UNIVERSITY OF SOUTHAMPTON

MEASUREMENTS AND PREDICTIONS OF WHEEL / RAIL VIBRATION USING A 1/5TH SCALE RIG

by

Tristan Daniel Armstrong

Thesis submitted for the degree of

Doctor of Philosophy

Institute of Sound and Vibration Research

Faculty of Engineering, Science and Mathematics

June 2004

Abstract

Rolling noise of railway vehicles is caused by the metal to metal contact of wheels on rails. This is a major source of noise from railway traffic. It is caused by variations in the geometrical profiles and the surface roughness of railway wheels and rails that initiate vibrations, which are then radiated as noise.

This thesis presents comparisons of measured and predicted (rolling noise) vibration where surface roughness and discontinuities are present on the railhead surface. This has been done with the help of extensive laboratory measurements made on a 1/5 scale wheel / rail rig.

The scale rig, which was donated by London Underground Ltd, has been modified to incorporate a new track bed that resembles a mainline concrete sleeper track. Rail lengths can be interchanged to allow measurements of vibration due to different railhead profiles.

Several practical methods have been devised. For example, a new method of the measurement of wheel and railhead surface profiles has been developed to improve the quality of these inputs to the prediction models. Another method is presented, for the situation of a surface roughness input, which determines the decay of vibration along the length of the track. This has been formed from measurements of rolling vibration by estimating the rail acceleration at the point of wheel / rail contact and comparing this with the average acceleration over a length of track. The estimate of rail acceleration at the point of contact has also been used to estimate the effect of wheel / rail contact patch filtering by comparing this (the acceleration at the point of contact) with a prediction of rail vibration.

The performance of two types of prediction models are considered: existing linear and non-linear wheel / rail contact models are investigated, adapted, and improved for application to the 1/5 scale rig. These existing prediction models have been investigated in the form of transfer functions (displacement divided by roughness) to demonstrate the effect of various contact stiffness values whilst the wheel remains in contact with the rail. It has been found that low contact stiffness attenuates the transfer function from the high frequencies. The transfer functions have also been expressed as poles and zeros and were found to remain stable for a wide range of contact force (or stiffness) values.

The outputs from the prediction models have been compared with measurements of rail vibration on the scale rig for surface roughness, step-joint, dipped rail, and simulated

wheel flat profiles. A method of splitting the input to the prediction models has been implemented to allow separate analysis of the surface roughness and discontinuity parts of the input. Good agreement is shown between the measurements and predictions for the majority of the railhead surface profiles considered.

The predicted contact force from the two types of prediction models have been compared with each other to show the amplitudes and frequencies at which differences in level between the non-linear and the linear predictions occur. Regions of non-linear contact behaviour are thereby identified.

Acknowledgements

Acknowledgements of the theses published in the ISVR library often demonstrate the author's gratitude towards the support given by their partners and spouses. This thesis is no exception. Without the help of my lovely, beautiful, wife Mara who gave the most support of all I do not think that I could have survived the tortuous process of completing a PhD.

Lots of other people helped me during my time at the ISVR, but none as much as my supervisor Professor David Thompson who has spent vast amounts of his busy time providing suggestions, encouragement, and help with my writing.

I would also like to thank John Edwards of Infraco BCV (ex-London Underground) for arranging a track walk in Brixton, and also to thank the ISVR technicians – past and present – for their help with the rig.

Finally, I am grateful to the EPSRC who provided the necessary funds for this research.

Contents

Abbreviations

AD	Anno Domini
ANSYS	A finite element software package
BEng	Bachelors of engineering
BILINEAR	s-plane to z-plane mapping routine in MATLAB software package
BT	Bandwidth time product
B&K	Brüel and Kjær
CF	Contact filter
CNC	Computer numeric control
DFT	Discrete Fourier transform
DPRS	Distributed point reacting spring
EPSRC	Engineering and physical sciences research council
FE	Finite element
FILTER	Difference equation filtering routine in MATLAB software package
FILTFILT	Difference equation filtering routine in MATLAB software package
FIR	Finite impulse response
FRF	Frequency response function
ICE	Inter city express
INVFREQS	Curve fitting routine in MATLAB software package
ISVR	Institute of sound and vibration research
LUL	London underground Ltd
LH	Left hand
LTSM	Linear time stepping model
LVDT	Linear variable differential transformer
MATLAB	A mathematical software package
MDOF	Multiple degree of freedom
MR	Measurement rail

MRS	Measurement rail sleeper spacing
MSc	Master of science
NLTSM	Non-linear time stepping model
ORE	Organisation for research and experiment
PSD	Power spectral density
PTFE	Polytetrafluoroethene
RH	Right hand
RMS	Root mean squared
RODEL	Rail on double elastic layer
S	Space or spacing between sleepers
SDOF	Single degree of freedom
SPL	Sound pressure level
SR	Surface roughness
TF2ZP	Transfer function conversion routine in MATLAB software package
TSM	Time stepping model
TWINS	Track-wheel interaction noise software
2DOF	Two degree of freedom

1 Introduction and literature review

1.1 Introduction

Evidence of the first railways originates from the 12th century AD where miners used trolleys and wooden tracks for the transportation of coal [Berghaus, 1964]. A boom period starting from the mid-nineteenth century with the introduction of iron rails and the steam locomotive saw railways in many different forms (for example, freight routes, light railways, trams, national networks, and links between continents) being built across the globe.

Shortly after the Second World War, closures and under-investment in railways were common in many first world countries as governments preferred development of road networks and air travel. However, railways now seem to be making a comeback. New high-speed rail links are competing with airlines, metro links are being improved and introduced, even trams have returned to some of our roads. The European Commission published a white paper in September 2001 making a high capacity rail crossing over the Pyrenees a priority, also including plans for a bridge or tunnel between Germany and Denmark, and a high speed route between Paris, Stuttgart, and Vienna [Railway Gazette International, October 2001].

Despite a recent widespread increase in the use of rail transport, which has arguably improved many people's lives, people's attitudes towards negative aspects of technology are becoming more intolerant. One such aspect is noise. Railway noise has been included in noise regulations in several countries [Thompson and Jones, 2000, and Jaecker-Cueppers, 2001].

Railway noise may be broadly categorised into three areas: motive power and ancillary noise, aerodynamic noise, and wheel / rail rolling noise. Rolling noise is of particular interest as it is the dominant source of railway operational noise for most speeds less than that at which aerodynamic noise exceeds that of all other sources. For example this 'critical' speed for the German Intercity Express (ICE) is 250 km/h [King, 1990]. Many trains, however, either never reach such speeds (as they were not designed to do so), or spend a large percentage of the time operating at speeds where rolling noise is dominant. Furthermore, it is highly probable that in built up areas where complaints about noise are most likely to originate, trains are less likely to be operating at very high

speeds. For this reason, the modelling of railway rolling noise has been an ongoing concern since the 1970's in order to devise means of reducing this type of noise.

Much work has been based on the, now well established, theory first proposed by [Remington, 1976] that vibrations of the wheel and rail are initiated from their point of contact due to irregularities or surface roughness. These vibrations induce noise radiation from the wheel and rail at frequencies in the range 100Hz to 5kHz [Thompson, 1996]. Measurements of rolling noise have demonstrated a difference of up to 10dB between rail vehicles with tread or disc brakes [Hemsworth, 1979]. In tread-braked vehicles brake blocks are applied to their wheel running surfaces, which roughen the wheel tyre. Disc-braked vehicles generally possess wheels with smoother running surfaces, as their braking force is applied to a separate surface (the disc), and they are therefore quieter in normal rolling. These measurements and findings helped to verify the theory that rough surfaces initiated wheel and rail vibration.

Fundamental studies of railway rolling noise are concerned, amongst other things, with the dynamic responses of wheels and rails [Thompson, 1990]. The work presented in this thesis is strictly concerned with the modelling and measurement of wheel and rail vibrations. Although only vibration data is presented the implications for noise levels could be inferred from the results. Methods of predicting noise from measured vibration data are typically in better agreement with measured noise levels, than for methods of predicting vibration from surface roughness measurements [Thompson, 1990]. Thus the need for development and improvements are greater for the prediction of vibration from surface roughness measurements, than modelling noise from measured vibration.

The improvements and developments in the methods of predicting vibration from surface profile data presented in this thesis have been made with the use of a 1/5 scale wheel / rail rig on which measurements of vibration have been made. Whilst this thesis includes work concerning the response of a wheel and a rail to surface roughness inputs, the primary motivation of this research is to make measurements and predictions of vibration due to particular surface profile discontinuities. The types of these discontinuities are discussed in section 1.6 below. A detailed description of the 1/5 scale rig used in this research is presented in Chapter 3.

This chapter gives an overview of the different types and methods of vibration prediction models used to date and provides the motivation for the research contained in

this thesis. Chapter 2 presents an introduction to the prediction models used throughout this thesis.

1.2 Prediction models

Many wheel / rail interaction models have been formulated to predict wheel and rail vibration. A primary categorisation of these models is their choice of fixed point of reference. Some models use the wheel as their fixed point and follow it along a continuous track, whilst the alternative approach regards wheels or vehicles passing over a finite (or infinite) section of track. Analysis of a system with a fixed point of reference at a wheel allows it to be simplified to a 'moving irregularity' model provided that the wheel speeds are much lower than that of the wave propagating along the rail [Grassie et al, 1982]. Rail wave speeds are typically in the order of hundreds of metres per second [Wu and Thompson 2000(a)], whilst typical train speeds are of the order of tens of metres per second. This means that a moving irregularity model is valid for modelling the majority of situations, provided that changes in track dynamic behaviour along the track can be neglected. These models consider a combined roughness of the wheel and rail as a relative displacement input, which is effectively 'pulled' between the representations of these two bodies. This is shown in Figure 1–1. Such an approximation can considerably simplify models, and is therefore the most commonly used.

The next categorisation (of existing models) is whether they are realised in the time or frequency domain. Frequency-domain models [for example Remington, 1987, and Thompson, 1993(a)] are necessarily linear models, which contain a linear approximation of the contact between wheel and rail. Wheel / rail contact, however, is a non-linear phenomenon (see section 1.4), and therefore the performance of the linear models is not reliable for every situation.

Time-domain models (for example [Newton and Clark, 1979, Clark et al, 1982, Nielsen, 1993, and Andersson and Dahlberg, 1998]) are able to account for non-linear behaviour but have been less widely favoured for noise prediction as they often involve long computation time, and their results are less easily interpreted.

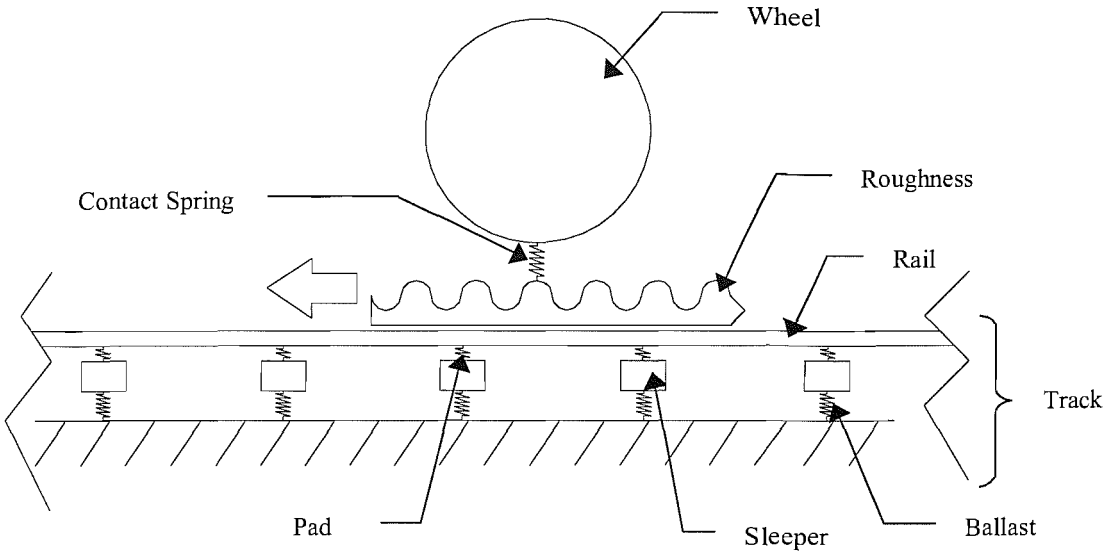

Figure 1–1 Schematic diagram of the relative displacement model.

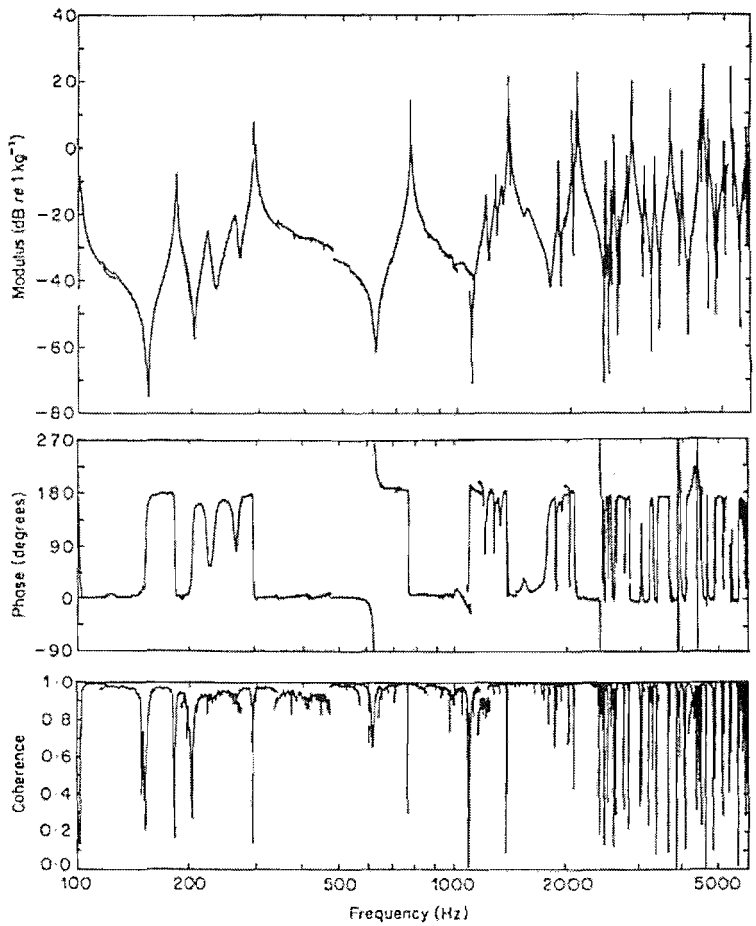

Figure 1–2 A point axial accelerance measurement of a Commonwealth railway wheel (extracted from [Thompson, 1993(b)]).

Historically the problem of rolling noise prediction has been divided into subsections. Broadly these are:

- Wheel and track dynamics
- Wheel / rail interaction
- Other effects at the wheel / rail contact

Each of these areas are considered in turn below, after which, specific situations of wheel and rail rolling noise are reviewed, followed by a discussion of previous research concerning scale models. This chapter is then concluded by a statement of the objectives of the present research.

1.3 Modelling the wheel and track dynamics

The two main components of a wheel / rail interaction model are of course the wheel and the rail. Examples of how these components have each been modelled and how they have been combined to form an interaction model, are presented next.

Generally speaking, simple approximations of the two main components result in a limited frequency range in which the model is applicable. Therefore, more complicated representations have been made to increase the performance of wheel / rail interaction models over larger frequency ranges. The features included in a particular model depend on the purpose for which it is intended.

1.3.1 The wheel

As a first approximation, a wheel can be simplified to just a mass which acts at the point of contact [Igeland, 1997 and Andersson and Dahlberg, 1998]. An extension of this model includes a spring and a damper attached in series [Wu and Thompson 2001(a)] that will give the first anti-resonance of vibration (typically at 500Hz for full size wheels). Other models have used discs [Ferguson, 1988] and rings [Remington, 1987] to represent the wheel. Multibody models have also been used to describe vehicle dynamics. For example [Jenkins et al, 1974] used a mass to represent a wheel, together with a bogie and body represented by masses and connected by suspension stiffnesses. However, for audio frequencies the suspension spring effectively isolates the wheel from the bogie.

More detailed analysis can be made by using finite element models to predict a wheel's many lightly damped resonances [Remington, 1988], examples of which can be seen in

Figure 1–2. This shows a measurement of a point accelerance of the wheel, which is a ratio of the measured acceleration to the measured input force as a function of frequency at a point of contact on the wheel tread. It is possible with finite element analysis to take advantage of a wheel's axisymmetric structure (see Figure 1–3), which can simplify and reduce the numerical calculations required (for example [Thompson, 1993(b)]). Natural frequencies, mode shapes, and modal masses are obtained using finite element models and used to form an estimation of the wheel frequency response functions (FRF) by a modal summation [Thompson, 1993(b), and Jones and Thompson, 2000]. Damping values used in the FRF calculation are typically obtained from measured data.

Adjustments for the dynamic effects of a rolling wheel have been presented and verified by [Thompson, 1993(c)], improving the predicted response of the web (a major contributor of wheel noise radiation) and the lateral response of the tyre. Models of single wheels have also been extended to include the effects of axles [Thompson et al, 1996], adjacent wheels [Wu and Thompson, 2001(a)], and even complete trains (for example [Andersson and Dahlberg, 1998]).

1.3.2 The rail and its support structure

In conventional track, rails are supported on sleepers in ballast. If the sleepers are made from concrete, a visco-elastic pad is fitted between the rail and the sleeper to help prevent the sleeper from cracking (see Figure 1–1 for a schematic of this configuration). Clips are used to hold the rail in place.

A very simple model of a rail could be a mass on a spring. Here the mass would represent the rail, with the low frequency response of the model dominated by the stiffness that would represent the ballast. Better models of rail response, however, represent the rail as a beam to allow for wave propagation along the track. Various types and combinations of beams have been used, for example:

- Euler beams [Remington, 1987]
- Timoshenko beams i.e. including shear deformation and rotational inertia [Grassie et al, 1982]
- A combination of two Timoshenko beams for high frequency vertical vibration analysis [Wu and Thompson, 1999(a)]

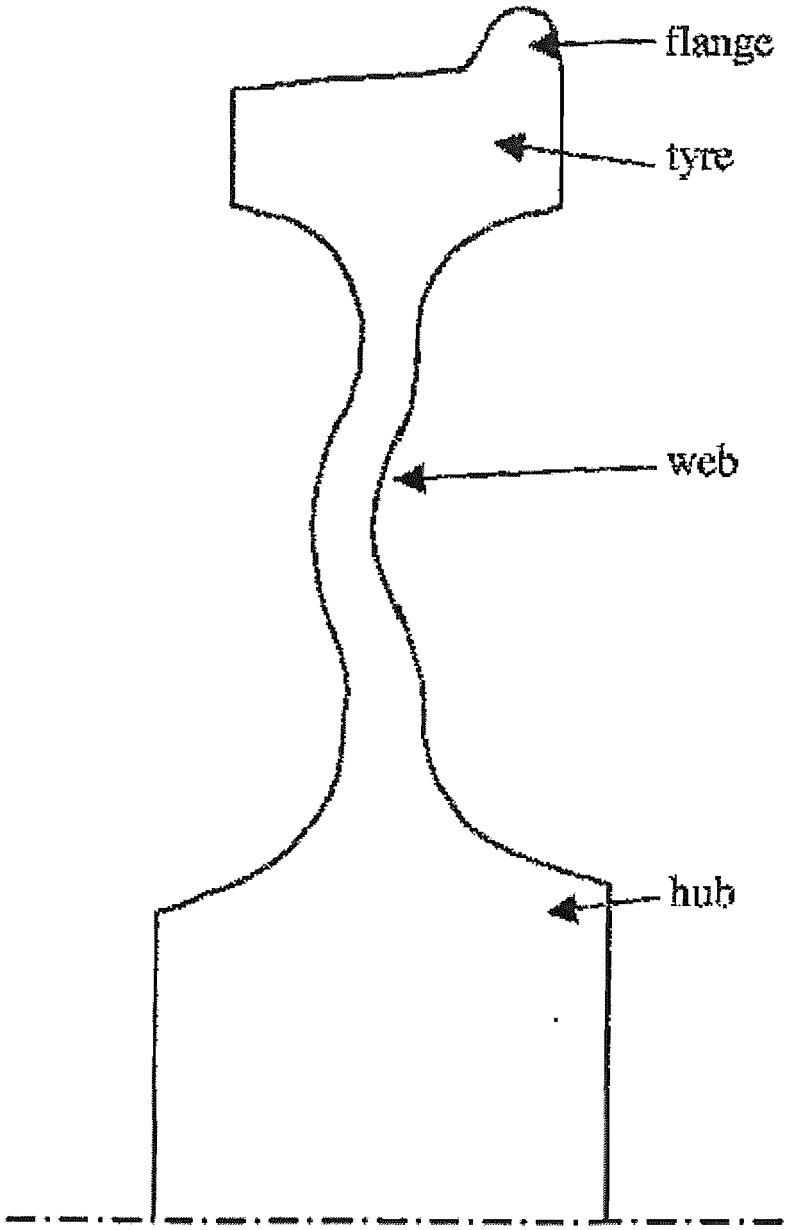

Figure 1–3 An example of a wheel cross-section: a UIC 920mm freight wheel (only a half of the wheel is shown) reproduced from [Thompson and Jones, 2002].

Euler beams have been found to be suitable as a first approximation of rail behaviour, but as Timoshenko beams include shear deformation and rotational inertia they are considered to be a more appropriate model in the range above 500Hz [Grassie et al, 1982]. More complicated models are needed, however, to analyse higher frequencies, as well as lateral vibration. The study of lateral rail vibration requires analysis of the cross-sectional deformation of the rail; more specifically the bending, torsion and relative motions of the railhead, rail foot, and web [Wu and Thompson, 1999(b)]. Finite element models have been used for this purpose [Thompson 1993(d), Knothe et al, 1994, and Thompson 1997] as well as multiple beam analytical models [Wu and Thompson, 1999(a and b)].

Use of finite element models to predict rail vibration, can be categorised into three methods that have been used to obtain the desired infinite behaviour (free from reflections in the longitudinal direction) found on most modern continuously welded rails. The first of these methods (described by [Thompson, 1997]) is to apply symmetric and/or antisymmetric boundary conditions to the finite ends of a length of modelled rail. This allows the free wave behaviour to be determined, but not the forced response. The second method is to use periodic structure theory to consider a length of rail modelled as a periodic structure of arbitrary period [Thompson 1993(d)]. The third method is to model the cross-section of the rail in two dimensions, rather than in three, and introduce a wave propagation factor along the length of the rail [Gavric 1995].

Finite element models tend to be complicated and need to be implemented numerically, which normally takes a lot of computational time and effort. Furthermore when the rail supports are considered in addition to the rail, it becomes harder to model dynamic situations of wheels rolling on the rail. Analytical models have proved themselves to be more versatile [Wu and Thompson, 1999(a and b)].

Apart from the rail, the track has also been modelled in many ways. These can be roughly grouped into two categories: continuous and discrete. Continuous support models ignore the discrete nature of real track supports by merging the effects of the ballast, sleeper, and rail pad into equivalent continuous layers along the track. A single continuous layer model of this nature was used to estimate wooden sleeper track behaviour [Grassie et al, 1982]. Double layered continuous support models are more common as they represent more realistically the majority of modern high-speed track.

The pad, is introduced as a spring, the sleeper as a mass, and the ballast as a second spring.

Discrete support models can allow for the periodic nature of the support. This introduces a pinned-pinned resonance formed by a standing wave between the sleepers, with its nodes at the supports [Grassie et al, 1982, and Thompson and Vincent, 1995]. Investigations into the discrete nature of railway track supports have been made using these models. For example the effect of varying sleeper spacing [Heckl, 1995, Wu and Thompson, 2000(b), and de France, 1998], and the effects of localised pre-loading of the pads and ballast as wheels pass over sleepers [Wu and Thompson, 1999(c) and 2001(a)].

The performance of this type of model has been shown to be realistic for most situations. The stiffness of the pad and ballast, however, are non-linear and load dependent. [Wu and Thompson, 1999 (c)] present analysis of this non-linear behaviour by modelling the track behaviour for different wheel loads. They found that the wheel pre-load has a strong effect on the behaviour of the track close to the point of loading, but it has a limited effect on the average behaviour of the track support. This type of non-linearity is not considered in the models used in this thesis.

Finally, models of different forms of track support have also been derived for specific cases such as bridges [Janssens and Thompson, 1996, and Walker et al, 1996], elevated railway lines [Crockett and Pyke, 2000], and underground railways (metro lines) [Nelson, 1996]. Whilst these models have considered the track and its support, they are more concerned with vibration transmission into the supporting structure or ground, which is not pertinent to this research.

1.4 Modelling the interaction between wheels and rails

Descriptions of models for wheels and rails have been given thus far but no mention has been made of how they interact. A wheel / rail interaction model can be considered to consist of three parts, namely, the wheel, the rail, and the contact (spring) as shown in Figure 1–1.

Hertz calculated the contact area between two spherical bodies in 1882 [Johnson, 1985]. This theory has been implemented to estimate the effects of local deformation of wheel and rail, and to formulate what is known as the contact spring. The contact spring, however, is non-linear ($F \approx kx^{1.5}$, where F is force, k is the spring constant, and x is

deflection). This is due to the contact geometry and the localised deformation, and the contact spring has to be linearised around a specific wheel load for use in the more common (linear) frequency-domain models. Investigations into the effect of this approximation for typical wheel loads and roughness amplitudes have shown that non-linear effects under normal circumstances are small [Wu and Thompson 2000(a)]. So the use of a linearised contact spring is adequate for most situations. However, for the cases of extreme surface roughness, rail corrugation, wheel flats, and rail joints (or any other discontinuity)[1] a non-linear relationship is required to describe fully the unloading between wheel and rail due to these surface profiles.

Whilst the wheel and rail remain in contact, the Hertzian relationship described above is valid. Despite large changes in contact deflection, a linearised estimation of the Hertzian contact stiffness could still be used in a prediction, although a non-linear relationship would be more accurate. A non-linear model is, however, essential if the wheel and rail are expected to lose contact. Specific relationships of the wheel and rail contact are presented in Chapter 2 where the non-linear models used in this research are introduced.

1.5 Roughness and the wheel / rail contact zone

As the models presented thus far are all based on the theory that roughness of the running surfaces generates vibration, measurements of surface profiles are a crucial part of the prediction of wheel and rail vibration. This, however, is not a trivial task.

Typical roughness values for full-scale track have amplitudes from below 1μm to 50μm depending on the wavelength [Thompson and Jones, 2000]. The wavelength is a longitudinal quantity that is used to help define the vertical sinusoidal content of the roughness amplitudes. A Fourier Transform of the roughness amplitudes, could for example, be presented as a function of wavelength (or distance along a surface) or as a function of time (for a speed at which the distance is traversed). As surface roughness wavelengths of relevance to noise are in the range 5mm to 200mm [Dings and Dittrich, 1996, Thompson et al, 1996], this means that a roughness measurement must measure small amplitudes across a wide range of wavelengths.

[1] See section 1.6 for a discussion of these types of surface profiles.

The frequency (f) of excitation induced by surface roughness of wavelength (λ) at the speed of a passing train (V) is:

$$f = V/\lambda \tag{1-1}$$

Particular roughness wavelengths will therefore produce different excitation frequencies at different train speeds. For example, a given wavelength will produce a doubling of excitation frequency with a corresponding doubling of train speed. A detailed description of the roughness measurement method (and subsequent processing) used during this research is presented in Chapter 4. However, an introductory review of surface profile measurement techniques is presented here.

Surface geometry measurements are typically made with displacement transducers, although some accelerometer-based methods have been developed (for example [Galaitsis and Bender, 1976, and Grassie et al, 1999]). [Thompson, 1996 and ORE report C163/RP9, 1988] compares surface profile measurement data from several different accelerometer and displacement transducer based methods. Results from five methods were reported in [Thompson 1996]. One method was based on an accelerometer mounted on a trolley system, two other methods involved displacement transducers mounted on trolleys, and the last two methods used displacement transducers coupled to beams. Accelerometer systems were found to require relatively high speeds of profile measurement (about 1m/s in this case) as they are sensitive to noise at low frequencies (and therefore low measurement speeds). Conversely, displacement transducers were found to be sensitive to noise at high frequencies and therefore require very slow surface profile measurements. Displacement transducers were thought to be preferable to accelerometers, for the measurement of surface profiles, as they were less likely to lose contact with the surface geometry during their slow measurement process.

Surface profile measurement techniques using accelerometers combined with a trolley arrangement allow long distances of a surface profile to be measured [Grassie et al, 1999]. As accelerometers use an inertial reference point, the combination of this transducer type with a trolley has good potential for measuring long wavelengths. However, in order to do this, an accelerometer that is sensitive at very low frequencies is necessary.

A displacement transducer measures the position of its probe relative to that of some reference point. Therefore, for a measurement along a length of track, a reference 'beam' is often used, combined with a sliding arrangement that allows the displacement transducer probe to follow the railhead [Grassie et al, 1999]. Any undulations of the beam and sliding arrangement are measured by passing the transducer probe over a calibrated 'smooth' surface. In this way any movement of the reference point can be estimated and removed from the measurement of railhead geometry. An example of this system that is available commercially is the Muller BBM RM1200E [Holm, 1999]. This uses a combination of a precision sliding guide rail assembly coupled with a measurement probe that is linked to a displacement transducer. Calibration of the sliding arrangement is performed by comparison with the surface of a high quality polishing stone. This system can measure lengths of track of up to 1.2m.

The five methods discussed above [Thompson, 1996], gave similar results for measurements of corrugation where a dominant frequency was present. However, they did not give such good agreement for smoother surface profiles. This suggests that it is easier to measure a discontinuity or a surface with a dominant narrow band frequency content, than it is to measure smoother surface profiles where their frequency content has a broader band content.

Each measurement of vertical amplitude (for any method of measurement) needs to be made at known distances (x) along the length of the track. This can be done by measuring at fixed time intervals (t) at a constant speed (v) (i.e. using $x = vt$) or alternatively directly measuring the probe position (x) corresponding with each measurement of vertical amplitude. Several two-dimensional surface measurements can be made along parallel lines so that analysis of the true three-dimensional input can be performed [Remington and Webb, 1996]. Measurements of both the wheel and the rail surface need to be made and then combined to form the input to the model. This can be done by a summation in the time domain, spatial domain, or frequency domain.

The length of the contact area between a wheel and rail is also known to affect the dynamic response to a roughness input. At high frequencies, the wavelengths are short compared with the length of the contact patch which has the effect that their effective amplitudes are attenuated due to averaging over the length of the contact patch[2]. This

[2] Contact patches are typically 10mm to 15mm long at full scale [Thompson and Jones 2000].

attenuating effect has resulted in the term 'contact filter' [Remington, 1987]. An analytical model of the contact filter was first produced by [Remington, 1976], whilst a numerical contact filter model has more recently been developed which includes the effect of many parallel roughness measurements along the surfaces of both the wheel and the rail [Remington and Webb, 1996]. These two approaches are compared in [Thompson, 2003] and shown to be in good agreement for wavelengths larger than 7mm.

The assumption of an elliptical contact patch (which follows where surfaces are assumed to have fixed radii of curvature) has been found to be incorrect for many cases of wheel / rail contact, particularly for worn profiles [Poole, 1986]. Many methods of measuring contact patches (a large majority of which still assume elliptical contact) are documented in [Poole, 1986]. More importantly, it includes a novel method of measuring the contact patch dynamically for a full-sized wheel with the use of compressed air and a perforated rail. Although this method is restricted to a low running speed of 0.035m/s (0.126km/h) and it is constrained to a specific measurement location, it does demonstrate that an elliptical contact patch is unlikely in the majority of cases. Unfortunately, as there is no other known method of making dynamic measurements of contact patches and including their effects in wheel/ rail interaction models, the elliptical contact patch based on Hertz theory is still used widely.

Contact (rather than dynamic) effects between a rolling wheel and the rail, such as small relative tangential motions called creepage, occurring in longitudinal, lateral and spin directions, have been investigated and summarised by [Kalker, 1979]. The transverse behaviour of wheel / rail contact, specifically slip, creepage and adhesion, are not, however, primary concerns of this research.

1.6 Situations represented using wheel / rail interaction models

Thus far, a broad outline of the different types of wheel / rail interaction model has been given. In this section a discussion is given concerning the situations for which predictions are required. Typical areas of research related to railway noise have been:

1. Noise due to wheel and rail roughness on continuously welded track

   Analysis of this case has been extensively researched resulting in various models, most of which are linear frequency-domain models. These are widely used, for

example the TWINS (Track-Wheel Interaction Noise Software) package [Thompson et al, 1996]. In [Wu and Thompson 2000(a)] the influence of non-linearities is investigated and shown to be small for typical roughness amplitudes and wheel loads.

2. Rolling noise on jointed track

   Jointed track is commonly found on many rail systems. It is the traditional form of track construction where rails are held together with fishplate assemblies. Jointed track produces more noise than continuously welded track. Until recently, little research has been made in this area. However, simple theoretical models of the expected sound pressure level (SPL) of a wheel passing over several discontinuities (step-up, step-down and level joints) have been compared with both scale model and full size measurements [Ver et al, 1976]. This research showed that a step-up joint produced a peak SPL that increased monotonically with increasing wheel velocity. The peak SPL of a wheel rolling over a step-down joint, however, was found to increase only up to a certain velocity and to remain constant beyond this. Increases in axle load were found not to influence the step-up case, but did raise the SPL for the step-down joint. A drop test, where the wheel of one side of an axle is dropped from a known height onto the rail, was also successfully introduced as a means of estimating a step-down joint peak SPL.

   Additional theoretical analysis for the case of step-up and step-down joints has been undertaken as part of the EPSRC research project that funded this thesis [Wu and Thompson, 2001(b)]. This is discussed in more detail in Chapter 2, but basically involved forming a time domain wheel / rail interaction model from which an equivalent roughness spectrum is deduced that can then be used with the TWINS package to predict noise. The geometry of the rail joint, train speed, and static wheel load were found to influence the results.

3. Response due to dipped weld joints

   The modern alternative to jointed track is to omit the fishplate assemblies as a method of joining track and to weld rail lengths together instead. The method of continuously welding railway track has primarily been introduced to high speed lines to reduce maintenance of both wheels and rails, but has the added advantage of being much quieter than jointed track. The process of manufacturing rails, however,

often results in a downwards curvature of the rail ends (in the vertical plane). When welded together, this forms a dip over a length of about one metre.

[Jenkins et al, 1974] made a series of comprehensive measurements and predictions of wheel / rail interaction due to the dipped joint geometry. This research was largely motivated to try to predict the forces at the connecting bolt holes in order to try to prevent the structural failure of the joint. [Wu and Thompson, 2001(b)] studied the effect of a dipped joint in conjunction with a step in the centre of the dip for the case of a jointed track. The geometric profiles of the joints in this case were approximated from analytical relationships. This is described in detail in Chapter 2.

4. Response due to turnouts (points) and crossings

   Turnouts and crossings are parts of the track that allow trains to move from (or across) one piece of track to another. At a turnout a wheel has to transfer from one rail to another. A model of a turnout, and its response to a train passing straight through at a constant speed, has been made with a finite element model [Andersson and Dahlberg, 1998]. Their theoretical analysis has shown that under a smooth transition, with the wheel running over three sections of the turnout (switch rail to wing rail to the turnout nose), an increase of 30 to 50% in the contact forces can be expected compared with normal tangent track. However, with an irregularity between only two of the sections of the turnout (switch rail and wing rail) the contact force increases significantly. A doubling of the contact force was found at only 70km/h. Their model assumes that the turnout joint is similar to a dipped weld joint in one rail, thus they are actually analysing a mixture of situations. Unfortunately this means that specific turnout geometry has been replaced by an approximation.

5. The influence of wheel flats

   Wheel flats are an unwanted product of severe or defective braking, or lack of adhesion at the railhead. If a wheel stops turning on a moving train, the resulting sliding action wears the wheel running surface to a flat. A typical wheel flat is around 50mm long, but may extend to over 100mm long [Wu and Thompson, 2002]. The impacting response of a wheel flat can cause damage to the vehicle, wheel, and the track, but it also noticeably increases noise levels.

A novel method of measuring the response to wheel flats was performed by grinding the inverse profile of a flat into a railhead and then measuring the response as a train passed [Newton and Clark, 1979]. By fixing the wheel flat position in the railhead, measurement equipment could be placed at optimal positions, which is hard to do for the case of a flat on a wheel. An extensive set of measurements were made comprising sixty-four strain and force measurements for train speeds of up to 117km/h. These were then compared with predictions from four models of track behaviour. At low speeds the measurements compared well with beam on elastic foundation models, although at high speeds (above 70km/h) the predictions were too high. From these results it was recommended that discretely supported track models should be used for predictions of contact forces at high speeds, and Timoshenko beams to predict shear and bending strains of the rail. Additional analysis was made of paint removal from the railhead due to passing trains. It was found that at low speeds (approximately 40 km/h) the wheels remained in contact with the rail as they travelled through the simulated wheel flat. At 79 km/h slight loss of contact with the rail occurred, whilst at 117 km/h complete loss of contact occurred followed by an elliptical contact mark just before normal running was resumed.

Measurements of the impacts of wheel flats and rail joints have shown that two peaks occur in the force time history [Jenkins et al, 1974]. These findings were verified by [Nielsen and Igeland, 1995] with the use of a non-linear time-domain model in which the track was represented by a modal solution from a finite element model. At speeds where there is loss of contact between the wheel flat and the rail, the wheel falls as the rail rises until contact is resumed. When the wheel and rail meet, a high frequency dominated impact termed the P1 force results. The frequency content associated with the time between the start of the P1 force pulse and the maximum force corresponds approximately to the resonance frequency of the vehicle's unsprung mass and the track mass connected by the Hertzian stiffness [Jenkins et al, 1974]. A second (P2) peak in the force time history is due to the low frequency resonance of the bogie on the track stiffness [Nielsen and Igeland, 1995].

A non-linear, time-domain, theoretical model of the effect of wheel flats including the consequent noise radiation has been made as part of this research contract [Wu and Thompson, 2002] and will be discussed further in Chapter 2.

6. The formation of rail corrugation

Rail corrugation is a periodic or near-periodic wear pattern on the railhead. Its formation leads to an increase in rolling noise but it is not always clear why it occurs. In an attempt to improve understanding, corrugations have been categorised by their damage mechanisms and their wavelengths [Grassie and Kalousek, 1993], but no definite explanation has been presented to date. Work in recent years has concentrated on short wave 'roaring rail' corrugations formed on straight high-speed passenger and / or mixed traffic railways.

As there is no clear explanation of such rail corrugation, many models have been developed that attempt to show how the corrugations are formed (see for example [Frederick, 1986, Ripke and Hempelmann, 1994, and Igeland, 1997]). Another example is presented by [Clark et al, 1988] who give an interesting explanation, based on slip–stick vibrations due to lateral creep by poorly aligned vehicle axles. [Igeland, 1997], on the other hand, attributes corrugation to longitudinal creepage of wheels under traction or braking. Generally speaking contact patch mechanics and Hertzian stiffness are assumed to be mechanisms associated with corrugation wavelengths, but [Ripke and Hempelmann, 1994] present a model which links structural dynamics to a wear process. Thus there are varied explanations of this phenomenon.

A study of the response to a corrugated rail had previously been performed at 1/8 scale on the same wheel / rail rig used in the present research [ORE report C163/RP11, 1988]. Unfortunately the resources required to repeat the manufacturing process of such a corrugated rail were not available for the research presented in this thesis. A study of corrugation growth, on the other hand, would require prolonged running of the wheel / rail test rig and might not actually occur in practice. Therefore, due to manufacturing and resource restrictions vibration due to corrugations has not been considered in this thesis.

7. Curve squeal

In tight curves the coning of the wheels that are fixed to a rigid axle, is insufficient for the curve they are negotiating. Individual wheels are then subject to a 'wheel crabbing' motion, the unstable friction from which drives the bending oscillations of the wheel which radiate a squeal noise [Heckl, 1998, and de Beer et al, 2000].

Investigations of curve squeal are not included in this research, but are intended for future work using the 1/5 scale rig (described in Chapter 3) that has been used for this research.

Although non-linearities exist in situation 1, these effects are small for the cases of typical (rail vehicle) wheel loading and may be modelled effectively by a linear representation [Wu and Thompson 2000(a)]. However, situations 2 to 7 listed above require models that allow for significant non-linear behaviour. As seen above, this means that a time-domain approach has to be considered. The research presented in this thesis investigates the subjects listed as items 1, 2, 3, and 5 above. Items 6 and 7 are beyond the scope of this thesis.

1.7 The use of scale models

The majority of this thesis is concerned with the measurements and predictions of vibration using a 1/5 scale wheel / rail rig. Therefore a brief review of the use of scale models is given here.

Although fluid dynamicists have used scale models for many years, since the development of the concepts of dimensional analysis and factors such as Reynold's number (see for example [Anderson, 1991]), the use of scale models in structural dynamics is very much less widespread. The work of this thesis is based on scaling by dimension, as was the work presented by [Ver et al, 1976]. If all dimensions are reduced by a scale factor, the dynamic behaviour remains the same but corresponding frequencies are increased by the scale factor. Derivation of the scaling used in this research is presented in Chapter 3.

[Ver et al, 1976] used a 1/8 scale model track and a three axle bogie assembly to measure peak sound pressure levels of impact noise for step-up and step-down joints. Their measurements confirmed their theoretical findings as described above (see section 1.6, item 2). All the measurements made on their scale rig were made in terms of peak sound pressure level as a function of wheel speed. This type of research, however, is very rare, although measurements of the effectiveness of shielding fitted to trains to reduce rolling noise has been presented by [Geerlings et al, 2001]. Here scale models were used to assess sound radiation from a static wheel.

London Underground Limited (LUL) performed extensive tests on a 1/8 scale single wheel and track model [ORE report C163/RP11, 1988 and ORE report C163/RP16, 1990] to try to ascertain whether a scale model could be used to represent rolling noise, and to investigate the influence of roughness on the wheel and rail vibration. Unfortunately, whilst several ingenious ways of manufacturing rough rail surfaces were used, their measurements appeared to be strongly influenced by an unknown non-linear behaviour. The rig described in Chapter 3 is a development of the LUL rig, but in a 1/5 scale form.

Scale models have also been used to study the effects of dynamic stability of railway vehicles for example [Iwnicki and Wickens, 1998] and [Jaschinski et al 1999] where both full scale and smaller scale roller rigs are considered.

1.8 Objectives of the EPSRC project and the work for this thesis

This thesis has been carried out within the framework of an EPSRC project [Thompson, 1999]. The main objectives of the project were:

1. To improve the accuracy and scope of wheel / rail noise prediction models by including the influence of non-linearities at the wheel / rail interface. This was done by producing a time-domain model of wheel / rail interaction valid at high frequencies.
2. To utilise this improved interaction model to extend the capabilities of prediction models for rolling noise, which apply on relatively smooth track, to enable them to deal with the noise from severe track discontinuities including impact noise at rail joints, points and crossings, dipped welds and other discontinuities in the rail running surface.
3. To verify the non-linear model with a laboratory test facility consisting of a scale model wheel running on a circular track.

The research presented in this thesis was mainly concerned with these objectives, but a greater degree of flexibility was permitted. The objectives of this thesis are defined as:

a. To commission the 1/5 scale wheel / rail rig that was donated by London Underground Ltd. This was to involve the design and construction of a new track bed.

b. Design and manufacture rails for the rig, some of which need to have smooth running surfaces, and others that need to have particular surface profiles that represent the discontinuities listed above in items 2,3, and 5 of section 1.6.

c. Formulate a method of measuring the surface profiles of the rig wheel and the rig rail.

d. Measure wheel and rail vibration on the 1/5 scale rig due to different railhead surface profiles which are expected to produce both linear and non-linear behaviour of wheel and rail contact.

e. Verify the performance of existing prediction models with measurements of the scale rig for the situations listed above in items 1,2,3, and 5 of section 1.6.

f. To make any necessary improvements to the models so that they are in better agreement with the measurements.

g. Investigate the non-linear contact spring behaviour by comparing the predicted linear contact force with the predicted non-linear contact force.

The prediction models that were used in this research are introduced in Chapter 2 where models that represent the contact between the wheel and the rail use linear and non-linear relationships. The model rig that was used to confirm the behaviour of the prediction models is described in Chapter 3. Chapter 4 introduces the measurement and processing of surface roughness and railhead discontinuities. Experiments on a relatively smooth rail are described in Chapter 5 and Chapter 6. Chapters 7 to 10 are concerned with discontinuities on the railhead, namely: step rail joints, dip rail joints, and wheel flats. A discussion and conclusions are presented in Chapter 11.

2 Wheel / rail interaction models

As described in Chapter 1, wheel / rail interaction can be modelled in the frequency domain or in the time domain. A frequency-domain model is inherently linear, whereas a time-domain model can allow for non-linear behaviour. Both of these model types have been used during this research. This chapter introduces a linear frequency-domain model that has been used to predict the behaviour of the 1/5 scale rig (described in Chapter 3), due to a surface roughness input. It also introduces a non-linear time-domain model that was used to predict vibration due to different railhead surface profiles.

All of the models described below concern only vertical vibration, and are of the moving irregularity type (i.e. are only relevant for train speeds much lower than the propagating wave speed in the track).

2.1 The linear, frequency-domain model

The linear, frequency-domain model used throughout this thesis is based upon the theory, proposed by [Remington, 1976], that surface roughness of the wheel and rail induces a relative movement between the two, which initiates vibrations. It is assumed in the model that local deformation of the wheel and rail can be considered as a linear (contact) spring. The frequency response functions of each component of the model (the rail, wheel, and contact spring) can be joined to predict the vertical response of either the wheel or rail at the point of contact, at a given frequency. This model is described by the following equations. (In this form, these equations are attributed to [Grassie et al, 1982], and developed by [Thompson et al, 1996]).

$$U_r = \frac{\alpha_r R}{\alpha_r + \alpha_c + \alpha_w} \tag{2-1}$$

$$U_w = \frac{-\alpha_w R}{\alpha_r + \alpha_c + \alpha_w} \tag{2-2}$$

where:
- α_r is the frequency response function of the rail,
- U_r is the displacement amplitude of the rail (as a function of frequency),
- α_w is the frequency response function of the wheel,
- U_w is the displacement amplitude of the wheel (as a function of frequency),

α_c is the frequency response function of the contact spring,

R is the roughness amplitude (as a function of frequency).

The frequency response functions in equations (2-1) and (2-2) are presented as receptances, the displacement response due to a unit force. The derivation of these equations is given in Appendix A. Either measurements or predictions of the frequency response functions can be used in these equations. Other transfer functions could equally be utilised, for example, accelerance or mobility (ratios of acceleration to force, and velocity to force respectively) provided that the same transfer functions are used throughout. This is possible because the ratios U_r/R and U_w/R are non-dimensional (as the output displacement of the rail and the wheel have the same units as the roughness input), so any factor of angular frequency implied by the use of different types of transfer functions (other than receptance) is cancelled out.

Manipulation of equation (2-1) and equation (2-2) can reveal several important relationships that help to explain wheel and rail interaction. For example when the modulus of the rail receptance is dominant, i.e. $|\alpha_r| >> |\alpha_c + \alpha_w|$:

$$\frac{U_r}{R} = \frac{\alpha_r}{\alpha_r + \alpha_c + \alpha_w} \approx 1 \qquad \text{thus} \quad U_r \approx R \qquad (2\text{-}3a)$$

This means that if the rail receptance is the greatest of the three receptances at a particular frequency, the rail displacement is comparable with the roughness, and thus the rail moves more than the contact spring or the wheel. Similarly the wheel displacement (equation (2-2)) becomes:

$$\left|\frac{U_w}{R}\right| \approx \left|\frac{\alpha_w}{\alpha_r}\right| << 1 \qquad (2\text{-}3b)$$

Thus it is demonstrated that a larger rail receptance will make the system transfer function U_w/R tend towards zero, so the predicted wheel displacement will be smaller.

When the wheel receptance dominates the system transfer function U_w/R, i.e. $|\alpha_w| >> |\alpha_c + \alpha_r|$, equation (2-2) yields a similar relationship to that shown above:

$$\frac{U_w}{R} = \frac{-\alpha_w}{\alpha_w + \alpha_c + \alpha_r} \approx -1 \qquad \text{thus} \quad |U_w| \approx |R| \qquad (2\text{-}3c)$$

This means that if the wheel receptance is largest at a particular frequency the wheel displacement has approximately the same magnitude as the surface roughness, and the movement of the rail and the contact spring will be small in comparison.

Furthermore, when the contact spring receptance dominates the wheel /rail interaction models, i.e. $|\alpha_c| >> |\alpha_r + \alpha_w|$:

$$|U_r|, |U_w| < |R| \tag{2-3d}$$

Therefore the motion of the contact spring exceeds that of the wheel and the rail. This analysis shows that when the receptance of a part of the model exceeds that of the other parts the motion of that part will exceed that of the others. Further analysis of these relationships is presented for the parts of the 1/5 wheel / rail rig in Chapter 5.

A final comment regarding equations (2-1) and (2-2) is that the vibration amplitude of either the wheel or the rail appears to be limited by the roughness (R). In fact if α_w is mass-like and α_c is a receptance of a stiffness, the denominator can be less than α_w, and U_w can exceed R; similarly for U_r. This occurs at frequencies where system transfer functions U_r/R and U_w/R are greater than unity, and therefore magnify the roughness or input to the model. Further consideration of the behaviour of these prediction models (in the form of their system transfer functions) is presented in Chapter 5.

Equation (2-1) gives the vibration of the rail at the wheel / rail contact point. Of more interest, in practice, is the average vibration of the rail as the wheel approaches and then passes a point on the rail. This is easier to measure. It is given by [Thompson and Janssens, 1997] under the assumption of a single decaying wave as:

$$\overline{U_r^2} = \frac{1}{L}\int_{-L/2}^{L/2} |U_r(0)|^2 e^{-2\beta|x|} dx = U_r(0)^2 \frac{\left(1-e^{-\beta L}\right)}{\beta L} \approx \frac{U_r(0)^2}{\beta L} \tag{2-4}$$

where: U_r is the displacement of the rail (as a function of frequency and position x),

β is the real part of the propagation constant (decaying part of wave number),

$U_r(0)$ is the displacement of the rail at the contact point (as a function of frequency) see equation (2-1),

L is the length of the measurement along the track.

Consideration of equation (2-4) shows that $\overline{U_r^2} < |U_r(0)|^2$ depending on β and L. So for a given decay characteristic β an increase in measurement length L will result in a lower average. The relationship presented in equation (2-4) provides a method of predicting the average rail vibration at a point on the rail during passage of the wheel from the prediction of rail vibration at the point of wheel / rail contact (see equation (2-1)). This is an important situation, as in practice, it is the only realistic method of measuring rail vibration.

Comparisons of this linear model with measurements from the rig are presented and discussed in Chapter 6.

2.2 The non-linear time-domain model

The complicated response of the track is commonly modelled analytically (see Chapter 1). This has advantages for a frequency-domain realisation, but these types of model are difficult to use for time-domain calculations. The time-domain model conceived by [Wu and Thompson, 2000(a)] approximates the response of an analytical model in a form that is easily utilised by a time stepping routine.

[Wu and Thompson 2000(a), 2001(b) and 2002] have presented three slightly different non-linear models for the cases of non-linear interaction due to surface roughness, the dynamic interaction due to wheel flats, and impacts of wheels passing over rail joints. Each of these time-domain models is essentially the same but in slightly different configurations to suit the situation that is being modelled. Essentially, the model is based on an elegant state-space representation of the track that simplifies the frequency response function of an infinite track, and considers the wheel as a point mass and a spring.

In [Wu and Thompson 2000(a)] an appropriate representation of the track response was obtained by constructing a multiple degree of freedom (MDOF) system that closely resembles the frequency response of a double elastic layered continuously supported Timoshenko beam model. This was obtained by utilisation of a MATLAB routine, which constructs an s-plane model from a frequency response curve, using a least-squares curve fitting technique. A transfer function is obtained in the form:

$$H(s) = \frac{B(s)}{A(s)} = \frac{b_1 s^m + b_2 s^{m-1} + \cdots + b_{m-1}}{s^n + a_1 s^{n-1} + \cdots + a_n} \tag{2-5}$$

The result is governed by the frequency range considered (in [Wu and Thompson, 2000(a)] 50Hz to 5000Hz) and the choice of the order of the polynomials A and B representing the transfer function, i.e. the number of poles and zeros. Higher polynomial orders were not found to behave better than m=3 for the zeros (shown in the numerator of equation (2-5)), and n=4 for the poles (shown in the denominator).

The s-plane model was then expressed in a time-domain state-space representation (via an equivalent differential equation), which would allow interaction with the wheel (here represented as a mass) and contact spring.

$$\begin{bmatrix} \dot{x}_1 \\ \dot{x}_2 \\ \dot{x}_3 \\ \dot{x}_4 \end{bmatrix} = \begin{bmatrix} -a_1 & 1 & 0 & 0 \\ -a_2 & 0 & 1 & 0 \\ -a_3 & 0 & 0 & 1 \\ -a_4 & 0 & 0 & 0 \end{bmatrix} \begin{bmatrix} x_1 \\ x_2 \\ x_3 \\ x_4 \end{bmatrix} + \begin{bmatrix} b_1 \\ b_2 \\ b_3 \\ b_4 \end{bmatrix} f_c \tag{2-6a}$$

$$\begin{aligned} \dot{x}_5 &= x_6 \\ \dot{x}_6 &= (W - f_c)/M_W \end{aligned} \tag{2-6b}$$

$$f_c = \begin{cases} C_H (x_5 - x_1 - r)^{3/2}, & x_5 - x_1 - r > 0 \\ 0, & x_5 - x_1 - r \le 0 \end{cases} \tag{2-6c}$$

where:

x_1	is the displacement of the rail,
x_2, x_3, x_4	have no physical meaning,
f_c	is the non-linear wheel / rail interaction force,
r	is the roughness excitation,
x_5	is the wheel displacement.
W	is the static wheel load,
M_W	is the unsprung wheel mass,
a_n, b_n	have no physical meaning,
C_H	is the Hertzian constant, (see section 2.3)

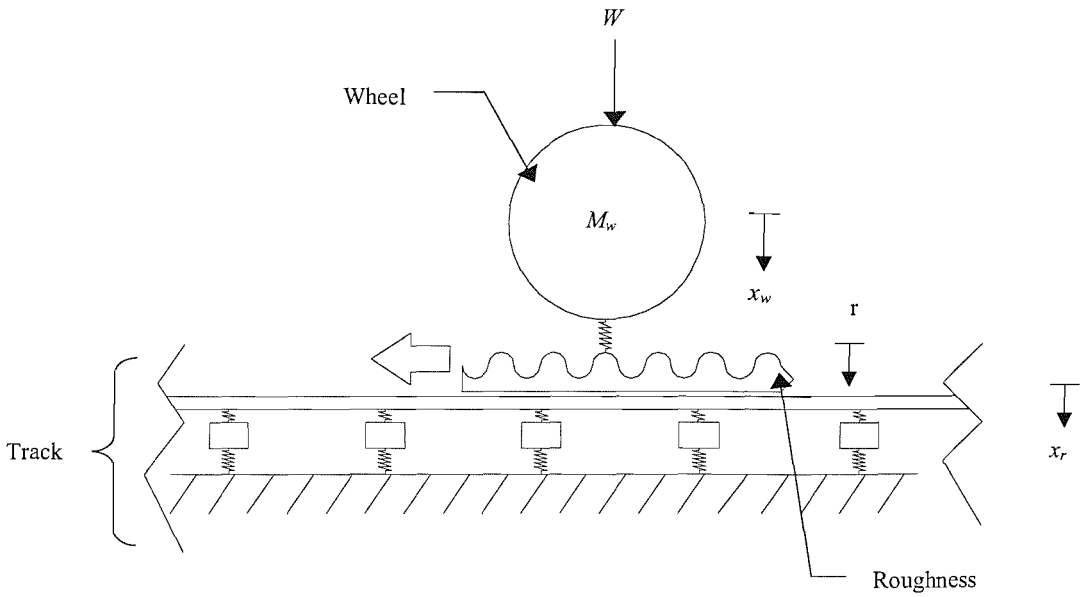

Figure 2–1 The moving irregularity wheel / rail interaction model as used by [Wu and Thompson, 2000(a)] where a downwards deflection of the wheel is defined as positive.

These equations assume that a positive deflection in the wheel / rail system is downwards (see Figure 2–1). They can be solved numerically using a fourth order Runge-Kutta method. Equations (2-6a), (2-6b), and (2-6c) show the complete state-space representation [Wu and Thompson, 2000(a)] of the non-linear models used to predict the theoretical analyses discussed in the following sections. Note that the rail (equation (2-6a)) and the wheel (equation (2-6b)) are linear whereas the contact spring (equation (2-6c)) contains non-linear terms. As stated in Chapter 1, a primary objective of this research is to verify the models produced by Wu and Thompson. Each of the following situations were simulated on the 1/5 scale wheel / rail rig (see Chapter 3) and were predicted using a non-linear model that was modified from that shown above (equations (2-6)). This modification of the Wu and Thompson model is presented in section 2.3. The theoretical results of the Wu and Thompson models are summarised next.

2.2.1 Non-linear interaction due to surface roughness

Simulations were made with harmonic and broadband random roughness inputs [Wu and Thompson, 2000(a)], where various wheel loads were considered. This included a simulated unloaded freight wagon (wheel load of 25kN), a typical passenger train (wheel load of 50kN), and a loaded freight wagon (wheel load of 100kN). The responses from the non-linear models were compared in each case to a linear prediction for the frequency range between 50Hz and 5kHz.

Provided that there is no loss of contact (due to large roughness amplitudes) the non-linear effects were found to be weak for larger wheel loads. Linear models are therefore suitable for the prediction of this situation as the difference between the non-linear stiffness and the tangent (linearised) stiffness[3] is small. Conversely the non-linear effects were found to be more significant for smaller wheel loads.

Two frequency regions were identified as being areas in which the non-linear effects were insignificant.

- Firstly at low frequencies, below 100Hz, the wheel and track dynamic stiffnesses are much smaller than the contact stiffness, which means that the contact spring is effectively rigid. The non-linear effects can therefore be ignored, provided that the

[3] An explanation of non-linear and tangent stiffness is presented in section 2.3.

roughness amplitudes are not so large that they cause loss of contact between the wheel and the rail.

- Secondly a high frequency region was identified, above 1kHz, where roughness amplitudes (with short wavelengths) are typically very small, resulting in small dynamic deflections. These small dynamic deflections can be well represented by a linear model.

A harmonic input study showed that non-linear effects generally existed in the region between 200Hz and 900Hz, though the predicted differences between the linear and non-linear models were small.

Studies using broad band (roughness) excitation studies showed that for a typical spectrum of roughness, at RMS amplitudes below 15μm (i.e. wheels and track in good condition), the linear and non-linear models were in good agreement. Linear and non-linear models were also in good agreement for RMS roughness amplitudes of 25μm with wheel loads of 50kN and above, though lower wheel loads at this roughness amplitude showed greater differences between the two models. Wheel loads of less than 25kN showed greater effects, although such loads were considered unrealistic.

The studies [Wu and Thompson, 2000(a)] based on the comparisons between linear and non-linear prediction models indicated that for the majority of roughness amplitudes, and the majority of wheel loads that occur in practice, non-linear contact spring effects at the wheel/rail interface are minimal and may be ignored.

2.2.2 Impacts of wheels passing over rail joints

The track model for the analysis of rail joints was slightly altered from the previous track model [Wu and Thompson, 2000(a)] to accommodate the rail joint geometry and characteristics [Wu and Thompson, 2001(b)]. Non-welded joints are typically held together by fishplates. These are connecting pieces of metal held in place by two bolts through each of the two ends of the rails. The track model was altered from the infinite case to a model with a pair of semi-infinite Timoshenko beams connected by a pinned joint. The presence of the pinned joint allowed shear forces to be transmitted from one rail to another, but prohibited the transmission of bending moments. This is only an approximation of a fishplate joint.

[Wu and Thompson, 2001(b)] characterised the geometry of rail joints by their height difference and distance apart (gap length). The geometry at the step is not the only change in surface profile. In addition to the step, rails tend to curve downwards towards

the joint due to the way they are manufactured. The curved nature of the rail near to the joints was modelled with a quadratic function. These geometric factors resulted in consideration of three possible types of step-up or step-down joint with dipped ends:

- Firstly, when the gap between the rails is narrow and there is a relatively deep dip; the wheel and rail are always tangentially in contact.
- Secondly, when the dip and gap are small but the step height is relatively large; here the wheel will pivot around the highest point of the joint until it makes contact with the next rail.
- Finally, a situation which rarely occurs in practice, where the gap is large resulting in a non-tangential (pivoting) contact on each of the rails.

The relative displacement between the two elastic bodies (the wheel and the rail) was calculated from the wheel's centre point trajectory assuming (at this stage) a rigid wheel and rail. This was used as a relative displacement input for the interaction model.

An additional, simpler, case was also considered where the ends of the rail were not dipped, and thus only a gap and step height dimension was needed to describe the joint. Analysis of 1m long dipped rail joints was made at 80km/h and 160km/h. For a step-up rail joint (height 1mm, gap 7mm, static load 100kN) loss of contact occurred at both speeds. It was found that as the wheel approaches the dip before the joint, the wheel falls and the rail rises to meet it. Due to its high inertia, the wheel is not able to follow the geometry of the dip resulting in partial wheel unloading at low speeds, or loss of contact at high speeds. After this, the wheel and rail meet, resulting in either a single impact at low speeds or a double impact at high speeds.

For a specific geometry, the time-domain model was used to calculate the force produced by the rail joints. This was then converted to an equivalent roughness spectrum, which was used to predict noise using the linear TWINS package. It was found that the impacts due to rail joints are related to train speed, static wheel load, and joint geometry. Noise from a single joint increases at a rate of approximately 20 $\log_{10}$ V (where V is the wheel velocity), but for many regularly spaced joints the average noise increases at 30 $\log_{10}$ V, much like that from surface roughness.

Lightly dipped rails with larger height differences were found to be noisier than deeper dipped rails. Step-up joints for the lightly dipped cases were noisier than step down joints, but were found to be similar for the deeper dipped cases. Light static loads were

found to increase the tendency for wheel unloading, and therefore produced more noise. This difference reduced with an increase in speed.

2.2.3 Dynamic interaction due to wheel flats

As described in Chapter 1, wheel flats are an unfortunate result of excessive braking by a train. A newly shaped flat spot on a wheel may be considered to have sharp edges at its ends which causes the wheel to pivot on the flat's corners as the wheel rotates. In time these sharp edges round off to form a more gradual transition from the curved surface of the wheel to the flat and vice versa. [Wu and Thompson, 2002] studied the excitation due to both newly formed and rounded wheel flats. They used a method similar to that used by [Newton and Clark, 1979] where a simulated wheel flat was included in the surface of a railhead.

The profiles of both new and rounded wheel flats were approximated by analytical functions and used to determine the wheel centre trajectory while assuming a rigid wheel and rail. This gives the relative displacement between the wheel and the rail that can then be used as an equivalent roughness input to the state-space model after taking account of the geometric effects of the wheel on the rail.

Analysis of a severe, rounded wheel flat with a depth of 2mm and length of 121mm (static wheel load 100kN, wheel radius 0.46m) showed a partial unloading at 30km/h and a double loss of contact occurring at 80km/h. When the wheel flat meets the rail it was found that the wheel would fall and the rail would rise to meet it. The static wheel load is sufficient to maintain contact at low speeds, but this is not so at higher speeds. A sharp increase in the contact force was seen to occur when the relative displacement reached its maximum. After this first impact, the momentum of the wheel and rail is changed dramatically and the wheel and rail are forced to move apart from each other resulting in the second loss of contact at 80km/h and above.

Investigations of a newly formed wheel flat (depth 2mm, but with length 86mm) demonstrated a higher impact force than the rounded wheel flat for the low speed case. This was because, although the magnitude of the displacement input is the same in both cases, as the excitation period is shorter for the newly formed flat the accelerations and peak force are higher. However, at 80km/h the newly formed flat produced a smaller impact force than the rounded flat, again due to its shorter dimensions. In this case the wheel turns so quickly that contact with the rail is re-established nearer the end of the wheel flat equivalent profile, thus reducing the accelerations and peak force.

Noise predictions that used a method of combining the non-linear model with the TWINS package showed an increase with train speed at a rate of approximately 20 $\log_{10}V$ (where V is the velocity) once loss of contact occurs. Flats with a depth of 1 and 2mm were found to be noisier than normal rolling noise for speeds up to 200km/h.

The hypothesis that a critical speed exists for a wheel flat, above which the noise level reaches a value independent of speed [Ver et al, 1976], was not verified. It was found that wheel flat noise continued to increase with speed after loss of contact occurred; it also increased with wheel load.

2.3 Verification and development of the non-linear models

As stated in Chapter 1, the non-linear model discussed above in Section 2.2 needs to be compared with measured data so that its performance can be verified. The model performance has been studied for cases with several railhead profiles using a 1/5 scale wheel / rail rig (described in Chapter 3).

Slight modifications to the non-linear models were required to predict the response of the 1/5 scale rig. Primarily a change of notation was adopted so that a positive input displacement was defined to be upwards (see Figure 2–2). This meant that equation (2-6c) was altered to:

$$f_c = \begin{cases} C_H (x_5 - x_1 + r)^{3/2}, & x_5 - x_1 + r > 0 \\ 0, & x_5 - x_1 + r \le 0 \end{cases} \qquad (2\text{-}7)$$

The Hertzian constant (C_H) used for the non-linear models is defined as [Thompson, 1990]:

$$C_H = \left(\frac{2}{3}\right)\left(\frac{2}{\xi}\right)^{3/2} E^* \sqrt{R_e} \qquad (2\text{-}8a)$$

where: E^* is a material constant (plane strain elastic modulus),

ξ is a geometrical constant that depends on the wheel and rail radii (which can be found from tables [Thompson, 1990][4]),

R_e is an equivalent radius given by [Thompson, 1990]:

---

[4] ξ =2 for a circular contact patch.

$$R_e = \frac{1}{1/R_{rt} + 1/R_{wt} + 1/R_w} \tag{2-8b}$$

where: R_{rt} is the transverse radius of the rail,

R_{wt} is the transverse radius of the wheel (positive for convex),

R_w is the radius of the wheel.

An example of the Hertzian non-linear contact effects is presented in Figure 2–3 where the resulting deflection (x) is plotted for a range of wheel pre-loads (P_0). The range of wheel pre-loads shown correspond with those that were used throughout this research. Figure 2–3 shows that for the lightest wheel pre-loads considered, small changes in wheel pre-load can result in large changes in deflection. At the highest wheel pre-loads considered, however, the changes in deflection are smaller.

Linear versions of the time-stepping models were also used during the research for comparative purposes. Conversion from a non-linear model to a linear time stepping model resulted in an alteration of equation (2-7) to:

$$f_c = k_H (x_5 - x_1 + r) \tag{2-9}$$

Equation (2-9) uses a linearised (tangent) approximation of the Hertzian stiffness for a specific wheel pre-load. This is defined as [Thompson, 1993(e)]:

$$k_H = \frac{2}{\xi}\left(\frac{3E^{*2}R_e P_0}{2}\right)^{1/3} \tag{2-10}$$

where: P_0 is the wheel pre-load

Contact patch dimensions (where an elliptical contact is assumed) are given by [Thompson, 1990]:

$$a = \sigma_1\left(\frac{3P_0R_e}{2E^*}\right)^{1/3} \qquad b = \sigma_2\left(\frac{3P_0R_e}{2E^*}\right)^{1/3} \tag{2-11}$$

where:

a is the contact patch length,

b is the contact patch width,

σ is a geometrical constant given in [Thompson, 1990].

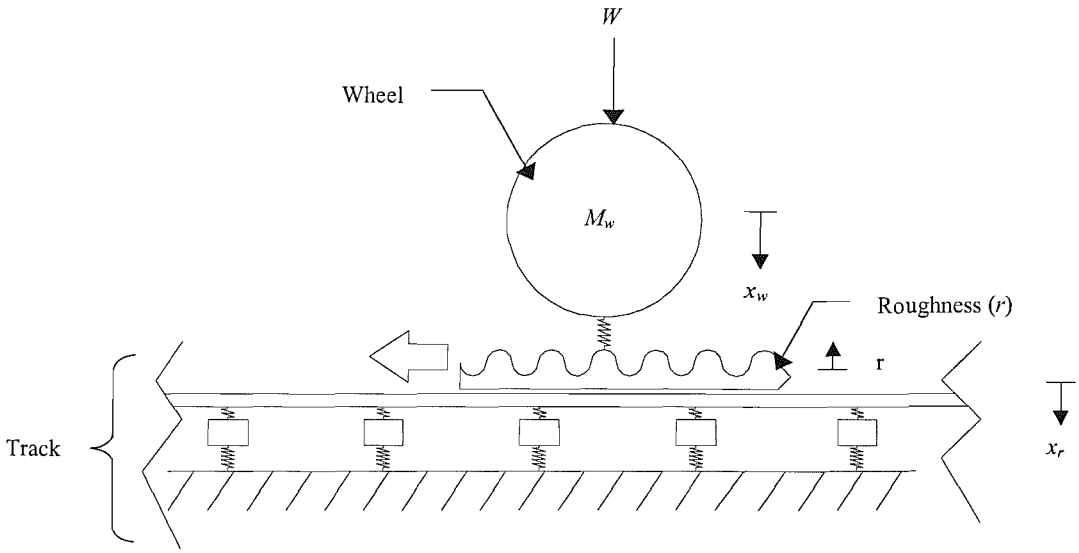

Figure 2–2 The moving irregularity model used in this thesis where a positive input is considered to be upwards.

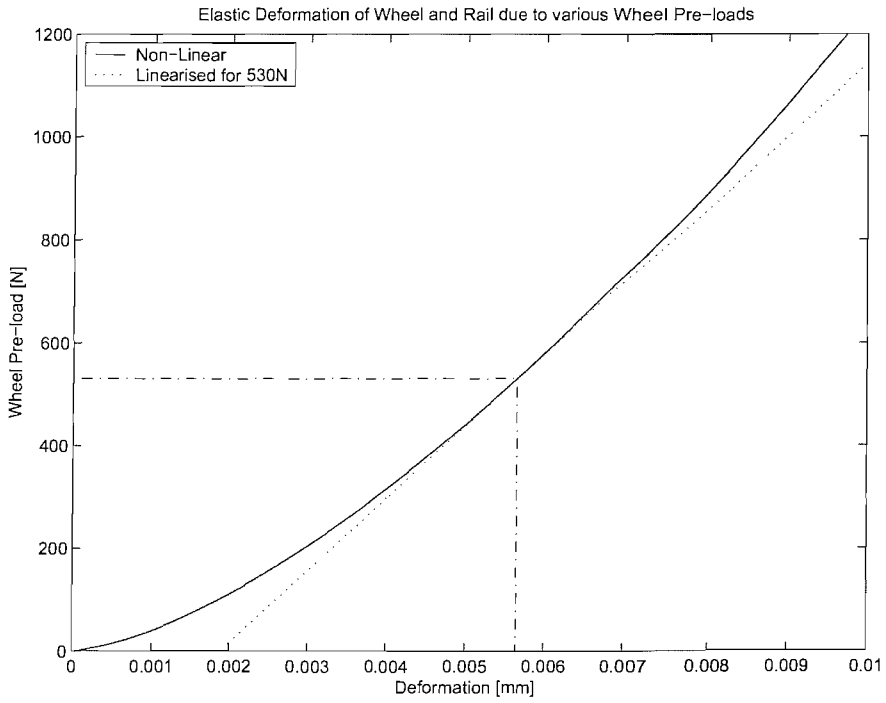

Figure 2–3 Predicted non-linear (Hertzian) contact deformation between a wheel (with a 0.1m radius) and a rail (with a 40mm railhead curvature). A linearised version for a wheel pre-load of 530N is also shown.

An example of a tangent (linearised) stiffness is shown in Figure 2–3 for a wheel pre-load of 530N. This demonstrates that if the wheel pre-load fluctuates greatly about this point, then the linear approximation differs considerable from the Hertzian non-linear estimate. However, it can be seen that the wheel pre-load (at 530N) can vary between approximately 400N and 700N before the approximation is in poor agreement with the non-linear representation.

The time-stepping models required a set of initial conditions before the routines could be started. These were found from static conditions. The deflection of the wheel and railhead due to a wheel pre-load (P_0) was calculated from:

$$z = \frac{\xi}{2R_e}\left(\frac{3P_0R_e}{2E^*}\right)^{2/3} \tag{2-12}$$

Equation (2-12) was then used with either equation (2-8a) or equation (2-10), depending upon the choice of contact spring relationship that was to be used in the time-stepping model, to find the contact force (f_c). The linear contact spring relationship used $f_c = kz$, whilst the non-linear contact spring relationship used $f_c = C_H(z^{3/2})$.

The deflections of each part of the time-stepping routine were then found by assuming that the initial velocity of each part of the model is zero when the routine is started. From this, the initial deflection of x_1 is calculated by a manipulation of equation (2-6a), after which the other deflections are found.

Additional alterations made to the time stepping prediction models conceived by [Wu and Thompson 2000(a)] concerned physical attributes of the 1/5 scale wheel / rail rig. These were the representations of the 1/5 scale track bed and the 1/5 scale wheel transfer function responses. These alterations are presented in Chapter 5. The 1/5 scale rig is described next.

3 Wheel / rail test rig

3.1 Background

London Underground developed a scale model wheel / rail test rig in the 1980's for use in research into wheel / rail rolling noise [ORE report C163/RP11, 1988, and ORE report C163/RP16, 1990]. Originally built to a scale of 1:8 it was later fitted with different wheels and rails, which are nominally to a scale 1:5.

In 1997 London Underground donated the rig to the ISVR and it was installed in a laboratory. A BEng project [East, 1998] was dedicated to commissioning the rig and a MSc project [Palluat de Besset, 1998] was subsequently carried out using the rig to study the effect of wheel design on noise and vibration. From the latter, it was clear that measurements of vibration suffered from severe instrumentation noise contamination and were unusable. Furthermore, on inspecting the rig at the start of this work, it was found that the main fixing had worked loose necessitating major structural refurbishment.

An introductory description of the rig is given below, followed by a description concerning the modification and recommissioning work carried out on the rig.

3.2 Basic description of the rig

Figure 3-1 shows an overview of the test rig. It consists of a beam mounted on a central pivot; two wheels, a measuring and guide wheel, at one end of the beam; two sections of circular track (upon which the wheels run); and an electric motor / drive belt (which rotates the beam assembly). The beam is designed to rotate in an anti-clockwise direction as seen from the perspective in Figure 3-1. The choice of a curved track section was decided by the designers of the rig [ORE report C163/RP11, 1988], because it allows a relatively easy way of measuring constant (fast) wheel speeds. A straight section of track would, for example, require long lengths of track where acceleration / deceleration sections would have to be incorporated to ensure constant wheel speeds.

In Chapter 1 a phenomena called curve squeal was described. This is produced where railway wheels negotiate tight curves, and therefore might be expected to occur on the circular 1/5 scale wheel / rail rig. [Rudd, 1976] presents a simple formula for when curve squeal is likely to occur, which relates the rail curvature to the length of a bogie.

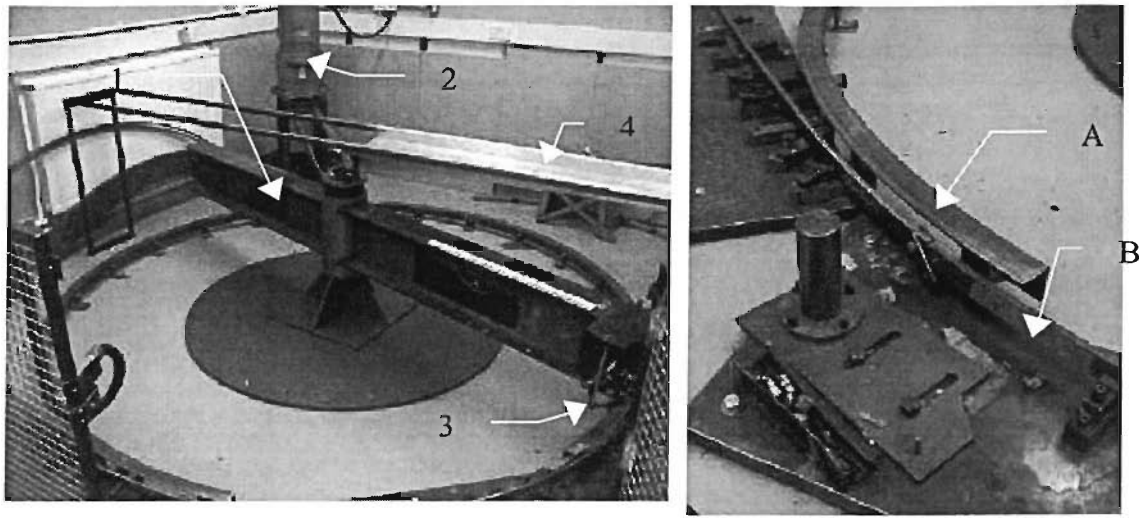

(a) General View (b) Measuring and Guide Rails

Figure 3–1 Rotary wheel / rail rig 1. Rotating beam, 2. Drive motor, 3. Wheel / spring assembly, 4. Instrumentation gantry, A. Guide rail, B. Measuring rail

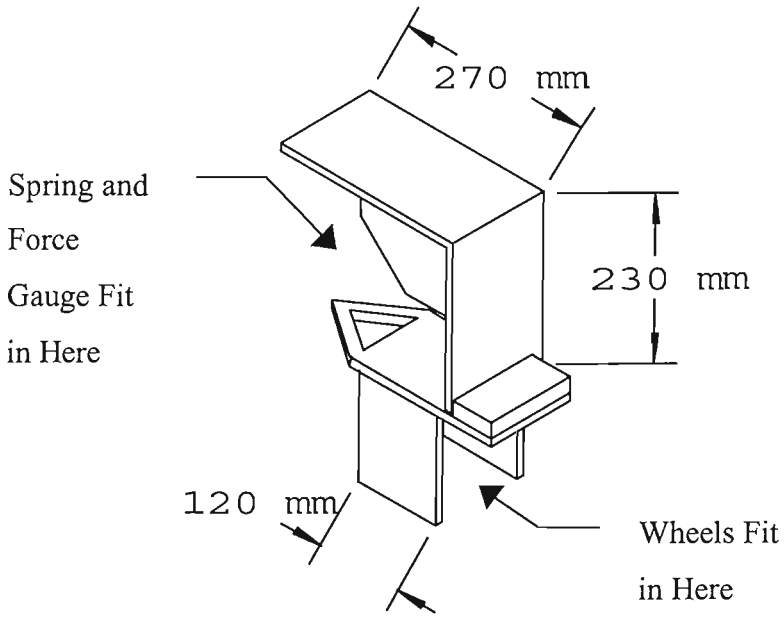

Figure 3–2 Sketch of the wheel and spring assembly

It can be inferred from this formula that curve squeal is only likely to occur when the wheel is not tangentially aligned to the curvature of the rail. As the rig wheel was always tangentially aligned with the rail radius, wheel squeal did not occur during the research presented in this thesis. The subject of wheel squeal, however, is intended to be researched with the use of the 1/5 scale rig at a future date.

The main features of the 1/5 scale rig are as follows:

1. A deep 'I' section steel beam rotates on a pivot in the centre of two tracks (1, Figure 3-1 (a)). At one end of the beam there is a wheel and spring assembly (3, Figure 3-1 (a), Figure 3-2, and Figure 3-3), which is counter balanced at the opposite end by a 30kg weight.

2. A guide rail encompasses approximately 80% of the circumferential rotation of the beam (Figure 3-1 (b) denoted 'A', and Figure 3-4). During the remaining section of the beam's rotation, the measurement wheel runs on the measuring rail (denoted 'B' in Figure 3-1 (b)). The ends of the measurement rail extend 2m tangentially to the guide rail circle to reduce the effects of standing waves in this finite section. These end pieces are attached by fish plated joints.

3. An electric drive motor and belt configuration is used to rotate the beam at constant angular velocities, and is seen at the rear of Figure 3-1 (a) (2).

4. An accelerometer is mounted on the web of the measuring wheel (Figure 3-5). This is wired through two slip ring units, one mounted at the wheel and spring assembly (Figure 3-5), and the other at the top of the beam pivot. The instrumentation wiring gantry keeps the wiring away from the rig's rotating parts (4, Figure 3-1 (a)).

5. A safety fence encloses the experimental area. An electrical isolating trip switch on the access gate prevents rig operation when open.

6. The pre-load applied to the rig wheel can be adjusted in the range of 380N to 850N by compressing a spring within the wheel / spring assembly. This is measured by a force gauge situated between the bottom of the spring and the wheel axle housing (see Figure 3-2, and Figure 3-3).

7. Wheel speed is measured by means of an optical tachometer situated at the end of the axle (see Figure 3-3).

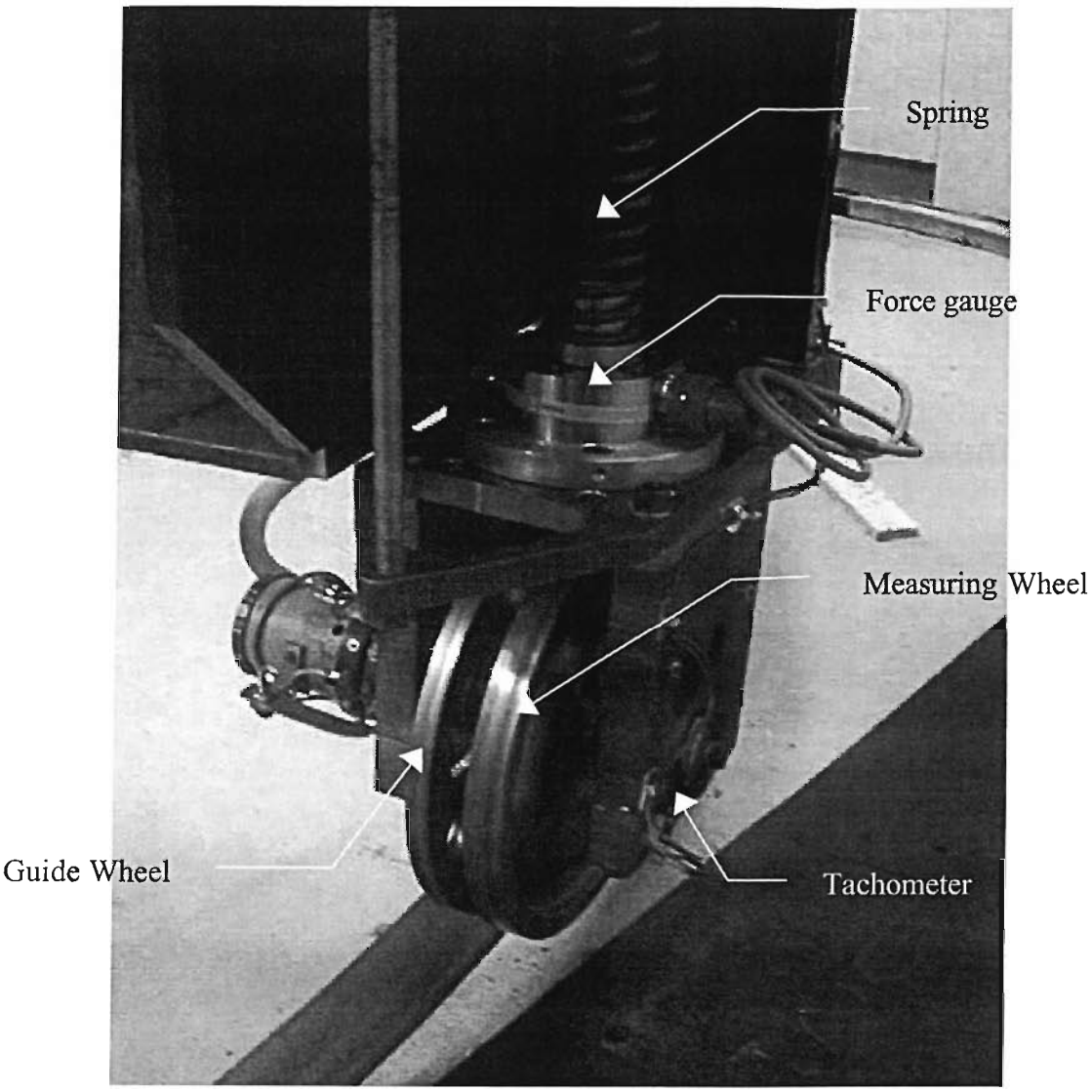

Figure 3–3 Wheel and spring assembly

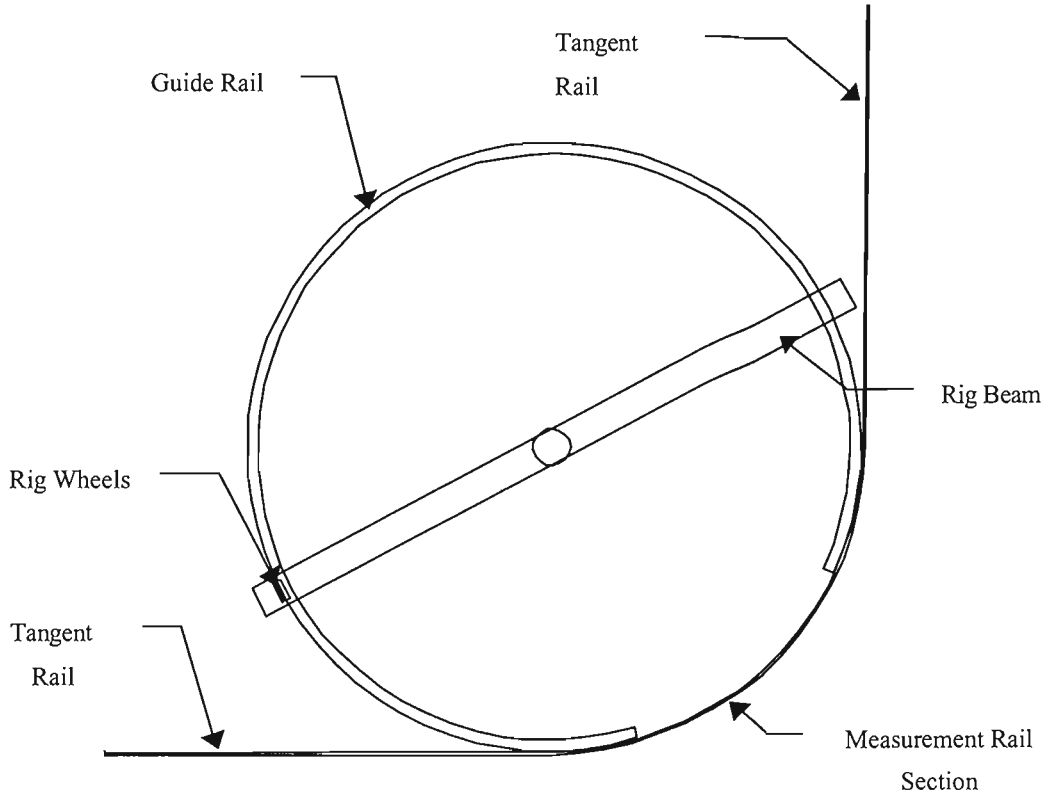

Figure 3–4 Sketch of the plan view of the rig

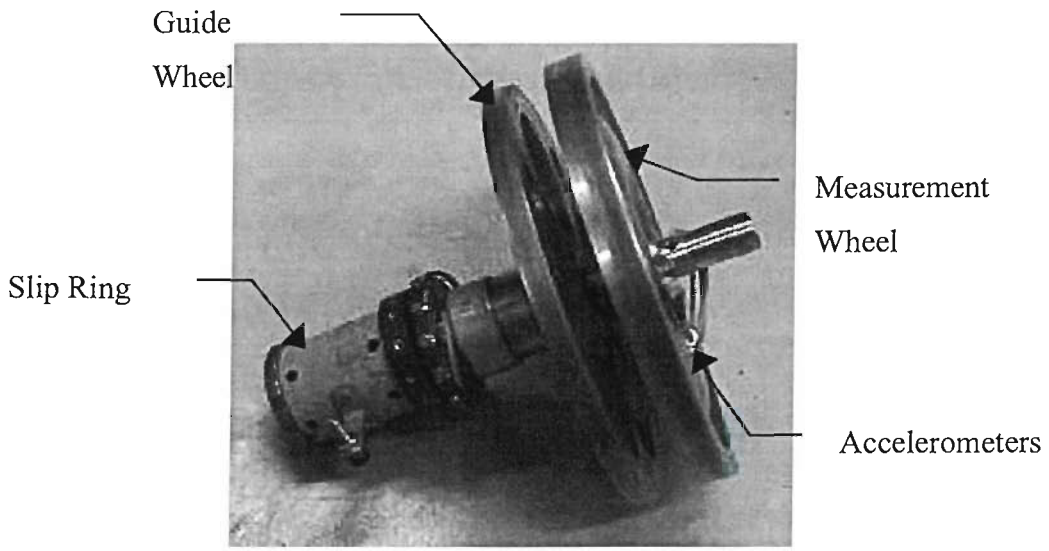

Figure 3–5 Unfitted wheel and slip ring assembly

3.3 Description of the wheel and spring assembly

The wheel and spring assembly performs two important functions:

- It holds both the measuring and guide wheels in position,
- It provides a way of applying a pre-load to the rig wheel.

Figure 3-2 and Figure 3-3 shows the wheel and spring assembly. The wheels are fitted to a hinged lower section of the assembly in between which the spring sits. This allows the wheels to be pre-loaded whilst allowing the wheels to move with any undulations of the track.

3.3.1 Modifications to wheel / spring assembly

A force gauge had at one time been fitted to the rig, though this had not originally been included during the initial installation at the ISVR. In [East, 1998] the spring had been calibrated to give an indication of pre-load from a measurement of the compression. The wheel pre-load had therefore been estimated from measurements of the compressed spring length. This method was not thought to be particularly reliable.

The wheel and spring assembly has now been modified by positioning an ENTRAN ELIM D1 load cell between the lower mounting point of the spring and the assembly housing. This is shown in Figure 3-3.

This was felt to be an important addition to the instrumentation system, as it would now enable monitoring of the static pre-load, during undulations of the track. The manufacturers of the load cell state that the bandwidth of the dynamic response of the transducer is from 0Hz to 500Hz. The usefulness of this transducer is assessed in an alternative method of surface profile measurement in Chapter 4. However, it proved to be most useful to provide a measurement of static wheel pre-load.

3.4 Faults found with the primary installation and configuration

A number of faults were identified in the first installation of the rig at the ISVR. These are listed below.

- The greatest problem with the initial installation of the scaled rig was that the fixings to the floor of the laboratory were working loose. Upon further inspection it

was found that the quality of the concrete laboratory floor was very poor. Rectification of this fault required the re-fitting of the guide rails and measuring section track bed along with a reinforced base plate for the beam pivot support. The new base can be seen as the large circular plate in Figure 3-1 (a) that is welded to the original square base, and secured to the floor with 12 chemical fixings.

- The instrumentation system was found to be in a poor state of repair and needed to be completely rewired.

- Previous measurements [Palluat de Besset, 1998] had used B&K charge based accelerometers to measure vibration of the measuring wheel. In order to do this it is necessary to feed signals from a transducer mounted on the rotating wheel, through a slip ring, to a charge amplifier mounted on the beam. It is suspected that the slip ring assembly caused noise contamination of the results. An alternative capacitance based accelerometer system has been fitted to try to reduce any influence of the necessary slip ring. This accelerometer produces an amplified signal which is therefore less susceptible to noise contamination.

- The original measuring rail cross-sections were rectangular. This, in combination with the alignment of the wheel, meant that the wheel would run on the corner of the rail, as shown in Figure 3-6.

- The track bed properties (which were unknown) were not thought to be an adequate representation of a full size railway partly because no allowance for a resilient layer representing the ballast had been made.

3.5 Improvements made to the measuring track section

3.5.1 New rail section

Figure 3-6 shows the difference between the original and desired contact between the measuring wheel and rail. To rectify this problem, new rails were manufactured to have a 40mm radius on their running surface as shown in Figure 3-7 (the choice of this value is discussed later). The other dimensions of the rail are the same as the previous configuration. After machining, the rails were rolled to a radius of 1.5m in the horizontal plane.

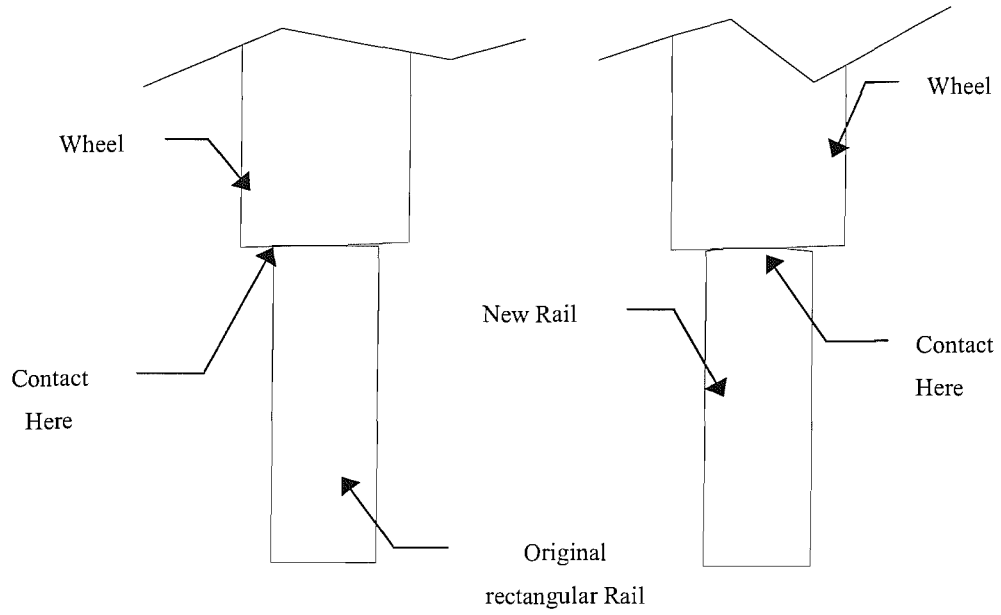

Figure 3–6 Original and desired wheel / rail contact

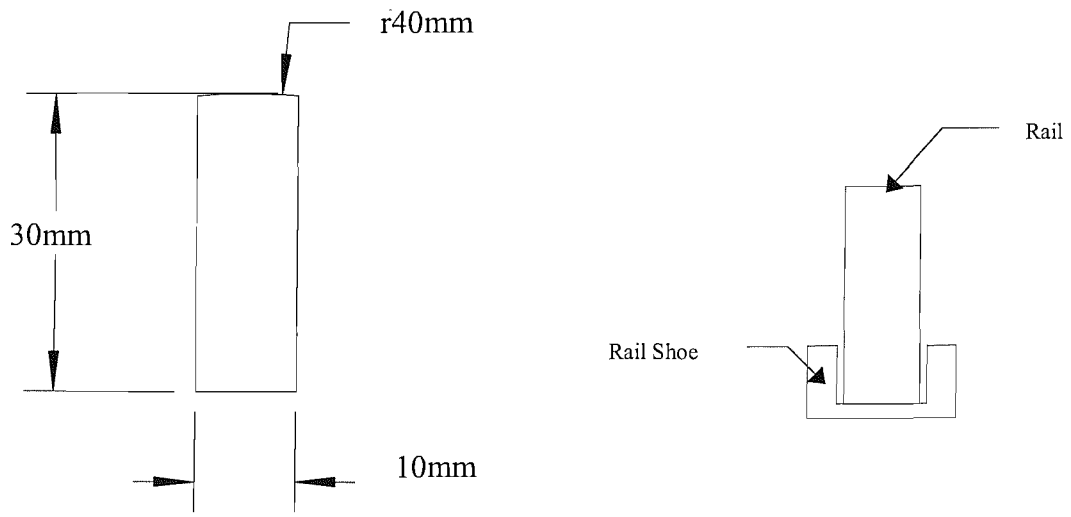

(a) Rail dimensions (b) Rail fitted to rail shoe

Figure 3–7 (a) New measuring rail profile, (b) Rail and shoe configuration

3.5.2 The original foundation

The original configuration of the measuring section of the track as supplied by London Underground is shown in Figure 3-8. Here stiff clamps held the rails to a Paxian sleeper, with elastomeric pads fitted between the rail shoe (Figure 3-7) and the sleeper. The sleeper spacing was approximately 90mm, which corresponds with the original 1/8 scale dimensions. The sleepers were bolted directly on to a 20mm thick steel base plate.

This design was considered to be inappropriate. Firstly, it did not have a ballast layer like a real track bed, and secondly, it did not have a sleeper scaled for a 1/5 scale track. The opportunity was therefore taken to redesign the whole support structure. This involved finding material with suitable dynamic properties for a 1/5 scale model track. These properties were determined from the scaling laws discussed next.

3.5.3 Scaling of the track bed parameters

Guidelines for the parameters for the rig scale model track were based upon a full size track with bibloc concrete sleepers in ballast. Parameters for this (full size) track were measured and presented in table 4.2 of [Thompson and Janssens, 1997]. These are reproduced in Table 3-1.

To produce a scale model a series of scaling laws needs to be adopted. If the sizes of all elements are reduced by the same factor N, while the material properties are kept the same, a model structure is obtained with natural frequencies that are multiplied by the factor N. Using this as a basis, the scaling factors given in Table 3-2 were derived. For example, the value for mass (m) is obtained by keeping the density (ρ) constant and multiplying the volume (V) by $1/N^3$ ($m = \rho V$). The value for stiffness is obtained by consideration of a block of elastic material of height h and area A and constant Young's modulus E:

$$k = \frac{EA}{h} \tag{3-1}$$

For a given material, the Young's Modulus E is fixed so it can be seen that the stiffness varies by N/N^2, which equals $1/N$.

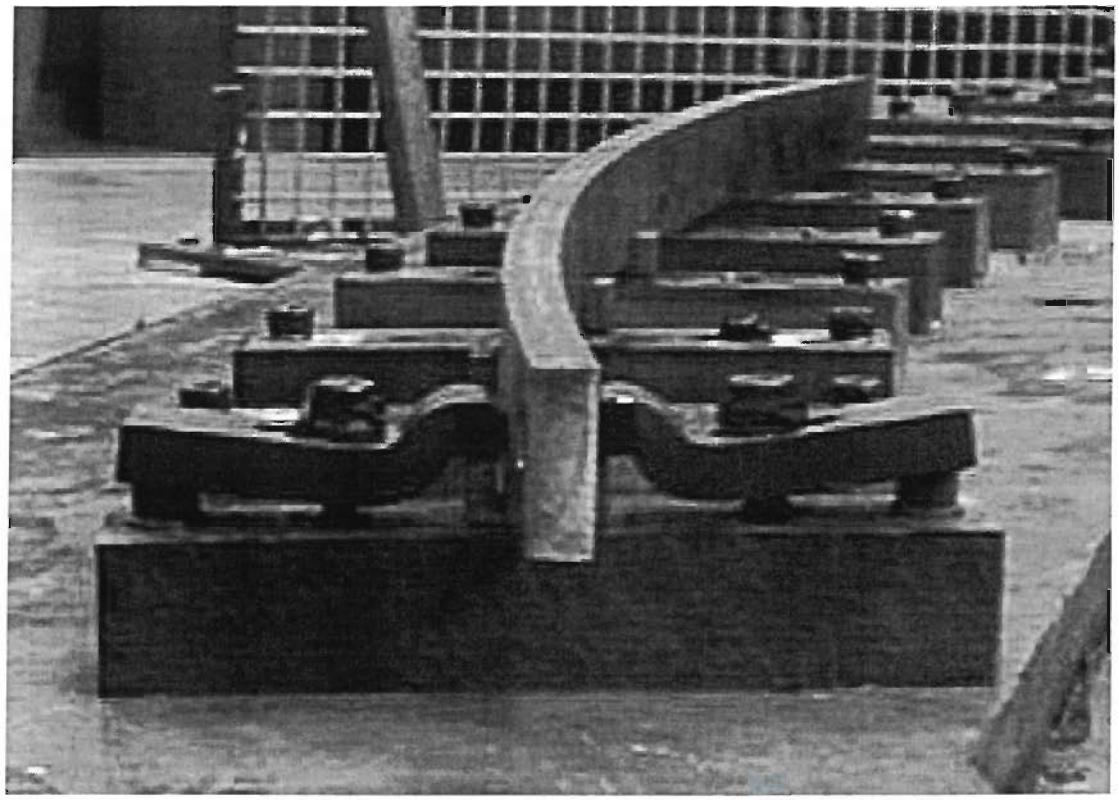

Figure 3–8 London underground track bed design

Table 3-1 Full size and scaled track bed parameters

Component	Full Size Value	1/5 Scaled Value
Rail vertical EI product	$4.92MNm^2$	$7872Nm^2$
Rail lateral EI product	$870kNm^2$	$1392Nm^2$
Rail mass per unit length	54kg/m	2.16kg/m
Rail vertical loss factor	0.02	0.02
Rail lateral loss factor	0.02	0.02
Sleeper spacing	0.6m	0.12m
Sleeper mass	122kg	0.976kg
Vertical pad loss factor	0.25	0.25
Lateral pad loss factor	0.25	0.25
Vertical pad stiffness	1.3GN/m	260MN/m
Lateral pad stiffness	100MN/m	20MN/m
Vertical ballast stiffness	67MN/m	13.4MN/m
Lateral ballast stiffness	34MN/m	6.8MN/m
Vertical ballast loss factor	2.0	2.0
Lateral ballast loss factor	2.0	2.0
Clip stiffness	500kN/m	100kN/m
Clip pre-load	10kN	400N
Wheel load	50kN	2kN

Table 3-2 Dimensional scaling factors

Variable	Notation	Units	Scaling Factor
Distance	L	m	1/N
Second Moment of Area	I	m^4	$1/N^4$
Mass	m	kg	$1/N^3$
Mass per unit length	ρA	kg/m	$1/N^2$
Force	F	N	$1/N^2$
Stiffness	k	N/m	1/N
Loss factor	η	none	none
Frequency	f	Hz	N
Time	t	s	1/N

Problems can arise with the scaling method presented thus far for the scaling of a force. For example, the relationship $F = ma$ could be used to give a scaling for a force of:

$$(1/N^3)((1/N)(N^2/1)) = 1/N^2 \qquad (3\text{-}2)$$

This scaling, however, appears at first not to correspond with the scaling for the relationship $F = mg$, which provides a scaling factor of $1/N^3$ when 'g' is considered to be a constant. This problem was noted by [ORE report C163/RP11, 1988] where it was suggested that wheel pre-loads could be scaled either by the factor $1/N^2$ or $1/N^3$. Ideally, the gravitational constant g should also be scaled from a full-size value of $9.81\,m/s^2$ at sea level. A value of acceleration is scaled by $(1/N)(N^2/1) = N$. This gives a value of $49.05\,m/s^2$ (9.81×5) for the 1/5 scale case. A 1/5 scale model should therefore be subjected to a gravitational force five times that of the full scale case. Clearly this is not possible in practice.

This highlights a problem with scaling dynamic models by the method of reducing dimensions by a constant factor. This analysis has shown that the resulting model will be subjected to a gravitational force that will be five times less than its full-scale equivalent. The contact patch dimensions are therefore not comparable with the full scale case.

[Jaschinski et al, 1999] document similar problems for the scaling of roller rigs used for the study of dynamic stability of railway vehicles. They suggested remedies for this problem by applying an external force to the model to obtain the correct contact patch dimensions, or to scale the density of the elements used in the scale rig. These methods, however, were not adopted for this research for the following reasons:

- It was felt not to be practical to apply any further load to the rig wheel other than that provided for by the wheel pre-load spring (within the wheel / spring assembly shown in Figure 3-3) due to uncertainty regarding the integrity of the rotating beam support structure on the rig room floor.
- Use of alternative materials with a scaled density for the rig wheel and rail were not considered to be practical for the situations that were to be investigated with the scale rig. Such materials, if they were available, might not necessarily have similar properties to steel. It was felt that steel was most likely to have the best damping and wear / impact resistant characteristics for the purposes of the project.

An alteration was made, however, to the scaling of the railhead radius (which at full size is 300mm) so that a realistic contact patch length would be obtained. This is important because the attenuation of the contact filter commences at a frequency that is related to the contact patch length [Remington, 1976]. An incorrect contact patch length would result in an unrealistic measurement of the vertical vibration on the rig.

To obtain the desired contact filter effect, the maximum rig wheel pre-load of 1kN was converted into a full size wheel pre-load with use of the scaling factor $1/N^2$. The Hertzian contact patch dimensions were then calculated for the equivalent full size case (equations (2-11)), from which the 1/5 scaled value was obtained. The railhead radius was therefore adjusted until a desired contact patch length of 1mm was obtained. A railhead radius of 40mm provided the desired contact patch length. This adjustment unfortunately resulted in a contact patch width that was not correctly scaled. This, however, was thought to be a small compromise as [Remington, 1976] indicates that the contact patch length influences the contact patch filtering effect.

The scaling laws (Table 3-2) are used to obtain the ideal scale model parameter values listed in Table 3-1. These were verified by use of a module of the TWINS package called RODEL which models the rail as a Timoshenko beam on a continuous spring-mass-spring foundation [Thompson and Vincent 1995]. Results of this are shown in Figure 3-9 and Figure 3-10. These curves are the same shape; the modulus is scaled by $1/N^3 = 1/125$, as accelerance has units of $m/Ns^2 \equiv 1/kg$, and the frequency is shifted by a factor of $N = 5$. The scaling laws are therefore verified from the performance of the existing prediction models.

3.5.4 Implementation of the track bed scaled values

From the scaling values found from the method described above, in section 3.5.3, a new design of track bed has been manufactured. This is shown in Figure 3-11. It can be seen that the new design has elastomeric sections for the ballast and pads, together with scaled sleepers. The sleepers are steel masses of dimensions 102mm x 51mm x 24mm. This gives a mass of 0.976kg excluding the spring clip assemblies. This mass corresponds with a full size sleeper mass of 122kg ($0.976\text{kg} \times \text{N}^3$).

A system similar to that of a full size track is used for connecting the measuring rail sections to the discrete supports. Here a simple cantilever spring is used to pre-load the pad located between the sleeper and rail. The spring, which is rigidly clamped at each

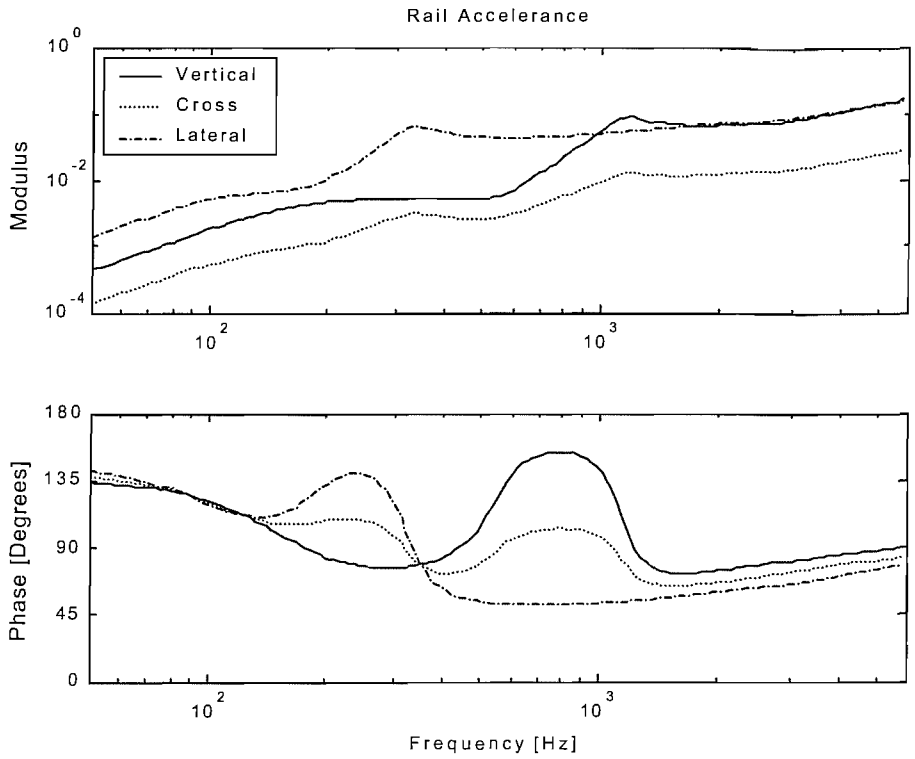

Figure 3–9 Full size track point accelerance predicted using Rodel (parameters from Table 3-1).

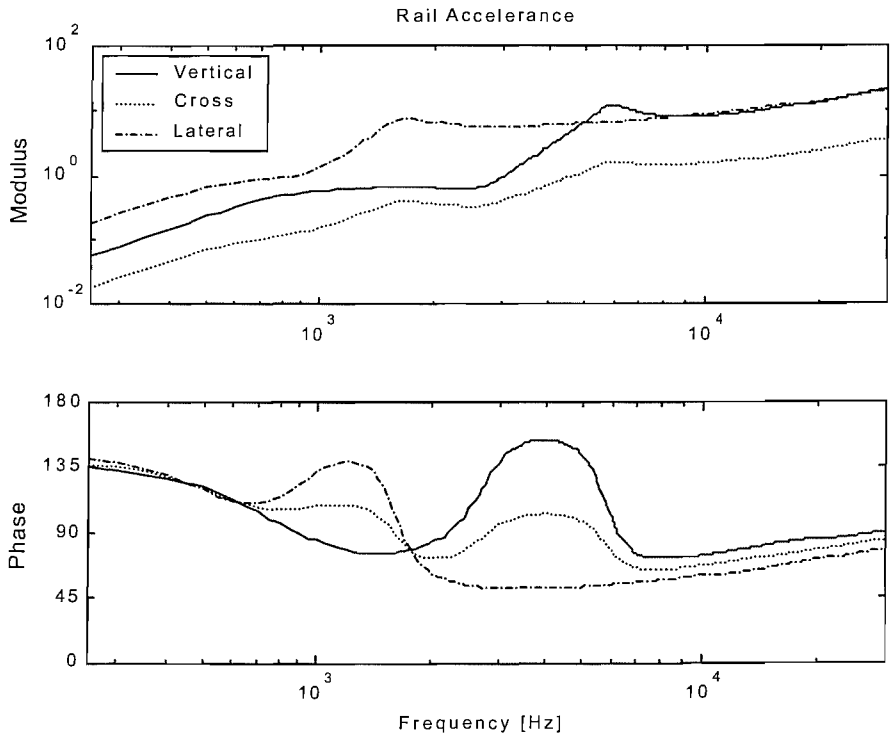

Figure 3–10 1/5 Scaled track point accelerance predicted using Rodel (parameters from Table 3-1)

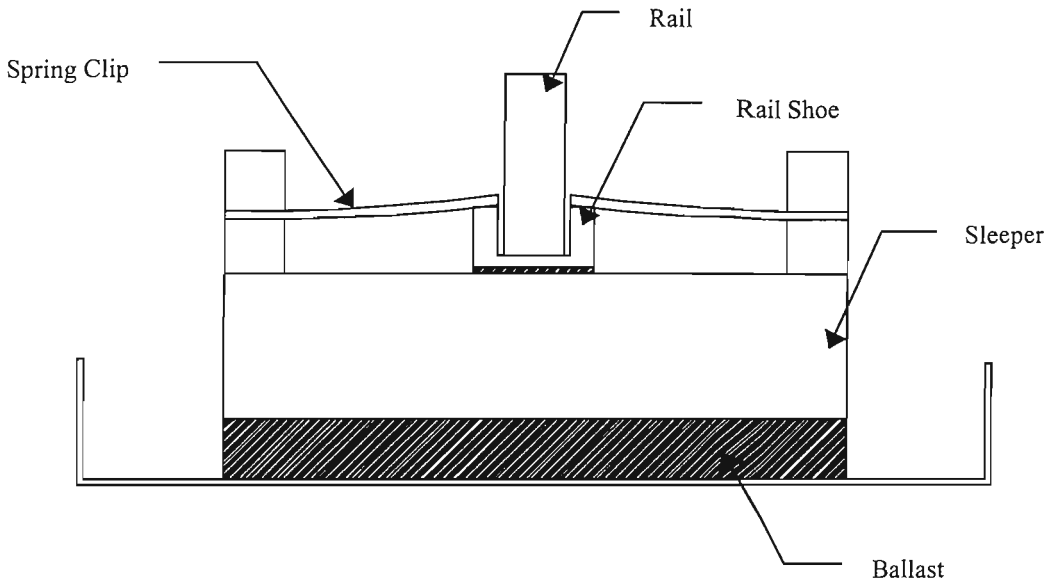

Figure 3–11 New design for model track bed

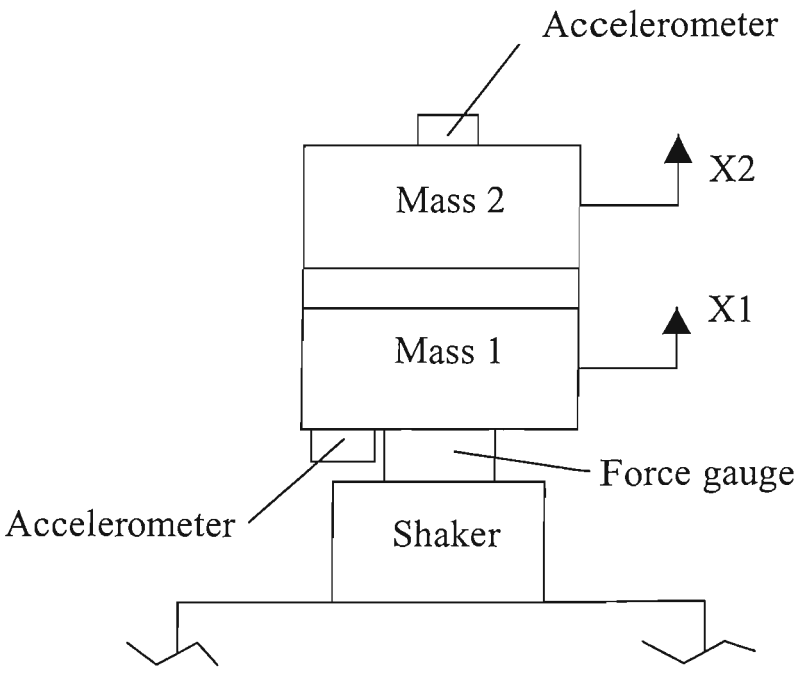

Figure 3–12 Polymeric property measurement apparatus

end of the sleeper, is designed to have a stiffness of 100kN/m and to give a pre-load force of 400N at the shoe. The rail shoe is a necessary addition to the model. It simply provides a way in which to locate the rail, without having to manufacture a complicated rail shape as in the full-scale example. The rail shoe adds 22.5g to each support section. As each support section effectively contains a 120mm section of the rail, which has a mass of 282.6g, this means that the rail shoe is 8% of the mass of the rail for a section in between the spacing of the sleepers. The addition of the rail shoe is therefore negligible.

The whole arrangement is mounted on a tray that has slotted holes and securing bolts for lateral adjustment. This adjustment does not provide a means to alter the lateral position of the rail, as the rail is much more rigid than the lateral stiffness of the supports; it merely permits the discrete supports to be positioned correctly under the measuring rail.

The process of measuring and selecting the ballast and pad elastomeric materials is presented next.

3.5.5 Polymeric material measurement

A suitable material for the ballast had previously been identified from data measured for the Silent Track Project [Thompson, Briscoe, and Jones, 2000] with a Young's Modulus E of 26MN/m^2. By using equation (3-1) (taking h the height of the pad to be 10mm, and the area of the sleeper (51mm x 102mm)) the stiffness of this material would be 13MN/m. This value compares well with the 1/5 scaled vertical ballast stiffness of 13.4MN/m shown in Table 3-1.

Dynamic measurements were made of several polymeric materials in order to obtain a suitable material for modelling of the pad. The following method for dynamic measurements of the polymeric materials was devised.

The sample materials were glued in turn between two 0.976kg steel masses (Figure 3-12). The combined 2DOF system was then mounted on a force gauge and attached to an electrodynamic shaker. This was excited with random (white noise) vibration, and the responses of the two masses were measured with accelerometers. The results were then compared with a two-degree of freedom model of the expected system response. This is given in state space form as:

$$\begin{bmatrix} \dot{x}_1 \\ \ddot{x}_1 \\ \dot{x}_2 \\ \ddot{x}_2 \end{bmatrix} = \begin{bmatrix} 0 & 1 & 0 & 0 \\ \frac{-k}{m_1} & 0 & \frac{k}{m_1} & 0 \\ 0 & 0 & 0 & 1 \\ \frac{k}{m_2} & 0 & \frac{-k}{m_2} & 0 \end{bmatrix} \begin{bmatrix} x_1 \\ \dot{x}_1 \\ x_2 \\ \dot{x}_2 \end{bmatrix} + \begin{bmatrix} 0 \\ \frac{1}{m_1} \\ 0 \\ 0 \end{bmatrix} [F] \tag{3-3}$$

$$\begin{bmatrix} y_1 \\ y_2 \end{bmatrix} = \begin{bmatrix} 1 & 0 & 0 & 0 \\ 0 & 0 & 1 & 0 \end{bmatrix} \begin{bmatrix} x_1 \\ \dot{x}_1 \\ x_2 \\ \dot{x}_2 \end{bmatrix} + \begin{bmatrix} 0 \\ 0 \end{bmatrix} [F] \tag{3-4}$$

where: x refers to the displacement of each mass,

y refers to the output for a given input force F,

m is the mass of each steel mass,

k is the stiffness of the resilient layer.

Equation (3-3) and equation (3-4) were used to obtain an estimate of the stiffness and the viscous damping by fitting the outputs to the measurements. An example of these results is shown in Figure 3-13.

The material found that best suited the design requirements for the pad gave a stiffness value closest to the 1/5 scaled value of 260MN/m for the area of contact between the sleeper and the rail shoe. This area of contact between the sleeper and the rail was made as small as possible to reduce the weight of the rail shoes (see Figure 3-11). After the polymeric material had been chosen for each of the track resilient layers, pieces were cut to shape for each of the discrete supports, and the track bed was assembled.

3.6 Commissioning

Once the new track design had been manufactured and assembled, its free vibration response was measured by using impact excitation with an instrumented hammer. These static tests were made at many positions along the measurement and tangent rails. The frequency response functions (arranged to measure accelerance) were then compared with results from the RODEL model [Thompson and Vincent 1995]. Additionally, the measurement rail was removed and the frequency responses of the individual sleepers were measured and compared with a simple mass-spring-damper model.

Prior to the measurements, for purposes of identification, each sleeper and sleeper spacing was numbered, as shown in Figure 3-14. The tangent rail sections are labelled

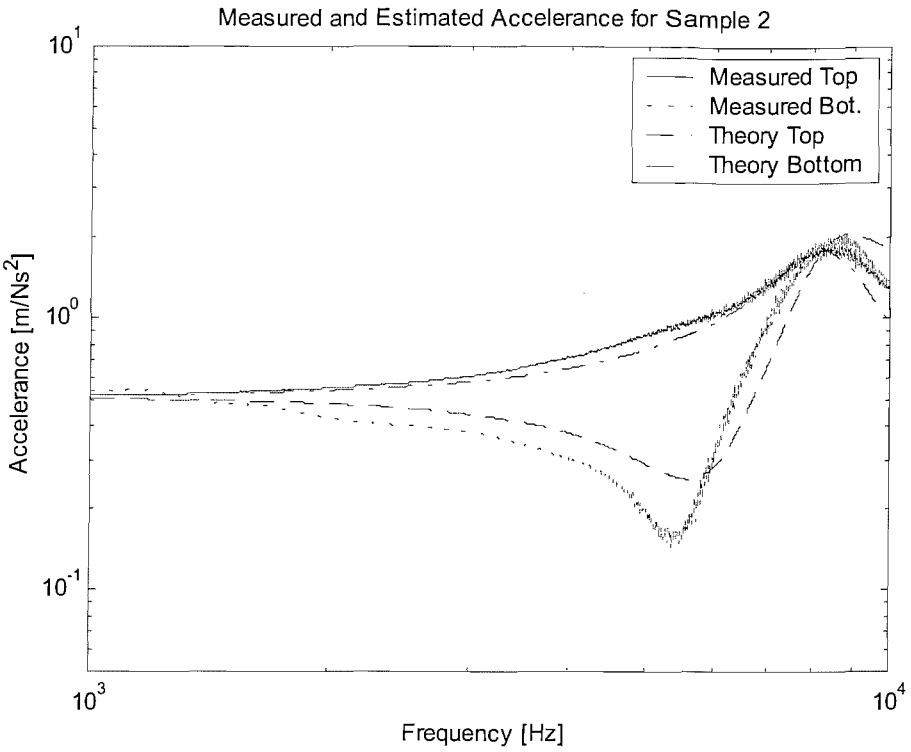

Figure 3–13 Estimated and measured response of material 2: Parameters for estimate, k = 1.3e9 N/m, ζ = 0.15, area of rubber = 3.6e-3 m^2, rubber height = 1 mm

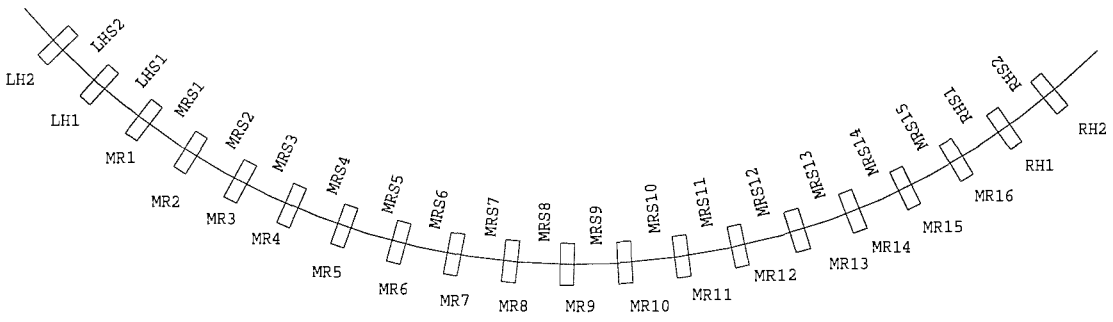

Figure 3–14 Sleepers and sleeper spacing positions

with either a 'LH' or 'RH' prefix, whilst the measurement rail is given an 'MR' prefix. Sleeper positions are simply given numbers at each point whereas the spaces between are denoted with an 'S'. For example 'MR2' refers to sleeper number two on the measurement rail, whilst 'MRS2' refers to the space between the sleepers numbered one and two on the measurement rail.

Measurements, comprising an average of ten hammer impacts for each measurement point, were made of the following:

- Drive point accelerance of the ballast and sleepers under the measurement rail (MR1 to MR16) without the rail fitted,
- A drive point accelerance of the measuring rail with the rail fitted at position MRS8,
- Transfer accelerance of the measuring rail (in between the sleepers) with the tangent rails fitted (LH3 to RH3), with a fixed accelerometer position at MRS8.

3.6.1 Measurements of the sleepers

Point accelerance measurements of each of the discrete supports without the rail fitted or the rail pads (but with the rail spring clip assemblies still in position) were made on the upper surface of each sleeper within the measurement rail section. This was done to try to quantify the behaviour of each of the rail discrete supports. In these measurements the instrumented hammer and accelerometer could not be positioned at the same point, but hammer taps were made as close as possible to the accelerometer. An average of ten hammer taps was taken for each of the accelerance measurements.

The measurements of the accelerance of the ballast and sleeper were compared with the expected response of a single degree of freedom (SDOF) system. The theoretical response of such a system is:

$$\frac{\ddot{X}}{F} = \frac{1}{m + c/j\omega + k/-\omega^2} \tag{3-5}$$

where: m is the mass,

c is the coefficient of damping,

k is the stiffness.

An example of the response is shown in Figure 3-15 The measured accelerance of the sleeper and ballast showed a resonance peak at approximately 100Hz. At frequencies below this peak the SDOF system is stiffness controlled, at frequencies above it the system is mass controlled, and the height of the peak is limited by the damping. By measuring the response of each of the sleeper and ballast supports and comparing it with the theoretical response of equation (3-5), estimates of the stiffness, damping, and mass could be made. The measurements also showed an anti-resonance and resonance at high frequencies (see Figure 3-15). This is probably caused by a bending mode of the sleeper, but is in a frequency range much higher than the expected resonance of the sleeper mass bouncing on the ballast stiffness.

Coherence measurements were made for each measurement. A coherence of less than 0.9 for a given frequency was considered to be a poor representation of the transfer function as it indicates noise contamination of the two signals. Generally it was found that the coherence would be poor at low and high frequencies or at frequencies corresponding with the resonance peaks. Coherence measurements were used as a guide to the quality of the transfer functions. A set of ten averages were accepted providing the coherence was above 0.9 between 80Hz and 12.8kHz with the exception of frequencies corresponding with the resonance behaviour depicted by the transfer function response.

The estimates of the modal parameters obtained from the measurements of the sleeper and ballast at each point along the measuring rail are summarised in Table 3-3. These were found by adjusting the inputs to the SDOF model so that its response corresponded with the measured response in each case. The damping is expressed in terms of the damping ratio $\zeta = c/\sqrt{km}$.

The variation in measured ballast stiffness (k_b), from the frequency response functions of individual sleepers, is shown in Figure 3-16. Here the ballast stiffness is shown as $20\log_{10}(k_b)$ for each of the discrete support positions. Figure 3-16 shows a difference of 17dB between the maximum and minimum measured stiffness. This demonstrates that the highest stiffness measured was approximately 7 times greater than the lowest stiffness measured. These variations are thought to be due to the manufacturing method of the discrete supports. This theory is confirmed by further investigations described in Chapter 5. The variations found in the effective mass (Table 3-3) are much smaller in comparison with the stiffness.

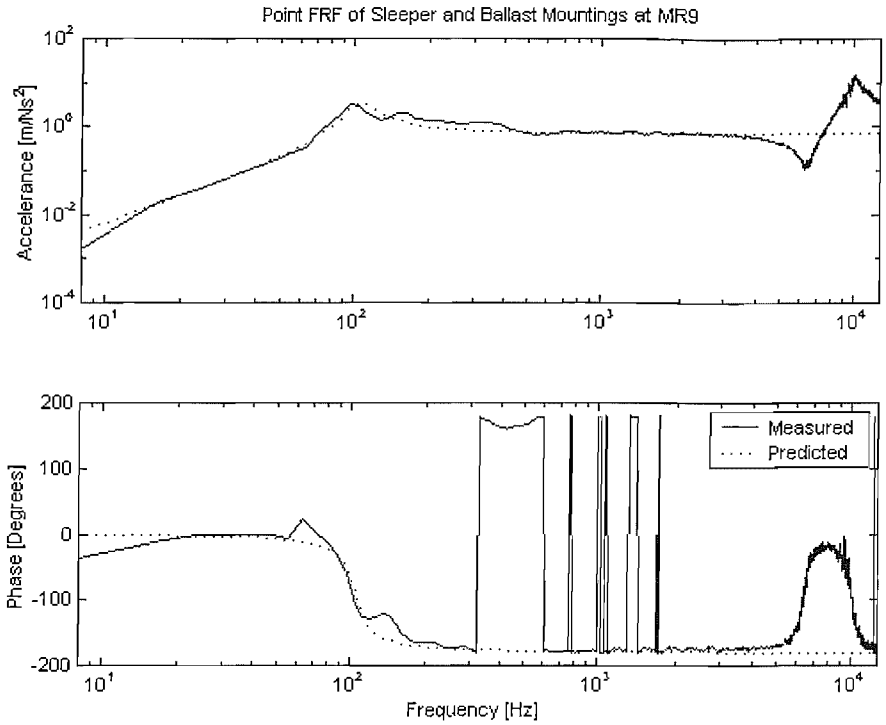

Figure 3–15 Measured and predicted sleeper and ballast response

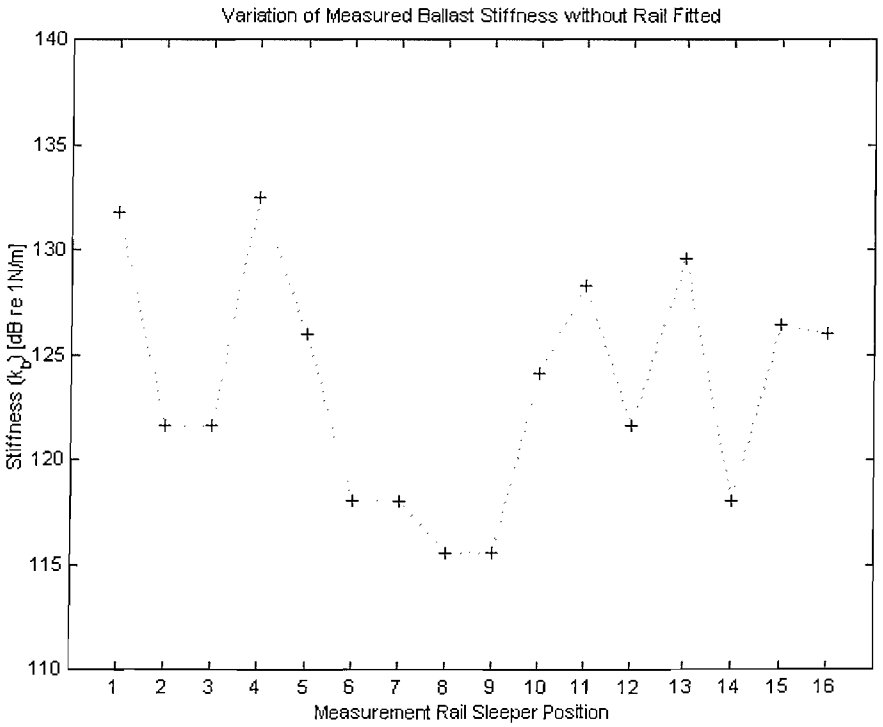

Figure 3–16 Variations in measured ballast stiffness from FRFs of individual sleepers

Table 3-3 Estimated values of ballast and sleeper assembly properties

Sleeper Number	Stiffness (k) [MN/m]	Damping Ratio (ζ)	Estimated Mass (m) [kg]	Actual Mass [kg]
MR1	3.9	0.2	1.25	1.205
MR2	1.2	0.2	1.4	1.217
MR3	1.2	0.2	1.4	1.207
MR4	4.2	0.2	1.5	1.217
MR5	2.0	0.2	1.5	1.175
MR6	0.8	0.15	1.5	1.177
MR7	0.8	0.1	1.65	1.177
MR8	0.6	0.1	1.65	1.177
MR9	0.6	0.1	1.4	1.171
MR10	0.1	0.15	1.5	1.175
MR11	2.6	0.15	1.25	1.175
MR12	1.2	0.1	1.5	1.171
MR13	3	0.1	1.4	1.219
MR14	0.8	0.1	1.5	1.215
MR15	2.1	0.1	1.5	1.213
MR16	2	0.1	1.5	1.211

3.6.2 Point accelerances of the rail

Point accelerance measurements of the track, with the rail fitted, were made at positions between the sleepers along the length of the rail. This measurement provides a good representation of the rig model track properties. Unlike the measurement of the discrete supports, it was easy to make (vertical) point accelerance measurements in between the sleepers as the instrumented hammer was used to excite the top of the rail, whilst the accelerometer was positioned on the underside of the rail. As for the measurements of sleeper accelerance, an average of ten hammer taps was made to provide the measurement at each point along the length of the track.

These measurements were compared with predictions from the TWINS track module RODEL. This module has been mentioned previously where it was used to demonstrate the effect of scaling in section 3.5.3, and it consists of a Timoshenko beam supported by two continuous elastic layers. Here the role of the RODEL model was to provide a simple way of characterising the 1/5 scale model track properties.

Values of the track ballast stiffness, sleeper mass, and rail pad stiffness were found by comparing the measured response with a fitted version of a prediction made by using RODEL. An example of this process is presented in Figure 3-17. The values used to obtain an adequate agreement between the RODEL prediction and the measurements are presented in Table 3-4 for each of the locations along the measurement rail section.

Table 3-4 shows that attaching the rail to the discrete supports causes great changes in the behaviour of the track bed. The estimated sleeper masses in Table 3-4 are, for example, seen to be lower than both the measured sleeper masses, and the predicted sleeper masses without the rail fitted (see Table 3-3).

The variations of ballast stiffness given in Table 3-4 are shown in Figure 3-18. This highlights a discrepancy between the estimated stiffnesses at individual sleeper supports with and without the rail fitted. Previously, Figure 3-16 showed the variation of ballast stiffness at each of the discrete supports along the length of the measurement rail. This showed a difference of 17dB between the lowest and highest stiffness measurements.

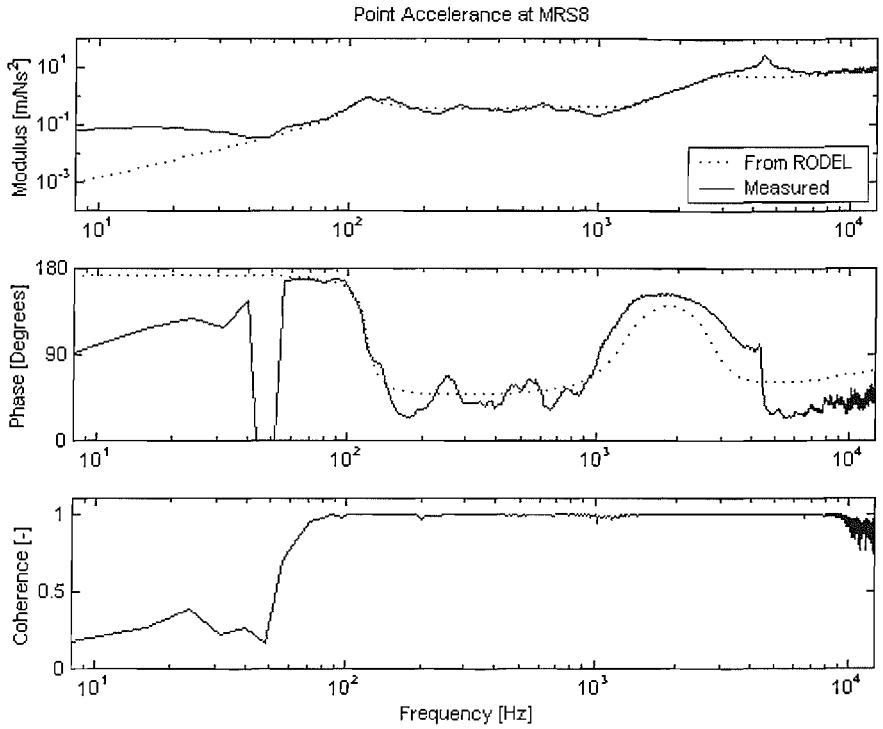

Figure 3–17 Predicted (using the RODEL model) and measured point accelerance at position MRS8

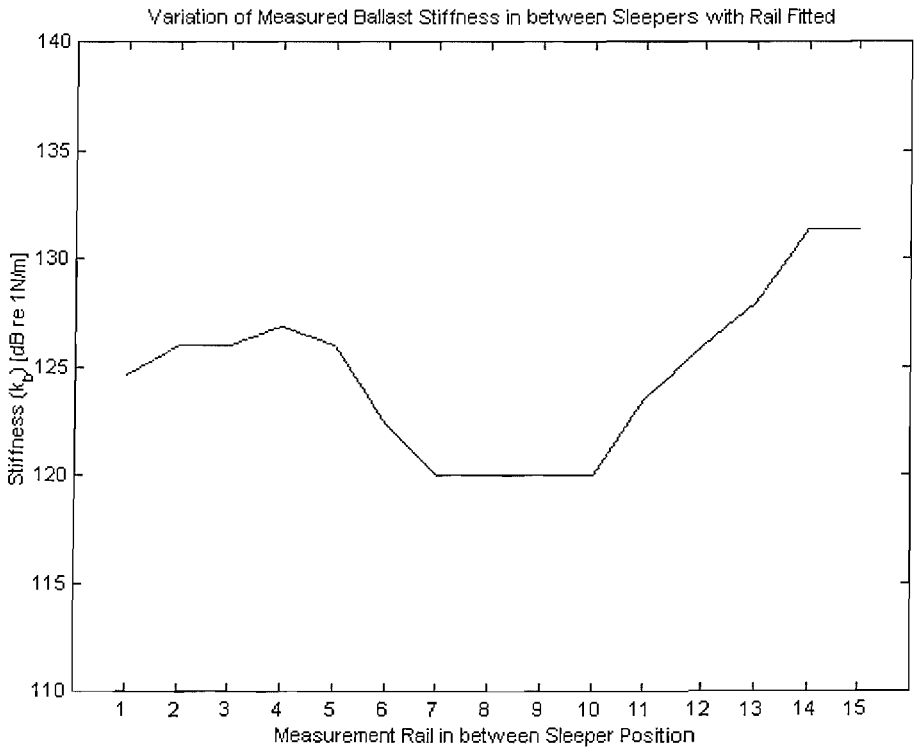

Figure 3–18 Estimation of ballast stiffness with all rails fitted

Table 3-4 Estimated parameter variations of measurement track with rail fitted

Position	Sleeper mass [kg]	Ballast Stiffness (k_b) [MN/m]	Ballast loss factor (η_b)	Pad stiffness (k_p) [MN/m]	Pad loss factor (η_p)
MRS1	1.1	1.7	0.4	70	0.2
MRS2	1.1	2	0.4	80	0.15
MRS3	1.1	2	0.4	80	0.15
MRS4	1.1	2.2	0.4	80	0.15
MRS5	1.1	2	0.4	80	0.15
MRS6	1.1	1.3	0.4	80	0.2
MRS7	1.1	1	0.4	80	0.2
MRS8	1.1	1	0.4	80	0.2
MRS9	1.1	1	0.4	80	0.2
MRS10	1.1	1	0.4	80	0.2
MRS11	1.1	1.5	0.4	80	0.2
MRS12	1.1	2	0.3	80	0.15
MRS13	1.1	2.5	0.4	80	0.2
MRS14	1.0	3.7	0.4	80	0.2
MRS15	1.0	3.7	0.4	80	0.2

The estimated stiffness from point accelerances measured in between the sleepers in Figure 3-18 show a difference of 11dB. This is a smaller difference, and therefore an improvement. But, Figure 3-18 also shows that by fitting the rail a smoothing effect is applied to the variation of each of the discrete support stiffnesses, due to the bending stiffness of the rails. The stiffness of the ballast of the supports towards the end of the measurement section (MRS 13 to 15) are seen to be higher than when they were measured separately (see Figure 3-16) due to the influence of the tangent rail.

The following behaviour of the track can be seen from Figure 3-17. At low frequencies the response is dominated by the stiffness of the ballast layer. The resonance peak due to the track mass bouncing on the ballast stiffness occurs at 120Hz. In the mid-frequencies, up to 1kHz, the accelerance is characterised by travelling waves that include the sleeper mass.

At higher frequencies the rail becomes decoupled from the sleeper due to the resilience of the rail pad. An anti-resonance dip occurs at 1.2kHz. This is also seen in the phase plot by a strong phase change at this point. At this frequency the sleeper vibrates between the two elastic layers. Next, the rail bouncing on the pad leads to a broad resonance at 3-4kHz. Superimposed on this is the pinned-pinned resonance of the discretely supported track, evident at 4.2kHz. The prediction model RODEL does not predict this peak as it is based on a continuous support model, as this is a feature of a discrete support structure. Above 8kHz the quality of the measured transfer function estimate reduces due to the poor signal level of the force and response in this frequency range.

The measurement made of the track point accelerance at MRS8 is an important static measurement, as it describes position at which the majority of the rail vibration measurements were made. The quality of the measurement therefore needs to be as good as possible, so that accurate model representations can be made. The measurement made at MRS8 is therefore shown in Figure 3-17 with the measured coherence of the transfer function. The measured coherence indicates a good quality (noise free) measurement between 90Hz and 8kHz with the exception of the track resonances at 120Hz and 4.2kHz.

3.6.3 Transfer accelerances

Transfer accelerances were made along the length of the measurement rail section in order to obtain the track decay properties. Decay rates are typically used to characterise the behaviour of a railway track. A track with low decay at a particular frequency, for example, is likely to radiate more noise than a track with a high decay rate at that particular frequency. A track with high decay characteristics therefore contains more damping, thus limiting the vibration due to wheel / rail interaction. A measurement of track decay is also used to provide a frequency-domain adjustment to allow predictions of rail vibration to be made corresponding to the average during the passage of a wheel. The track decay is proportional to the decaying part of the wavenumber β which is used in equation (2-4).

Decay rates along the rail were determined from the transfer accelerances in the following manner. An accelerometer was positioned in the centre of the measurement rail length at MRS8, on the underside of the rail. The measurement rail section was then excited by the use of an instrumented hammer on the upper surface of the rail (the railhead) at positions between the discrete supports of the track. An average of 10 hammer taps was taken for each transfer accelerance made between the positions LHS3 to RHS3 with the accelerometer at MRS8 (see Figure 3-14 for specific sleeper mid-span positions).

The magnitude of the transfer accelerance was typically found to increase as the excitation position was moved nearer to the accelerometer position at MRS8. The largest measured magnitude was found to be the (point accelerance) measurement made at MRS8. This is often referred to as the driving point accelerance and is shown in Figure 3-17. The decay along the length of the track is calculated by plotting the measured one-third octave-band levels as a function of distance from the driving point accelerance. The decay in each one-third octave-band is then found by estimating the gradient of the measured levels as a function of distance along the track, away from the driving point accelerance position at MRS8. These results are referred to as 'manual' measurements.

Figure 3-19 and Figure 3-20 shows the decay in dB/m against frequency obtained for the measurement rail with tangent rails fitted. The two figures correspond with measurements on either side of the accelerometer positioned at MRS8. The decay rates

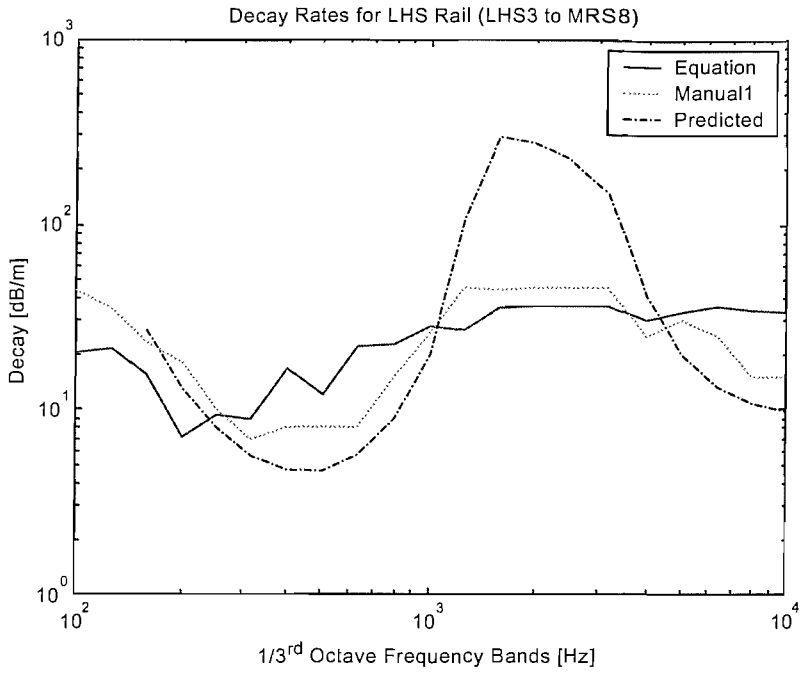

Figure 3–19 Decay rates along the measurement rail with tangent rails fitted (LHS3 to MRS8)

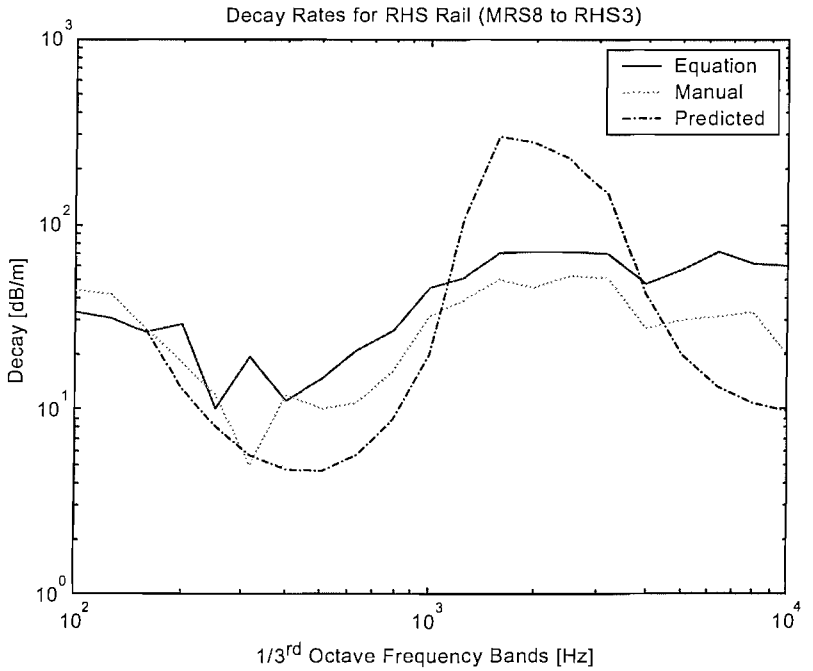

Figure 3–20 Decay rates along the measurement rail with tangent rails fitted (MRS8 to RHS3)

were also determined from the measured frequency response functions using the following procedure [de France 1998]:

$$Decay[dB/m] = \frac{10\log_{10} e}{\sum_i \left(\frac{A_i}{A_0}\right)^2 \Delta z_i} \tag{3-6}$$

where: A_i is the amplitude at an incremental distance,

A_0 is the driving point amplitude at the position of the accelerometer,

Δz_i is the incremental distance between each measurement position.

The results in Figure 3-19 and Figure 3-20 are also compared with predictions from the RODEL model [Thompson and Vincent 1995] using the vertical input parameters presented in Table 3-5. The predicted decay rates, obtained using RODEL, are seen to be lower than the measurements between 100Hz and 300Hz, larger between 1kHz and 4kHz, and lower again at high frequencies. A possible explanation for this discrepancy is presented in Chapter 5 where an alternative method of measuring the track decay rates is described.

Table 3-5 Vertical input values to RODEL

Vertical Value Input to RODEL Program	
Rail vertical EI product	4657.5Nm^2
Rail vertical loss factor	0.02
Mass per unit length of the rail	2.355kg/m
Vertical pad stiffness	100MN/m
Vertical pad loss factor	0.2
Vertical ballast stiffness	1.2MN/m
Vertical ballast loss factor	0.4
Sleeper mass	1.2kg

3.6.4 Joints between tangent and measuring rails

Provisions were made to enable the measurement rails to be removed and refitted, so that different rail surfaces could be measured. Fishplates were used to join the three sections of rail, an example of which is shown in Figure 3-21. The presence of these fishplate joints, and the discontinuous nature of the rail, however, was found to lead to reflections (modal behaviour) in the track response.

Fluctuations occur in the modulus and phase of the accelerance in the region between 150Hz and 1kHz (see Figure 3-17). Figure 3-22 shows an enlargement of this frequency range. These are attributed to reflections due to the finite nature of the track. This was confirmed by comparisons between predictions and measurements of the track. Analysis of the response of a half-length of the measurement rail, that had been cut to make a step-up / step-down joint, initially helped these investigations, as the fluctuations in the frequency response of a rail with a free end were found to be much larger in amplitude than those shown in Figure 3-22. The findings from this analysis proved to be applicable to a full-length rail as well. For reasons of brevity only the results for the full length rail are presented here.

The drive point response of the full-length rail was measured at a position between two sleepers in a sleeper bay in the centre of the rail length at MRS8. This position is shown in Figure 3-14. Even though the measurement section of the rail is supported at 15 points along its length, it was found to be behaving much like a clamped-clamped beam. It could be considered that the fishplates were behaving like clamps that attached the measurement rail section to the tangential rails at each of its ends (see Figure 3-14: LH and RH rail).

The natural frequencies of a clamped-clamped beam of length L can be found from [Kinsler et al, 1982]:

$$\tan\frac{kL}{2} = \pm\tanh\frac{kL}{2} \qquad (3\text{-}7a)$$

where k is the wave number associated with each mode. The solutions to this are given as:

$$L = \frac{n}{4}\lambda \quad where \quad n = 3.0112, 5, 7, 9, 11, 13, \ldots \qquad (3\text{-}7b)$$

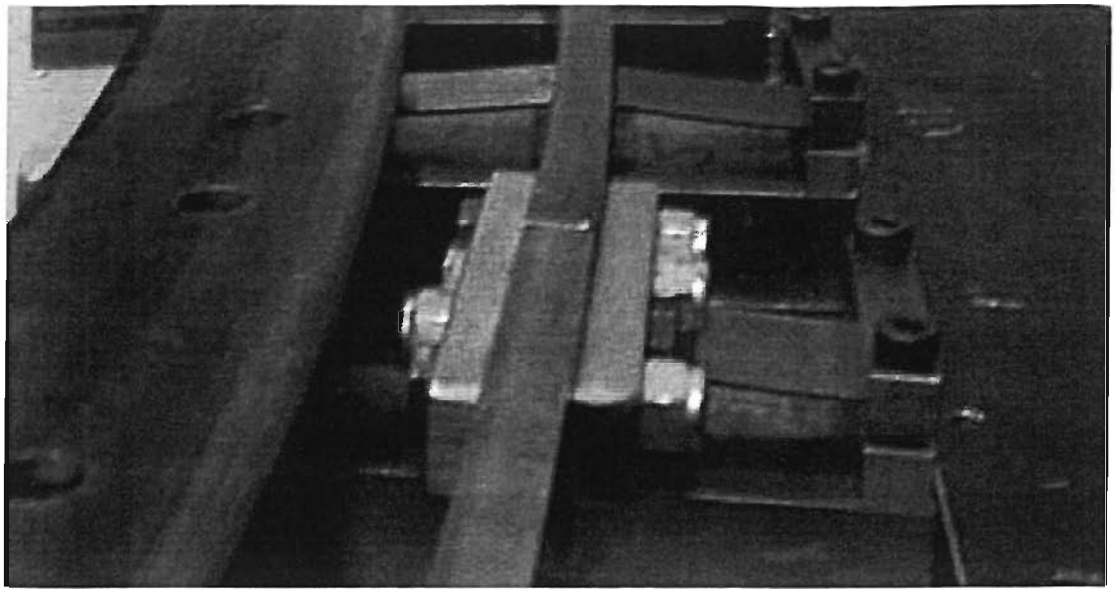

Figure 3–21 Picture of the fishplate arrangement used to connect the tangent rails to the measurement rail section.

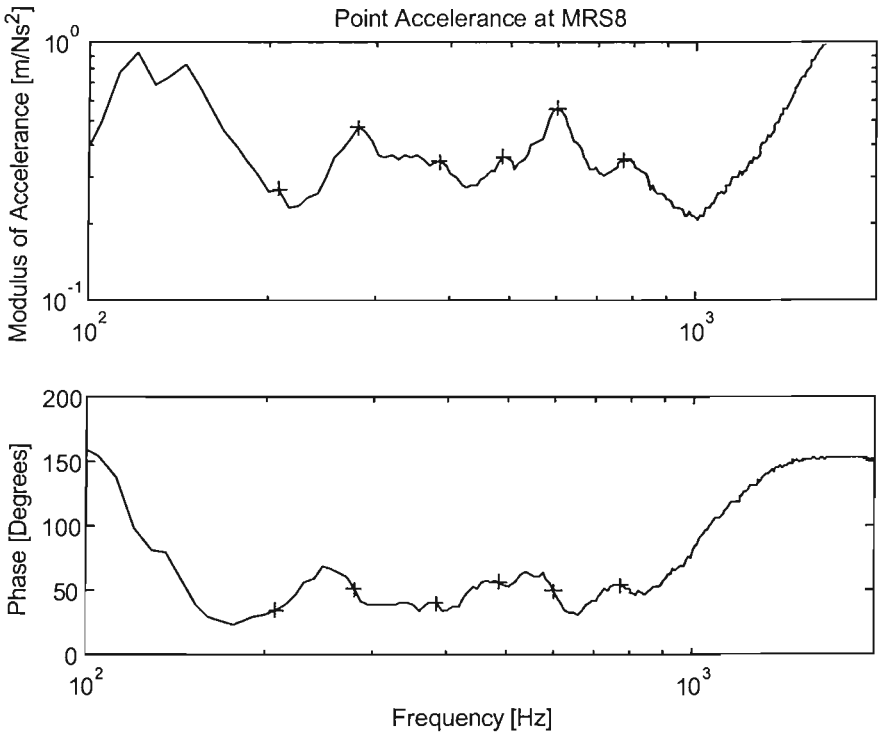

Figure 3–22 Enlarged view of the point accelerance measurement made at MRS8 including the positions of the peaks and troughs in the modulus and phase.

$$k = \frac{2\pi}{\lambda} \qquad \text{i.e.} \qquad k = \frac{\pi n}{2L} \tag{3-7c}$$

The peaks in the modulus and points of maximum change of the phase of the point accelerance measurement were found (Figure 3-22) and the frequencies of these were then used to calculate the assumed wave numbers using equation (3-7b) and equations (3-7c). The results (see Figure 3-23), using a value of L=2m which is the length of the 'measurement' rail section, were then compared with the predictions of a beam on a double elastic layer (RODEL [Thompson and Janssens, 1997]) used above. Good agreement was found by using $n = 7$ to $n = 23$ (odd numbers) in equation (3-7b), as shown in Figure 3-23.

These findings showed that the ripples in the frequency response between 150Hz and 1kHz correspond with the modal behaviour of a (2m long) clamped-clamped beam and the predicted behaviour of the track from the RODEL model. The good agreement between the RODEL model prediction, and the estimated wavenumber (found by converting a value of frequency that corresponds with a ripple in the frequency response and assuming clamped-clamped beam behaviour) indicates that it is likely that the fishplate joints cause reflections in the track response, rather than this being due to the free ends of the rail, for which a larger value of L would be required in equation (3-7a).

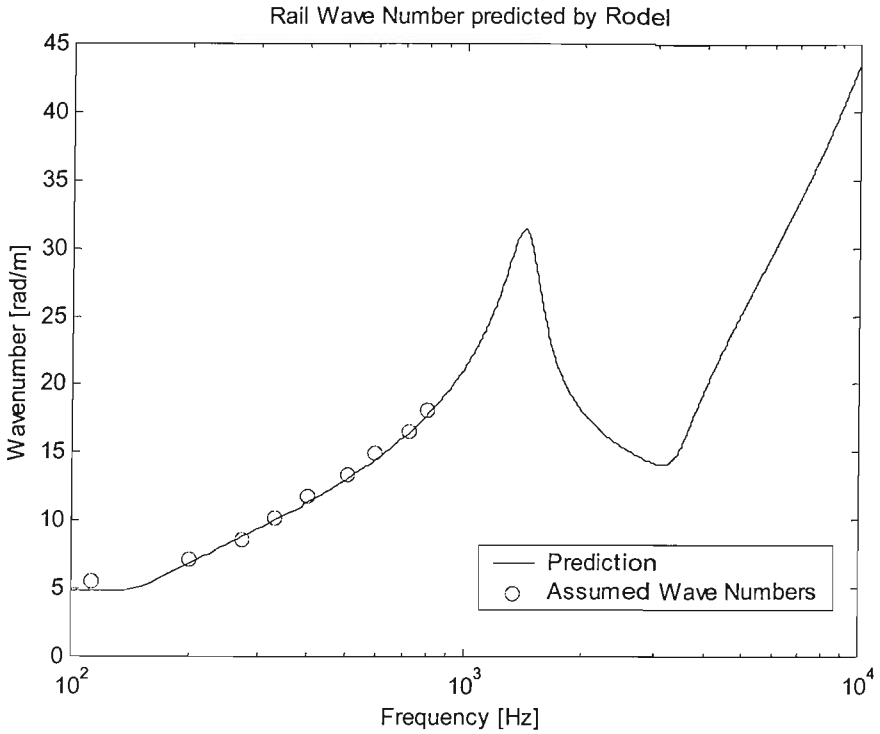

Figure 3–23 Comparisons of the calculated wave numbers (assuming clamped-clamped beam behaviour) with the predicted wave number as a function of frequency made with the RODEL model.

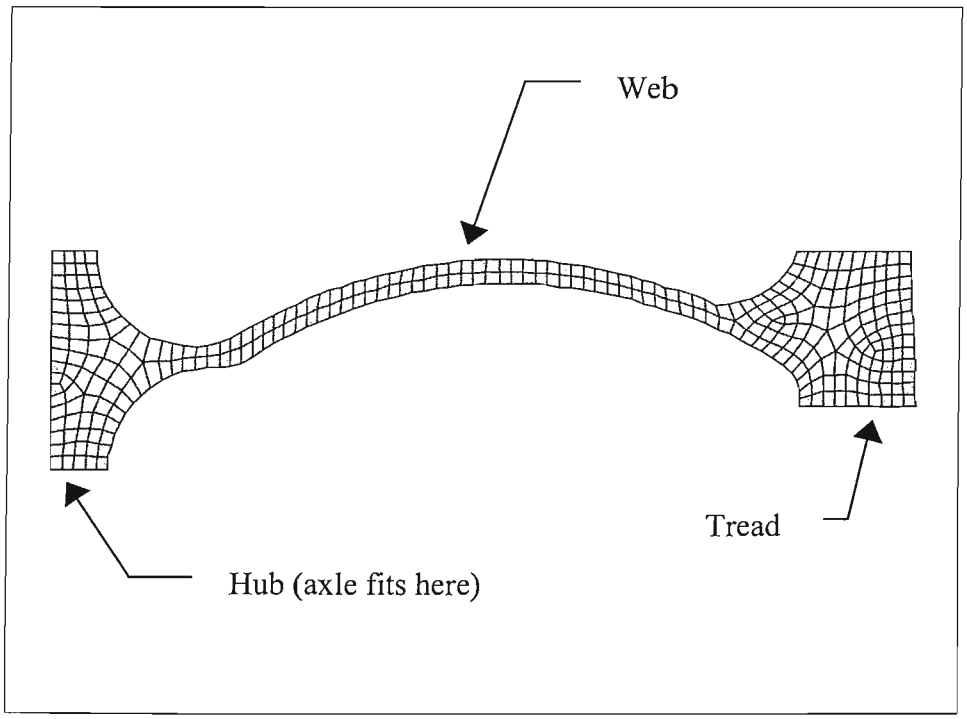

Figure 3–24 Finite element mesh of the rig wheel cross section.

3.7 Measurements of the rig wheel and spring assembly

Measurements of the rig wheel were made both with it unfitted and fitted in the wheel and spring assembly. These measurements were primarily made to help characterise the behaviour of the wheel by comparing its measured accelerance with a predicted accelerance generated from a finite element model.

The measurement of the rig wheel accelerance was made by removing the wheel from the rig and suspending it above an electrodynamic shaker. The shaker was used to excite the wheel via an impedance head and 'stinger' arrangement at a point of the wheel tread. This measurement represents the behaviour of the rig wheel at the point of wheel / rail contact.

In order to verify the measurements of the wheel a finite element (FE) model made using a package called ANSYS, was constructed from careful measurements of the wheel dimensions. Only the wheel cross section was modelled as the FE package could make allowances for the wheel axi-symmetry. This is shown in Figure 3-24. Comparisons between the measured and predicted wheel point accelerance are presented in Figure 3-25. This shows that only some of the features predicted by the FE model correspond with the measurement. It is assumed that this is because of the position of the impedance head on the circumference of the rig wheel, thus not all of the modes of wheel vibration are seen at this position. Whilst agreement between the FE model and the measured FRF is not particularly good across the whole frequency range considered (100Hz to 12.8kHz) the predicted behaviour does have similar characteristics. The similarities are sufficient to permit a conclusion that the measurements were reasonable representations of the wheel behaviour.

Additional point accelerance measurements were made of the rig wheel when it was fitted to the rig spring assembly. An example of this measurement is presented in Figure 3-26. This shows that the measurement of the wheel point accelerance does not dramatically change when it is fitted to the spring assembly.

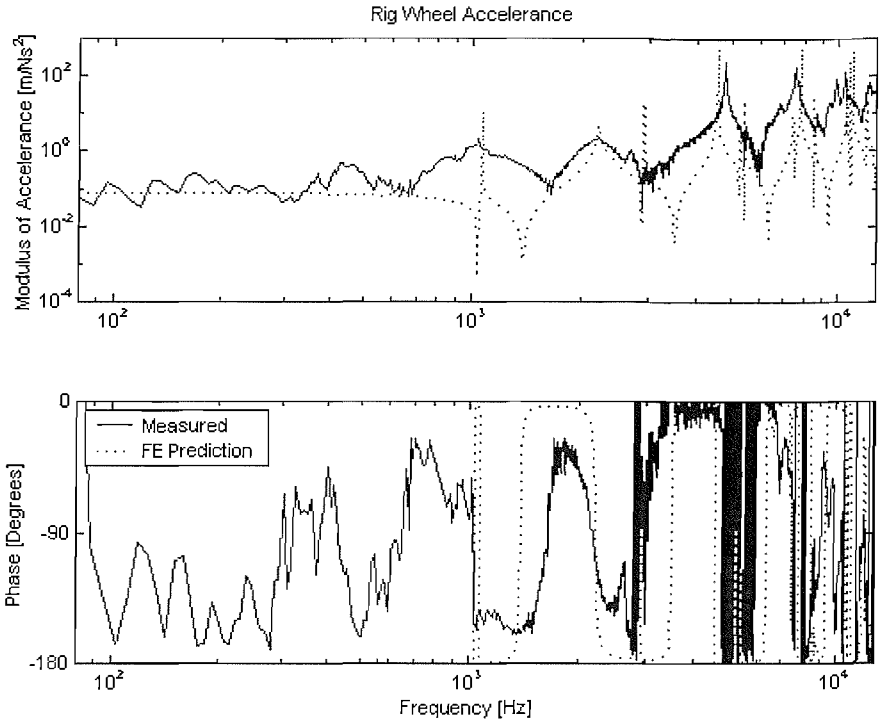

Figure 3–25 Measured wheel point accelerance and predicted point accelerance made from the finite element package ANSYS.

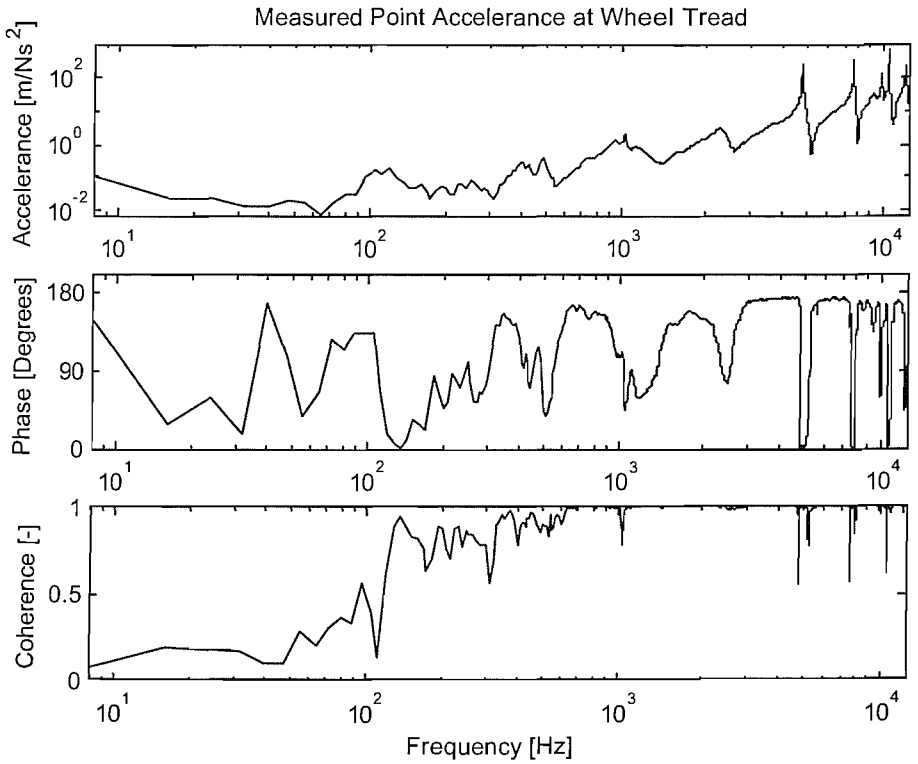

Figure 3–26 Measured wheel point accelerance when fitted to spring assembly.

3.7.1 Calibration of the rig wheel pre-load spring

Before any rolling wheel measurements of vibration were made, the wheel pre-load spring was calibrated. This was primarily done to find out the maximum wheel pre-load that could be applied to the rig wheel, but this calibration also proved to be useful in attempting to develop an alternative method of surface profile measurement using the force gauge as a transducer. This method is described in Chapter 4, where it is seen to be adequate for wavelengths larger than the wheel / rail contact patch dimensions.

Calibration of the rig pre-load spring was performed primarily with a static test rig (in the Mechanical Engineering department of the University of Southampton). This rig slowly applies a load to the spring whilst measuring its deflection. The results shown in Figure 3-27. Here a linear trend is seen for compressive loads applied to the spring in the range 10N to 1kN. This linear trend can be expressed as a stiffness (k) of 11.5kN/m.

A measurement of the point receptance of this spring was also made. This was done by attaching a shaker and an impedance head to one end of the spring, clamping the other end of the spring to a solid base plate, and exciting it with a white noise signal via the electrodynamic shaker. The result of this experiment is presented in Figure 3-28. This shows that the vertical vibration of the pre-load spring is much like an idealised spring receptance at very low frequencies. At higher frequencies, however, strong modal behaviour is seen to dominate the response. This is due to standing waves in the spring. The measurement shown in Figure 3-28, makes it clear that above 30Hz, the spring does not behave like its idealised representation. Further investigations into this effect were not made, however, as it did not obviously have any influence on the measurements of wheel / rail interaction made on the rig.

3.8 Discussion and summary

The re-construction of the rig's track bed was a lengthy and difficult task, but has resulted in a free vibration response close to the predictions of the RODEL [Thompson and Janssens, 1997] model. In-depth analysis of the track performance has been made.

Variations of the bonding between each of the sleepers and ballast layers appear to be responsible for the different levels of stiffness and mass found when comparing the measured frequency response functions with the SDOF model. Comparisons with the

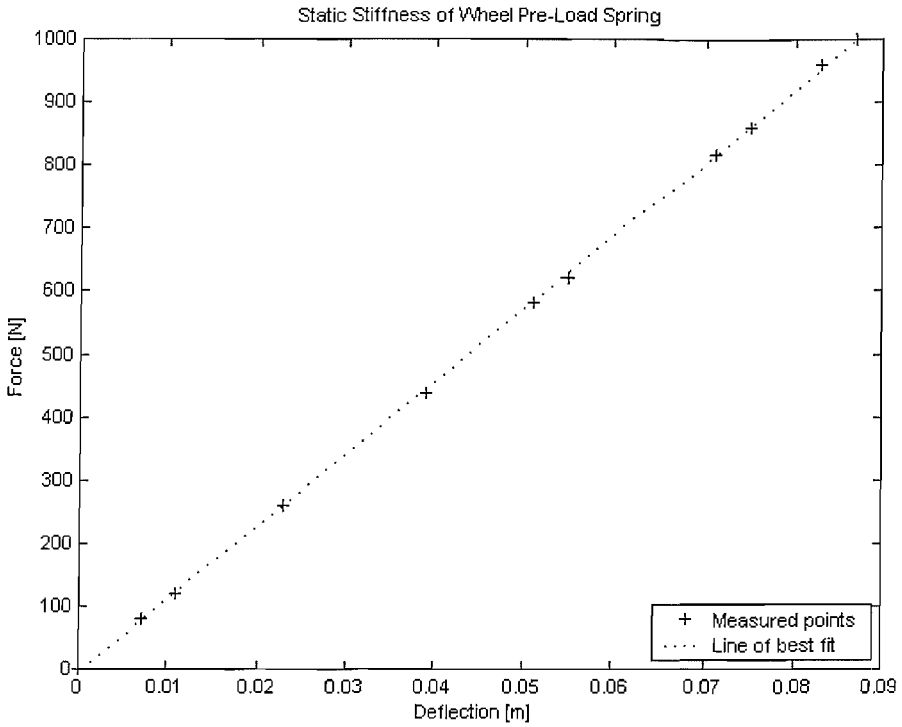

Figure 3–27 Measured force and compression of the rig wheel pre-load spring. Stiffness constant (k) was found to be 11.5kN/m.

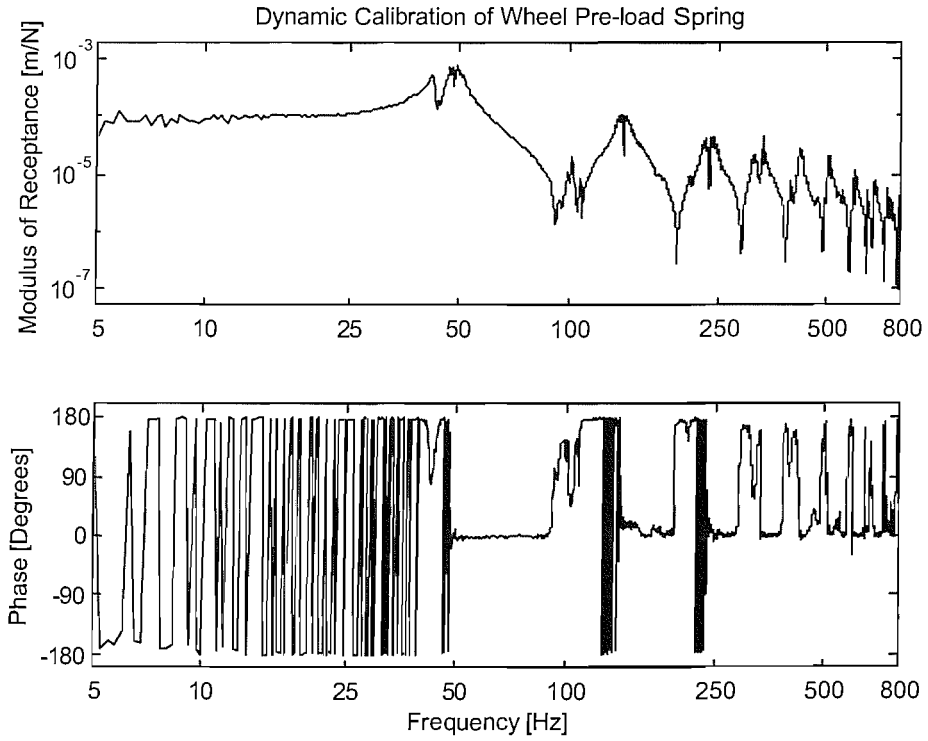

Figure 3–28 Measured point receptance of the rig wheel pre-load spring.

stiffnesses derived from the mid-span measurements of the track response, using RODEL, demonstrate an averaging effect of the variation in support stiffness when the rail is fitted. This is shown by the results in Figure 3-16 and Figure 3-18 and the values in Table 3-3 and Table 3-4.

A comparison between the parameters applying to the model rig and those of an equivalent full size track is given in Table 3-6. This shows that the model rail is not quite as stiff as a comparable full size track. This is because the model rail cross section was based on a rectangular extrusion for ease of manufacture. The mass per unit length of the rail however is quite typical at an equivalent of nearly 60kg/m.

The equivalent vertical stiffness value for the pad of 400MN/m gives a representation of a medium-stiff pad and therefore corresponds quite well with a full size case. The vertical stiffness of the 1/5 scale rig 'ballast' is rather low. This has a minimal effect on the frequency range of interest (a resonance frequency of 180Hz on the model scaling down to 36Hz on the full-scale track). Unfortunately the ballast loss factor does have an effect on the track decay rate. The loss factor for the rig (which according to the scaling laws in Table 3-2 does not change) only has a value of 0.4 compared with 1 to 2 for the full size track. Even so, the measured decay rates shown in Figure 3-19 and Figure 3-20 indicate large levels of decay in the frequency range considered. This means that the vibration of the track at the wheel / rail contact point is expected to decay quite quickly with distance.

It has been shown that the decay rates, in 1/3-octave bands, of the rail differ considerably from the RODEL prediction. Nevertheless the decay rate in both cases is quite large in most of the frequency bands. Both the smallest and largest decay rate is predicted by the RODEL model which estimates decay rates in the range 2.5dB/m to 150dB/m (see Figure 3-19 and Figure 3-20). The measured decay rates show a smaller range, from 10dB/m to 80dB/m. The method used to calculate these results is compared later in Chapter 5 with an alternative method of assessing the decay along the length of the 1/5 scale track bed. Comparison of these two methods suggests that the manufacture of the 1/5 scale track bed was not as good as had been expected and may have influenced the results.

Table 3-6 Comparisons between model and equivalent full size track

	Measured / Calculated	Equivalent Full Size[5]
Rail vertical EI product	4657.5Nm^2	2.91MNm^2
Rail lateral EI product	517.5Nm^2	323kNm^2
Rail vertical loss factor	-	0.02
Mass per unit length of the rail	2.355kg/m	58.9kg/m
Vertical pad stiffness	Measured independently 201.13 MN/m, Measured on model to be 70 to 80MN/m	400MN/m
Vertical pad loss factor	0.15 to 0.2	0.15 to 0.2
Vertical ballast stiffness	Measured on model to be 1 to 3.7MN/m	5 MN/m to 18.5MN/m
Vertical ballast loss factor	0.4	0.4
Sleeper mass	1 to 1.1kg	125kg to 137.5kg

[5] Calculated from scaling values given in Table 3-2

Analysis of a point accelerance measurement of the 1/5 scale rig track bed has indicated that reflections are evident in the track response due to standing waves in the finite length of the measurement rail section and the fishplate connections. This effect was not thought to have a strong influence on the outcomes of the forthcoming investigations because the fluctuations measured were small.

The frequency response of the rig wheel has been investigated together with measurements of the pre-load spring. Each element of the 1/5 scale wheel / rail rig has thus been measured and analysed so that the performance of the rig may be assessed for the situations of rolling (vertical) vibration presented in the following chapters.

The investigations described in this chapter have allowed the parameters to be established for the vibration prediction models (described in Chapter 2) This will enable comparisons to be made between the measurements and predictions of wheel / rail interaction due to different railhead profiles. A list of the 1/5 scale wheel / rail rig parameters is presented in Table 3-6 and Table 3-7. A method of obtaining the inputs for the prediction models (the surface profiles) is presented next.

Table 3-7 Other 1/5 scale wheel / rail rig specifications used for the prediction models

Item	Symbol	Value
Rig wheel radius	R_w	0.1m
Rail transverse radius	R_{rt}	40mm
Effective radius	R_e	28.6mm
Wheel and spring assembly mass	m	15kg
Elliptical contact patch length for the lowest wheel pre-load (530N)	a	0.8mm
Elliptical contact patch width for the lowest wheel pre-load (530N)	b	0.44mm
Linearised Hertzian contact stiffness for the lowest wheel pre-load (530N)	k_H	141MN/m
Elliptical contact patch length for a highest wheel pre-load (1kN)	a	1mm
Elliptical contact patch width for a highest wheel pre-load (1kN)	b	0.5mm
Linearised Hertzian contact stiffness for the highest wheel pre-load (1kN)	k_H	174MN/m

4 The measurement of surface geometry

4.1 Introduction

The models used in this thesis are all based upon the assumption that wheel and rail vibration is initiated by surface roughness [Remington, 1976]. Accurate measurement of surface profiles is therefore a vital part of the prediction of wheel / rail vibration, as the response of a model is directly influenced by its input. This chapter discusses the method of measuring surface profiles. The discussion and results presented in this chapter are thus a crucial part of the research. Predictions of wheel and rail vibration cannot be expected to be in good agreement with measurements if the input is not correct.

In Chapter 1 several forms of wheel and rail surface geometry were introduced. These are wheel flats, dipped (welded) rail joints, stepped rail joints, railhead corrugation, surface roughness, and discontinuities caused by points and crossings. As an input to a model, such surface geometry should ideally be measured, although some geometrical forms can be, and have been, approximated by idealised forms (see for example [Anderson and Dahlberg, 1998, and Wu and Thompson, 2001 (a and b)]).

The surface geometry, however, not only provides an input to the model, but can also indicate the most appropriate type of prediction model to be used. This was demonstrated by [Wu and Thompson, 2000(a)] who compared the performance of a linear model (in which a continual contact between the wheel and rail is assumed) with a non-linear model that allowed loss of contact. It was found that the likelihood of loss of contact between the wheel and the rail was a function of wheel load and surface geometry. Larger amplitudes of surface profile were more likely to lead to the wheel unloading from the rail. Where wheel unloading is likely to occur, a linear contact spring relationship cannot reliably be used.

A measurement of surface geometry is preferable to an idealised approximation, as it more likely to contain more detailed information. The process of measurement, however, is not a trivial task. Ideally, the surface measurement should be long enough to contain the largest wavelengths of interest. For measurements of railhead corrugation this can mean measurement lengths over several metres of track [Grassie and Kalousek, 1993].

4.2 Choice of transducer for the measurement of wheel and rail surface geometry

Different methods of measuring surface roughness have been discussed in Chapter 1. There it was stated that two types of transducer are commonly used to measured surface roughness. These are accelerometers or displacement transducers. Only displacement transducers are considered in this chapter. These were used in the research due to:

- the short distances of measurement length (less than 1.5m),
- the availability of a fixed reference point for a displacement transducer (the rig beam) for the measurement of the railhead surface profile,
- the situation that the wavelengths of interest in the scale model are shorter than full-scale (see section 4.3.1) making accelerometers less able to cover the required range,
- ease of availability,
- relatively low cost.

The performance of the displacement transducer needs to meet the following demanding criteria:

1. It should have a dynamic range that can enable measurements of the smallest amplitudes from less than a micron [Jones and Thompson, 2000], to corrugations as large as 0.2mm [Clark et al, 1982], and possibly even greater amplitudes to allow for any long wavelength fluctuations (or trends) within the measurement length.
2. The transducer response should be linear in the frequency and amplitude range of interest.
3. A good signal-to-noise ratio is required so that accurate measurement of the smallest amplitudes is ensured. Ideally the signal-to-noise ratio should be as large as possible. [Grassie et al, 1999] suggest a typical rule of thumb for satisfactory instrumentation, that the instrumentation precision should be at least ten times greater than the measurement required. This corresponds with a signal-to-noise ratio of 20dB.

4. Loss of contact between the transducer probe and the surface during the measurement must not occur. This means that the displacement transducer probe has to be spring loaded.

5. As the transducer probe has mass and is sprung loaded it has a dynamic response. Its dynamic effects should have a negligible effect on the measurement process. The measurement of surface geometry is therefore made at a very low speed so that the surface geometry wavelengths do not excite the dynamic effects of the probe and contact is maintained throughout the measurement.

6. Finally, the probe tip diameter needs to be large enough to be able to negotiate the surface amplitudes without getting stuck. It also needs to be either the same size, or preferably smaller than the diameter of the wheel to ensure that an accurate representation of the surface geometry as seen by the wheel / rail contact can be obtained. Typically, the probe diameter is much smaller than the wheel diameter, which results in a more detailed than necessary roughness measurement. Allowances are made for this in processing the data and are described below in Section 4.4.

A common displacement transducer that is capable of meeting these requirements is a linear variable differential transformer (LVDT). This transducer typically consists of a magnetic core that moves within a coil arrangement [Haslam et al, 1981]. The coils are excited with a high frequency alternating current that is modulated by changes in the position of the core displacement. After de-modulation, the resulting signal output is proportional to the displacement applied to the probe. The LVDT used throughout this research was a spring-loaded LVDT (probe radius 1mm) manufactured by RDP Electronics (Model D5 combined with the S7AC in-line amplifier).

The following section describes the methods used to measure profiles on the 1/5 scale rig, including an investigation of the suitability of the LVDT used for this purpose.

4.3 Measurement of roughness on the 1/5 scale rig

4.3.1 Determining the wavelength range required for a prediction

As indicated previously, in Chapter 1, an ideal surface geometry input to a wheel / rail prediction model would be a three-dimensional representation made from many parallel measurements of surface geometry across the contact zone. This is not possible on the

1/5 scale rig because the dimensions prohibit such parallel measurements, as the estimated contact patch width for a typical wheel load (800N) is only 0.5mm. Therefore only single line measurements of surface geometry were made on the railhead centreline along as much of the length of the railhead as possible.

In [Thompson, 1996] it is stated that, for train speeds in the range 50km/h to 300km/h, the roughness wavelengths that need to be measured fall within a range 3mm to 830mm. The range of wavelengths required for the predictions of the vibration on the 1/5 scale rig are calculated from the relationship ($\lambda = V/f$) presented previously in Chapter 1 (equation (1-1)).

The range of wavelengths that are required on the 1/5 scale wheel / rail rig are tabulated in Table 4-1 for a speed range 1m/s to 6m/s. This shows that for frequencies between 50Hz and 10kz the largest wavelength required is 120mm and the shortest wavelength is 0.1mm. Measurement of components at a wavelength of 120mm, assuming that they exist (and are large enough to be measured), should not be a problem for the measurement method detailed below, but measurement of components of the shortest wavelength is not so easy. If it is assumed that the amplitudes at the shortest wavelength are large enough to be measurable, then the longitudinal spatial increments at which this wavelength is measured (or sampled) must themselves have a finer resolution.

Table 4-1 shows that the shortest wavelength of 100μm corresponds with the highest frequency at the lowest rig wheel speed. Shannon sampling theorem, which is widely quoted in many texts such as [Oppenheim and Schafer, 1975], requires a sample rate of at least twice the highest frequency that is being measured. From this the following analysis can be made. To obtain a 10kHz frequency a sampling frequency of at least 20kHz must be used. The reciprocal value of this corresponds with a time spacing or sampling interval ($\Delta t = 1/f_s$) which can be substituted into equation (1-1) to find the corresponding shortest distance spacing. This was found hence to be 50μm. Thus the minimum number of points that can be used to describe a wavelength (according to the Shannon sampling theorem) is two. A more detailed representation might use six points to describe a 100μm wavelength. This would require a spatial resolution of 17μm.

The following sections describe how an adequate spatial resolution is obtained and how the effects of the transducer are considered. Then a description of the measurement method will be given.

Table 4-1 Wavelengths of consideration

Frequency		Wheel Speed	
		1m/s	6m/s
	50Hz	20mm	120mm
	100Hz	10mm	60mm
	1kHz	1mm	6mm
	10kHz	0.1mm	0.6mm

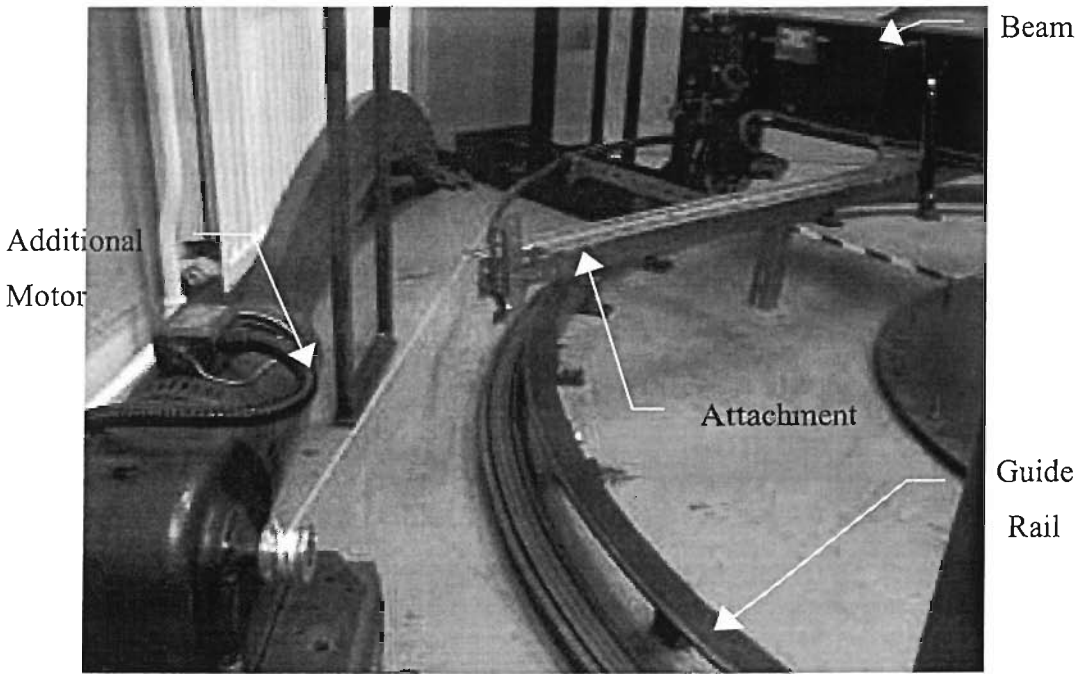

Figure 4-1 The method of roughness measurement on the 1/5 scale rig as developed by London Underground [ORE report C163/RP11, 1988].

4.3.2 Determination of spatial position on the 1/5 scale rig

A previously devised method of measuring railhead roughness on the rig is described in [ORE report C 163/RP11, 1988]. This method relied upon an auxiliary motor to pull the rotating beam at a constant speed (see Figure 4-1). An attachment to the rig guided a 'pulling' wire from the end of the beam in a tangential direction towards the auxiliary motor, where it was wound around a pulley. A LVDT was attached to the other end of the rig beam (out of picture) for the measurement of the vertical surface roughness amplitudes. In this method it was attempted to measure surface roughness amplitudes, at a constant speed, in the time domain. The measurement could be expressed as a function of distance (x) by multiplying the measurement time (t) by the constant measurement speed (V). This could then in turn be converted back to a time base for a different wheel speed, according to the requirements of a prediction. This method of converting a spatial measurement into a time domain representation for a particular wheel speed has been discussed previously in Chapter 1.

Under ideal circumstances this method should produce good results. However, it was found in practice to be hard to maintain a constant speed whilst turning the beam in this manner. The connection between the auxiliary motor (see Figure 4-1) and the rig beam was not always rigid (as the rig beam bearing suffered from 'stiction' / friction at low speeds), resulting in a jerky horizontal movement of the LVDT probe. A similar problem of maintaining a constant speed for the wheel surface profile measurements was also found. For this method of surface profile measurement to be reliable, a constant speed is crucial to allow the roughness to be sampled at fixed distance intervals along the surface. If the measurement speed varies, then the relationship $x = Vt$ cannot be used over the entire length of the measurement section, and the calculation of the distance measured is inaccurate.

An alternative approach has therefore been devised here, similar to that presented by [Dings and Dittrich, 1996] for wheel roughness measurements, where a fine resolution tachometer is incorporated into the sampling process. In this way it is possible to measure the surface roughness at fixed spatial intervals along a surface without having to ensure a constant velocity. A diagram of the tachometer assembly developed here is given in Figure 4-2.

The tachometer assembly consists of a wheel that is rigidly mounted on a shaft, which is then attached to the tachometer via a flexible tubular coupling. The shaft is secured to a

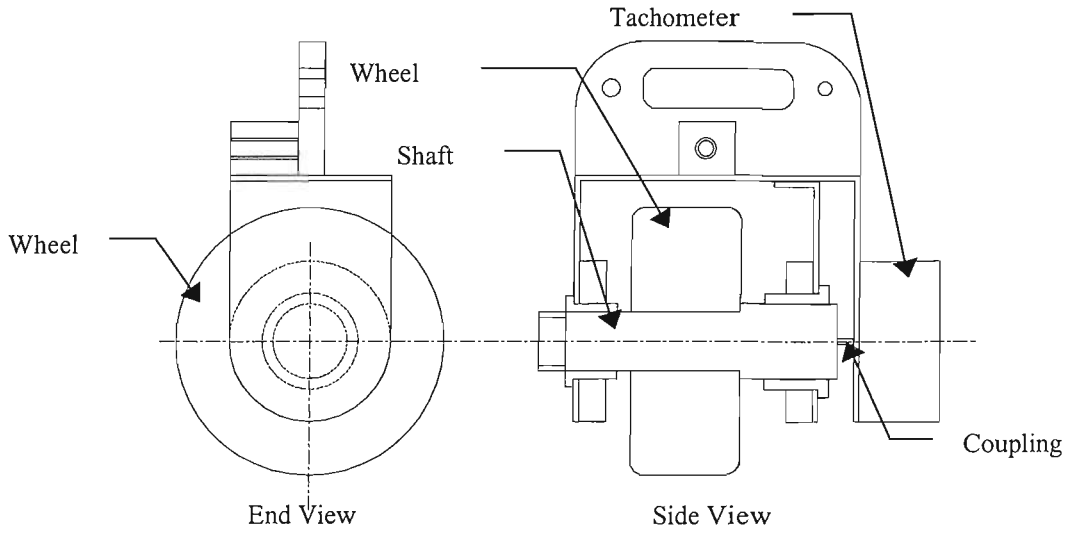

Figure 4-2 Schematic diagram of the tachometer assembly.

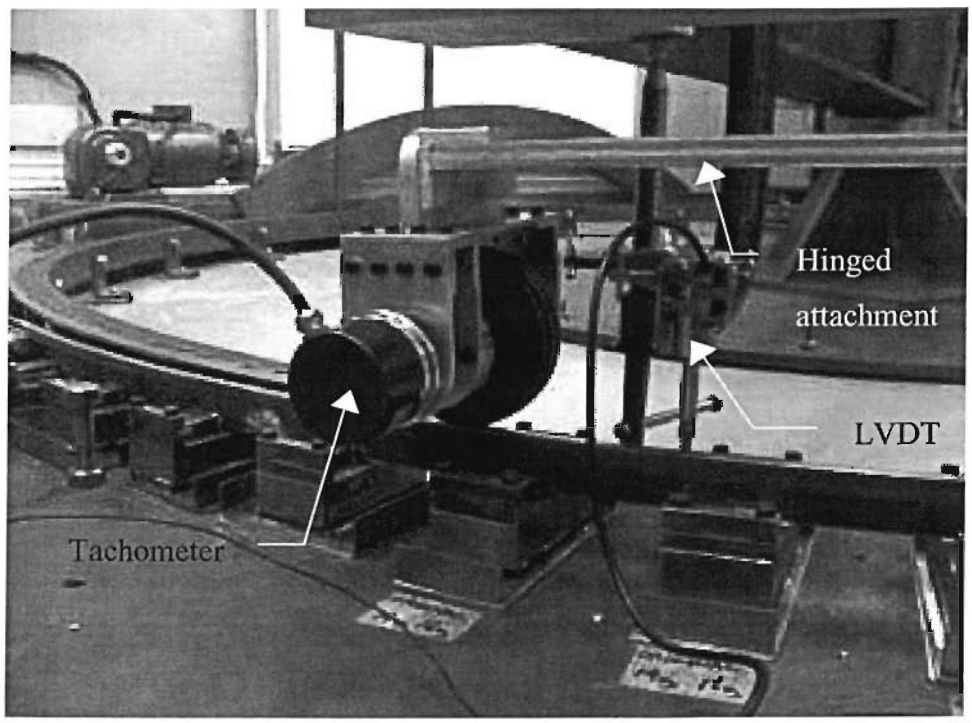

Figure 4-3 The tachometer assembly connected to the rig beam with the hinged attachment and the tachometer wheel running on the 'measurement' railhead to the left of the LVDT.

rigid frame by two plain bearings. The tachometer has a fine resolution of 2048 pulses per revolution. The distance between each pulse equates to a distance of 0.15mm for the 50mm tachometer-wheel radius. It should be noted that although the tachometer pulse spacing is small, it is of comparable dimensions of the smaller roughness wavelengths considered in Table 4-1. The consequence of this is considered and accounted for later in Section 4.3.4.

An additional hinged attachment has also been developed to attach the tachometer assembly to the rig beam for the measurement of a railhead profile. This is shown in Figure 4-3 and Figure 4-4. The hinged beam allows the tachometer-wheel to move freely in a vertical direction, thus ensuring contact with the rail is maintained despite any railhead discontinuities. After the tachometer assembly is secured to the beam (see Figure 4-3), the beam is turned slowly by hand, so that a distance of about 1.2 metres is measured during an acquisition time of approximately 65 seconds. This speed, of about 19mm/s, has been found to give acceptable results when using the LVDT to measure (vertical) surface amplitudes. No skipping or juddering of the LVDT probe was noticed during the measurement, which meant that there were no excessively large spikes in the roughness measurement data. Spikes had sometimes been observed at measurement speeds greater than 30mm/s. For railhead measurements the path of the LVDT probe was chosen to be as representative of the wheel / rail contact as possible by measuring along the visible line of wheel / rail contact on the dull railhead surface. This was formed after many passes of the wheel on the rail and was about 0.5mm wide.

When measuring a wheel profile, the tachometer assembly is held in contact with the (rig) wheel whilst it is slowly turned by hand. The use of the tachometer assembly therefore allows for small changes in the measurement speed. Great care is taken to ensure that the tachometer wheel remains in contact with the measured surface (with no slippage) so that the distance along the surface is measured correctly.

Measurements of surface roughness and railhead discontinuities were performed throughout this research with the use of the tachometer assembly, rather than the method used by the previous research project [ORE report C 163/RP11, 1988]. Each of the different railhead cases was measured with an LVDT together with the newly designed tachometer assembly. This transducer was used throughout the research project as a 'known method' of measuring surface geometry profiles. An alternative

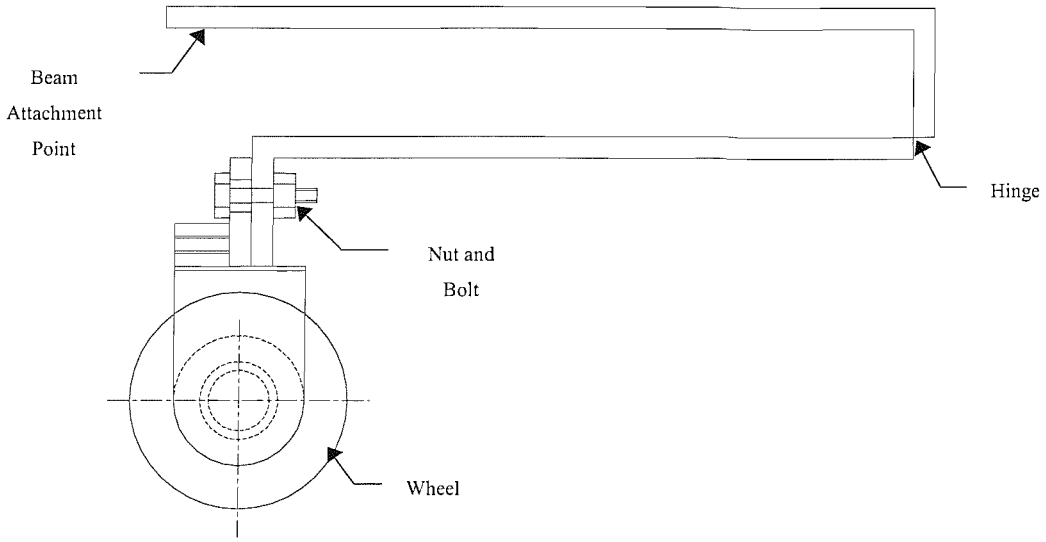

Figure 4-4 Schematic diagram of the tachometer assembly with its hinged attachment that enabled the connection of the tachometer assembly to the rig beam.

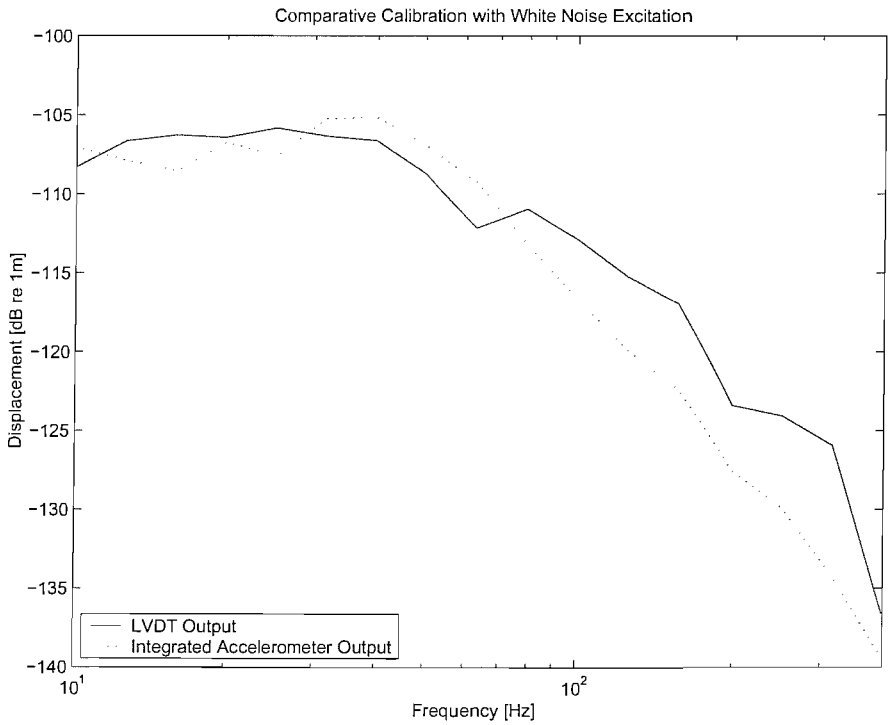

Figure 4-5 Comparative calibration of the LVDT transducer due to white noise excitation and an accelerometer of known frequency response.

measurement method using the force gauge and wheel loading spring is presented and compared with the LVDT performance in section 4.5.

4.3.3 LVDT transducer effects

It is important in any dynamic measurement that the frequency response of the transducer is taken into account. This is particularly the case for displacement transducers, as their usable (flat) frequency response regions tend to be limited to rather low frequencies and thus they have smaller bandwidths than other transducer types.

To determine the frequency response of the LVDT it was excited by an electrodynamic shaker driven with a random (white noise) input. The output of the LVDT is compared with the output from an accelerometer suitable for low frequencies (B&K type 4635) for the frequency range of 10Hz to 400Hz in Figure 4-5. Here the accelerometer has been integrated twice to give displacement. The accelerometer is known to have a flat response from 10Hz to 5kHz. The two results in Figure 4-5 are seen to be comparable in the frequency range considered (10Hz to 400Hz), but are in best agreement at frequencies lower than 80Hz. The spectra for each of the transducers are seen to reduce in amplitude with an increase in frequency due to the combined frequency response of the white noise generator and the electrodynamic shaker upon which the transducers were placed. A slight dip in the output of the LVDT is seen at 63Hz.

It is preferable to ensure that the measurement speed along any surface geometry is low enough that this frequency of 63Hz is not excited by the required wavelengths as listed in Table 4-1. For example, as the smallest wavelength that needs to be measured on the railhead is 100μm, the highest measurement velocity that can be used to traverse the LVDT probe along the railhead is 6mm/s (using $V = f\lambda$). Unfortunately this profile measurement speed is difficult to achieve, at a steady state, (on the 1/5 scale wheel / rail rig) due to friction of the rig beam PTFE bearing at low speeds. Many attempts were made to try to measure at very low speeds using different methods. However, the method described below gave the best (consistently steady) results. Another consequence of the requirement for such a slow measurement speed would be a time capture length of 200 seconds for a 1.2 metre length of track, resulting in huge data files.

The best results were made over a time capture length of 65 seconds at an average speed of 18.8mm/s. This speed is over three times faster than the optimal speed, so

wavelengths of 300μm were expected to coincide with the resonance frequency of the LVDT.

[Dings and Dittrich, 1996] present results of railhead surface geometry profiles for three cases ranging from what they describe as a smooth railhead to a rough railhead. Each of these cases shows a trend that decays by approximately 10dB over a wavelength range of 80mm to 8mm. This indicates that surface roughness amplitudes are proportionately smaller at shorter wavelengths. Therefore, whilst it might be possible that the LVDT resonant behaviour at 63Hz matches that of the smaller wavelengths at the traversing speed of the transducer, the amplitude of excitation is likely to be small. This is confirmed by a measurement of railhead roughness shown in Figure 4-6. It can be seen that the response of the LVDT follows a consistent trend where no noticeable resonant behaviour is apparent.

Attempts were made to try to alter the resonance frequency of the LVDT by changing the stiffness of the probe spring. Stiffer springs were fitted to the LVDT probe, to try to raise the resonance frequency, but these were found to apply too great a force to the transducer probe causing a lateral juddering due to friction. Increasing the stiffness of the probe spring was therefore found to be more detrimental than the possible resonance effect at a frequency of 63Hz.

It should be noted that the transducer resonance only needs to be considered here because of the wavelengths required for the prediction of the vibration on the 1/5 scale rig. In [Thompson, 1996] it is stated that the shortest wavelength of consideration for full-scale measurements need only be 3mm. Thus for the LVDT used here, the measurement speed could be as high as 180mm/s for a full scale railhead surface.

A source of error when using an LVDT is that as the probe itself has a contact patch. This could influence the values of measured vertical amplitudes on the surface being measured. For example, the LVDT probe contact patch length is about 18μm when a 1N load is applied to the probe tip. The maximum difference in height across to the 1mm radius of the LVDT tip for this contact patch dimension is 0.04μm. It was therefore not likely that the contact patch of the LVDT probe would have a significant influence on the measurements of vertical amplitude.

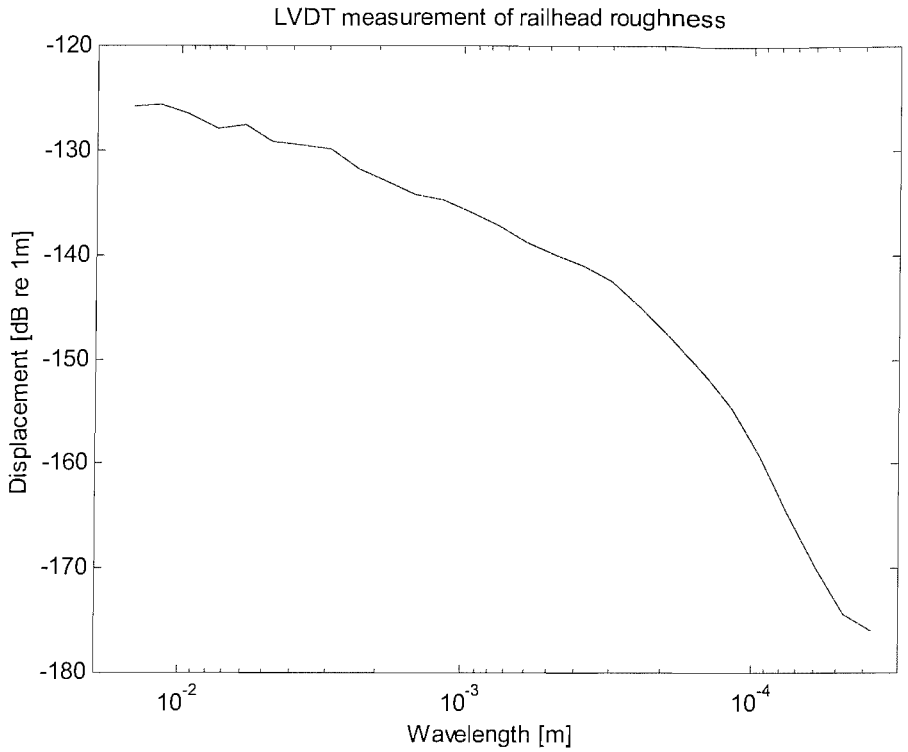

Figure 4-6 LVDT Measurement of railhead roughness shown as a one-third octave spectrum as a function of wavelength.

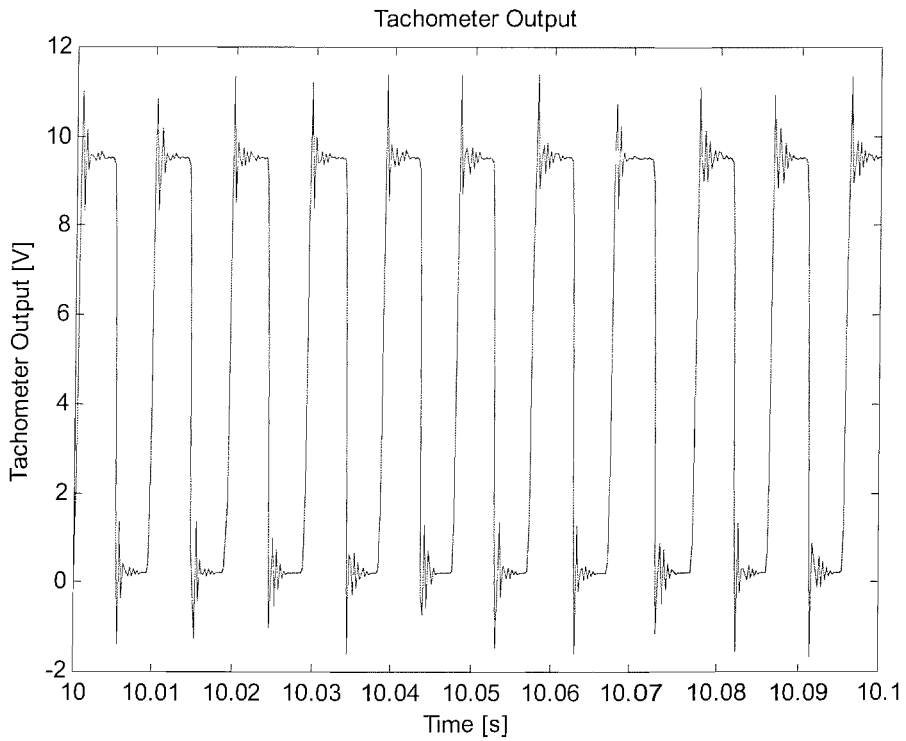

Figure 4-7 An example of the time-domain output from the tachometer.

4.3.4 Data acquisition method

The following procedure was adopted, when using the tachometer assembly, to obtain a measurement of surface profile:

1. Digital time-captures were used to record the output of the tachometer and the displacement transducer.

   The frequency analyser, used for this purpose, can be set to acquire data in the time domain at intervals between 312.5μs and 31.25μs. This results in a half sample frequency ($f_S/2$) of 1.6kHz to 16kHz respectively. After allowing for the effects of the analyser anti-aliasing filters (on the frequency content in the time-capture) an upper frequency limit of 1.28kHz to 12.8kHz remains. The initial time-capture data therefore has an upper frequency content that greatly exceeds the requirements of the low frequency pulses from the tachometer and the output from the displacement transducer.

   Nevertheless it is preferable to have a small time spacing between each sample so that the time-capture can be re-sampled at points that correspond as closely as possible with the tachometer pulses. Therefore a high sampling rate is necessary. In addition to a high sampling rate, a long time-capture length was also required so that the larger wavelengths of the surface profiles were included in the measurement. This resulted in large data files.

2. A simple algorithm has been written to find the start and the end of each tachometer pulse. This is implemented in MATLAB. Every other data point is then discarded so that a set of positions for either the start, or the end, of each tachometer pulse remains. An example of the tachometer output is shown in Figure 4-7. Although the speed of the surface profile measurement undoubtedly changes during the measurement (as the beam is turned by hand) it is assumed that the measurement speed is virtually constant between successive pulses.

3. The roughness data can now be re-sampled at positions that correspond with each tachometer pulse from the original time-captures.

   Although the tachometer has a fine resolution of 2048 points per revolution, it has been seen that the distance between each of these points did not give a fine enough spatial resolution (see Section 4.3.2). The distance between each tachometer pulse was only 150μm whereas approximately 17μm was required to describe the shortest

wavelength required (100μm) with six points. Therefore the space between each tachometer pulse was divided into ten equal parts, thus increasing the number of re-sampling points to provide a spatial resolution of 15μm. This allowed a sufficient number of points to describe the smallest required wavelength of 100μm.

4. The largest time interval between each of the re-sampling points was calculated, and the inverse of twice this value was used to form the upper frequency limit for a new low-pass anti-aliasing filter.

The data recorded from the roughness measurement transducer is then low-pass filtered in MATLAB before the values at the points corresponding with the re-sampling points are extracted into a new vector. This vector contains roughness amplitudes sampled at fixed distances apart along the measurement surface.

4.3.5 Effect of filtering and noise floor

The low-pass anti-aliasing filtering was performed in MATLAB using a routine called 'FILTFILT' with a third order Butterworth filter. This first filtered the surface profile data forwards through the filter and then time-reversed this filtered data back through the filter. By filtering the data twice in this manner, the effects of the phase distortion of the Butterworth filter are removed. The modulus of the filter response, however, is the square of the original. This means that the 3^{rd}-order Butterworth filter is equivalent to a 6^{th}-order filter when used with the FILTFILT routine.

By applying an anti-aliasing filter, the frequency content of the surface profile data was obviously altered. This effect is shown in Figure 4-8, which presents spectra in terms of frequency for a wheel speed equivalent to that at which the surface profile measurement was recorded (18.8mm/s). The vertical dotted line shows the position of the anti-aliasing filter cut-off frequency at 148Hz. The solid line in Figure 4-8, shows the 'raw' spectrum of the surface profile measurement before it has been re-sampled. The other dotted line shows the re-sampled data, while the dash-dot line shows the noise floor of the LVDT, which has been measured separately. It should be noted that the solid line was produced without any account for changes in measurement velocity during the measurement of the surface profile. Therefore this measurement is not strictly accurate, even though the differences between this result and the re-sampled data (where changes of measurement velocity are removed) are small.

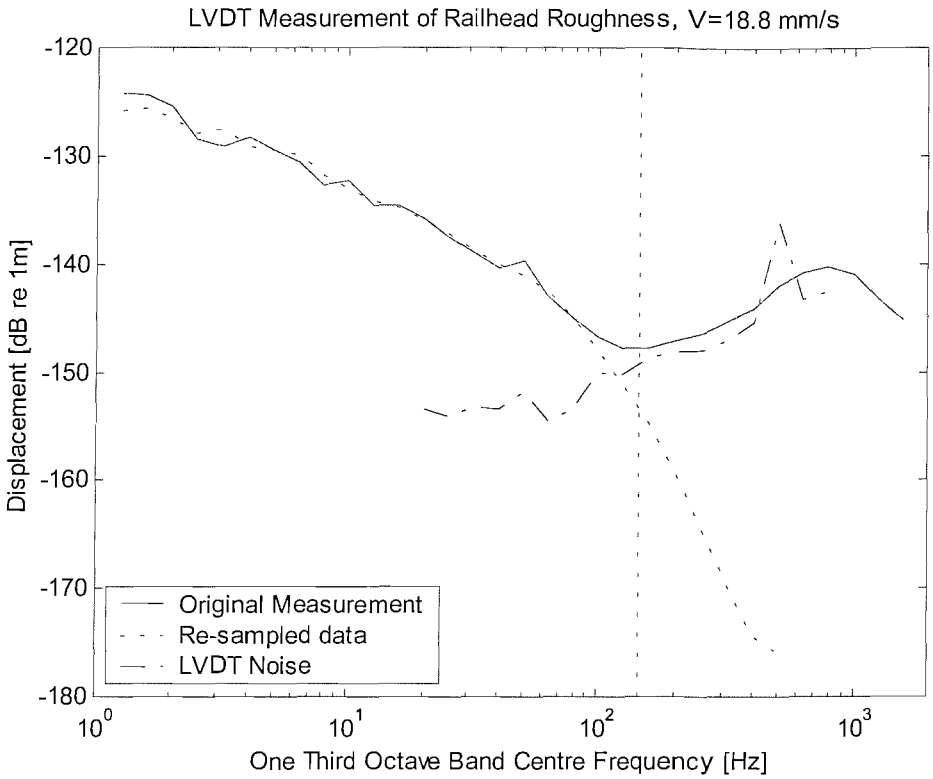

Figure 4-8 Comparison of a 'raw' LVDT railhead measurement, the re-sampled LVDT data, and the LVDT noise (which has been measured separately). The dotted vertical line represents the position of the cut off frequency of the anti-aliasing filter.

The differences between the 'raw' measurement and its re-sampled version, shown in Figure 4-8, are interesting. The fluctuations in the 'raw' measurement spectrum at low frequencies (less than 70Hz) are assumed to be due to variations in the measurement velocity as they are not apparent in the re-sampled version of this measurement. At frequencies above 100Hz the original measurement data shows a rising trend that coincides with the separately measured LVDT noise floor. The downwards trend at frequencies above 800Hz is attributed to the anti-aliasing filters of the frequency analyser used to make the time capture of this measurement. It should be noted that the re-sampled data (with corrections for measurement velocity) shows a much smoother trend in Figure 4-8 than the 'raw' roughness measurement, although the spectra above 100Hz are clearly affected by the anti aliasing filter applied by the re-sampling routine in MATLAB (see step 4 of the acquisition method described above).

The smallest one-third octave band amplitude that was measured in the original data was 0.039μm (equivalent to -148 dB re 1m) at a frequency of 100Hz and a corresponding wavelength of 188μm. The LVDT could not measure smaller amplitudes at this transducer measurement velocity. Smaller amplitudes could be measured by the LVDT, but this would require an even lower measurement velocity, since the noise floor is fixed relative to the frequency axis whereas the roughness is fixed relative to the wavelength axis.

The re-sampled data, shown by the dotted line in Figure 4-8, follows the trend of the 'raw' data at frequencies below 100Hz. However, as the anti-aliasing filter (for the re-sampling process) has been applied at 148Hz the re-sampled data continues to fall in the higher frequency range at a rate of 6dB per octave. The roughness in this short wavelength region is rarely required for the predictions. Only a small section of the spectrum affected by the anti-aliasing filter is expected to be used for a prediction for the lowest wheel speed. The anti-aliasing cut-off (at a wavelength of 188μm) corresponds with 7.8kHz for a wheel speed of 1m/s (i.e. 53 times faster than the speed of measurement) and 46.8kHz for a wheel speed of 6m/s (316 times faster). Thus, although the short wavelength roughness data is unreliable, this would only be used for one or two one-third octave bands at low speeds. Since the shape of the spectrum is reasonable this will nevertheless be used in the predictions for simplicity.

4.3.6 Sampling resolution and frequency content

In the above it has been shown that the tachometer pulse distance and re-sampling point resolution must be sufficient to enable an adequate frequency bandwidth of roughness data for the desired wheel speed range. It is also desirable that the anti-aliasing filter does not affect the high frequency surface profile data at the lowest wheel speeds. This is not always possible as the upper frequency limit is ultimately governed by resonances of the LVDT (see Figure 4-5), the noise floor, and the measurement velocity. However, more re-sampling points could be used to enhance the frequency range of the low wheel speed predictions by using a finer resolution tachometer, for example, or by taking a greater number of points between each tachometer pulse. The penalty for using a finer spatial resolution within a surface profile measurement, however, is that the calculation time required for the prediction models increases, especially for the time-stepping model. With the present measurement there would be no benefit in increasing the number of resampling points as the noise floor precludes obtaining useful data above 148Hz.

Conversely, as the frequency spectrum is effectively stretched for higher wheel speeds, the spacing between each frequency line is also increased. This has the result that, as the wheel speeds are increased, the frequency resolution at the lower end of the spectrum is reduced. Therefore the lower frequency one-third-octave bands of the surface profile are less likely to contain a sufficient number of narrow-band frequency points to allow a valid estimate to be made. This effect is particularly noticeable for the linear frequency-domain model introduced in Chapter 2. Thus low frequency predictions at higher wheel speeds will suffer if the length of the measured profile is not large enough.

A check was made to ensure that sufficient data lengths were measured for the highest wheel speed that needed to be considered. The frequency resolution was calculated for the highest wheel speed, and then the lowest one-third octave band was determined that contained at least three narrow-band frequency points. For a measurement of surface profile 1.2m long, at the maximum wheel speed (V=6m/s), the equivalent input would last 0.2 seconds. This corresponds with a frequency spacing of 5Hz (1/0.2s), which means the narrow-band estimates at 45Hz, 50Hz, and 55Hz fall within the 50Hz one-third octave band (as it has a lower limit of 44.5Hz, and an upper limit of 56Hz). Three narrow-band points fall within the 63Hz and 80Hz bands also. Therefore the roughness measurement lengths are more than adequate for the range of wheel speeds on the 1/5

scale rig using this criterion. Alternatively the BT product (B = bandwidth, T = analysis time) is 12×0.2=6 at 50Hz or 12 at 100Hz which is sufficient.

4.3.7 Trend removal

Unfortunately, problems were encountered with the surface profile measurement of the railhead that are inherent to the use of a displacement transducer.

As stated previously, a displacement transducer requires a fixed reference point from which all measurements are taken. To measure railhead geometry, the end of the rotating beam was assumed to be vertically rigid whilst providing the necessary horizontal sweep above the rail. The LVDT body was clamped onto the beam (Figure 4-3) and the probe tip was allowed to make contact with the railhead surface. The beam was then slowly turned (by hand at approximately 19mm/s) so that the surface roughness along the length of the railhead could be measured.

In practice the track bed was found not to be perfectly level. The measurement of the rail surface therefore had a considerable low frequency trend. This is shown in Figure 4-9. The presence of such large amplitude low frequency components is common to roughness measurements on full size rails. The spectrum of vertical alignment continues down to very low frequencies corresponding with hundreds of metres, which are not relevant to noise generation (see for example [Esveld, 1989]). If this surface profile measurement is converted to a 'raw' PSD (where no windowing or frequency-domain averaging was applied) it is found to have a strong fictitious low frequency content, due to the discontinuity in the data between the two ends (the DFT assumes the signal is periodic beyond the section available). This would affect the predictions from the linear frequency-domain model, resulting in predictions of rail acceleration that could greatly exceed the measurements.

Investigations were made to try to find a suitable method that could remove the unwanted low frequency trend from the measured railhead profile. Two signal processing methods, that were initially considered, were high pass filtering and windowing (see for example [Oppenheim and Schafer, 1975]).

Signal processing windowing techniques could be used to remove the trend, but as will be shown here this would adversely affect the frequency content of a surface profile measurement. This is because roughness profiles contain very large low frequency components and small high frequency components, the latter being of interest. Furthermore, the introduction of a window length restricts the wavelength content of the

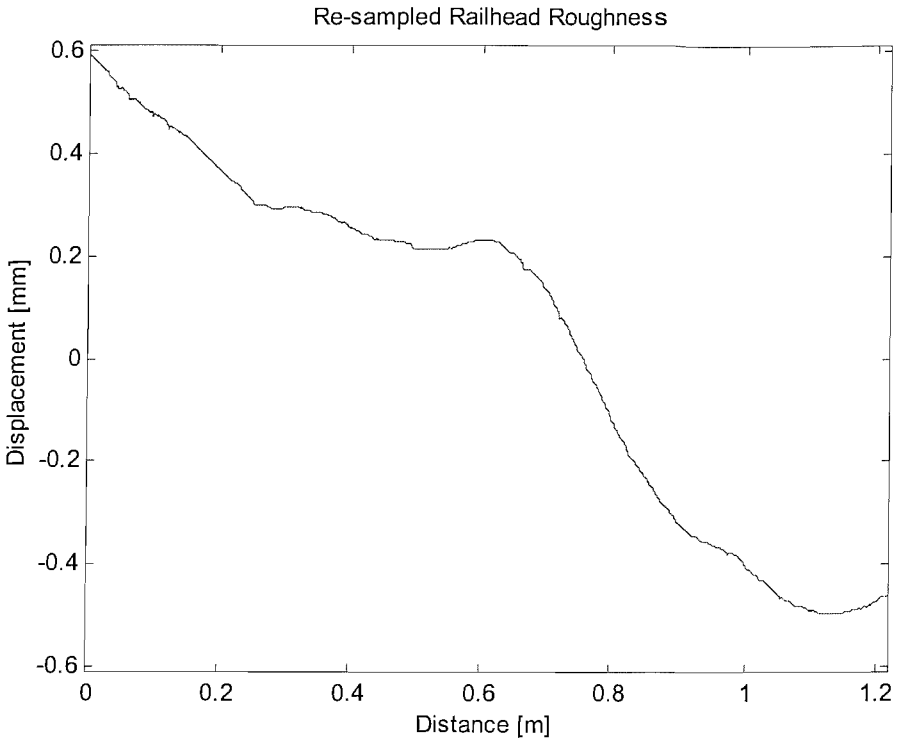

Figure 4-9 Measurement of railhead surface roughness.

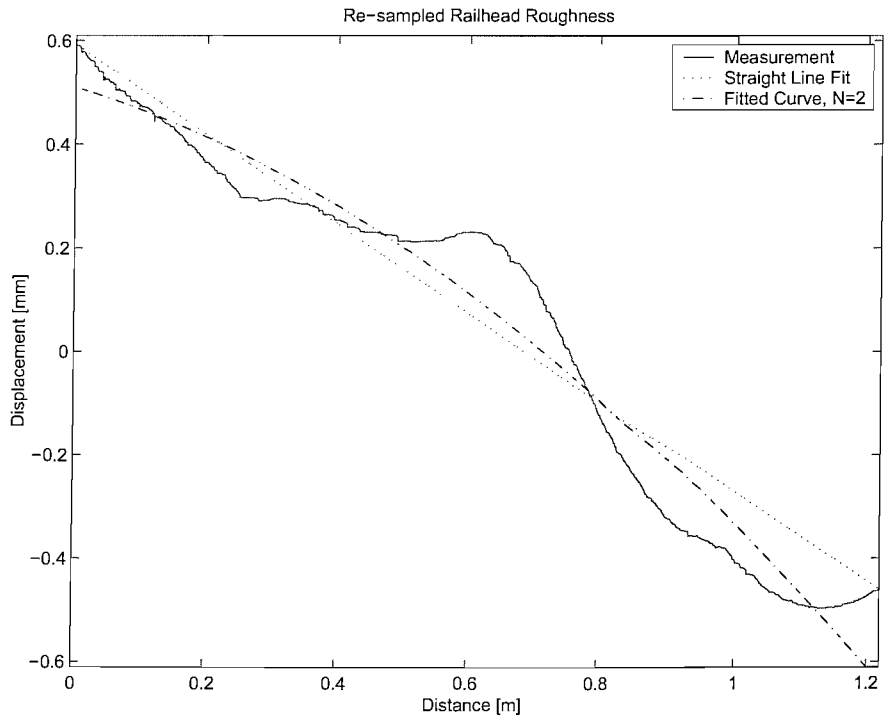

Figure 4-10 The measurement of the railhead roughness compared with a simple straight line fitted as a linear trend, and a complicated fitted curve.

surface profile measurement. A window that is too short could affect the largest wavelength component available.

High-pass filtering the measured (sampled) data using difference equations offers the potential of a fast solution to the problem. In practice, however, it is found that the starting transients of these routines dominated the filtered response. Cut-on frequencies have to be at correspondingly large wavelengths in order not to influence large starting transients. This effectively reduces the larger wavelength content of the measurements and thus limits the frequency bandwidth at high wheel speeds.

So, rather than using windowing or filtering techniques to limit the effect of the discontinuous nature of the railhead roughness measurement, trends were removed from the surface profile data in the spatial domain. Two methods of trend removal were considered: firstly by removing a linear trend so that both ends of the measurement were equal to zero, and secondly by subtracting a fitted polynomial function. These are shown in Figure 4-10. In order to demonstrate that removing the trends from the surface profile is preferable to using a windowing technique, the following analysis was made.

Figure 4-11 shows two sine waves for a time interval of one second. The solid line shows a 1Hz sine wave, whilst the dotted line shows half a cycle of a 0.5Hz sine wave. A raw PSD (i.e. a scaled FFT) of both of these signals was made and is presented for the frequency range 0.5Hz to 5Hz in Figure 4-12, where their responses are compared with the response of a 0.5Hz sine wave of a complete period. Figure 4-12 shows that for each of the complete sine waves their power is concentrated in the frequency bands corresponding with their fundamental frequency (0.5Hz or 1Hz). The spectra of the whole sine waves decay quickly (by 60dB) before the second point in the frequency estimate. The power of the truncated 0.5Hz sine wave, however, is smeared across many frequency bands. This means that by truncating a sine wave, higher frequency spectral estimates will be contaminated.

This analysis is repeated for cosine waves in Figure 4-13 where a full cosine wave and a half cosine wave form are considered. The half cosine wave is also considered when a linear trend (between 0 and 1 seconds) has been removed. The raw PSD of these waves are presented in Figure 4-14. As for the complete 1Hz sine wave, the PSD of the 1Hz cosine wave has its power concentrated at the fundamental frequency. Again it can be seen that the truncated wave produces spectra that are smeared across many frequency bands. Therefore it can be assumed that a truncated low frequency trend such as that of

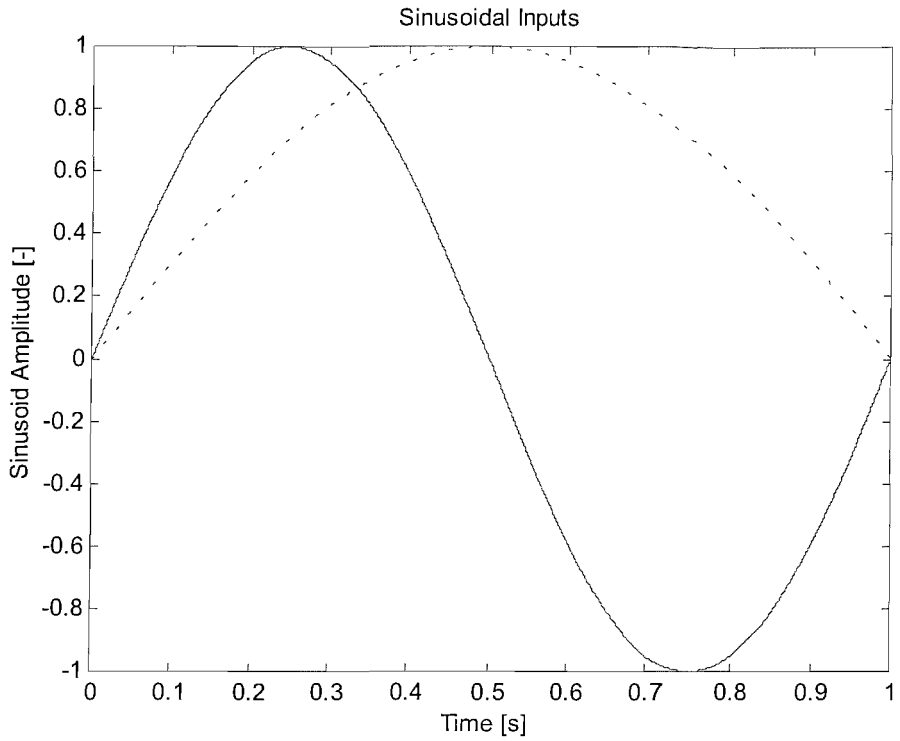

Figure 4-11 A 1Hz and 0.5Hz sinusoidal input.

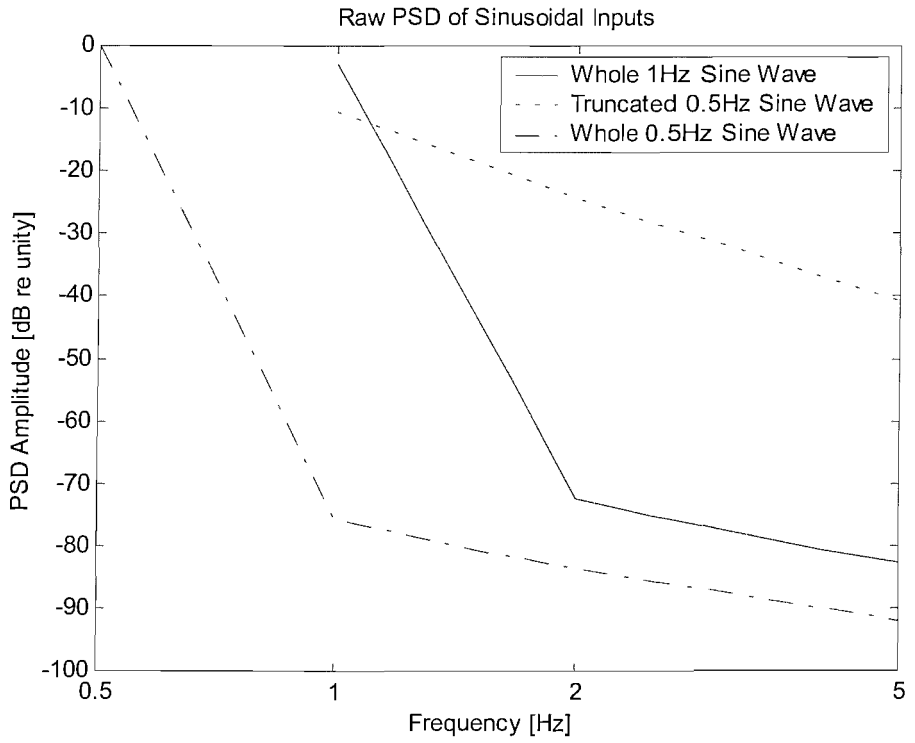

Figure 4-12 'Raw PSD' of the sinusoidal inputs shown in Figure 4-11, where the whole 1Hz sign wave and the truncated 0.5Hz sine wave have a frequency resolution of 1Hz, whilst the whole 0.5Hz sine wave has a 0.5Hz frequency resolution.

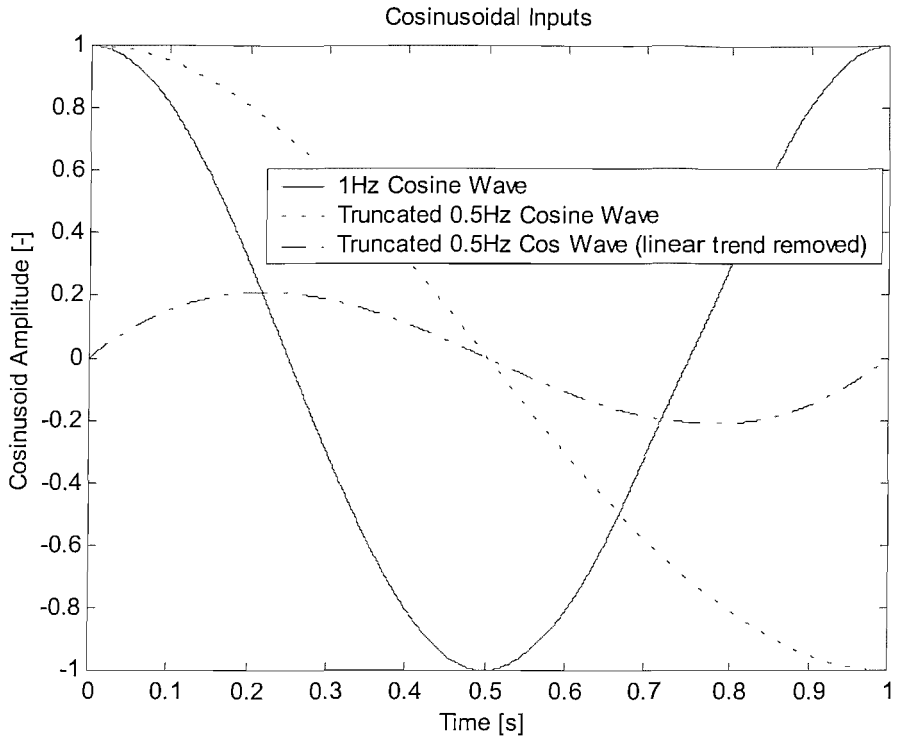

Figure 4-13 1Hz and 0.5Hz cosine waves.

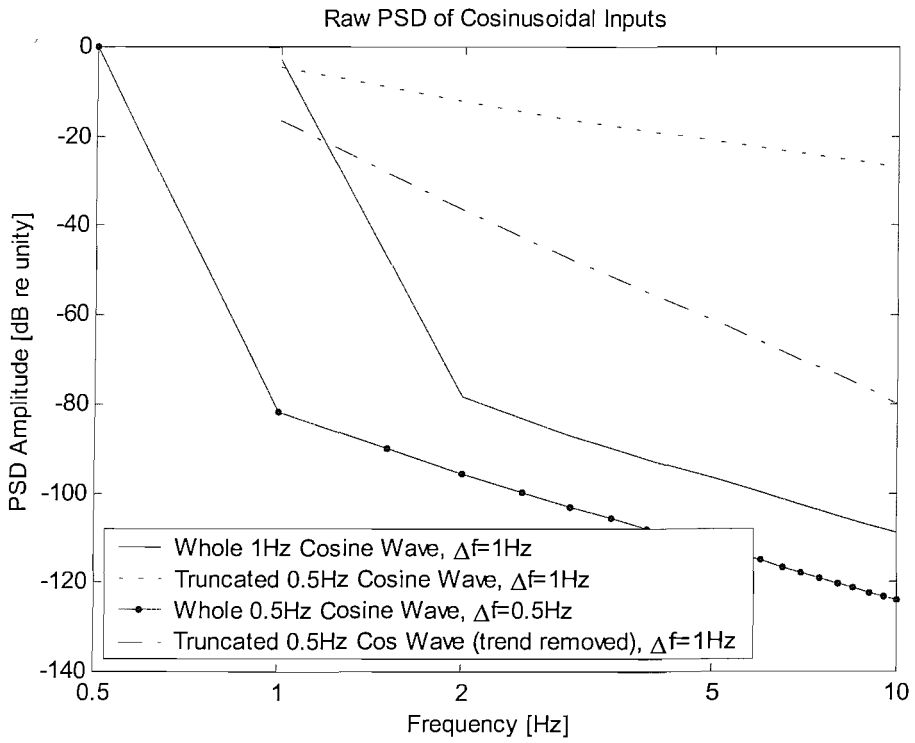

Figure 4-14 'Raw PSD' of the cosine waves shown in Figure 4-13.

the railhead surface roughness shown in Figure 4-9 will not only cause a poor PSD estimate at the frequency of the trend, but that it will influence the higher frequency content of the estimate. Removal of the linear trend reduces this effect considerably.

Figure 4-15 shows a comparison of the raw PSD of the complete cosine wave (shown previously in Figure 4-14) with a Han windowed version, in which 4 windows have been used with a 50% overlap. This demonstrates that by using windowing techniques, a truncation of the waveform is introduced and thus the power from the frequency of excitation is smeared into the neighbouring frequency bands. Although commonly used in signal processing, this is inappropriate for signals containing large amplitude very low frequency trends.

Figure 4-14 shows that removing a linear trend from a truncated cosine wave considerably reduces the over-estimate of the PSD at higher frequencies. However, removing the linear trend from the half sine wave would have no effect. Therefore the method of removing a trend by applying a simple straight line is not always good enough if the low frequency content of the signal is to be utilised. To improve this, the subtraction of a higher-order polynomial fitted curve was considered. Whilst it is felt that this process would most definitely remove the unwanted trend, it might also remove higher frequency content that is needed in the prediction. Therefore a compromise has to be made, using a fairly low order polynomial curve. Linear trend removal must also be applied to ensure there is no discontinuity at the ends of the data block.

As the purpose of the trend removal process was to remove the low frequency content that represented the discontinuous nature, a second order fitted polynomial was first subtracted from the measurement. Next the remaining linear trend was removed from the data so that it no longer had a discontinuity at its ends. This process is demonstrated in Figure 4-10 where the 2^{nd} order fitted curve is shown with the roughness measurement, and in Figure 4-16 where this and the remaining linear trend has been removed. By removal of the trend from the surface profile measurement it is assumed that any of the undesired effects of the uneven track bed are omitted.

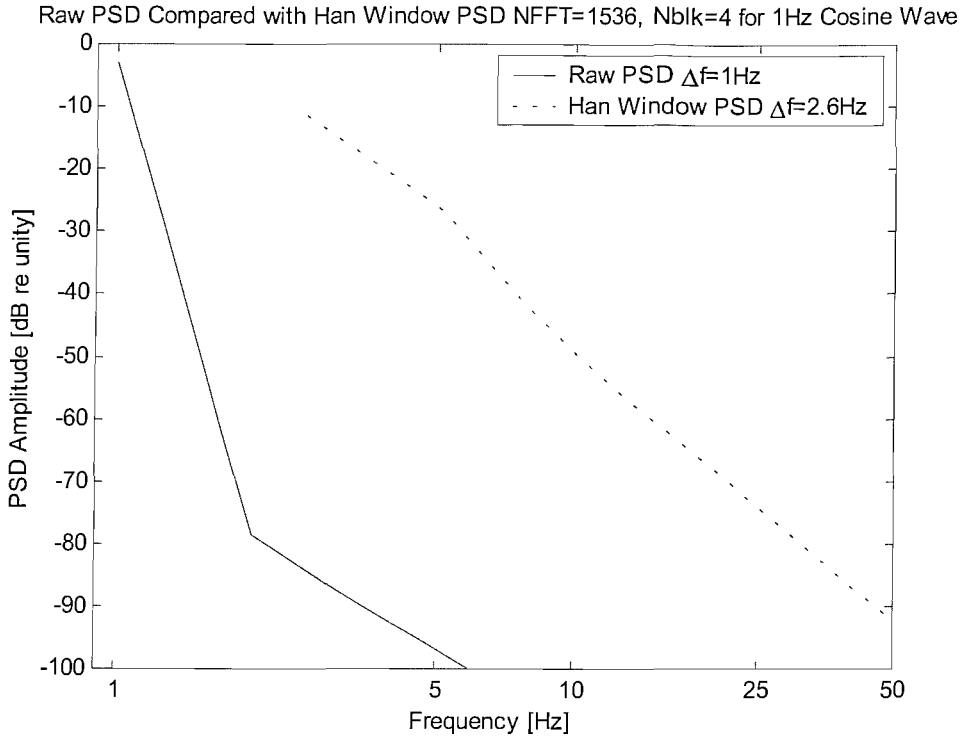

Figure 4-15 Comparison of a 'raw PSD' of a 1Hz cosine wave and a PSD of the same signal using a Han window.

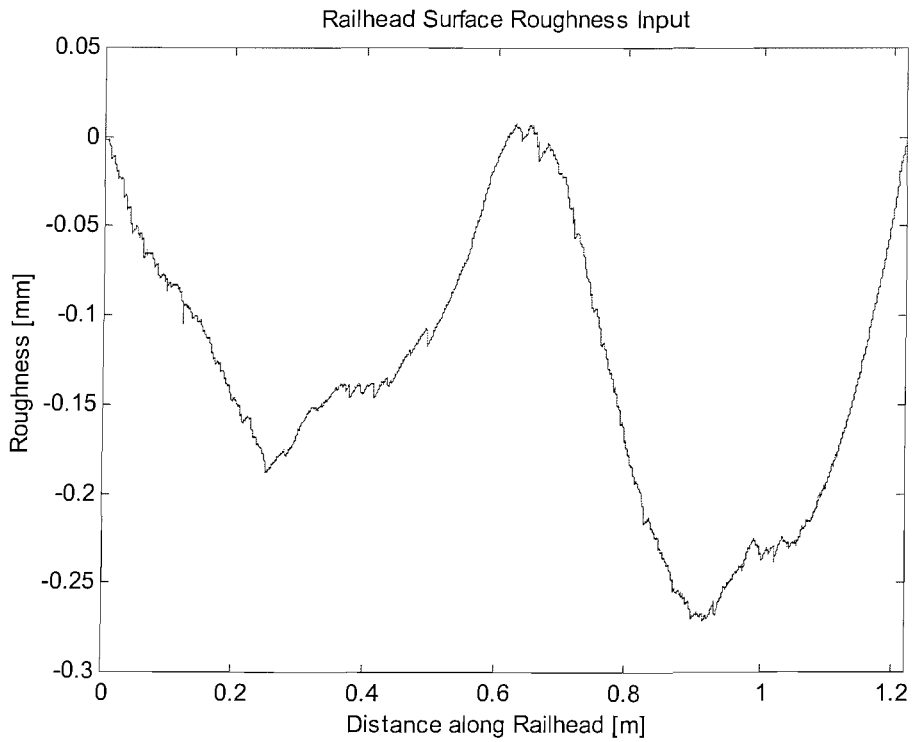

Figure 4-16 Resulting roughness input after removal of a fitted second order curve and then the remaining linear trend.

4.3.8 Summary of the surface profile measurement process

A summary of the considerations needed to make a surface profile measurement are presented in Figure 4-17. This contains a flow chart that demonstrates the relationship between:

- The wavelengths of interest defined by equation (1-1).
- The frequency response of the LVDT as considered in Section 4.3.3.
- The difficulty of measuring at a constant velocity as described in Section 4.3.3 and Section 4.3.4.
- The resulting requirements of the time capture length and the resolution of each data point.

The trend removal process described in section 4.3.7 was not required for the surface roughness measurements of the rig wheel. Although the process of maintaining a constant measurement speed was difficult, when turning the rig wheel by hand, little trend removal of the measured data was required. With a lot of patience, good measurements of the wheel surface profile could be made that contained surface roughness measurements of one complete revolution of the rig wheel. These measurements were of comparable length with the measurements of the railhead surface profiles, as the circumference of the rig wheel was 1.26m. Any differences between the measured amplitudes between the start and end of a rig wheel surface profile measurement were usually very small. An example of a measurement of the wheel surface roughness, is shown in Figure 4-18. If required, these small discrepancies were removed by use of a linear trend removal process.

Inputs to the prediction models based on LVDT measurements generally require a measurement of both the railhead and the wheel surface, as both profiles contribute towards the excitation of vibrations. The maximum roughness amplitudes on the wheel, however, are only about 3-4μm. An example of the measured railhead roughness has already been presented in Figure 4-10.

By adding their amplitudes together in the spatial domain, the combined roughness input (of the railhead and wheel) can be formed. Figure 4-19 shows the one-third octave band spectra of the wheel and rail roughnesses. These are presented as a function of wavelength using equation (1-1). Although the roughnesses of both the wheel and the rail should be used as an input to the models, the rail roughness was found to be the

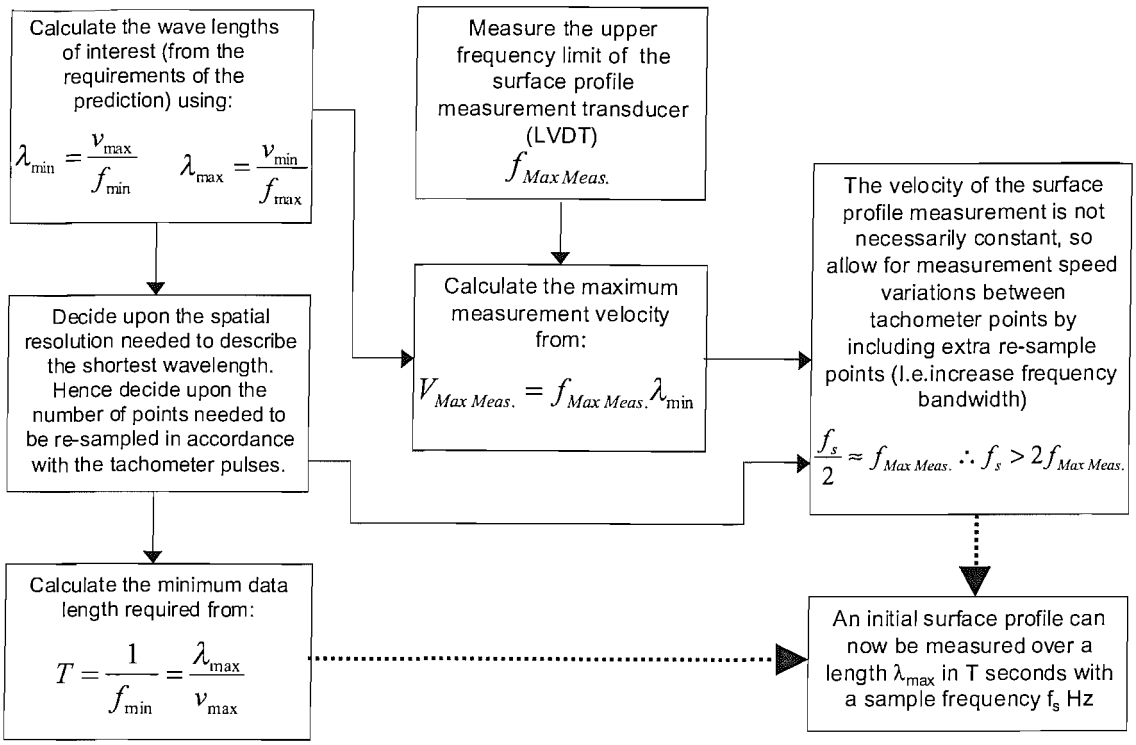

Figure 4-17 Flow chart of the procedure required to ensure an adequate roughness measurement prior to re-sampling.

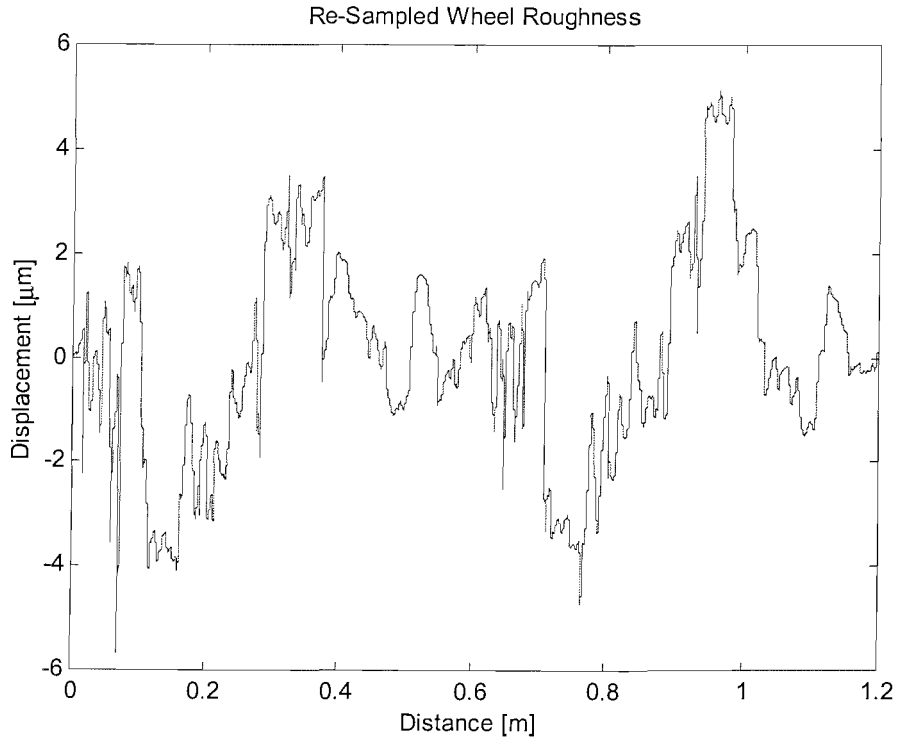

Figure 4-18 Measurement of the rig wheel roughness.

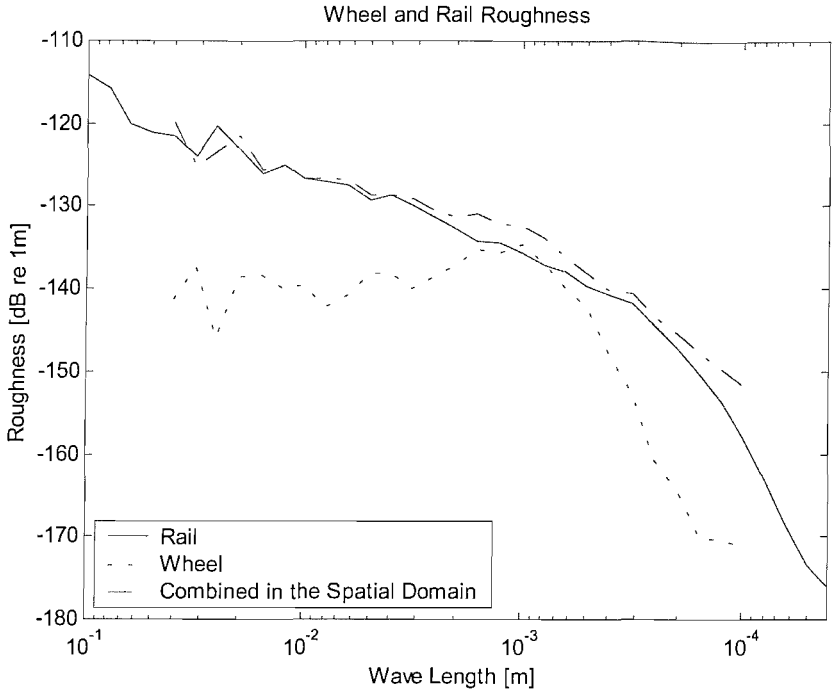

Figure 4-19 Comparison of the rig wheel and rail roughness presented as one-third octave spectra as a function of wave length. These measurements are shown together with a spectrum obtained from the combined wheel and rail surface roughness. The rail roughness is seen to be the major contributor to the combined surface roughness.

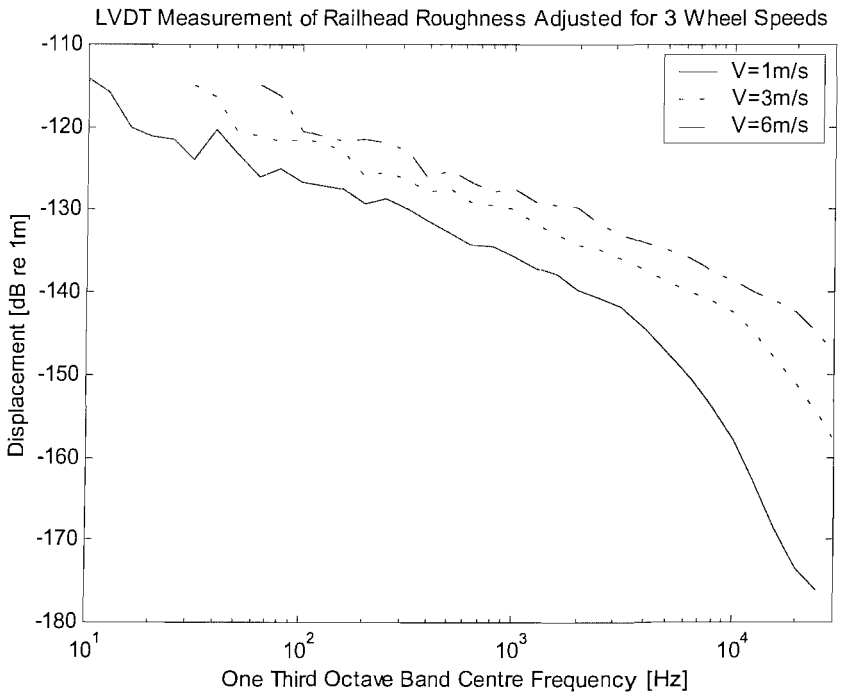

Figure 4-20 Railhead roughness measured with the LVDT, presented as a function of frequency for 3 wheel speeds.

major contributor. This is shown by the combined wheel and rail spectra where the roughnesses have been combined by addition of their amplitudes in the spatial domain.

To use the combined roughness measurement for a specific wheel speed (V), it is converted into a function of time ($t = x/V$) before it is used by the model. The combined roughness can now be used (with some modifications, see Section 4.4) as an input to a time-stepping routine. For use in the frequency-domain model, the PSD of this input is formed and then used to estimate one-third octave spectra. The one-third octave spectra from this are shown in Figure 4-20 for three wheel speeds. It can be seen that an increase in wheel speed causes a horizontal shift towards higher frequencies of the one-third octave spectra while the amplitudes remain the same for a given wavelength. As the calculation of the one-third octave spectra from narrow-band spectra requires the average of at least three frequency points per one-third octave band for reliable estimates, the lower bands are not calculated for the higher wheel speeds as the frequency spectra are effectively stretched by the relationship $f = v/\lambda$.

4.4 Post-processing of the measured roughness

4.4.1 Geometric filtering effects

The LVDT has a spherical probe of radius 1mm, which is considerably smaller than the radius of curvature of the wheel (0.1m). The profile measured with the LVDT is therefore more detailed than is necessary. It contains high frequency (short wavelength) components that are not fully registered by a wheel rolling over this surface. A geometric filtering process is therefore required to alter the measurement to a roughness input corresponding with that 'seen' by the wheel.

Figure 4-21 illustrates the case of contact between a rough surface on a rail and an 'ideal' smooth wheel, to provide an insight into the performance of a 'geometric filter'. It is assumed at this stage that a single contact point exists between the wheel and the rail on which the roughness amplitudes are present [Thompson, 1996]. At each longitudinal sample of the measurement, the wheel is effectively lowered towards the rail and the height of the wheel at which contact would first occur is determined. Thus it can be seen that small troughs around the point of contact are ignored, so the result corresponds with an approximation of the roughness 'as seen' by the wheel. Although the high frequency components of the roughness data are removed, this differs from a low-pass filter in that peaks and dips in the roughness are treated differently.

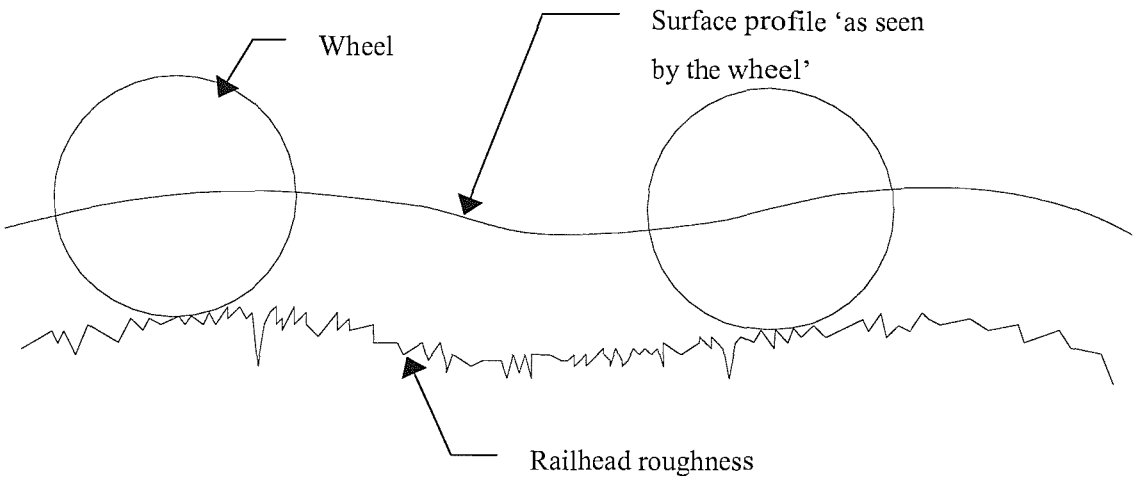

Figure 4-21 Roughness at the contact point of a smooth wheel: an explanation of the geometrical filtering effect.

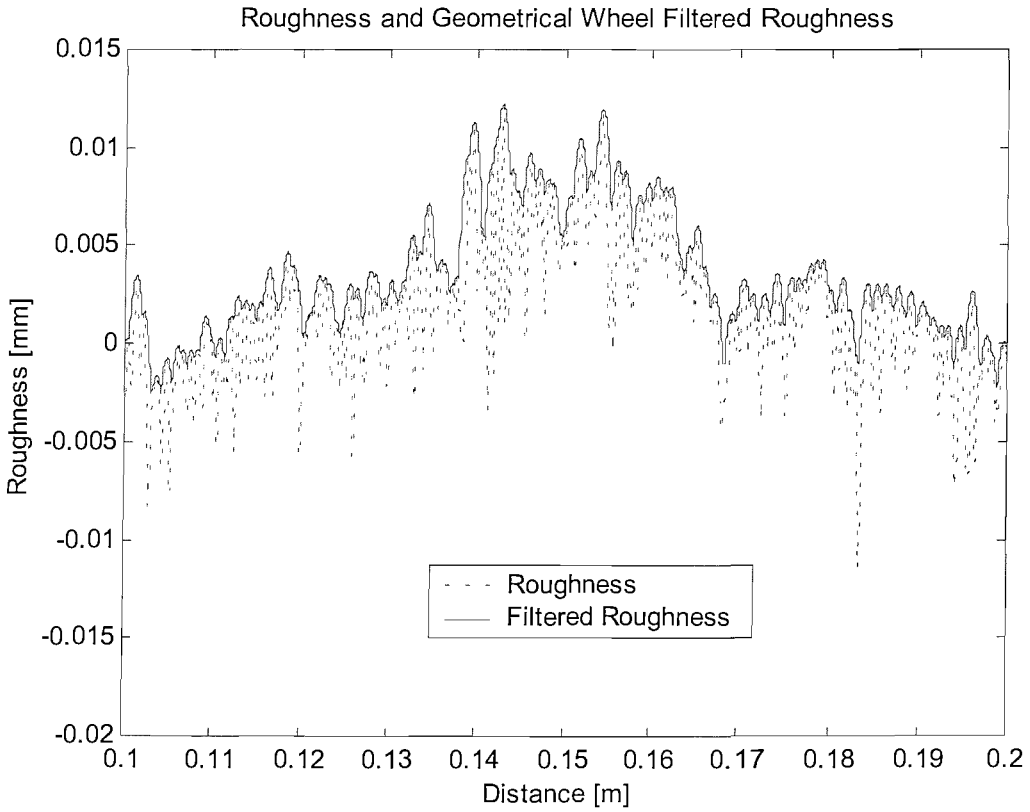

Figure 4-22 An example of geometrical wheel filtering in the spatial domain.

An example of the effect of a geometrical filter based on that described in [Thompson, 1996] is shown in Figure 4-22 for a section of the railhead roughness measurement (see Figure 4-6) in the spatial domain. Here it can be seen that the troughs are ignored whilst the wheel rolls over the peaks. Figure 4-23 shows frequency spectra (as a function of wavelength) of the roughness with and without the effect of geometrical filtering. The large wavelength content of the geometrically filtered signal is similar to the original, whilst the short wavelengths are attenuated.

Results of the geometrically filtered railhead surface roughness, the rig wheel surface roughness and a combined surface roughness (of the wheel and the rail) are presented in Figure 4-24. Previously in Figure 4-19 the wheel and rail measured roughness before geometrical filtering were shown to be of similar magnitude at wavelengths between 0.5mm and 1mm. This effect is reduced after geometrical filtering.

The geometrical filter devised by [Thompson, 1996] works on the principle that an arc of a perfectly round wheel is considered at each point along the length of the measurement. The arc dimensions are chosen at the start of the filtering operation and therefore have an equivalent fixed length of consideration throughout the filtering process. The choice of this filter length (that is related to an equivalent arc dimension) is important as it can have a strong effect on the roughness spectrum. This is shown in Figure 4-25 where the result of using different filter lengths is presented for a railhead surface roughness measurement.

The smallest filter length considered (54 points) corresponds with the estimated Hertzian contact patch length (0.8mm at a wheel pre-load of 527N). An increase of filter length by a factor of ten or one hundred is seen to produce the same attenuation of the shorter surface roughness wavelengths. The over predicted filter length (5400 points, shown in Figure 4-25) is also seen to affect the larger wavelengths for the surface roughness input. This is due to a reduction in the length of the data after the geometrical filtering process, which thus has the effect of truncating the data and influencing the spectral estimate of the large wavelength region.

Therefore, too large a filter length will affect the long wavelength content of the data. It also leads to long computation times. Conversely, more realistic filter lengths that are comparable with the estimated Hertzian contact patch dimensions have been seen not to apply the correct geometrical filtering effect. It is therefore necessary to adjust the filter length (i.e. increase the number of points in the filter) to ensure that the maximum

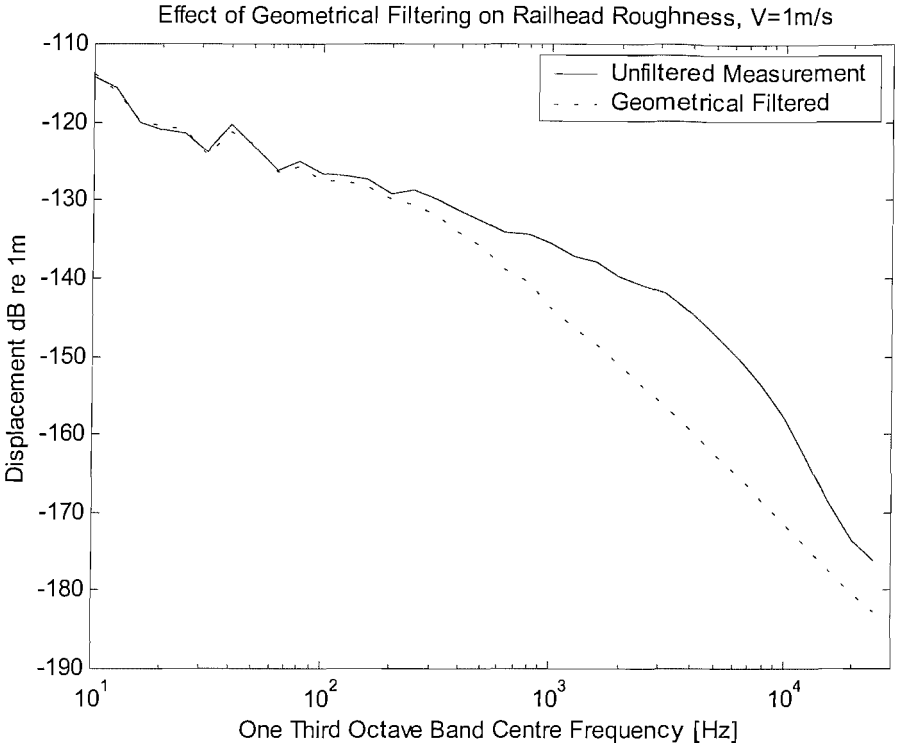

Figure 4-23 Geometrical wheel filtering PSD for the railhead surface roughness.

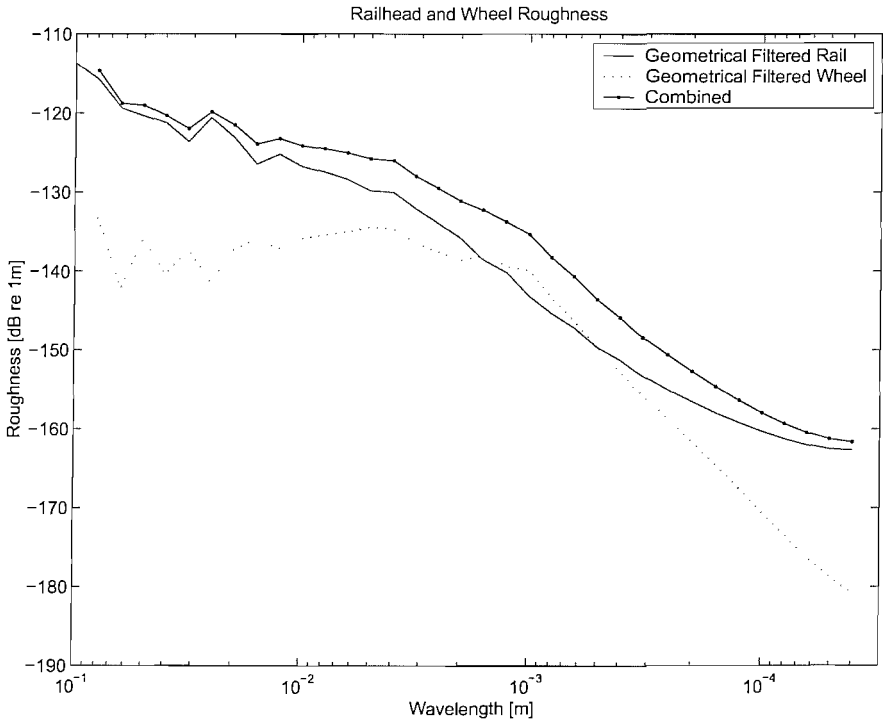

Figure 4-24 Geometrical wheel filtering PSD for the railhead surface roughness and the combined wheel and rail surface roughness.

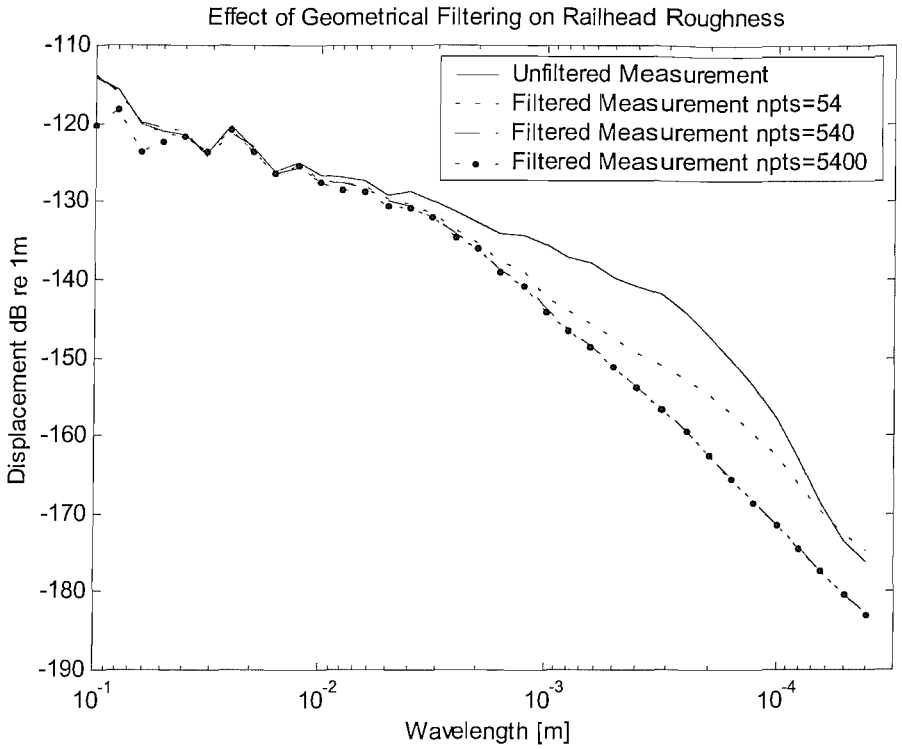

Figure 4-25 Effect of the geometrical filter length considered in the process of geometrical wheel filtering the railhead roughness using 54, 540, and 5400 point filter lengths.

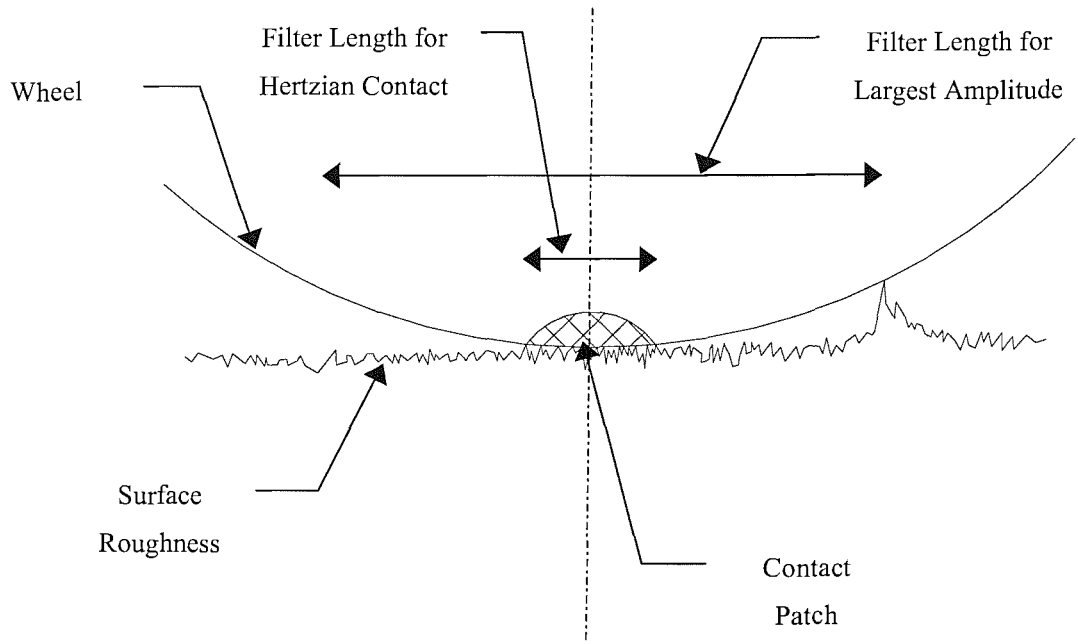

Figure 4-26 Schematic diagram showing the difference between the geometrical filter length from a Hertzian contact patch estimate and the filter length found by trial and error to include the greatest roughness amplitude.

height differences of the surface profile found by the filtering process is contained between the first and the last point of the filter length considered. This is shown schematically in Figure 4-26.

The geometrical filter discussed in this section does not, however, consider localised deformation of the wheel and rail. For this a 'contact' filter is required, which is introduced next.

4.4.2 Contact filtering effects

The length of the contact area between a wheel and rail, which is typically 10-15mm at full scale [Thompson and Jones 2000], is known to affect the dynamic response due to a roughness input. At high frequencies the roughness wavelengths are short compared with the length of the contact patch and therefore their effect is attenuated due to averaging over this length. This attenuation is referred to as the 'contact filter' [Remington, 1987].

An analytical contact patch filter for the case of a circular contact patch of radius a is given by [Remington, 1976]:

$$|H(k)|^2 = \frac{4}{\alpha}\frac{1}{(ka)^2}\int_0^{\tan^{-1}\alpha} J_1^2(ka\sec\psi)d\psi \qquad (4\text{-}2)$$

where: H is the attenuation of the filter,

k is the roughness wave number ($k = 2\pi/\lambda$),

α is a correlation factor for the roughness running across the contact patch,

J_1 is the Bessel function of order 1.

Another contact filter, a numerical model, has been developed more recently [Remington and Webb, 1996] which includes the effect of many parallel roughness measurements along the surfaces of both the wheel and the rail. This is referred to as the distributed point reacting springs (DPRS) model. These two approaches are compared in [Thompson, 2001] and shown to be in good agreement down to about 7mm wavelength for a contact patch length of 11mm.

A graph showing the result calculated using equation (4-2) for typical values of the 1/5 scale wheel / rail rig (and a value for a equal to the contact patch length) is shown in Figure 4-27 along with data from the DPRS model that has been adapted from [Thompson, 2001] to correspond with a contact patch length of 0.8mm. Ideally the

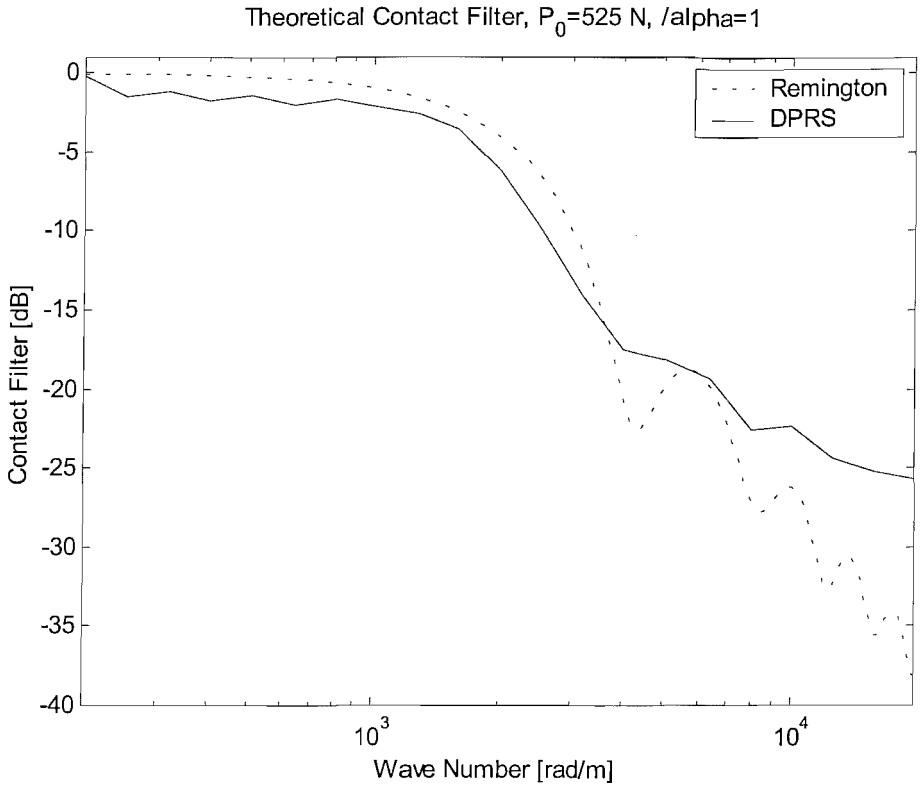

Figure 4-27 Contact filter calculated for wheel radius 0.1m, rail radius 40mm, contact patch length 0.8mm, static load of 525N (typical values for the rig), and α=1.

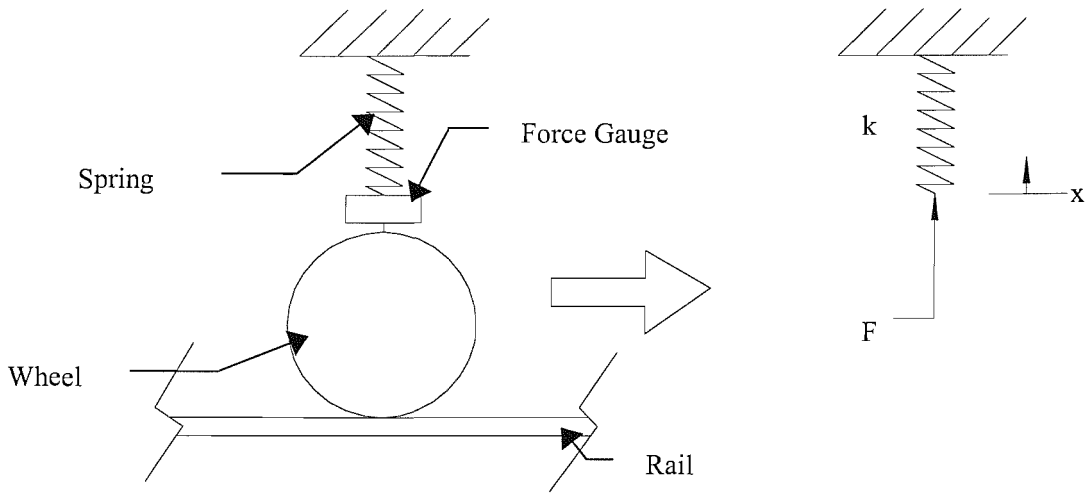

Figure 4-28 Schematic diagram of a roughness measurement using the force gauge. The force gauge output can be converted into a displacement providing the spring stiffness is known.

DPRS model would be used. At full-scale measurements made for the DPRS model often cover at least 5 parallel lines of roughness across the contact patch. This cannot be done reliably on the 1/5 scale rig due to the smaller contact patch width. Direct use of the DPRS method was therefore not appropriate.

Even so, it is still necessary to modify the roughness data by applying a contact filter, so, of these two approaches, only the Remington model (equation (4-2)) is applicable to the 1/5 scale rig. Further discussions regarding the performance of the Remington contact filter are presented in Chapter 5. These lead to an approximate contact filter that is developed on the basis of measured results from the rig.

4.5 Surface profile measurements made with the force gauge

The 1/5 scale wheel / rail rig contains a pre-loading spring and force gauge to apply and measure the wheel pre-load (see Figure 3-5). Although not its primary purpose, this configuration allows an alternative method of surface profile measurement. The force gauge output can be monitored as the wheel runs on the surface of the rail at very low rolling speeds. This 'blocked force' should be proportional to the wheel vertical displacement. A schematic diagram of this method is shown in Figure 4-28. A vertical displacement of the wheel (x) compresses the spring (k), thus changing the measured output of the force gauge (F). It is assumed that during the measurement the wheel and track are rigid. This method requires the wheel speed to be very low, so that the modal properties of the wheel and track are not excited.

4.5.1 Introduction to the alternative method

The procedure adopted for measuring the surface profile by this method was similar to that used with the LVDT transducer described in Section 4.3. The tachometer assembly was mounted at the free end of the rig beam and the rig wheel was lowered onto the measurement rail section. As for the LVDT surface profile measurements, the rig beam was rotated by hand at very low speeds and the data from the tachometer and the force gauge were acquired as described in Section 4.3.4. The force gauge output (F) was then converted into a corresponding deflection (x) using Hooke's law ($x = F/k$).

A measurement of roughness that is based on using the force gauge in this way has the potential to measure the resulting roughness 'seen' by the wheel. Moreover it measures

the sum of the wheel and rail surface profiles directly, so only a single profile measurement is required.

The performance of the force gauge method is best demonstrated by a comparison with an LVDT surface profile measurement of a railhead discontinuity. A measurement of a 2mm dipped 'rail joint' is shown in Figure 4-29, where the results of the two methods look very similar. Further comparisons of the two methods are given in section 4.5.2 below.

In order to calculate the wheel loading spring stiffness (k), the spring was calibrated on a static load rig. This has been presented in Chapter 3. The stiffness was found to be 11.5kN/m. Further analysis of the spring was made to dominate its dynamic properties. A measurement of the driving point receptance of the spring with the opposite end blocked, when excited by an electrodynamic shaker driven with a white noise signal, was also shown in Chapter 3. Figure 3-29 shows there is evidence of strong resonant behaviour for frequencies above 35Hz. This resonant behaviour limits the usefulness of this method, so frequencies above 35Hz (at the measurement speed) were excluded from the results.

A point accelerance measurement of the rig wheel was presented earlier in Figure 3-28. Unfortunately the results at low frequencies were adversely affected by measurement noise. An improved measurement of the low frequency response of the wheel assembly was attempted, but accurate point measurements were found not to be possible with the (relatively) low sensitivity impedance heads available. It is therefore unclear whether modal behaviour of the wheel will affect the measurement of roughness via the force gauge. However, it is clear that the bending modes of the wheel itself will not occur in the region below about 500Hz (100Hz full-scale) [Hemsworth, 1979].

The frequency response of the force gauge also needs to be considered. The force gauge was positioned between an electrodynamic shaker and a known mass and excited with white noise. The force gauge output was then converted into acceleration by dividing by the mass before comparing it with that from an accelerometer (of known performance). The result of this is shown in Figure 4-30 in terms of the ratio of accelerometer output divided by the converted force gauge output. This shows that the force gauge response is generally in agreement with the accelerometer throughout the frequency range 10Hz to 500Hz, to within +/- 2dB. Fluctuations at higher frequencies (>100Hz) could be due to rotation of the mass on top of the force gauge during the measurement. The results at

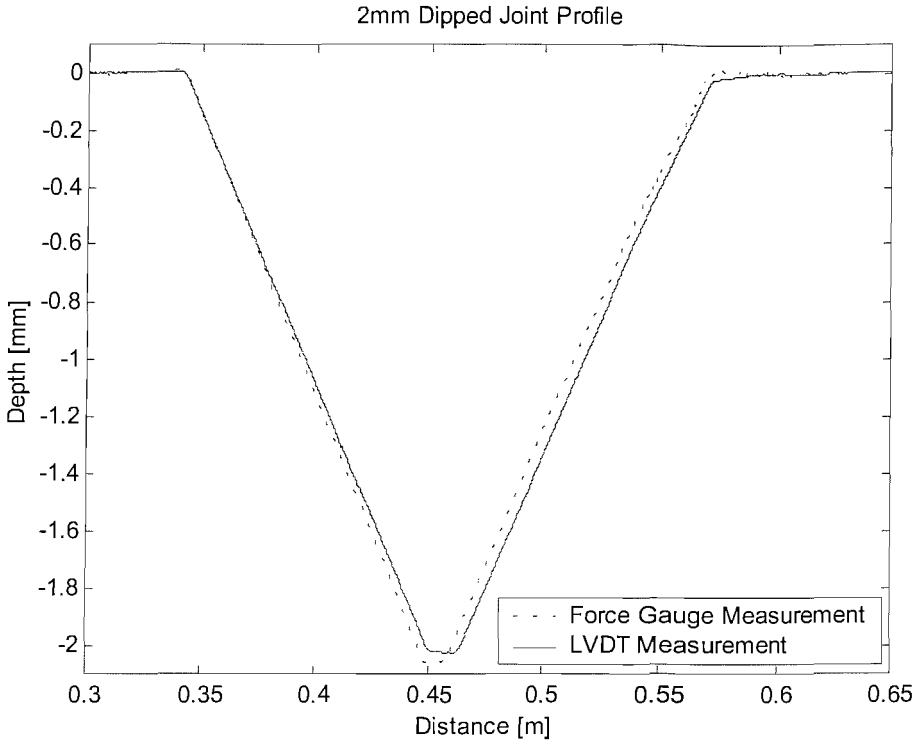

Figure 4-29 A comparison of a force gauge and an LVDT roughness measurement of a 2mm dipped joint.

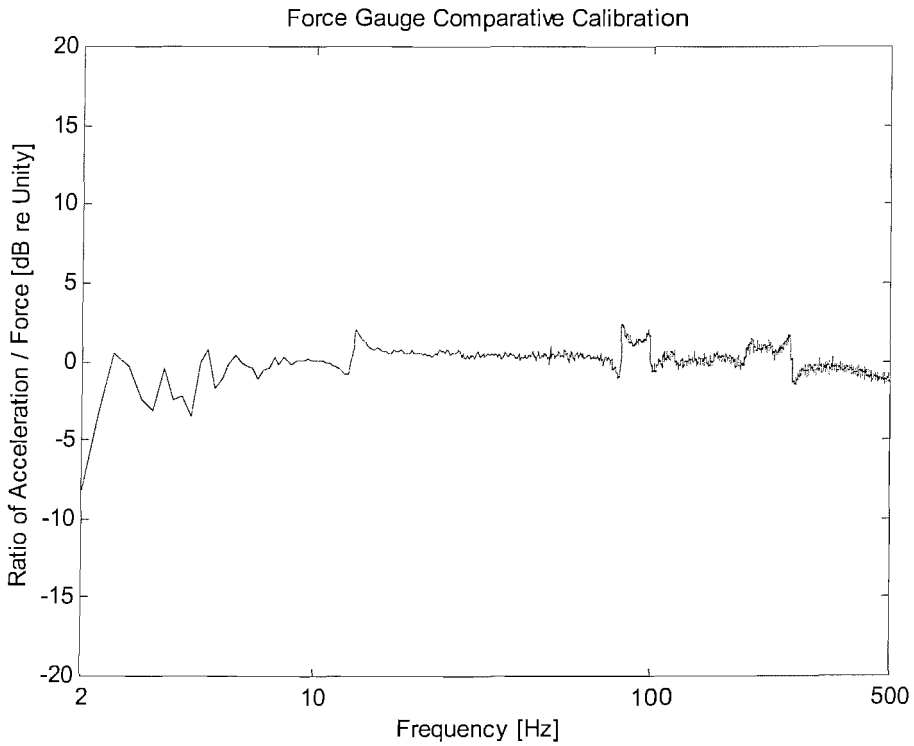

Figure 4-30 Result of the force gauge comparative calibration due to white noise excitation. This is shown as the output of the accelerometer (on a known mass) divided by the converted output of force gauge plotted as a function of frequency.

low frequencies are adversely affected by low accelerometer amplitudes produced by the electrodynamic shaker.

The investigations described above indicate that the combined effects of the rig wheel, force gauge and wheel assembly pre-load spring are not likely to influence a measurement of surface profiles made with this alternative method.

4.5.2 Comparisons of the force gauge and LVDT measurement methods

Measurements were made of the relatively smooth railhead using both the force gauge method and the LVDT. This railhead was chosen so that any effects from intended discontinuities would not bias the results.

A comparison in terms of spectra of the roughness derived from the force gauge output, an LVDT measurement of the rail roughness, and a geometrically filtered version of the LVDT measurement, is shown in Figure 4-31. As each of the measurements were made at different measurement speeds, they have been converted to a function of wavelength so that comparisons may be made. Figure 4-31 shows that the large wavelength components of the force gauge output are approximately the same as those from the LVDT. This explains why the spatial domain comparisons in Figure 4-29 look similar. The output from the force gauge, however, was found to be different from the LVDT for shorter wavelengths (smaller than 1mm), as at these wavelengths the measurements made with the force gauge were found to be affected by noise.

This is shown in Figure 4-32 where the high frequency (short wavelength) range of the force gauge method results are seen to be affected by the anti-aliasing filter that is applied during the re-sampling process (solid line). The effect of the anti-aliasing filter is shown (in Figure 4-32) by the dotted line which represents the force gauge measurement before the re-sampling process (and therefore without the anti-aliasing filter effect). Another straight chain-dot line is shown in Figure 4-32. This inclined line describes a trend that rises at 10dB per decade of frequency. This trend corresponds with that of white noise when converted into one-third octave bands. The noise in the force gauge measurement appears to occur at a higher level (20 to 30dB) than that found at the corresponding frequencies in the LVDT measurement shown in Figure 4-8. The force gauge data for wavelengths shorter than 1mm should be discounted as they consist of filtered noise.

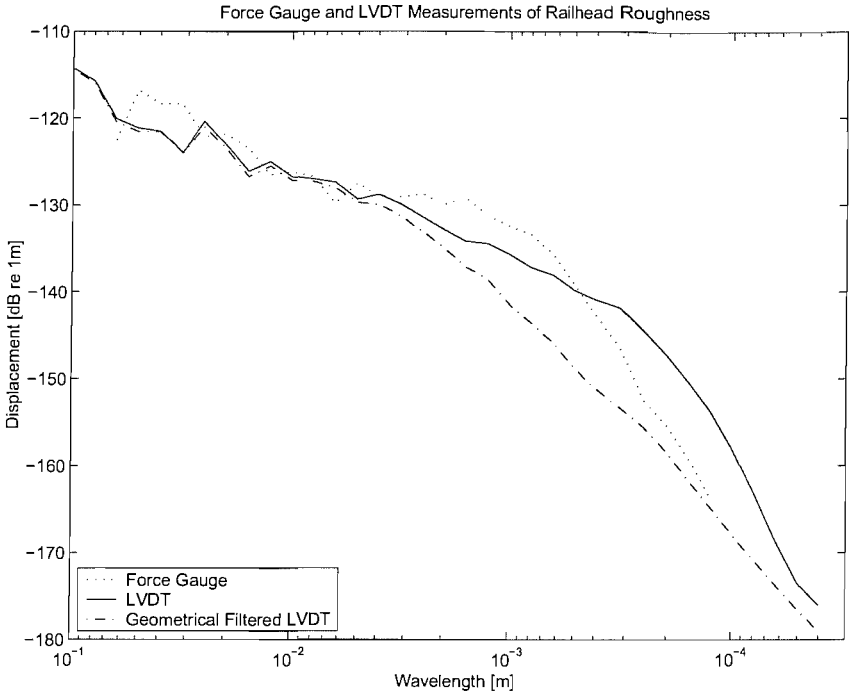

Figure 4-31 Comparison of the LVDT measurement, the LVDT geometrical filtered response and the force gauge measurement for railhead roughness.

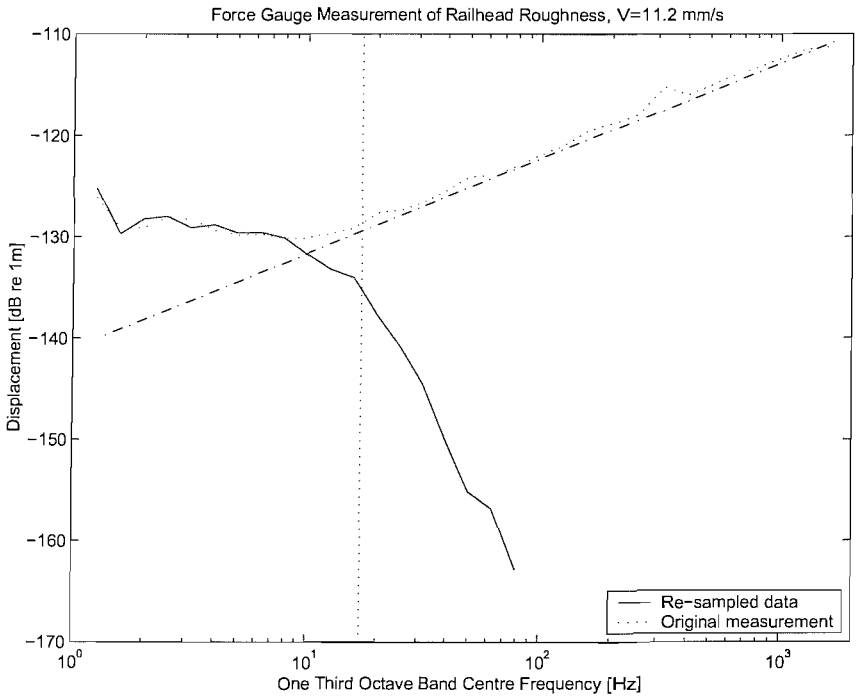

Figure 4-32 Comparison of the frequency response of force gauge measurement of railhead roughness without any corrections for change in measurement speed and the re-sampled data. The dotted vertical line indicates the frequency of the anti-aliasing filter.

Figure 4-33 shows spectra of two 'raw' measurements (before re-sampling) from the force gauge made at 11mm/s and 17mm/s. The 17mm/s measurement is adversely affected by dynamic effects possibly of the wheel, although this is not certain due to the poor low frequency measurement of the wheel assembly in Figure 3-45.

As the useful frequency content of the force gauge measurement, was limited to wavelengths greater than 1mm, this measurement method was not used to obtain inputs for the prediction models.

4.6 Summary

Measurement of the rig surface profiles has proved to be a difficult task. Much time and effort has been spent trying to obtain the best possible representation of the surface profiles. In this chapter the measurements of the rig wheel and railhead (where no intended discontinuities are present) have been used as an example case to study the following aspects:

- Determination of the wavelength required for the prediction
- Choice of measurement transducer
- Calibration of measurement transducer
- Determination of spatial position
- Trend removal
- Post processing considerations

These techniques have been summarised in a flow chart (see Figure 4-17). To summarise the following conclusions are made:

1. The choice of transducer is important. If the method of measurement involves a device that relies upon contact with the surface then it has to have a probe that is able to negotiate the surface profiles of the wheel and the rail without getting stuck. The probe must also be spring loaded so that contact with the surface during the measurement is ensured. The frequency response of the transducer needs to be identified, so that the frequency and amplitude at which loss of contact is likely to occur can be avoided (if it is practical to do so).

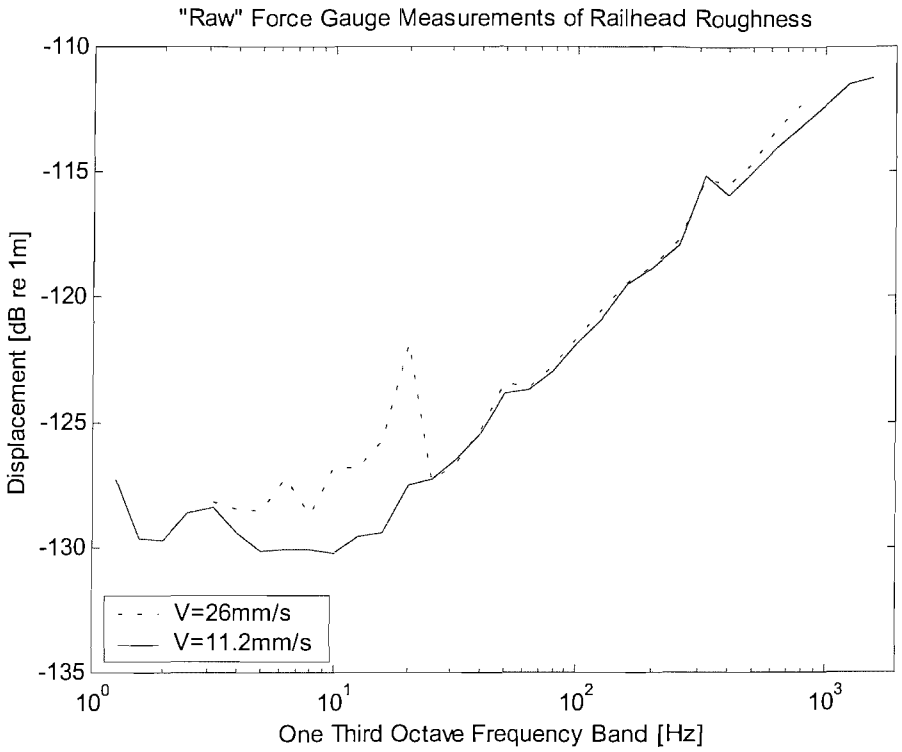

Figure 4-33 Raw roughness measurements at 2 different speeds plotted as a function of frequency.

2. The probe tip must also be able to slide in a vertical direction without excessive lateral movement. A possible source of error found during this research was a very slight juddering of the LVDT probe in the direction of travel along the surface of the railhead whilst traversing an awkward geometrical shape or rough surface. Cleaning of the LVDT probe and the surface of the railhead alleviated this problem.

3. The dynamic range of the transducer must be sufficient to allow for the height differences of any discontinuities and any unevenness of the measurement profile whilst ensuring sufficient signal-to-noise ratio for the small amplitude, short wavelength (high frequency) content of the signal.

4. If a reliable constant velocity can not be ensured along the length of surface profile, then a method of acquiring data at fixed spatial intervals is required. This is particularly important for the measurement of large discontinuities rather than typical levels of surface roughness. This is because the measured shape of a discontinuity could be significantly different from the real case if the spatial positioning of the measurement is not carefully controlled.

5. The frequency bandwidths of both the transducer and the method of data acquisition need to be considered in conjunction with the required wavelength range and the measurement speed.

6. Great care is required to remove any effects from the measurement that may (unintentionally) be discontinuous between the start and end of the measurement. These discontinuities have been found to contaminate estimates of a roughness measurement spectral density, by increasing estimates of frequencies higher than the lower frequency trends. This effect has been demonstrated by considerations of the behaviour of sinusoidal trends in section 4.3.7.

7. The time capture length (T) and time spacing (Δt) can be determined with reference to the required frequency range as shown in Figure 4-17.

The effect of geometrical filtering was shown to attenuate the short wavelengths (high frequencies) of a surface profile measurement. The geometrical filter used in this thesis [Thompson, 1996] was found to behave differently according to the number of points (or distance) the filter considered. For a realistic over-estimation of the number of points used in this filter, the frequency content of the surface roughness was not found to alter, but, the computational time of such a filter was seen to increase dramatically. It is necessary to obtain a geometrical filter of an adequate length (for a correct alteration of the surface roughness) but without unnecessary computational times.

An alternative method of measuring surface profiles by using the wheel load spring and force gauge did not prove to be useful for the measurement of discontinuities and railhead roughness, due to noise contamination at frequencies corresponding with a wavelength of 1mm and smaller.

The measurement of the railhead profile shown in Figure 4-16 (after the trend removal process has been applied) and the measurement of the wheel roughness shown in Figure 4-18 were both used in Chapter 6 for the purpose of validating the scale rig and the prediction models. First, however, the next chapter considers some aspects of the performance of the prediction models that were used throughout this thesis.

5 Analysis of prediction models and methods used to improve the predictions of vibration

5.1 Analysis of the models used to predict wheel / rail vibration

Chapter 2 introduced two general types of prediction model that have been used in this thesis. These are models formulated in both the frequency domain and in the time domain. To avoid confusion the following terminology is introduced:

- the frequency-domain model [based on Remington, 1976] is called the FRF model,
- the time-domain models are called either the non-linear time-stepping model, or the linear time-stepping model depending upon the choice of contact spring relationship used in the model.

The FRF model is a special case as it can be used with measurements of the rig wheel and track together with an approximation of the linearised contact stiffness (converted into a FRF) to form a very detailed model. This is not possible for the time-domain models, as they are only able to use analytical approximations of these measurements.

All of the models have been constructed from frequency response functions (or their time-domain equivalents) of the track, the wheel, and the contact spring. Frequency response functions of these elements have been used from either measurements or analytical approximations to form different "models". For clarity the term model is only used here to describe the three main time-domain or frequency-domain models listed above. Differences in the way each model has been formed are from now on referred to as variants of the model. For example, two analytical approximations of the wheel and track frequency response functions have been used in this thesis:

1. A variant in which the wheel is approximated as a mass, and the track is modelled by a $m = 3$ polynomial in the numerator and $n = 4$ polynomial in the denominator (in the same manner as [Wu and Thompson, 2000(a)]). This is called the 'simple' variant, and has been utilised in the frequency-domain and time-domain models.
2. A more complicated variant where the wheel is modelled by a $m = 15$ polynomial in the numerator and $n = 16$ polynomial in the denominator. This is called the 'modal wheel' variant, and has also been utilised in the frequency-domain and time-domain models.

To demonstrate the effectiveness of the analytical approximations the performance of the variants (i.e. the measured FRF variant, simple variant, and the modal wheel variant) are illustrated below using the FRF model (for example equation (2-1)), in the form of their transfer functions. This method of analysing the performance of the FRF model is slightly different from the analysis presented in Chapter 2 where the relationships of the elements of the model were considered. The analysis made here considers how the elements of the model combine to make a transfer function; thus an explanation of the (combined) interaction is formed.

A transfer function in the frequency domain is defined as the ratio of the output to the input signal at a particular (sinusoidal) frequency [Dorf and Bishop, 1995]. The transfer functions corresponding to equations (2-1) and (2-2) can therefore be expressed in terms of a ratio of displacement to roughness input.

Three different transfer functions are considered in this chapter as they correspond with measurements made at various points on the rig. The transfer functions considered are the ratios of:

- Displacement of the rail (at the contact point) to the roughness input (U_r / R).
- Displacement of the axle to the roughness input (U_a / R).
- Displacement of the wheel (at the contact point) to the roughness input (U_w / R).

Each of the transfer functions is considered within the following sub-sections for the measured FRF, simple, and modal wheel variants discussed above.

5.1.1 Measured FRF variant

This variant of the FRF model is constructed from narrow-band transfer function measurements of the rig wheel and the track. Examples of the measured wheel and track response have been presented in Figure 3-17 and Figure 3-26. These measurements can only be used in the FRF model, as the measurements are not in an analytical form, which is necessary for the time-stepping models. The measured FRF model however cannot be used reliably to predict wheel and rail vibration where wheel unloading is likely. Even so the measured FRF variant does provide an important insight into the wheel / rail dynamic contact where the contact spring relationship is (approximately) linear.

Despite being restricted to linear interaction, the measured FRF variant gives potentially the best representation of the rig as it contains the most detail of the rig wheel and track

response with the minimum of assumptions. This is verified in Chapter 6 where comparisons with the measurements and predictions of rail vibration due to a surface roughness input are made. The reason why these results are in best agreement with each other is because, in the absence of discontinuities, the amplitudes of the surface roughness input are not large enough to cause strong variations in the contact between the rig wheel and rail, and thus the linearised contact spring relationship in the prediction is realistic.

5.1.1.1 Rail transfer function U_r / R

The FRF model introduced in Chapter 2 can be expressed as a transfer function of either receptances (α) or accelerances (A) as shown in equation (5-1):

$$\frac{U_r}{R} = \frac{\alpha_r}{\alpha_r + \alpha_w + \alpha_c} = \frac{A_r}{A_r + A_w + A_c} \tag{5-1}$$

The point receptance of the linearised contact spring (k_H) is given as:

$$\alpha_c = \frac{1}{k_H} \tag{5-2a}$$

Alternatively, the accelerance (A_c) is:

$$A_c = \frac{-\omega^2}{k_H} \tag{5-2b}$$

The measurements of the wheel and the track frequency response functions are shown in Figure 5–1 in the form of receptances. The contact spring receptance is also shown from equation (5-2a) and corresponds with a linearised stiffness for a wheel load of 527N, calculated using equation (2-10).

The transfer function U_r / R based on these measured values of the wheel and rail frequency response functions is shown in Figure 5–2. This transfer function resembles a low pass filter combined with a 'notch filter' effect at 1kHz. High frequencies are attenuated above 5kHz. This attenuating trend occurs in a frequency range that coincides with the strong resonant behaviour of the wheel, as does the 'notch filter' effect at 1kHz.

The transfer function shows how the frequency content of an input will be altered. Thus the input frequency content below 5kHz will barely be modified, with the exception of the dip in the response close to 1kHz.

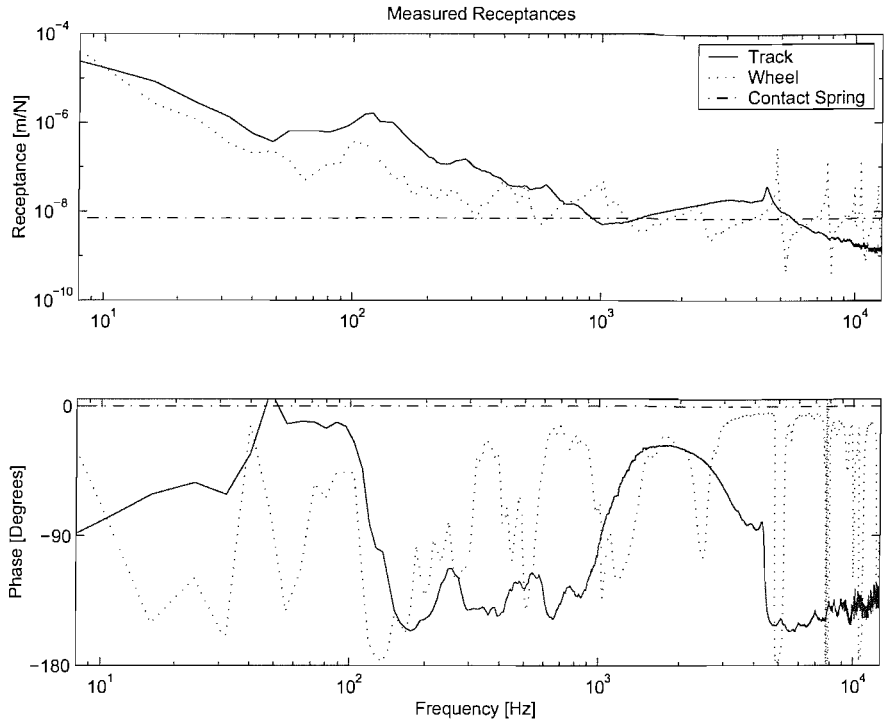

Figure 5–1 Narrow band measurements (shown as receptances) of the elements that make up the measured FRF variant.

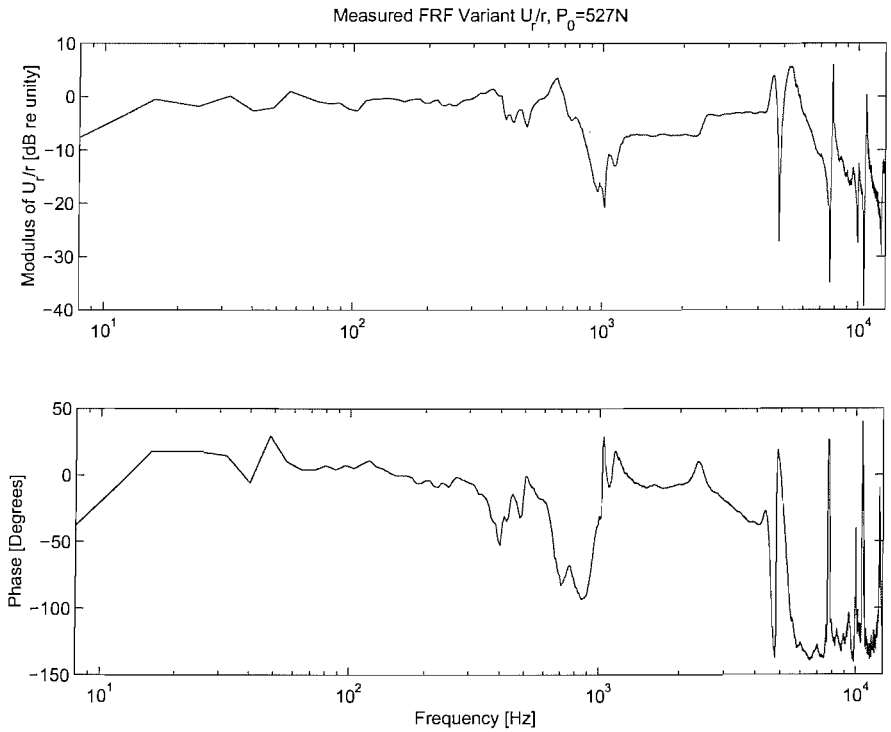

Figure 5–2 Transfer function U_r / R obtained using measured frequency response functions.

5.1.1.2 Axle transfer function U_a/R

The model for the predictions of the axle vibration is a slight modification of equation (5-1):

$$\frac{U_a}{R} = \frac{-\alpha_a}{\alpha_r + \alpha_w + \alpha_c} = \frac{-A_a}{A_r + A_w + A_c} \tag{5-3}$$

where: U_a is the displacement of the axle as a function of frequency,

α_a is the transfer receptance between the wheel tread and axle accelerometer,

A_a is the transfer accelerance between the wheel tread and axle accelerometer.

A measurement of the FRF between the tread of the wheel and the accelerometer on the axle housing is shown in Figure 5–3 in the form of a transfer receptance. Unfortunately a good quality measurement proved to be very difficult to make. The coherence in the lower plot of Figure 5–3 indicates the presence of noise contamination at frequencies below 100Hz and between 3kHz and 7kHz. The higher frequency coherence dips occur in a frequency region where many resonances occur, which coincide with the many modes of the wheel (see Figure 5–1). Attempts were made to try to improve this measurement by applying a load to the axle so that it made better contact with the bearings in the axle housings, but this was not found to make any significant improvements.

The axle transfer receptance is compared with the wheel, rail and contact spring receptances in Figure 5–4. The transfer receptance between the wheel tread and the axle is very similar to the wheel point receptance at low frequencies (up to 1kHz) although its amplitude is slightly lower. Between about 1kHz and 4kHz, the tread to axle transfer accelerance falls relative to the wheel receptance. At high frequencies, above 5kHz, the transfer receptance appears to have a similar modal character to that of the wheel although it is approximately 100 times smaller in amplitude.

Comparisons between the wheel point accelerance and the axle transfer receptance therefore show that the responses are of a similar nature, albeit at different amplitudes, in the lower and higher frequency ranges measured. This is because the axle becomes dynamically decoupled from the wheel above 1kHz. This can also be seen in the phase of the transfer receptance (Figure 5–3) which is mass-like below 1kHz but tends towards stiffness-like behaviour above 3kHz (180°).

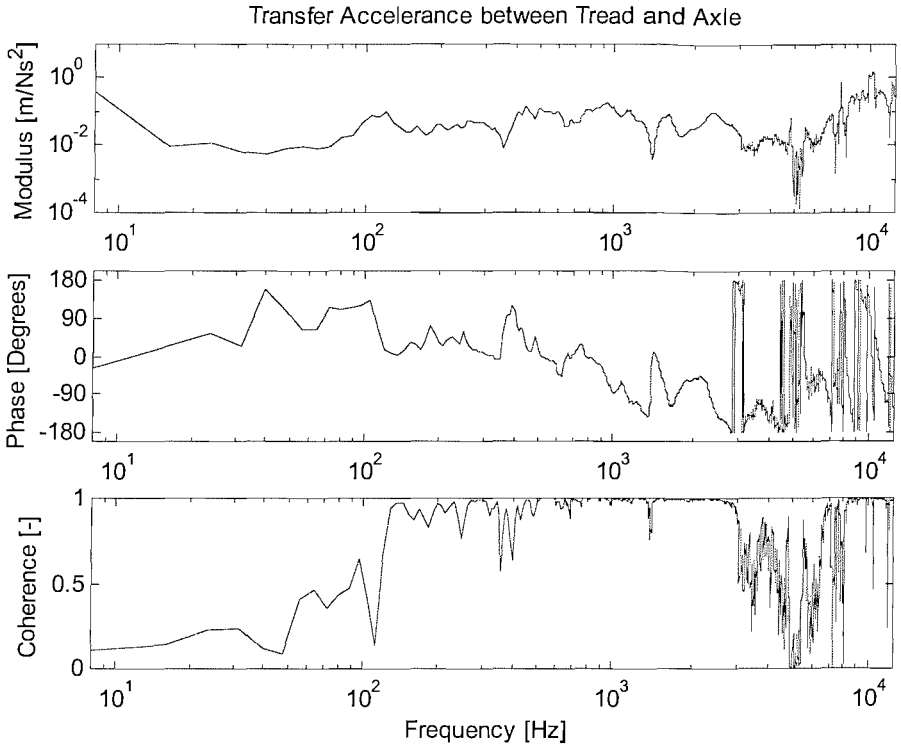

Figure 5–3 Transfer accelerance measured from wheel tread to the axle measurement position.

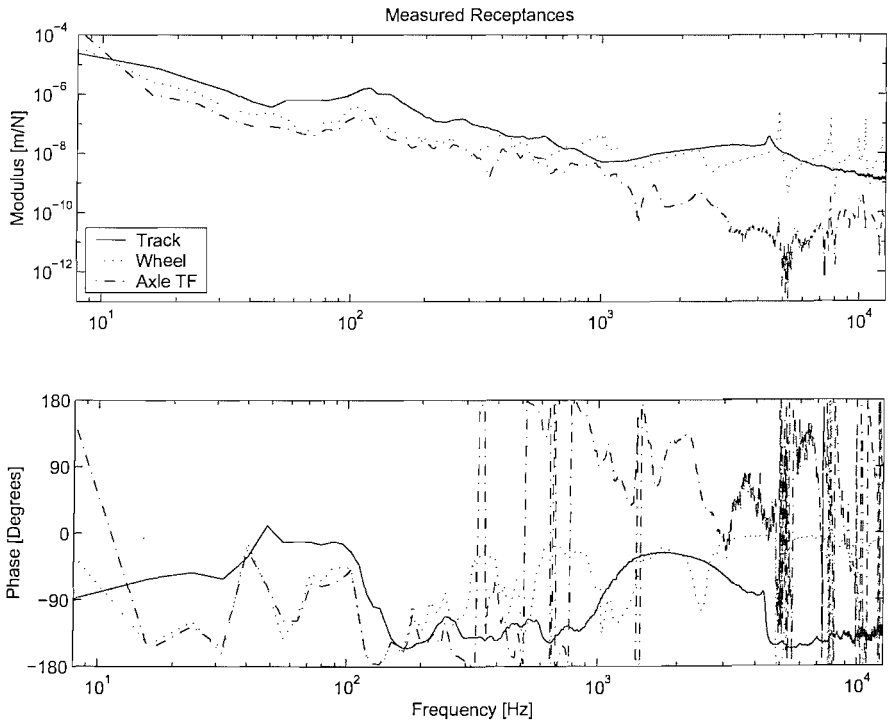

Figure 5–4 Narrow-band measurements (shown as receptance) of the rig elements (excluding contact stiffness) that make up the measured FRF model Transfer function U_a / R.

The transfer function U_a/R, is shown in Figure 5–5. At frequencies below 1kHz this shows a fairly constant attenuation of about 20dB, caused by the roughly constant difference between α_a and α_r seen in Figure 5–4. Above 1kHz U_a/R falls markedly to an attenuation of almost 90dB at 5kHz. Above 5kHz, the attenuation of U_a/R is not so great, rising to about –30dB at 10kHz.

5.1.1.3 Wheel transfer function U_w/R

Predictions and measurements of the wheel response are not as straight forward as the axle response, because the wheel is not a stationary object relative to either the track bed or the rig beam. The model for the prediction of wheel vibration, like the axle prediction model, is a slight modification of equation (5-1):

$$\frac{U_a}{R} = \frac{-\alpha_w^T}{\alpha_r + \alpha_w + \alpha_c} = \frac{-A_w^T}{A_r + A_w + A_c} \qquad (5\text{-}4)$$

where: U_w is the displacement as a function of frequency of the wheel,

α_w^T is the transfer receptance from the contact point to the required location,

A_w^T is the transfer accelerance from the contact point to the required location.

The response of the wheel could be predicted by use of the wheel point accelerance measurement that is also used in the denominator of this model. However this gives a response of the wheel as though it is a stationary body. As the wheel actually turns, and its vibration is measured at a point that rotates with the wheel, an average response during wheel rotation is required. Furthermore, the position of the accelerometer is on the inner rim of the wheel, whilst the point of contact is on the tread. This means that account should be taken of the transfer function between the point of excitation and the point of measurement in addition to the effects of the wheel rotation. Thus α_w^T will not correspond with α_w. It is obtained by averaging several transfer accelerance measurements made at different points around the wheel.

To do this, the wheel was excited at the tread using an electrodynamic shaker supplied with a white noise input and acceleration was measured at 10 points randomly selected around the inner circumference of the tread. These points are shown in Figure 5–6. The average was then calculated of the squared modulus of these measurements. The average result in the form of accelerance is shown in Figure 5–7 where it is compared with the point accelerance measurement. This shows that the averaged accelerance is

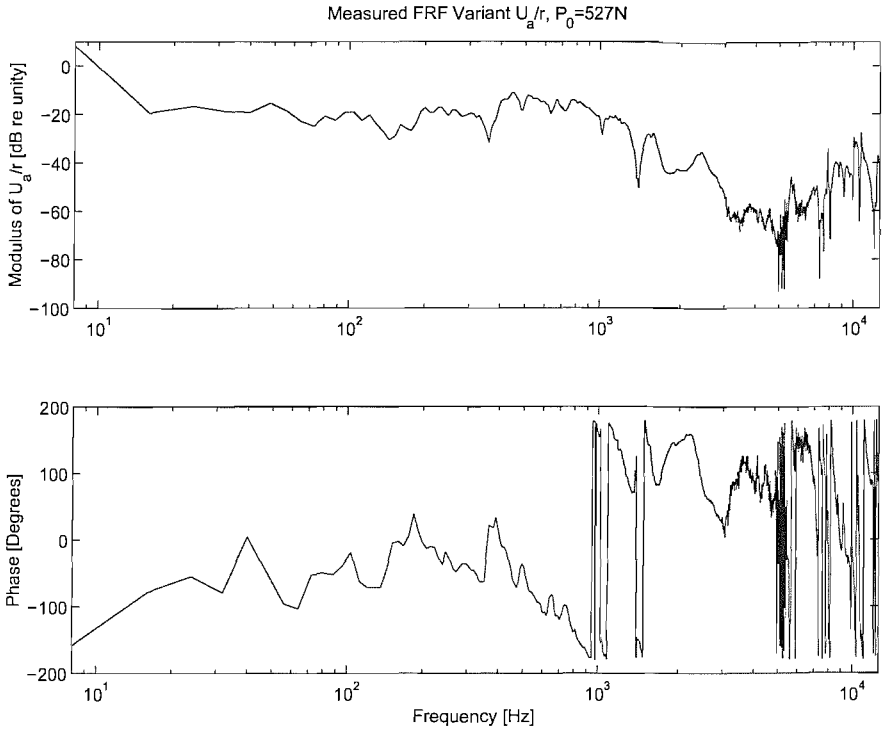

Figure 5–5 Transfer function U_a / R obtained using measured frequency response functions.

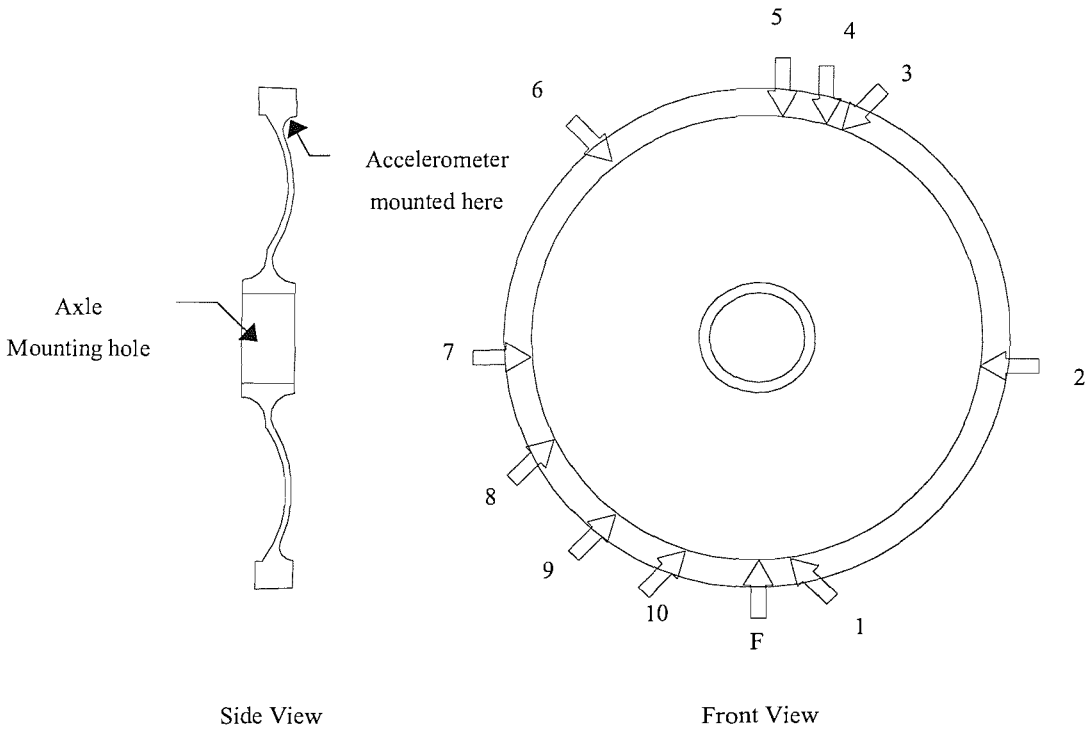

Figure 5–6 Position of the accelerometer mounted on the rig wheel. Position 'F' indicates the forcing point, and the positions numbered 1 to 10 were chosen randomly.

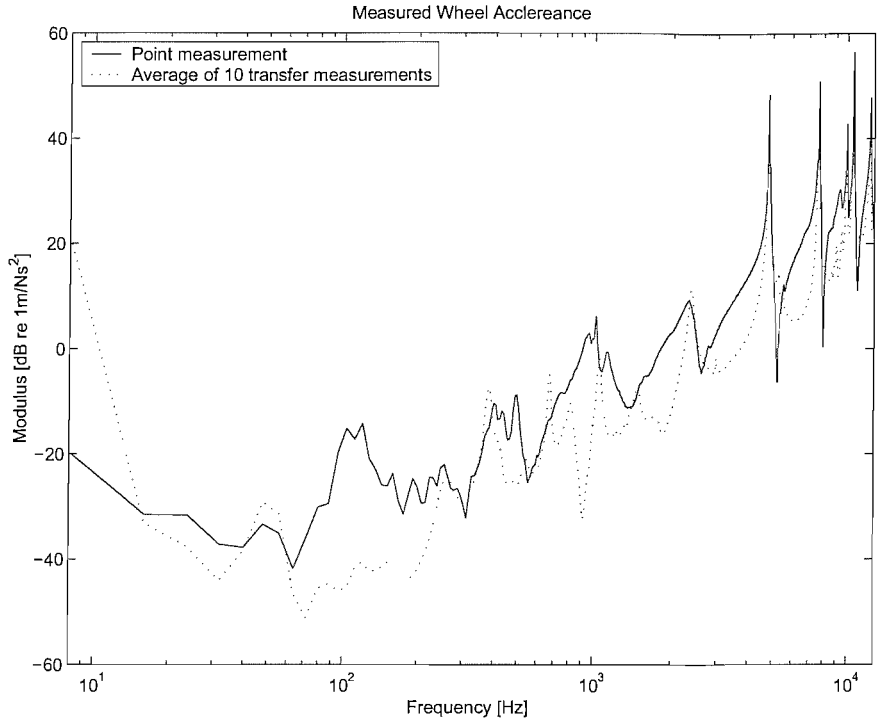

Figure 5–7 Modulus of the average wheel response (A_w^T) measurement and the point accelerance measurement.

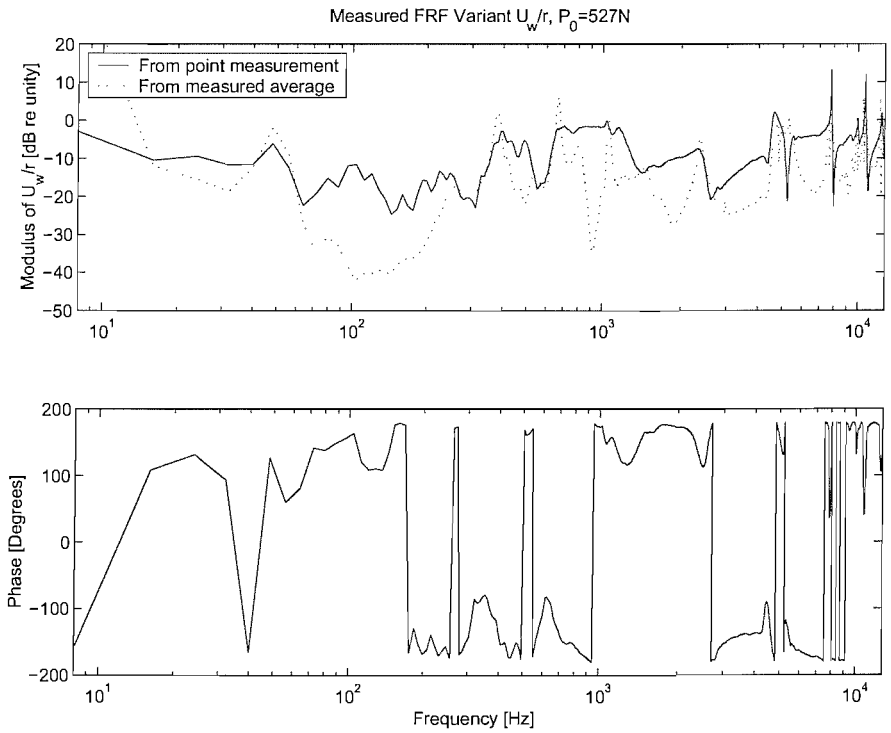

Figure 5–8 Transfer function U_w / R calculated using a point accelerance measurement and an average response measurement of the wheel.

typically lower than the point accelerance measurement in the frequency range 20Hz to 10kHz. It can also be seen that due to the averaging process, the averaged accelerance has no pronounced dips in its modulus.

The transfer function U_w/R was calculated using both the wheel point accelerance measurement and the average wheel accelerance in the numerator of equation (5-4). The results are shown in Figure 5–8 where it can be seen that both of these results are rather complicated. They do not show any simple trends that can be identified as for the transfer function U_r / R. Strong modal behaviour is evident across the whole frequency range considered.

As demonstrated in Figure 5–7, the inclusion of the averaged measured wheel response in the numerator of equation (5-4) produced a lower transfer function response between 100Hz and 10kHz than using the point accelerance. This is also seen in Figure 5–8.

5.1.2 'Simple' variant

Rather than using measured frequency response functions of the elements to make up the transfer function, simple approximations are utilised in this variant. The track is represented by an approximation made using the method devised by [Wu and Thompson, 2000(a)], which has been discussed in Chapter 2. A simple mass is used to approximate the wheel.

Figure 5–9 shows a comparison of the approximated (curve fitted) track response with a measurement of the point accelerance between two sleeper supports at a position in the centre of the track (position MRS8 shown in Figure 3-14). This shows that the simplified variant captures the main features of the measured accelerance, apart from the peak at 4.3kHz due to the pinned-pinned resonance. The approximated track FRF is also compared with a measurement made above a sleeper at position MR8 (see Figure 3-14) in Figure 5–10. The modulus of the measurement above the sleeper is seen to be at a slightly higher level across the frequency range considered (100Hz to 10kHz) when compared with the modulus of the measurement at the mid span sleeper position in Figure 5–9. Despite the differences between the measured frequency response functions at the two different positions along the track, the comparison in Figure 5–10 shows that the approximate track FRF is quite a good representation of the track frequency response at positions above and in between the discrete track supports. Therefore effects due to the discrete nature of the 1/5 scale track bed are quite well represented by the approximate track FRF.

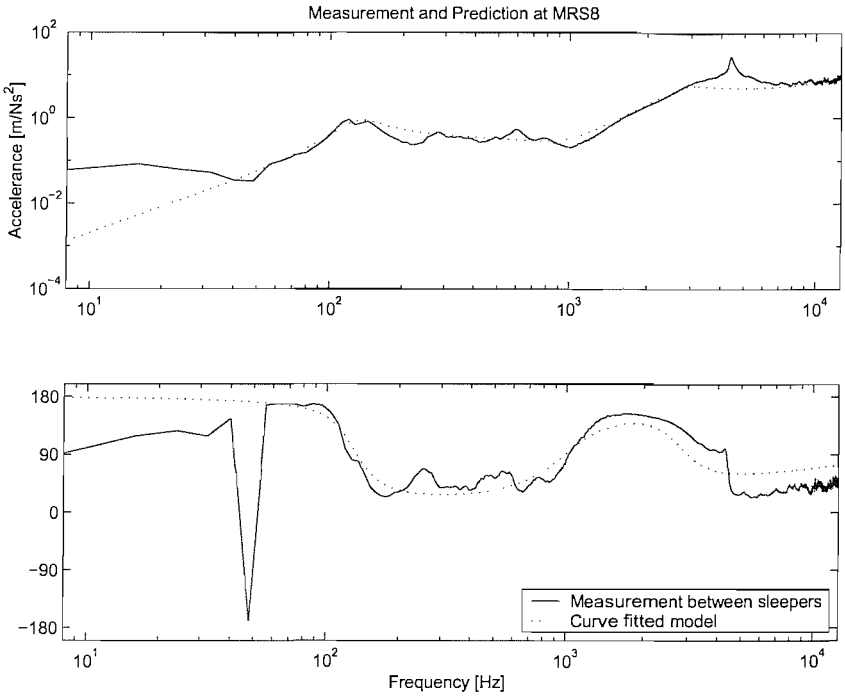

Figure 5–9 Prediction using a fourth order polynomial fit [Wu and Thompson, 2000(a)] to a track point accelerance measurement in between two sleepers at position MRS8.

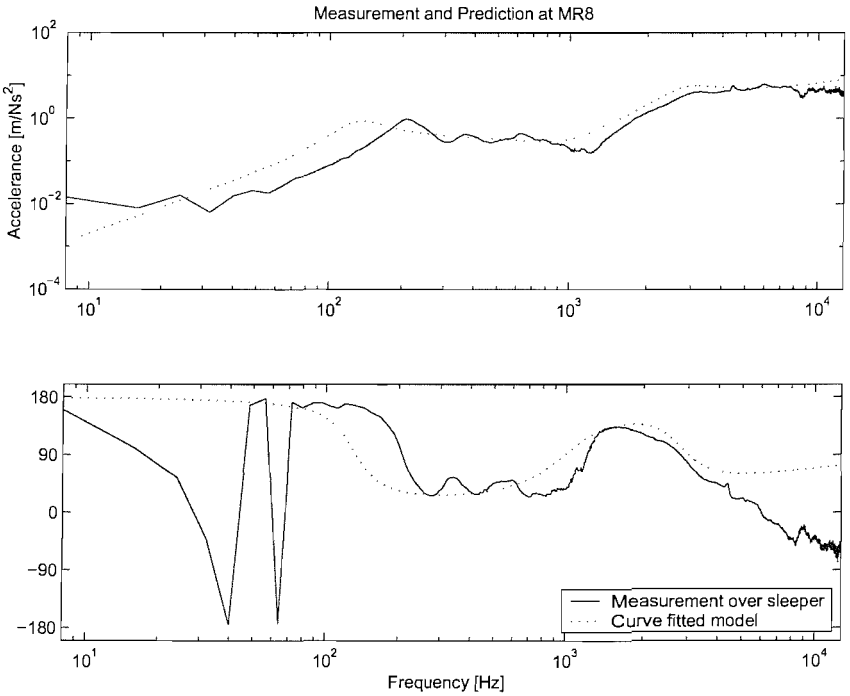

Figure 5–10 Comparison of a fourth order polynomial fit [Wu and Thompson, 2000(a)] with a track point accelerance measurement above a sleeper at position MR8.

Values of the polynomial used to represent the track FRF are presented in Table 5-1.

5.1.2.1 Rail transfer function U_r / R

The point receptances that make up the transfer function U_r / R are shown in Figure 5–11 for the simple variant. Again the receptance of the contact spring is calculated using equation (5-2a) with the linearised Hertzian stiffness derived from equation (2-10) for a wheel pre-load of 527N. These elements are combined as shown in equation (5-1) to form the transfer function in Figure 5–12. This is compared with the previous result from the measured FRF variant described in section 5.1.1.1.

Figure 5–12 shows that the transfer function for the simple variant is close to 0dB between 100Hz and 4kHz. In the simple variant, however, the receptance of the wheel dominates the denominator at low frequencies, leading to an attenuation of the transfer function at low frequencies. As 0Hz is approached, the simple variant of U_r / R tends towards zero due to the infinite receptance of the simple mass model. A resonance occurs at about 50Hz where the mass of the wheel bounces on the stiffness of the track, as the wheel and track receptances have equal magnitude and opposite phase at this frequency.

The idealised receptances of the wheel and track differ from their measured counterparts at frequencies below 100Hz. However, the quality of the measurements that are used in the measured FRF variant below 100Hz are thought to be influenced by noise. This is shown in Figure 3-17 and Figure 3-27 where the coherence of each measurement is seen to be between 0 and 0.5 at low frequencies. The FRF of the track (see Figure 3-17) should behave much like a stiffness at frequencies up to 80Hz, representing the ballast stiffness, but the measured response here looks almost mass-like. The measurement therefore does not correspond with the expected behaviour in this lower frequency range.

It is interesting to note that the strong dip in U_r / R at 1kHz found for the measured FRF variant is mirrored by a lesser fluctuation in the simple variant. This indicates that the dip in track receptance at this frequency (see Figure 5–11) contributes to this feature in addition to the wheel modal behaviour noted previously.

The differences between the two transfer functions in Figure 5–12 demonstrate that the simple wheel / rail variants are unlikely to produce a prediction that performs as well as the measured FRF variant. Even though, in the high frequency range, the simplified

Table 5-1 Track bed model parameters

Numerator Values		Denominator Values	
b_1	9.1×10^{-5}	a_1	1
b_2	3.2	a_2	9.8×10^{3}
b_3	17.8×10^{3}	a_3	312×10^{6}
b_4	113.4×10^{6}	a_4	133×10^{9}
		a_5	199×10^{12}

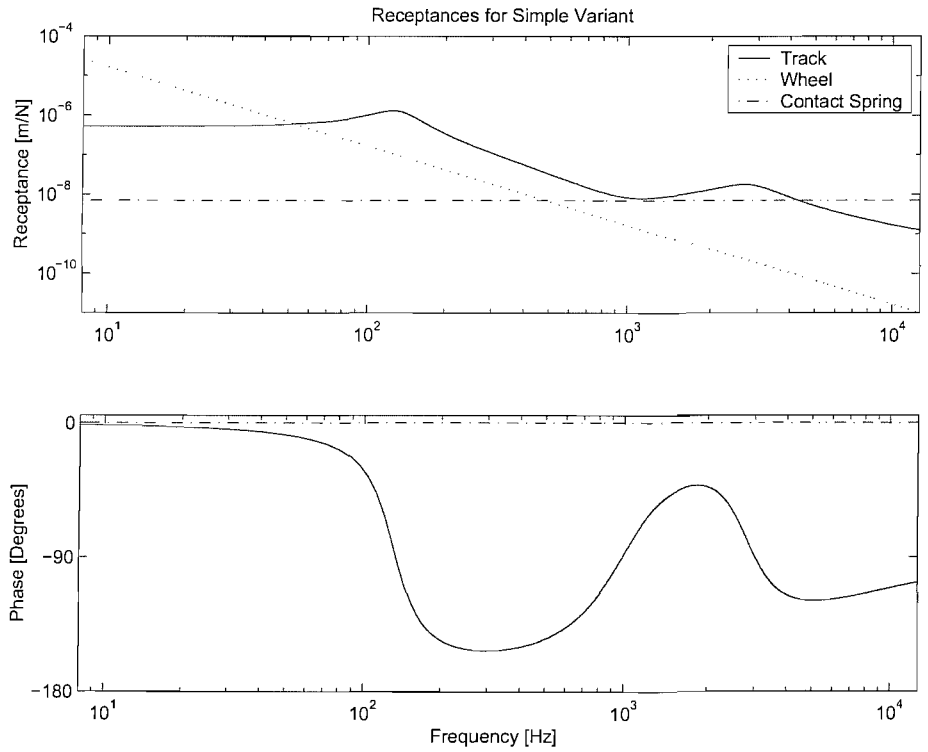

Figure 5–11 Frequency responses of the elements that make up the simple variant transfer function U_r / R.

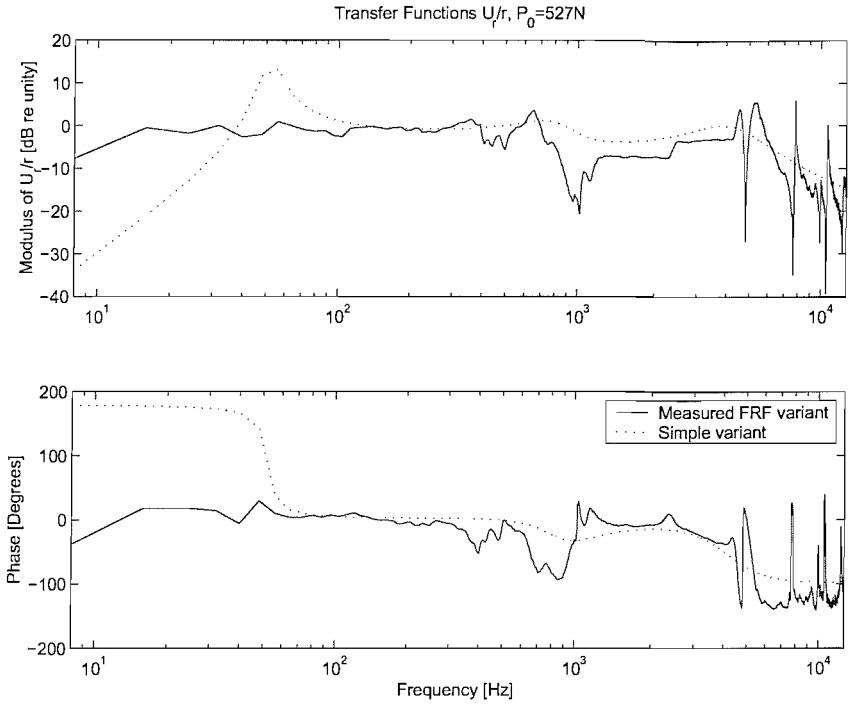

Figure 5–12 Comparison of the measured FRF variant transfer function U_r / R with the simple variant representation of U_r / R.

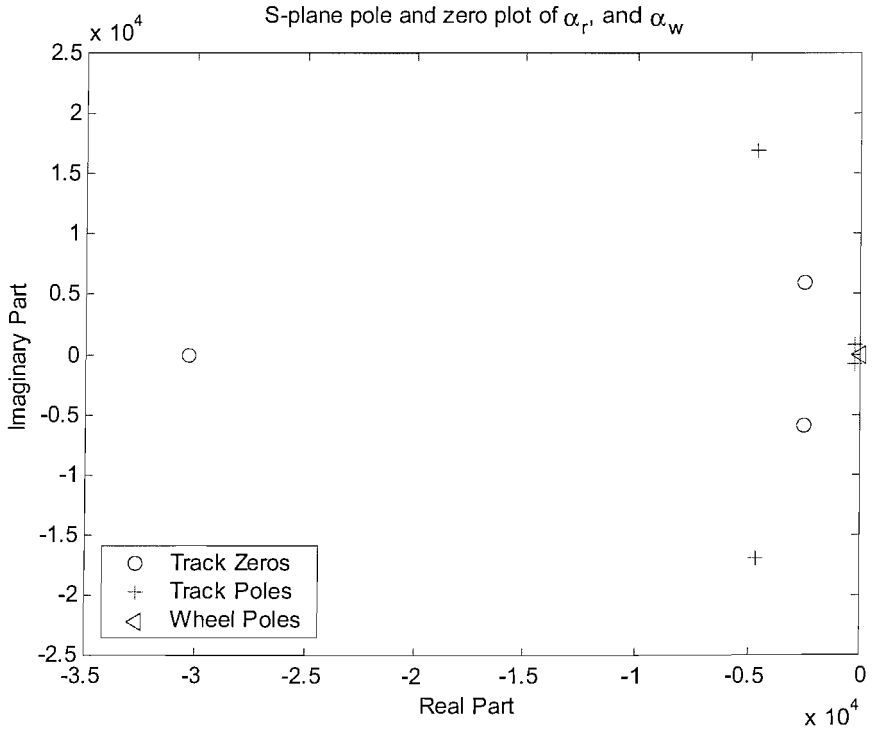

Figure 5–13 Pole and zero plot of the simple variant wheel and track representations. Only the poles of the wheel model are shown, as there are no zeros for this variant.

variant does not adequately describe the modal response of the wheel, the transfer function U_r / R is still similar to the measured FRF variant. In this frequency region it is determined predominantly by α_r/α_c .

5.1.2.2 Alternative method of analysing U_r / R

Analysis of the transfer function U_r / R of the simple variant in the form of its poles and zeros provides an interesting, alternative, insight into how the wheel and rail interact. This is done by calculating the complex roots of the polynomial equations in the denominator and numerator. By ensuring that the real parts of the filter poles always remain negative, or on the left-hand side of the s-plane, stability of the equivalent filter is ensured. This is called the Nyquist stability criterion and is widely documented in control system textbooks (for example [Golten and Verwer, 1991]).

If equation (5-1) is re-written using the form of the simple variant polynomial representation of the wheel, track, and contact spring the following relationship is obtained.

$$\frac{U_r}{R} = \frac{\dfrac{b_1 s^3 + b_2 s^2 + b_3 s + b_4}{s^4 + a_1 s^3 + a_2 s^2 + a_3 s + a_4}}{\dfrac{b_1 s^3 + b_2 s^2 + b_3 s + b_4}{s^4 + a_1 s^3 + a_2 s^2 + a_3 s + a_4} + \dfrac{d_1}{c_1 s^2} + \dfrac{f_1}{e_1}} \qquad (5\text{-}5)$$

where: the coefficients b_n correspond to the track numerator polynomial,

a_n correspond to the track denominator polynomial,

c_1 is equal to the wheel mass,

e_1 is equal to the linearised contact spring stiffness,

and $d_1 = f_1 = 1$ for the simple variant.

The polynomial coefficients of this relationship can be simplified in the following manner:

$$\frac{\frac{B}{A}}{\frac{B}{A}+\frac{D}{C}+\frac{F}{E}} = \frac{BCE}{BCE+ADE+ACF} \tag{5-6}$$

where: A and B represent the polynomial expressions of the track model,
C and D represent the coefficients of the wheel model,
E and F represent the coefficients of the linear contact spring.

Two things should be noted from equation (5-5) above. Firstly the receptance of the linearised contact stiffness contributes to the denominator of the transfer function in the form of a pure gain, and the receptance of the wheel mass is just a second order term. This is confirmed by the responses previously shown in Figure 5–11 where, for example, the modulus of the linearised stiffness is shown as a horizontal line. Secondly the zeros of the transfer function U_r / R (BCE) are seen to be a factor of the zeros of the approximate track FRF (B) combined with the poles of the wheel analytical representation (C) multiplied by the linear stiffness (k_H). The poles of the transfer function are a combination of all of the poles and zeros of each part of the wheel / rail interaction model. Therefore whilst it has been important to ensure that the poles of the fitted polynomial curve exist on the left-hand side of the s-plane, to ensure stability, all the zeros of the resulting curve fitting routine must also be on the left-hand side of the s-plane to ensure stability of the overall transfer function U_r / R.

The poles and zeros of the approximate track FRF, and the poles of the analytical wheel variant (as no zeros are present) are shown in Figure 5–13. The wheel model has a double pole at the origin, while the poles and zeros of the track model are indeed in the left-hand half-plane.

With reference to equation (5-6), three factors of the polynomial coefficients can be found. These are:

$$BCE = c_1 e_1 \left(0 + b_1 s^5 + b_2 s^4 + b_3 s^3 + b_4 s^2 + 0 + 0\right) \tag{5-7a}$$

$$ADE = d_1 e_1 \left(0 + 0 + a_1 s^4 + a_2 s^3 + a_3 s^2 + a_4 s + a_5\right) \tag{5-7b}$$

$$ACF = c_1 f_1 \left(a_1 s^6 + a_2 s^5 + a_3 s^4 + a_4 s^3 + a_5 s^2 + 0 + 0\right) \tag{5-7c}$$

The symbol zero ('0') has been used in equations (5-7) above as a 'place holder' to clarify the relative positions of each polynomial coefficient. The final representation of the transfer function U_r / R is shown in equation (5-8).

$$\frac{U_r}{R} = \frac{c_1 e_1 \left(0 + b_1 s^5 + b_2 s^4 + b_3 s^3 + b_4 s^2 + 0 + 0\right)}{a_1 c_1 f_1 s^6 + a_2 b_1 c_1^2 e_1 f_1 s^5 + G_1 s^4 + G_2 s^3 + G_3 s^2 + a_4 d_1 e_1 s + a_5 d_1 e_1} \tag{5-8}$$

where:

$$G_1 = a_1 a_3 b_2 c_1^2 d_1 e_1^2 f_1$$
$$G_2 = a_2 a_4 b_3 c_1^2 d_1 e_1^2 f_1$$
$$G_3 = a_3 a_5 b_4 c_1^2 d_1 e_1^2 f_1$$

Equation (5-8) was converted into its poles and zeros by use of the MATLAB routine TF2ZP. The results are shown in Figure 5–14. This shows that the transfer function is stable as the poles are all on the left-hand side of the origin. The double zeros at the origin, were previously the poles of the wheel model shown in Figure 5–13. Further comparisons between Figure 5–13 and Figure 5–14 show that the zeros of the track model match those of the transfer function U_r / R (with the exception of the new double zeros at the origin). The poles, however, are seen to move to new positions.

Equation (5-8) can be used to form a digital filter of the transfer function U_r / R for a fixed value contact force (k_H). This provides an alternative prediction model that is presented in Appendix B.

5.1.2.3 Wheel transfer function U_w / R

In the simple variant there is no allowance for the distinction between the wheel and the axle response as only a simple relationship is used to describe the wheel and wheel assembly as a mass. Therefore only the wheel transfer function U_w / R is considered. Further, in the simple variant the difference between the point FRF and average FRF of the wheel is not accounted for, as the effect of the average response can not reliably be included in the simple variant.

The frequency response of the simple variant elements shown in Figure 5–11 were used to form the transfer function U_w / R, according to equation (5-4). This is given in Figure 5–15 where it is compared with the result from the measured FRF variant based on the wheel point accelerance measurement, shown previously in Figure 5–7.

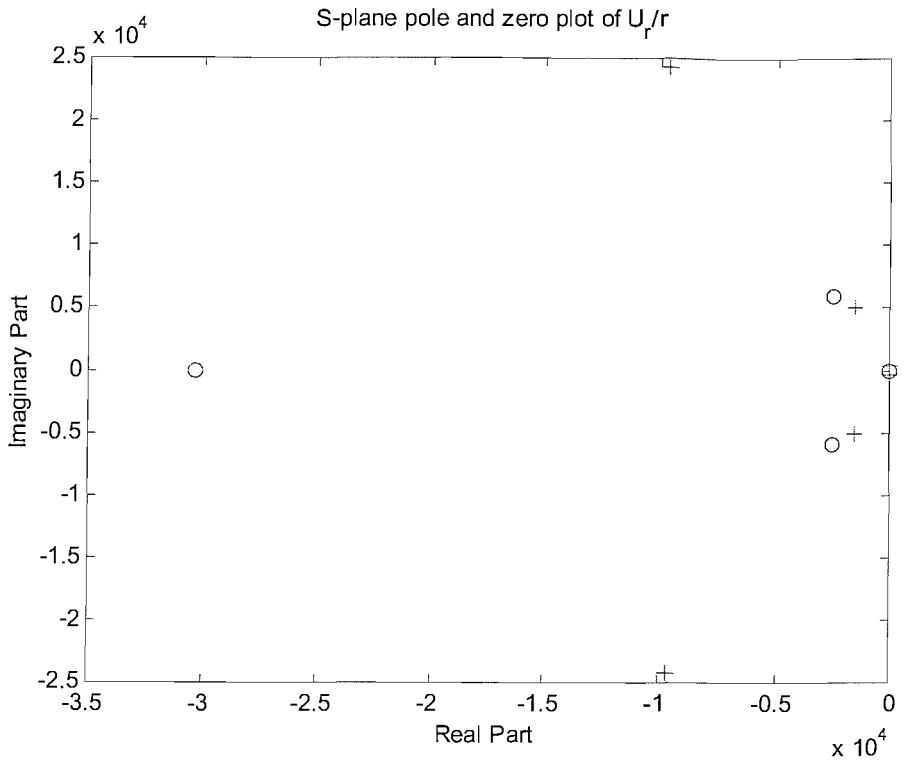

Figure 5–14 Pole and zero plot of the simple variant transfer function U_r / R (o= zeros, += poles).

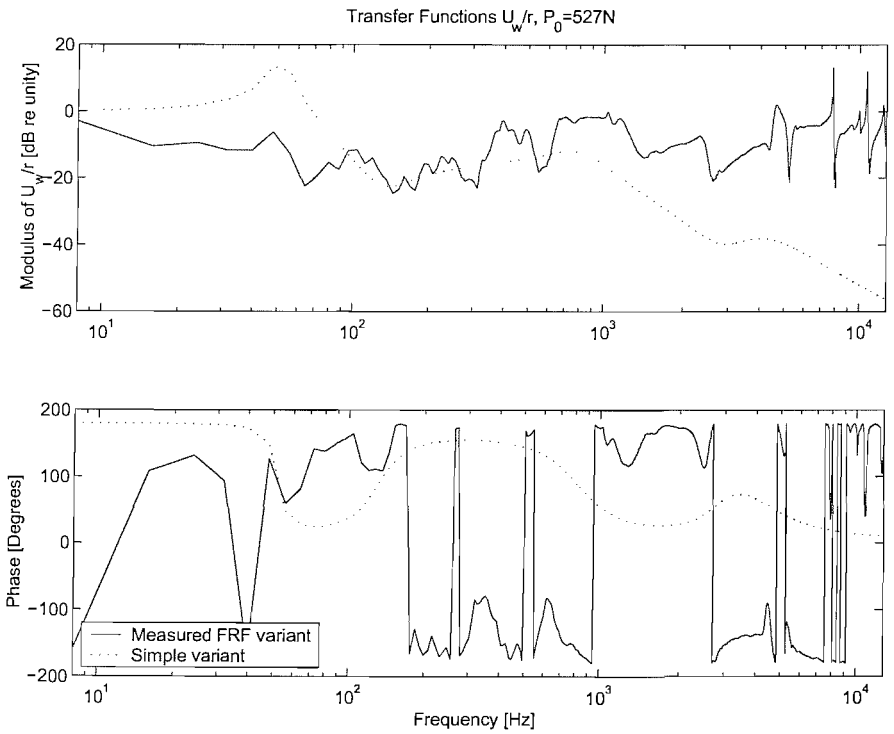

Figure 5–15 Comparison of the measured FRF variant transfer function U_w / R with the simple model variant U_w / R.

The transfer function U_w / R of the simple variant is close to 0dB at very low frequencies, where the wheel has the highest receptance. The wheel on track resonance at 50Hz, seen in the transfer function U_r / R, is seen again here. Above this frequency U_w / R falls initially to around –15dB to –20dB, and above 1kHz it falls again due to the widening difference between the rail and wheel receptances, see Figure 5–11. These results shown in Figure 5–15 demonstrate the limitation of the simple variant. Whereas the transfer function U_r / R was not found to be greatly affected by the simplifications of this variant, U_w / R is seen to be greatly influenced at high frequencies.

5.1.2.4 Alternative method of analysing U_w / R

As in section 5.1.2.1, where U_r / R was considered, the simple variant representation of the transfer function U_w / R can also be described in polynomial form. The receptances of the track, wheel and linear contact spring, converted into their polynomial equivalents are shown below in equation (5-9). The numerator of the transfer function U_w / R differs from equation (5-5), in the same way that equation (2-1) differs from equation (2-2).

$$\frac{U_w}{r} = \frac{\dfrac{-d_1}{c_1 s^2}}{\dfrac{b_1 s^3 + b_2 s^2 + b_3 s + b_4}{s^4 + a_1 s^3 + a_2 s^2 + a_3 s + a_4} + \dfrac{d_1}{c_1 s^2} + \dfrac{f_1}{e_1}} \tag{5-9}$$

The polynomial coefficients of this transfer function were simplified in a similar manner to that shown in section 5.1.2.1.

$$\frac{-\dfrac{D}{C}}{\dfrac{B}{A} + \dfrac{D}{C} + \dfrac{F}{E}} = \frac{-ADE}{BCE + ADE + ACF} \tag{5-10}$$

This provided the following result.

$$\frac{U_w}{r} = \frac{-d_1 e_1 \left(0 + 0 + a_1 s^4 + a_2 s^3 + a_3 s^2 + a_4 s + a_5\right)}{a_1 c_1 f_1 s^6 + a_2 b_1 c_1^2 e_1 f_1 s^5 + G_1 s^4 + G_2 s^3 + G_3 s^2 + a_4 d_1 e_1 s + a_5 d_1 e_1} \tag{5-11}$$

The poles and zeros of the simple variant transfer function U_w / R are shown in Figure 5–16. As for U_r / R the transfer function U_w / R is seen to be a stable system as all of the poles are on the left hand side of the origin. The original positions of the track and

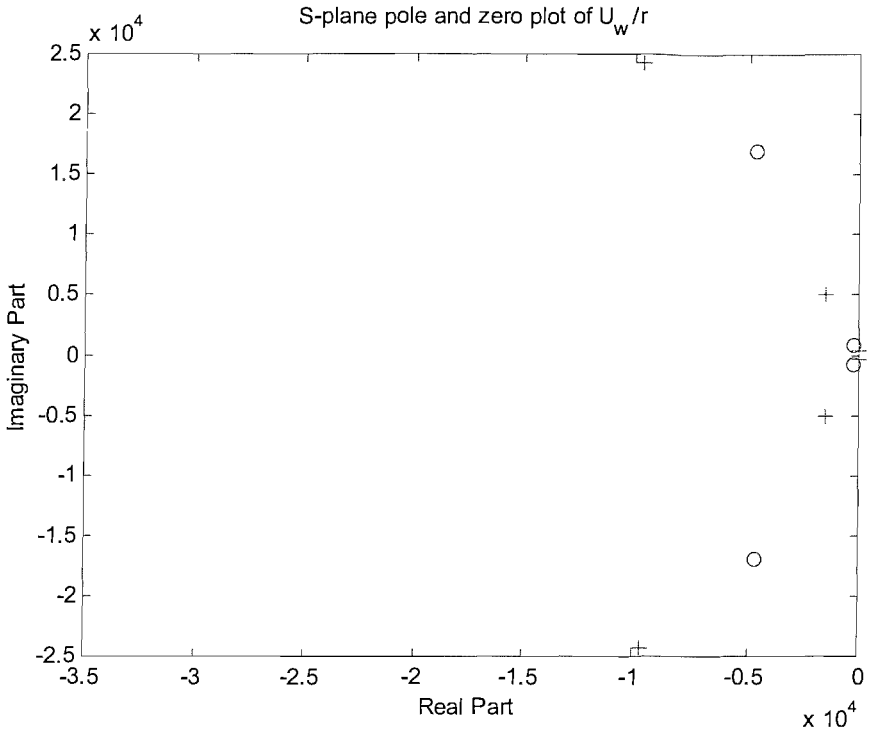

Figure 5–16 Pole and zero plot of the simple variant transfer function U_w / R (o= zeros, += poles).

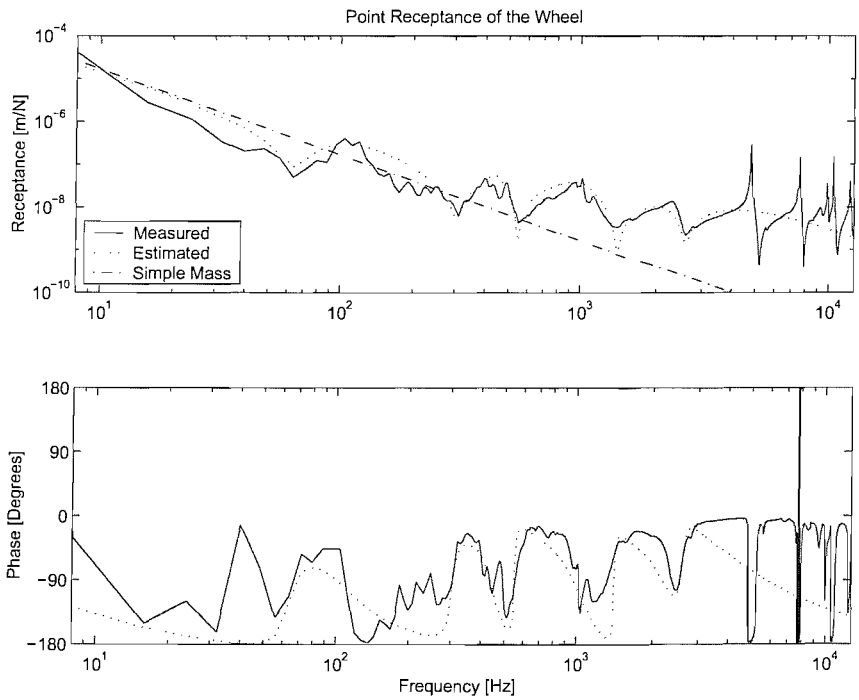

Figure 5–17 Point receptance measurement of the wheel compared with the modelled wheel response obtained using a $m=15$, $n=16$, polynomial curve fitting method.

wheel model poles and zeros shown in Figure 5–13 are seen to move to new positions in Figure 5–16. Pole and zero cancellation is evident as the double poles of the wheel model at the origin no longer exist, nor does the pole from the track model furthest away from the origin.

5.1.3 Introduction to the 'modal wheel' variant

Prediction of wheel vibration using the simple variant has been seen to give poor results at high frequencies. Despite the noise contamination at low frequencies in the measurements, the variant based on the measured frequency responses of the wheel and the rail has the greatest potential for predicting wheel and rail vibration accurately (above 100Hz). However such a model cannot be used in the time domain as no analytical representation of the measured frequency response functions exists. Therefore a model for the wheel frequency response has been produced in a manner similar to that of the polynomial representation of the track response.

A series of first and second order systems were fitted to the point receptance measurement of the wheel, using assumed values of mass, damping, and stiffness in order to obtain an acceptable representation of a modal response. Although time consuming, this method was found to provide better results than by using the MATLAB function INVFREQS used by [Wu and Thompson, 2000(a)][6]. When assembled, these lower order systems of each modal response of the wheel were found to combine to form a $m = 15$ polynomial in the numerator and $n = 16$ polynomial in the denominator. The frequency response of this fitted curve is compared with the measurement in Figure 5–17.

Great care was taken to ensure that the phase of the curve fitted response remained between $-180°$ and $0°$, so that it represented a valid driving point receptance. The modelling of the lower frequency wheel modes, below 3kHz, was quite straightforward. However, the higher frequency wheel modes proved to be harder to represent. These high frequency modes were therefore approximated by an 'average' response as shown in Figure 5–17. Table 5-2 presents the values of the polynomial coefficients used to describe the rig wheel.

---

[6] This was due to the many lightly damped modes of the wheel (see Chapter 3), that proved difficult for the least squares fitting routine to represent.

Table 5-2 Coefficients for complicated wheel response polynomial

Numerator Values		Denominator Values	
b_1	13.1	a_1	1
b_2	24.7×10^{3}	a_2	54.5×10^{3}
b_3	4.8×10^{9}	a_3	1.6×10^{9}
b_4	4.9×10^{12}	a_4	22.6×10^{12}
b_5	3.6×10^{17}	a_5	3.2×10^{17}
b_6	1.6×10^{20}	a_6	1.6×10^{21}
b_7	4.7×10^{24}	a_7	1.2×10^{25}
b_8	1.2×10^{27}	a_8	2.1×10^{28}
b_9	1.3×10^{31}	a_9	7.7×10^{31}
b_{10}	1×10^{33}	a_{10}	4.5×10^{34}
b_{11}	2×10^{36}	a_{11}	3.2×10^{37}
		a_{12}	1.5×10^{39}
		a_{13}	2.4×10^{40}

5.1.3.1 Rail transfer function U_r / R

The transfer function (U_r / R) obtained using the modal wheel variant is shown in Figure 5–18. As before, the value of the linearised contact stiffness (k_H) corresponds with a wheel load of 527N. Here the transfer function of the modal wheel variant is compared with that of the simple variant and the variant based on measured frequency response functions, shown previously in Figure 5–2 and in Figure 5–12 respectively.

Figure 5–18 demonstrates that the response of the modal wheel variant and the measured FRF variant are in good agreement in the frequency range from 100Hz to 3kHz. The modal wheel model gives a better representation of the 1kHz dip than the simple variant, although, it tends to under-predict the effect of the higher frequency wheel modes. This is because the high frequency wheel modes are not included in the modal wheel variant, as shown in Figure 5–17.

5.1.3.2 Alternative method of analysing U_r / R

The use of polynomial relationships to model the behaviour of the wheel assembly and the track receptances enabled similar investigations to be made of the transfer functions as shown previously in section 5.1.2. The equation for the modal wheel variant of U_r / R is shown below.

$$\frac{U_r}{R} = \frac{\dfrac{b_1 s^3 + b_2 s^2 + b_3 s + b_4}{s^4 + a_1 s^3 + a_2 s^2 + a_3 s + a_4}}{\dfrac{b_1 s^3 + b_2 s^2 + b_3 s + b_4}{s^4 + a_1 s^3 + a_2 s^2 + a_3 s + a_4} + \dfrac{d_1 s^{15} + \cdots + d_{16}}{c_1 s^{16} + \cdots + c_{17}} + \dfrac{f_1}{e_1}} \qquad (5\text{-}12)$$

This equation is very similar to equation (5-8) which described the simple variant transfer function U_r / R, except that the wheel polynomial is much more complicated. The position of the poles and zeros of the track polynomial and the wheel polynomial are shown in Figure 5–19. Using the same method of simplification as shown in section 5.1.2, the modal wheel variant transfer function was split into three factors that could be combined as shown by equations (5-7) to form the final equation.

$$\begin{aligned} BCE &= e_1\left(b_1 c_1 s^{19} + \cdots + b_4 c_{17}\right) \\ ADE &= e_1\left(a_1 d_1 s^{19} + \cdots + a_5 d_{16}\right) \\ ACF &= f_1\left(a_1 c_1 s^{20} + \cdots + a_5 c_{17}\right) \end{aligned} \qquad (5\text{-}13)$$

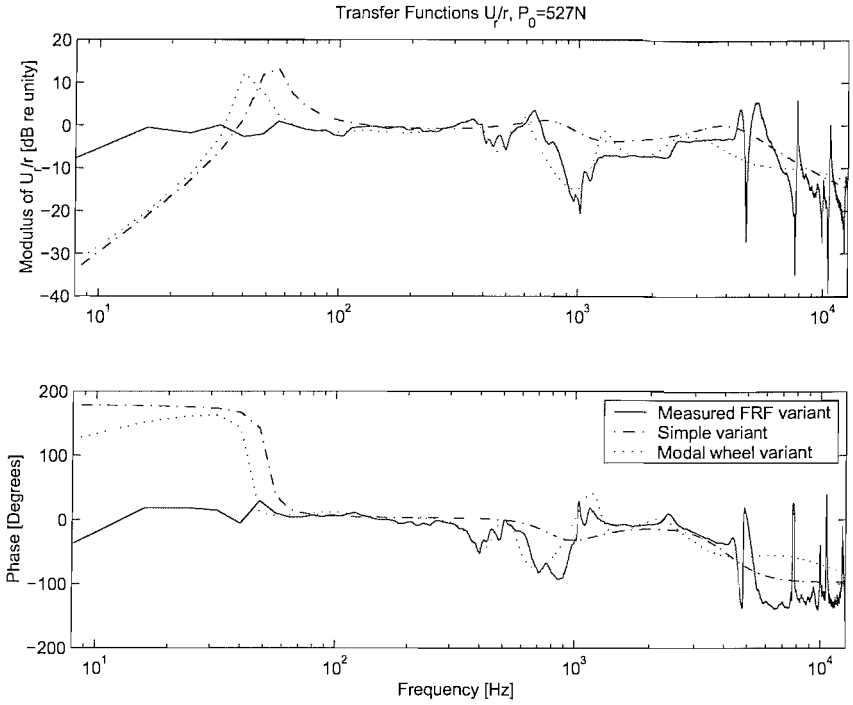

Figure 5–18 Modal wheel variant transfer function U_r / R compared with transfer functions of the measured FRF and the simple variations.

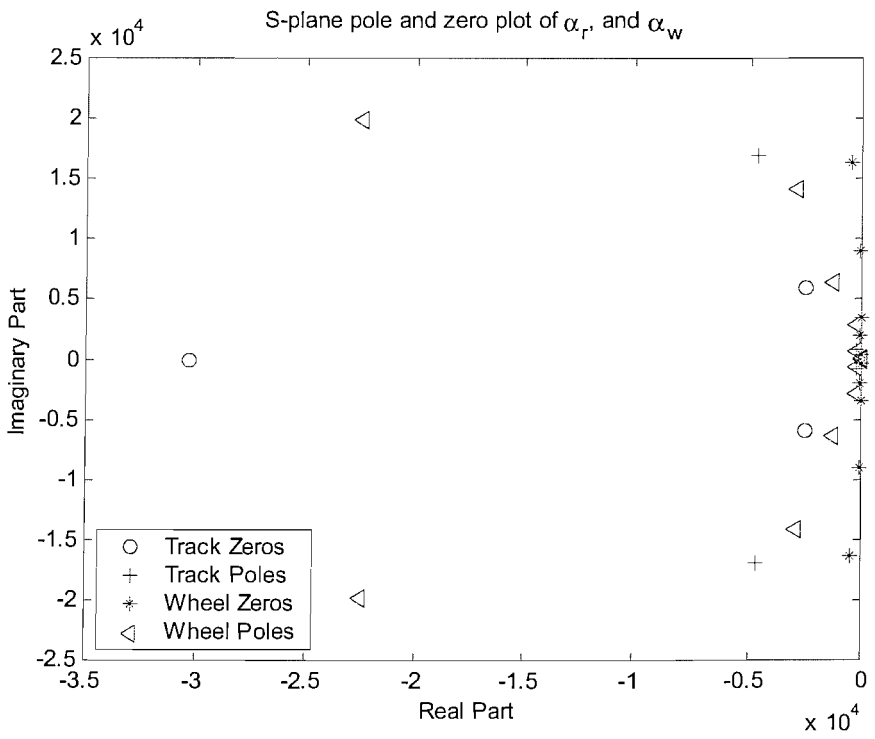

Figure 5–19 Pole and zero plot of the modal wheel variant wheel and track representations (o= zeros, += poles).

$$\frac{U_r}{R} = \frac{e_1\left(b_1c_1s^{19} + \cdots + b_4c_{17}\right)}{f_1a_1c_1s^{20} + \cdots + a_5^2b_4c_{17}^2d_{16}} \tag{5-18}$$

Comparisons between Figure 5–19 and Figure 5–20, where the poles and zeros of U_r / R from the modal variant are presented, show that the zeros of the track model remain in the same positions. This was also observed for U_r / R from the simple variant in section 5.1.2.

5.1.3.3 Wheel transfer function U_w / R

As for the simple variant, there is no distinction between the modelling of the axle and of the wheel, as the behaviour of the wheel assembly cannot be verified, nor is the effect of the wheel rotation taken into account. The analysis of the wheel response was therefore based only on the estimate of the wheel point FRF.

The transfer function U_w / R is compared with those of the simple variant and the measured FRF variant (both using a point FRF of the wheel) in Figure 5–21. This shows that the transfer function for the modal wheel variant agrees well with that of the measured FRF variant in the frequency range 100Hz to 10kHz. The discrepancies at low frequencies, below 100Hz, are due to the effects in the measured track FRF, as discussed previously.

Figure 5–21 demonstrates that, to obtain a realistic response of the wheel, it is necessary to include its modal behaviour. The simple variant has been seen to fail to be useful above 1kHz, but the results of the modal wheel variant agrees more closely with those of the measured FRF variant for frequencies above 80Hz.

5.1.3.4 Alternative method of analysing U_w / R

Using the same method employed in section 5.1.2 and the equations (5-7) the polynomial form of the transfer function U_w / R for the modal wheel variant is shown below in equation (5-14). The pole and zero plot for this relationship is shown in Figure 5–22.

$$\frac{U_w}{R} = \frac{-e_1\left(a_1d_1s^{19} + \cdots + a_5d_{16}\right)}{f_1a_1c_1s^{20} + \cdots + a_5^2b_4c_{17}^2d_{16}} \tag{5-14}$$

Comparisons between the poles and zeros of the modal wheel and track variant shown in Figure 5–19 and the resulting transfer function poles and zeros of U_w / R presented

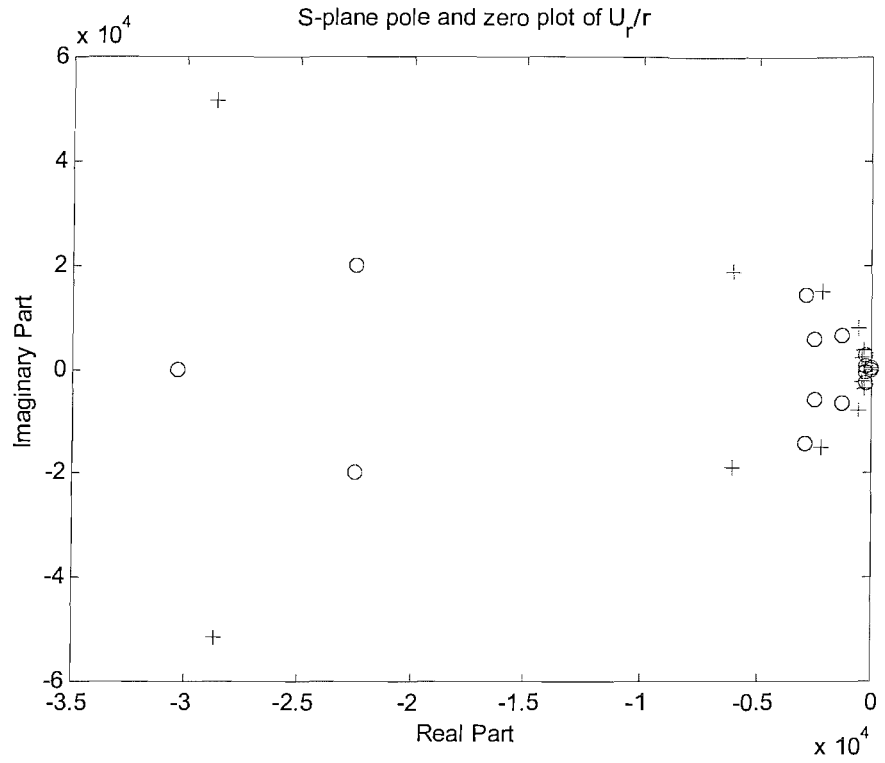

Figure 5–20 Pole and zero plot of the modal wheel variant transfer function U_r / R (o= zeros, += poles).

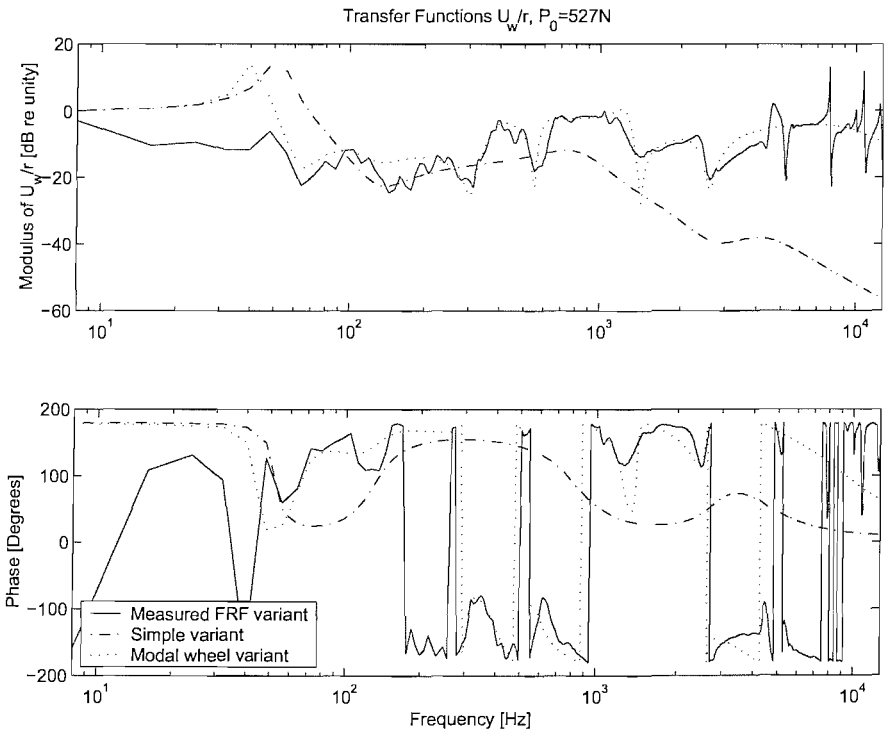

Figure 5–21 Modal wheel variant transfer function U_w / R compared with transfer functions of the measured FRF variant and the simple variant.

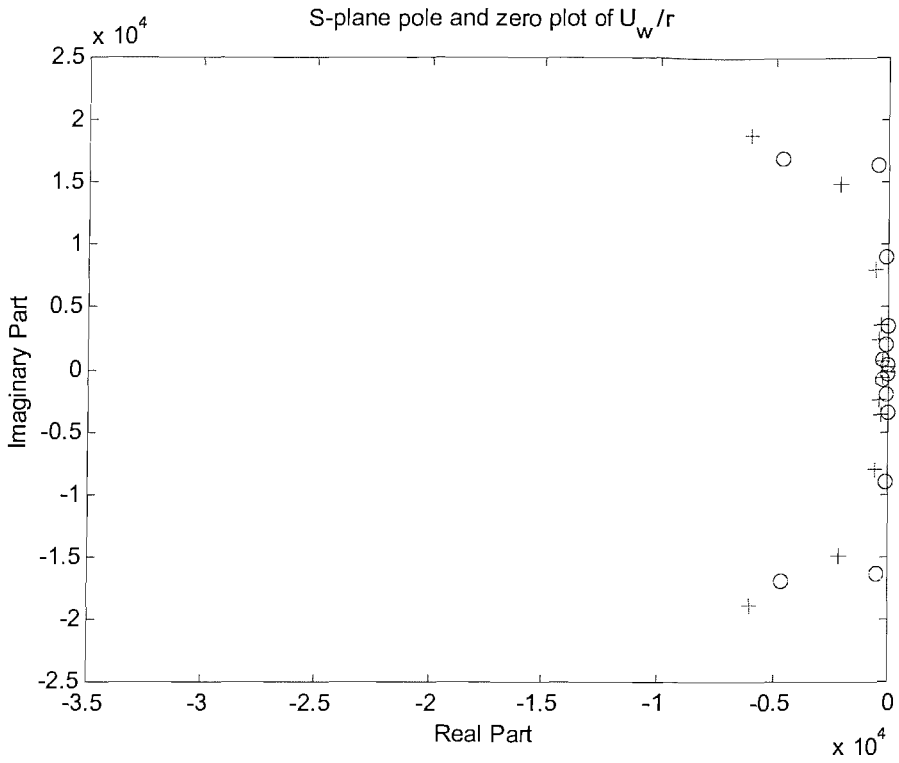

Figure 5–22 Pole and zero plot of the modal wheel variant transfer function U_w / R (o= zeros, += poles).

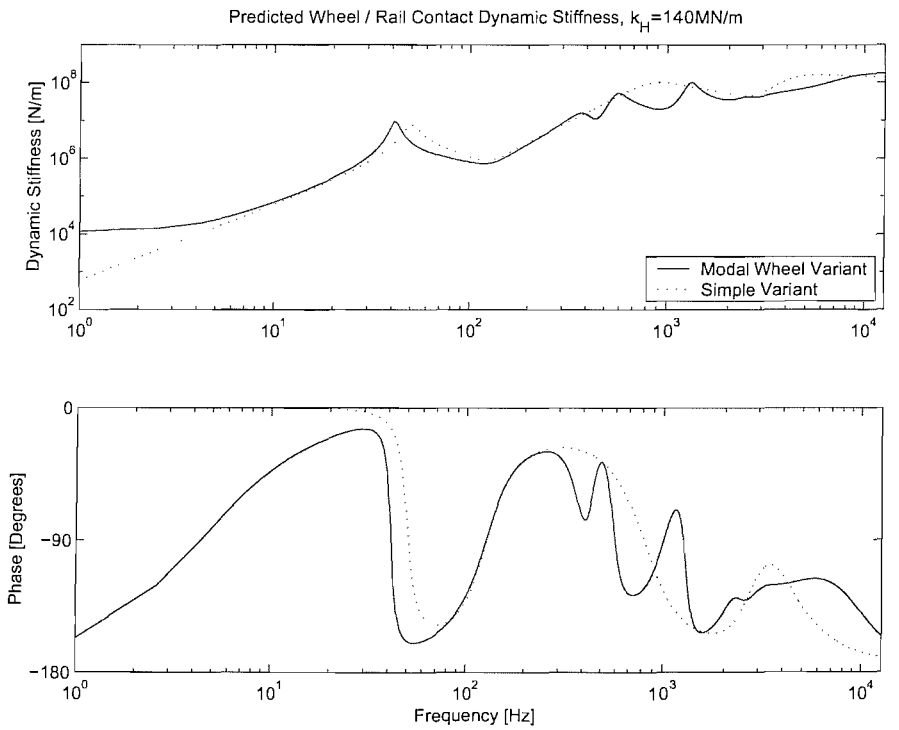

Figure 5–23 Simple variant and modal wheel variant transfer function representing their dynamic (contact) stiffness.

in Figure 5–22, show that all of the poles and zeros move to different positions. Pole and zero cancellation is also evident.

5.1.3.5 Comparison of the modal wheel variant and the simple variant

A final comparison is made between the simple variant and the modal wheel variant by comparing transfer functions for each variant in terms of the contact force divided by roughness. Contact force (F) as a function of frequency is given by [Wu and Thompson 2000(a)]:

$$\frac{F}{R} = \frac{-1}{\alpha_r + \alpha_w + \alpha_c} \tag{5-15}$$

This can be easily expressed in the 'alternative' forms of each model variant (i.e. using the method in section 5.1.2) to produce the transfer function shown in Figure 5–23. It should be noted that this transfer function is not non-dimensional like the previous transfer functions considered. It has the units of N/m which corresponds with a dynamic stiffness. The results shown in Figure 5–23 show that the simple variant and modal wheel variant transfer functions are quite similar. Differences are seen, however, at the lowest frequencies below 10Hz because in the simple variant the wheel is modelled as a mass, whereas in the modal wheel variant the wheel is modelled as a stiffness that represents the rig wheel assembly pre-load spring. Between 30Hz and 70Hz, the differences are attributed to the location of the wheel on track resonance, and at about 1kHz differences are seen because of the more complicated wheel representation of the modal wheel variant.

The similarities between the simple variant and modal wheel variant in Figure 5–23 suggest that the simple variant can be used effectively to predict the contact force despite its simple representation of the wheel FRF. This is interesting as the comparisons made between the modal and simple variants demonstrated that the simple variant was not suitable for predicting wheel vibration.

5.1.4 Variation of the linearised contact stiffness (k_H)

A study of the input parameters for the FRF model was performed to try to ascertain where improvements could be made. As the measured FRF variant is constructed from measurements, the best 'quality' measurements are required. The frequency response of both the wheel and the track has been extensively measured (see Chapter 3). These measurements seemed to be the best available, despite the noisy responses at low

frequencies. This meant that the only remaining part of the FRF model that had not been investigated was the contact spring.

The linearised contact spring stiffness (k_H) is evaluated using equation (2-9). This gives an approximation of the non-linear Hertzian contact stiffness. The lowest wheel load considered was 527N, which corresponds with a contact patch length of 0.8mm and a value of stiffness (k_H) of 140MN/m. The highest wheel load was 966N which corresponds with a contact patch length of 0.9mm and a value of stiffness of 172MN/m. The differences between these two values is small corresponding to only 2dB in the receptance level.

To test the sensitivity of the results to the value of k_H, the transfer function (U_r / R) based on the measured frequency response functions of the wheel and the rail is shown in Figure 5–24 for three different values of contact stiffness. These are derived from the value corresponding with the lowest wheel load of 527N increased by a factor of 100 and decreased by a factor of 10 and 100. These results demonstrate that an over-prediction of the contact stiffness has little effect upon the response of the model. However an under-prediction of the contact stiffness has a much greater effect. If the contact stiffness is reduced, the corresponding receptance becomes larger than those of the wheel and the rail. This is particularly apparent at high frequencies, and more of the roughness (or input) is absorbed by the contact spring. If the contact stiffness is increased the receptance falls below the others, and further increases have a negligible effect on the transfer function.

The use of polynomial relationships for the simple and modal wheel variants enables an additional method of analysing the effect of changes in the linear contact stiffness (k_H). As the contact receptance (k_H) is modelled as a pure gain, this factor can be analysed in the form of the transfer function poles and zeros. This analysis is only made for the simple variant, as the complicated densely positioned poles and zeros of the modal wheel model make it more difficult to observe.

The poles and zeros of the simple model transfer function (U_r / R) were calculated from the polynomial forms described by equation (5-8). This was done for various values of linearised stiffness (k_H) for a corresponding contact force varying from 10N to 10kN. The results are shown in Figure 5–25. This shows that an increase in the wheel pre-load causes the poles to move away from the origin.

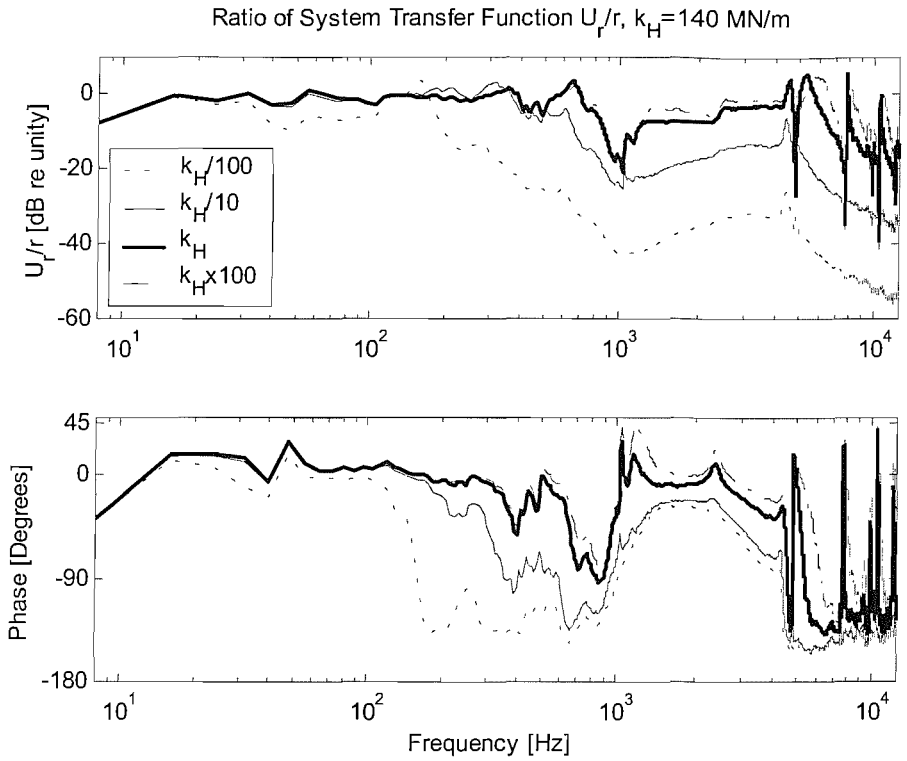

Figure 5–24 Variation of k_H and its effect upon the narrow band formed transfer function U_r / R.

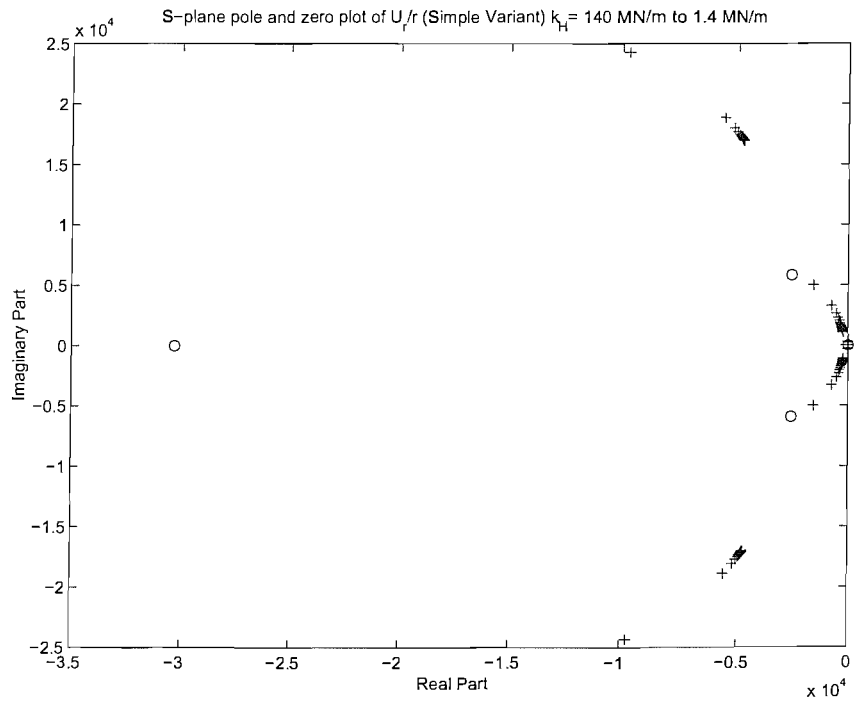

Figure 5–25 Pole and zero plot for simple variant U_r / R with contact stiffness variation from 140MN/m to 1.4MN/m. The zeros remain in the same position, whilst the poles move towards the origin with a decrease of contact stiffness.

The effect of variations of the contact stiffness (k_H) is shown in Figure 5–26 for the transfer function U_a / R. Again much like in the transfer function U_r / R, the effects of an under-estimated contact stiffness are more noticeable than the effects due to a similarly scaled over-estimation. This is also confirmed in Figure 5–27 for the transfer function U_w / R. Whilst at the high frequencies U_w / R is attenuated in a similar manner to the other transfer functions, it can be seen from Figure 5–27 that the high frequency modal behaviour of the wheel appears to be amplified. This effect can be explained by consideration of equation (5-4). If the contact spring receptance becomes large the following approximation can be made.

$$\frac{U_w}{R} \approx \frac{\alpha_w}{\alpha_c}$$

This means that the resonances of the numerator described by the wheel receptance (α_w) can be clearly seen in U_w / R. For lower values of α_c, the rail receptance α_r has a damping effect on the wheel modes.

As for the transfer function U_r / R, the changes in the position of the poles and zeros of the simple variant of the wheel transfer function (U_w / R) (see equation (5-11)) were investigated for estimated linearised contact stiffnesses due to wheel pre-loads ranging from 10N to 10kN. The results are shown in Figure 5–28. As for the rail transfer function (U_r / R), only the poles in the wheel transfer function (U_w / R) are seen to move with a corresponding increase of wheel pre-load. The behaviour of this transfer function is seen to be similar to that of the rail transfer function shown in Figure 5–25.

5.2 Estimation of track properties from operational measurements

This section presents an analysis of alterations that were found to be necessary to improve agreement between the models discussed above in section 5.1 and the measurements made on the 1/5 scale wheel / rail rig.

5.2.1 Introduction

The behaviour of the measured FRF variant, the simple variant, and the modal wheel variant has been extensively investigated in section 5.1 with use of the FRF model. A detailed method of obtaining reliable input profiles for the models has been presented in Chapter 4. It was hoped, at this point, that comparisons between predictions and

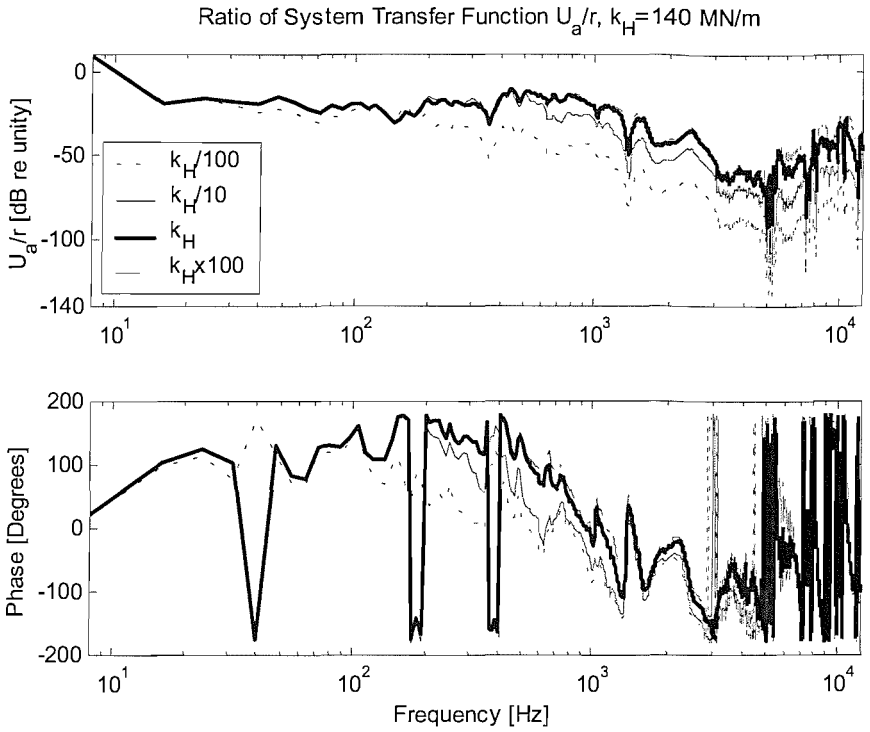

Figure 5–26 Variation of k_H and its effect upon the narrow band formed transfer function U_a / R.

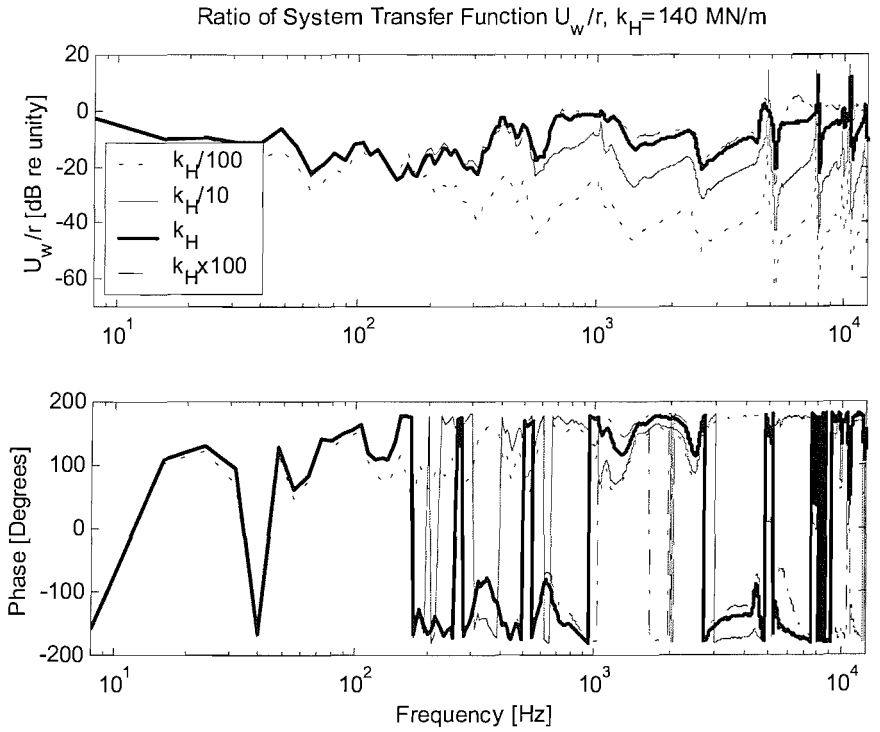

Figure 5–27 Variation of k_H and its effect upon the narrow band formed transfer function U_w / R.

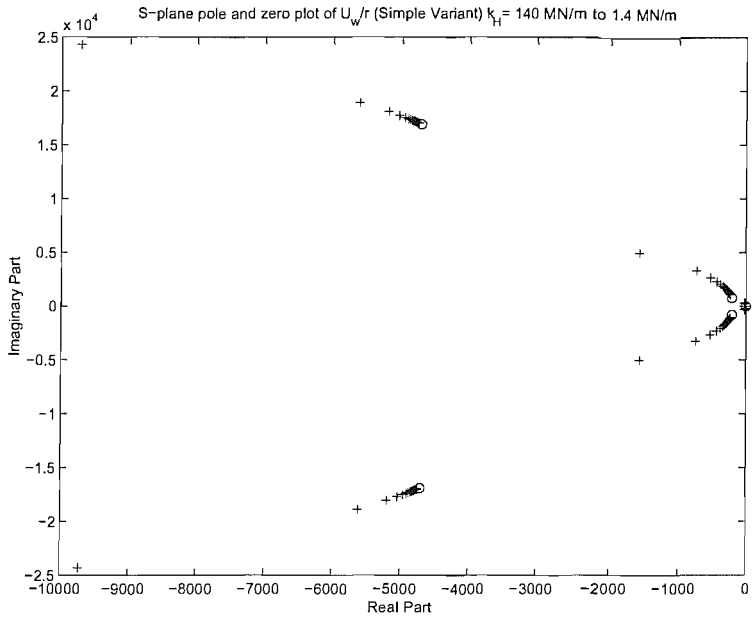

Figure 5–28 Pole and zero plot for simple variant U_w / R with contact stiffness variation from 140MN/m to 1.4MN/m. The zeros remain in the same position, whilst the poles move towards the origin and the zeros (eventually causing cancellation) with a decrease of contact stiffness.

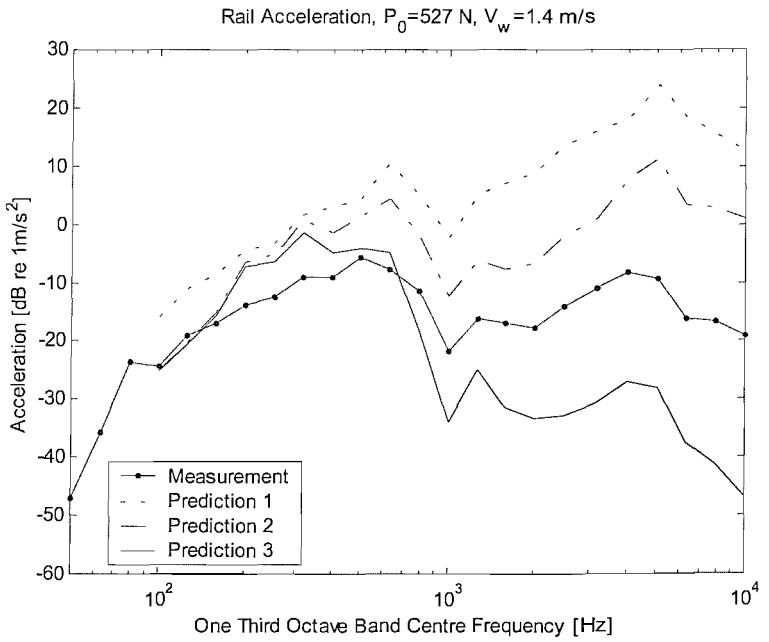

Figure 5–29 Comparisons between a measurement and three frequency-domain model predictions of rail acceleration. Prediction 1 is a prediction at the wheel / rail contact point. Prediction 2 is a modified version of prediction 1 including an adjustment for the decay of vibration along the rail. Prediction 3 is derived from prediction 2 by including Remington contact filter effects.

measurements would be in good agreement. Unfortunately this was not the case, necessitating further analysis.

An example of rail vibration predicted using the measured FRF variant and a measurement (as a function of frequency presented in one-third-octave band spectra) is given in Figure 5–29 for a wheel pre-load of 527N and a wheel speed of 1.2m/s. This shows the following:

1. A measurement of the rail vibration of the wheel rolling past the measurement position MRS8 (refer to Figure 3-14 for this position on the track).
2. A prediction of rail vibration at the point of wheel / rail contact that does not include corrections for contact filter effects (see Chapter 4). This is labelled 'Prediction 1'.
3. A prediction that includes a correction using statically measured track decay rates, as shown by equation (2-4), so that the average rail vibration is formed. This prediction also does not include any contact filter corrections. This is labelled 'Prediction 2'.
4. A prediction that includes both the correction of equation (2-4) and a Remington contact filter (see equation (4-2)). This is labelled 'Prediction 3'.

The predictions of the rail vibration in Figure 5–29 show the results of various stages of adjustments of the prediction at the point of contact (Prediction 1), that are designed to improve comparisons with the measurements. 'Prediction 1' in Figure 5–29 is much greater than the measurement for all frequencies. 'Prediction 2' shows the effect of altering the prediction from a point that moves with the wheel / rail contact to the average at a fixed position on the rail. Here a factor based on the track decay rates has been used to modify the prediction (see equation (2-4)). These track decay rates were calculated from measurements of transfer accelerances (see Chapter 3).

'Prediction 3' includes both the alteration described by 'Prediction 2' and a Remington contact filter estimate, where a high correlation of roughness across the contact patch is assumed ($\alpha = 1$, see equation (4-2)). The inclusion of the Remington contact filter results in an additional attenuation of the high frequency region (above 1kHz) of the prediction.

Predictions containing all of the corrections, based upon published methods, were found not to agree well with the measurements. As demonstrated in Figure 5–29, in the high frequency range the predictions are always smaller than the measurements, sometimes

by as much as 20dB. This was thought to be because of an over-attenuation from the contact filter. The predictions at the lowest one-third-octave bands (particularly 100Hz and 125Hz) were also found to be consistently smaller than the measurements. It was apparent that neither the published correction was adequate to enable good comparisons with the measurements made on the 1/5 scale wheel / rail rig. Alternative methods to estimate these alterations were therefore required.

In order to obtain reliable predictions using the FRF model (for example equation (2-4)) two aspects of the model required further refinement. These were the contact filter and the effect of the vibration decay along the rail. Techniques to investigate these two aspects using rolling wheel measurements are described in this section.

5.2.2 An alternative method of estimating track decay rates

The method of using static measurements of the track decay was found not to produce predictions that agreed well with the measurements. It is thought that this is due to a manufacturing defect of the 1/5-scale track bed, where the parts of the track bed had been glued together (the ballast resilient layer, the sleeper mass, and the tray). As previously mentioned in Chapter 3, the ballast stiffness was found to be much softer than expected once the track bed was assembled and constructed. It is assumed that the weight of the wheel on the track bed 'takes out the slack' in the track bed supports and therefore gives a different decay characteristic than when the track bed is unloaded.

Equation (2-4) shows that the average rail vibration differs from the rail displacement at the contact point (equation (2-1)) by a factor that depends on the decay rate. This factor may be found from transfer function measurements on the rail by the method given in Chapter 3, or alternatively it may be found by manipulating the information within a time-domain measurement of the rail vibration at a fixed point as the wheel passes.

The first step of this method is to estimate the response of the rail at the wheel / rail contact point ($U_r(0)^2$). Figure 5–30 shows the vibration signal (acceleration) from measurements on the rail as the rig wheel passes a fixed point (on the rail) for a wheel speed of 1.4m/s. This shows that the vibration increases as the wheel approaches the accelerometer, and then reduces again as it passes. For position MRS8, the wheel is above the accelerometer at a time of about 0.6 seconds. A short section of this time series could be extracted and used to form an estimate of the acceleration at the point of contact. This method, however, would not provide an adequate statistical representation of this quantity for the range of wheel speeds considered. Examination of the

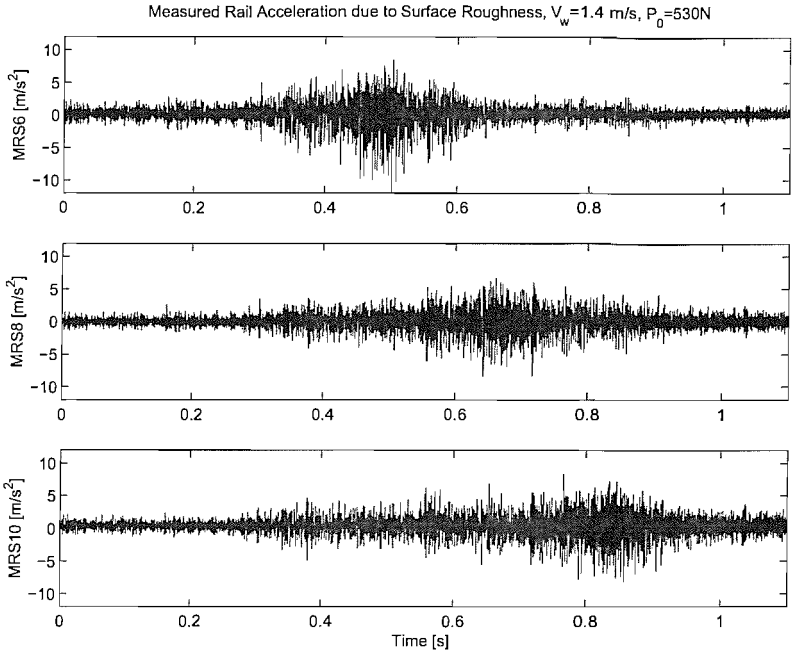

Figure 5–30 An example of the measured rail acceleration due to surface roughness of the rig wheel and rail. This has been measured at three points on the track at MRS6, MRS8, and MRS10 for a wheel speed of 1.4m/s and a wheel pre-load of 530N.

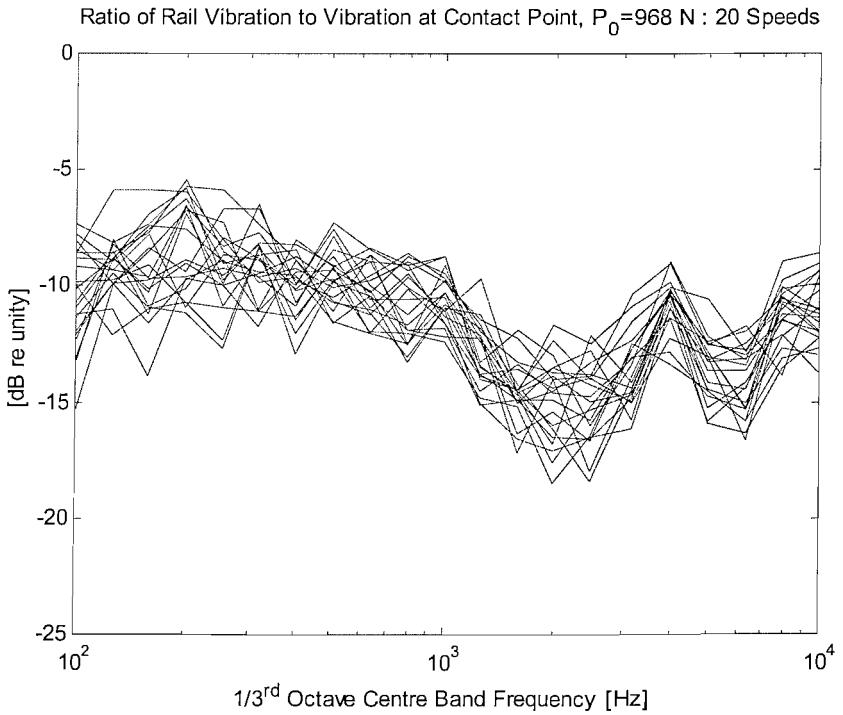

Figure 5–31 Ratio of average rail vibration to rail vibration at point of contact at all wheel speeds measured (1m/s to 6m/s) for the greatest wheel pre-load (968N).

bandwidth-time (BT) product for the lowest frequency band (the 100Hz one-third octave band, that has a bandwidth of approximately 23Hz) and a section 0.04 seconds long produces a value of 0.92. To allow for sufficient statistical degrees of freedom, the BT product should be at least unity [Oppenheim and Schafer, 1975]. BT products for higher wheel speeds would necessitate smaller time intervals to be used (so that the effect of the decay of the signal is minimised) thus this method becomes less appropriate. A method relying upon the removal a section from the measurement, therefore cannot be used to provide a reliable estimate of the point acceleration. Another method to find the acceleration at the point of contact has therefore been devised.

The measured rail acceleration (Figure 5–30) can be filtered in the time-domain to give a response in a single one-third octave band. In this way, sets of filtered responses of the measurement for each one-third octave band, between 100Hz and 10kHz, have been calculated. This process was performed in MATLAB using a digital 3rd order Butterworth band-pass filter. The order of the filter was chosen to be the largest order value that did not cause any numerical errors due to the close spacing of the cut-off and cut-on frequencies (especially for the low frequency bands) within the MATLAB filter routine. When used in conjunction with a MATLAB routine that filters the data twice (a routine called FILTFILT in the signal processing toolbox), which results in a sixth order filter. This meets the requirements of the British Standard for a third-octave filter [BSI, 1964]. Moreover as FILTFILT filters in the forward and then reverse direction, it removes any effect of phase distortion of the band-pass filter from the data.

Next, for each one-third octave band, the maximum RMS value was found. It is assumed that this corresponds with the time when the wheel was directly over the accelerometer on the rail. By assembling all these maximum responses for each band, an estimation of the acceleration spectrum at the wheel position ($U_r(0)^2$) as a function of frequency (in one-third octave bands) was obtained.

The original, complete, measurement of the average vibration as the wheel passes over the rail (Figure 5–30) has also been used to estimate a PSD from which a one-third octave spectrum is derived. By dividing this spectrum ($\overline{U_r^2}$) by the estimated response at the contact point ($U_r(0)^2$) an estimate of the decay rate in the form of $1/\beta L$ is obtained according to equation (2-4).

Figure 5–31 shows the results in the form of the ratio $\overline{U_r^2}/U_r^2(0)$ from measurements of over twenty wheel speeds ranging from 1m/s to 6m/s for a pre-load of 968N. Similar

results were obtained for other pre-loads. Figure 5–32 shows the average in each one-third octave band of all the wheel speeds for each of the wheel pre-loads. The average values shown in Figure 5–32 are not found to vary with pre-load by more than 1dB for the majority of the frequency range considered.

Figure 5–33 shows the average of the four wheel load estimations of $\overline{U_r^2}/U_r^2(0)$ compared with estimates of $1/\beta L$ derived from the decay rates obtained from the instrumented hammer measurements given in Chapter 3. The greatest discrepancies occur between 200Hz and 800Hz, indicating that the effective decay rate is up to a factor of 4 (6dB) greater than that measured in the unloaded situation. The results above 1kHz, which will be determined by the stiffness of the pad rather than the 'ballast', agree much more closely.

It should be noted that this method can only be used where the excitation at the wheel/ rail contact is stationary. If the measurements contain a strong effect of a discontinuity, then the maximum value in each filtered one-third-octave band will not necessarily correspond with the point where the wheel is above the accelerometer. This would mean that the relationship between the average at the accelerometer position and the maximum value would differ from that used above.

The method for finding the estimated point accelerance with time-domain filtering for the lowest one-third octave bands was verified by making a comparison with an octave band result. This was to ensure that the representation of the smallest bandwidths was correct. For example, the 50Hz one-third octave band only has a bandwidth of 11.6Hz which might be too small to be sufficiently represented by 3rd order Butterworth filters.

To check the (time) filtering process it was decided that if the sum of the squares of three one-third octave bands was approximately the same as the octave band estimate (that has a much larger bandwidth), then it was reasonable to assume that the method was working correctly. By forming estimates of the one-third octave bands and octave bands from time-domain filtered data it was found that the 50Hz band can be reliably considered with this method. Results are shown in Figure 5–34 for the fastest measured wheel speed response and therefore shortest data length. The solid line, in Figure 5–34, shows the point acceleration found using one-third octave band analysis, and the dotted line shows the point acceleration found using octave band analysis. The sum of each one-third octave band is also shown in Figure 5–34 by a cross. Each of the crosses were found to approximate the octave band response in the frequency range 50Hz to 2.5kHz.

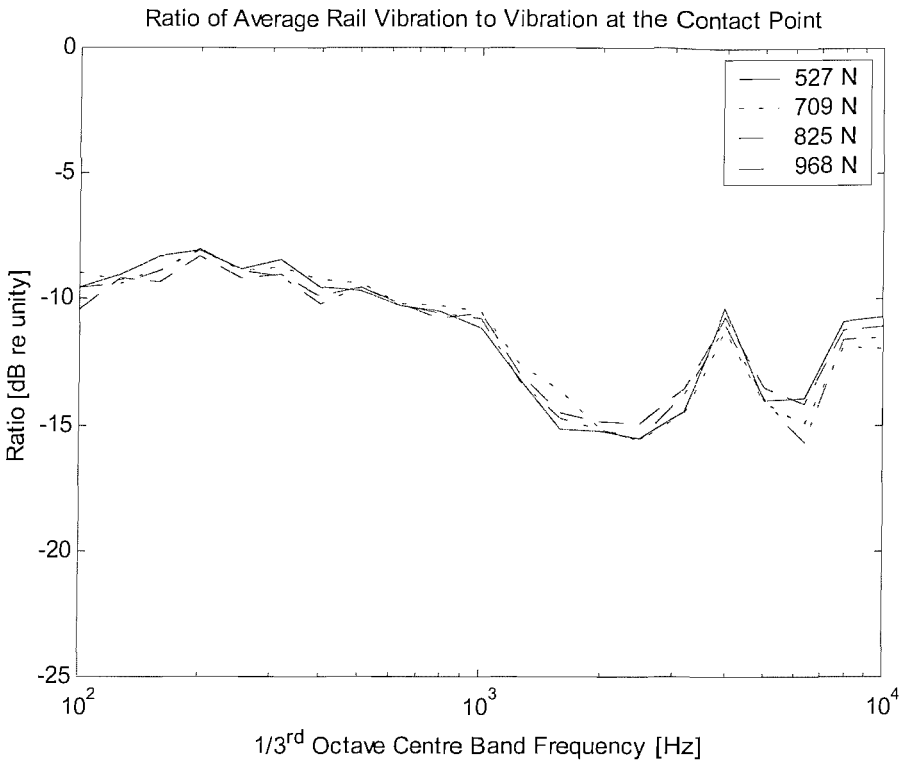

Figure 5–32 Results of the average one-third-octave band response of many wheel speeds for each of the four rig wheel pre-loads.

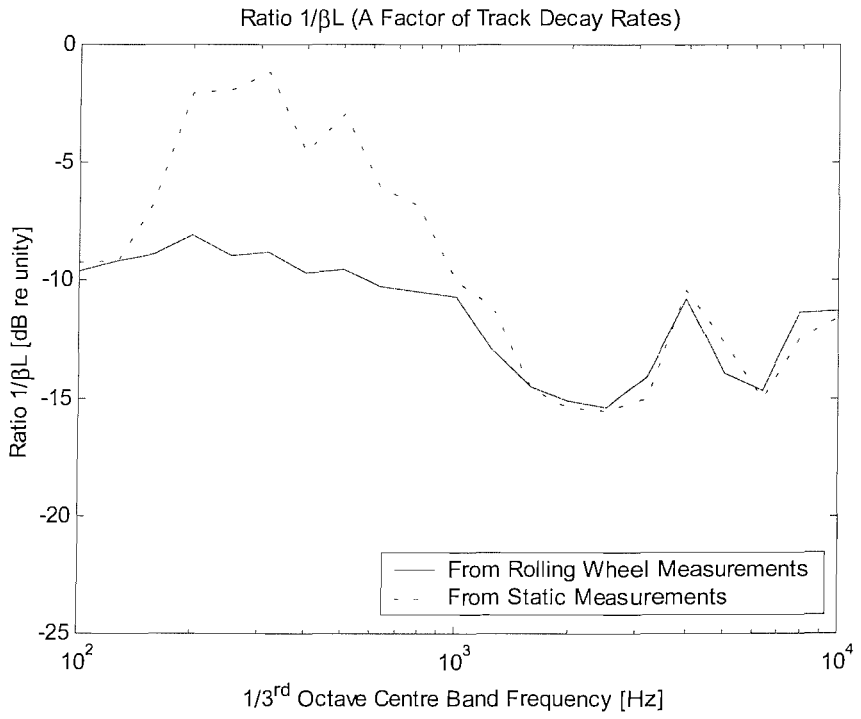

Figure 5–33 Comparison of the ratio $1/\beta L$ calculated from instrumented hammer tests with the ratio $1/\beta L$ calculated from 'rolling wheel' measurements.

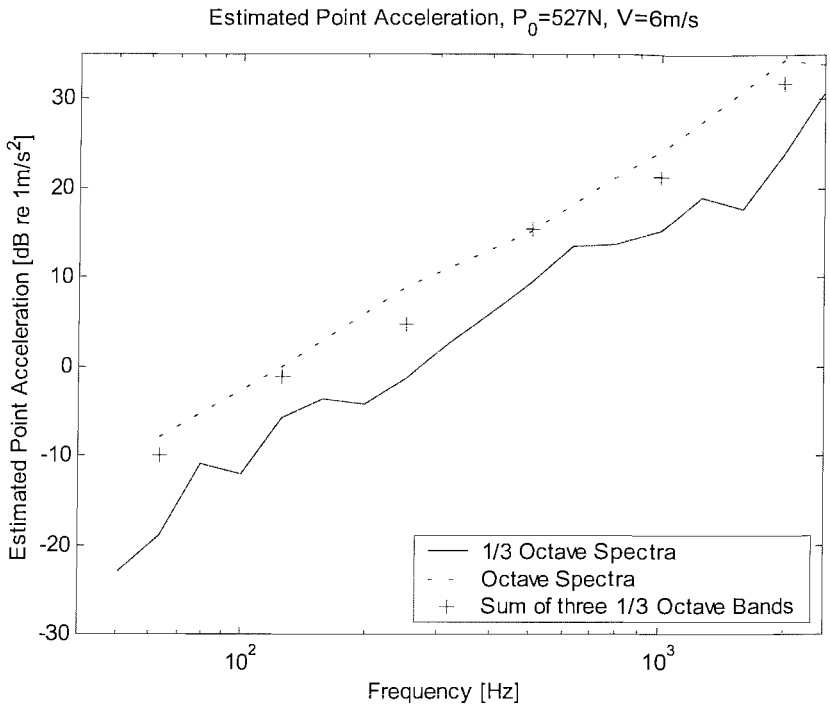

Figure 5–34 Verification of the method of obtaining an estimation of the point acceleration from operational measurements where time-domain filtered outputs in 1/3 octave and octave bands are compared. The sum of three 1/3 octave bands approximates the octave value.

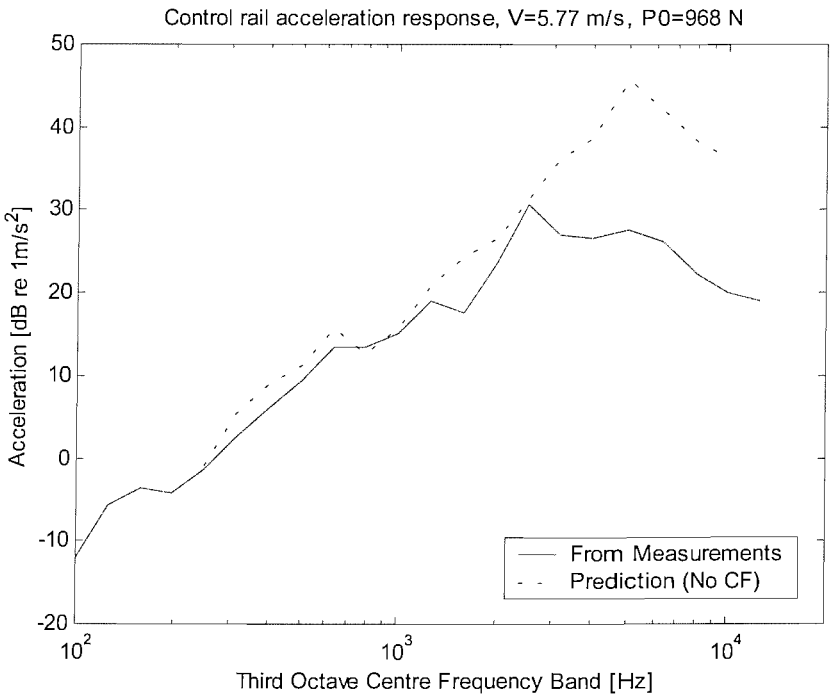

Figure 5–35 Prediction of rail acceleration at point of wheel / rail contact (contact filter effects excluded) and estimated acceleration at contact point calculated from measurements.

Thus no adverse effects due to the time-domain filtering process were evident for the measurements made on the 1/5-scale rig. The averaged track decay rates in the form of $(1/\beta L)$ found from rolling wheel measurements shown in Figure 5–33 have therefore been used throughout this thesis in preference to the results from hammer excitation.

5.2.3 Estimation of a contact filter

The acceleration at the wheel / rail contact point estimated from the measurements (used above to determine the effect of the decay rates along the track) has also been used to estimate the contact filter behaviour. This was done in the following manner.

An FRF model prediction of rail acceleration at the wheel / rail point of contact was made as discussed previously in section 5.2.1 using the measured FRF variant. The measured FRF variant was used here as it was expected to provide the best representation of the elements that make up the model. Figure 5–35 shows an example prediction along with the estimated measured acceleration at the point of contact (obtained using the method described in section 5.2.2). The difference between the predicted and measured spectra in Figure 5–35 provides an estimate of the contact filter.

This process was repeated using measured data at each wheel speed (1m/s to 6m/s) and at each wheel load. The results for the lowest pre-load are shown in Figure 5–36, and the results for the highest pre-load are shown in Figure 5–37. These are shown as a function of wavelength, $\lambda = V / f$, so that the spectra in terms of frequency at different speeds are shifted laterally before plotting. It can be seen that the difference is near to 0dB at large wavelengths but falls to around –10dB at smaller wavelengths. This can be attributed to the contact filter effect. These results are compared with those from the Remington analytical contact filter [Remington, 1987], and also the average effect from the DPRS numerical model from six sets of measured roughness on different wheels [Thompson, 2001]. In both cases, these contact filter results are adjusted to correspond with a contact patch semi-axis length equivalent to a Hertzian estimate for the 1/5 scale rig at its particular wheel pre-load. Adjustment of the DPRS data to an equivalent contact patch length is an appropriate method in accordance with [Thompson, 2001].

Figure 5–36 and Figure 5–37 show that the analytical contact filter predicts too great an attenuation for small wavelengths (<0.5mm), but better agreement is found with the more recently developed DPRS filter (based on a numerical calculation for many parallel lines of roughness). The comparisons shown in Figure 5–36 and Figure 5–37

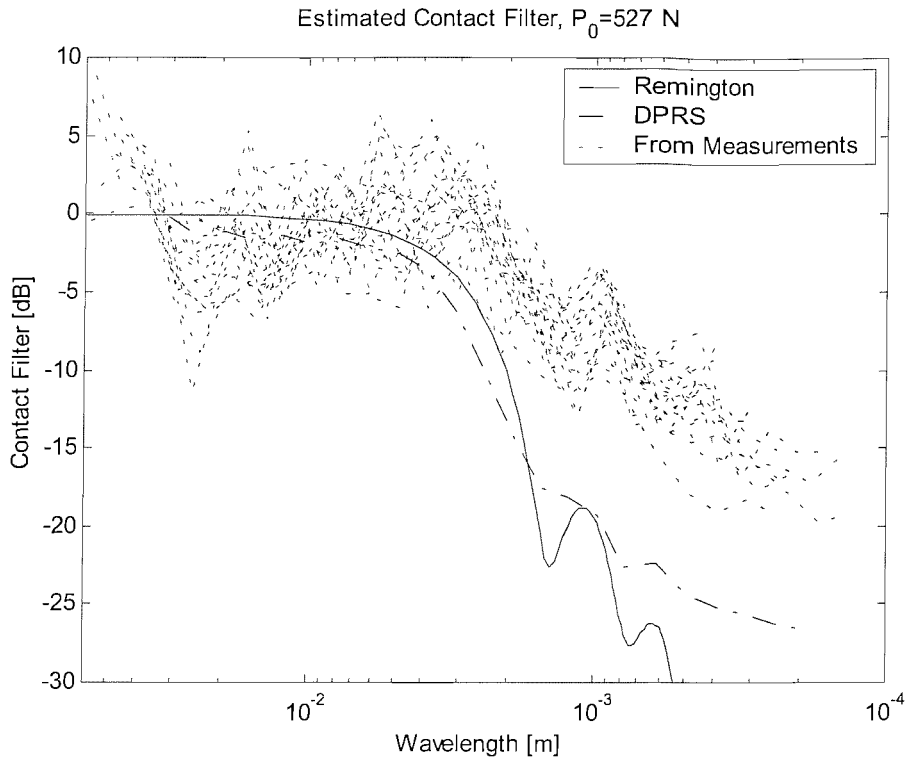

Figure 5–36 Estimation of the lowest rig wheel pre-load contact filter, and comparisons with published contact filter models.

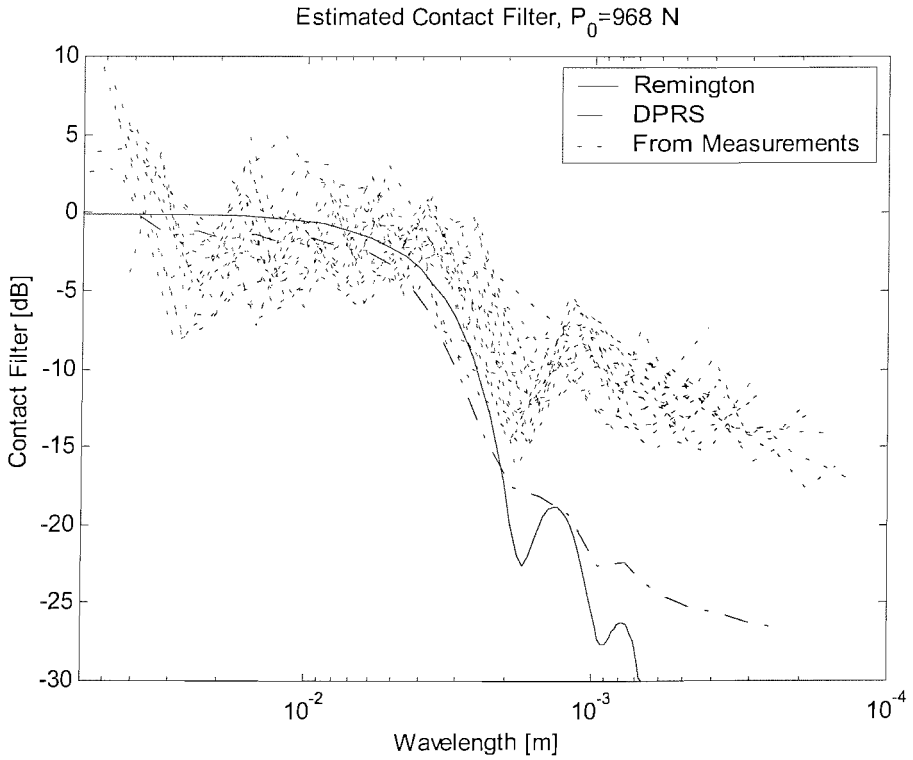

Figure 5–37 Estimation of the maximum rig wheel pre-load contact filter, and comparisons with published contact filter models.

indicate that the measured contact filter is shifted to slightly shorter wavelengths than both the DPRS and analytical Remington models. The reason for this is not known.

5.2.3.1 Approximation of the estimated contact filter

The Remington contact filter has been seen to over-attenuate the high frequency response (as shown in Figure 5–29). The alternative option, the DPRS contact filter, is constructed from measurements of many parallel lines of surface roughness. As discussed in Chapter 4, this method cannot be used on the 1/5 scale rig as the physical dimensions prohibit the measurement of parallel lines of surface roughness across the contact patch width. A new, alternative, contact filter representation was therefore conceived from the findings presented above.

The trend in the contact filter effect found from the rig measurements can be approximated by the response of a combination of 2nd and 3rd order filters. This allows the formation of an approximate contact filter that could be used to improve predictions of the rig vibration. State space values were found from appropriate values for springs, masses, and dampers from the following equations.

$$f_c = \frac{V}{4a} \qquad \text{(5-15a)}$$

$$m_1 = \frac{k_H}{(2\pi f_c)^2} \qquad m_2 = \frac{k_H}{(4\pi f_c)^2} \qquad \text{(5-15b and 5-15c)}$$

$$c_1 = 2\zeta_1\sqrt{k_H m_1} \qquad c_2 = 2\zeta_2\sqrt{k_H m_2} \qquad \text{(5-15d and 5-15e)}$$

$$J = \frac{c_1}{6(2\pi f_c)^2} \qquad \text{(5-15f)}$$

where: f_c is the filter cut-off frequency,

a is the contact patch semi-axis length,

V is the wheel velocity,

c_1, c_2 are scaled damping ratios,

m_1, m_2, are scaled masses,

k_H is the Hertzian stiffness,

ζ_1 is a damping ratio and was chosen to be 0.65,

ζ_2 is a damping ratio and was chosen to be 0.25,

J is a scaled 3rd-order term.

This leads to:

$$\left(Js^3 + m_1 s^2 + c_1 s + k_H\right)X = \left(m_2 s^2 + c_2 s + k_H\right)Y \qquad (5\text{-}16a)$$

where: X is a representation of an idealised output,

Y is a representation of an idealised input.

Hence the filter transfer function is given by:

$$\frac{X(s)}{Y(s)} = \frac{m_2 s^2 + c_2 s + k_H}{Js^3 + m_1 s^2 + c_1 s + k_H} = H(s) \qquad (5\text{-}16b)$$

This transfer function for $s = j\omega$ is shown in Figure 5–38 for an appropriate choice of parameters in form of $20\log_{10}|H|$. It is seen to compare well with the estimated trend of the measured contact filter. Equation (5-16b) can be used to provide a frequency weighting in this form and is in a form that has been demonstrated previously in the modelling of the rig wheel FRF.

The modulus and phase of the above approximate contact filter (equation (5-16b)) is shown in Figure 5–39. The modulus of the approximate filter is seen to tend towards unity at low frequencies (large wavelengths) as required. This can be seen in equation (5-16b) by letting $s \to 0$. Further analysis of equation (5-16b) shows that the approximate filter tends to m_2/Js at high frequencies. This forms an attenuation of 20dB per decade. Only the modulus of this correction has been used in the FRF model used in Chapter 6 but in a time-domain model the phase would also play a role. This is an undesirable effect, as the phase characteristics of a contact filter have not been investigated thoroughly.

The values of the above contact filter polynomial coefficients all depend on the value of the filter cut-off frequency, see equations (5-15). By using the MATLAB function TF2ZP the polynomial coefficients can be converted into the values of the filter poles and zeros. The poles and zeros of the contact filter (equation (5-16b)) were calculated for a fixed wheel speed (1m/s) with various contact patch lengths ranging from 0.001mm to 2mm obtained by varying the wheel pre-load[7]. The results are shown in Figure 5–40. This shows that small contact patch lengths cause the poles to move away from the origin, and that larger contact patch lengths cause the poles to converge

[7] Equivalently the speed could be raised for a fixed contact patch length, see equation (5-15).

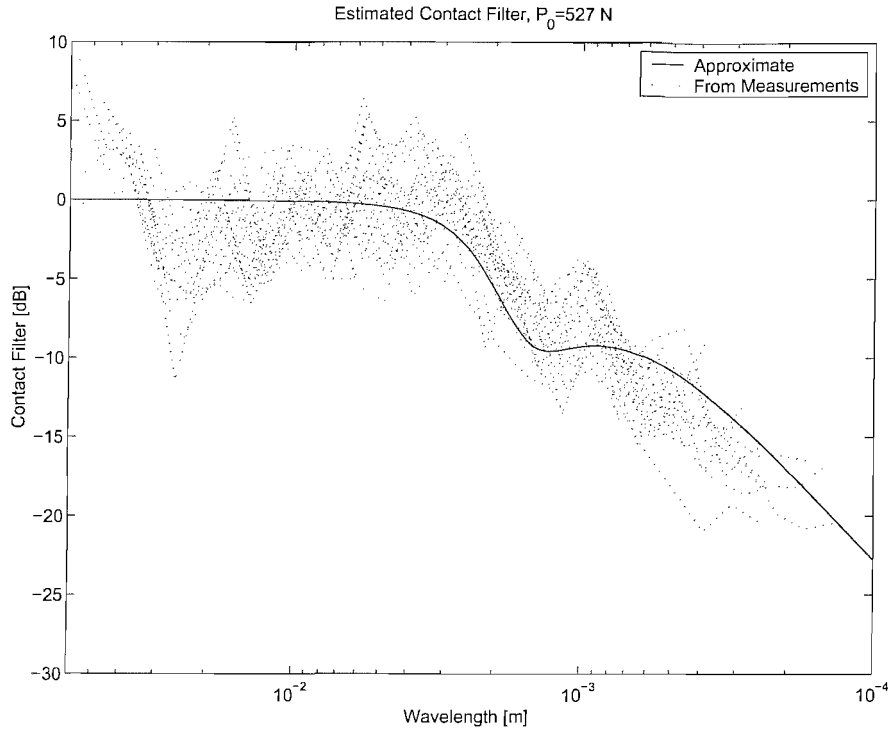

Figure 5–38 Approximation of the estimated (measured) contact filter trend.

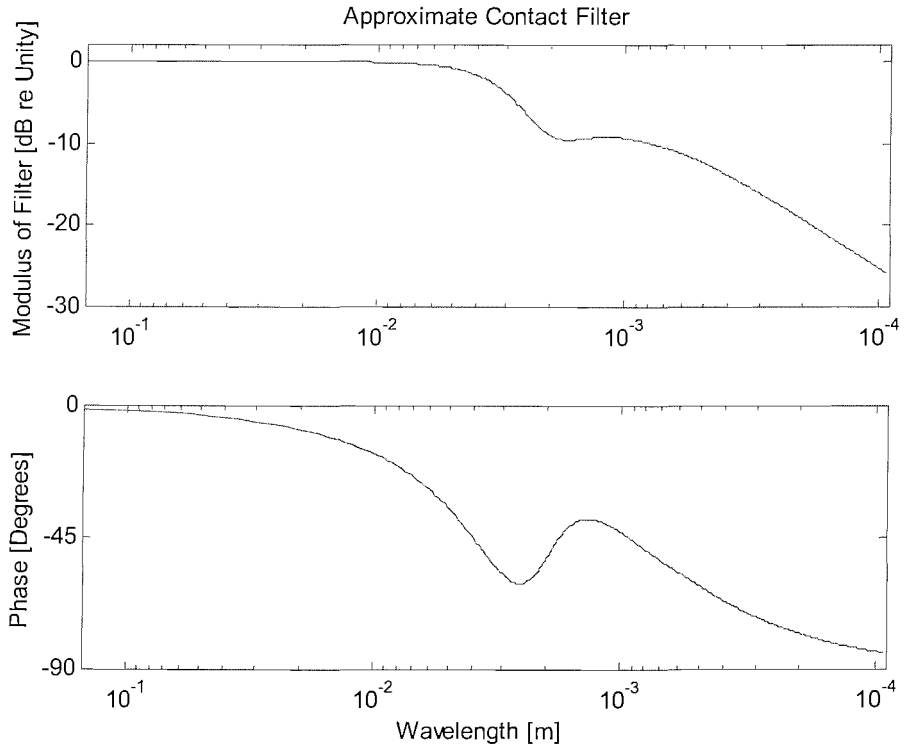

Figure 5–39 Modulus and phase of the approximate contact filter.

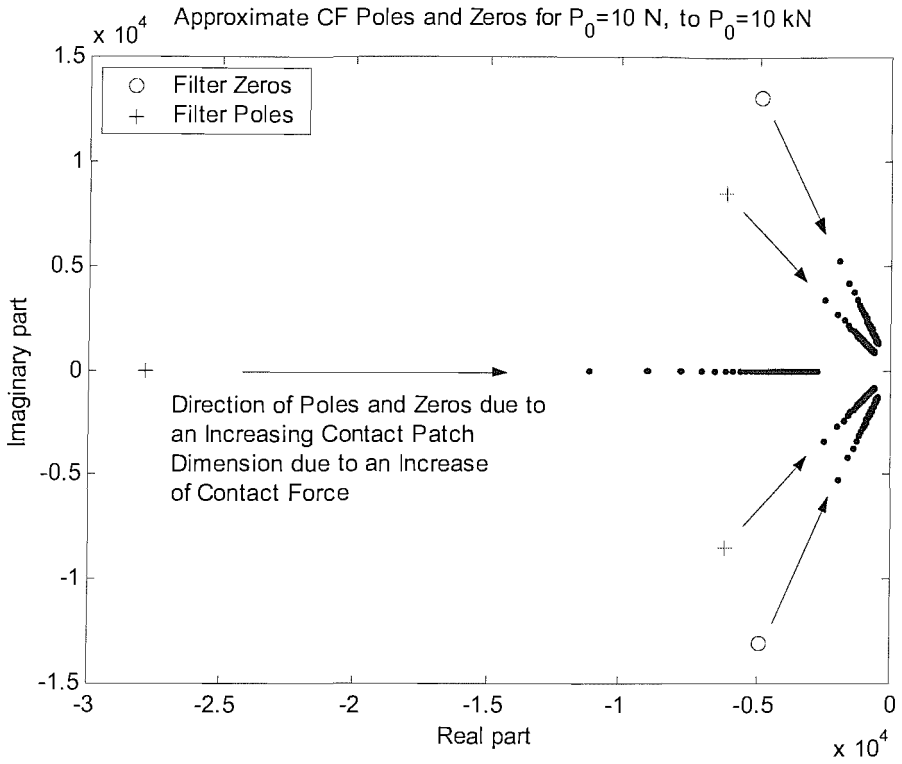

Figure 5–40 Position of the approximate contact filter poles and zeros estimated for rig wheel pre-loads (or contact force) in the range of 10N to 10kN. The positions of the '+' and 'o' represent the 10N wheel load. An increase of wheel load promotes a movement of the poles and zeros towards the origin.

towards the origin. The imaginary part of s corresponds to angular frequency, which increases as the contact patch length reduces.

Setting the variable $s = j\omega$ enables the calculation of the frequency response of the filter. The positions of the poles of the filter in relation to the value of the angular frequency (ω), as it increases from the origin along the $x = 0$ axis, demonstrates where the maximum response of the filter occurs. Therefore large contact patch sizes result in the poles of the filter approaching the origin, and the cut-off frequency tending towards 0Hz. Smaller contact patch lengths move the poles away from the origin, and the cut-off frequency therefore tends towards infinity. This is also confirmed by consideration of equation (5-15a). Analysis of the poles and zeros of this model confirms that the model remains stable even for large contact patch dimensions.

For a situation where minimal non-linear behaviour of the contact spring is expected, the approximate contact filter can be applied by estimating the average contact patch dimension and then correcting a prediction (without contact filter effects) in the frequency domain. For a situation where non-linear behaviour is expected, however, the contact filter ideally needs to be included in the time-stepping prediction.

Attempts were made to alter the roughness input within the time-stepping routine by incorporating the approximate contact filter described by equation (5-16b). Instantaneous values of the contact force (produced by the time-stepping routine) were used to form an estimate of the linear contact stiffness (k_H) and contact patch semi axis length (a) using Hertzian contact theory. These values were then used to calculate the coefficients for equation (5-16b). Unfortunately the numerical routine would often produce large values that were considered to be unrealistic. Improvements could be made to the results by limiting the approximate contact filter cut-off frequency (equation (5-15)) to a maximum value of 10kHz, as frequencies higher than 10kHz were not required for the prediction. This did improve the results of the time-stepping routine by containing the varying natural frequencies within the frequency range of the time-stepping routine. However, even after taking this effect into account, the predictions with a varying contact filter still proved to be unreliable. This could have been because of the degree at which the approximate filter cut-off frequency could vary (this was generally between 1kHz and 10kHz). Time-varying properties are notoriously difficult to implement in an integrating routine.

Another problem with implementing the approximate contact filter shown in Figure 5–38 is that it is based upon operational measurements that are expected to have fairly constant contact patch dimensions. Verification of this filter characteristic for contact patch dimensions (estimated from Hertzian contact theory) outside of the range 0.8mm to 1mm was not performed. It is therefore not necessarily appropriate to apply the approximate contact filter trend shown above to situations where different contact patch dimensions are expected.

5.2.3.2 Conversion of the approximate contact filter into a Finite Impulse Response (FIR) filter

As stated previously the filter trend presented above in section 5.2.3.1 can be applied as an adjustment to a measurement in the frequency domain, but could not be incorporated as part of a time-stepping routine, as previously explained. This meant that outputs from the time-stepping models could only have contact filter adjustments made as a post-processing step in the frequency domain. This is not always desirable, especially when comparisons in the time-domain between measured and predicted values are required. It is possible to take a FFT of the time-domain data, and then apply the frequency weighting, and finally take an inverse FFT for the alteration back into the time-domain. This method can be rather laborious for long data lengths. A faster method of applying a frequency weighting to a sampled data record is by the use of 'digital filtering' techniques, or namely by the utilisation of difference equations.

The approximate contact filter (equation (5-16b)) can be converted from a continuous function in the s-plane to a discrete function in the z-plane by a method known as bilinear mapping. A method of bilinear mapping is presented by [Oppenheim and Schafer, 1975] where conversion from the s-plane to the z-plane is performed with the following equation.

$$z = \frac{1 + (T/2)s}{1 - (T/2)s} \tag{5-17}$$

where: z is the z-plane sample delay operator,

T is the time of the data length (the reciprocal value of the frequency resolution),

s is the s-plane operator.

Equation (5-17) is incorporated into a MATLAB function called BILINEAR that produces digital filter coefficients for a fixed frequency range of consideration. The

poles and zeros of the s-plane function described by equation (5-17) are positioned in the z-plane according to the chosen sample frequency. This sample frequency must correspond to that of the data that is to be filtered, as otherwise the frequency weighting will occur at incorrect frequencies.

A digital filter can be applied in MATLAB with use of a function called FILTER. This routine applies both the modulus and phase characteristics of the filter to the data. Another routine, which has been discussed previously, called FILTFILT can also be used to ensure that the phase characteristics of the filter may be removed by filtered the data first forwards and then in reverse. Unfortunately FILTFILT results in the amplitude attenuation being applied twice, i.e. the filter characteristic is $|H|^2$. Adjustments were therefore made to the equations that make up the approximate filter so that the desired attenuation could be obtained with the use of the FILTFILT routine.

The following adjustments were made to the s-plane approximate filter. Equation (5-15c) was altered to equation (5-18) and the damping ratios were modified.

$$m_2 = \frac{k_H}{(2.6\pi f_c)^2} \tag{5-18}$$

New damping values (ζ_1) and (ζ_2) were chosen to be 0.5 and 0.45. These alterations provided the response shown in Figure 5–41. This response is compared with the original *s*-plane approximate contact filter and a modulus-squared version of the new digital filter.

The comparisons shown in Figure 5–41 are in agreement for the large wavelength region of the filter, prior to the filter cut-off point. Agreement of the shorter wavelength regions however, is not as favourable, due to the necessity of mapping an *s*-plane representation of the approximate contact filter with a square root of the modulus. Any discrepancies between the *s*-plane and *z*-plane versions of the frequency response are exaggerated by taking the square of the modulus of the bilinear mapped (FIR) filter. However, comparisons of the FIR filter with the trends estimated from the measurements, from which the approximate contact filter was formed, are still in fairly good agreement. This is shown in Figure 5–42. The shorter wavelengths of this comparison, however, are in worst agreement, and the FIR version of the approximate contact filter is seen to under-attenuate.

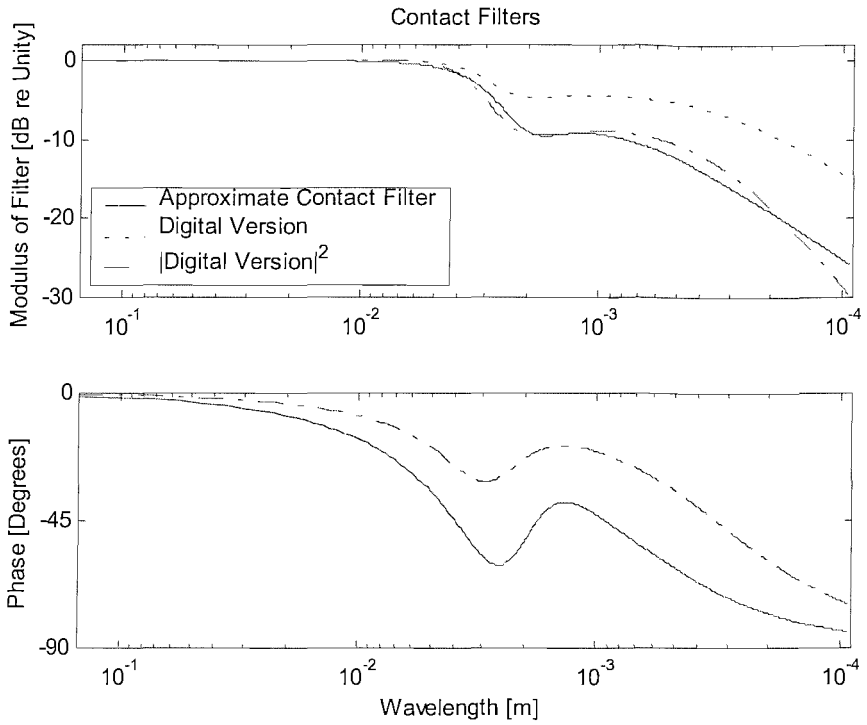

Figure 5–41 Comparison of the digital filter version of approximate contact filter with the original approximate contact filter.

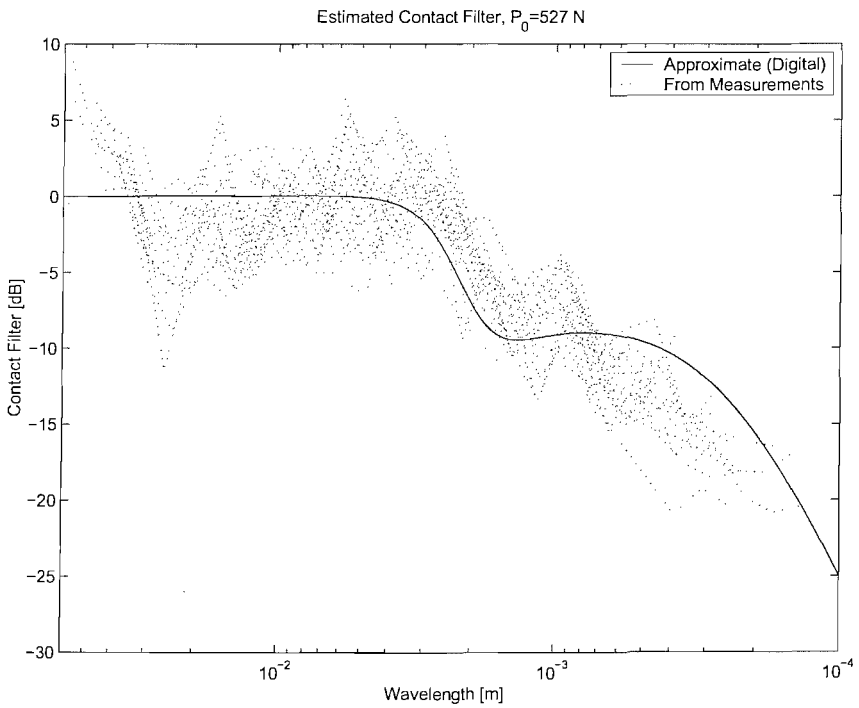

Figure 5–42 Comparison of the digital filter version of approximate contact filter with the estimated contact filter for the lowest wheel load.

The difference equation version of the approximate contact filter was used to provide a quick modification of the time-domain outputs of the time-stepping models. It could also be used to provide a modification of the surface roughness prior to use in a time-stepping model, but this was not done in the research presented in this thesis.

5.3 Summary

Analysis of the prediction models for different values of linearised contact stiffness has been considered in the form of a transfer function. This has demonstrated the differences between the models that have been used in this research. It was found that:

- A discrepancy exists at low frequencies between the idealised elements (used in the formation of the simple variant and the modal wheel variant) and their measured responses. This is thought to be because of poor measurement quality at low frequencies.
- Predictions of rail vibration can be performed adequately with the wheel represented as a simple mass.
- Conversely, predictions of wheel vibration cannot be performed adequately with this simple wheel representation, as a more complicated model including the wheel modes is required.
- The modal wheel variant and the simple variant both exhibit a strong wheel-on-track resonance at low frequencies. It is not clear whether this occurs in reality, to the extent shown, as measurements at these frequencies are affected by noise.
- The contact stiffness forces predicted with the simple variant and the modal wheel variant FRF models have been found to be rather similar at frequencies above their respective wheel on track resonances.

Analysis of a predicted transfer function with different linearised stiffness values has shown that in the high frequency range the transfer functions are attenuated when the wheel / rail contact stiffness is reduced. Conversely, it was found that as the contact stiffness between the wheel and the rail is reduced, the contact filter effects are shifted to higher frequencies.

Whilst these results show that an under-estimation of the linear contact stiffness (k_H) has more effect on the FRF model predictions than an over-estimate of similar magnitude, it is not likely that realistic discrepancies due to a surface roughness input will have such a great influence on the model transfer function. This is shown by the

variation of contact deflection (x) for a linearised contact stiffness (k_H) as a function of wheel load in Figure 2-1. This demonstrates that large variations in deflection only occur when the wheel load is much smaller than the lowest wheel load considered.

Despite the efforts made to obtain a good quality input (Chapter 4) and detailed analysis of the prediction models, initial comparisons between predictions and measurements were not found to show good agreement. Further investigations were therefore made. This highlighted a problem with the manufacture of the 1/5 scale rig track bed, and inadequacy of the published contact filter models to provide a reasonable adjustment for the 1/5 scale rig. Adjustments in the form of an approximate contact filter and decay rates estimated from operational measurements have been obtained for the case of a surface roughness input. These have been presented in section 5.2.

Comparisons of predictions and measurements due to a surface roughness input are presented next in Chapter 6 where the approximate contact filter (section 5.2.3) and the measured track decay rates (section 5.2.2) are incorporated into the prediction process.

6 Measurements and predictions of wheel / rail vibration due to surface roughness

6.1 Introduction

This chapter presents measurements and predictions of wheel and rail vibration for a situation with wheel and railhead surfaces that were manufactured to be relatively smooth. The models and their variants that were used for this purpose have been described previously in Chapter 2 and Chapter 5, and certain adjustments have been introduced (namely an approximate contact filter and a method of predicting the average rail vibration during a wheel passage) to improve agreement between predictions and measurements.

The purpose of this chapter is to:

- Present measurements obtained on the rig.
- Demonstrate that the measurements made on the rig were reasonable, that they were comparable (through the scaling laws in Table 3-1) with full-scale responses, and that these responses could be predicted using the FRF model.
- Show that the time-stepping models (described in Chapter 2) can also be used to predict reasonable levels, comparable not only with measured data, but with the outputs from the FRF model.
- Define to what extent the prediction models are reliable for the current situation.

The measurements and predictions of vibration for the 'smooth' wheel and rail considered here are treated as the 'control' or standard case. This was because the contact spring behaviour was not expected to vary greatly as there were no sudden large changes in either the rail or the wheel surface profile geometry. It was hoped therefore that the vibration (due to the surface roughness input) could be predicted satisfactorily using a linear wheel / rail contact model.

The non-linear wheel / rail contact effects were therefore expected to be minimal, so the outputs from linear and non-linear models were expected to be similar, enabling comparisons with each other and with the measurements. Consequently, any obvious differences between the performance of a non-linear model and a linear model should highlight an error in the formulation in one of the models, rather than a difference between the methods of prediction.

6.2 Measurements of wheel and rail vibration

Many measurements were made of rail, axle, and wheel acceleration. These measurements were made at approximately 20 different wheel speeds (in the range of 1m/s to 6m/s) for 4 wheel pre-loads that were applied by compressing the rig spring to produce a force between 380N and 821N. These pre-loads are expressed throughout this thesis in a form that includes the mass of the wheel and spring assembly (15kg=147N), making the smallest wheel load 527N, and the highest 968N.

Accelerometers were positioned on the following parts of the rig:

- The rail, at three positions on the underside of the rail between the track discrete supports,
- The axle bearings,
- The wheel rim.

For the measurements of the rail vibration presented in this chapter the accelerometers were positioned at MRS6, MRS8, and MRS10 (see Figure 3-14). The outputs from these accelerometers (B&K Type 4375V) were each found to have a maximum amplitude occurring at different times (see Figure 5-30). These times related to their relative positions, which were 240mm apart. An example of the measured rail acceleration for a wheel speed of 1.4m/s is presented in Figure 5-30 for each of the three points on the rail. In each case, the acceleration amplitude is seen to rise as the wheel approaches the point at which the accelerometer is fixed on the rail. After this point the acceleration amplitude is seen to steadily reduce as the wheel continues along the track, moving away from the accelerometer measurement positions. Only the output from the accelerometer at MRS8 is presented in this chapter, as the other measurements (when converted into the frequency domain) were very similar.

The position of the axle accelerometer was chosen to be above the expected wheel / rail contact point. A stud was used to securely hold the accelerometer (B&K Type 4375V). This was glued to the base of the wheel assembly near to the axle housing and the wheel speed tachometer (see Figure 3-3). A charge amplifier for the accelerometer was strapped to the rotating beam, close to the pivot. The output from the charge amplifier was then fed through a single slip ring unit, and the amplified signal was then recorded by the frequency analyser.

A single capacitance accelerometer (ENDEVCO Type 35C) was used to measure the wheel vibration at a position on the inner rim of the wheel. This type of accelerometer has an internal amplifier that provides a sufficiently large output permitting the signal to be fed directly through a slip ring. A second stage amplifier and power distribution box attached to the beam increased the signal before it was fed through a second slip ring on the axis of the beam.

Examples of the measured acceleration at the wheel and axle are presented in Figure 6–1. These are from the same set of measurements as shown in Figure 5-30, i.e. they are measurements of rig vibration made with a wheel pre-load of 530N at a wheel speed of 1.4m/s. Comparisons of the measurements in Figure 5-30 and Figure 6–1 show that the maximum amplitudes are smallest for the axle measurement, and largest for the rail measurements.

In addition to the measurements of the rail, axle, and wheel vibration, measurements of the wheel pre-load (from the force gauge), and the wheel speed (from a tachometer) were made. These were used to identify each set of vibration measurements, and to find some of the input parameters for the prediction models. For example, a measurement could be classified as follows: a 527N wheel pre-load, at a wheel speed of 1.4m/s for the case of a surface roughness input. This classification allowed direct comparisons between a measurement and a prediction for the specific input parameters.

The input data required by all the models includes physical parameters of the rig listed in Chapter 3 (see Table 3-7). In addition, a roughness measurement is required as discussed in Chapter 4.

6.3 Comparison of measurements and predictions made using the measured FRF model

In this section predictions obtained using the frequency domain model are based on measurements of the wheel and track frequency response functions (i.e. the measured FRF model).

6.3.1 Rail acceleration

Predictions of rail vibration have been made for each corresponding measurement of wheel and rail vibration. The predictions of rail acceleration are expressed in terms of a one third octave band spectrum of the average vibration during a wheel passage and are

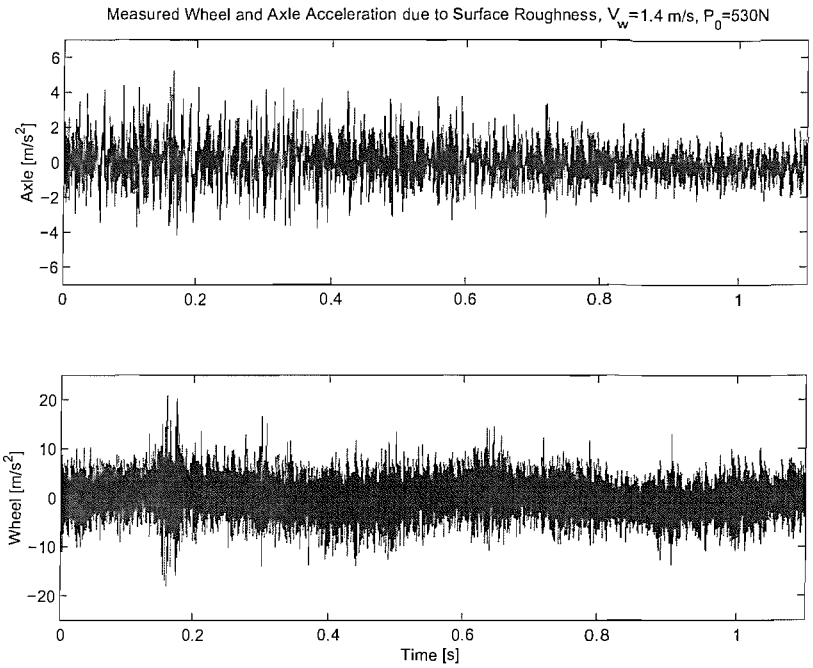

Figure 6-1 An example of the measured axle and wheel acceleration, due to surface roughness of the rig wheel and rail, for a wheel speed of 1.4m/s and a wheel pre-load of 530N.

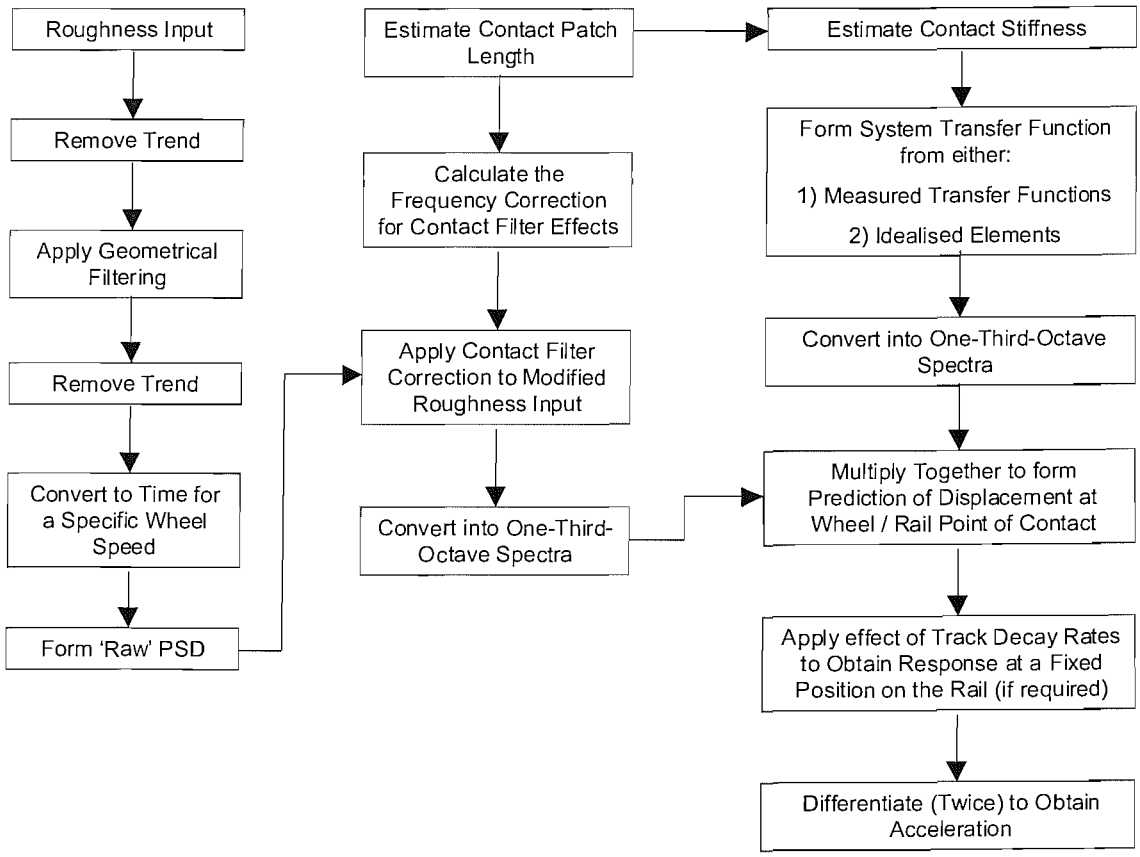

Figure 6-2 FRF model flow chart.

compared with a measurement of the rail acceleration at a point in the centre of the track section (position MRS8 in Figure 3-14).

As previously described in Chapter 5, the measured FRF variant is the most detailed model considered, with the smallest number of simplifications. The following results are therefore expected to be in best agreement.

At a particular frequency the displacement amplitude of the rail at the wheel / rail contact point is given by equation (2-4). The transfer function U_r / R was calculated as described in Chapter 5 using the narrow band measurements of the point accelerance of the wheel and the rail between 8Hz and 12.8kHz).

The approximate contact filter described in section 5.3.3 was applied to the roughness spectrum (as a frequency domain weighting) as detailed in Chapter 5. As the roughness spectrum did not have the same frequency resolution as the transfer function, both U_r / R and the roughness were converted into one-third octave bands before the spectrum of U_r was calculated. The displacement prediction was then modified to give the average vibration at a fixed point on the rail as the wheel passes, which is the situation that was measured. The method used to derive this modification is presented above in Chapter 5. The factor $1/\beta L$ (see Figure 5-33) was used for all of the rail acceleration predictions in this chapter. Finally, the displacement was multiplied by angular frequency to obtain an acceleration spectrum. A flow chart of the processes used to obtain a frequency-domain prediction is shown in Figure 6–2.

An example of a measurement and prediction of rail acceleration is given in Figure 6–3. This shows that the prediction follows the same trend as the measurement[8]. As the measurements were repeated for about twenty different wheel speeds and four wheel-loads approximately eighty of these graphs could be made. A more convenient way of comparing the results of the measurements and predictions is to form the difference of the predicted level minus the measured level (dB). This is equivalent to a ratio of predicted acceleration to measured acceleration in linear values (m/s^2). Many different measurements can now be plotted together, as shown in Figure 6–4. Ideally these graphs would show many straight horizontal lines, all at 0dB. This would mean that the predictions perfectly match the measurements. Whilst perfect agreement is not

[8] This is to be expected given the fact that the corrections in Chapter 5 are based on these measurements. However, the corrections have been shown to be entirely reasonable in comparison with published data.

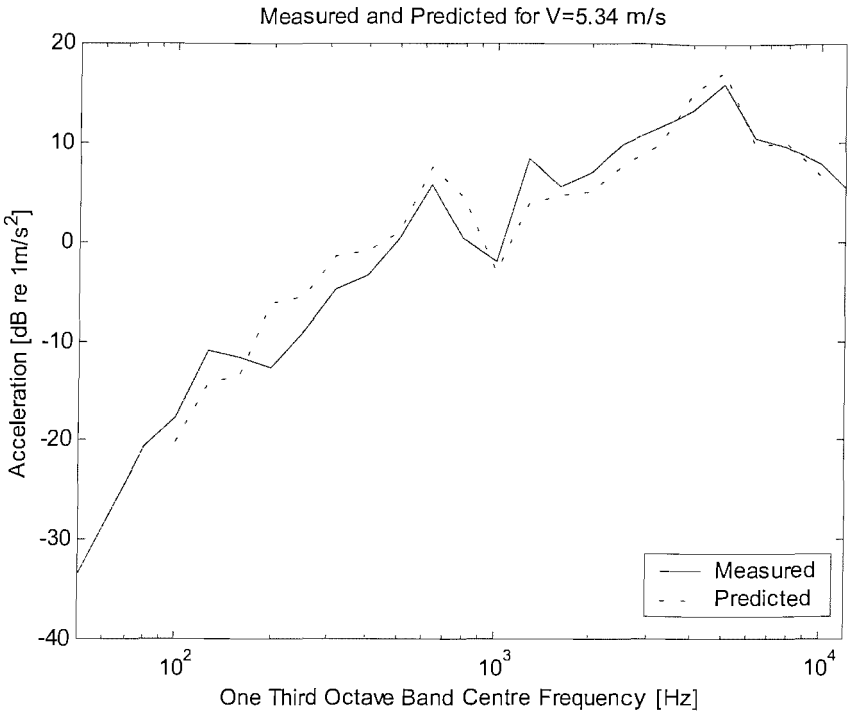

Figure 6-3 Predicted (measured variant of the FRF model) and measured rail acceleration for a wheel pre-load of 527N, and a wheel speed of 5.3m/s.

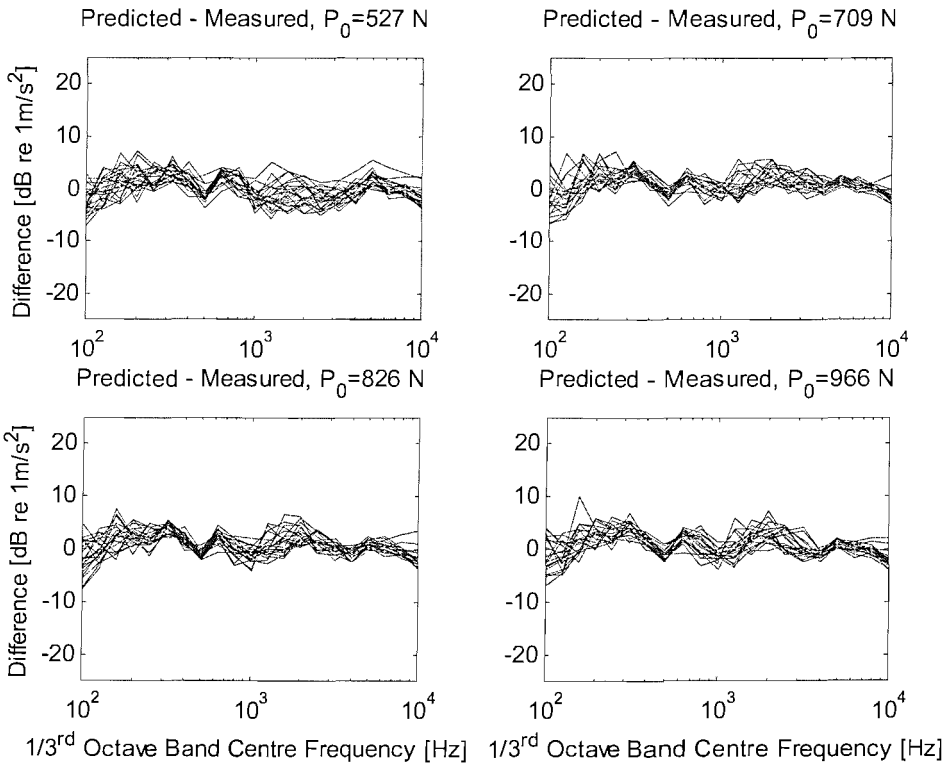

Figure 6-4 Predicted (measured variant of the FRF model) minus measured rail acceleration for the four rig wheel pre-loads considered. Each graph shows the predicted minus measured level at approximately 20 different wheel speeds.

achieved, the results tend to resemble the required horizontal straight line with a certain amount of scatter.

As this prediction has the most detailed representation of the wheel and the rail, the other models and their variations are not expected to improve upon these results. They demonstrate that the response of the rig, due to the dominant surface roughness on the railhead, is at a level that agrees with the frequency-domain model [Remington, 1976]. As this model has been extensively developed (see Chapter 2), it is reasonable to assume that the rig is behaving as it was designed. Conversely it can also be argued that as the predictions agree with the measured response, the measured FRF model is also working correctly.

6.3.2 Axle acceleration

Comparisons of the measured and predicted axle vibration were made in addition to the wheel vibration as the measurement instrumentation only used a single slip ring. As slip rings are a possible source of noise, it was hoped that the axle measurements would be an alternative method of measuring the wheel.

An example of the measured and predicted axle vibration is shown in Figure 6–5 for two wheel speeds, 1.4m/s and 5.6m/s, but with the same wheel load of 527N. The predictions are found to be lower than the measurements for frequencies below 200Hz. This region coincides with the poor coherence in the FRF measurements identified in Chapter 5 (see Figure 5-3). Similar problems arise in the frequency range 2kHz to 7kHz where the coherence of the axle transfer function measurement was seen to drop in Figure 5-3. The results for all of the wheel speeds at each of the four wheel pre-loads are presented in Figure 6–6 in the form of predicted level minus measured level. All of these predictions have been made using the measured FRF variant of the axle prediction model transfer function (U_a / R), shown in Figure 5-5.

The following trends are observed from Figure 6–6:

- The predictions are seen to be lower than the measurements by approximately 25dB in the range 100Hz to 200Hz.
- The model is typically found to over-predict at 400Hz and 500Hz by about 10dB.
- The best agreement of the predicted and measured acceleration is seen between 600Hz and 2kHz.

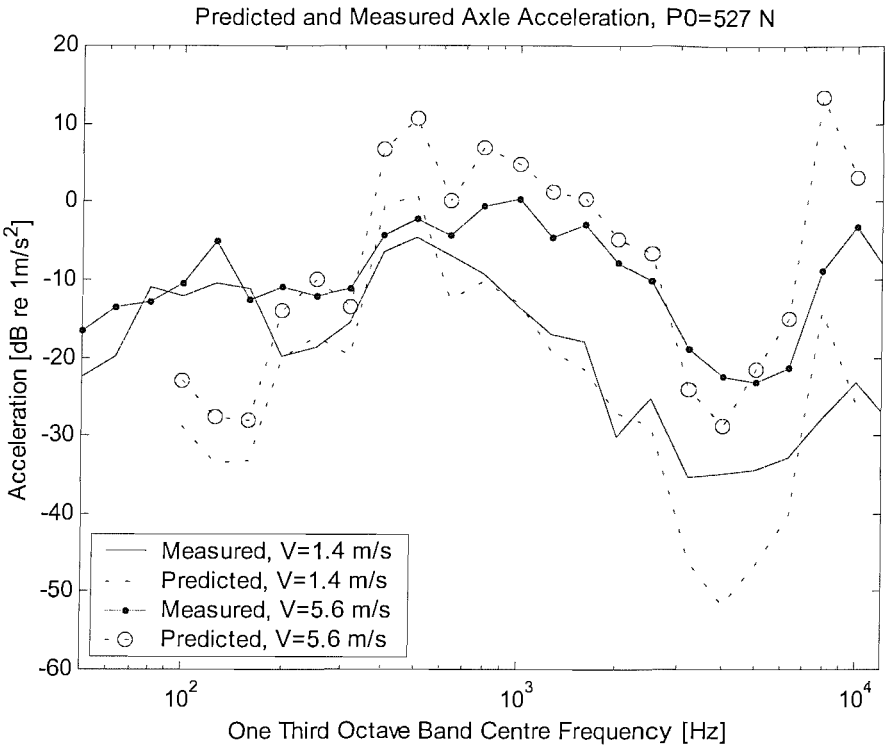

Figure 6-5 Predicted (measured variant of the FRF model) and measured axle acceleration for two wheel speeds (1.4m/s and 5.6m/s) at a 527N wheel pre-load.

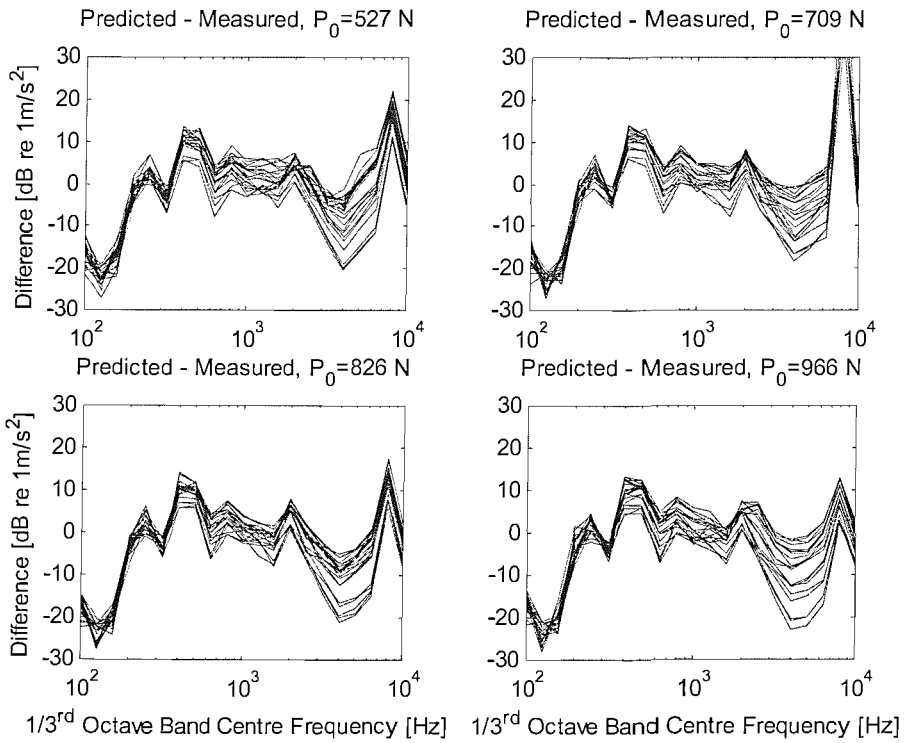

Figure 6-6 Predicted (measured variant of the FRF model) minus measured axle acceleration for the four rig wheel pre-loads considered. Each graph shows the predicted minus measured level at approximately 20 different wheel speeds.

- A strange peak is seen in the 8kHz one-third-octave band which varies with wheel load.

Figure 6–6 shows that the predicted minus measured levels varied with wheel speed in the range between 2kHz and 6kHz. This can also be seen in Figure 6–5 where the low wheel speed predictions are similar to the measurements, but as the wheel speed increases the difference between the measurements and predictions grow, resulting in an under-prediction from the model at the highest wheel speed of 6m/s.

The poor agreement at low frequencies in Figure 6–6 could be explained by the noisy low frequency measured frequency response functions that made up the transfer function. However, the other discrepancies at 400Hz and 500Hz, and at 8kHz, that were noted, cannot be so easily explained. It is plausible that the axle bearing could behave in a non-linear manner that causes the discrepancies observed in the measurements. However, this has not been verified experimentally. Only the static measurement shown in Figure 5-3 was possible. An alternative possibility is that the measurements of the axle vibration were contaminated by an unknown effect within the instrumentation slip ring. This is discussed further in the next section.

The comparisons shown in this section demonstrate that the predictions and measurements of axle vibration are generally rather unreliable, partly because of the transfer function measurement made between the tread and the axle, but mainly due to the inconsistencies that are related to wheel speed.

6.3.3 Wheel acceleration

As described in Chapter 5, the transfer function (U_w / R) for the measured FRF model can be formed by either using a point accelerance measurement or an average accelerance measurement. The results based on a point accelerance measurement are shown for a wheel speed of 5.3m/s with a wheel load of 527N in Figure 6–7, and for all the wheel speeds at each wheel pre-load in Figure 6–8. It can be seen that for the majority of the frequency range considered, the difference in level between the predicted and measured acceleration varies with wheel speed. Variations with wheel speed of up to 10 dB in some frequency bands can be seen (for example in the 1kHz band).

The measured FRF variant prediction based on the average wheel accelerance measurement gives a better agreement with the measurements, as shown in Figure 6–9 and Figure 6–10. Nevertheless, in certain frequency ranges the predictions do not agree

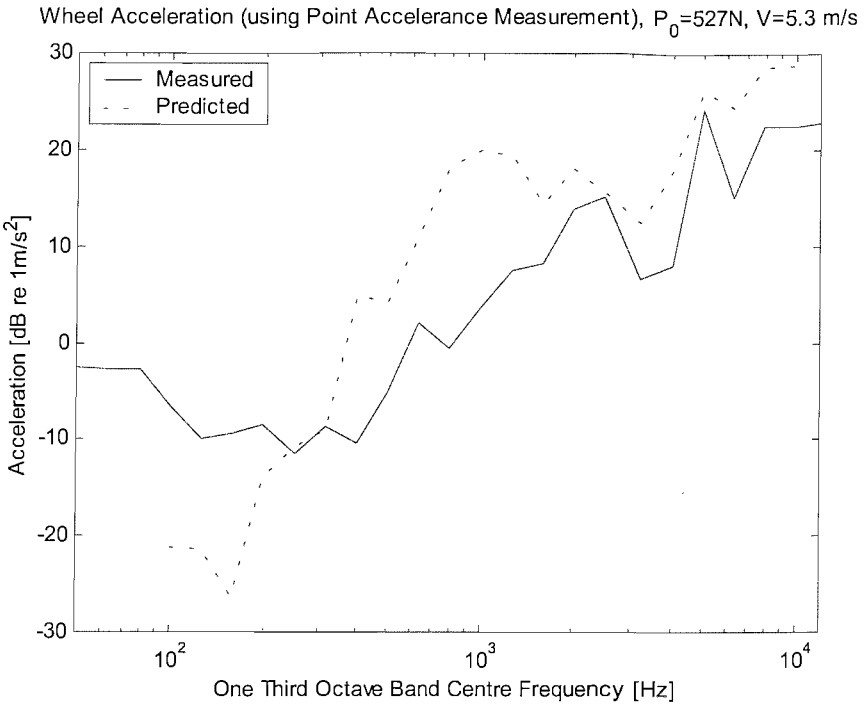

Figure 6-7 Predicted (measured variant of the FRF model using a point accelerance measurement) and measured wheel acceleration for a wheel load of 527N, and a wheel speed of 5.3m/s.

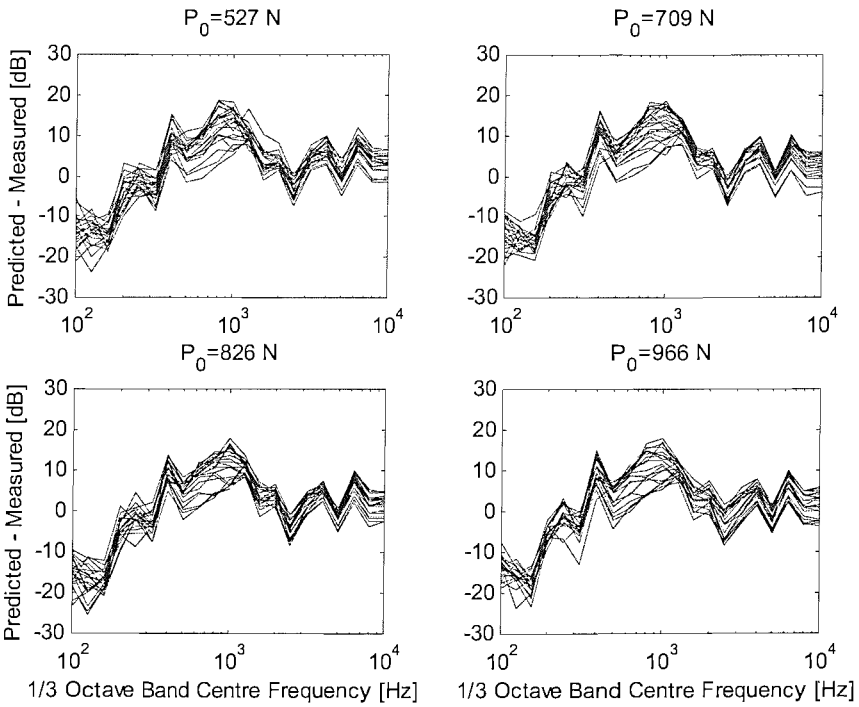

Figure 6-8 Predicted (measured variant of the FRF model using a point accelerance measurement) minus measured wheel acceleration for the four rig wheel pre-loads considered. Each graph shows the predicted minus measured level at approximately 20 different wheel speeds.

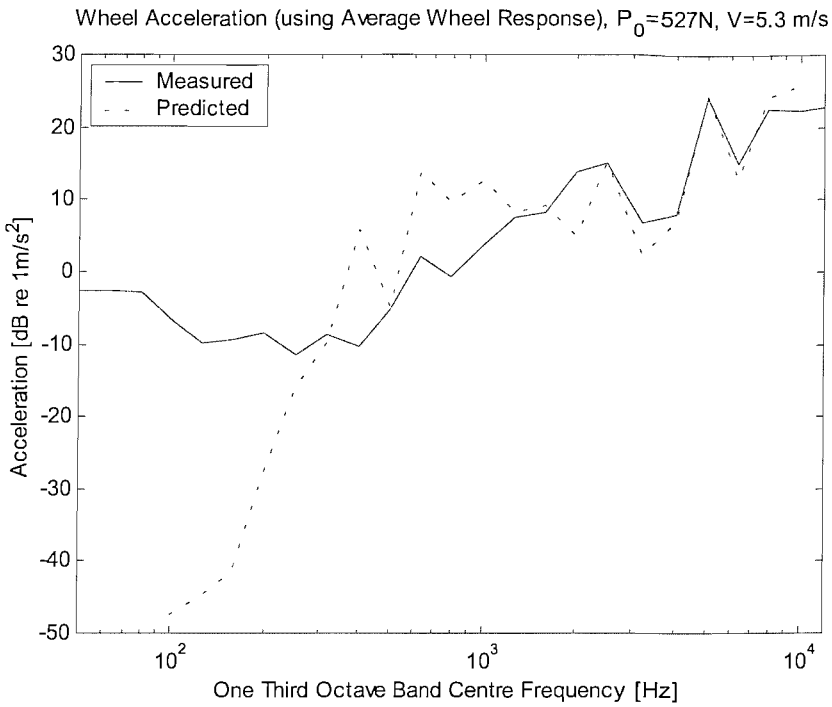

Figure 6-9 Predicted (measured variant of the FRF model using the average accelerance measurement of the wheel response) and measured wheel acceleration for a wheel load of 527N, and a wheel speed of 5.3m/s.

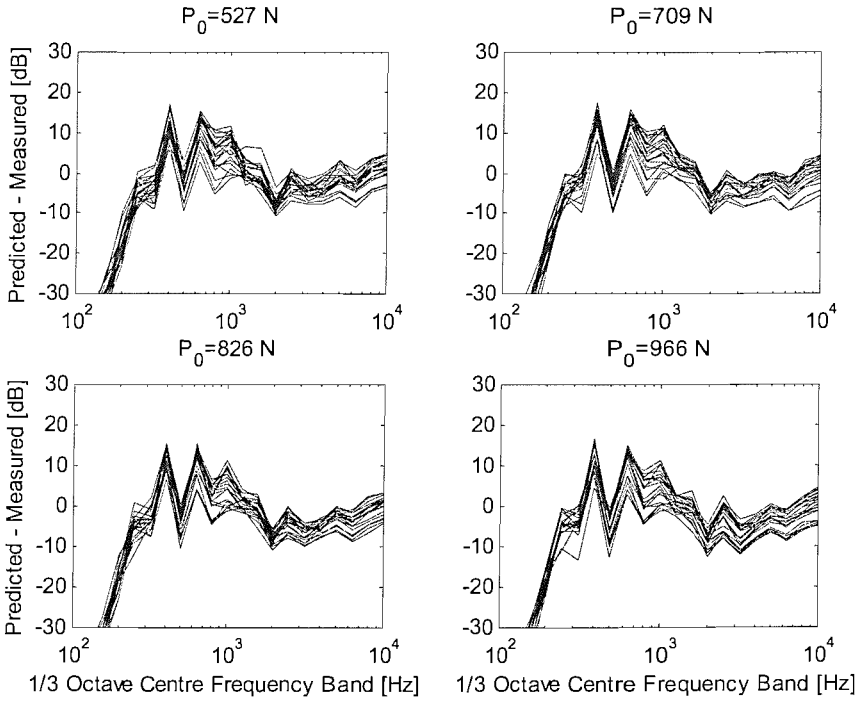

Figure 6-10 Predicted (measured variant of the FRF model using the average accelerance measurement of the wheel response) minus measured wheel acceleration for the four rig wheel pre-loads considered. Each graph shows the predicted minus measured level at approximately 20 different wheel speeds.

well with the measurements, particularly at frequencies below 200 Hz where the predictions are much smaller than the measurements. Again, as for the predictions made with the point accelerance measurement of the wheel, variations with wheel speed are seen across the majority of the frequency range considered.

It is not immediately apparent why the predictions of the wheel acceleration and the axle acceleration are in poor agreement with the measurements. For the case of the measured FRF variant it is possible that one of more of the measurements could be the cause, as the predictions are based almost entirely on measurements.

It is thought that the static measurements, that had been extensively made, were of fairly high quality, despite the low frequency content of these measurements having been found to be unreliable (see Chapter 5). Comparisons of predictions (based upon measurements) of rail acceleration with the measured rail acceleration above 100Hz have been seen to be in good agreement (section 6.3.1). This appears to confirm the validity of the static measurements.

The dynamic measurements of both the wheel and axle, however, have not been verified. A possible problem with these measurements is that the slip rings (that are a necessary part of the instrumentation) may introduce an effect that varies with wheel speed. To verify this an extensive set of measurements of the slip ring noise would have to be made at different speeds of rotation. Alternatively, a different instrumentation system could be used that does not have any moving electrical contacts between the moving parts of the rig. Project constraints, however, in the form of both time and money, prohibited such an investigation or inclusion of a more advanced instrumentation system.

6.4 Comparison of measurements with predictions using the 'simple' variant

6.4.1 Rail acceleration predicted using the 'simple' variant of the FRF model

The predictions of rail acceleration shown above in section 6.3.1 were repeated for the simple variant of the FRF model. These predictions were made to enable comparisons with the time-stepping models. They were also used for comparison with the modal wheel model, and to demonstrate any differences between the linear and non-linear predictions.

As described previously, the simple model represents the track as a fourth order rational polynomial. The coefficients were found from a curve fitting method described in Chapter 2, and are given in Table 5-1. The wheel was modelled as a mass that includes the wheel, its axle, the slip ring, the rig pre-load spring, the force gauge and the part of the wheel assembly that pivots about the beam end (see Figure 3-4). This mass was measured and found to be 15kg.

The contact spring was modelled, in the same manner as for the measured FRF model prediction above, with a linear spring (k_H) at a fixed value for each wheel pre-load. The frequency response functions of each of the model elements were shown previously in Figure 5-11, and the process of obtaining a prediction was made in accordance with the flow chart shown in Figure 6–2.

The results are given in terms of the predicted level minus the measured level for each wheel load in Figure 6–11. Whilst the results show that the predictions are not always in agreement with the measurements, they do show a surprisingly good trend. Certain features are noticeable that are independent of the wheel load and the wheel speed. This indicates that they are due to the behaviour of the system, and are therefore attributed to an over-simplification of the model. A good example of this is seen in the 1kHz one-third octave band for all of the wheel pre-loads considered.

6.4.2 Verification of the time-stepping routine using the simple variant

A time-stepping model with a linear contact spring was made to ascertain whether identical inputs for a time-stepping model and the FRF model would produce the same outputs. The purpose of this comparison was to verify that the time-stepping routine was working correctly. The simple variant wheel and track representations were used in both the time-stepping model and the frequency-domain model, and the roughness input was interpolated before it was used in either model to provide an adequate time step size for the time-domain model. Roughness input interpolation was found to be necessary to improve the high frequency predictions of the time-stepping model. This was done by artificially raising the frequency content of the input past the highest frequency of interest. The frequency content of the input had already been adjusted to ensure that it contained an adequate content for all of wheel speeds by the methods of surface profile measurement presented in Chapter 4. So the interpolation was only done to help comparisons with the frequency domain models in the higher one-third octave

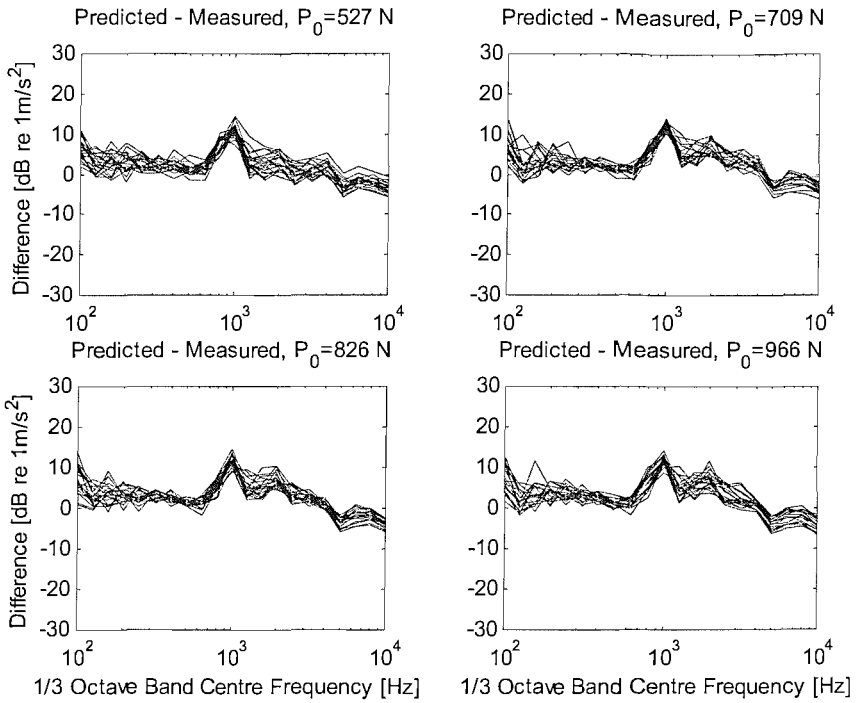

Figure 6-11 Predicted (simple variant FRF model) minus measured rail acceleration for the four rig wheel pre-loads considered. Each graph shows the predicted minus measured level at approximately 20 different wheel speeds.

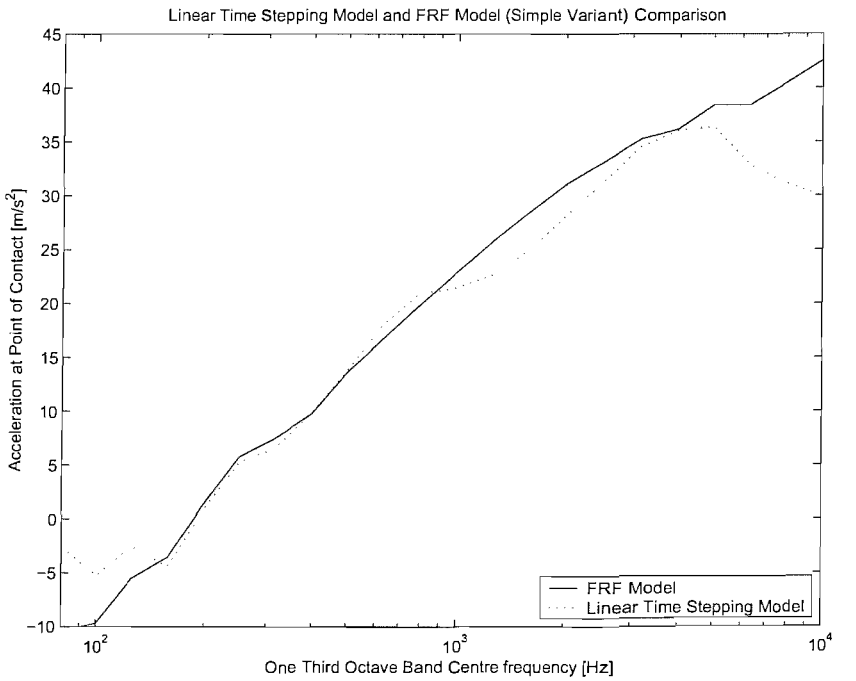

Figure 6-12 Comparison of a prediction made with the simple variant of the linear time stepping model and the simple variant of the FRF model. High frequency differences are due to the sample frequency (which was 60kHz) chosen for the time-stepping model.

frequency bands (e.g. the 10kHz band) of the frequency range of interest. It was found that a sample frequency of 60kHz provided an adequate comparison with the frequency-domain model predictions in the 10kHz one-third octave band whilst ensuring a reasonable computation time for the time-stepping routines.

A comparison between the time-stepping model and FRF model outputs is shown in Figure 6–12, from which it can be seen that there is good agreement for the majority of the frequency range considered. Better agreement at high frequencies is achievable, but much higher sample frequencies (>2MHz) are required.

6.4.3 The 'simple' variant non-linear time-stepping model

This section presents predictions using the non-linear time-stepping model conceived by [Wu and Thompson, 2000(a)]. This model is also used in later chapters where non-linear effects are expected to be present.

The outputs of the time-stepping routines are the displacements of the wheel and the rail as a function of time. Examples of the predicted wheel and rail displacements are given in Figure 6–13. Here it can be seen that the rail vibration has a strong sinusoidal trend throughout. The frequency of this trend (45Hz) corresponds with the wheel-on-track resonance shown in Figure 5-12. Unlike the rail displacement, the wheel displacement, however, is seen to follow the main features of the roughness input, or surface of the rail, that is shown in Figure 4-17.

Simple comparisons in the time domain were made between the measurements and predictions, where the peak value of acceleration was compared. As the measurements were already in the form of acceleration, only the predictions had to be differentiated in the time domain. This was done by a first order difference routine in MATLAB. After differentiation, the contact filter effects were applied by the use of the digital version of the approximate contact filter described in Chapter 5. The predicted peak rail acceleration in Figure 6–14 is somewhat larger than the measurements. There is at least 10dB between the measured and predicted peak values within the wheel speed range 1m/s to 6m/s. Part of this discrepancy is likely to be due to the effect of the track decay rates that has not been included. A frequency-domain correction for this effect has been presented in Chapter 5, but a time-domain correction or filter for this characteristic has not been devised. Unlike the contact filter, no simple physical trend or mathematical relationship exists to approximate $1/\beta L$.

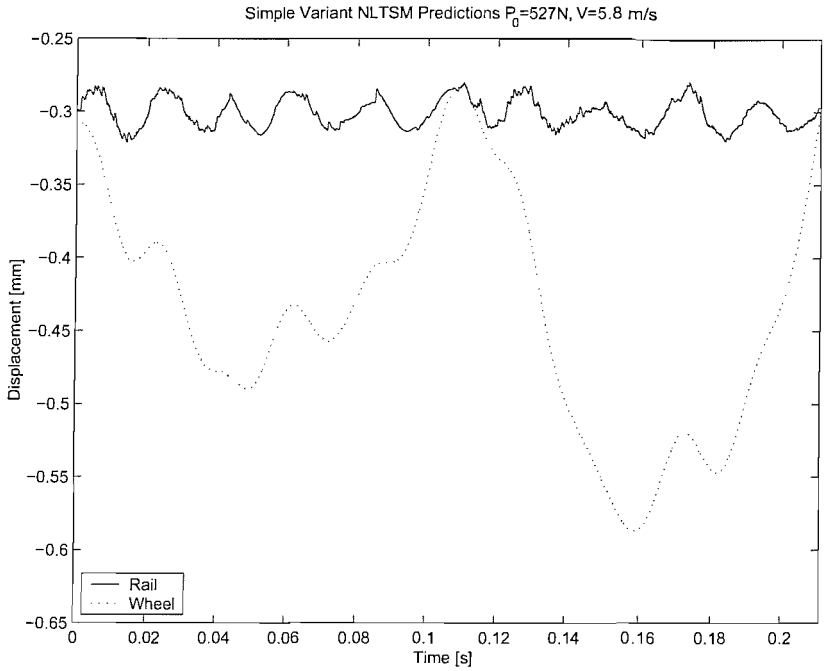

Figure 6-13 Simple variant non-linear time-stepping model prediction of wheel and rail displacement for a wheel speed of 5.8m/s at a 527N wheel pre-load.

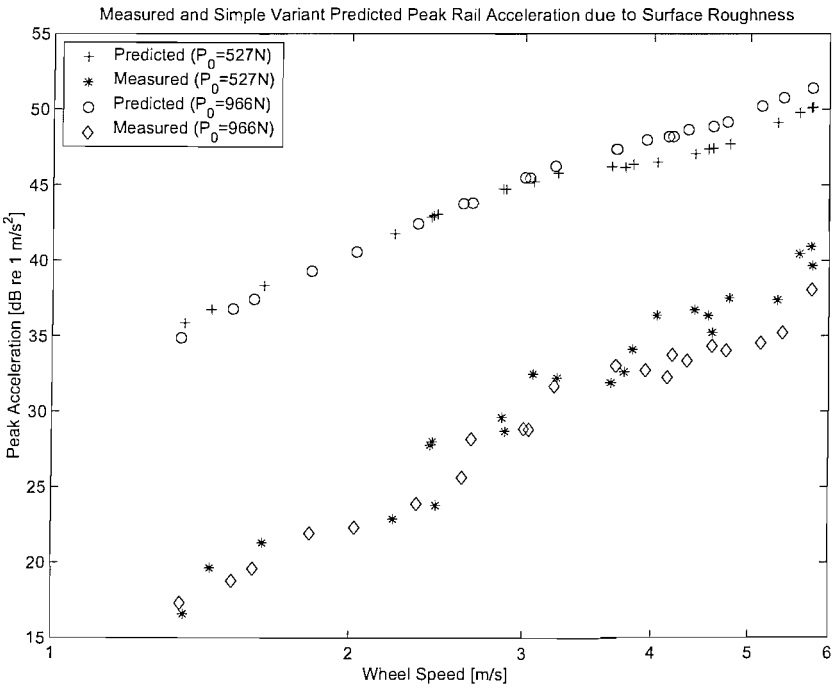

Figure 6-14 Measurements and predictions, using the simple variant of the non-linear time stepping model where contact filter effects have been included, of peak rail acceleration for two rig wheel pre-loads.

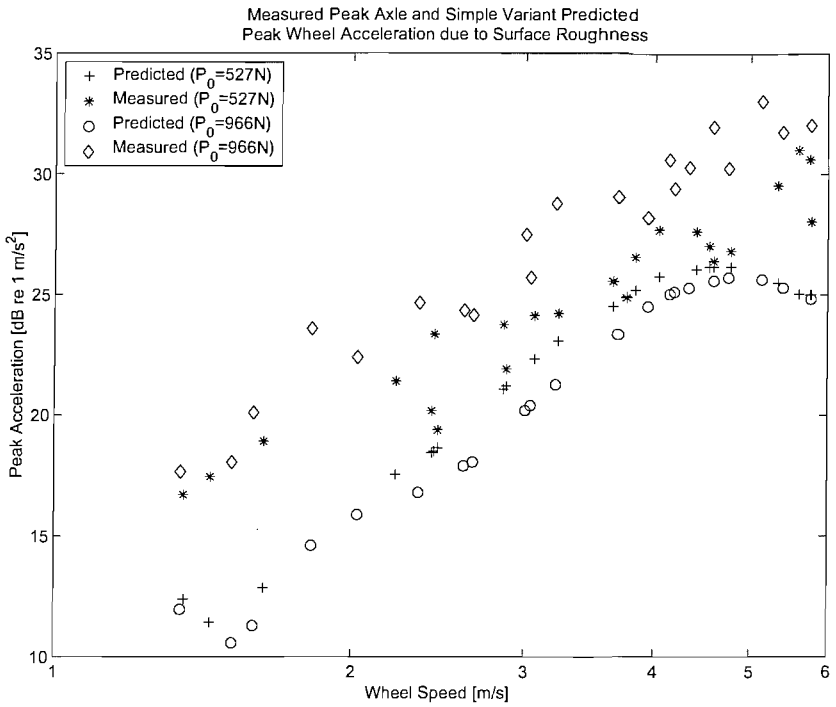

Figure 6-15 Measurements and predictions, using the simple variant of the non-linear time stepping model where contact filter effects have been included, of peak wheel acceleration for two rig wheel pre-loads.

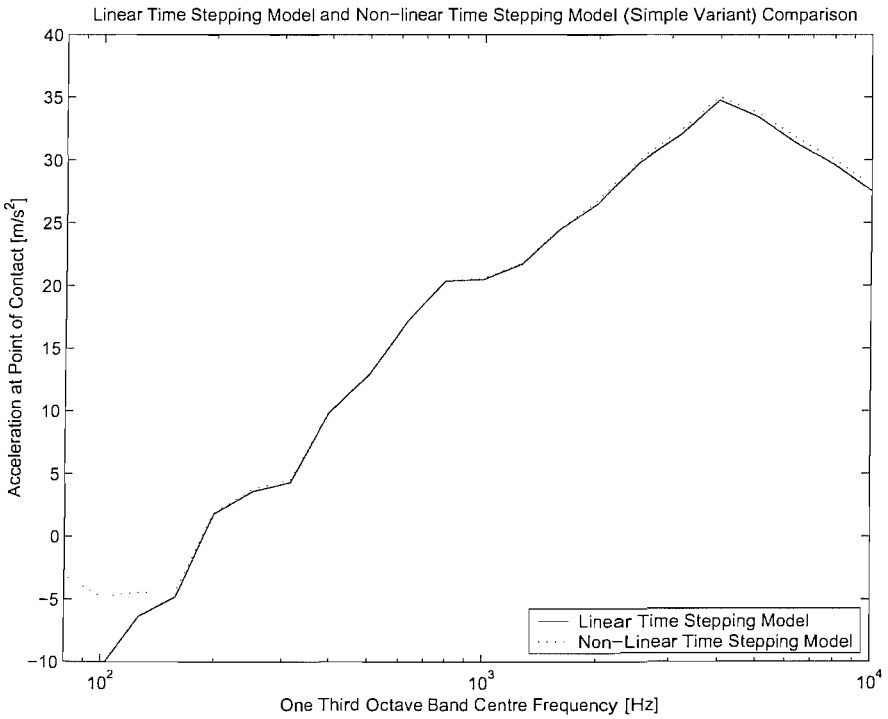

Figure 6-16 Predicted rail acceleration made with the simple variant of the linear time-stepping model and the equivalent non-linear time-stepping model.

The results of the wheel peak acceleration are shown in Figure 6–15. These show better agreement, than for the rail as the track decay rates have no effect on the wheel vibration. The peak acceleration measurements of the wheel exceed the predicted levels by about 5dB across the range of wheel speeds considered (1m/s to 6m/s).

The use of fairly smooth wheel and railhead surfaces was intended to avoid any noticeable non-linear behaviour. This is confirmed in Figure 6–16 where predictions of rail vibration from both the linear and non-linear time-stepping models are compared. It can be seen that their outputs are similar at all the frequencies considered. The comparison of the two models therefore suggests that the railhead with 'normal' surface roughness does not cause any noticeable non-linear behaviour and can therefore be modelled successfully using a linear frequency-domain model. This is also confirmed by the results shown in Figure 6–4 where the FRF model predictions were shown to agree with the measurements.

The results from this non-linear time-stepping model were then compared with the measurements in terms of frequency spectra. As results of the time-stepping model are functions of time, the following process was used to convert these predictions into a frequency spectrum that could be compared with measured acceleration spectra:

- Firstly a PSD of the displacement output of the time-stepping model was determined.
- The predictions were then differentiated twice in the frequency-domain (multiplied by ω^4 as the PSD is a squared quantity) to form a PSD of acceleration.
- The PSD was then converted into one-third octave frequency bands.
- Next the approximate contact filter was applied to the predictions in the form of a one-third octave band frequency weighting (as in section 5.3.3).
- The predictions of rail vibration were then adjusted in the frequency-domain for the effects of rail decay rate (as in section 5.3.2).

Ideally the inclusion of the contact filter effects would have been made at a point either during the time-stepping routine, or prior to the commencement of the routine by adjusting the input. Applying the contact filter at the end of the time-stepping routine is likely to highlight any non-linearities as greater high frequency excitation has been included in the model, which might contribute to any non-linear behaviour. However, if the wheel / rail interaction can be represented by a linear model as is expected (and has

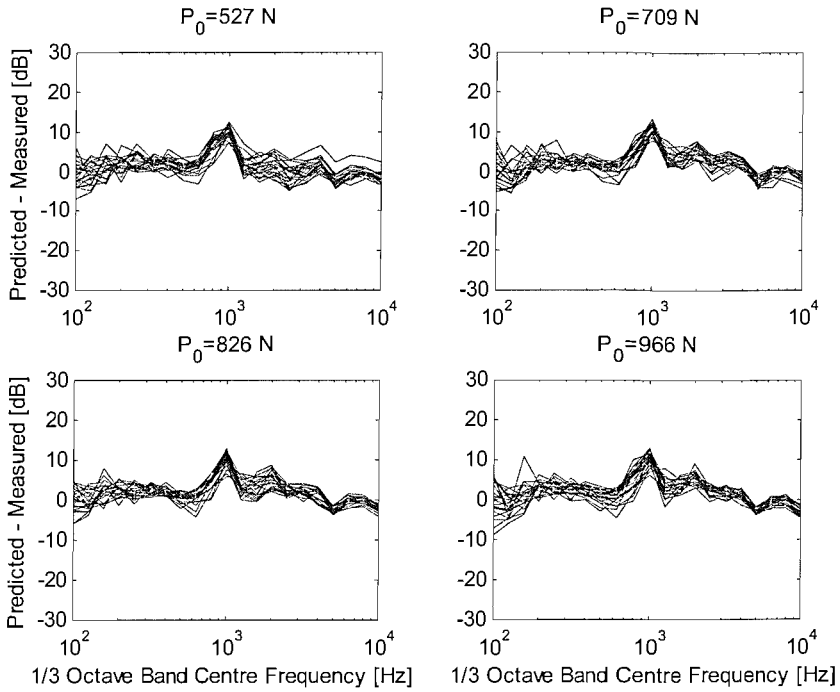

Figure 6-17 Predicted (simple variant non-linear time stepping model) minus measured rail acceleration for the four wheel pre-loads considered. Each graph shows the predicted minus measured level at approximately 20 different wheel speeds.

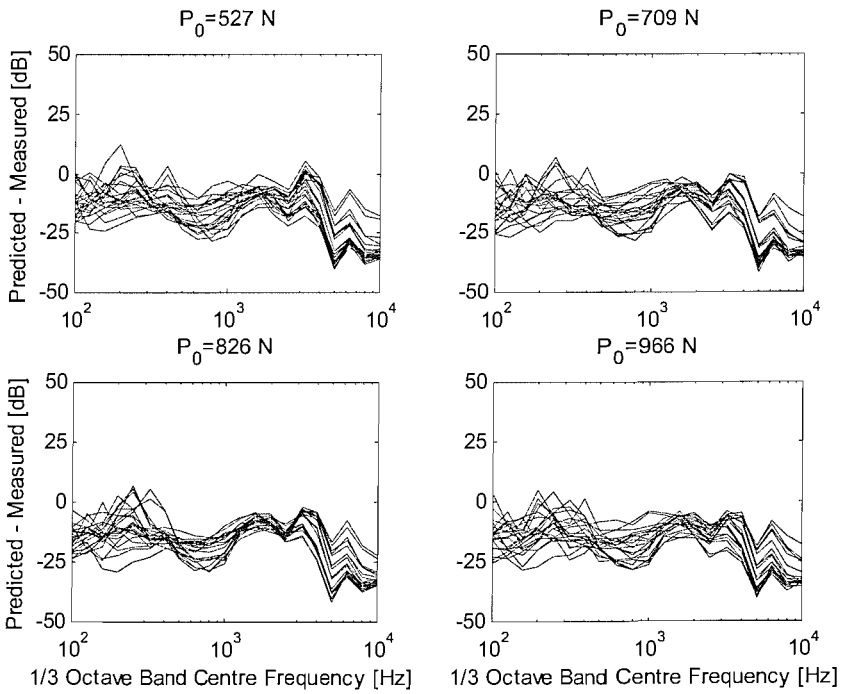

Figure 6-18 Predicted (simple variant non-linear time stepping model) minus measured wheel acceleration for the four wheel pre-loads considered. Each graph shows the predicted minus measured level of approximately 20 different wheel speeds.

been shown by Figure 6–4 and Figure 6–16) then it will not matter at what stage the contact filter effects are applied.

The difference between the predicted and measured rail acceleration level (for the simple variant of the non-linear time-stepping routine) is presented in Figure 6–17 for the four wheel pre-loads. Similar results are found to those from the equivalent frequency-domain model, given in Figure 6–11. The corresponding results for the wheel acceleration are presented in Figure 6–18. This demonstrates that the simple wheel mass model cannot adequately describe the response of the wheel, particularly at high frequencies. This was expected and has been discussed in Chapter 5. However, again it can be seen that the difference between the predicted and measured wheel acceleration varies with wheel speed. As the measurements of the wheel vibration have not been verified, and confirmed to be reasonable, it is possible that the 25dB variations in the predicted minus measured level could be due to an unknown effect of the slip rings used in the wheel accelerometer instrumentation.

6.5 Comparison of measurements with predictions from the 'modal wheel' variant

6.5.1 Verification of time-stepping routine using the modal wheel model

In order to ascertain that the non-linear time-stepping model was performing correctly, its response was compared with that of the FRF model with the same inputs. This meant that the wheel and track representations from the modal wheel variant were used in both the time-stepping model and the FRF model. This comparison is shown in Figure 6–19, which indicates that there is good agreement for most of the frequency range considered. The discrepancy at high frequencies is again attributed to the resolution of the input roughness data, as explained in section 6.4.2.

6.5.2 Modal wheel non-linear time-stepping model

The predictions from the non-linear time-stepping model, that has been developed further to include the modal response of the rig wheel, are compared with the measurements in this section. The purpose of such a model is to try to reproduce the modal characteristics of the measured FRF as the latter can only be used in a linear model. Another motivation for this model is to attempt to improve the predictions of the wheel response. This has been shown by the findings in Chapter 5 where the simple

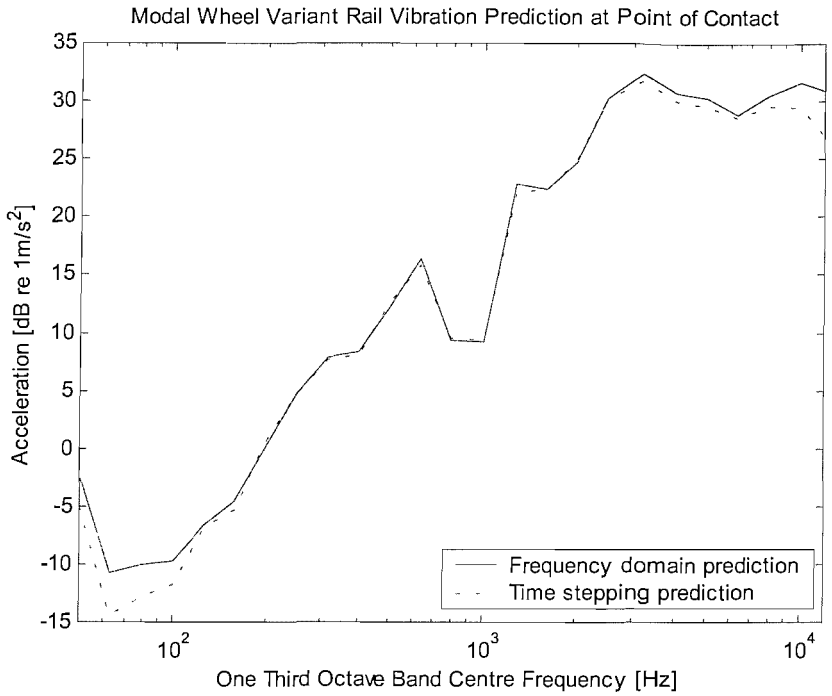

Figure 6-19 Comparison of the rail acceleration predicted using the modal wheel variant FRF model and non-linear time-stepping model outputs for the same roughness input (interpolated to have a 60kHz sample frequency), for a wheel load of 527N, and a wheel speed of 5.8m/s.

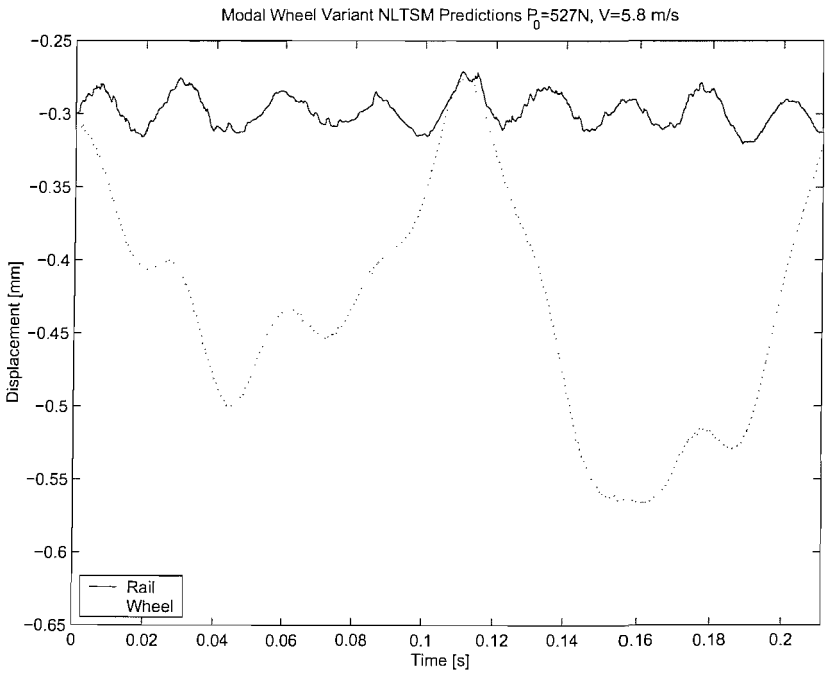

Figure 6-20 Predicted wheel and rail displacement from the modal wheel variant of the non-linear time-stepping model for a wheel speed of 5.8m/s and a 527N wheel pre-load.

mass model was found only to produce an acceptable prediction in the frequency range 100Hz to 1kHz. The modal wheel model was therefore designed to improve these results.

An example of the predicted wheel and rail displacements from the modal wheel non-linear time-stepping model is given in Figure 6–20. Again it can be seen that the rail displacement has a strong sinusoidal trend that corresponds with the wheel-on-track resonance of 40Hz, shown in Figure 5-18. The wheel displacement is seen to follow the main trends of the surface of the rail, that is shown in Chapter 4, in a similar way to the results for the simple variant of the time-stepping model (see Figure 6–13).

The predictions from the modal wheel non-linear time-stepping model were compared with the measurements in terms of frequency spectra. The same process of conversion of the time domain outputs into one-third octave bands was used as for the simple model. This process is described in section 6.4.3. The predicted minus measured rail acceleration (for the modal wheel variant of the non-linear time-stepping routine) is presented in Figure 6–21 for the four wheel pre-loads. This shows that, as described in Chapter 5, the modal wheel variant improves the agreement between the measured and predicted acceleration in the 1kHz band (compared with the simple variant). However this occurs at the expense of the neighbouring 800Hz band. A dip in the predicted minus measured levels at 5kHz occurs for the modal wheel variant. This indicates that, as the modal wheel variant does not perform well in these two one third octave bands, the simple variant is arguably the better model to use. This however, is not expected to be the case for the prediction of wheel vibration (see Chapter 5).

The predicted minus measured wheel acceleration is presented in Figure 6–22. Only small variations are found as a function of wheel speed. The differences in level are smaller than those shown previously in Figure 6–18 which has a scale of –50dB to 50dB whereas Figure 6–22 has a smaller scale (-30dB to 30dB). The predictions of wheel acceleration made with the simple variant of the non-linear time-stepping model in Figure 6–18 (see also Figure 5-17) demonstrate that the simplified representation of the wheel as a mass is not an adequate model. Better agreement with the measurements is seen with the modal wheel variant in Figure 6–22, but the differences remain due to the poor quality of the measured wheel vibration, because of noisy instrumentation.

The results for the rail vibration shown in Figure 6–17 and Figure 6–21 indicate that, whilst the modal wheel variant is better for the prediction of wheel acceleration, the simple variant arguably provides a better prediction of rail acceleration. The comparison

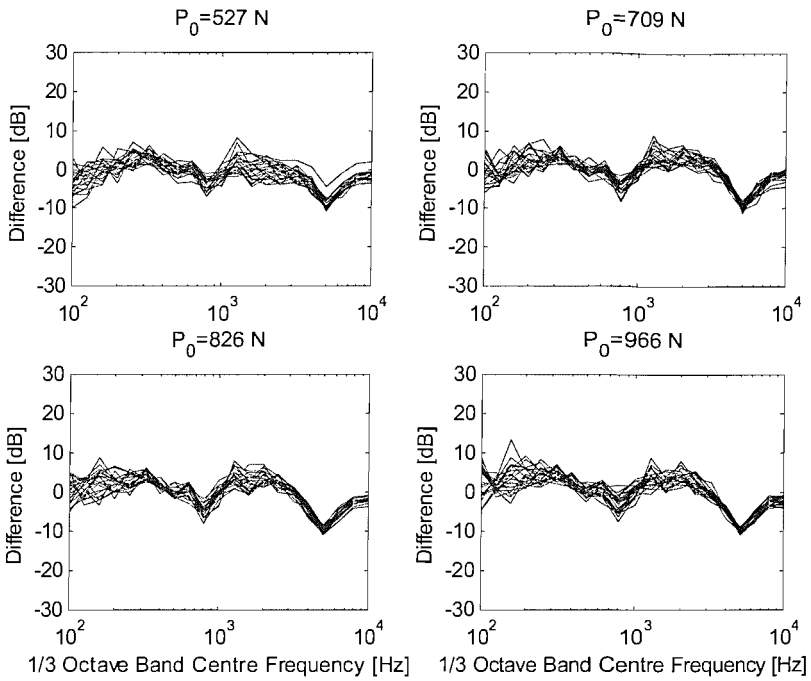

Figure 6-21 Predicted (modal wheel variant non-linear time stepping model) minus measured rail acceleration for the four wheel pre-loads considered. Each graph shows the predicted minus measured level of approximately 20 different wheel speeds.

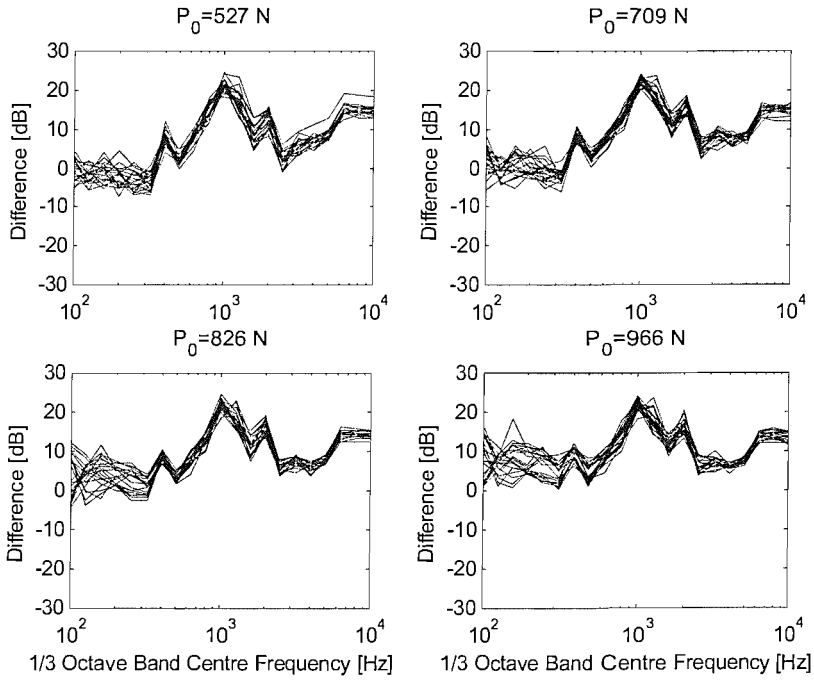

Figure 6-22 Predicted (modal wheel variant non-linear time stepping model) minus measured wheel acceleration for the four wheel pre-loads considered. Each graph shows the predicted minus measured level of approximately 20 different wheel speeds.

of the dynamic stiffness of the two variants shown in Chapter 5 (Figure 5-23) highlighted two frequency regions where the simple variant and the modal wheel variant differed. These were at frequencies close to 1kHz and close to the wheel on track resonance of each variant. The differences below 100Hz are not considered here as the measured rail acceleration was not reliable at such low frequencies, but the higher frequency discrepancies appear to favour the simple variant predictions as these results are in better agreement with the measured levels. This suggests that the simple variant is the more reliable model not only for the prediction of rail acceleration, but also for the prediction of contact force.

6.6 Conclusions

The comparisons between each of the models have demonstrated that the prediction of rail vibration using the measured FRF model gives the best agreement with the measurements. This confirms that the measurements of acceleration made on the 1/5-scale rig are reasonable, as such a model has been widely used (see Chapter 2) to predict rail vibration.

It is expected that the measured FRF model cannot be reliably used to predict wheel / rail vibration where large variations of the contact stiffness are expected. To account for this, a time-stepping routine with a non-linear contact spring is required. The measured FRF model however, cannot be used in a time-stepping routine, so whilst it has been shown to agree well with the measurements of rail vibration it cannot be used for the forthcoming chapters concerning railhead discontinuities.

Two models that use analytical representations of the wheel and track have been presented in this and the previous chapter, and their performance has been investigated. The different shapes of the curves of predicted minus measured rail vibration shown in Figure 6–17 and Figure 6–21 highlights the characteristics of each model. For the prediction of rail vibration, despite its relative crudeness, the simple variant is seen to give good agreement with the measurements for most of the frequency range. A contribution of a 1kHz wheel mode in the measured vibration is not predicted by this model, and a discrepancy at this frequency is shown. The differences in levels at the highest frequency one-third octave band also indicate some deficiencies of the simple variant.

The more complicated modal wheel variant gives a slight improvement on the simple variant. Its performance, however, is not as good as had been hoped. The motivation to

include the wheel modes in an analytical model was to try to obtain a model that would match the performance of the measured variant of the FRF model. An exact match has not been achieved for the prediction of rail vibration. Comparison of Figure 6–17 and Figure 6–21 shows that whilst the simple variant failed to represent adequately a wheel mode at 1kHz, the modal wheel variant has improved the agreement with the measurements. However, this occurs at the expense of the performance in neighbouring frequency bands. The lightly damped high frequency wheel modes were not easy to model and thus this frequency region was only crudely approximated in the modal wheel variation. This has resulted in a dip in the predicted minus measured levels at 5kHz.

Unfortunately problems relating to the quality of the acceleration measurements hindered analysis of the predictions for the wheel and axle. However, it is felt that, as comparisons between the models and the measurements of rail vibration have been successful, the predicted vibration of the wheel should be better than has been indicated by the comparisons with the measurements of both the wheel and the axle. It is therefore more likely that the measurements of the wheel and axle vibration are influenced by noise. It is possible that this is due to the slip rings used in the instrumentation of both the wheel and axle measurements.

One of the main purposes of this chapter was to verify the time-stepping models by comparing them with the existing FRF model and measured responses of the rig. The non-linear model gave very similar results to those of the linear time-stepping model and therefore the FRF model using simplified representations of the wheel and the rail. The performance of the models based on these simplified representations of the rig wheel and track has been extensively investigated.

The different methods used to model various parts of the rig, highlighted the following points:

- Rail vibration can be fairly accurately represented by a model with a simple mass for the wheel.
- Wheel vibration, however, requires a good representation of the many wheel modes in order to obtain an adequate prediction.
- The measurements of wheel and axle vibration are most likely to be influenced by an undetermined effect, that is probably associated with the slip rings.

Despite the problems that have been found with the measurement and prediction of the axle and wheel response, the aims of this chapter have been met. The predictions and measurements of rail vibration have been found to be reliable enough to achieve this. The time-stepping model performance has been verified and can now be used to predict vibration where non-linear wheel and rail interaction is likely.

The next chapter describes further adjustments that were required to obtain good agreement between the predictions and the measurements particularly for inputs with discontinuities, after which measurements and predictions of vibration due to step joints dip joints and wheel flats are presented.

7 Methods to analyse and predict vibration due to discontinuities on the railhead

7.1 Introduction

This chapter introduces two methods that are used to improve and analyse the predicted behaviour of wheel / rail interaction due to discontinuities on the railhead surface. These methods have been designed to:

- Allow the inclusion of contact patch filtering and rail decay rates in the predictions of wheel and rail vibration due to a discontinuity on the railhead,
- compare non-linear predictions with linear predictions to investigate the behaviour of the contact spring when passing over a given railhead discontinuity.

Both of these methods are used in the following investigations for railheads with intended discontinuities on their surfaces (Chapters 8, 9, and 10). Additional material is also presented in this chapter which supplements the research commenced in Chapter 5. This includes methods that:

- identify when contact filter effects need not be applied to the vibration predictions if large variations of wheel pre-load are expected,
- investigate the effect of varying contact force on the model transfer function for different inputs,

These latter methods have not been used in the following chapters but have sufficient worth to warrant inclusion in this thesis. They have been found to be useful ways of demonstrating certain aspects of wheel / rail interaction.

7.2 Method used to allow the inclusion of contact patch filtering and rail decay rates in predictions of vibration due to a discontinuity on the railhead

The method of obtaining and preparing a surface profile measurement, so that it can be used as an input for a time-stepping model, has been presented in Chapter 4. Chapter 6 presented comparisons of predictions with measured vibration, which demonstrated that the methods developed thus far (in Chapter 4 and Chapter 5) produce relatively good agreement for the case of a surface roughness input. Chapter 5 notably presents two important corrections to the predictions that have been found to be necessary. These

were (i) a frequency domain alteration that converted the predicted vibration from a point that moved with the wheel / rail contact to the average at a fixed position on the rail, and (ii) an approximate contact filter effect. These methods, however, are found not to produce particularly good results when surface profile inputs containing a discontinuity are used with the non-linear time-stepping models.

The surface profile used in Chapter 6 fortunately had sufficiently small amplitudes for non-linear wheel / rail interaction to be negligible. This meant that the above two corrections to the predictions could in effect be applied either to the input prior to use in the non-linear prediction model, or to the output from the prediction model. Applying the corrections in either of these ways was found to produce similar results. However, where any non-linear behaviour is evident in the prediction, the option of applying the contact filter correction to the output from the prediction is not available. As previously indicated (Chapter 4 and Chapter 5) these sorts of adjustments should ideally be included within the time-stepping routine.

At present, it is not possible to include these corrections within a time-stepping model; thus the options that were readily available were either, not to apply any corrections or to apply corrections before or after the non-linear prediction.

Chapter 5 demonstrates the importance of the two corrections, so it was known that without some form of correction (for a change in position for the prediction of rail vibration, and the inclusion of contact filter effects) is required.

The contact filter adjustments could have been applied to the surface profile input prior to use in the prediction model. This option was, however, disregarded, as the methods used previously do not apply to non-stationary roughness. Both of the corrections presented in Chapter 5 are based upon an estimate of the acceleration at the wheel / rail contact point. As previously mentioned, if this method was utilised for a discrete discontinuity on the railhead, the estimate of the acceleration would be biased by the presence of the discontinuity. The behaviour therefore cannot be guaranteed. Further problems also exist with the application of the approximate contact filter adjustment, namely, that wheel pre-loads below 500N or above 1kN have not been investigated. This effect has therefore only been verified for a rather small range of pre-loads. If the predicted contact force leaves the small region that has been considered, then the contact filter, strictly, should not be applied. Intuitively, it appears safer to try to adjust the output after the prediction model. This at least meant that a reliable estimate of the

wheel and rail behaviour could be obtained albeit without these two important adjustments.

To alleviate this problem, the following method has been devised. This enables the two corrections presented in Chapter 5 to be safely applied to a part of the prediction. The method is to split the measured surface profile into two parts; one part that represents the discontinuity, and the other part that represents the surface roughness contribution. This means that this method requires two predictions of wheel / rail vibration for each case.

The surface roughness input is formed by removing the discontinuity part from the original measurement in the time (or spatial) domain. An example of this is shown in Figure 7–1 where a step joint discontinuity is considered. Artificially smooth sections are used to replace the section of the measurement where the discontinuity was formerly positioned. This is demonstrated in Figure 7–2 where a curve fitting process has been used to ensure a smooth transition from one side of the roughness measurement to the other. The data have also been extended here to a length of 1m.

The discontinuity part of the input is obtained by adding artificially smooth sections to either end of the small section of surface profile measurement removed above. This is shown in Figure 7–3 where the discontinuity has been repositioned so that a small (artificially) smooth section exists prior to the discontinuity. This ensures that any starting transients of the numerical time-stepping routine have decayed before the profile of the discontinuity is reached. A second, longer, section of artificially smooth surface profile is added after the discontinuity (see Figure 7–3) so that decay from the wheel / rail interaction model can be included in the prediction. The process of trend removal and preparation of the inputs for use in the prediction models is then carried out as described in Chapter 4, and the inputs are then used in their respective prediction models.

The discontinuity part of the input was used in conjunction with the non-linear time-stepping model, as wheel unloading from the rail was expected at the discontinuities. This process was very time intensive due to long input data lengths. These were necessary to ensure that an adequate time existed after the discontinuity so that wheel and rail vibration decay may be properly gauged, and small time step sizes were used so that the higher frequency bands may be accurately estimated. Predictions of the surface roughness contribution of an input, however, were completed in much less time as they could use the FRF model (see Chapter 2). The results of this model, when compared

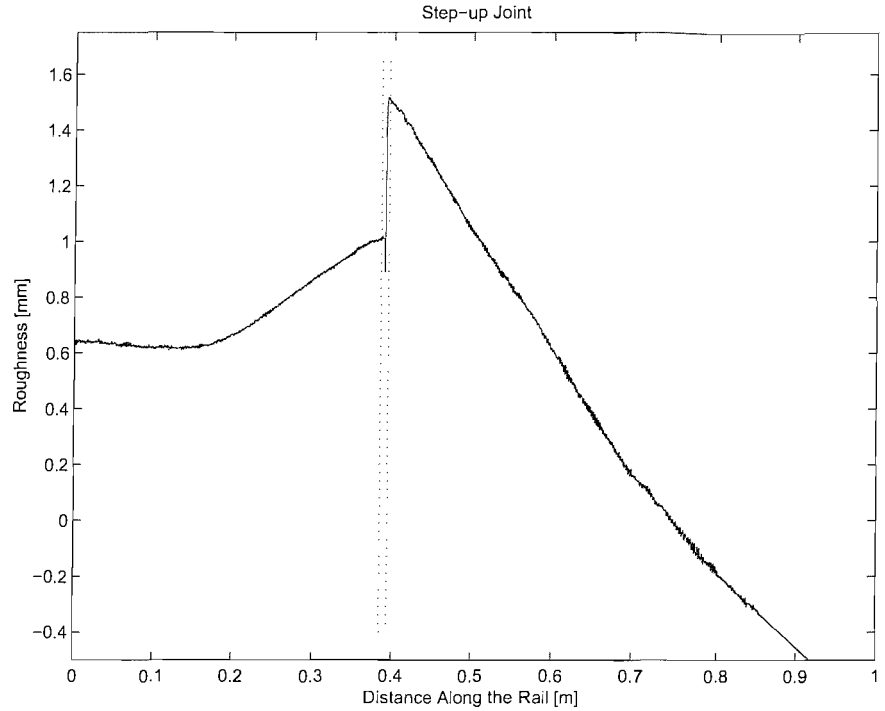

Figure 7–1 Example of the removal of a discontinuity from a surface profile measurement.

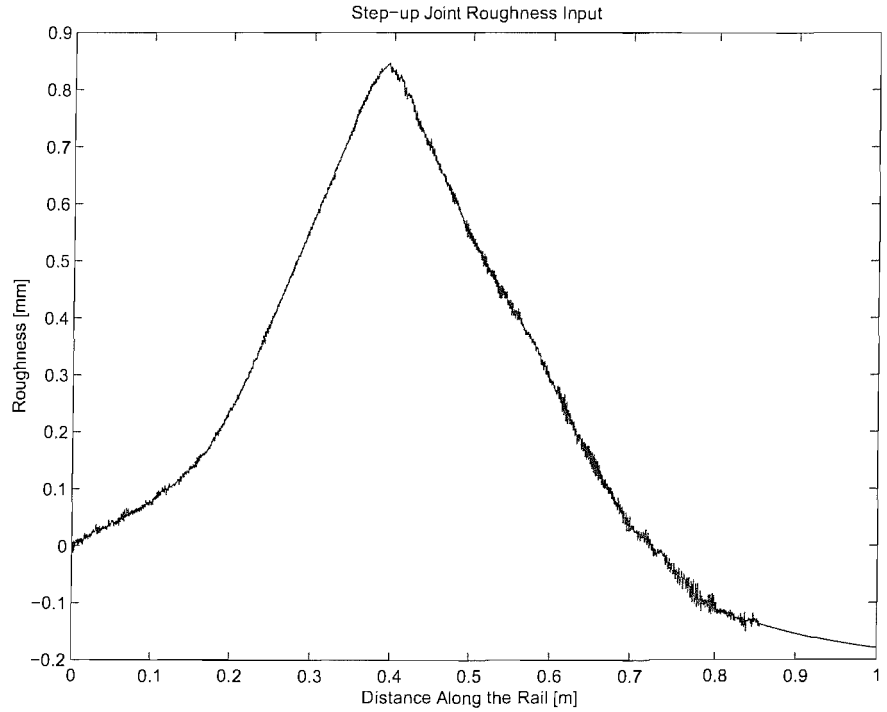

Figure 7–2 The formation of the surface roughness contribution after removal of the discontinuity from the surface profile measurement.

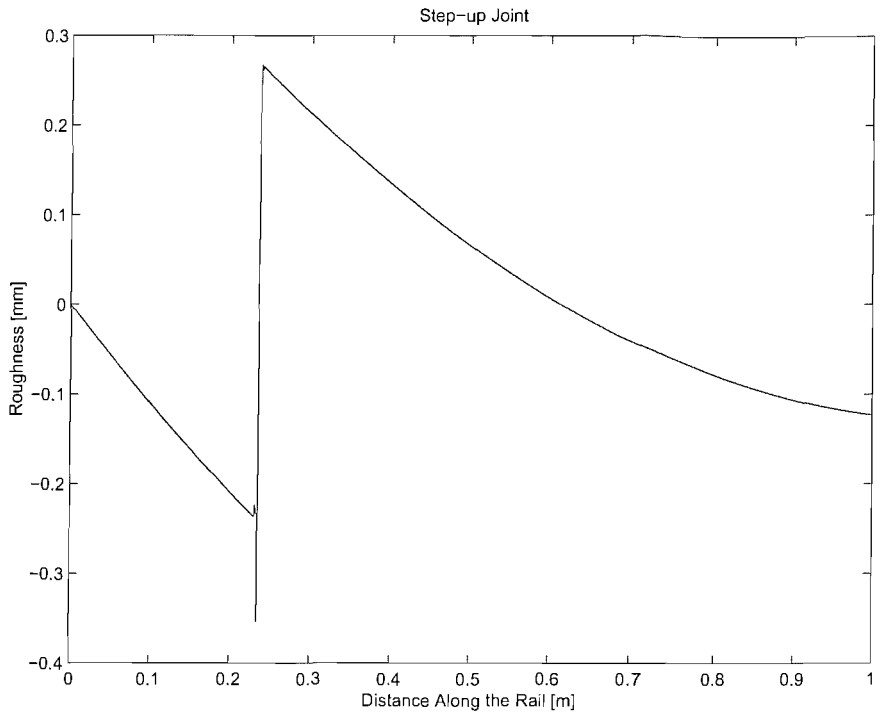

Figure 7–3 An example of a discontinuity input.

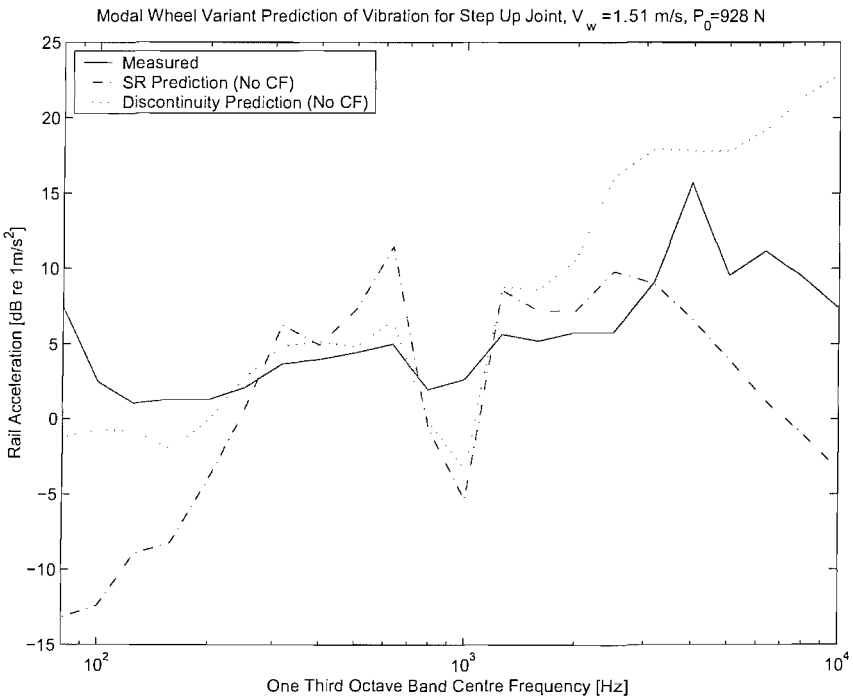

Figure 7–4 Prediction of rail acceleration due to a step-up joint without contact filter (CF) adjustments. Predictions from the surface roughness (SR) and discontinuity contributions are presented for a wheel speed of 1.5m/s and a 925N wheel pre-load along with the measured vibration.

with the non-linear time-stepping model in Chapter 6, had been found to be virtually identical. Thus this enabled a quicker solution for each of the many predictions.

Once the two predictions had been completed they were combined to form the overall prediction in the following way. The prediction due to the surface roughness contribution already exists as a function of frequency, as it had been formed by the FRF model. The prediction formed from the discontinuity part of the input using the non-linear model, however, is as a function of time. This result was therefore converted into the frequency domain and the two predictions were combined by a simple summation of powers, assuming the two inputs are incoherent.

By predicting the surface roughness contribution of an input separately from the discontinuity on the railhead, the adjustments in Chapter 5 (contact filter and track decay effects) can be safely applied to the part of the prediction that is formed from surface roughness contribution. As before (in Chapter 5) these adjustments may be applied either before or after the prediction. Unfortunately, the prediction formed from the discontinuity part of the input, that is made separately using the non-linear time-stepping model, strictly cannot have the corrections safely applied. Thus the problem still remains for this part of the prediction.

Initially, no corrections were applied to the discontinuity parts of the prediction, and the two outputs from the models were combined to form the overall prediction. Unfortunately, the results where large discontinuities were present in the railhead surface profile (for example the step joint and wheel flat profiles in Chapter 8 and Chapter 10) were not found to be in good agreement with the measurements of rail vibration.

Due to the nature of the step joints and the simulated wheel flat discontinuities, and the high decay of the track, it was found that the effects of the vibration due to the discontinuity were limited to an area close to the discontinuity. This effect is demonstrated in the subsequent chapters, Chapter 8 and Chapter 10. This indicated that the adjustment for the track decay rates would not be appropriate for these cases when the measurement point on the rail is close to the discontinuity. Therefore, provided that the vibration was measured close to the discontinuity, the effects of track decay were assumed to be insignificant, and thus they were omitted. Further analysis of the application of the track decay rate correction is presented in the following chapters for each of the discontinuities considered.

Ideally a contact filter model should be used in conjunction with the discontinuity part of the input during the prediction of wheel / rail vibration. Despite recent advances [Ford and Thompson, 2003] this was not yet possible here. Thus, splitting the input into two parts is a compromise. Nevertheless this method does demonstrate the influence of the contributions of the two distinct parts of the surface profile input. An example is shown in Figure 7–4. Predicted results of rail vibration at the step-up joint are shown with contact filter adjustments included. This discontinuity is described in detail in Chapter 8, but is used here to demonstrate that a prediction without any contact filter adjustment does not agree well with the measured result obtained on the rig. Inclusion of the approximate contact filter effects (in the form of a frequency domain weighting) are shown for the same prediction in Figure 7–5. This shows that the predicted and measured rail acceleration are in better agreement even though the contact filter adjustment that has been applied to the prediction is not expected to be a good representation of the contact effects for the discontinuity part.

In summary, the method presented above consists of the following steps:

- The surface roughness measurement is split into two parts; one that contains the discontinuity, and the other that contains the surface roughness contribution. Artificially smooth surfaces are introduced into these inputs as necessary.
- These inputs are prepared for use in the prediction models as before (see Chapter 4).
- Two predictions of wheel / rail vibration are made, using the models presented previously in Chapter 2. The non-linear time-stepping model is used for the discontinuity, and the linear FRF model is used for the roughness input. Both are expressed as one-third octave spectra.
- Contact filter adjustments are applied (as a frequency weighting) to the results of both of the predictions.
- Effects of the track decay (i.e. an adjustment that converts the prediction from a point that moves with the wheel / rail contact to the average at a fixed point on the rail) are only applied to the prediction formed from the surface roughness input.
- The spectra of the adjusted predictions are added together in the frequency domain. These are then compared with the measurements.

This method was used in the following chapters where vibration due to railheads with intended discontinuities are investigated. For the step joints and the simulated wheel flat

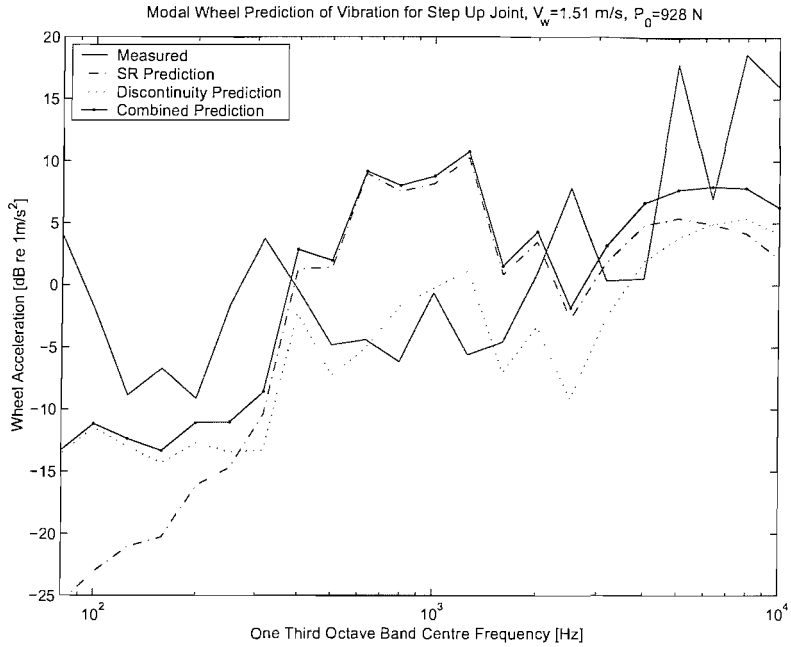

Figure 7–5 Prediction of rail acceleration due to a step-up joint with contact filter adjustments. Predictions from the surface roughness (SR) and discontinuity contributions are presented for a wheel speed of 1.5m/s and a 925N wheel pre-load along with the measured vibration.

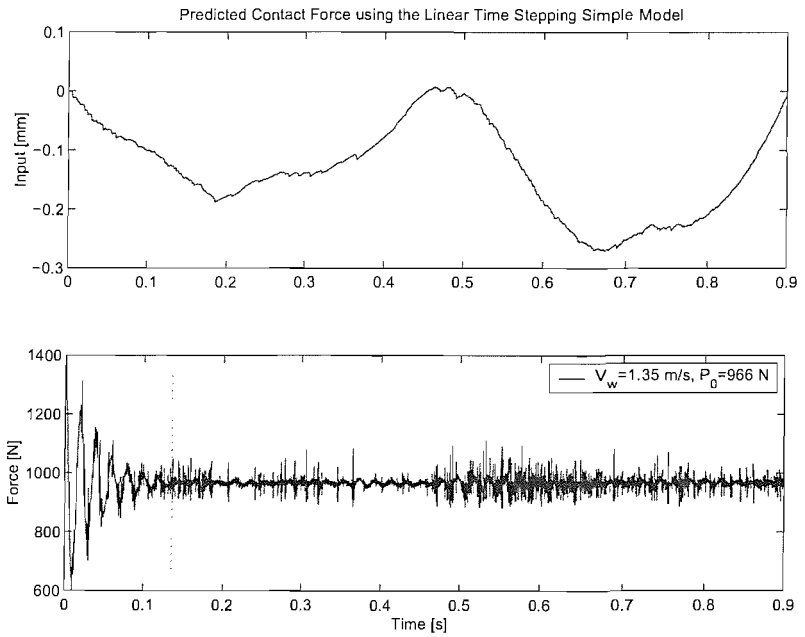

Figure 7–6 Example of the linear time-stepping model predicted contact force compared with the surface roughness input for a wheel speed of 1.4m/s at a wheel pre-load of 966N. This clearly shows the numerical routine starting transients at the beginning of the prediction.

the formation of the two parts of the inputs was exactly as has been described here. The inputs of the dip joints (see Chapter 9), however, were made using a slightly different method, described at the beginning of Chapter 9.

7.3 A method to estimate the degree of non-linear behaviour experienced by a wheel / rail prediction model

The comparisons made between the various linear and non-linear models detailed in Chapter 5 indicate that, for a surface roughness input, a linear model can be used to predict accurately wheel and rail vibration. It has been shown that, for the surface roughness input measured on the 1/5 scale rig, use of a non-linear model is not necessary. This indicates that the contact spring does not behave in a significantly non-linear manner. In this section, a method is developed that attempts to assess the degree of non-linear behaviour by comparing the predicted contact force from a non-linear time-stepping model with that from a linear time-stepping model.

For simplicity, the method is based on comparisons in the frequency domain. The comparisons are made between the predicted non-linear and linear contact force for a particular input, as shown below in equation (7-1).

$$F_c(f)_{Non-linear\ effect}[dB] = F_c(f)_{Non-linear}[dB] - F_c(f)_{Linear}[dB] \qquad (7\text{-}1)$$

where: F_c is the spectra of the contact force as a function of frequency (f)

The ratio of the non-linear and linear contact force predictions will be unity (0dB) when they are in agreement. Large positive values indicate that the non-linear levels are larger than the linear prediction levels (in a particular one-third octave band), and, large negative (dB) levels indicate that the linear predicted contact force is the largest. This simple method can be used to show trends in the frequency domain of the detected non-linear effects as the wheel speed and wheel pre-load of the predictions is altered.

Unfortunately this method was found to be strongly influenced by the starting transients of the linear time-stepping numerical routine. This is illustrated in Figure 7–6 where fluctuations in the predictions are seen at the beginning of the output. These fluctuations are not desirable as they effectively include an influence of an unintended discontinuity due to a poor choice of the initial conditions. The method of choosing the initial conditions for the time-stepping routines has been presented previously in Chapter 2.

Whilst good initial conditions were found for the non-linear time-stepping routine, the method failed to give good results for the linear time-stepping routine.

An example of a force PSD is shown in Figure 7–7, which shows that the output is dominated by the wheel on track resonance at 50Hz. This effect was removed by high pass filtering (with a cut on frequency of 80Hz) the outputs from each of the models before the frequency spectra of each output was estimated. Thus the outputs from the time-stepping models did not contain any unwanted effects due to the starting transients.

This method is considered below for the case of surface roughness presented in Chapter 5. As this was a situation where little difference between the non-linear and linear predictions of wheel /rail vibration were noted, the results shown below provide a benchmark with which the predictions due to other surface profiles (where greater non-linear behaviour is expected) may be compared.

Figure 7–8 shows results in terms of the non-linear contact force divided by the linear spectra. These are obtained using the simple model variant for surface roughness input. Wheel speeds range from 1m/s to 6m/s and four wheel pre-loads are considered. Differences in level between the two predictions of contact force in the frequency range 100Hz to 10kHz are very small.

The greatest differences in predicted contact force levels are evident at frequencies above 1kHz. Here the linear prediction levels are generally larger than the non-linear ones, giving negative differences. The largest differences are, however, still small and do not exceed 0.5dB. The differences reduce as the wheel pre-load is increased.

Figure 7–9 shows equivalent results for the modal wheel model. The largest differences between the non-linear and linear predictions of contact force are again seen to be above 1kHz. The differences between the non-linear and linear predictions are, however, seen to be slightly lower than those obtained for the simple model.

The results shown in Figure 7–8 and Figure 7–9, where an onset of non-linear behaviour begins with the highest frequency bands, agrees quite well with the findings of [Wu and Thompson, 2000(a)]. They, however, identified another region where non-linear behaviour was evident due to a simulated surface roughness input (the simulations were made for full-scale dimensions). The region where they found the greatest difference between the linear and non-linear predicted contact force was in the mid frequency range of consideration where the wheel and track receptances were of similar magnitude to that of the linearised contact stiffness receptance. The equivalent positions for the 1/5

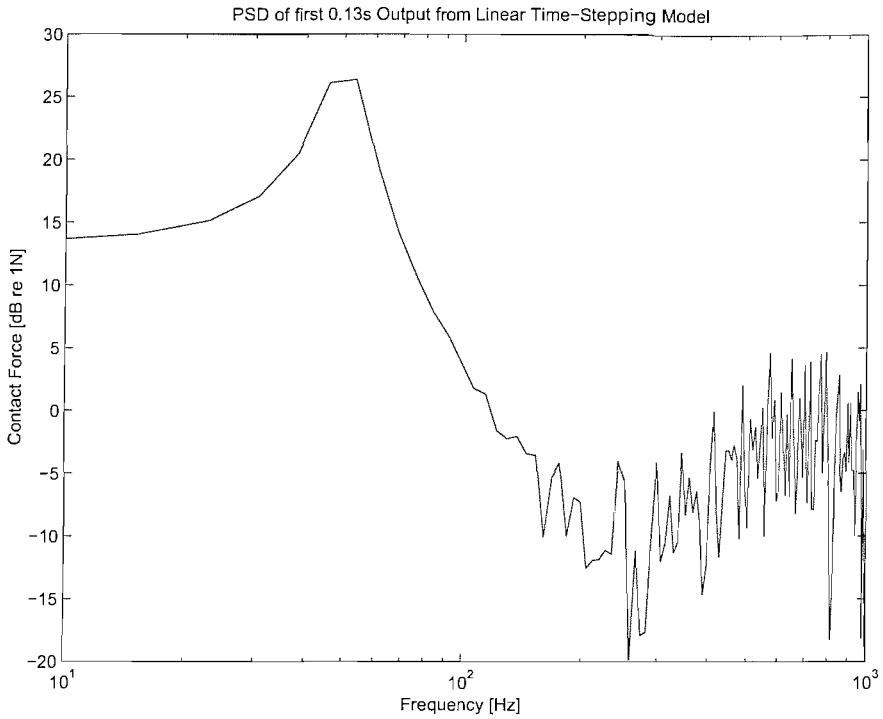

Figure 7–7 PSD of the first 0.1 seconds of the linear predicted contact force shown in Figure 7–6 above.

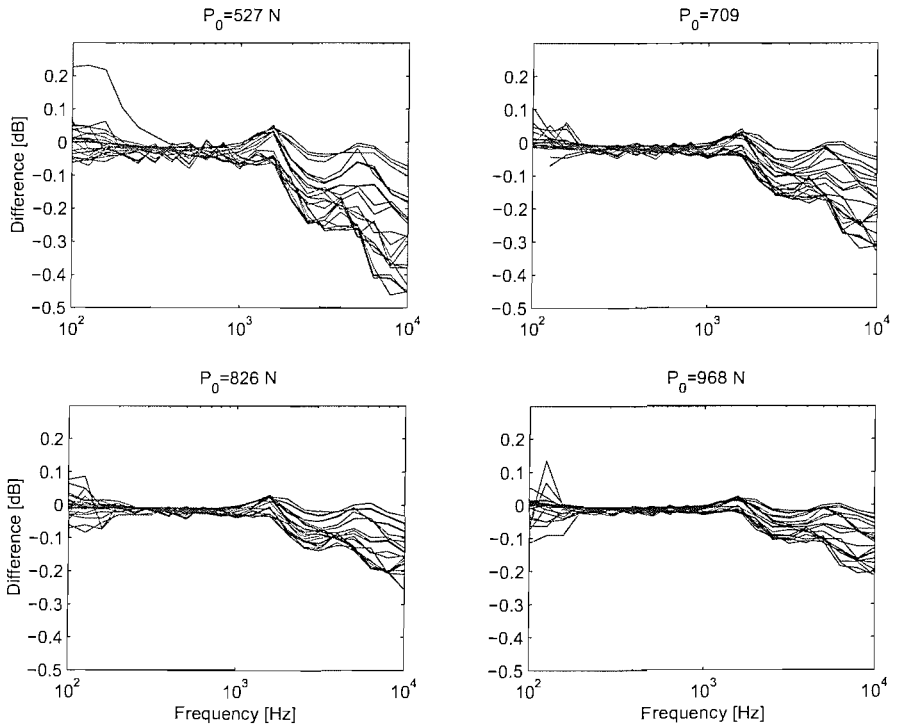

Figure 7–8 Predicted non-linear contact force level minus predicted linear contact force level for the simple model predictions due to a surface roughness input at wheel speeds ranging from 1m/s to 6m/s at four wheel pre-loads.

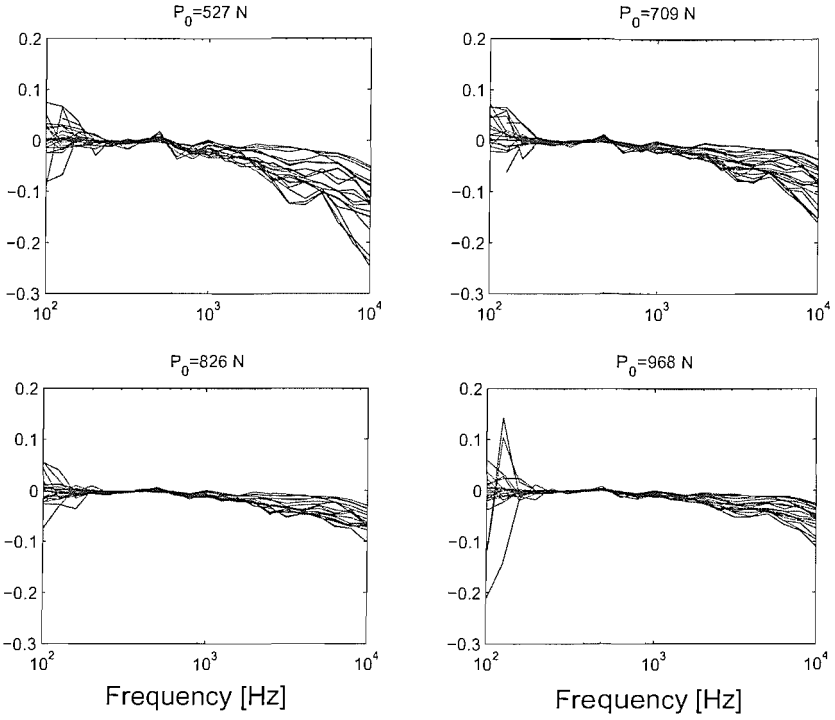

Figure 7–9 Predicted non-linear contact force level minus predicted linear contact force level for the modal wheel model predictions due to a surface roughness input at wheel speeds ranging from 1m/s to 6m/s at four wheel pre-loads.

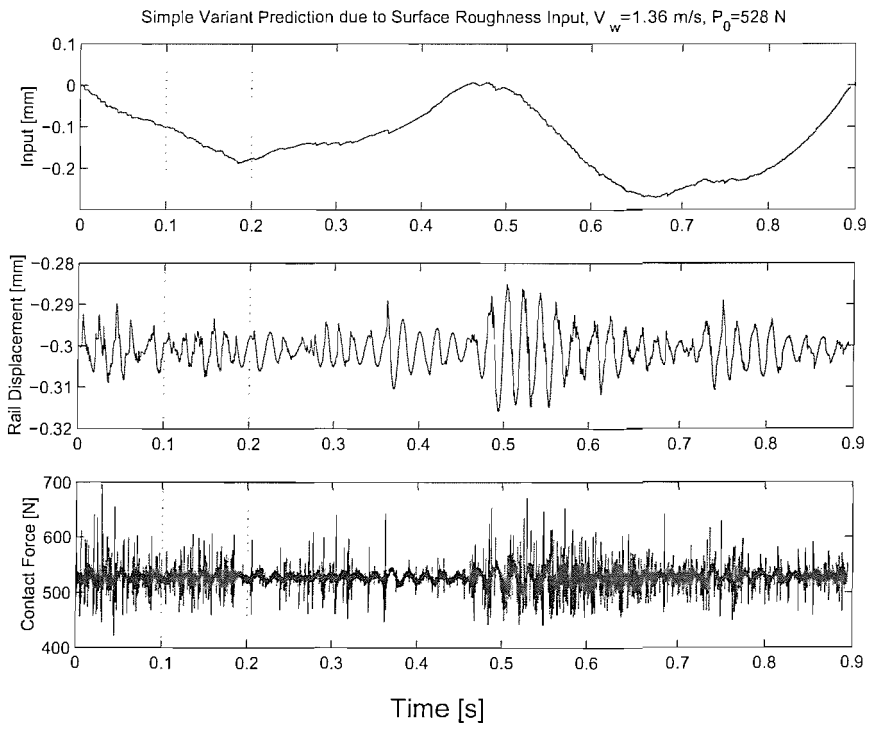

Figure 7–10 Simple model predicted rail displacement and contact force due to surface roughness (which is also shown) for a 1.4m/s wheel speed and a 527N wheel pre-load.

scale model occur at approximately 550Hz and 4.5kHz (see Chapter 5). Only one of these points is in the high frequency region where the greatest differences in Figure 7–8 and Figure 7–9 exist. The position where the track receptance and the contact stiffness receptance are of similar magnitude at 550Hz is shown to be within the low frequency region where the least non-linear behaviour has been observed. The results found in this chapter therefore do not completely agree with the full scale simulations made by [Wu and Thompson, 2000(a)].

[Wu and Thompson, 2000(a)] also identified a low frequency region (<100Hz at full scale) where they concluded that minimal non-linear effects existed as the wheel and track dynamic stiffnesses were much less than the dynamic stiffness of the contact spring, thus the contact between the two is effectively rigid. The region where this occurs for the 1/5 scale model is approximately at frequencies below 80Hz. This region, however, is not shown here due to the effects of the wheel on track resonance dominating the linear time-stepping model predictions. Further investigations at these low frequencies are therefore required.

7.4 Method of identifying transfer function properties from predicted outputs and measured inputs

This method was formulated to investigate how transfer functions behave for extreme contact force values by considering inputs and outputs of the transfer function U_r / R.

An example of this method is shown in conjunction with the input and the output of the non-linear time-stepping model, where the simple model transfer function U_r / R (that was used to make the prediction) can be verified by forming a spectral estimate of the predicted rail displacement (x_r) and dividing (or subtracting levels in dB) this by the spectral estimate of the input (r). The input (r) and output (x_r) of the transfer function are shown in Figure 7–10 for a wheel speed of 1.3m/s at a wheel pre-load of 966N.

Figure 7–10 shows a small section of time between 0.1s and 0.2s. The spectral estimate of this section along with the spectral estimate of the signal length from 0.1s to 0.9s (where the starting transients have been omitted by removal of the first 0.1seconds) is presented in Figure 7–11. This shows that the spectra of the surface roughness input and the predicted rail displacement are very similar for both the long section (0.1s to 0.9s) and the short section (0.1s to 0.2s). If the spectral levels (i.e. values in decibels) of the surface roughness (the input) are subtracted from the predicted rail displacement spectra

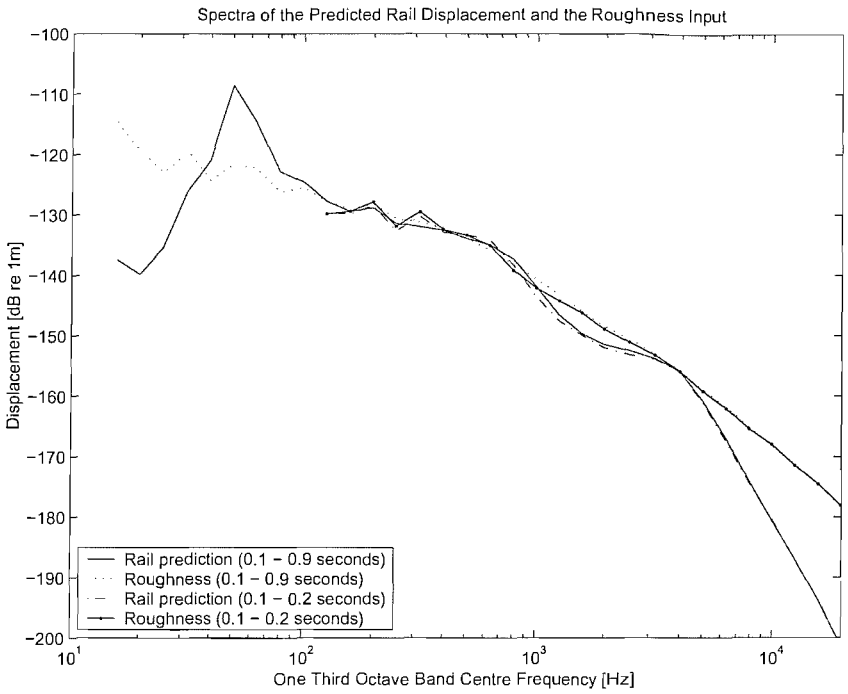

Figure 7–11 Spectra of the predicted rail displacement and roughness input made from time lengths between 0.1s to 0.9s and 0.1s to 0.2s for the results presented in Figure 7–10.

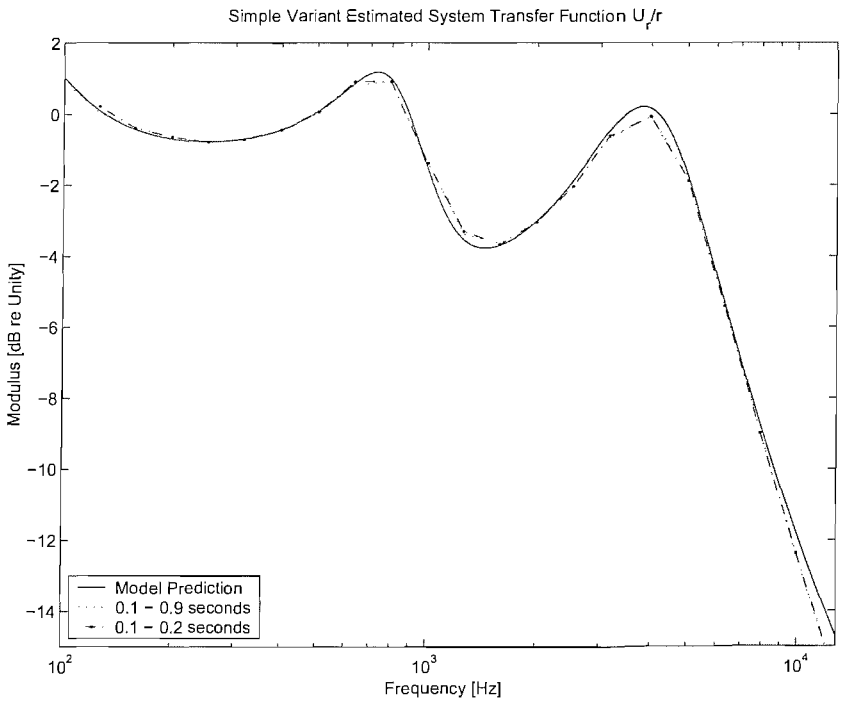

Figure 7–12 Estimates of the simple model system transfer function U_r / r formed from the spectral estimates of the non-linear model input and output shown for different lengths of time in Figure 7–11 above.

(the output) then an estimate of the transfer function is formed for each particular length of signal. This is shown in Figure 7–12, which demonstrates that the transfer function U_r / R, for a surface roughness input, remains constant for these two intervals. This is assumed to be because wheel unloading is not predicted by the simple model as the surface roughness input at a wheel speed of 1.3m/s is not sufficiently large enough to cause gross non-linear behaviour.

The above spectral estimates were obtained by removing any linear trend from both the input and output of the simple model before a PSD of each length of time-domain data was made. As in the rest of this thesis a rectangular window was applied.

Unfortunately this method of verifying the transfer function is not especially useful in practice, other than to ensure that prediction models are functioning correctly. It was found that the length of data that was required to obtain an adequate spectral resolution often resulted in a transfer function shape that was the average over a length of time. As the predicted contact force was generally seen to fluctuate near to the discontinuities (see Chapters 8, 9, and 10), over a relatively short length of time, the resulting shape of the transfer function would typically look very much like that formed using a contact spring receptance value based on the nominal wheel pre-load. This was only because the discontinuities that were considered for the work presented in this thesis were of comparatively short wavelengths. This might not be the case for an input such as rail corrugation. This method, however, demonstrates that the transfer functions are quite constant over relatively short data lengths.

7.5 Summary

This chapter has demonstrated a method to include contact patch filtering and the effect of rail decay rates in predictions of vibration where a discontinuity on the railhead is to be studied. This method allows the surface roughness contribution of an input to be considered separately from the discontinuity part of the input. The effect of adjustments such as the contact filter on each part of the prediction can therefore be assessed. Whilst a reliable representation of the contact filter effects, for wheel loads outside of the range 500N to 1kN, is not included in the predictions of this thesis, the method presented in section 7.2 does at least show how each part of a railhead surface profile is accounted for.

A method to identify the frequencies at which non-linear behaviour is apparent has also been presented This involves comparing the spectra of a non-linear prediction of contact

force with a linear prediction of contact force much like [Wu and Thompson 2000(a)]. This method shows that the non-linear effects are more prevalent in the one-third octave frequency bands above 1kHz.

Comparisons of the spectral content of the input and output to a prediction model have been used to verify the model transfer function. It was hoped that this method would show changes in model transfer functions when discontinuities in the input were considered. Unfortunately it was found that the model transfer functions did not vary during the time intervals considered. Therefore this method is not considered in the following chapters.

The two remaining methods developed within this chapter (section 7.2 and 7.3) are now applied to three different types of railhead discontinuity. Step joints are considered first.

8 Wheel / rail vibration due to stepped joints

8.1 Introduction

Lengths of rail are typically joined together in two ways. One method is to weld the lengths together and then grind the joint to provide a transition from one rail to the next so that is as smooth as possible [Esveld, 1989]. Rails are often welded into long lengths off site and these are joined on site into 'continuously welded' rail. This is extensively used on high speed (mainline) track. The second, more traditional way of joining rails together, is to use two metal plates (called fishplates) positioned on either side of the rail where the ends meet. The fishplates are designed to form a geometrical lock when fitted to the sides or webs of the rail sections between the rail head and the rail foot. This is shown in Figure 8–1. The fishplates are held in position with bolts. This may result in a small step or discontinuity in the railhead surface due to the difficulty of aligning the two adjoining rails. Additionally after installation, a step might evolve due to wear or slack in the fish plate joint. The wheel / rail interaction behaviour when passing over such step joints is the subject of this chapter. The behaviour of the continuously welded rail joint is considered in Chapter 9.

Steps on the railhead surface at the joints between two rail sections may be classified into three categories:

- Step-up joint,
- Step-down joint,
- Level joint.

The use of these three categories, however, can be misleading, so it is worth considering what this terminology means.

Firstly, it is important to note that the last category (the level joint) is an idealised situation, as in practice, there is bound to be some difference in height, however small, between one rail and the other. After use, and under load, a railway track is likely to settle into different positions forming more noticeable steps at the joints.

Secondly, the first two categories (step-up and step-down joints) are really the same from a geometrical point of view, apart from the direction of travel of the wheel (or train). Therefore the terms step-up or step-down relate to the direction of the train and not specifically to the joint itself. However, the influence of load is such that it tends to

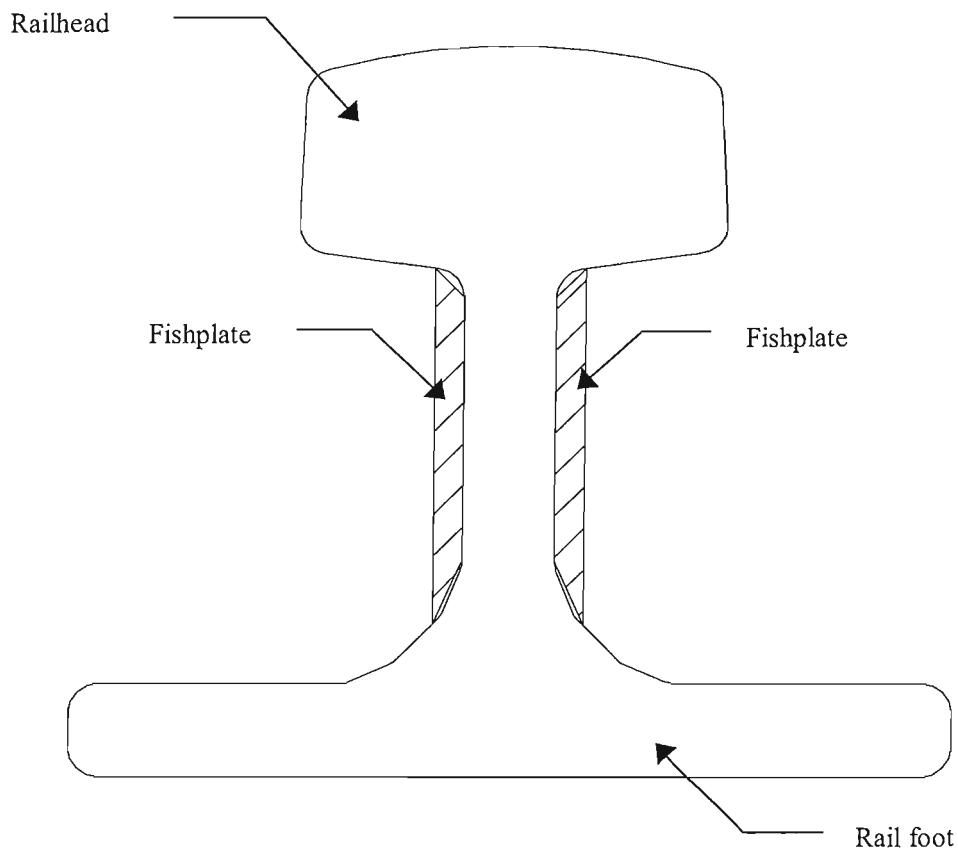

Figure 8–1 Schematic diagram of a full size rail and fishplate joint.

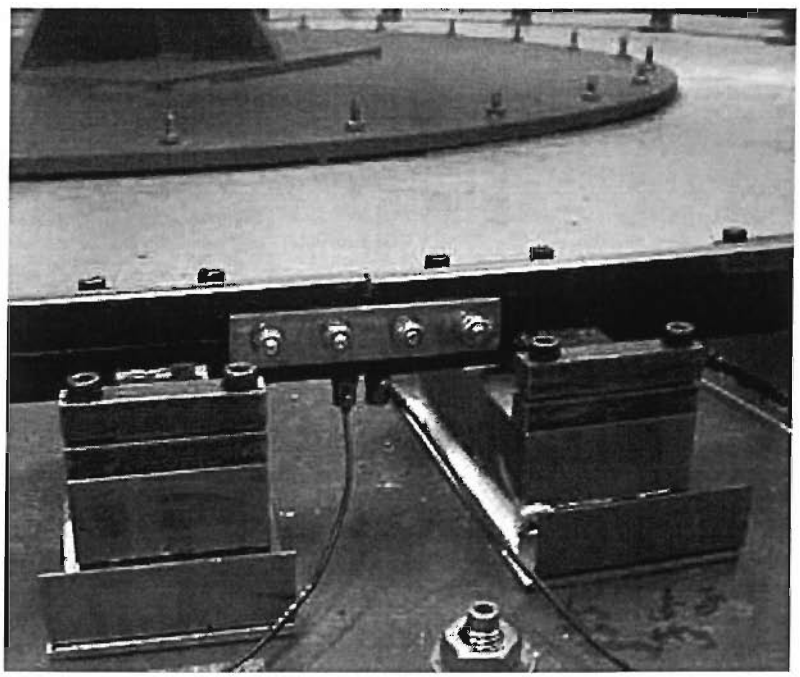

Figure 8–2 Photograph of the fishplates and a step joint (step-down joint) used on the 1/5 scale wheel / rail rig.

push down the rail before the joint so that an otherwise level joint appears as a step-up joint under load.

The rolling direction over a step joint does matter. More noise is produced by a wheel rolling over a step-up joint than over a step-down joint (see for example, [Ver et al, 1976, and Wu and Thompson, 2002]).

8.2 Manufacture of a rail with a fishplate joint

Step joints for the 1/5 scale rig were produced by taking a rail that had been manufactured to include a 40mm radius of curvature on the railhead, curved to the radius of the track (see Chapter 3), and cutting it in half. This was done at a position such that the joint would be in the middle of the measurement rail at the mid-span position MRS8 (see Figure 3-14). To join the rail lengths, fishplates (80mm long and 10mm high) were cut from 1mm thick aluminium sheet and bent to fit the 1.5m curvature of the measuring rail section. Clearance holes were then drilled into the fish plates and the rail ends, and four M6 bolts, washers, and nuts were used to clamp the fishplates and the rails together. This is shown in Figure 8–2. The total weight of the fishplates and connecting hardware that was added to the rail was 90g. This weight is 32% of a 120mm rail section (282.6g) between two discrete supports of the rig, and is therefore a considerable addition to the rail. The fishplates used for the step joint discontinuity at MRS8 were much lighter than the fishplates used to connect the measurement rails to the extension rails at LHS1 and RHS1 (see Figure 3-14). It was hoped that the step joint fishplates would have a minimal effect on the track frequency response. Measurements of the track FRF are presented in section 8.3.

The fishplates were not scaled replicas of the full scale case. In fact the 1/5 scale rail did not have the same cross-section as a full size rail (see Figure 3-7 and Figure 8–1) so the fishplates could not form a geometrical lock between the railhead and the rail foot. This meant that the 1/5 scale step joints with fishplates relied upon the grip of the connecting bolts to maintain the step geometry. At the values of the wheel pre-load used during the experiments (500N to 1kN) the loads applied to the fishplate joint were unlikely to lead to relative motion in the joint. However, prior to the experiments (and the subsequent predictions of vibration) the loads applied to the rail due to the dynamic behaviour of wheel / rail interaction were unknown. Therefore surface profile measurements of the joints were made before and after the rolling wheel measurements to confirm that the

geometry of the joints had not changed during the experiments. No evidence was found that indicated that any slippage of the joint had occurred during the measurements.

The height of each step joint was determined by adjusting the height of the discrete track supports on either side of the discontinuity. This was done by carefully adding shims under each support, beneath the plate under the 'ballast' layer, until the desired joint profile was obtained. This process was awkward and time-consuming, but, was the best method available to ensure that the rail was held evenly by each of the discrete track supports. This was not a particularly versatile method of obtaining specific step joint heights. It was found that the resulting step height, after shimming, would depend not only on the height of the shims at either side of the joint, but also on the height of the adjacent supports due to the rail bending stiffness.

Each of the three types of step joint have been considered in the investigations below. First, however, results of the static measurements are presented.

8.3 Static measurements of the fishplate joint track

The presence of a joint can be expected to modify the dynamic behaviour of the track. This is demonstrated by the measurement result shown in Figure 8–3. An accelerometer was fixed close to the joint (on the underside of the rail) and the top of the rail was excited with an instrumented hammer. An average of twenty 'taps' was taken to form the FRF shown in Figure 8–3. The frequency response measurement of the track with a joint (at MRS8) is shown with the measurement of the track without a joint (i.e. a measurement of the whole rail made at MRS8). The frequency response of the whole rail fitted to the track support structure has been presented previously in Chapter 3 and Chapter 5. Figure 8–3 shows that the frequency response of the track close to the joint has a much larger amplitude than the frequency response without a joint (approximately a factor of 4 between 200Hz and 2kHz). This measurement, however, is of the step joint without the fishplates fitted; measurements with the fishplates fitted do not demonstrate such large amplitudes (see Figure 8–4).

Chapter 3 presented a method that used frequency response measurements close to the ends of a rail (such as that shown in Figure 8–3) to formulate a method of associating fluctuations in the measured modulus and phase with predictions of the track behaviour, and the assumed behaviour of a clamped-clamped beam. Fluctuations in the measured modulus and phase between 100Hz and 1kHz were found to be due to reflections. Such

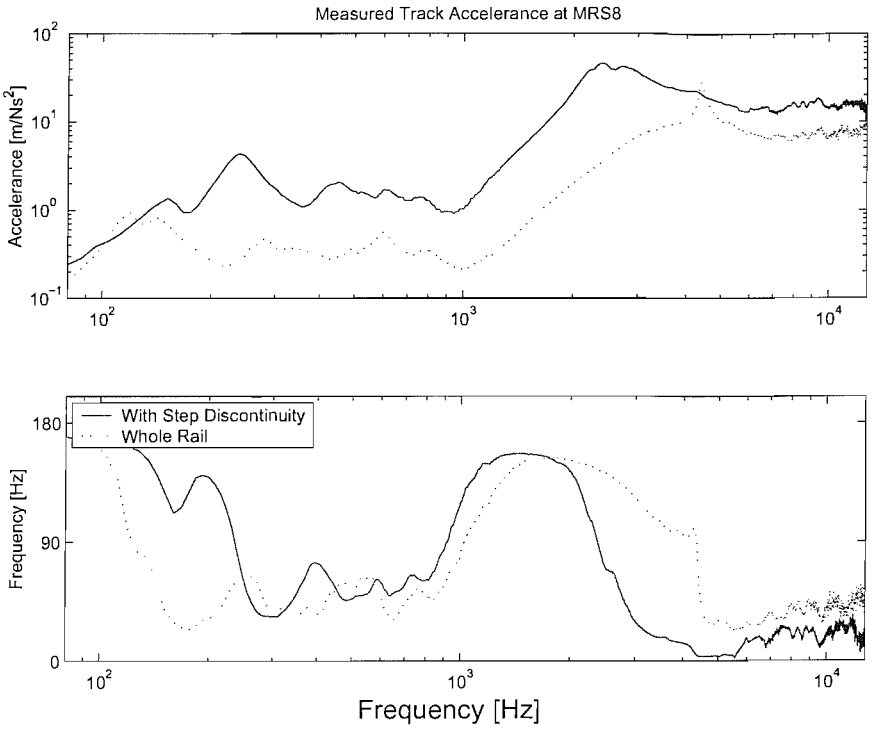

Figure 8–3 Comparison of the measured point accelerance at MRS8 of the whole rail (used in Chapter 5) and the measured point accelerance at MRS8 of the step joint, close to the discontinuity without the step joint fishplates fitted.

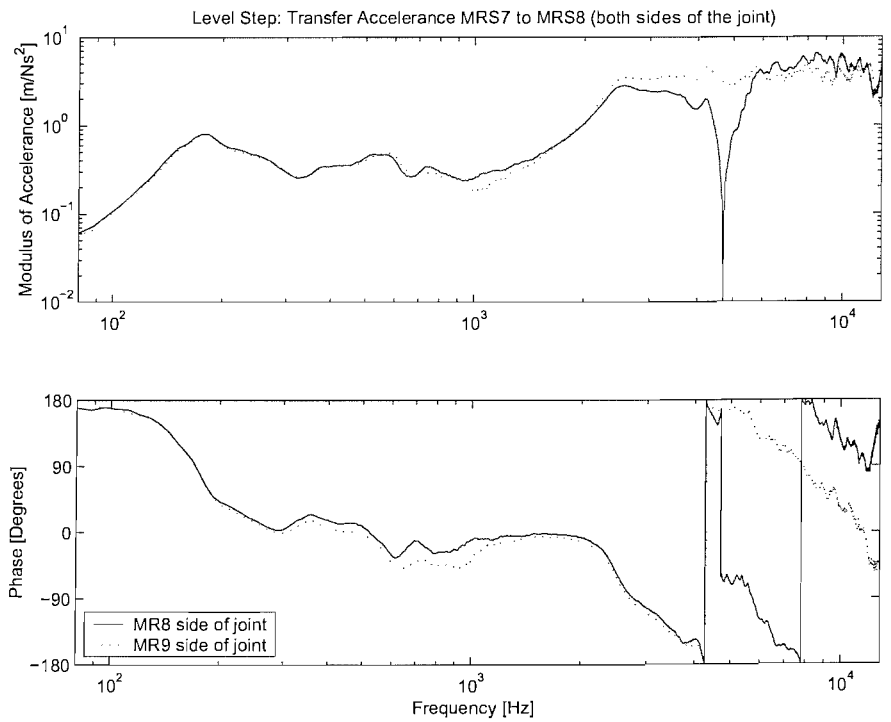

Figure 8–4 Transfer accelerance excited from each side of the joint (MRS8) to MRS7.

evidence of reflections is also seen in Figure 8–3 in the same frequency range between 100Hz and 1kHz of this point accelerance measurement.

The presence of the joint is also seen in the transfer accelerance measurements shown in Figure 8–4 and Figure 8–5. Here the measurements were made with accelerometers fixed at MRS7 and MRS9, and then an instrumented hammer was used to excite the track at MRS8 on either side of the joint. Measurements made where the rail is excited on the same side of the joint as the accelerometer are seen to contain a drop in the modulus at approximately 5kHz whereas the measurements excited on the other side of the joint do not. This result, however, is seen to be the only noticeable difference between the four transfer accelerance measurements made across the step joint.

Although the results in Figure 8–3, Figure 8–4, and Figure 8–5 show that the track close to the step joint discontinuity is influenced by reflections, it was found that this behaviour was localised at the discontinuity. This was shown by additional measurements of the track frequency response at positions away from the step joint that are considered next.

To find the average frequency response of the track, a series of point and transfer accelerances were measured with an accelerometer fixed on either side of the step joint discontinuity. As the step joint discontinuity was positioned at MRS8, the accelerometers were placed between the supports of the track in the sleeper bays at MRS7 and MRS9. The accelerometers were therefore placed a distance of 120mm along the track on either side of the step joint discontinuity. Two sets of transfer accelerances were made for each of the fixed points (MRS7 and MRS9), where the track was excited at the mid-span positions from MRS1 to MRS15. Sample results displaying the modulus of these transfer accelerances along the length of the track are shown in Figure 8–6 where the accelerometer was positioned at MRS7 and the track was excited from positions MRS1 through to MRS15. This demonstrates that the measured accelerance varies greatly between 1×10^{-4} m/Ns^2 and 10m/Ns^2. However, these variations appear to be similar to those found for the whole rail presented in Chapter 5.

To verify this observation the following comparisons were made. Each of the two sets of the transfer accelerances made along the length of the track containing the step joint rail and one set of the measurements of the transfer accelerances made for the whole rail (previously presented in Chapter 5) were averaged in the frequency-domain. The results are shown in Figure 8–7 in the form of the average of the modulus of accelerances in

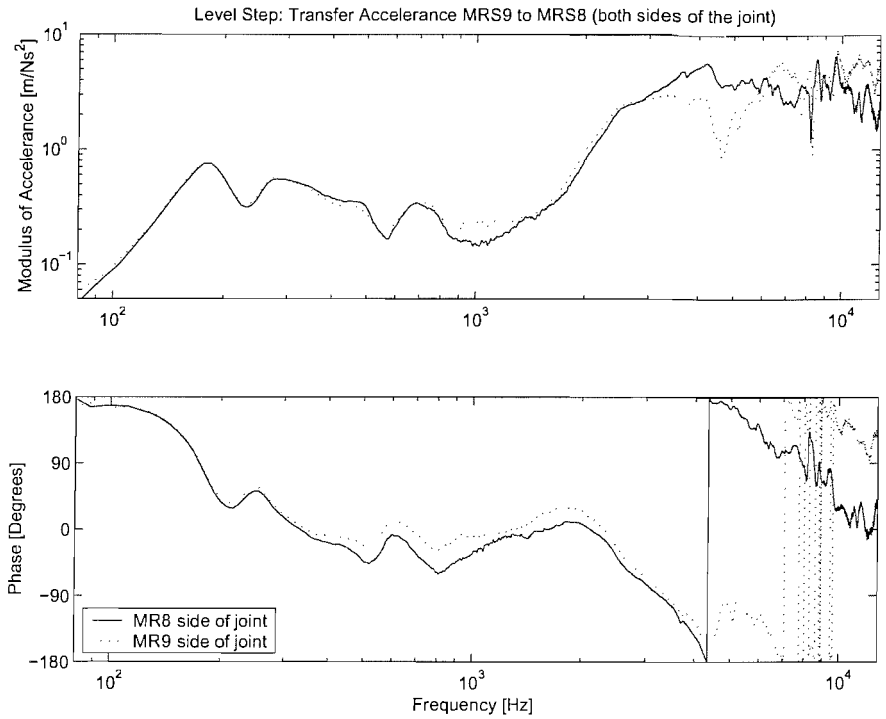

Figure 8–5 Transfer accelerance excited from each side of the step joint (MRS8) to MRS9.

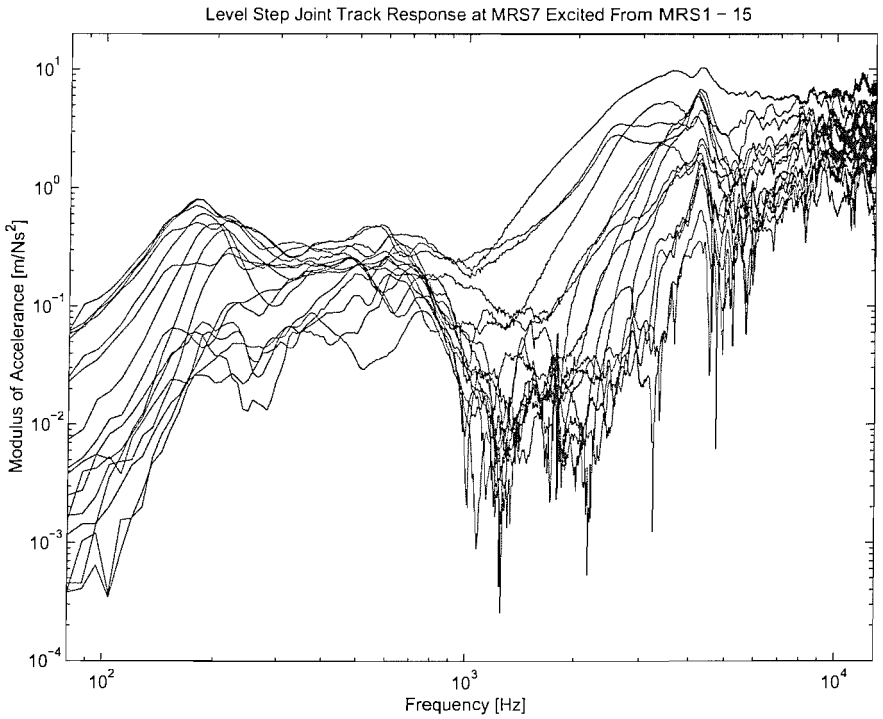

Figure 8–6 Transfer accelerance measurements along the length of the level joint rail measured from an accelerometer at MRS7 and excited with an instrumented hammer from positions MRS1 to MRS15.

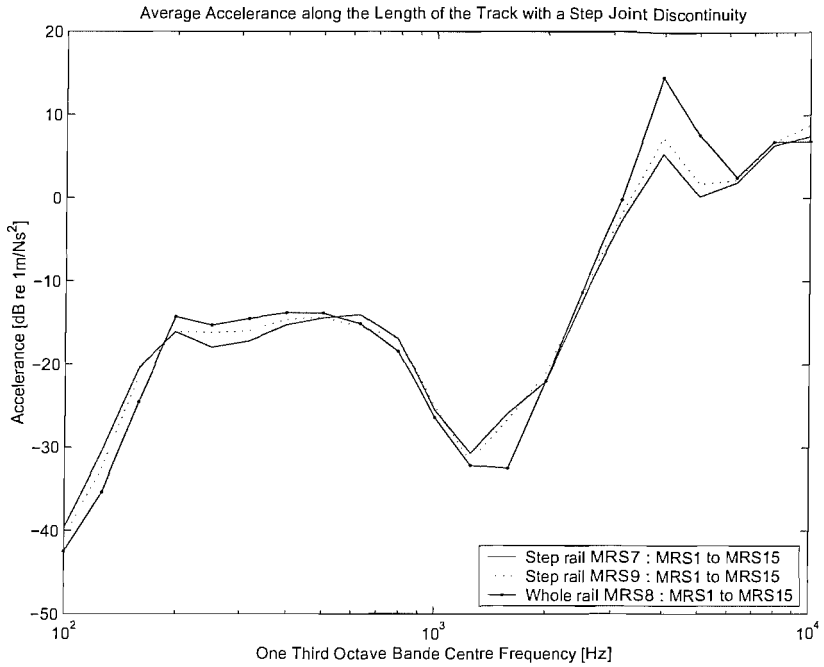

Figure 8–7 Comparison between the average transfer accelerance of the control rail and average transfer accelerance of the level step joint rail measured from two points on the track.

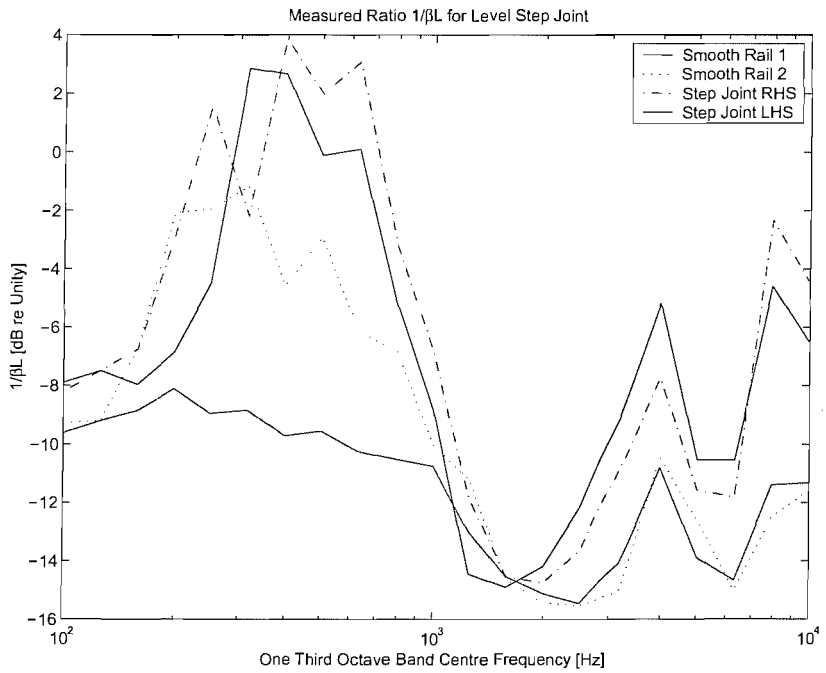

Figure 8–8 The measured ratio $1/\beta L$ for two types of rail. Smooth rail 1 shows the results made using 'operational' measurements on a rail with an 'as smooth as possible' surface. Smooth rail 2 shows instrumented hammer test results for the same rail. The last two lines show results of instrumented hammer tests for each side of the level step joint.

each one-third octave band. This shows that they do not vary by much more than 3dB in the majority of the one-third octave bands. Larger variations are seen, however, in the 1.6kHz and 4kHz bands. Even so, the results in Figure 8–7 indicate that the average frequency response of the track containing the joint is approximately the same as a track without the joint.

Whilst the results in Figure 8–7 indicate that the presence of the joint at MRS8 appears to have little effect upon the average transfer accelerance along the complete length of the measurement rail, an interesting difference between the track with and without a joint is seen in the 4kHz frequency band. This difference is explained more clearly by consideration of Figure 8–3 where it can be seen that the point accelerance measurement of the whole track (i.e. without a joint discontinuity) contains a pinned-pinned resonance at 4.2kHz. This is not so clearly the case for the point accelerance measurement of the track that contains the joint.

Further comparisons of the track behaviour with and without the joint were made by studying the decay of vibration along the length of the track. The decay rates of the track with the joint were calculated from instrumented hammer measurements that included one point accelerance measurement and several transfer accelerance measurements made at positions between the discrete track supports. These measurements were used to calculate the decay along the length of the track for each one-third octave band ranging from 100Hz to 10kHz, by using equation (3-3). The results of this process are presented in terms of the ratio $1/\beta L$ in Figure 8–8, along with the results for the track without a joint from Chapter 5.

The results in Figure 8–8 for the track with the joint are shown for the left hand side of the joint (with the accelerometer fixed at MRS7 and the track excited from MRS1 to MRS15) and for the right hand side of the joint (with the accelerometer fixed at MRS9 and the track excited from MRS1 to MRS15). The track decay for each side of the discontinuity is compared along the whole length of the track, even though the rail is split into two parts (connected by the fishplates). Measurements at MRS8, the position of the joint, were included in this calculation. The measurements at this point included the position at which the instrumented hammer excited the end of the rail just before the joint on the same section of the rail as the accelerometer. So the results in Figure 8–4 and Figure 8–5 with the large dips in the modulus in the 5kHz one-third octave frequency band were used, but not the transfer accelerance measurements made by exciting the rail just past the joint.

From the results in Figure 8–8, it is clear that the static measurements of the jointed track are in good agreement with each other. The properties of the track decay have been found to be approximately the same no matter which side of the joint the accelerometer is fixed. The results of the track decay measured on the track containing the joint agree quite well with the static tests made on the whole rail presented previously in Chapter 3. There are, however, differences between the whole rail and the jointed rail at frequencies between 200Hz and 800Hz and between 2kHz and 10kHz. Even greater differences occur between the decay rates calculated from the operational 'rolling wheel' measurement method and the static measurement method. This discrepancy was considered in Chapter 5 and was found to be because of the effect of the track supports being compressed by the wheel pre-load.

The average accelerance along the length of the track in Figure 8–7, and the decay along the length of the track in Figure 8–8, demonstrate that the behaviour of the track containing a joint is similar to that of the track without the joint when the whole measurement rail is taken into consideration. This indicates that the effects of the joint are limited to an area close to the discontinuity. Further evidence is shown in Figure 8–9 and Figure 8–10 where point accelerance measurements at MRS7 and MRS9 are shown. These measurements look very similar to the measurements made at MRS8 on the whole rail presented previously in Chapter 3.

The point accelerance measurements at MRS7 and MRS9 presented in Figure 8–9 and Figure 8–10 are also seen to be well approximated by the 4^{th} order polynomial curve used in the prediction models in Chapter 5. The results in Figure 8–9 and Figure 8–10, when compared with the transfer accelerance measurements shown in Figure 8–4 and Figure 8–5, demonstrate that only if a point is either measured or excited at the discontinuity, does the joint have any great influence the frequency response of the track.

[Wu and Thompson, 2001(b)] presented a continuously supported track model in which a fishplate joint was modelled as a pinned joint. This method of modelling the step joint could have been incorporated into the prediction models so that a frequency response similar to the measured accelerance in Figure 8–3 could have been made. However, as the measurements of the track frequency response indicate that the presence of the step joint affects only a small section of the track within the sleeper bay MRS8 it was felt that this alteration might not be an appropriate alteration for the predictions. The track accelerance shown in Figure 8–3 is only applicable for a relatively short distance along

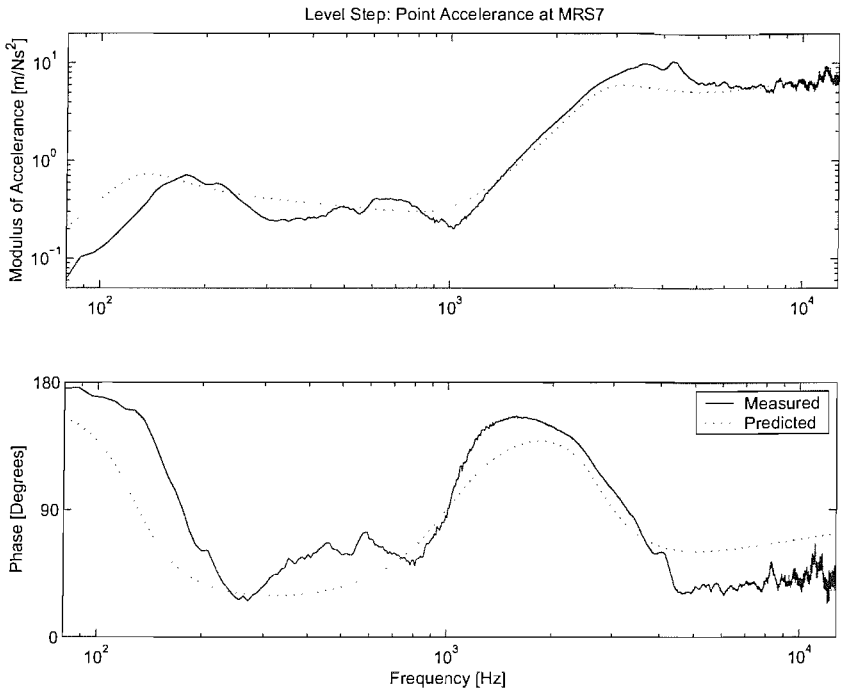

Figure 8–9 Point accelerance of the level step rail at MRS7 compared with the polynomial track model used in the simple variant and the modal wheel variant.

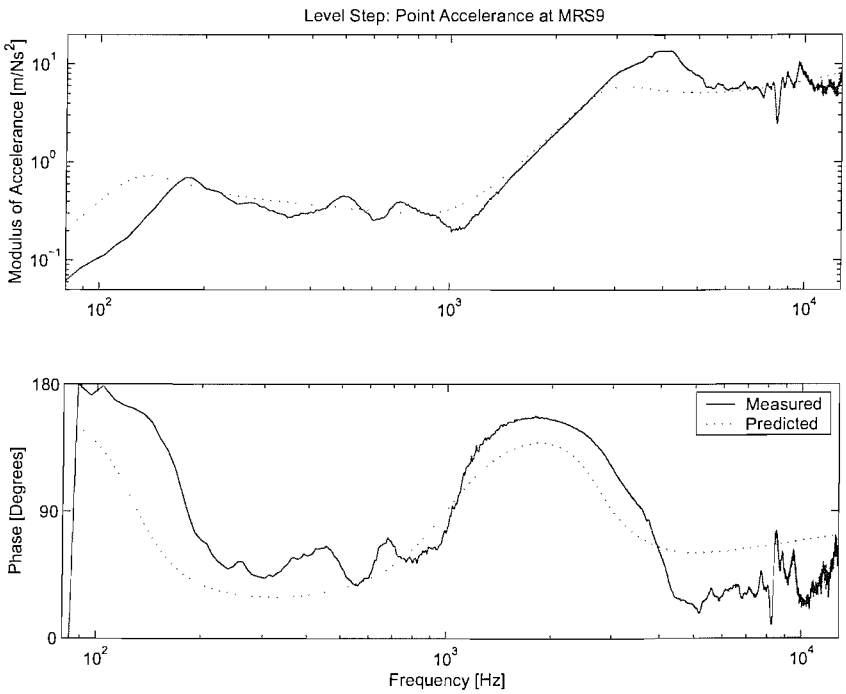

Figure 8–10 Point accelerance of the level step rail at MRS9 compared with the polynomial track model used in the simple variant and the modal wheel variant.

the track, whereas point accelerance measurements made at MRS7 and MRS9 are more representative of the majority of the track behaviour. The effects of the joint were therefore not included in the track model part of the prediction.

The low frequency response of the measurements in Figure 8–9 and Figure 8–10 close to the track on-ballast resonance shows a slight discrepancy with the 4^{th} order polynomial model. It is apparent that the ballast stiffness is slightly higher in the present tests than the value found from the measurements in Chapter 5. This could have been for the following reasons:

- Temperature changes resulting in a different stiffness of the resilient track supports
- Re-positioning of the track when two half length rails were used.

Most of the tests were made with an ambient air temperature close to 20°C. Fluctuations of a few degrees may have occurred, but, it is not likely that this would have caused such large discrepancies between the measurements and the track model shown in Figure 8–9 and Figure 8–10.

It appears more likely that the discrepancies were related to the position of the rail on the discrete supports. Prior to fitting the jointed rail to the rig track bed, the supports were positioned at heights for the whole rail length as they had just been used for the measurements presented in Chapter 5. When the two half rail lengths of the jointed rail were first positioned onto the track supports (with the fishplates not tightened) the heights of the top of the rails were found to be at slightly different levels at the joint. This difference in height formed the geometry of the first step joint that is considered in this chapter. This is the (almost) level step joint. It is assumed that as the support heights produced a small step joint (the 'level' step joint) when two half rails were fitted to the track bed, the smaller sections of rail were in better contact with the discrete supports. It is also assumed that as the half rails appeared to be supported better by the discrete supports, the track supports were likely to have been in both tension and compression when the whole rail was fitted.

If the discrete supports had been in both tension and compression along the track length with the whole rail fitted, then this might have led to a slightly softer average support structure when measured using the instrumented hammer tests. This assumption agrees with the measurements of the deflections of the track due to a wheel pre-load that were presented in Chapter 3, along with the measurements of the track properties when the track was compressed by the wheel pre-load (see Chapter 5). If in addition to being

poorly manufactured, the supports were not positioned correctly, so that the rail was supported to differing degrees at each of the 15 positions along the measurement rail length, then the glue used between the 'ballast' layer and the sleeper of the discrete support would have been more likely to fail. This offers an explanation for why the 1/5 scale track supports with the whole rail length behaved differently when they were under load.

8.3.1 Summary

The investigations described in this section have shown that the rail joint influences the behaviour of the track slightly. Some of the reasons for this behaviour have been considered, but, an in-depth investigation has not been made. This is because for a first approximation, it has been shown that the existing approximation of the track bed behaviour is similar to the measurements. Further adaptations of the approximate track bed behaviour that was used within the prediction models have therefore not been made.

No new corrections for the effect of track decay have been introduced, even though the measurements show a marked difference between the step joint track and the whole rail case. This is because the method used to obtain a true correction for track decay (see Chapter 5) cannot be used with a discontinuity on the railhead. Use of the statically measured decay rates shown in Figure 8–8 would not include a realistic adjustment as the (poorly constructed) track bed was not suitably compressed during these measurements (see discussion in Chapter 5).

The next three sections are concerned with each of the step joint profiles considered. In each case these sections include sample measurements, the inputs used for the predictions, comparisons between the measurements and the predictions. Analysis of the predicted contact force is presented for all three step joints in section 8.7.

8.4 Measurements and predictions of wheel and rail vibration due to a level joint

8.4.1 Examples of the measurements made on the rig

Similarly to the measurements presented in Chapter 6, measurements were made of the rail, wheel, and axle acceleration. Measurements were also made of the rig wheel speed, and rig wheel pre-load were made with a tachometer and a force gauge respectively. The positions of the wheel and axle accelerometers remained the same as described in Chapter 6. Accelerometers were positioned at three points on the test rail. Two

accelerometers were positioned in the sleeper mid-span position MRS8 (see Figure 3-14); one just before the joint, and the other just after the joint. The third accelerometer was placed in the sleeper mid-span position MRS10. The accelerometers close to the joint can be seen in Figure 8–2. Although the rail vibration was measured at three points, comparisons between the measurements and the predictions were made only using the output of the accelerometer just after the joint at MRS8. This position was chosen because it was close to the discontinuity, so the peak values of the rail vibration should give closet agreement with the predictions.

As for the case of a surface roughness input, presented in Chapter 6, measurements of wheel and rail vibration were made at four wheel pre-loads, at wheel speeds ranging from 1m/s to 5m/s. Generally speaking, wheel speeds faster than 5m/s were not used as problems were experienced with the rig drive belt system which tend to slip at faster speeds. Predictions were made for each set of the measured wheel speeds for a particular wheel pre-load so that direct comparisons between a measurement and a prediction could be made. These comparisons have been made in both the time domain and the frequency domain.

Examples of the rail vibration measured at the three positions described above are shown in Figure 8–11 for a wheel speed of 1.3m/s with a wheel pre-load of 976N due to the step joint. This shows that the peak acceleration occurs at the same time for the accelerometers positioned at MRS8 at 0.6 seconds. The peak acceleration at the measurement position MRS10 was also found to occur at 0.6 seconds. This shows that the effect of the discontinuity dominates the rail vibration both close to the discontinuity and at a position 240mm away, the wave speed in the rail being very high. Vibration due to surface roughness is seen at MRS10 to reach a maximum close to 0.8 seconds where the wheel is directly above the rail measurement position, but this is a smaller effect compared with the impulse due to the discontinuity.

The measured axle and wheel acceleration is shown in Figure 8–12 for the same wheel speed and wheel pre-load as that of Figure 8–11. This shows that the peak measured acceleration occurs at the same time (0.6 seconds) as that found for the rail at the point of the discontinuity. After the peak acceleration, outputs in Figure 8–11 and Figure 8–12 are dominated by a 80Hz fluctuation for about 0.06 seconds. It is reasonable to assume that this is the wheel on track resonance, although this was not confirmed due to the time restrictions of the project.

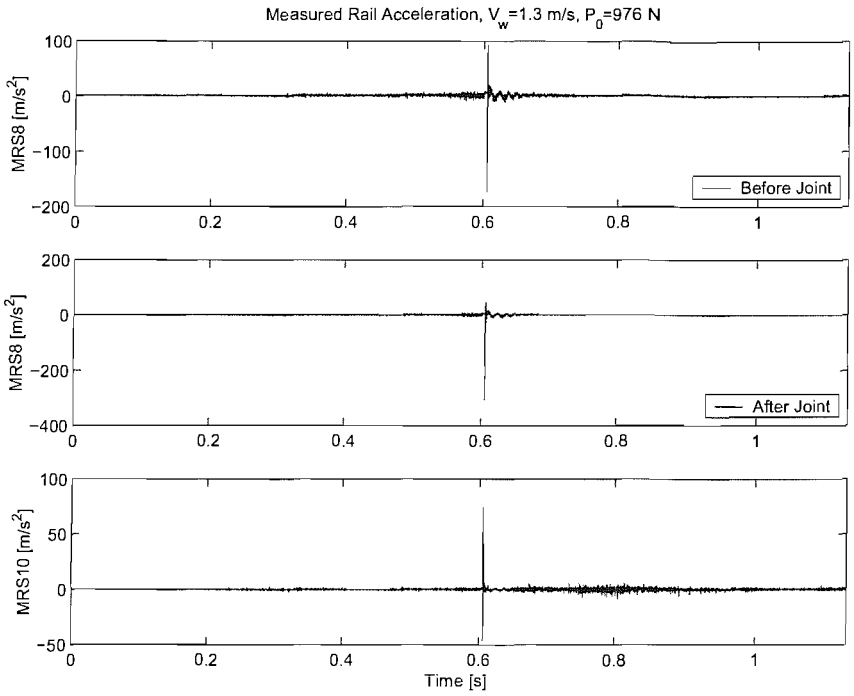

Figure 8–11 Measured rail acceleration due to a level joint at three points on the rail for a wheel speed of 1.3m/s and a 976N wheel pre-load.

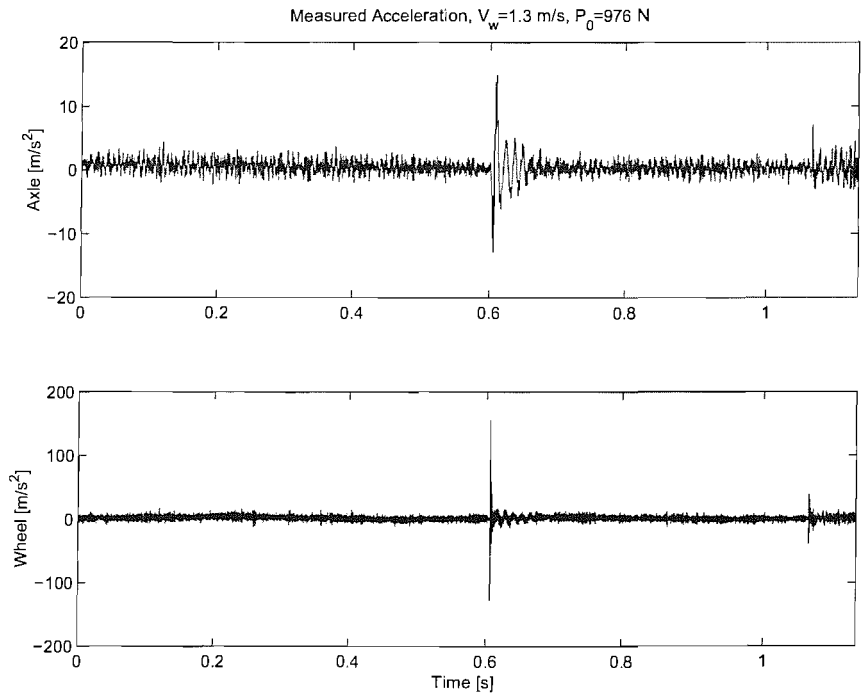

Figure 8–12 Measured rail acceleration due to a level joint at three points on the rail for a wheel speed of 1.3m/s and a 976N wheel pre-load.

The sample measurements of rail acceleration at three different points on the rail presented in Figure 8–11 showed similar results in the time domain. Comparisons of two of these measurements have been made to try to ascertain what are the effects the position of the accelerometers in relation to the rail discontinuity. Figure 8–13 shows the results of the measured acceleration spectral levels at MRS8 at the position just past the joint minus the measured acceleration spectral levels at MRS10. Differences between the spectral levels are shown for all of the measured wheel speeds (1m/s to 5m/s) and each of the four wheel pre-loads. This shows that in some frequency bands the difference between the two measurement positions can be as much as 20dB. This shows that whilst the impulse of the wheel at the joint is seen to dominate the time domain results away from the discontinuity, an effect of decay is noticeable over a relatively short length of track. The trend of this decay is similar but inverted to the shape of the decay rates expressed in the form $1/\beta L$ shown in Figure 8–8. A change in wheel pre-load does not appear to alter the shape of the effect shown in Figure 8–13. A change in wheel speed, however, can make variations as large as 5dB in some of the one-third octave frequency bands. The results in Figure 8–13 cannot, however, be used as a reliable measurement of decay between the two measurement positions, as the measured level from the accelerometer at MRS10 includes a contribution of the wheel rolling past this measurement point, as well as the impulse of the wheel hitting the track at MRS8.

Measurements of the measured peak rail acceleration for four wheel pre-loads at wheel speeds ranging from 1m/s to 5m/s are presented in Figure 8–14. This shows that a change in wheel pre-load has only a small effect on the trend of the measured peak acceleration. For a particular wheel speed, the peak acceleration values for the four wheel pre-loads are within 3 to 10dB of each other. The peak values in Figure 8–14 are seen to be within a range of 34dB to 56dB re $1m/s^2$ for wheel speeds between 1m/s and 5m/s.

8.4.2 Inputs used for the prediction of wheel and rail vibration

The method of splitting the surface profile measurement of the level joint into two parts was employed, as described in Chapter 7. The discontinuity part of this input is presented in Figure 8–15. Note that the joint is not exactly level – a step down of 0.13mm is present. Artificially smooth surfaces have been added to the input in Figure 8–15 to allow starting transients of the numerical routine to decay, and to allow the decay of the wheel and rail vibration due to the step joint.

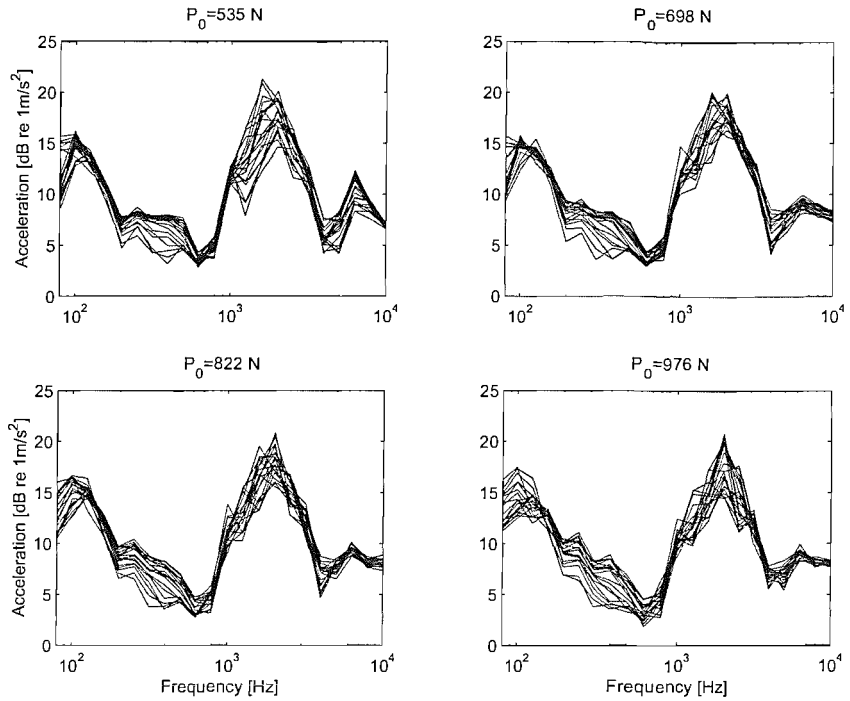

Figure 8–13 Measured rail acceleration spectra level at MRS8 (just after the level joint) minus the measured rail acceleration spectra level at MRS10, for four wheel pre-loads at wheel speeds ranging from 1m/s to 5m/s.

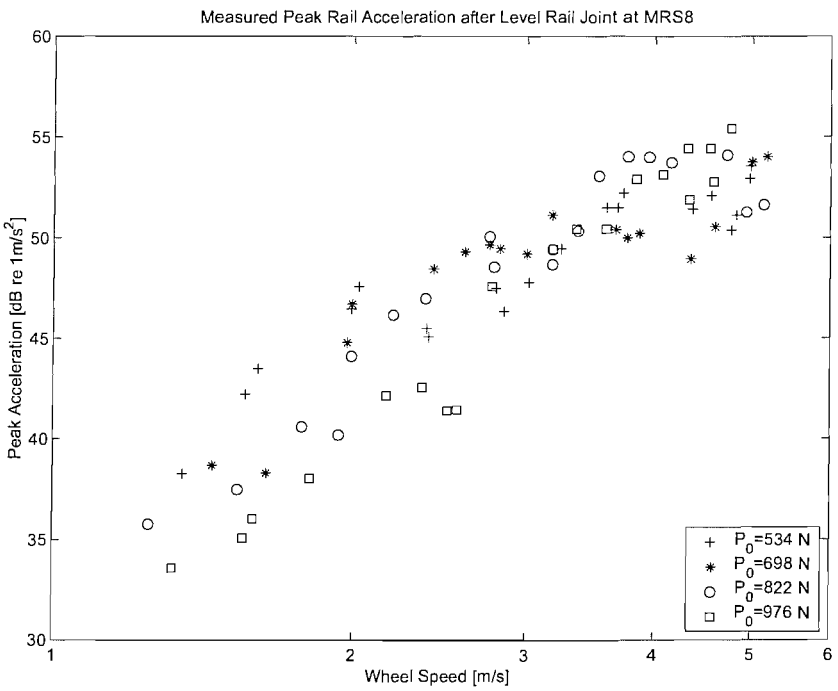

Figure 8–14 Measured peak rail acceleration at MRS8 for four wheel pre-loads at wheel speeds ranging from 1m/s to 6m/s due to the level joint.

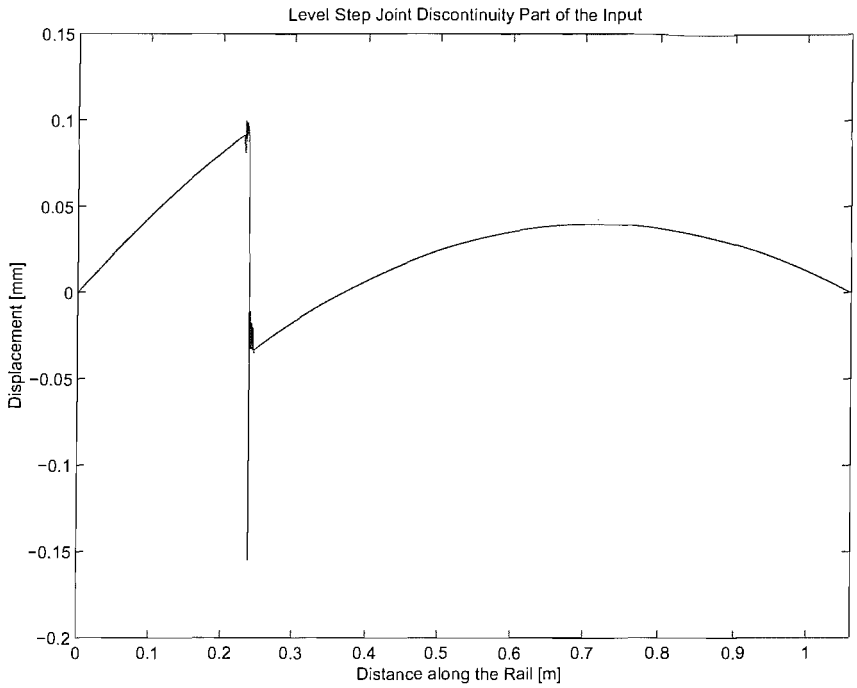

Figure 8–15 The discontinuity part of the level joint surface profile input. This has been repositioned to 0.23m for use as an input to the time-stepping routine.

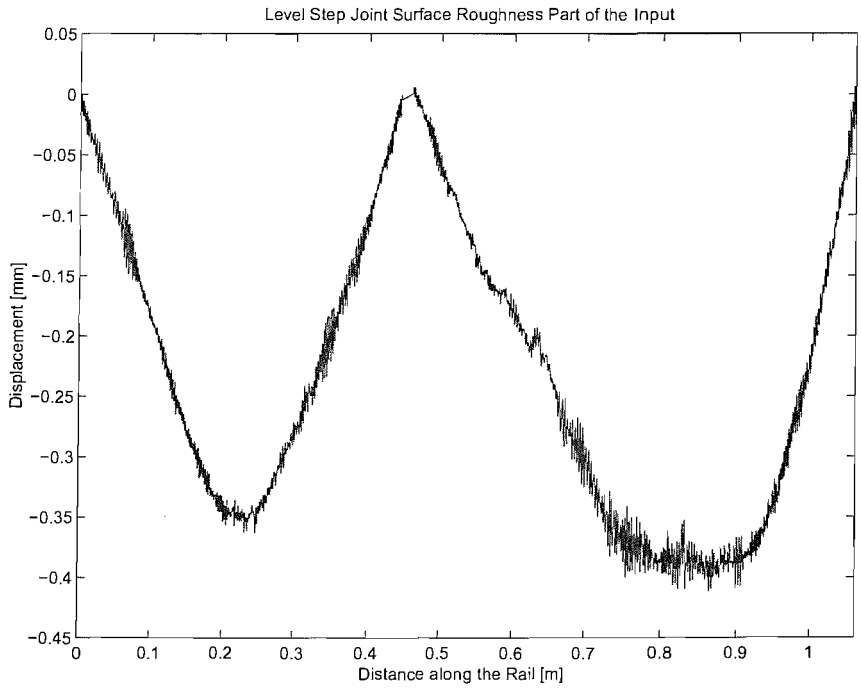

Figure 8–16 The remaining surface roughness input contribution for all of the step joints. The joint has been removed from this measurement at 0.44m.

The surface roughness (SR) contribution of the input is shown in Figure 8–16. Spectra of these two inputs (Figure 8–15 and Figure 8–16) are presented in Figure 8–17 as a function of wavelength. Here the spectra of the two inputs are also compared with the spectra of the inputs after they have been geometrically filtered. The process used to apply the geometrical filter to the inputs is described in Chapter 4.

Figure 8–17 shows that the discontinuity part of the level joint input dominates at the largest wavelengths considered. Prior to geometrical filtering the wavelengths larger than 5mm are seen to be dominated by the discontinuity part of the level joint input. Wavelengths smaller than this are seen to be dominated by the surface roughness contribution. A peak in the surface roughness contribution is seen in the spectra at approximately 3mm wavelength. It is not known why the spectrum at this wavelength is so large, but it is assumed to be related to the way in which the railhead surfaces have been manufactured because it is a characteristic of both of the half rail lengths.

After geometrical filtering, the large levels at a wavelength of 3mm in the surface roughness contribution are seen to have been reduced, but a strong component at this wavelength is still evident. Geometrical filtering is also seen to change the point at which the discontinuity part of the input is larger than the surface roughness contribution. The effect of the discontinuity part of the input is now seen only to dominate wavelengths larger than 11mm. This means that the discontinuity part of the input is now likely to be less influential in the predictions of vibration than it would have been if geometrical filtering had not been applied.

8.4.3 Measurements and predictions of wheel and rail vibration

The method of splitting the surface profile measurement into two parts, described in Chapter 7, means that two predictions are made:

- predictions using the discontinuity part of the input were made by using the non-linear time-stepping model (as non-linear wheel / rail interaction was expected),
- predictions based on the surface roughness contribution were made using the more (time) efficient FRF model.

An example of a time-domain output of the modal wheel variant non-linear time-stepping model formed using the discontinuity part of the input is shown in Figure 8–18. Here the displacements of the wheel and rail predicted for a wheel speed of 1.3m/s and a wheel pre-load of 976N, are compared with the discontinuity part of the input, and

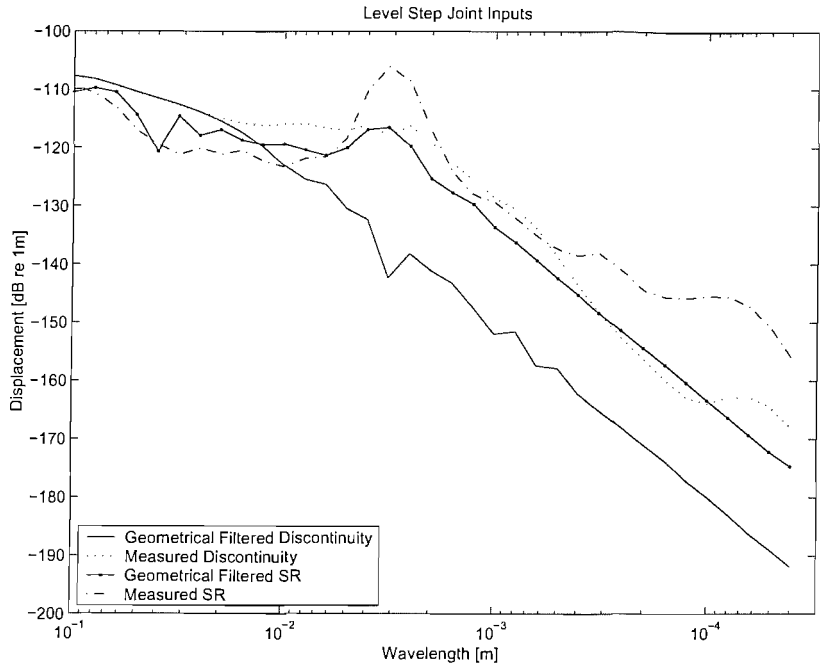

Figure 8–17 Spectra of the measured surface roughness and discontinuity parts of the level step joint input compared with the spectra of the surface roughness and discontinuity parts of the level joint input after geometrical filtering.

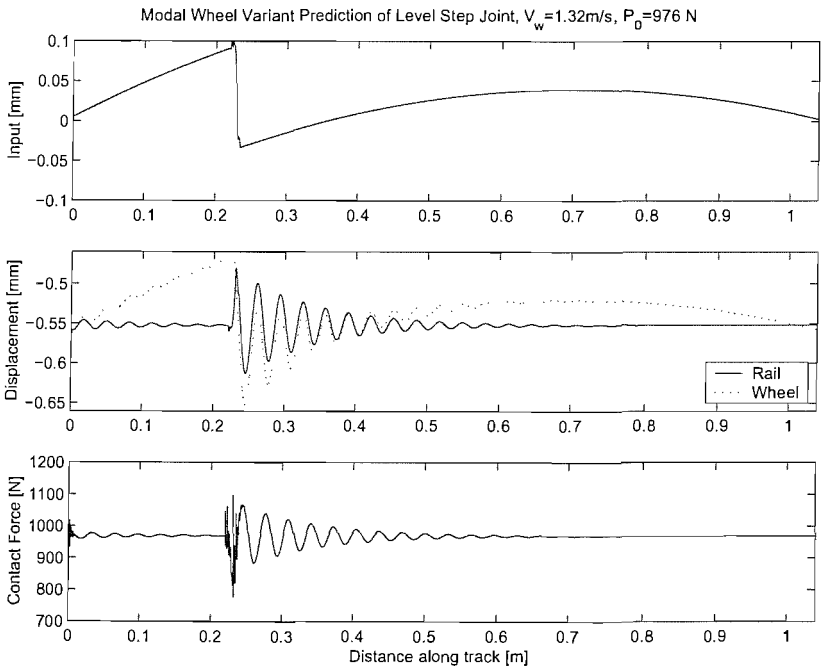

Figure 8–18 Modal wheel non-linear time-stepping model prediction of wheel and rail displacement due to the level joint for a wheel speed of 1.3m/s and a wheel pre-load of 976N shown as a function of distance along the track length. This is compared with the input to the simple variant and the predicted contact force.

the predicted contact force. The results are presented as a function of distance along the track so that forthcoming results can be compared easily.

The predicted displacements in Figure 8–18 show that as the wheel drops off the step joint geometry (at a position 225mm along the rail) the rail displacement is seen to rise upwards. This is because the wheel unloads as it falls to the lower rail height, thus enabling the compressed track to rise upwards to meet the wheel. The effect of the wheel unloading is also shown in the output of the predicted contact force where the wheel / rail contact force is seen momentarily to drop down to a value of approximately 750N. Even though the wheel is travelling along the rail at a speed of 1.3m/s, loss of contact between the wheel and the rail is not predicted for this wheel speed at this wheel load. Both the predicted displacements of the wheel and the rail and the predicted contact force are seen to fluctuate with a strong sinusoidal content after the wheel has met the discontinuity. This fluctuation has been found to be related to the wheel on track resonance of the modal wheel variant non-linear time-stepping model (60Hz) also seen in the measurement at about 80Hz.

More results of the predicted wheel and rail displacements are presented in Figure 8–19 for a wheel speed of 4.8m/s at a 976N wheel pre-load. Again the predicted displacements are compared with the input to the prediction model and the predicted contact force. As for the lower wheel speed, it is predicted that the wheel remains in contact with the rail. The wheel speeds at which wheel / rail unloading occurred for each of the wheel pre-loads are presented in Table 8-1. This shows that the outputs for the two highest wheel pre-loads of the modal wheel variant non-linear time stepping model (with the level joint input) did not predict loss of contact with the range of wheel speeds measured (1m/s to 5m/s).

Figure 8–19 shows that wheel and rail vibration is predicted to be larger than the example shown in Figure 8–18, and that the vibration takes a longer length of track to decay. The length along the track over which the vibration decayed in Figure 8–18 was about 0.24m. At a wheel speed of 1.3m/s this corresponds with a decay time of 0.18s. The results in Figure 8–19 were seen to decay over a length of about 0.85m, which at a wheel speed of 4.8m/s also meant a decay time of 0.18s. Thus the predictions show that the wheel and rail vibration due to the discontinuity decays within approximately the same length of time independent of the wheel speed. However, it is seen from the predictions in Figure 8–19 that a greater length of the rail is affected by the vibration of the wheel / rail interaction due to the level joint.

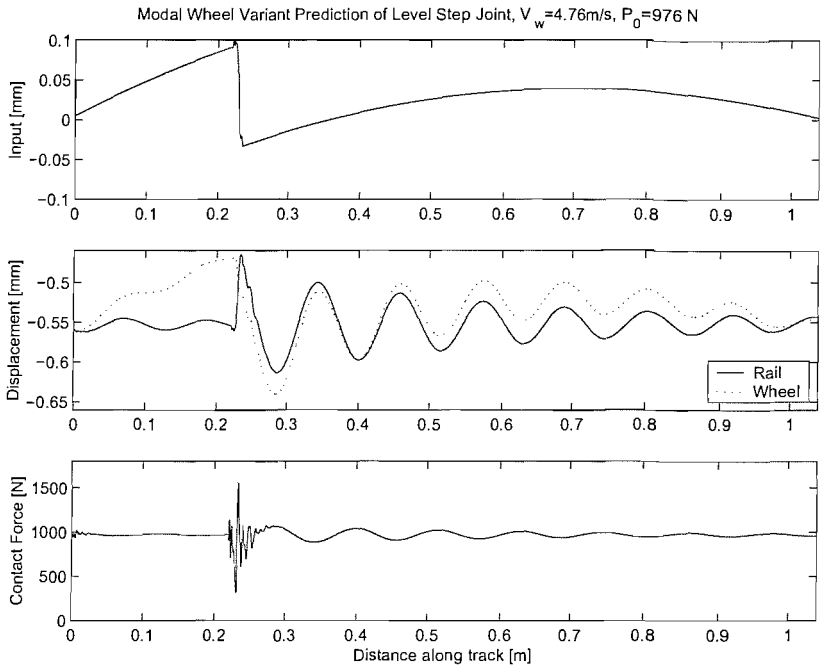

Figure 8–19 Modal wheel non-linear time-stepping variant prediction of wheel and rail displacement due to the level joint for a wheel speed of 4.8m/s and a wheel pre-load of 976N shown as a function of distance along the track length. This is compared with the input to the simple variant and the predicted contact force.

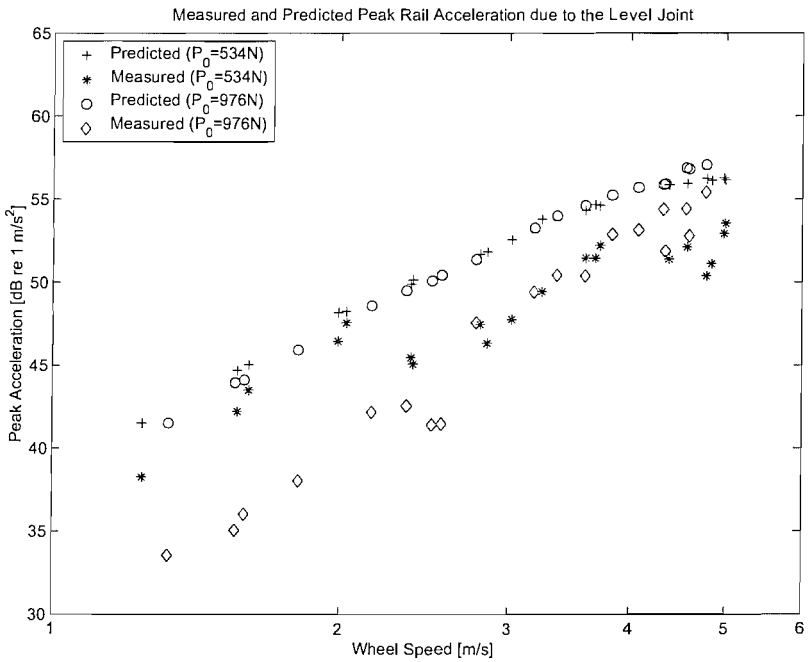

Figure 8–20 Modal wheel variant predicted (using the discontinuity part of the level joint input) peak rail acceleration and the measured peak rail acceleration for wheel speeds in the range of 1m/s to 5m/s at the lowest wheel pre-load of 535N and the highest wheel pre-load of 976N.

Table 8-1 Predicted wheel speed at which wheel / rail unloading occurred.

	Simple Variant	Modal Wheel Variant
Level step joint		
534N Wheel pre-load	3.7m/s	4.1m/s
698N Wheel pre-load	3.8m/s	5.0m/s
822N Wheel pre-load	4.2m/s	Out of measured range
976N Wheel pre-load	4.7m/s	Out of measured range
Step-down joint		
536N Wheel pre-load	1.3m/s	1.4m/s
669N Wheel pre-load	1.5m/s	1.6m/s
840N Wheel pre-load	1.8m/s	1.9m/s
978N Wheel pre-load	2.0m/s	2.5m/s
Step-up joint		
542N Wheel pre-load	3.1m/s	4.4m/s
681N Wheel pre-load	3.5m/s	4.8m/s
771N Wheel pre-load	3.8m/s	5.4m/s
928N Wheel pre-load	4.2m/s	Out of measured range

Comparisons of the measured and predicted peak rail acceleration are presented next in Figure 8–20 for the lowest (535N) and highest (976N) wheel pre-loads. Values for the predictions were first calculated by use of a first order (difference) differentiation routine, after which, the results were then filtered in the time domain for adjustments of the contact filter by use of the (FIR) approximate contact filter (see Chapter 5). Figure 8–20 shows the results of the peak rail acceleration for two wheel pre-loads at wheel speeds in the range 1m/s to 5m/s. The predictions are seen to be at a higher level than the measurements at low wheel speeds up to about 7dB at 1.2m/s, but at the highest wheel speeds considered the agreement is good. This however does not necessarily indicate that higher wheel speeds will always be in better agreement. Further comparisons are required to confirm such a relationship. The predicted peak acceleration values are seen to follow a trend that rises by approximately 10dB for a doubling of wheel speed below 3m/s. Above this speed, however, the trend is seen be closer to 8dB for a doubling of wheel speed.

Results of the predicted rail vibration are presented next in the frequency domain. These are shown in the form of acceleration spectra, where comparisons with the measurements are presented as one-third octave band spectra between 100Hz and 10kHz as shown in Figure 8–21, for a wheel pre-load of 976N, and a wheel speed of 1.3m/s.

A this speed a strong component is predicted at 400Hz, from the FRF model prediction made using the surface roughness contribution. This corresponds with the large spectral content of the surface roughness surface profile shown in Figure 8–17 at a wavelengths of 2 to 4mm. This peak manifests itself for a wheel speed of 4.8m/s at 1.2kHz. This is clearly shown in Figure 8–22 where predictions and measurements of rail acceleration due to the level step joint at a 4.8m/s wheel speed and a 976N wheel pre-load are presented. The predictions formed from the discontinuity part of the input are seen to be influential at the lowest frequency bands. This extends to higher frequency bands at higher wheel speeds. The overall predicted level is shown together with the predictions formed with the surface roughness part of the input and the discontinuity part of the input in Figure 8–21 and Figure 8–22.

The overall predicted level of acceleration minus the measured level of acceleration for four wheel pre-loads at speeds ranging from 1m/s to 5m/s is shown in Figure 8–23. Quite good agreement is seen between the measurements and the predictions. Certain trends are apparent from the results which are not related to wheel speed or wheel pre-

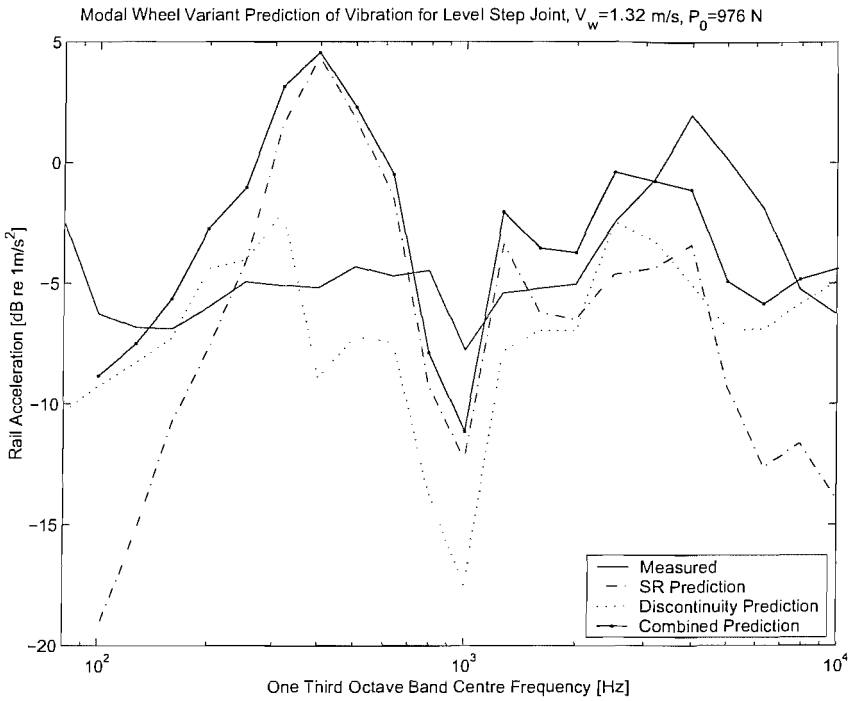

Figure 8–21 Modal wheel variant prediction (with contact filter effects) of rail acceleration due to the level joint compared with the measured rail acceleration for a wheel speed of 1.3m/s at a wheel pre-load of 976N.

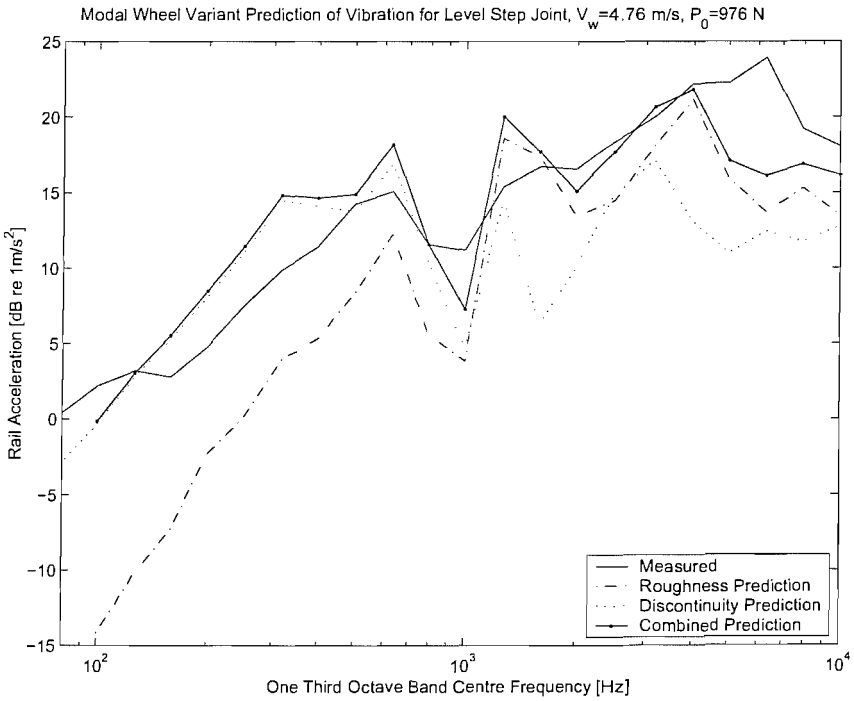

Figure 8–22 Modal wheel variant prediction (with contact filter effects) of rail acceleration due to the level joint compared with the measured rail acceleration for a wheel speed of 4.8m/s at a wheel pre-load of 976N.

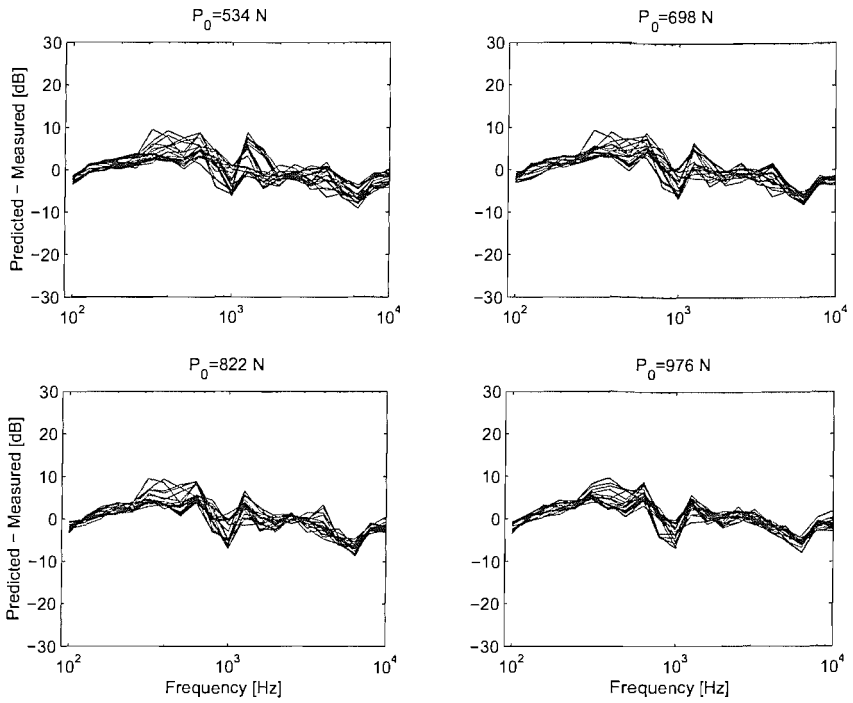

Figure 8–23 Modal wheel variant overall predicted (with contact filter effects) rail acceleration due to the level joint compared with the measured rail acceleration due to the level step joint for a wheel speeds in the range 1m/s to 5m/s at four wheel pre-loads.

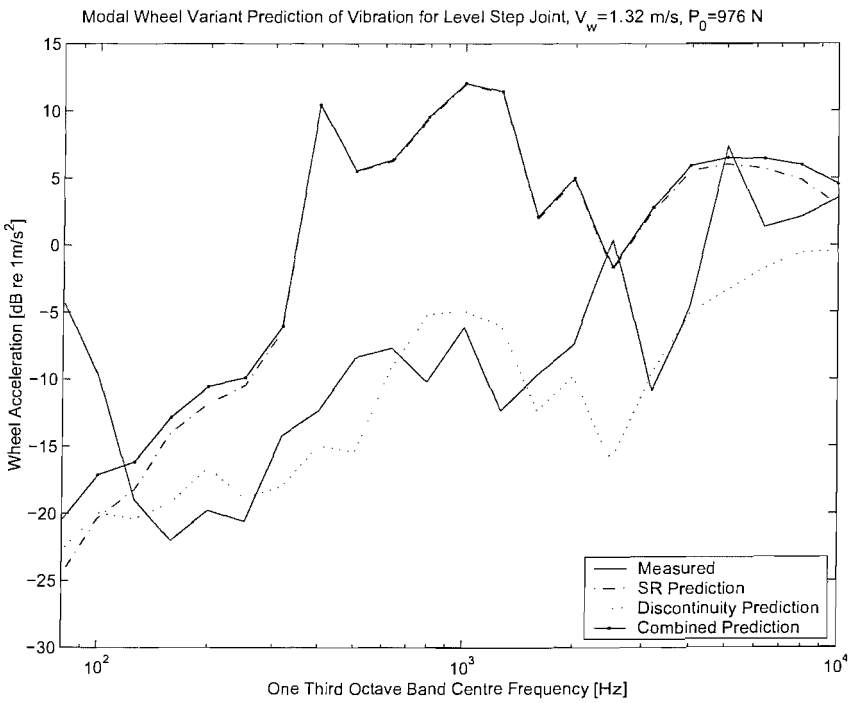

Figure 8–24 Modal wheel variant prediction (with contact filter effects) of wheel acceleration due to the level joint compared with the measured wheel acceleration for a wheel speed of 1.3m/s at a wheel pre-load of 976N.

load. For example, all of the comparisons are seen to have a dip at around 6kHz, where the measurements have larger levels than the predictions. These differences are most likely to be related to the modal wheel variant model. The contact filter attenuation appears to be approximately correct as the highest one-third octave bands (8kHz to 10kHz) show differences that are close to 0dB.

The predictions are also seen to be larger than the measurements by as much as 10dB at 1kHz. This also does not seem to be likely to be related to contact filter effects as the largest attenuation of a contact filter is expected to be at higher frequencies (see Chapter 5), so model differences could also be responsible here. Discrepancies of up to 10dB seen in the comparisons between the measured and predicted acceleration levels appear to be related to the performance of the prediction model. As the predictions are formed from an 'average' behaviour of the track, where no account for the presence of the step joint has been made, improvements of the model appears to be achieved by including the differences in the track behaviour close to the joint.

Results for the wheel acceleration predicted by the modal wheel variant are presented next. Whilst the measured wheel vibration has been shown to be unreliable, the predictions made using the modal wheel variant of the non-linear time-stepping model are included here so that the relationship between the two parts of the prediction (using the method described in Chapter 7) is shown.

Examples of the predicted wheel acceleration due to the level joint at a wheel speed of 1.3m/s and a wheel pre-load of 976N are presented in Figure 8–24. This shows that the prediction formed from the surface roughness part of the input is generally larger than the prediction formed from the discontinuity part of the input. Therefore in the frequency range 100Hz to 10kHz, the wheel vibration is not predicted to be greatly influenced by the level joint. It is assumed that the step joint has a greater influence at frequencies below 100Hz (see Figure 8–17).

The results shown in Figure 8–25 for a higher wheel speed of 4.8m/s demonstrate that the predictions formed from the discontinuity part of the input are larger than the predictions formed from the surface roughness contribution at frequencies up to 300Hz. However, at frequencies greater than 300Hz the predictions formed from the surface roughness part of the level joint rail surface profile are seen to contribute the most to the overall level of the predicted wheel acceleration. As expected, the comparisons between the overall predicted and measured wheel acceleration are not good.

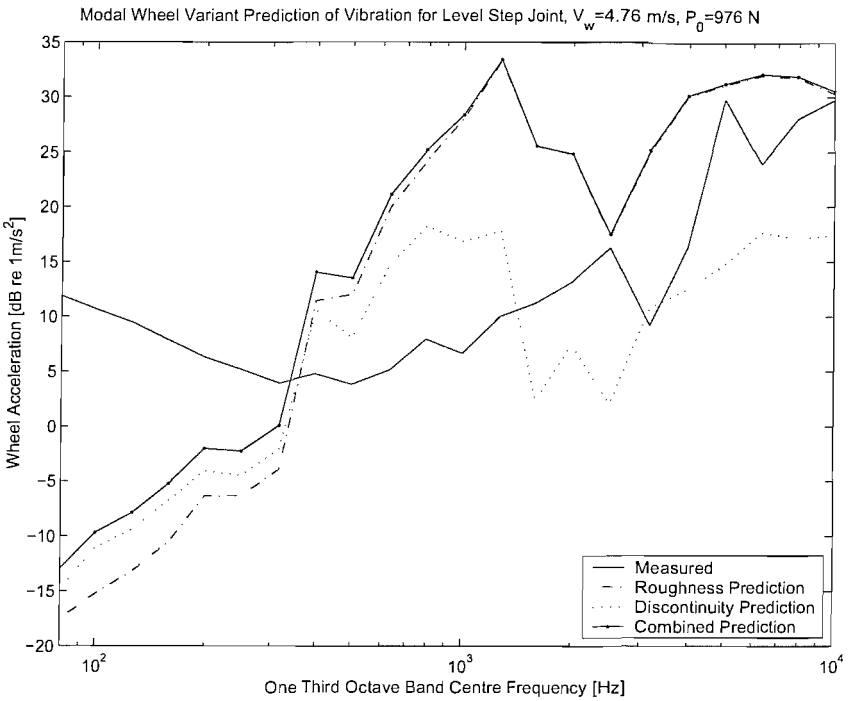

Figure 8–25 Modal wheel variant prediction (with contact filter effects) of wheel acceleration due to the level joint compared with the measured wheel acceleration for a wheel speed of 4.8m/s at a wheel pre-load of 976N.

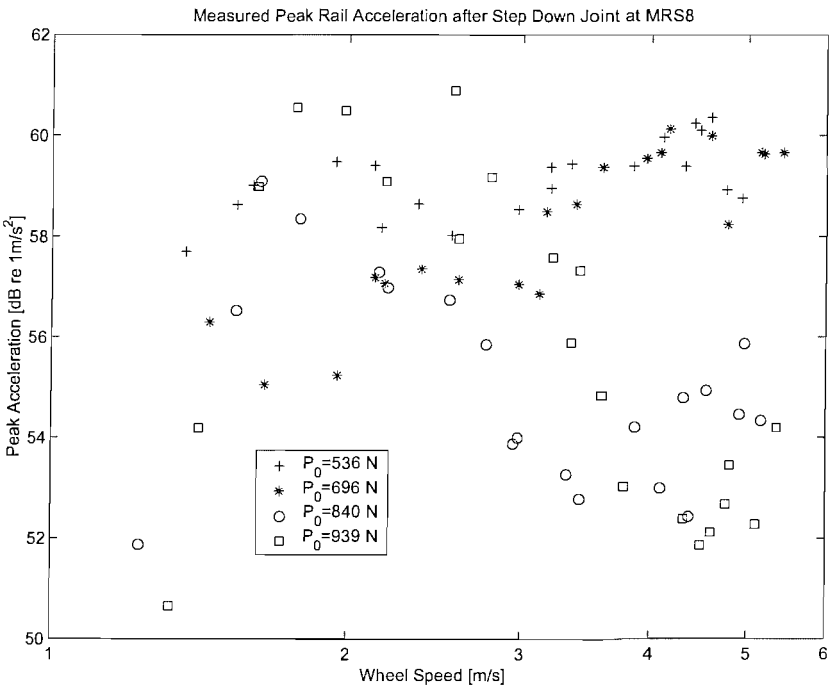

Figure 8–26 Measured peak rail acceleration at MRS8 (just after the joint) due to the step-down joint for wheel speeds in the range 1m/s to 6m/s.

8.5 Measurements and predictions of wheel and rail vibration due to a step-down joint

8.5.1 Examples of the measurements made on the rig

No changes, other than an increase of height of the step joint, were made to the rig for the measurements of the step-down joint presented in this section. The mode of operation and the method of making measurements was also the same as before. The profile of the level joint in Figure 8–15 showed that the level joint was actually a small step-down joint. The results in this section correspond to a greater step-down joint of height 0.83mm.

Results of the measured peak rail acceleration are shown for the step-down joint for four wheel pre-loads at wheel speeds ranging from 1m/s to 5m/s. These acceleration values (at MRS8 just after the joint) are presented in Figure 8–26. This shows that the measurements are strongly influenced by an increase in wheel pre-load as well as changes in wheel speed. The results measured with the lowest wheel pre-load (536N) are seen to lie between 57.5dB re $1m/s^2$ and 60.5dB re $1m/s^2$, whilst at the maximum wheel pre-load (939N) they lie between 50dB and 61dB. These values are much greater than the values of the 'level' joint shown in Figure 8–14. The peak value of the measured acceleration due to the step-down joint at the lowest wheel speed (1.2m/s) exceeds the measured peak acceleration due to the level joint at the high wheel speed considered (5.2m/s).

A clear distinction between the results for the lowest and the highest wheel pre-load is seen in Figure 8–26. The results at the lowest wheel pre-load (536N) are seen to be higher in level than those at the highest wheel pre-load (939N), and they change by little more than 2dB for an increase of wheel speed (in the range 1m/s to 6m/s). The results for the highest wheel pre-load (939N), however, are seen to rise from approximately 50dB at 1.3m/s to a maximum level of 61dB at 2.5m/s. At wheel speeds greater than 2.5m/s the measured peak acceleration level is seen to fall dramatically as the wheel speed increases to 6m/s. Similar behaviour is measured for a 840N wheel pre-load.

Some of these measured trends appear similar to the results presented by [Ver et al, 1976]. For example, much like their results, the step-down rail joint shown in Figure 8–26 the peak rail acceleration did not increase with faster wheel speeds at the highest wheel pre-load considered. The measured trend actually reduced with an increase of wheel speed. This trend, however, was not predicted by the time-stepping models, and

therefore it is unclear whether other effects have influenced the results. This is discussed later in section 8.5.3.

8.5.2 Inputs used for the prediction of wheel and rail vibration

As in section 8.4, predictions of the wheel and rail vibration were made so that comparisons could be made with the measurements. The discontinuity part of the step-down joint surface profile is shown in Figure 8–27. This shows that the height of the step-down joint is 0.83mm whereas the height of the 'level' joint was 0.14mm (see Figure 8–15). The step-down joint is almost 6 times larger than the level joint.

Spectra of each of the parts of the step-down joint input are presented in Figure 8–28. This shows that the discontinuity part of the input is much larger than the surface roughness contribution of the step-down joint for wavelengths larger than 0.3mm. As for the level step joint, a peak in the surface roughness spectrum is seen at a wavelengths between 2mm and 4mm. The effect of geometrical filtering (see Chapter 4) is also shown in Figure 8–28 for each part of the step-down joint inputs. Geometrical filtering is seen to attenuate the short wavelengths of each of the inputs. The filtered spectra are similar at a wavelength of 4mm.

8.5.3 Measurements and predictions of wheel and rail vibration

An example of the predicted wheel and rail displacements for the discontinuity part of the step-down joint is presented in Figure 8–29 for a wheel speed of 1.3m/s at a 939N wheel pre-load. The result in Figure 8–29 is compared with the step-down discontinuity part of the input, and the predicted contact force. This shows that, as for the level joint, no loss of wheel / rail contact is predicted for the lowest wheel speed. Higher wheel speeds did, however, result in the wheel losing contact with the rail. The wheel speeds at which the wheel / rail unloading was predicted are listed in Table 8-1 where results for the level joint were also presented. The simple variant of the non-linear time-stepping model was found to predict loss of contact at lower wheel speeds than the modal wheel variant. This highlights a difference between the two model variants used to make the predictions.

Predictions of the peak rail acceleration obtained using the modal wheel variant are compared with the measured peak rail acceleration in Figure 8–30. Results for the lowest wheel pre-load 536N and the highest wheel pre-load 939N at wheel speeds ranging from 1m/s to 6m/s are considered. Here (as in section 8.4) the predicted results have been differentiated twice to form acceleration using a first order differentiating

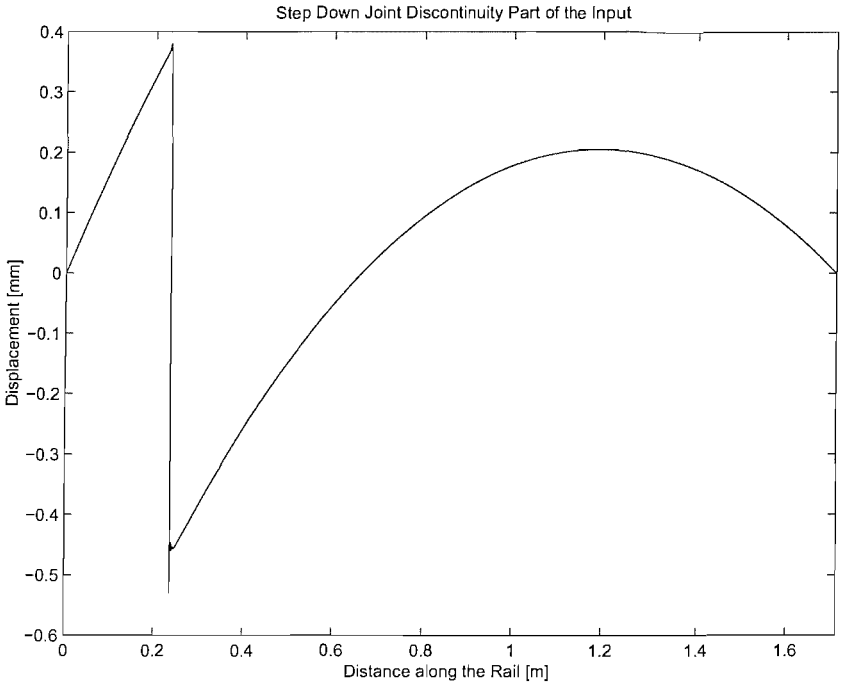

Figure 8–27 Discontinuity part of the step down joint input.

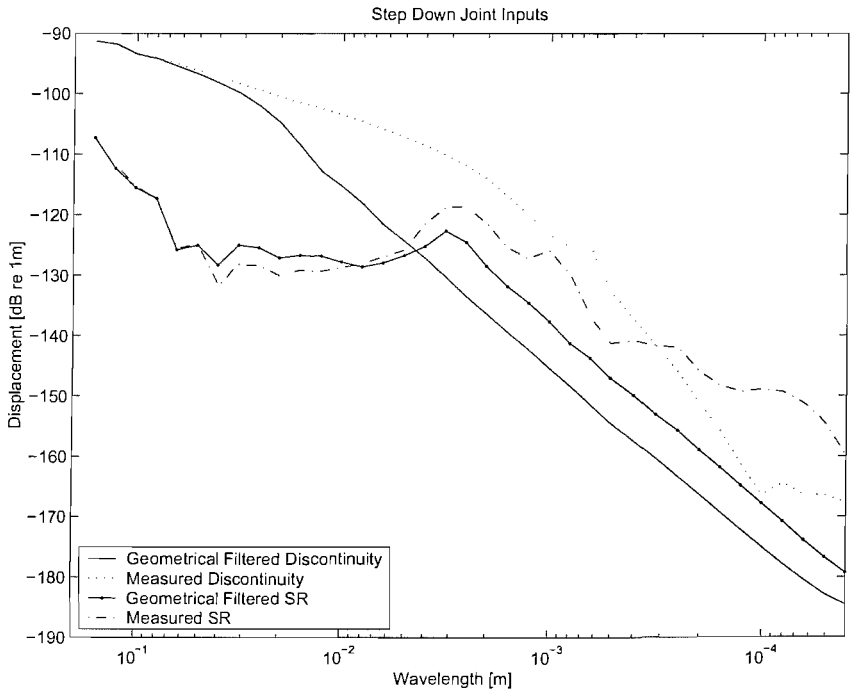

Figure 8–28 Spectra of the step-down joint discontinuity part of the input and the contribution of the surface roughness input before and after geometrical filtering. Spectra are shown as a function of wavelength.

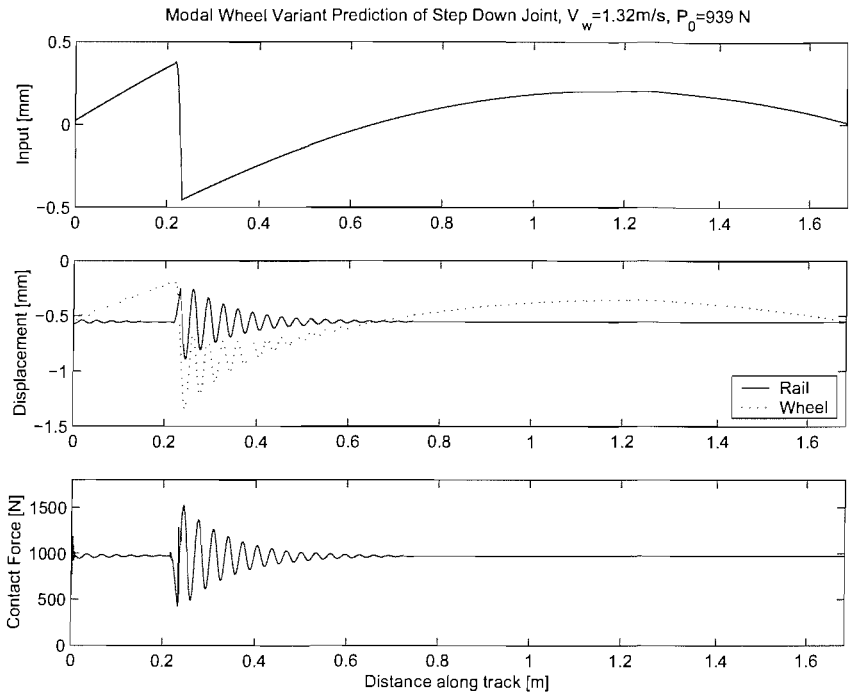

Figure 8–29 Modal wheel variant prediction of wheel and rail displacement due to the step down joint for a wheel speed of 1.3m/s and a wheel pre-load of 939N shown as a function of distance along the track length. This is compared with the input to the modal wheel variant and the predicted contact force.

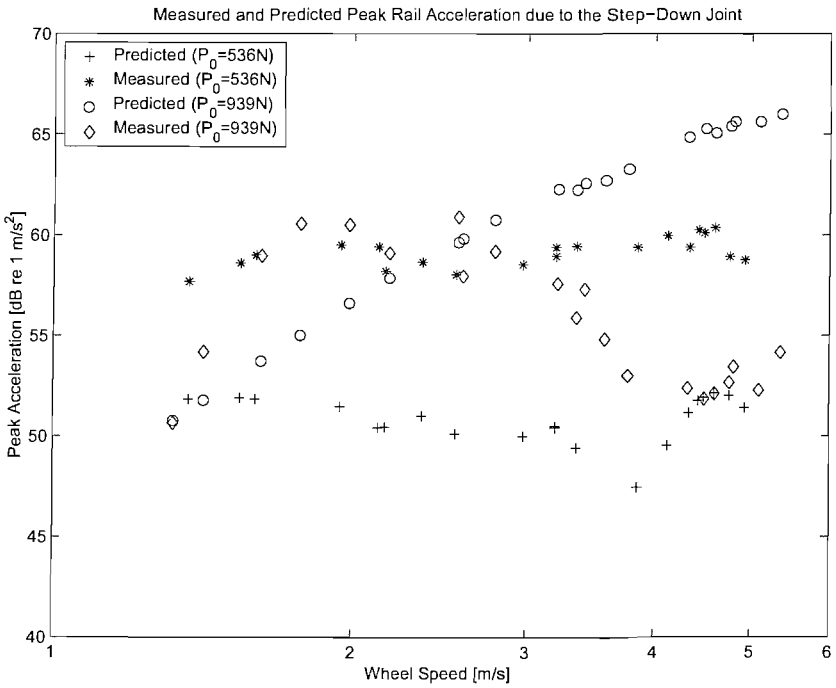

Figure 8–30 Measured and modal wheel variant predicted peak rail acceleration for the lowest wheel pre-load (536N) and the highest wheel pre-load (939N) at wheel speeds in the range 1m/s to 6m/s.

routine. Contact filter effects have been included but adjustments for the track decay have not been applied. As these predictions are outputs from the non-linear time-stepping model, the contribution from the surface roughness part of the input is not included in the comparisons. Agreement between the measurements and predictions in Figure 8–30 is not seen to be particularly good. The predicted peak values at the lowest wheel pre-load (536N) are at least 6dB lower than the measured values, but the trends of the measurements and the predictions show similar behaviour. A more or less constant peak acceleration value (at 51dB) is predicted for the range of wheel speeds considered, whilst a more or less constant value is measured at about 59dB.

At the highest wheel pre-load (939N) agreement between measured and predicted peak acceleration is not as good. The predicted values for this wheel pre-load are seen in Figure 8–30 to rise at a rate of approximately 10dB for a doubling of wheel speed whereas the measurements fall at higher speeds.

Frequency domain comparisons between the measured and predicted rail acceleration are presented in Figure 8–31 for a wheel speed of 1.3m/s and a wheel pre-load of 939N. Also shown are the contributions of the predictions formed from the surface roughness (SR) part of the input and the predictions formed from the discontinuity part of the input. The predictions formed from the surface roughness contributions are lower than those formed from the discontinuity input. The surface roughness contribution of the input has little influence on the overall prediction. Thus it is seen from Figure 8–31 that the overall predicted level is virtually identical to the predicted level formed with the discontinuity input. The overall predicted level is generally seen to be lower than the measured rail acceleration level. The two parts of the prediction, however, are seen to be quite close to each other at frequencies between 300Hz and 1kHz. The prediction formed from the surface roughness contribution of the step-down input is seen to contribute (in a small way) to the overall predicted level in these frequency bands at this low wheel speed of 1.32m/s. This peak in the prediction formed from the surface roughness is due to the peak in the measured spectra of the surface roughness contribution at a wavelengths of 2mm to 4mm.

Figure 8–32 shows the measured and predicted rail acceleration levels for a wheel speed of 5.1m/s at a 979N wheel pre-load. Again it is clear that the discontinuity predictions dominate the overall prediction levels. Comparisons of the measured levels with the overall predicted levels are seen to be in better agreement.

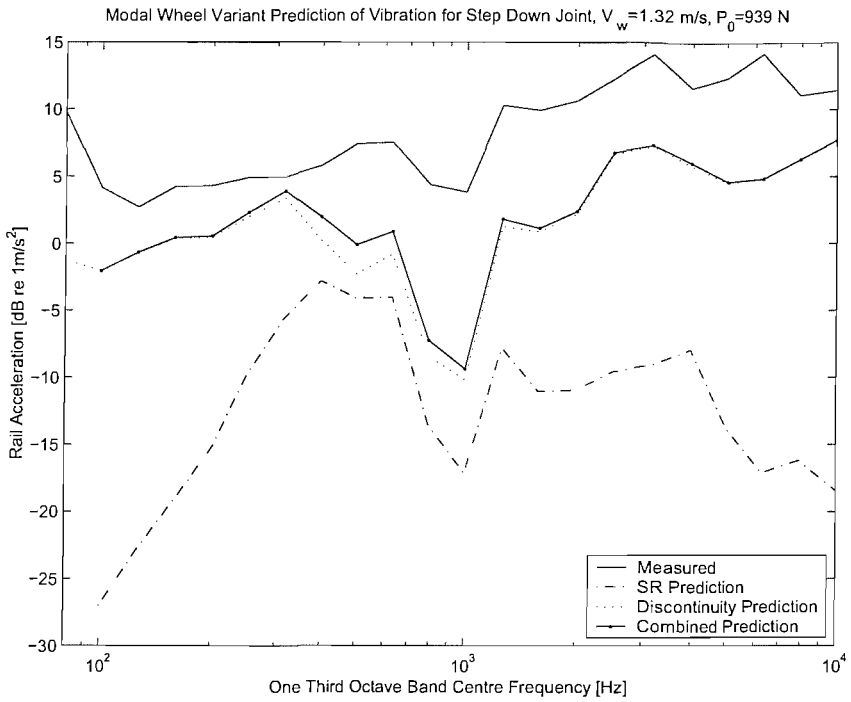

Figure 8–31 Modal wheel variant prediction (with contact filter effects) of rail acceleration due to the step down joint compared with the measured rail acceleration for a wheel speed of 1.3m/s at a wheel pre-load of 939N.

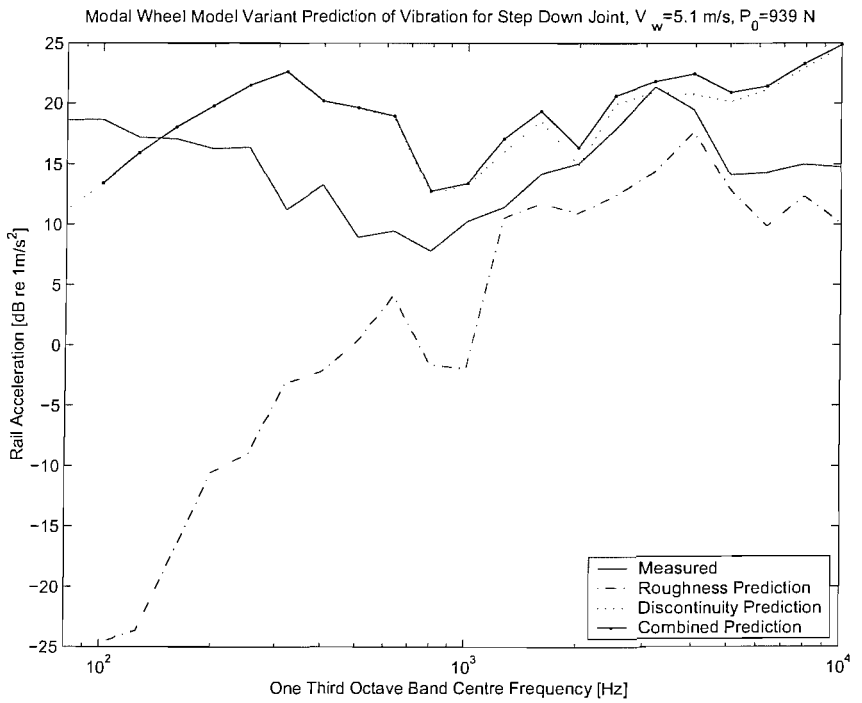

Figure 8–32 Modal wheel variant prediction (with contact filter effects) of rail acceleration due to the step down joint compared with the measured rail acceleration for a wheel speed of 5.1m/s at a wheel pre-load of 939N.

The results of the predicted minus measured rail acceleration levels are presented in Figure 8–33 for all four wheel pre-loads at all of the measured wheel speeds. Variations with wheel speed are evident, particularly for the greater wheel pre-loads of 840N and 939N. As shown in Figure 8–32 improvements in the predicted minus measured levels are seen at the highest wheel speeds considered.

Use of the modal wheel model has been shown to provide better predictions of wheel vibration than the simple model (see Chapter 5). However, as the reliability of the measurements of the wheel vibration (when converted into the frequency domain and presented as one-third octave spectra) is not good only two examples of the predicted wheel acceleration spectra are presented. These examples are shown to demonstrate the relationship between the two parts of the overall prediction.

The predicted levels of wheel acceleration are presented in Figure 8–34 for a low wheel speed of 1.3m/s and in Figure 8–35 for a wheel speed of 5.1m/s. Both of these comparisons were made for wheel pre-loads of 939N. Figure 8–34 shows that the prediction formed from the surface roughness and the prediction formed from the discontinuity part of the input have similar magnitudes. The two parts of the prediction of wheel vibration are much closer in magnitude than is the case for the prediction of rail vibration for most of the frequency range considered (100Hz to 10kHz). The prediction formed from the discontinuity part of the input, however, is still seen to dominate the overall predicted level. The results shown in Figure 8–34 demonstrate that at a wheel speed of 1.3m/s the prediction formed from the surface roughness contribution is only smaller in magnitude at frequencies below 300Hz and above 2kHz. Similar results are seen in Figure 8–35 for the faster wheel speed (5.1m/s), where the prediction formed from the surface roughness contribution is only smaller in magnitude in the low frequency range 100Hz to 600Hz and in the high frequency range 8kHz to 10kHz.

The results of the predicted wheel vibration shown in Figure 8–34 and Figure 8–35 demonstrate that whilst the surface roughness contribution of the step-down input plays an important role in the overall predicted levels, the discontinuity part of the input has a greater influence in the predictions for the step-down joint than for the level joint in section 8.4.3. The results demonstrate that for the rail vibration due to the step-down joint the surface roughness part of the input has negligible effect in the overall rail vibration, but that the predictions formed from the surface roughness part of the input were found to be significant in determining the wheel vibration.

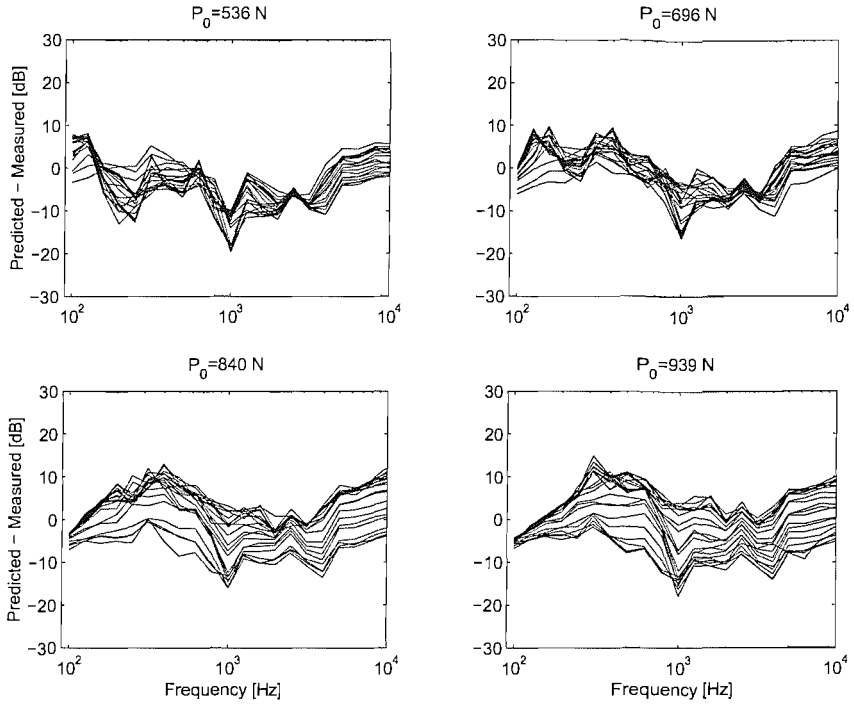

Figure 8–33 Modal wheel variant overall prediction of rail acceleration spectra level minus measured rail acceleration spectra level due to the step-down joint for four wheel pre-loads and wheel speeds ranging from 1m/s to 6m/s.

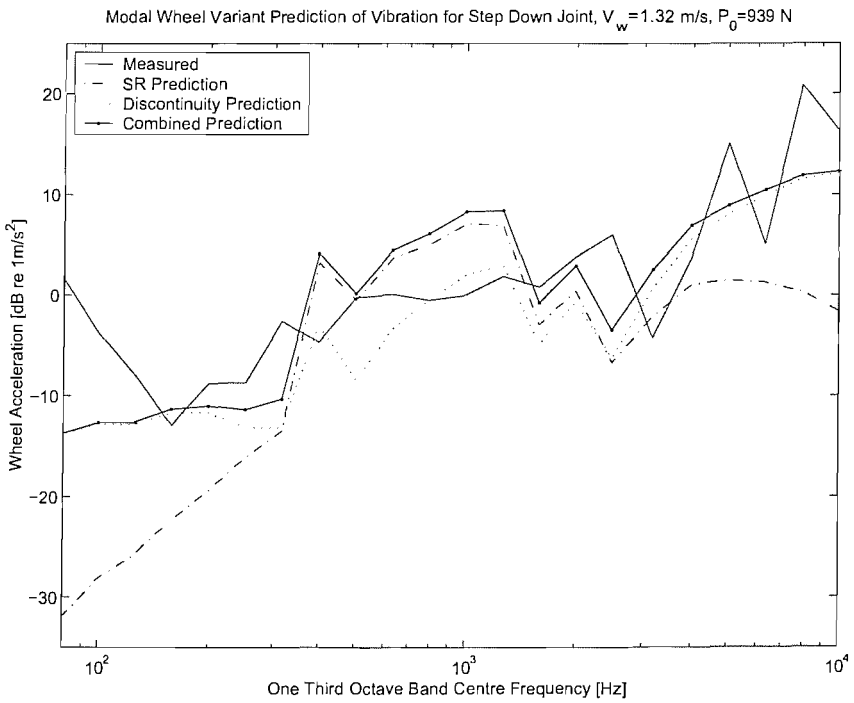

Figure 8–34 Modal wheel variant prediction (with contact filter effects) of wheel acceleration due to the step down joint compared with the measured wheel acceleration for a wheel speed of 1.3m/s at a wheel pre-load of 939N.

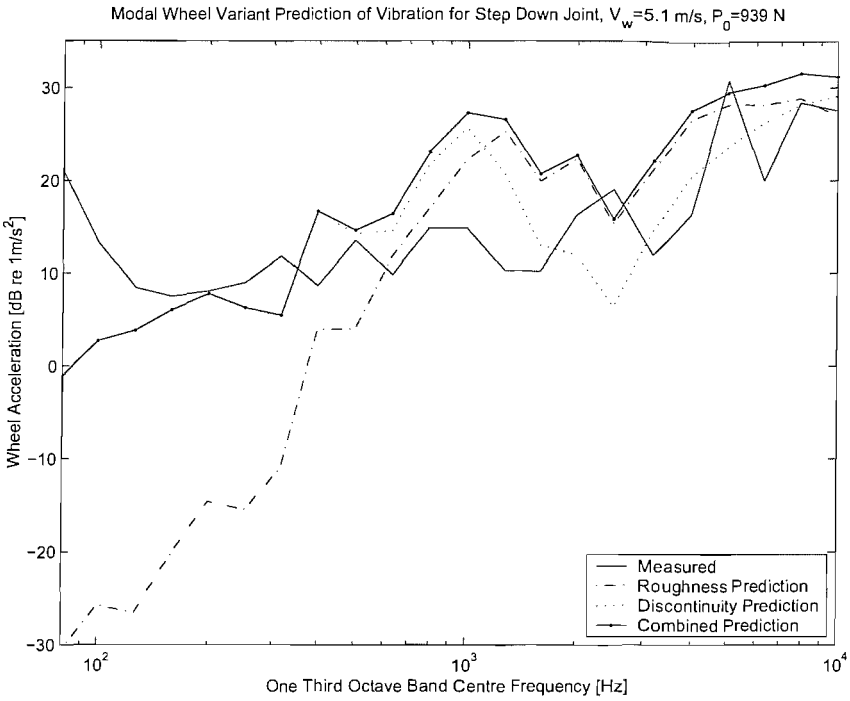

Figure 8–35 Modal wheel variant prediction (with contact filter effects) of wheel acceleration due to the step down joint compared with the measured wheel acceleration for a wheel speed of 5.1m/s at a wheel pre-load of 939N.

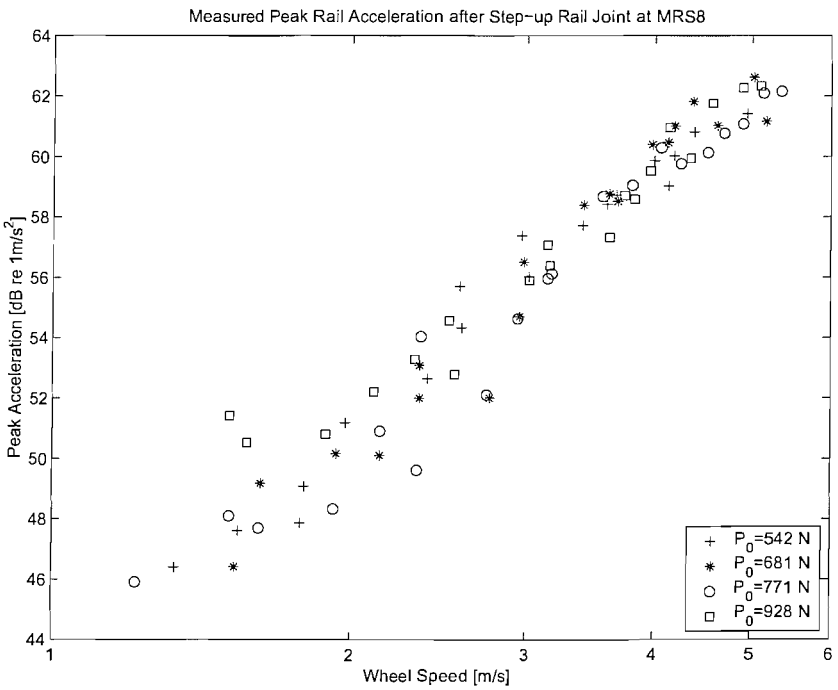

Figure 8–36 Measured peak rail acceleration at MRS8 (just after the step-up joint) for four wheel pre-loads and at wheel speeds in the range of 1m/s to 6m/s.

8.6 Measurements of wheel and rail vibration due to a step-up joint

Measurement and prediction of wheel and rail vibration due to a step-up railhead discontinuity is considered in this section. Measurements of the peak rail acceleration (at MRS8 just after the discontinuity) due to the step-up joint on the 1/5 scale rig are shown in Figure 8–36. This shows that the measured levels for the four wheel pre-loads considered, at wheel speeds in the range of 1m/s to 5m/s, are quite similar. For a particular wheel speed, the measured peak acceleration is not seen to be greater than 63dB re $1m/s^2$ for any of the four wheel pre-loads. The measured peak rail acceleration for smaller wheel pre-loads and wheel speeds is generally greater than that measured for the level joint in Figure 8–14. The levels of the step-down and step-up joint are seen to be within a similar range (50dB to 63dB), but the step-down results follow a different trend. The majority of the measurements in Figure 8–36 are not seen to vary by much more than 2dB due to a change in wheel pre-load at a particular wheel speed. This suggests that the measured peak rail acceleration values are not particularly dependant on the wheel pre-load within the range 500N to 1kN.

The discontinuity part of the step-up surface profile measurement is shown in Figure 8–37. This shows that the step-up joint has a height of 0.5mm. Spectra of the inputs used to predict the vibration of the 1/5 scale rig are presented in Figure 8–38. Here the measured discontinuity part of the input is seen to be of a larger magnitude than the measured surface roughness part of the contribution at wavelengths larger than 3mm. This relationship, however, is altered after the two inputs have been geometrically filtered.

The surface roughness contribution of the railhead once more has a peak at wavelengths between 2mm and 4mm. As for the other step joints at the largest wavelengths considered in Figure 8–38 the discontinuity part of the step joint has the highest levels.

8.6.1 Measurements and predictions of wheel and rail vibration

Predictions of wheel and rail displacements are presented in Figure 8–39. These are calculated using the modal wheel variant non-linear time-stepping model for a wheel speed of 1.5m/s at a 928N wheel pre-load. This model does not predict loss of contact between the wheel and the rail at this speed. Wheel / rail unloading was found to occur at higher speeds for the three lowest pre-loads. The wheel speeds and wheel pre-loads at which loss of contact was found to occur are listed in Table 8-1.

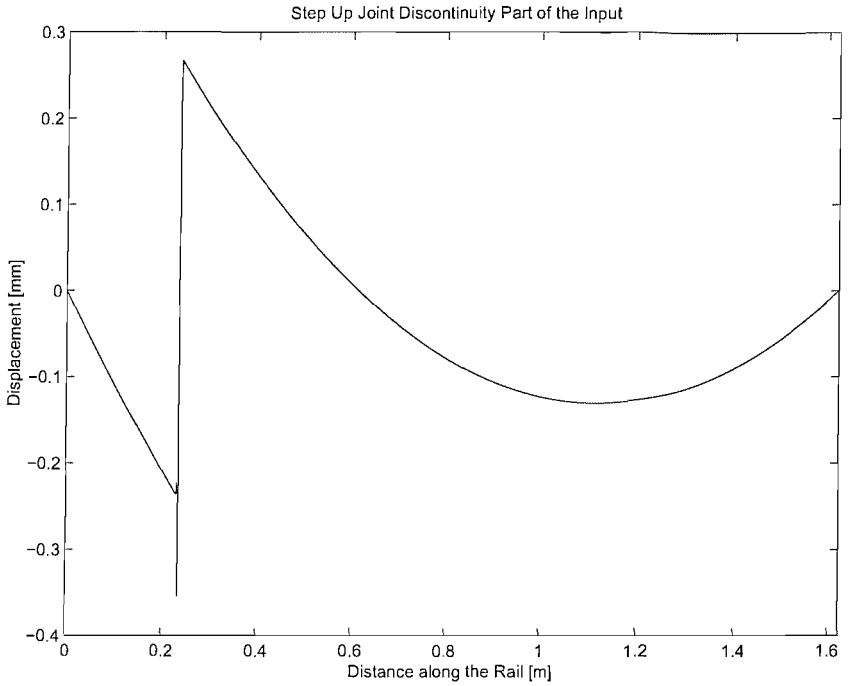

Figure 8–37 The step-up joint discontinuity part of the surface profile measurement.

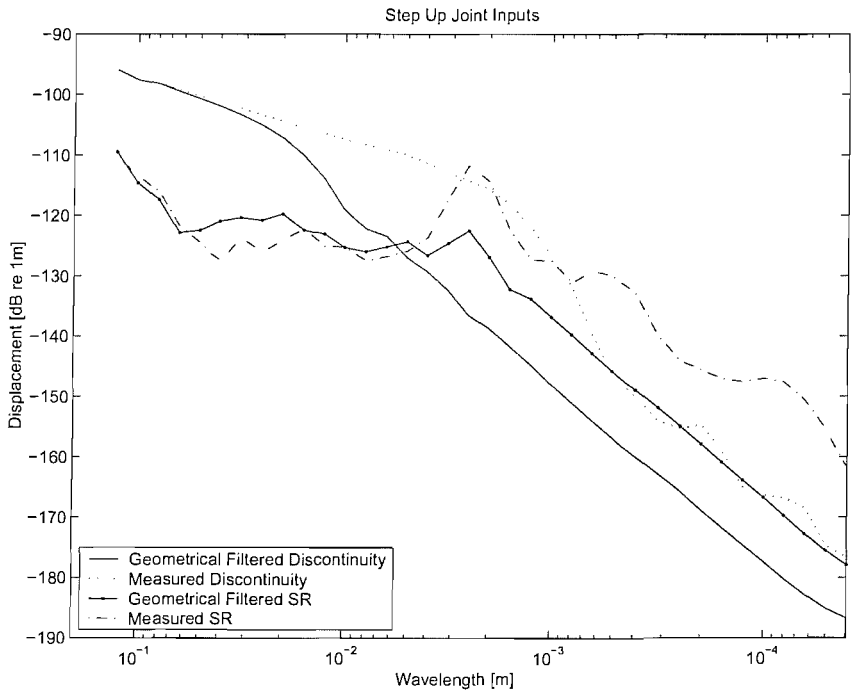

Figure 8–38 Spectra of the discontinuity part of the step-up joint input and the surface roughness contribution of the step-up joint input before and after geometrical filtering.

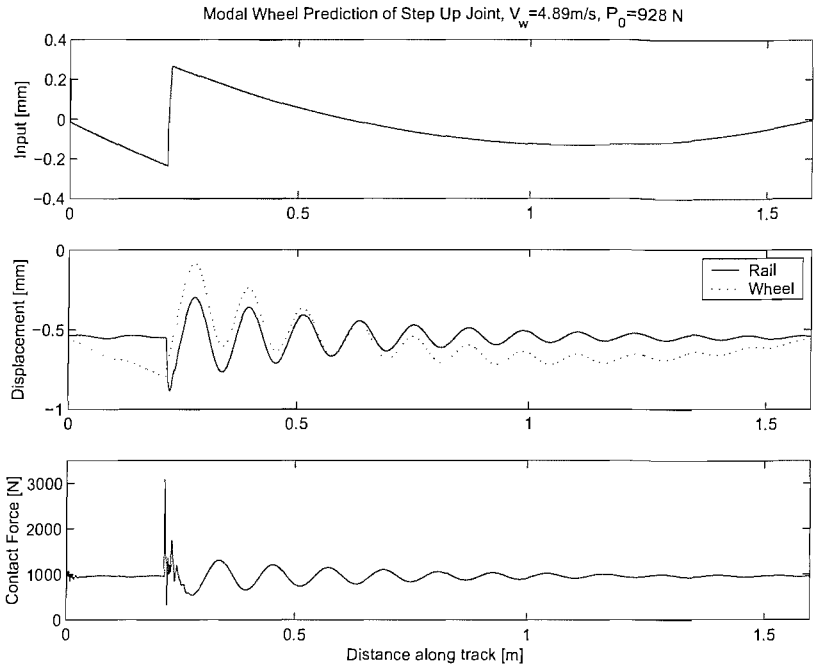

Figure 8–39 Modal wheel variant predicted wheel and rail displacements using the discontinuity part of the step-up input for a wheel speed of 5m/s and a wheel pre-load of 928N. The discontinuity part of the step-up input is also shown along with the predicted contact force.

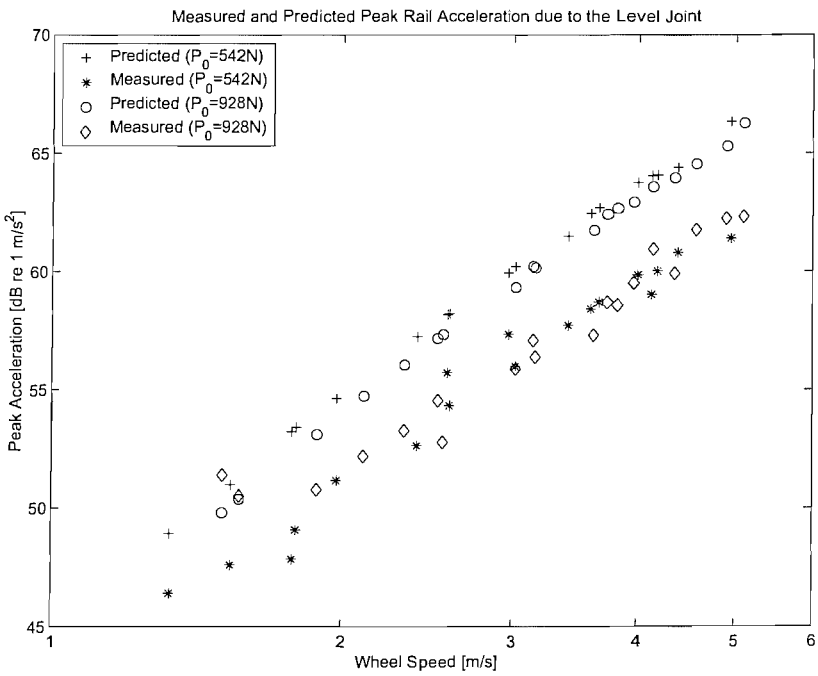

Figure 8–40 Modal wheel variant predicted peak rail acceleration (including contact filter effects) due to the step-up joint and measured peak rail velocity due to the step-up joint for the lowest wheel pre-load (542N) and the highest wheel pre-load (928N) for wheel speeds in the range 1m/s to 6m/s.

Figure 8–40 shows the peak rail acceleration predicted using the modal wheel variant for the lowest wheel pre-load (542N) and the highest wheel pre-load (928N) at wheel speeds between 1m/s and 6m/s. Here the predictions of peak rail acceleration are formed by twice performing first order differentiation in the time domain, after which contact filter effects are included by the time domain filtering technique described in Chapter 5. The predictions in Figure 8–40 are seen to rise with a trend that matches the measured values (10dB re 1m/s for a doubling of speed). The predictions, however, are seen to be approximately 2dB higher than the measurements. Even so, very good agreement is seen between the two sets of results.

The predictions of the rail vibration converted into the frequency domain and differentiated (as spectra) to form acceleration are presented in Figure 8–41 for a wheel speed of 1.5m/s and a 928N wheel pre-load. Here contact filter effects have been included in the prediction, and an overall predicted level (formed from predictions made for each part of the input) is compared with the measured acceleration levels. Figure 8–41 shows that the prediction formed from the surface roughness contribution is at a lower level than the discontinuity contribution. The overall predicted level therefore mainly consists of the prediction formed with the discontinuity part of the input. This was found to be the case for the other step joint predictions presented previously.

The results of the predictions and measurements of rail acceleration for a higher wheel speed of 4.9m/s are shown in Figure 8–42. This shows, again, that the surface roughness contribution does not have any significant effect upon the overall prediction and that the overall prediction is dominated by the discontinuity contribution.

The results of the differences between the overall predicted rail acceleration levels and the measured rail acceleration levels are presented in Figure 8–43 for the four wheel pre-loads at all of the wheel speeds measured. This shows that there is comparatively good agreement between the measurements and the predictions below 500Hz, but, at higher frequencies the predicted levels are larger than the measured levels by up to 10dB.

The differences in levels shown in Figure 8–43 can be attributed to modal characteristics of the modal wheel variant and the adjustments (introduced in Chapter 5) made to the predictions to improve agreement with the measurements. The differences in the 1kHz band, for example, are attributed to the modal wheel variant whilst the under attenuation of the high frequency part of the predictions (1.2kHz to 10kHz) may be due to the contact filter. The results in this frequency range suggest that, for the step-

Figure 8–41 Modal wheel variant predicted (with contact filter effects) rail acceleration and measured rail acceleration due to the step-up joint at a wheel pre-load of 928N at a wheel speed of 1.5m/s.

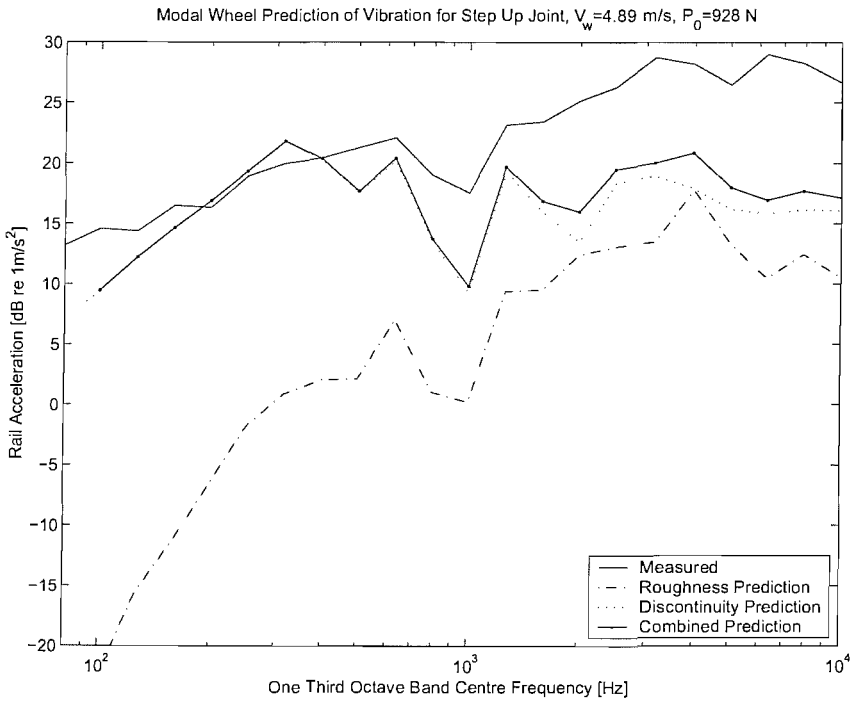

Figure 8–42 Modal wheel variant predicted (with contact filter effects) rail acceleration and measured rail acceleration due to the step-up joint at a wheel pre-load of 928N at a wheel speed of 4.9m/s.

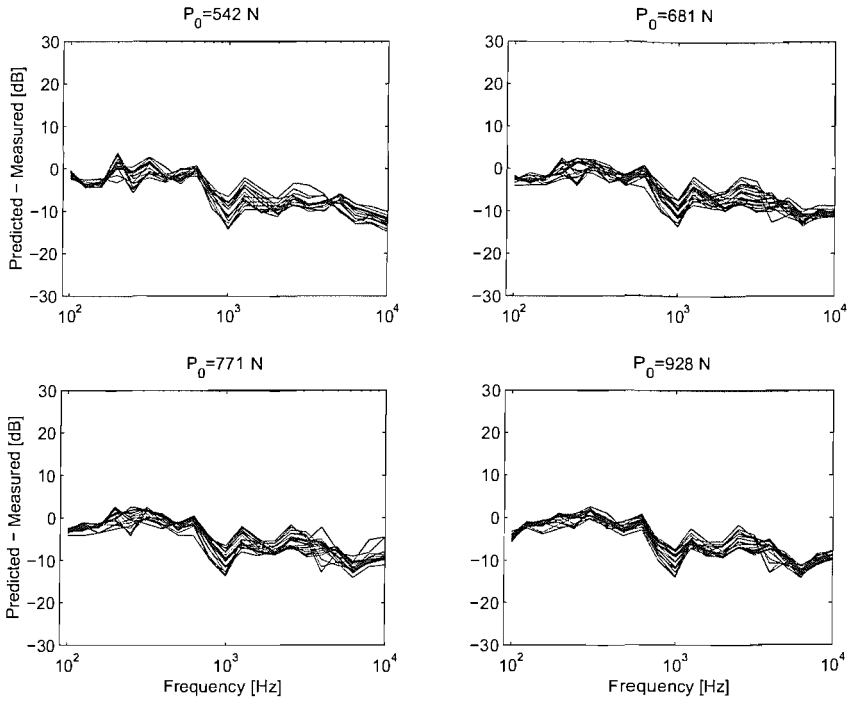

Figure 8–43 Modal wheel variant overall predicted rail acceleration (including contact filter effects) minus the measured rail acceleration for four wheel pre-loads at all the measured wheel speeds due to the step-up joint.

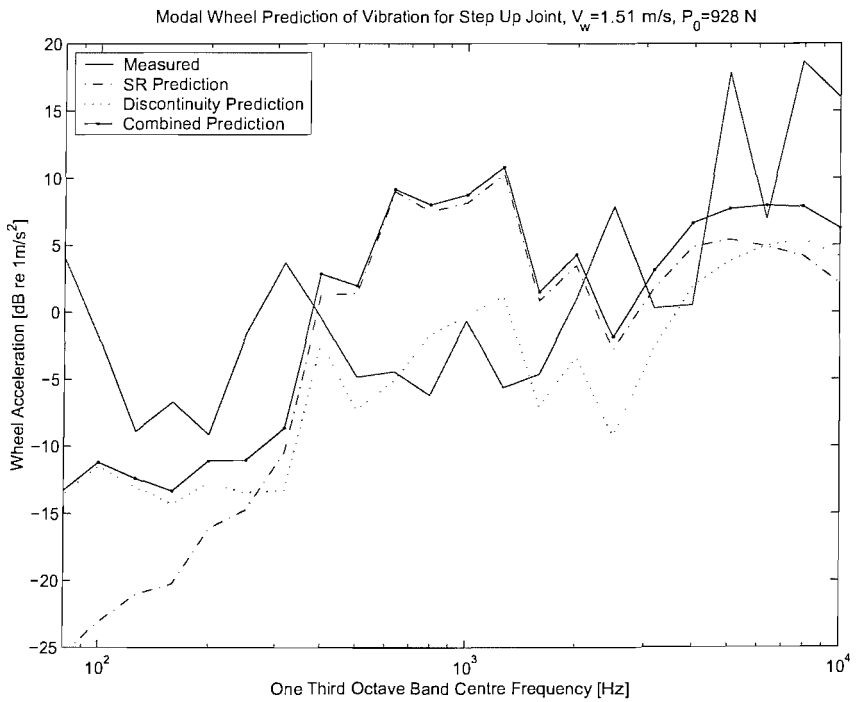

Figure 8–44 Modal wheel variant predicted (with contact filter effects) wheel acceleration and measured wheel acceleration due to the step-up joint at a wheel pre-load of 928N at a wheel speed of 1.5m/s.

up joint, the contact filter behaviour based on the smooth rail case is particularly unsuitable for the discontinuity considered here. This was not the case for the level joint or the step down joint (see Figure 8–23 and Figure 8–33).

Results of the predicted wheel acceleration are presented in Figure 8–44 for a wheel speed of 1.5m/s at a wheel pre-load of 928N. As has been found for the other step joint discontinuities presented previously, the prediction formed from the surface roughness contribution of the input plays a greater role in the overall predicted levels than it does for the prediction of rail vibration. It can be seen from Figure 8–44 that the predictions of wheel acceleration due to the surface roughness contributions are greater than the predicted levels formed with the discontinuity part of the input between 300Hz and 7kHz.

Again the results of the predictions show that the discontinuity part of the input dominates the prediction of rail vibration. The surface roughness part of the input, however, has been found to be important for the prediction of wheel vibration.

8.7 Analysis of the predicted contact force

Differences between the two model variants, such as at the wheel on track resonance, has been seen to alter the predictions of contact force. For example, predictions of the level joint using the modal variant indicated the wheel did not lose contact with the rail within the range of wheel speeds considered (1m/s to 5m/s) for the two highest wheel pre-loads. This is shown in Table 8-1, where similar predictions using the simple wheel variant predicted that loss of contact would occur within the wheel speed range considered at each of the wheel pre-loads.

Predictions of the peak contact force for the simple variant and the modal wheel variant are presented in Figure 8–45 for the level joint, Figure 8–46 for the step-down joint, and Figure 8–47 for the step-up joint. These three sets of results are presented as a ratio of peak contact force to static contact force. It is clear that the results are larger for the simple variant than for the modal wheel variant. This is particularly noticeable at higher wheel speeds, for each of the step joints considered. These results demonstrate that the properties of the prediction models should be carefully considered when discontinuities are included in an input. The wheel on track resonance, for example, should be carefully considered to ensure that the behaviour of wheel / rail interaction of discontinuities on the railhead surface are modelled correctly. This has been seen to play an important role in the prediction models as it manifests itself as a strong sinusoidal fluctuation in the

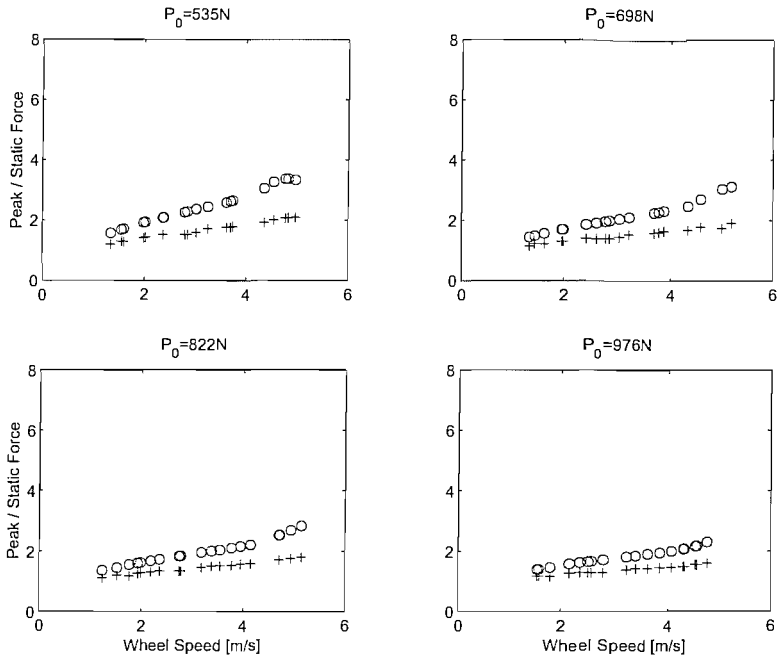

Figure 8–45 Ratio of predicted peak to static contact force due to the level joint as a function of wheel load and wheel speed. These predictions have been made using the discontinuity part of the level input. Key:- 'o'= Simple variant, '+'= modal wheel variant.

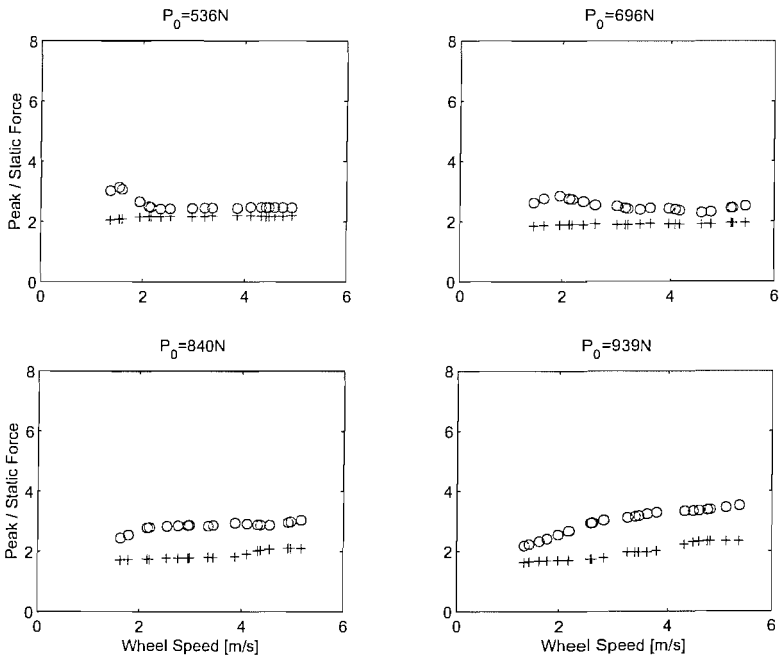

Figure 8–46 Ratio of predicted peak to static contact force due to the step-down joint as a function of wheel load and wheel speed. These predictions have been made using the discontinuity part of the step-down input. Key:- 'o'= Simple variant, '+'= modal wheel variant.

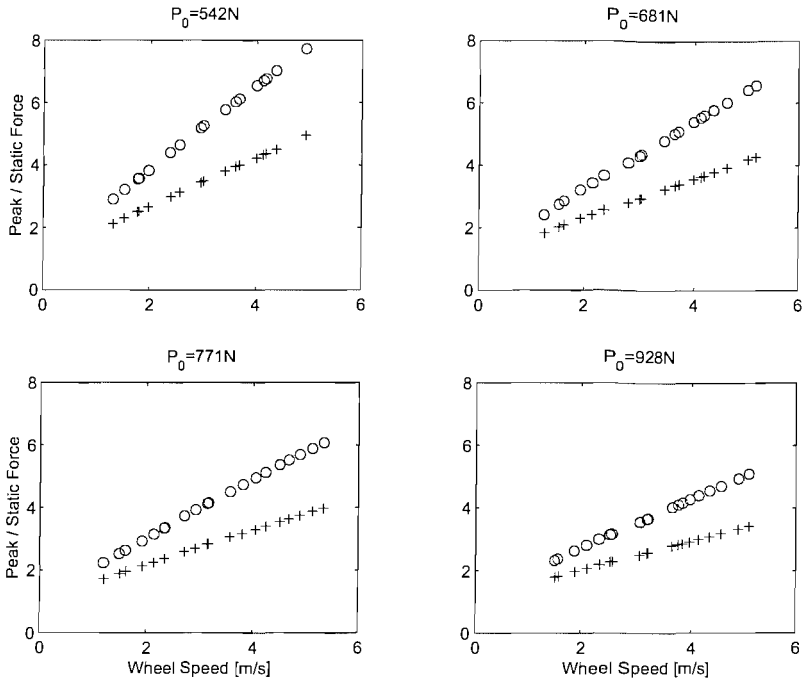

Figure 8–47 Ratio of predicted peak to static contact force due to the step-up joint as a function of wheel load and wheel speed. These predictions have been made using the discontinuity part of the step-up input. Key:- 'o'= Simple variant, '+'= modal wheel variant.

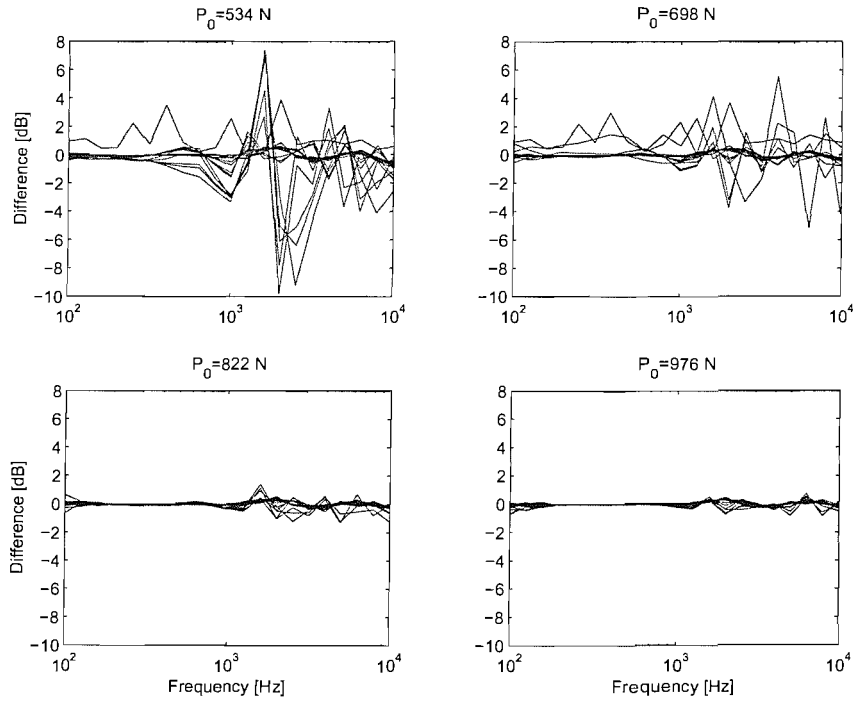

Figure 8–48 Non-linear contact force level minus linear contact force level predicted using the simple variant for the level joint, for wheel speeds in the range 1m/s to 5m/s at four wheel pre-loads.

output. Indications of the frequency at which the scale rig wheel on track resonance occurs have been shown in Figure 8–11 and Figure 8–12 where 80Hz fluctuations after the peak acceleration are evident. Unfortunately reliable measurements have not been made at the low frequencies associated with the wheel on track resonance. This is important information and should be investigated in the future to enable improved performance of the prediction models.

The predicted peak to static contact force ratios due to the level joint (Figure 8–45) show that the predicted contact force is close to the value of the static wheel pre-load at low wheel speeds, but that it is at least twice as large as the wheel pre-load at the highest wheel speeds considered. A linear trend is seen for each set of predictions no matter which model variant has been used.

This is not the case for the step-down joint predictions shown in Figure 8–46. At low wheel pre-loads (536N and 696N) the contact force ratio predicted using the modal wheel variant is seen to be fairly constant for predictions formed at wheel speeds within the range of 1m/s to 6m/s. It is generally twice a large as the wheel pre-load. The result from the simple variant at these wheel pre-loads, however, is seen to fall slightly with an increase of wheel speed. At wheel pre-loads of 840N and 939N both models are seen to predict small rises in the peak contact force when the wheel speed is increased from 1m/s to 6m/s.

The results for the step-up joint were found to differ from the other two step joints. Figure 8–47 shows that the simple variant predictions rise at a slightly higher rate than the modal wheel variant predictions. The differences between the two trends get larger for the faster wheel speeds considered. The predicted peak contact force is seen to rise from a level that is approximately twice that of the wheel pre-load to levels that as much as eight times the wheel pre-load. The results in Figure 8–47 indicate smaller ratios of peak to static contact force with a greater wheel pre-loads.

A method of assessing the predicted non-linear behaviour of wheel / rail interaction was presented in Chapter 7 where comparisons were made between results from a non-linear time stepping model and a linear time-stepping model. This method involved high-pass filtering the predicted contact force so that effects of the wheel on track resonance that had been incorrectly excited by the numerical routine starting transients were removed from the data. As explained previously, this was done to improve the spectra of the non-linear and linear predictions before the levels of the spectra were subtracted from each other. An example of these results using the contact force predicted using the simple

variant is shown in Figure 8–48 for the level joint. Here the predicted non-linear contact force level minus the predicted linear contact force level is presented for four wheel pre-loads at wheel speeds ranging from 1m/s to 5m/s.

A strong effect of pre-load is seen in the differences of predicted contact force in Figure 8–48. At the lowest wheel pre-load (534N), the largest differences in the predicted levels are as much as 10dB. The differences for the largest wheel pre-load (976N), however, are much smaller (less than 1dB). The differences are seen to have both positive and negative values across the frequency range considered (100Hz to 10kHz). This means that in particular frequency bands both the non-linear predicted levels and the linear predicted levels are larger than each other. For example at the lowest wheel pre-load (534N) in the 2kHz one-third octave band, the linear predicted contact force level is about 10dB larger than the non-linear predicted contact force level. The larger differences occur at the highest wheel speeds considered.

Similar results are shown in Figure 8–49 for the modal wheel variant predictions. Smaller differences in the levels are seen here than for the simple model. The maximum difference is 6.2dB compared with 10dB in Figure 8–48. As for the simple variant results, a reduction in the predicted difference levels occurs with an increase of wheel pre-load. These results therefore suggest that more non-linear behaviour occurs for the level joint at the lower wheel pre-loads. This agrees well with the conclusions of [Wu and Thompson 2000(a)]. Larger wheel pre-loads therefore have been seen to reduce the requirement for a non-linear prediction (for the level joint) across the frequency range considered (100Hz to 10kHz), as little difference between a non-linear prediction and a linear prediction is seen.

Results for the predicted contact force for the step-down joint were found to vary much more than those of the level joint. Large differences between the predicted non-linear contact force spectra and the linear contact force spectra are shown in Figure 8–50. These differences are seen to vary for each of the wheel pre-loads considered. The lower wheel pre-loads of 536N and 696N are seen to have the largest variations of the differences between the linear and non-linear predictions. The differences are seen to vary not only with wheel pre-load, but also with a change of wheel speed. The predictions at higher wheel speeds were found to be in better agreement with each other. The differences in the predicted levels are also seen to improve with an increase in wheel pre-load. For example the results at 840N and 939N are seen to contain smaller differences than the results at the lower wheel pre-loads.

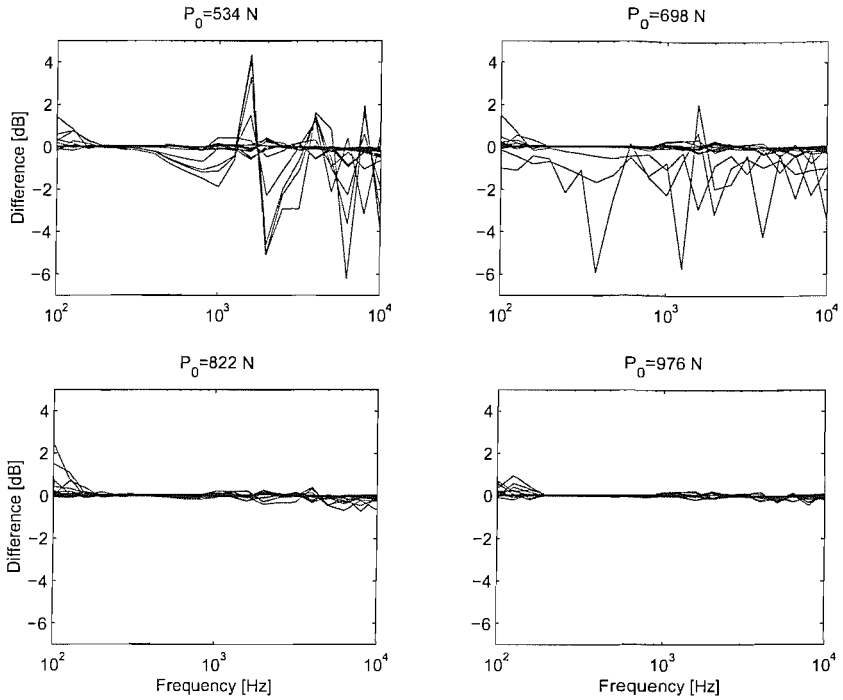

Figure 8–49 Non-linear contact force level minus linear contact force level predicted using the modal wheel variant for the level joint, for wheel speeds in the range 1m/s to 5m/s at four wheel pre-loads.

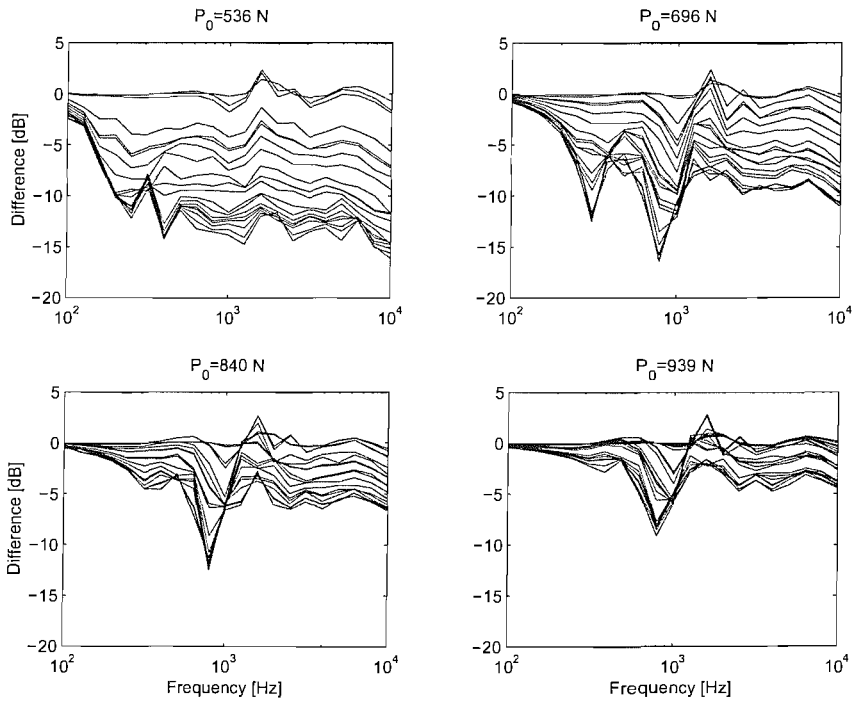

Figure 8–50 Non-linear contact force level minus linear contact force level predicted using the simple variant for the step-down joint, for wheel speeds in the range 1m/s to 5m/s at four wheel pre-loads.

Results of the differences of the predicted contact force spectra formed with the modal wheel model are presented in Figure 8–51. The results shown here are different from the results shown in Figure 8–50, but there are similarities. Similar tendencies in the results at the lower wheel pre-loads (536N and 696N) are seen. Improvements in the agreement of the linear and non-linear predictions are again found to occur for higher wheel speeds and for larger wheel pre-loads.

The difference between the linear and non-linear simple variant predicted contact force due to the step-up joint are presented in Figure 8–52. At the three lower wheel pre-loads both positive and negative differences in the predicted contact force spectra are seen. The results for the highest wheel pre-load (928N) are generally positive values. This means that the non-linear predicted levels were smaller than the linear predicted levels.

Figure 8–53 presents the modal wheel variant predictions for the step-up joint. This shows that for the four wheel pre-loads considered, the non-linear contact force spectra are larger than the linear contact force spectra at frequencies above 1kHz. Differences in the spectra below 1kHz are very small (less than 0.2dB).

8.8 Conclusions

Many measurements of the response were made for the wheel running across the step joint discontinuity. These measurements showed that the presence of the step joint only affected the accelerance of the track close to the discontinuity. For this reason the track frequency response described by the polynomial representation presented in Chapter 5 was used in the prediction models as it resembled the majority of the track behaviour. This choice may be questioned. Ideally the track model should be able to change as the wheel rolls along the rail. If this was to be incorporated into the prediction, the properties of the track either side of the discontinuity could have been the same as those used in Chapter 5, and another set of properties could have been used to describe the properties closer to the joint. This type of alteration, however, was not implemented into the predictions due to restrictions of time.

A problem associated with the manner in which the track frequency response was modelled at lower frequencies is that the ballast stiffness of the track made with two half lengths of rail was found to be greater than that measured for the whole rail length in Chapter 5. This is shown in Figure 8–9 and Figure 8–10. It is therefore unlikely that the wheel on track resonance of both of the prediction models agree well with the real case. The wheel on track resonance together with other differences between the two

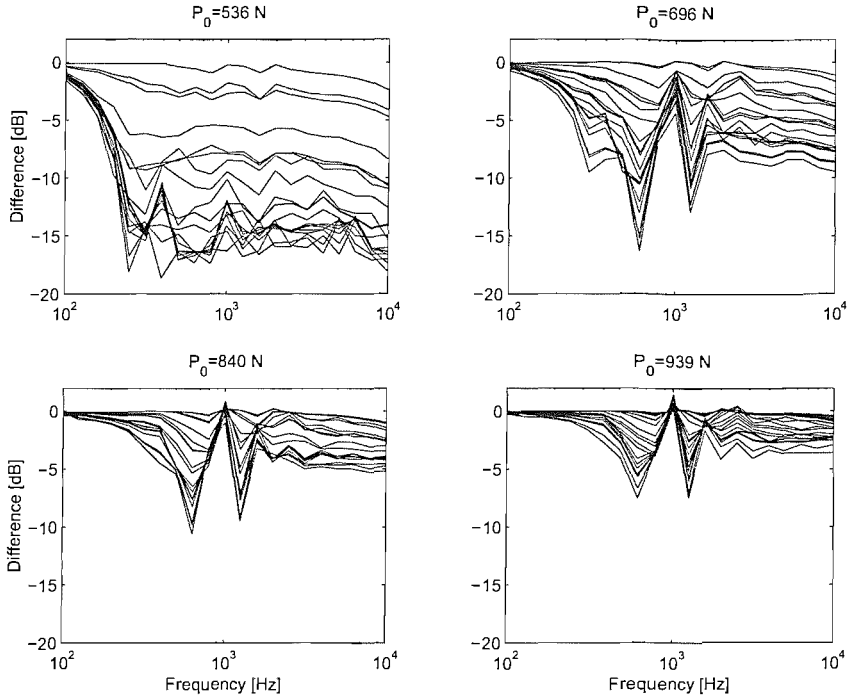

Figure 8–51 Non-linear contact force level minus linear contact force level predicted using the modal wheel variant for the step-down joint, for wheel speeds in the range 1m/s to 5m/s at four wheel pre-loads.

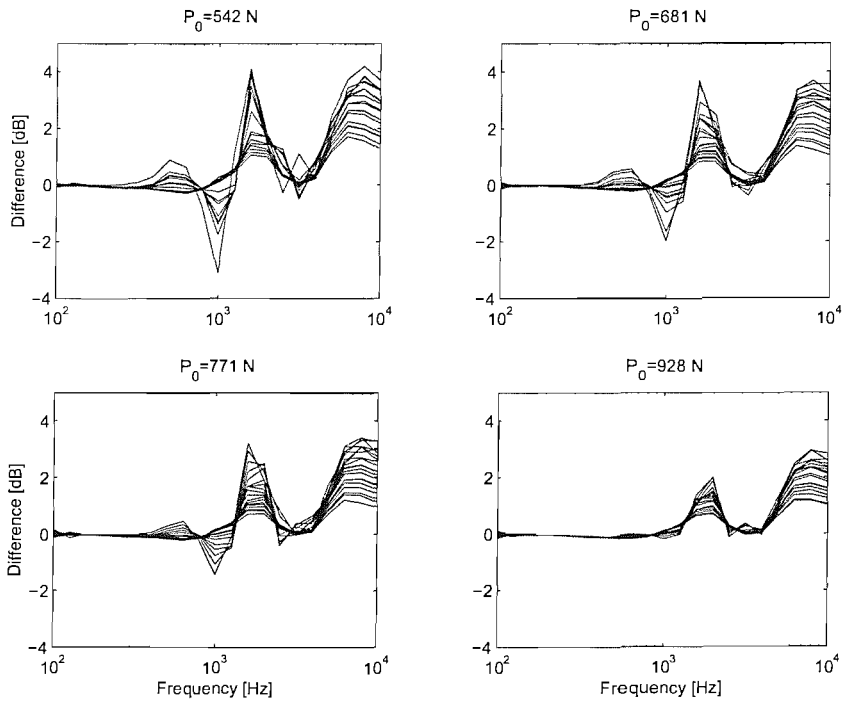

Figure 8–52 Non-linear contact force level minus linear contact force level predicted using the simple variant for the step-up joint, for wheel speeds in the range 1m/s to 5m/s at four wheel pre-loads.

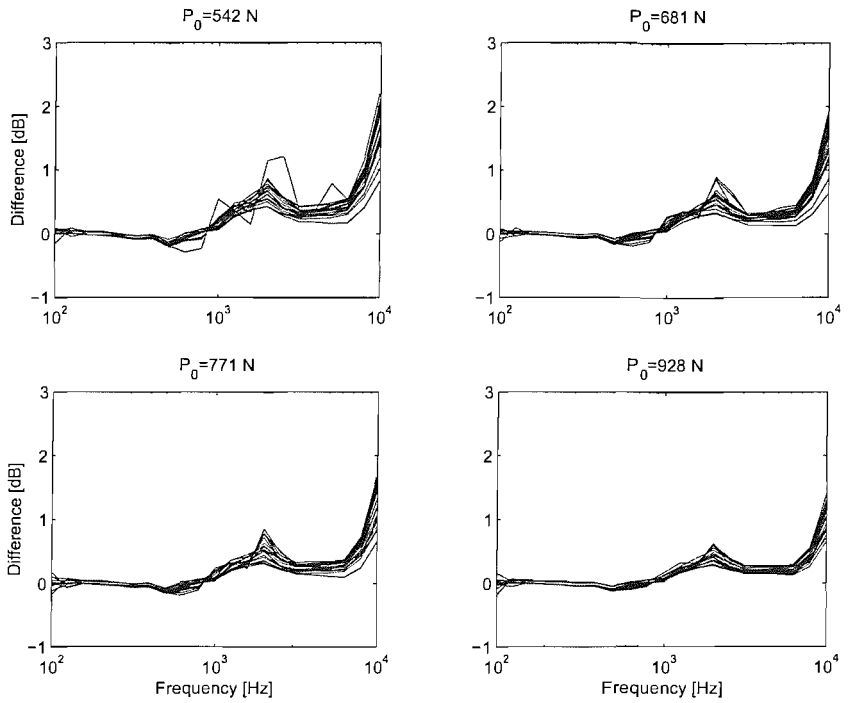

Figure 8–53 Non-linear contact force level minus linear contact force level predicted using the modal wheel variant for the step-up joint, for wheel speeds in the range 1m/s to 5m/s at four wheel pre-loads.

model variants have been seen to produce different results using the same input. This will have introduced errors into the predicted peak values of wheel / rail displacement and contact force.

Despite these problems, measurements and predictions of the vibration due to each of the step joints have shown good agreement. Comparisons of the measured and predicted rail acceleration made for the level joint and the step-up joint gave almost as good agreement as the case for the surface roughness input in Chapter 6. The predictions and measurements due to the step-down joint were found to be in worse agreement. It is not clear why this is so. Analysis of the contact force suggests that non-linear behaviour is less likely at the highest wheel pre-loads. Comparisons with the measurements, however, showed poorer agreement with the predictions for the higher wheel pre-loads, together with large variations in the differences for changes in wheel speed (see Figure 8–33). One possible explanation for this poor agreement, might be that the measurements were contaminated by unknown effects due to excessive compression of the rig track bed when the wheel hit the rail after the step joint. The size of the step-down joint may have been too large for the scale rig. Thorough investigations into any possible causes were not made due to time restrictions within the project.

The method presented in Chapter 7, in which the overall predicted level was constructed from the predictions formed from the discontinuity part of the input and the surface roughness part of the input demonstrated the relative importance of each part of the railhead surface profile. Generally it was found that for rail vibration, the predictions formed from the discontinuity part of the step input contributed the most towards the overall predicted level, although this is dependant upon the size of the step. The predictions formed with the discontinuity part of the level joint for example did not dominate the overall predicted level to the same extent as in the step-down joint case.

The requirement for a reliable two dimensional contact filter was quite apparent as the corrections applied to the predictions formed from the discontinuity parts of the inputs did not result in agreement with the measurements. This was the case even for the level joint where the overall predicted vibration is significantly influenced by the surface roughness of the wheel and railhead and therefore is less reliant on the prediction from the discontinuity part of the input.

Results of the difference in levels of the predicted contact force using a non-linear and a linear predictions were found to provide interesting insight into the extent of non-linear behaviour of the contact spring at each of the step joints. Generally it was found that

less non-linear behaviour was evident for the predictions of contact force (due to the step joints) at the higher wheel pre-loads (greater than 750N). The comparisons made for the step-up and level joint showed the most consistent trends. Whilst results for the step-down joint showed less variations with wheel speed for the higher wheel pre-loads (840N and 939N), the results were different from each other at each wheel speed.

Analysis of the spectra of non-linear and linear predictions of contact force has shown that for the step-down joint the differences in spectral levels (non-linear minus linear) are mainly negative, for small step joint dimensions (i.e. the level joint), the differences are both negative and positive, and for the step-up joint the differences are mainly positive. This result indicates that the non-linear contact spring force is mostly larger than the contact force due to the wheel pre-load for a step-up joint, whilst the non-linear contact force is mostly smaller than the contact force due to a wheel pre-load for a step down joint.

9 Wheel / rail vibration due to dipped rail joints

9.1 Introduction

Dipped rail joints are common features of railway track that occur where lengths of rail are joined together. Dips occur at the ends of the rail lengths as a by-product of their manufacturing process. This causes the ends of the rail to slope downwards. When two rails are joined together the combined profile results in a downward slope (at the end of one rail), to depths of up to 5mm, followed by a rise (at the start of the next rail) over a combined length of approximately 1m at full scale [Wu and Thompson, 2001(b)]. Rails are usually joined together either by the use of a fish-plate arrangement or by welding. 'Continuously welded' rail has become common-place over the last 30 years and is now widely used for mainline / high speed track. Geometry representing dipped welded joints is studied in this chapter using two dips that have been machined on to a 1/5 scale railhead.

9.2 Manufacture of the dipped rail profiles

Two dipped rail profiles were machined, using a computer numeric control (CNC) process, into the railheads of 1/5 scale rails at depths of 1mm and 2 mm. These depths correspond with full scale dimensions of 5mm and 10mm respectively, which are the same depths of the dip joints used by [Wu and Thompson, 2001] for their analytical investigations.

The intended shape of the dipped joints for the scale rig is shown schematically in Figure 9–1, where the vertical axis has been exaggerated to show the designed shape. Each of the dips was designed to be contained within a length of 250mm, and each dip was positioned in the middle of the measurement section, with the lowest point of each dip at the mid-span position MRS8 (see Figure 3-14). The lateral railhead curvature along the length of each dip was intended to be consistent with the railhead curvature of the rest of the track. Thus the CNC machining process not only involved the machining of the dip profile along the length of the railhead, but also a 40mm curvature across the railhead surface. The dips were designed to start and end with gentle gradients over the first and last 80mm of the dip lengths. The remaining 90mm section in the centre of the dip joint consisted of two sharp radii, that represented the ends of the joining rails.

Figure 9–2 and Figure 9–3 show the measured profiles of the rails from which it is clear that the CNC machining process was not able to follow the subtle curves along the

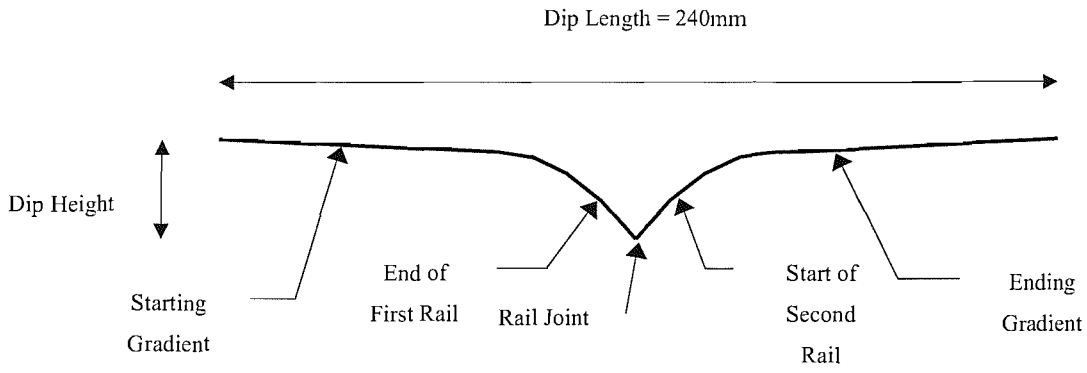

Figure 9–1 Schematic diagram of the 1mm and 2mm dipped rails.

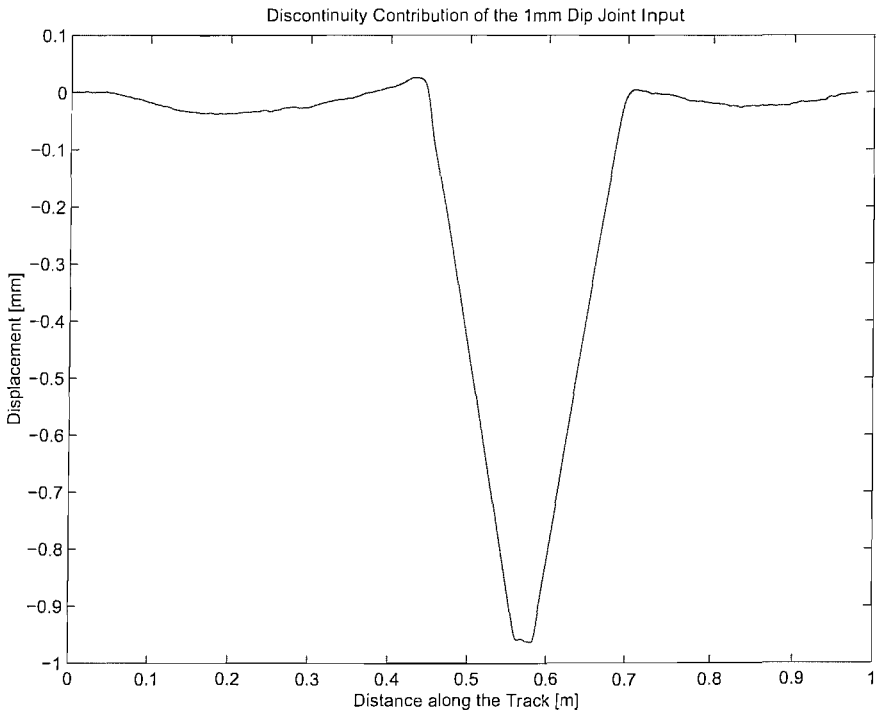

Figure 9–2 The 1mm dipped rail (discontinuity) input used for predictions.

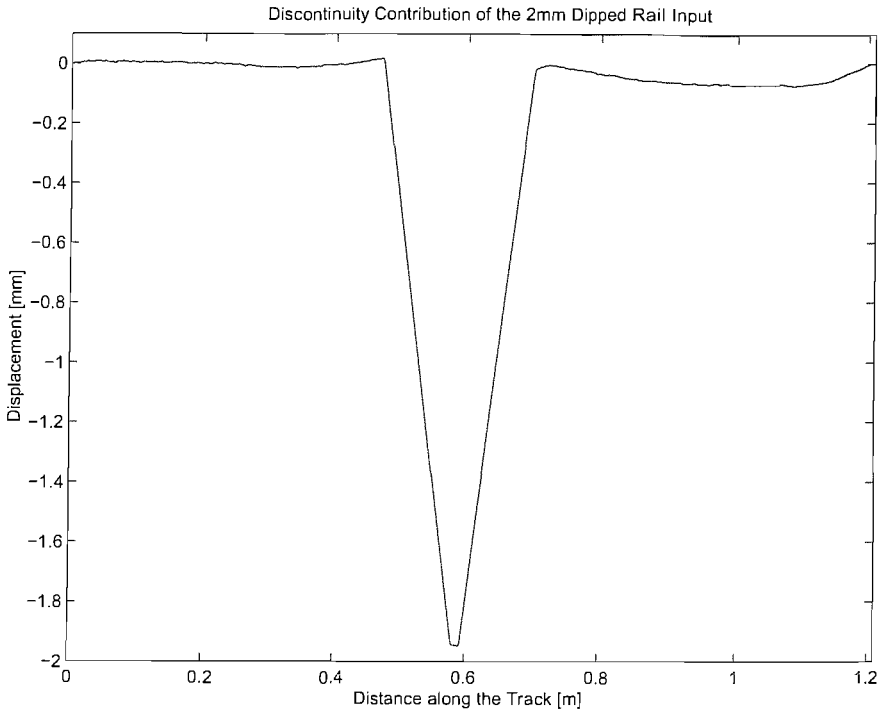

Figure 9–3 The 2mm dipped rail (discontinuity) input used for predictions.

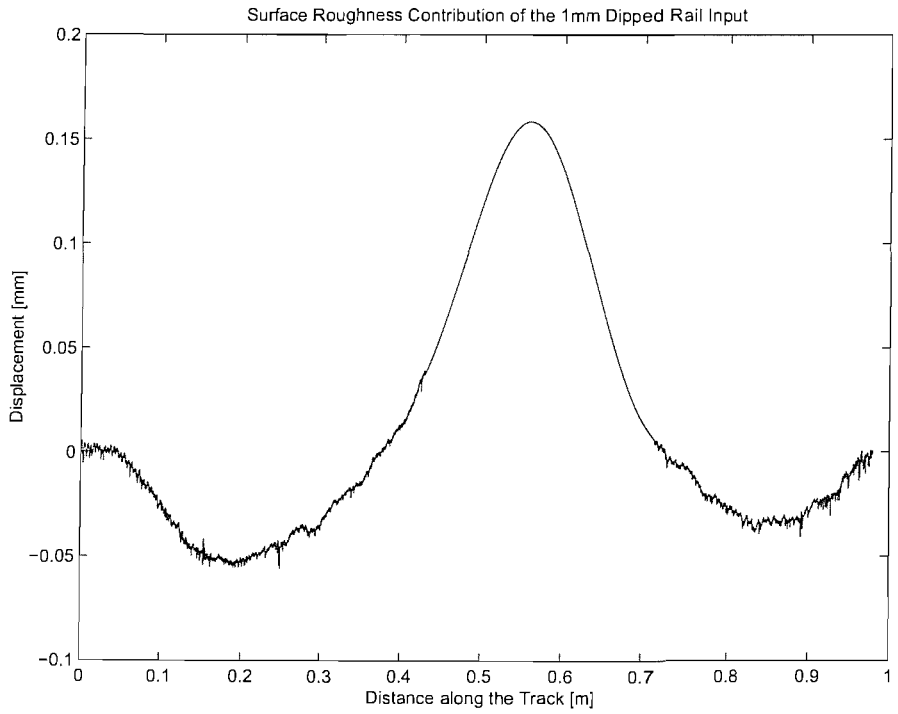

Figure 9–4 Example of the (1mm) dipped rail profile with the discontinuity part of the profile removed and replaced by an artificially smooth fitted curve section.

length of the rail shown in Figure 9–1. The transitions into the dip were not present; in fact they have been machined with a linear shape rather than a curved shape as in Figure 9–1. Furthermore, at the lowest point of the dip a small flat spot was evident for both of the dipped rails. The profiles shown in Figure 9–2 and Figure 9–3 suggest that the depths of the dips are also slightly less than the design requirements. This is not actually the case. As for other railhead profiles, measurements of the simulated dip joint profiles were made after many 'rolling wheel' measurements had been made over each discontinuity, when a line showing the wheel / rail contact path was distinguishable from the duller railhead surface. Measurements of the surface profile were made along this line to obtain an input to the prediction models that was as representative as possible of the real case. The rig wheel did not run exactly in the centre of the railhead due to manufacturing restrictions of the 1.5m long rig rail and slight lateral movements of the rig wheel on its axle shaft. Because of this, the geometry of the dips shown in Figure 9–2 and Figure 9–3 appears not to be as deep as their design requirements. Even though these dips do not match that of the design requirement, these measured profiles are representative of the input to the wheel / rail system, and these dipped rails provide useful measurement data.

9.3 Input profiles and their spectra

The dipped joint surface profiles presented in Figure 9–2 and Figure 9–3 show the discontinuity part of the inputs used for all of the predictions presented later in this chapter. These inputs have been constructed from measurements of each dipped joint surface profile in a manner similar to the method presented in Chapter 7. This method, however, has been modified so that longer discontinuities can be analysed.

Use of the existing method, presented in Chapter 7, would cause a problem with the dipped rail joints as these discontinuities on the 1/5 scale rig are 0.25m long whereas the other discontinuities that have been studied are under 4mm long. The length of the dipped joint profiles makes it difficult to separate the surface roughness contribution of the profile from the discontinuity part by simply cutting out the discontinuity from the measurement of the railhead. If the existing method was to be used for the dipped rail joints, it would produce two short input lengths of surface roughness coupled together by an artificially smooth section (where the discontinuity has been removed). This would mean that the spectral level of the surface roughness contribution would be incorrect as it would contain an artificially smooth section. This is not in itself a problem as corrections can be applied to adjust for the inclusion of the artificially

smooth section, but the discontinuity input would contain surface roughness as well as the change in geometry. This is not desirable, as the aim of the method in Chapter 7 is to separate the discontinuity from the surface roughness part of the input so that the effect of adjustments derived in Chapter 5 can be assessed.

An alternative method of obtaining inputs for the prediction of vibration due to dipped joint profiles was therefore devised. This involved the following steps:

1. The spectra of the roughness contribution of the railhead on either side of the dipped joint discontinuity was calculated. This was done by use of the existing method in Chapter 7, where a section of the measurement that represented the discontinuity was removed and replaced with an artificially smooth section. An example of this is shown in Figure 9–4. As stated previously, the level of the spectra calculated from this representation needs to be corrected. This is done by applying a ratio of the appropriate lengths, as shown in equation (9-1):

$$L_{tot} = L_s - 10\log_{10}([l_1 - l_2]/l_1) \qquad (9\text{-}1)$$

where: L_{tot} is the overall surface roughness spectral level,

L_s is the estimated surface roughness level calculated from the surface profile measurement with the artificially smooth surface roughness in place of the discontinuity,

l_1 is the length of the original surface profile measurement,

l_2 is the length of the discontinuity / artificially smooth section.

This correction needs to be made before the modified surface roughness contribution can be compared with the original surface profile measurement.

2. The estimate of the modified surface roughness spectrum (found from using step 1 above) was then compared with the spectrum formed from the original surface roughness measurement. This is shown in Figure 9–5. Here the whole surface profile spectral estimate is dominated at long wavelengths by the discontinuity part of the profile. This is not the case for the surface roughness contribution of the input. Figure 9–5 shows that the contributions from the discontinuity and surface roughness are of similar spectral amplitude at a wavelength of 9mm.

3. The wavelength at which the discontinuity and surface roughness contributions are similar is then used as a cut off point from which the measured surface profile data was filtered into two parts. A discontinuity input was constructed by using a low

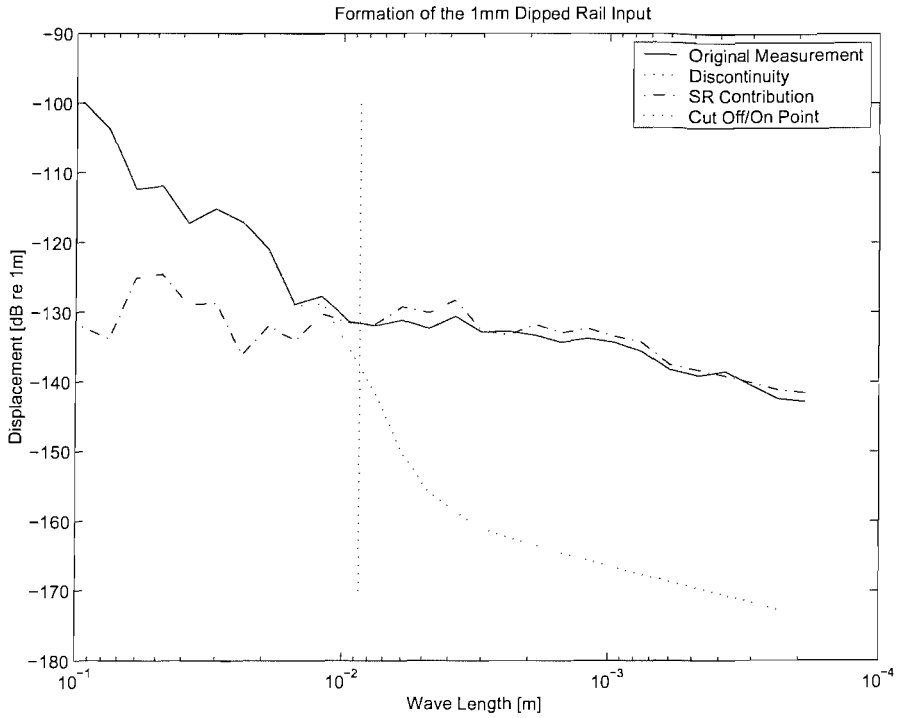

Figure 9–5 The 1mm dipped rail surface roughness and discontinuity contributions compared with the original measurement.

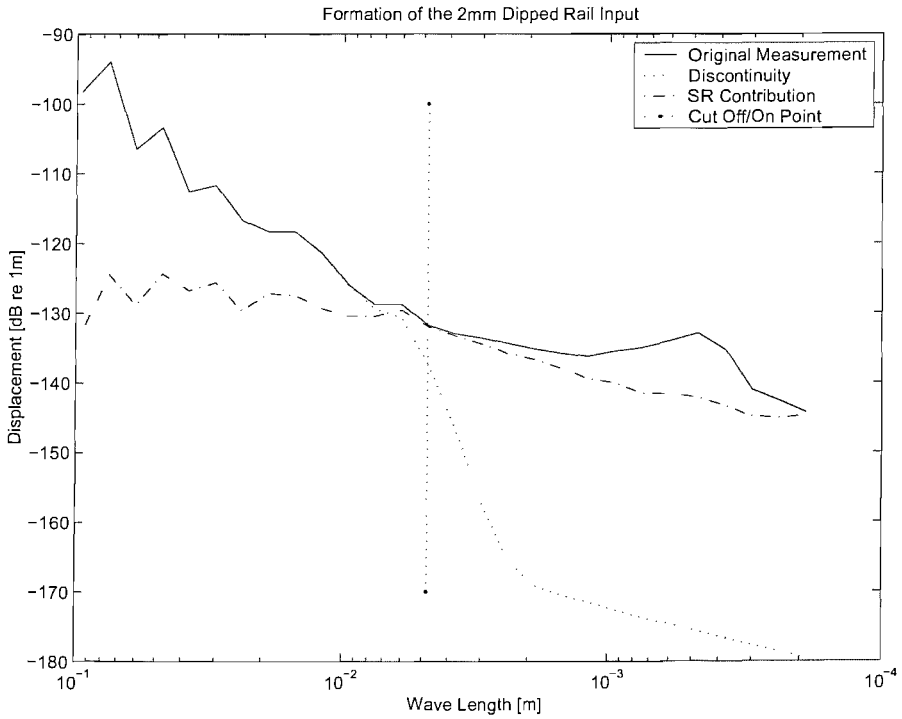

Figure 9–6 The 2mm dipped rail surface roughness and discontinuity contributions compared with the original measurement.

pass filter, and the surface roughness contribution input was constructed by high pass filtering the surface profile measurement. The filtering was performed in the time domain using 3rd order Butterworth filters within the FILTFILT routine in MATLAB. The cut-off or cut-on frequency of the low-pass and high-pass filters was the same for each of the dipped joint types. This was calculated for the measurement speed of the surface profile measurement (i.e. the average speed at which the LVDT transducer traversed the railhead) using the following relationship:

$$f_c = \frac{V_{meas}}{\lambda_c} \tag{9-2}$$

where: f_c is the filter cut-on / cut-off frequency,

V_{meas} is the measurement speed of the surface profile measurement,

λ_c is the wavelength of discontinuity and surface roughness similar amplitudes.

The cut off frequencies for each of the joints were different. The 1mm dipped joint spectra met at a wavelength of 9mm, whilst the 2mm dipped joint spectra met at a wavelength of 5mm. As the measurement speeds for each of the surface profiles were also slightly different, the resulting cut-off / cut-on filter frequencies were found to be 10Hz for the 1mm dip and 12Hz for the 2mm dip joint. Spectra of the surface roughness (SR) contribution, the discontinuity part of the input, and the position of the cut-off / cut-on point of the filter are shown in Figure 9–5 for the 1mm dipped joint and Figure 9–6 for the 2mm dipped joint.

Examples of the resulting discontinuity inputs for the 1mm dipped rail and the 2mm dipped rail have already been shown in Figure 9–2 and Figure 9–3 respectively. The surface roughness contributions of the 1mm dip and the 2mm dip are presented in Figure 9–7 and Figure 9–8. Both of the representations of the surface roughness contributions of the dipped joints show that the CNC machined sections are rougher than the neighbouring railhead surfaces. This is particularly noticeable for the 2mm dipped joint (see Figure 9–8).

As for all of the predictions presented in this thesis, the dipped joint inputs were geometrically filtered before being used in the prediction models. Figure 9–9 shows the spectra of the two 1mm dipped joint inputs after geometrical filtering. The large wavelengths are seen to be dominated by the discontinuity part of the input, whilst shorter wavelengths are dominated by the surface roughness contribution. The spectra

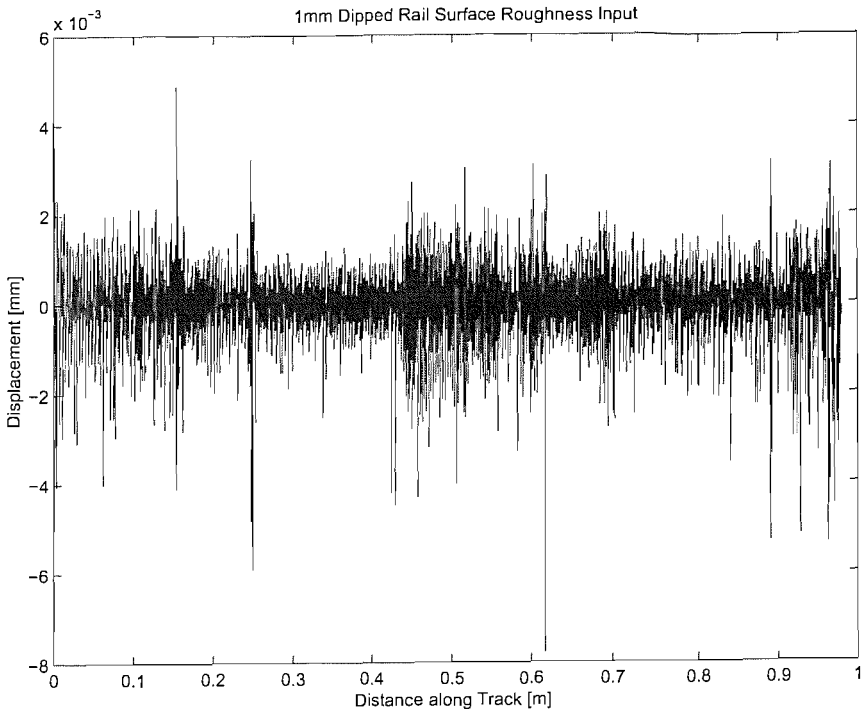

Figure 9–7 The 1mm dipped rail surface roughness contribution after (time domain) filtering.

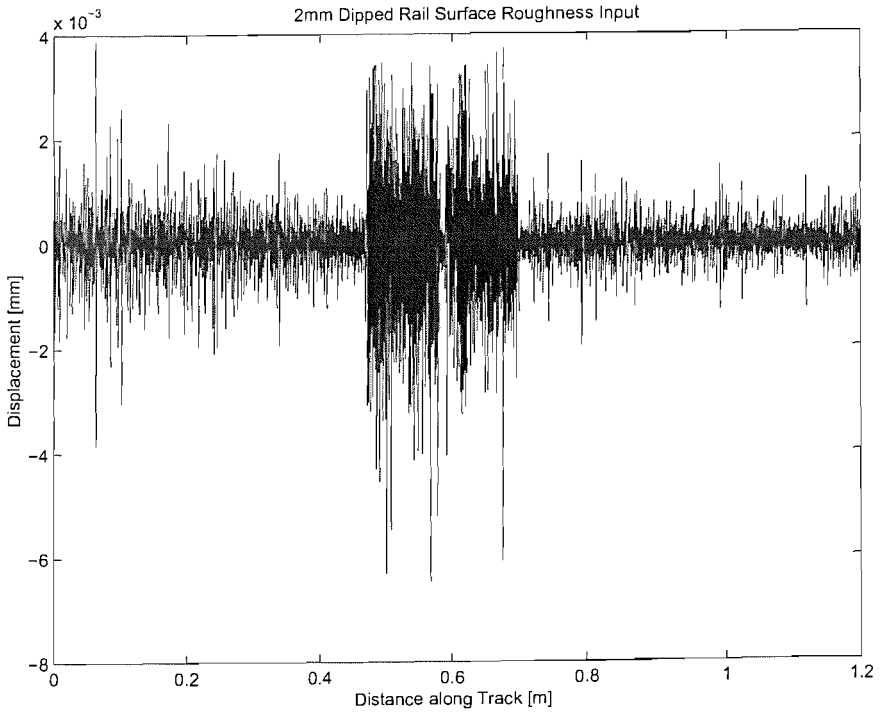

Figure 9–8 The 2mm dipped rail surface roughness contribution after (time domain) filtering.

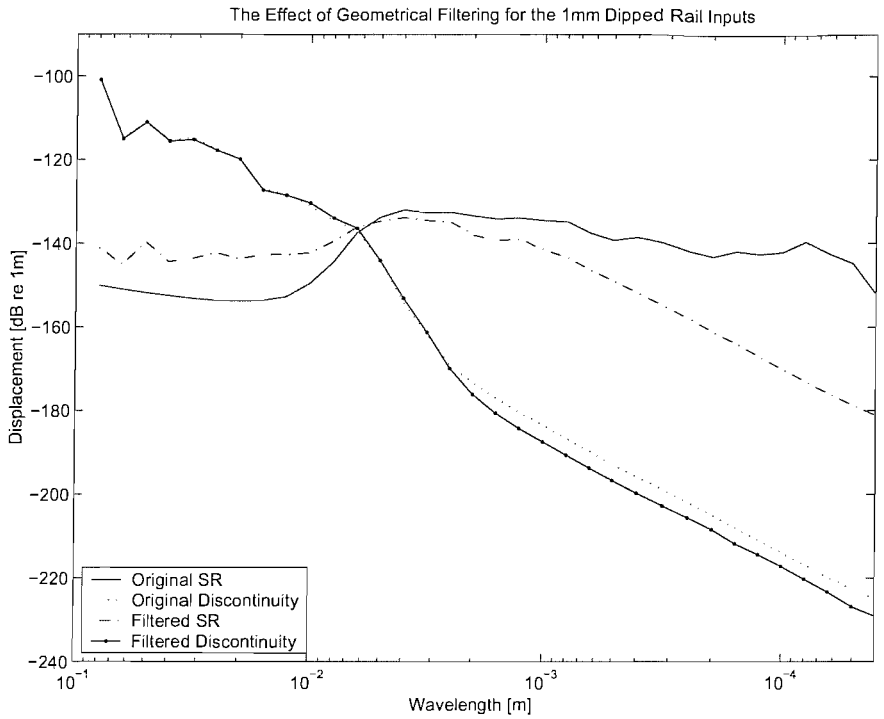

Figure 9–9 The 1mm dipped rail input spectra after geometrical filtering.

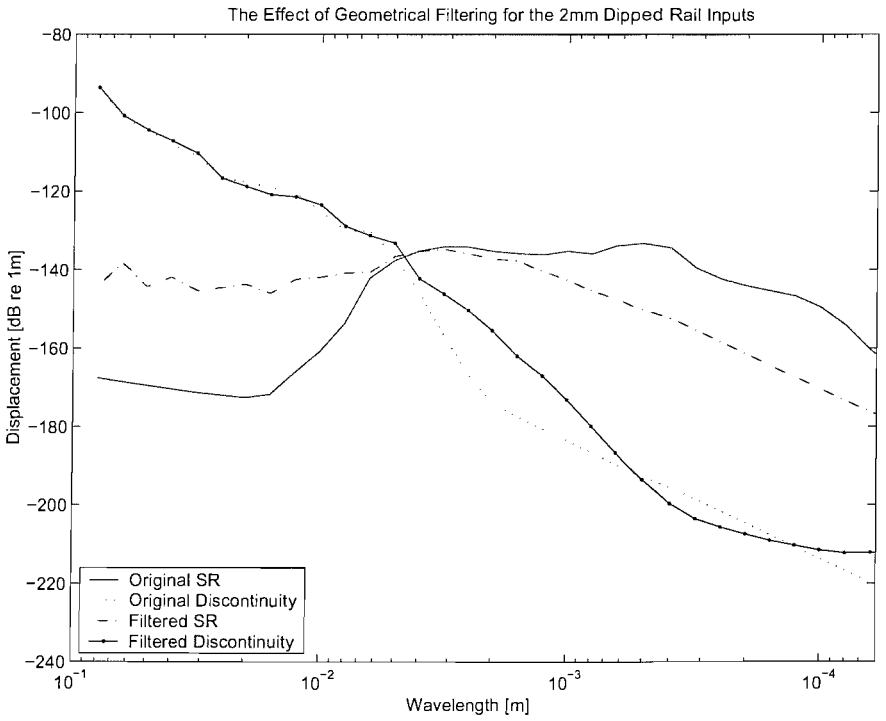

Figure 9–10 The 2mm dipped rail input spectra after geometrical filtering.

of the 2mm dip before and after geometrical filtering is presented in Figure 9–10. It can be seen that the discontinuity part of the input is left unaltered by this filtering process, as only wavelengths shorter than 5mm are affected where the discontinuity is less significant.

A surprising result is demonstrated in Figure 9–10. It can be seen that regions where the two-part inputs have been minimised by the low / high pass filter have actually been amplified by the geometrical filtering process. For example the level of the short wavelength region of the discontinuity input is much larger after geometrical filtering than it was when it had been formed by the process shown above. The same has happened to the surface roughness contribution formed from the measurement of the 2mm dipped joint. This effect, however, is seen not to affect the areas where each part of the input is dominant. Thus this effect of geometrical filtering on the 2mm dip joint is not likely to alter the predictions.

Figure 9–9 and Figure 9–10 show that the spectral amplitudes of both of the dipped joint inputs is larger than the surface roughness input shown in Figure 4-24 for the largest wavelengths (>0.01m). When converted into the frequency domain in one-third octave bands for a specific wheel speed, these spectra manifest themselves at specific frequencies. If the process is repeated for different wheel speeds, the spectrum in the 1/3 octave bands is seen to move to higher frequencies for greater wheel speeds, and to lower frequencies for lower wheel speeds. This is shown in Figure 9–11 for the 2mm dipped profile for speeds ranging from 1m/s to 5m/s. The large wavelength power related to the dipped joint geometry is therefore seen to move to higher frequency bands with a corresponding increase of wheel speed.

It is interesting to compare the spectra in Figure 9–11 for the 2mm dip joint with the spectra of the surface roughness input (see Figure 4-24) for similar wheel speeds. The level in the 100Hz band of the surface roughness input, for wheel speeds in the range of 1m/s to 5m/s, varies from –128dB to –120dB re 1m, whereas for the 2mm dip joint, the level in the 100Hz band varies from –129dB to –105dB re 1m. So the 2mm dipped joint has a much greater change in input level in the 100Hz band (24dB compared with 8dB for the roughness input) but starts at a similar value for the lowest wheel speed that was considered. The input level for the 10kHz band varies from –172dB to –152dB re 1m for both the surface roughness input and the 2 mm dip joint input. This shows again that at the high frequencies, the 2mm dip joint input is dominated by the roughness. Higher

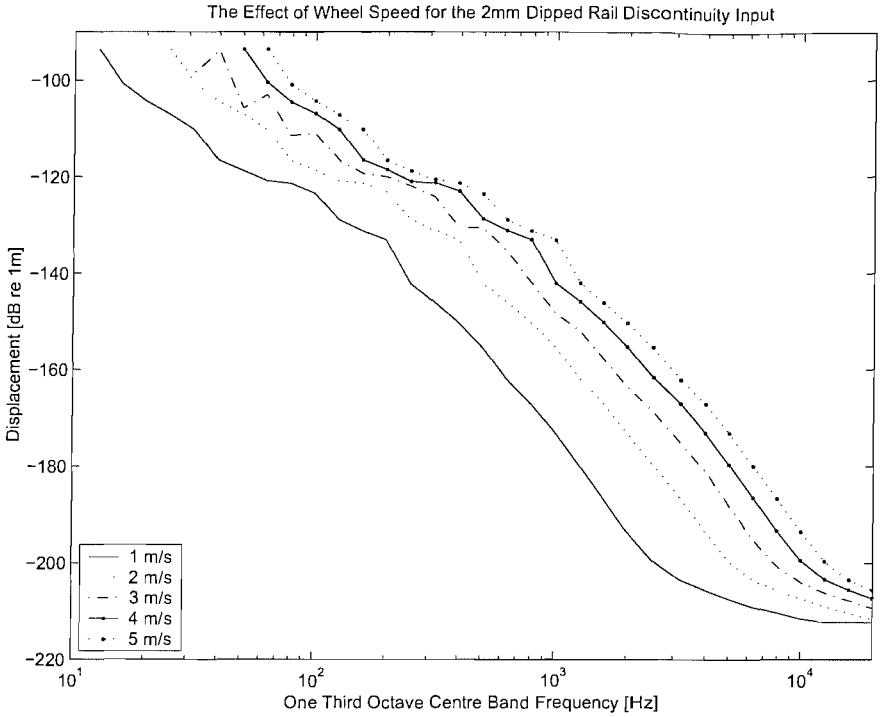

Figure 9–11 The 2mm dipped rail input (after geometrical filtering) at speeds ranging from 1m/s to 5m/s.

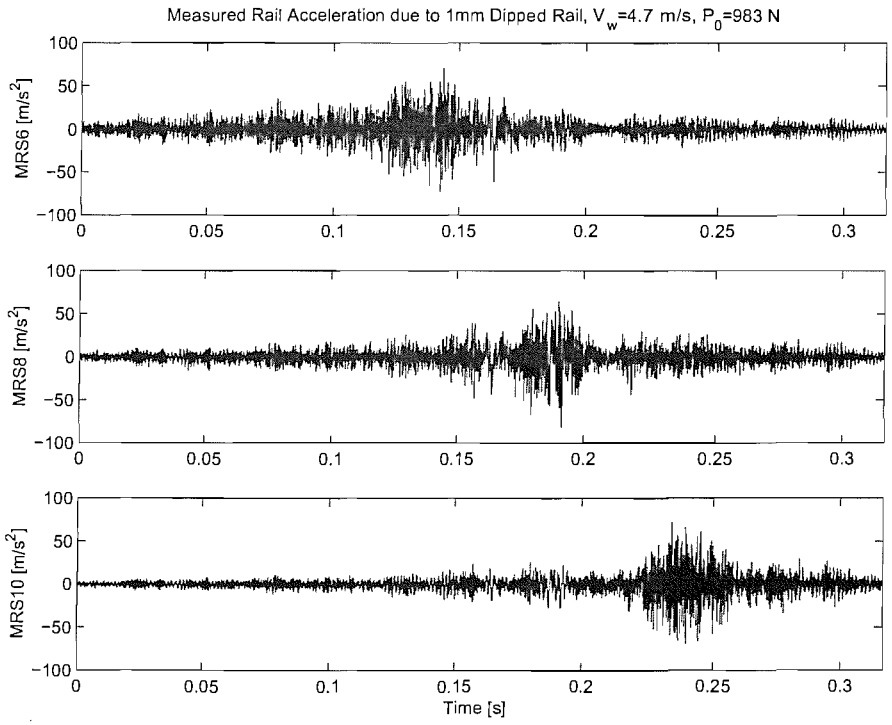

Figure 9–12 Measured rail acceleration at three points on the track for the 1mm dipped rail at a wheel speed of 5m/s and a wheel pre-load of 983N.

frequencies are seen to be unaffected by the 2mm dip geometry for the wheel speeds considered, as their spectra approximate those due to the surface roughness input.

9.4 Measured results

Measurements of vibration were made at several points on the 1/5 scale wheel / rail rig. As described in the previous chapters, measurements were made of the wheel speed, wheel pre-load, axle acceleration, wheel acceleration, and rail acceleration. These were all made at the same points as described before (see Chapter 6). For example, measurements of rail acceleration were made at three points along the track. These included a measurement of vibration before the dip joint at MRS6, a measurement at the centre of the joint at MRS8, and a measurement after the joint at MRS10 (see Figure 3-14). These are each separated by 0.24m.

Examples of the measured acceleration at the three points on the track are presented in Figure 9–12 for the 1mm dip rail joint, with a wheel speed of 5m/s at a wheel pre-load of 983N. These results show that the maximum accelerations occur when the wheel is at positions close to the accelerometers. A time delay of 0.05s at a wheel speed of 4.7m/s corresponds to the separation of 0.24m. Therefore the 1mm dip discontinuity is not seen to dominate the measured response of the rail in the way it did for the step joints in Chapter 8. Similar results were found for the 2mm dip joint in the speed range (1m/s to 5m/s) considered. So, despite the large vertical change in geometry of the dip joint it can be seen that, as the change of the discontinuity height occurs over a longer distance of the rail compared with the step joint, the dip joint has less of an influence on the rail acceleration than the step joints in the speed range considered.

The measured peak rail acceleration for the 1mm dipped joint is presented in Figure 9–13. These results show that the peak rail acceleration rises at a rate of approximately 10dB for a doubling in wheel speed. The peak accelerations are seen to lie between 20dB and 40dB re $1m/s^2$. These measured results are generally seen not to vary greatly with a change in wheel pre-load. The greatest difference for a specific wheel speed is seen to be about 6dB at 3.8m/s, but variations of less than 3dB are more usual. Two much higher results are seen for 516N at speeds below 2m/s, but the reason for this is unknown.

Equivalent results are shown in Figure 9–14 for the 2mm dipped joint. The measured peak acceleration levels of the 2mm dipped joint were found to be at least 7dB higher than for the 1mm dipped joint, and now lie between 27dB and 50dB re $1m/s^2$. These

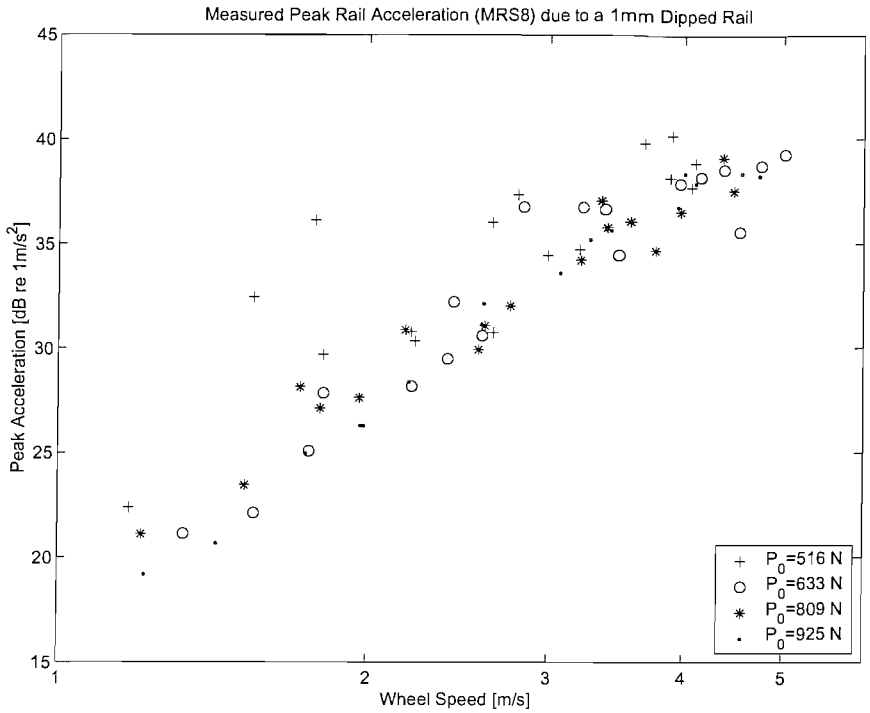

Figure 9–13 Measured peak rail acceleration due to the 1mm dipped rail at MRS8 as a function of wheel speed.

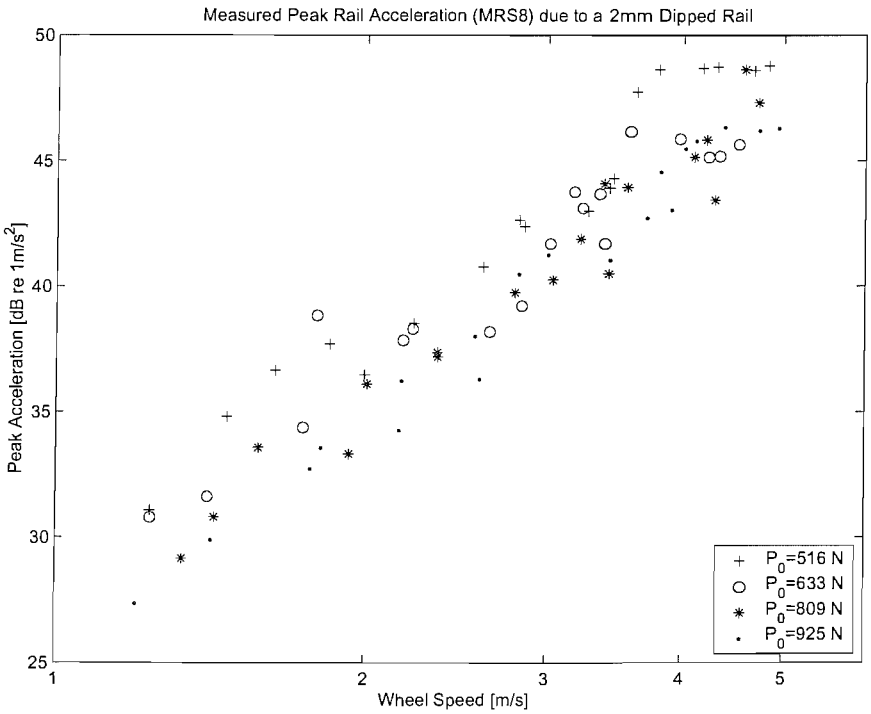

Figure 9–14 Measured peak rail acceleration due to the 2mm dipped rail at MRS8 as a function of wheel speed.

results are also seen to rise at a rate of approximately 10dB for a doubling of wheel speed.

9.5 Predictions of vibration due to a 1mm dipped rail

As for the other discontinuity profiles, the measurements of rig vibration due to the dipped joints were compared with predictions. Predictions were made using two inputs that were formed from measurements of the surface profile geometry. These inputs have been introduced above in section 9.3. As for the step joints (see Chapter 8), the discontinuity part of the dipped joint input was used with the non-linear time-stepping model (see Chapter 2) so that non-linear wheel and rail behaviour due to the surface geometry could be properly assessed. Predictions of the surface roughness contribution were made with the linear FRF model (see Chapter 2). Again, two models variants were used to predict wheel and rail vibration; namely the simple model and the modal wheel model. Comparisons between the measurements and the predictions have been made both in terms of peak amplitudes and in the frequency domain.

9.5.1 Predictions of rail and wheel vibration

An example of a prediction made with the modal wheel variant of the non-linear time-stepping model using the discontinuity input for the 1mm dip joint is presented in Figure 9–15. This shows the predicted wheel and rail displacements and the predicted contact force for a wheel speed of 1.2m/s at a wheel pre-load of 983N. It can be seen that at this wheel speed the wheel follows the surface of the railhead / input. This is also shown for comparison. As the wheel follows the surface of the input, minimal displacement of the rail is predicted. The variations in predicted contact force for this low wheel speed over the 1mm dipped joint, indicates that the wheel / rail contact is ensured much like the results shown in Chapter 6.

Figure 9–16 shows the corresponding results for a wheel speed of 4.7m/s and a wheel pre-load of 983N. This gives a clearer view of the wheel and rail interaction over the 1mm dipped joint. Before the discontinuity the contact force between the wheel and the rail fluctuates slightly about the wheel pre-load value (983N). The small fluctuations shown in this prediction are due to a low frequency content of the railhead surface profile that remained after the low pass filtering process was used to make the 1mm dip discontinuity profile. In Chapter 8 fluctuations did not occur in the regions before or after the step discontinuities because of the artificially smooth sections used in the input

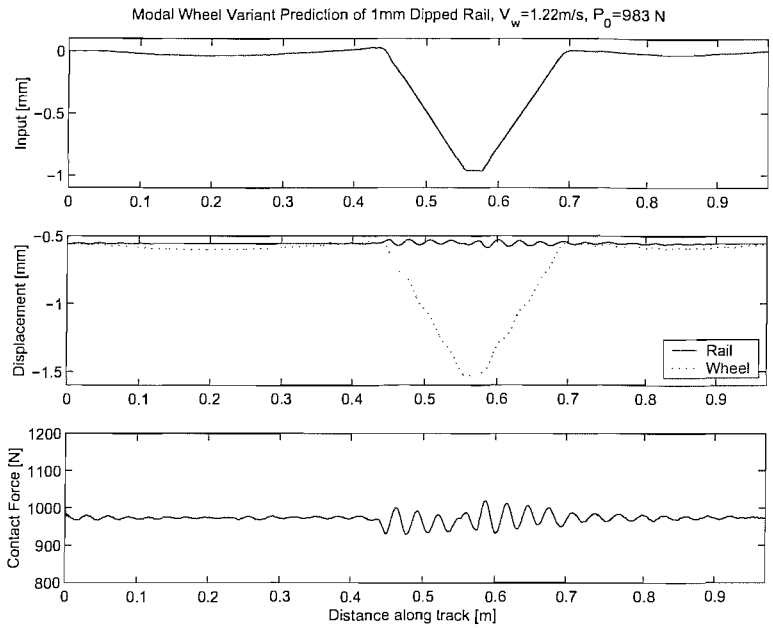

Figure 9–15 Modal wheel variant predicted wheel and rail displacements due to a 1mm dipped rail at a wheel speed of 1.2m/s at a wheel pre-load of 983N, compared with the 1mm discontinuity dipped rail input, and the predicted contact force, all plotted as a function of distance along the track.

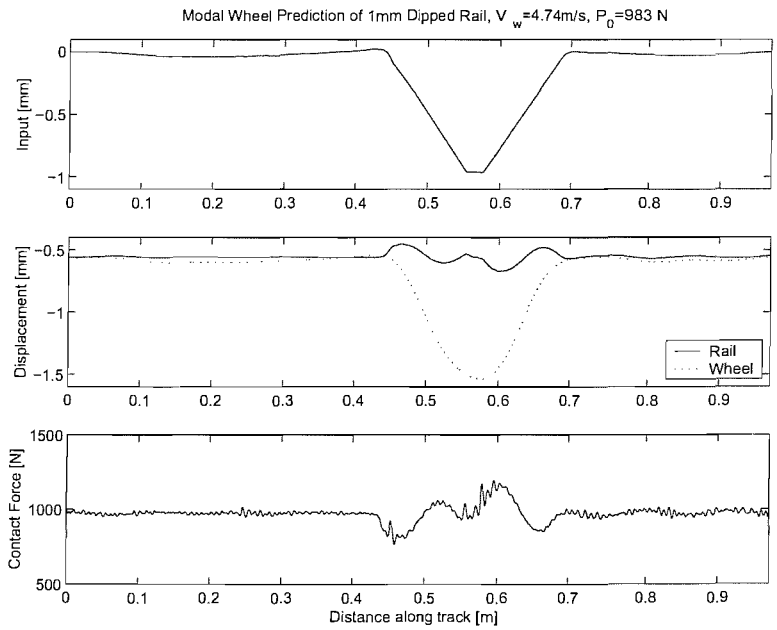

Figure 9–16 Modal wheel variant predicted wheel and rail displacements due to a 1mm dipped rail at a wheel speed of 4.7m/s at a wheel pre-load of 983N, compared with the 1mm discontinuity dipped rail input, and the predicted contact force, all plotted as a function of distance along the track.

representing the discontinuity. This highlights a difference between the types of inputs used.

After the small fluctuations at the start of the prediction, the wheel approaches, and then falls into the dip of the discontinuity. The wheel attempts to follow the surface profile of the input, as the shape of the predicted wheel displacement resembles that of the input. The predicted contact force is seen to reduce in value as the wheel drops into the dip, and the rail displacement is seen to rise to meet the wheel. This is because the ballast layer decompresses under the momentarily reduced contact force between the wheel and the rail. As the wheel reaches the bottom of the dip, the predicted contact force is seen to return back to its equilibrium position determined by the wheel pre-load value (983N). However, after this point the 1mm dip rail geometry forces the wheel back up its slope to the height of the railhead outside of the discontinuity. This results in a rise of contact force as the wheel meets the positive gradient of the 1mm dipped profile. As the wheel rejoins the height of the railhead profile outside of the discontinuity, further unloading of the wheel is demonstrated by a decrease in contact force before the equilibrium is reached once more.

Comparisons between the measured and predicted peak rail acceleration due to the 1mm dip discontinuity (converted in the time domain into acceleration by a first order differentiation routine) are shown in Figure 9–17. After differentiation, the predictions were adjusted for contact filter effects by application of the FIR filter version of the approximate contact filter (see Chapter 5). The peak rail acceleration is predicted to rise at a rate of approximately 10dB for a doubling of wheel speed within the range of 1m/s to 5m/s similar to the measurements. The predicted levels are between 3 and 6dB lower than the measurements.

Some fluctuations are seen within the general trend of the predicted peak acceleration as a function of wheel speed not found in the measurements. It is important to note that this comparison is made between the measurements and the predictions based on only one part of the dipped joint profile. It will be shown next that the discontinuity part of the input did not dominate the overall predicted level, so the comparisons in Figure 9–17 do not necessarily indicate good agreement between measurements and predictions as the contribution due to the surface roughness part of the input is not included.

An example of the predictions formed from the surface roughness part of the input and the discontinuity part of the input is presented in Figure 9–18. These results are for a wheel speed of 1.2m/s and a wheel pre-load of 983N, where contact filter effects

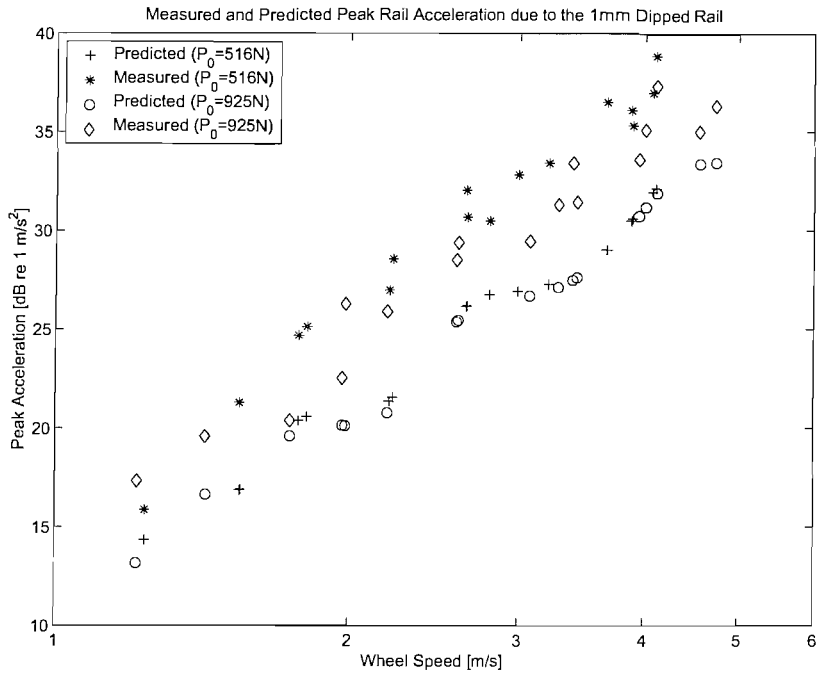

Figure 9–17 Measured and (modal wheel variant) predicted peak rail acceleration due to the 1mm dipped rail for wheel speeds in the range 1m/s to 5m/s at wheel pre-loads of 516N and 983N.

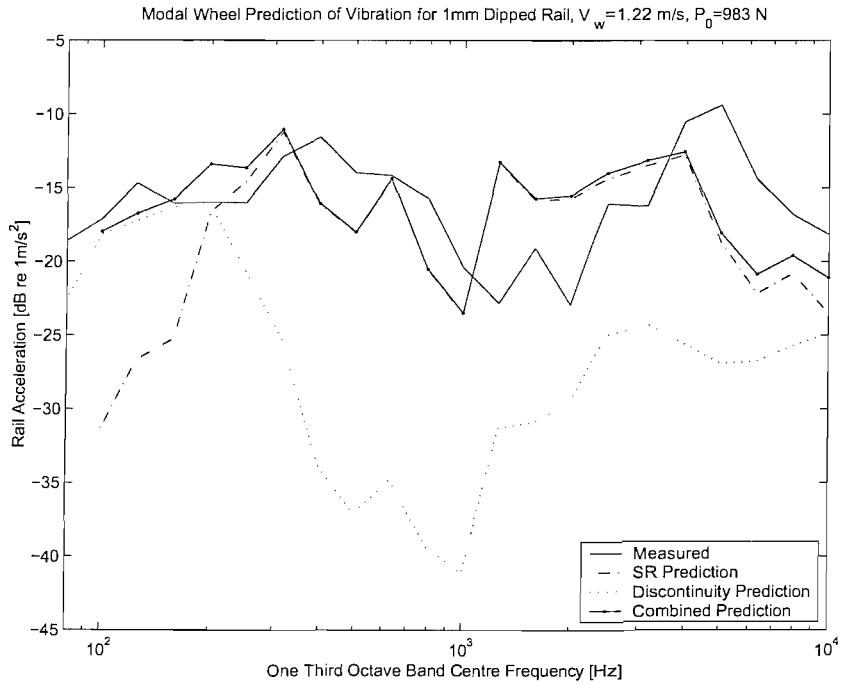

Figure 9–18 Modal wheel variant predicted (with adjustments) rail acceleration due to a 1mm dipped rail at a wheel speed of 1.2m/s at a wheel pre-load of 983N.

(applied in the form of a frequency weighting) have been included in both of the predictions. The prediction formed from the surface roughness contribution has additionally had the effect of track decay included. Figure 9–18 shows that for the modal wheel variant, the prediction formed from the discontinuity part of the input does not significantly contribute to the overall predicted level for frequencies above 200Hz.

The overall predicted level in Figure 9–18 is seen to be in good agreement with the measured acceleration level. Similar agreement was found for other wheel speeds and wheel pre-loads. This is demonstrated by the results of the overall predicted rail acceleration level (including contact filter effects) minus the measured rail acceleration level. This is presented in Figure 9–19 for four wheel pre-loads at wheel speeds ranging from approximately 1m/s to 5m/s. The results demonstrate quite good agreement between the measurements and the predictions. However, it is seen that the predictions are much smaller than the measurements in certain frequency bands. This has resulted in large negative differences in the acceleration levels at 1kHz, and 5kHz, much like the results presented in Chapter 6. The differences at 5kHz are attributed to a feature of the modal wheel variant, as little variation is seen with changes in wheel speed. The differences at 1kHz though, are influenced by wheel speed and therefore can not be explained purely by a deficiency in the model.

The predicted wheel acceleration level with adjustments for the contact filter effects are shown in Figure 9–20.This shows that the discontinuity part of the prediction does not influence the overall predicted level above 200Hz, thus the influence of the 1mm dip rail geometry is minimal for the prediction of wheel vibration. The predictions formed from the surface roughness contribution are seen to dominate in the majority of the mid and high frequency range of consideration, whilst the effects of the 1mm dip discontinuity were limited to the lowest frequencies. This was also found to be the case for the predictions of vibration due to step joints in Chapter 8.

9.6 Predictions due to a 2mm dipped rail

Results for the 2mm dipped rail are presented in this section. As for the 1mm dipped rail, the non-linear time-stepping model was used to predict vibration due to the discontinuity part of the input, whilst the FRF model was used to predict the vibration due to surface roughness.

An example of the output from the modal wheel variant of the non-linear time-stepping model is presented in Figure 9–21 for a wheel speed of 1.2m/s and a 942N wheel pre-

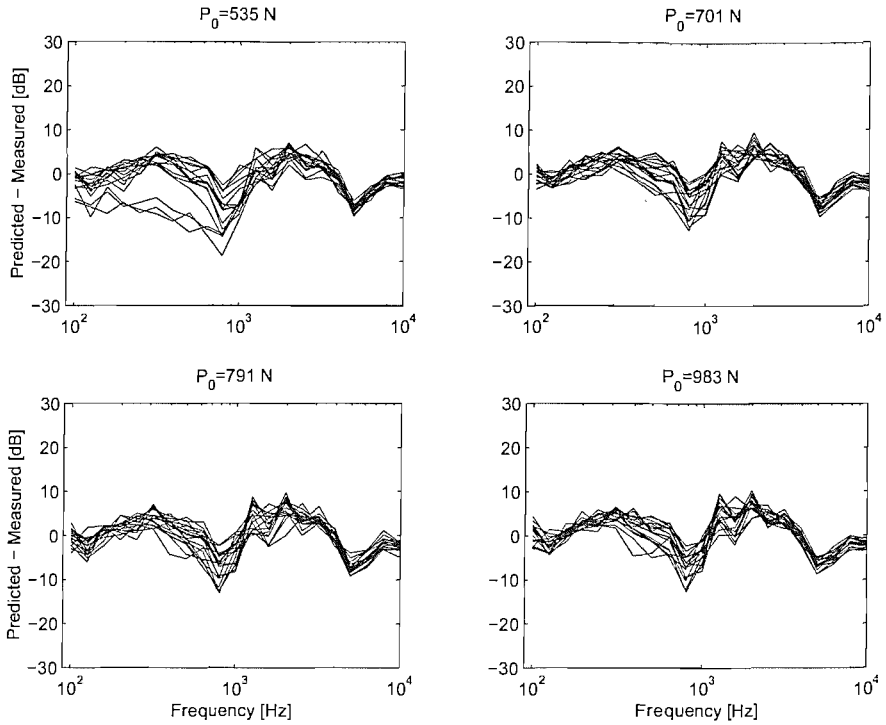

Figure 9–19 Modal wheel variant predicted (with adjustments) rail acceleration due to a 1mm dipped rail at all of the measured wheel speeds and wheel pre-loads.

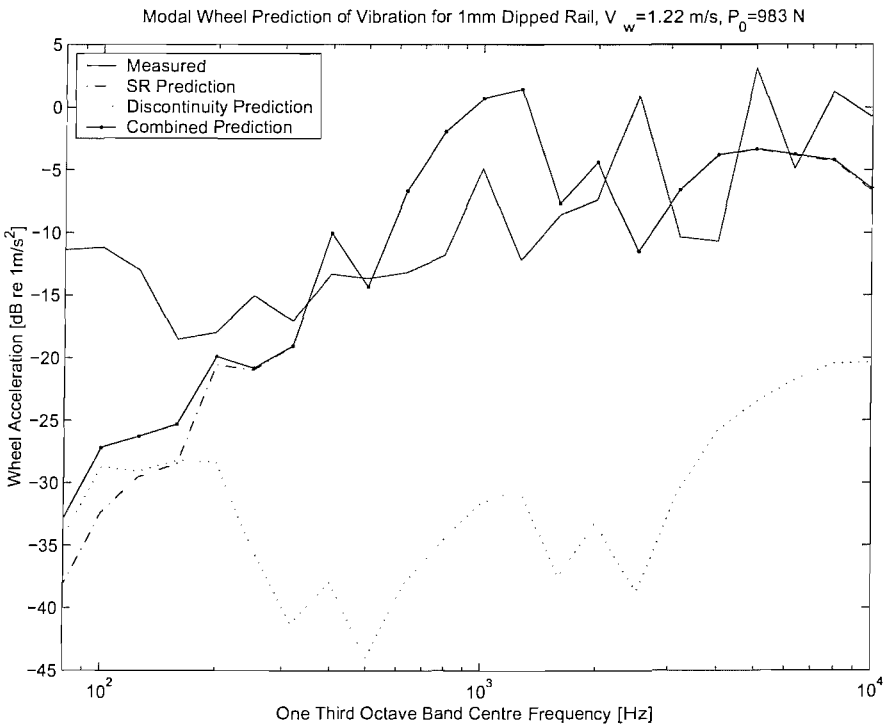

Figure 9–20 Modal wheel variant predicted (with adjustments) wheel acceleration due to a 1mm dipped rail at a wheel speed of 1.2m/s at a wheel pre-load of 983N.

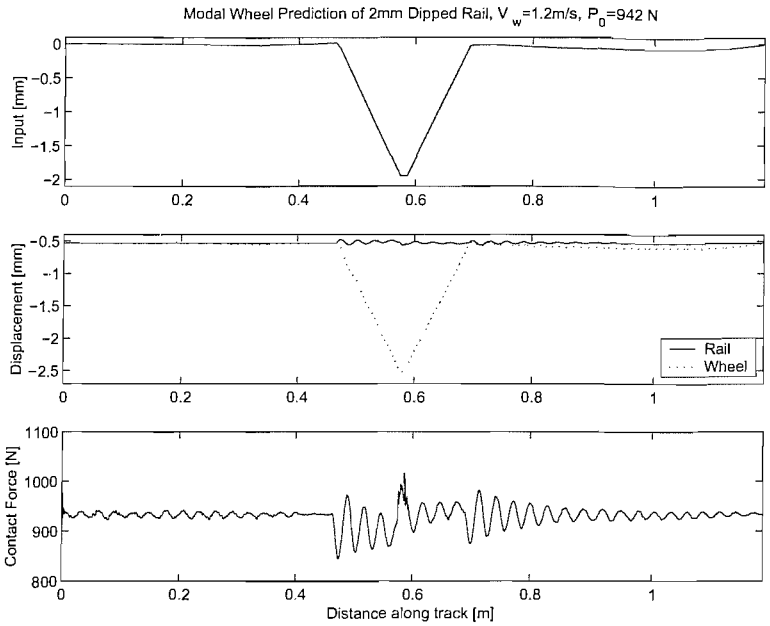

Figure 9–21 Modal wheel variant predicted wheel and rail displacements due to a 2mm dipped rail at a wheel speed of 1.2m/s at a wheel pre-load of 942N, compared with the 2mm discontinuity dipped rail input, and the predicted contact force, all plotted as a function of distance along the track.

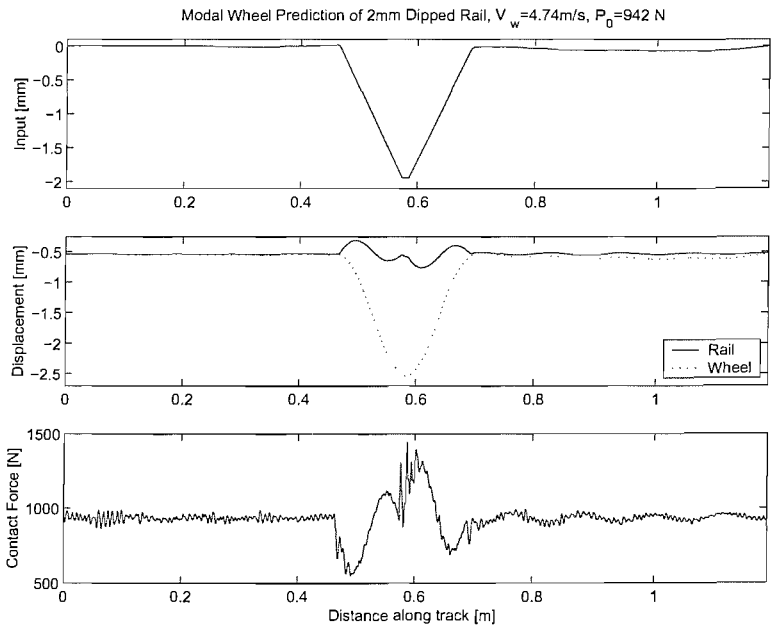

Figure 9–22 Modal wheel variant predicted wheel and rail displacements due to a 2mm dipped rail at a wheel speed of 4.7m/s at a wheel pre-load of 942N, compared with the 2mm discontinuity dipped rail input, and the predicted contact force, all plotted as a function of distance along the track.

load. The predicted wheel and rail displacements are presented as a function of distance along the length of the track, and are compared with the 2mm dip joint (discontinuity) input and the predicted contact force. The predicted contact force is seen to fluctuate between 830N and 1030N for this low wheel speed.

Results for a higher wheel speed of 4.7m/s at the same wheel pre-load of 942N are presented in Figure 9–22. This shows that the predicted contact force fluctuations now fluctuate between 500N and 1500N. The increase in wheel speed therefore has a stronger influence upon the wheel / rail interaction for the 2mm dipped rail than for the 1mm dipped rail.

The predicted peak rail acceleration (using the modal wheel variant) is compared with its measured equivalent in Figure 9–23 for wheel speeds in the range 1m/s to 5m/s, at two wheel pre-loads (532N and 942N). The predictions in Figure 9–23 are seen to rise at a rate of approximately 10dB for a doubling of wheel speed. This is similar to that of the measured trends. As before for the 1mm dip predictions formed from the surface roughness part of the input are not included in these comparisons, and thus the comparisons with the measurements are biased.

Comparisons of the predictions with the measurements in the frequency domain are considered next. Figure 9–24 shows the predicted rail vibration due to both parts of the inputs for a wheel speed of 1.2m/s and a wheel pre-load of 942N. The discontinuity part is seen to exceed the prediction formed with the surface roughness contribution at frequencies below 300Hz and above 5kHz.

Figure 9–25 presents the differences between the predicted overall rail acceleration level and the measured rail acceleration level at wheel speeds ranging from 1m/s to 5m/s for four wheel pre-loads. This shows a good agreement between the measured and predicted acceleration. The largest differences seen in the results are due to deficiencies (identified in Chapter 6) in the modal wheel variant model at 800Hz and 1kHz. Negative values in the differences above 5kHz are influenced by an over-attenuation of the contact filter adjustment. Nevertheless these comparisons are close to those shown for the results due to surface roughness presented in Chapter 6.

An example of the wheel acceleration predictions are shown in Figure 9–26 for a wheel speed of 1.2m/s and wheel pre-load of 942N. The prediction formed from the discontinuity part of the prediction is seen not to be a dominant part of the overall

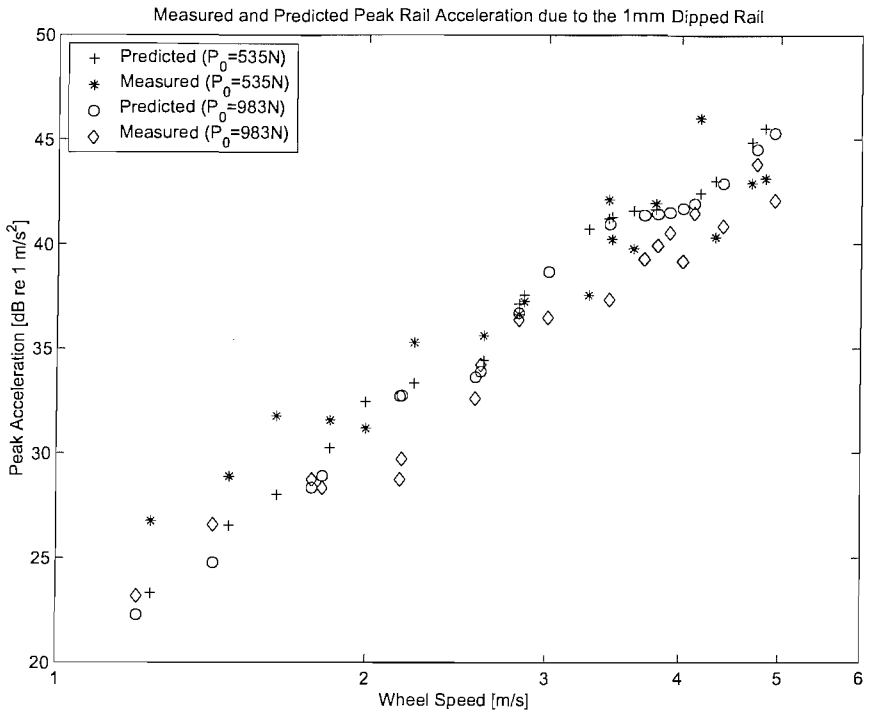

Figure 9–23 Measured and predicted (using the modal wheel variant) peak rail acceleration due to the 2mm dipped rail.

Figure 9–24 Modal wheel variant predicted (including adjustments) rail acceleration due to a 2mm dipped rail at a wheel speed of 1.2m/s at a wheel pre-load of 942N.

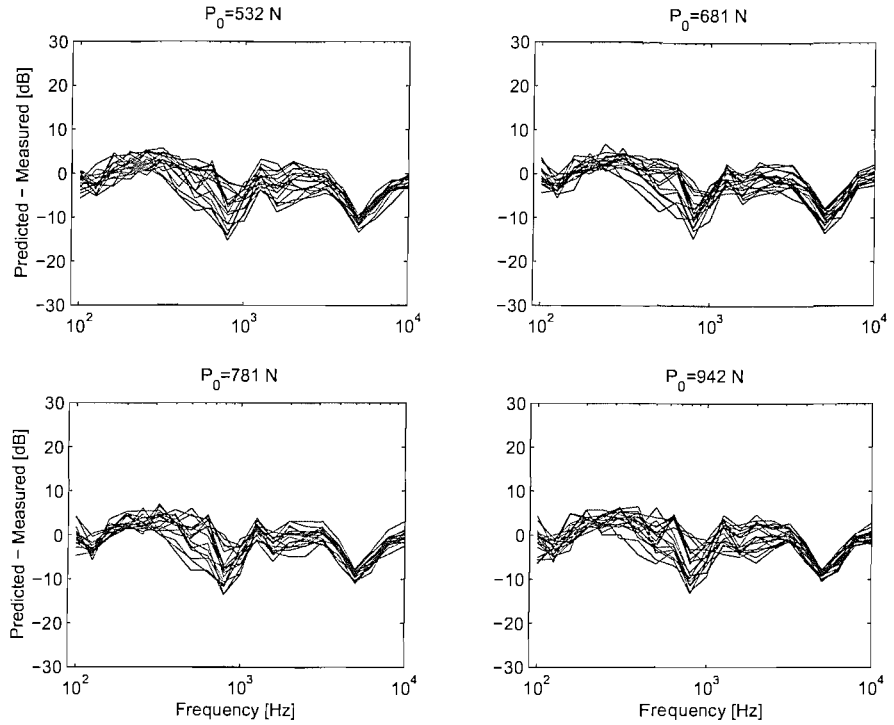

Figure 9–25 Modal wheel variant predicted (with adjustments) rail acceleration due to a 2mm dipped rail at all of the measured wheel speeds and wheel pre-loads.

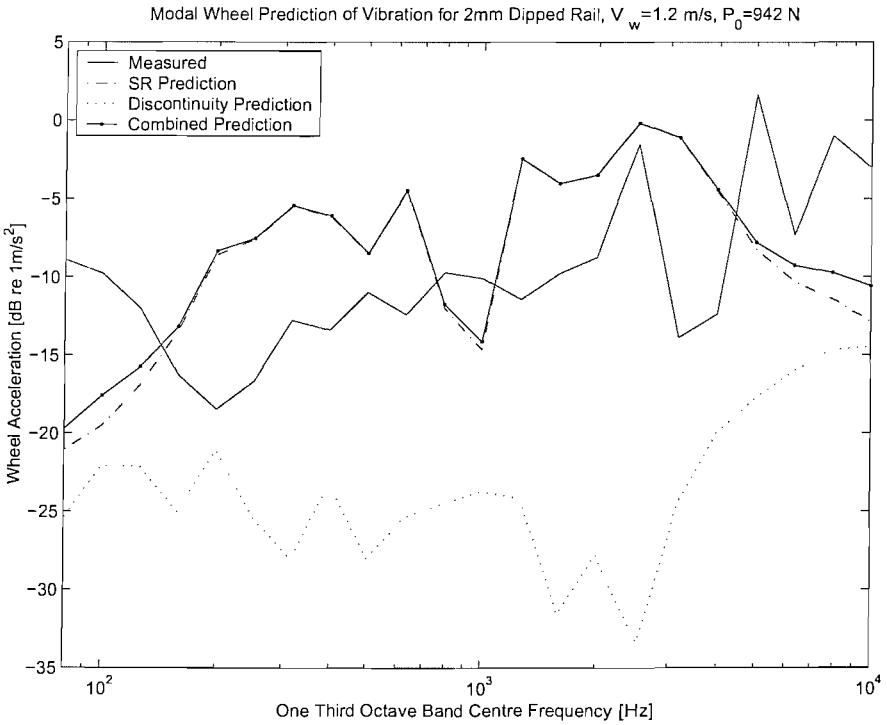

Figure 9–26 Modal wheel variant predicted (including contact filter adjustments) wheel acceleration due to a 2mm dipped rail at a wheel speed of 1.2m/s at a wheel pre-load of 942N.

predicted level. Predictions of wheel vibration are therefore more influenced by the surface roughness part of the input than the discontinuity part of the input.

9.7 Predictions of contact force

Results of the predicted contact force due to the dipped rails were different from the step joints as no wheel / rail loss of contact was predicted by either model variant for either of the dipped rail profiles at any of the wheel pre-loads or wheel speeds considered. It can therefore be expected that non-linear effects will be smaller.

9.7.1 Analysis of the predicted contact force for the 1mm dipped joint

The predicted peak contact force due the 1mm dip joint geometry at wheel speeds ranging from approximately 1m/s to 5m/s for four wheel pre-loads is presented in Figure 9–27. This shows the results for the lowest and highest wheel pre-loads for both the simple variant and the modal wheel variant predictions. The results are presented in the ratio of peak contact force to static wheel pre-load. It can be seen from Figure 9–27 that differences between the simple and modal wheel variants occur particularly at the highest wheel speeds (>3.5m/s).

The predicted ratio of peak to static contact force is seen to be close to unity at low wheel speeds (<3m/s). This means that the predicted peak contact force is not much larger than the wheel pre-load. This result, however, is biased by the exclusion of the predicted contact force due to the surface roughness contribution, which for the case of a 1mm dipped rail has been shown to be significant. The predicted contact force ratio is seen to rise to a value that indicates that the predicted contact force is almost one and a half times as large as the static wheel pre-load at the highest wheel speeds considered (>4m/s). A change in wheel pre-load is seen to reduce the maximum predicted contact force ratio within the speed range considered.

Comparisons of the predicted contact force spectra were made between linear and non-linear time-stepping versions of the two model variants (see Chapter 7). Figure 9–28 demonstrates that the differences between the contact force spectra from the non-linear prediction and the linear simple variant prediction vary most in the 1kHz to 10kHz one-third octave bands. Differences of up to 6dB are seen in some high frequency bands (for example the 2kHz band for the maximum wheel pre-load). The differences between the non-linear and linear predicted contact forces are found to give both positive and negative values.

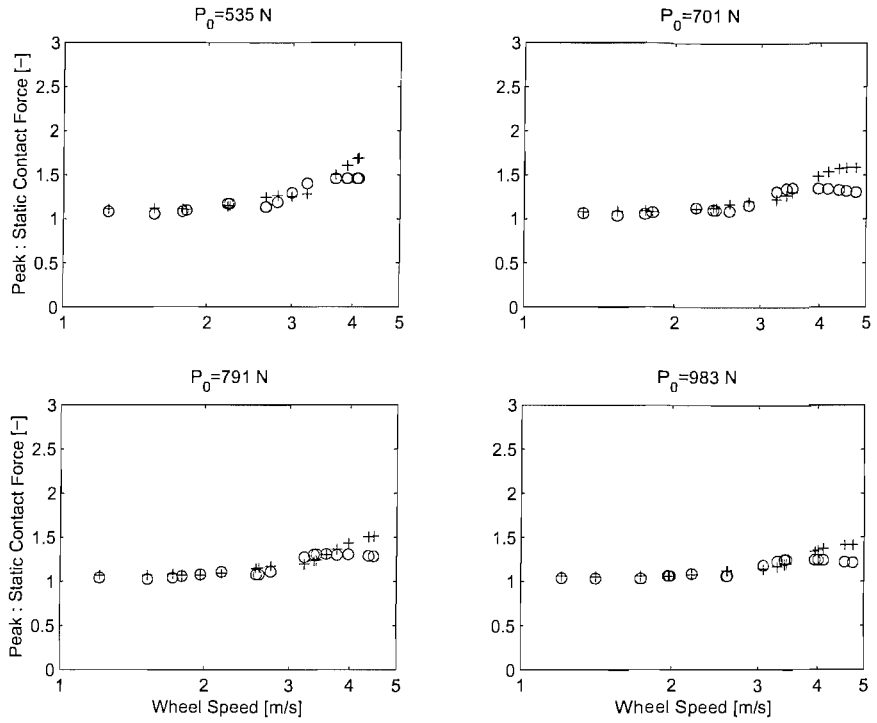

Figure 9–27 Comparison of predicted contact force using the modal wheel variant and the simple variant as a function of wheel speed for the four wheel pre-loads considered.

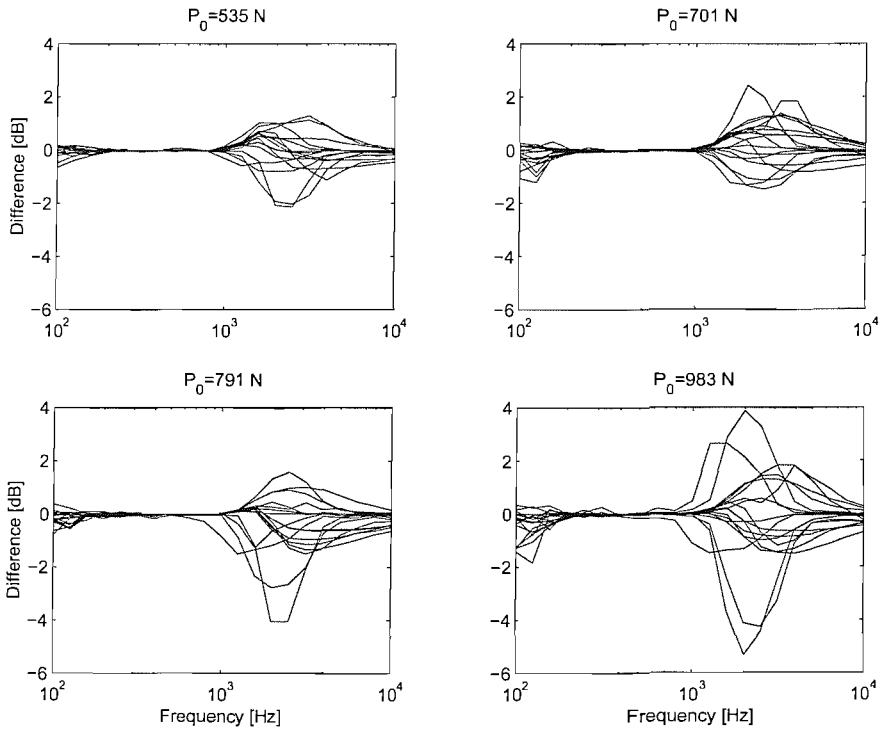

Figure 9–28 Comparisons of the simple variant predicted contact force due to a 1mm dipped rail using non-linear and linear time stepping models.

Results for the modal wheel variant are shown in Figure 9–29. These demonstrate that differences between the two predictions are again both positive and negative. Therefore neither the non-linear or linear predictions are consistently greater than the other. The differences shown for the modal wheel variant predictions are seen to be smaller than for the simple variant predictions.

9.7.2 Analysis of the predicted contact force for the 2mm dipped rail

As for the 1mm dipped rail results, a simple comparison between the modal wheel variant and the simple variant predicted in terms of the ration of the peak contact force to the wheel pre-load is presented in Figure 9–30. For the 2mm dipped rail this ratio is seen to increase to higher values than for the 1mm dipped rail. The 2mm dipped rail results are also seen to increase more rapidly with wheel speed. The peak predicted contact force due to the 2mm dipped rail is seen to be similar to the wheel pre-load at wheel speeds below 1.5m/s. At the highest wheel speeds considered the predicted peak contact force is about 2.5 times greater than the wheel pre-load for the lowest wheel pre-load (532N) according to the simple variant of the non-linear time-stepping model. The differences between the modal wheel variant and simple variant predictions are greater for the 2mm dipped rail than for the 1mm dipped rail.

Using the method of analysing the predicted levels of contact force formed from a non-linear prediction and a linear prediction, presented in Chapter 7, the results shown in Figure 9–31 are obtained for the simple model. These results demonstrate a difference in levels that are mainly positive. This means that the contact force predicted using the non-linear model is typically larger than the corresponding results from the linear model for the high frequency bands (above 1kHz). The largest differences are seen in the 2kHz band, and between 5kHz and 8kHz. The maximum differences (2.3dB) are seen to be at the lowest wheel pre-load, whilst an increase in wheel pre-load is seen to reduce the maximum difference to 1.5dB.

Figure 9–32 presents comparisons obtained using the modal wheel variant. These results show large differences at low frequencies (<500Hz), that are attributed to an unwanted influence of the wheel on track resonance which was inadvertently excited due to poor choice of initial conditions in the linear version of the time-stepping model.

As for the simple model predictions, the differences in predicted levels in Figure 9–32 are generally positive values. This means that the non-linear predictions of contact force

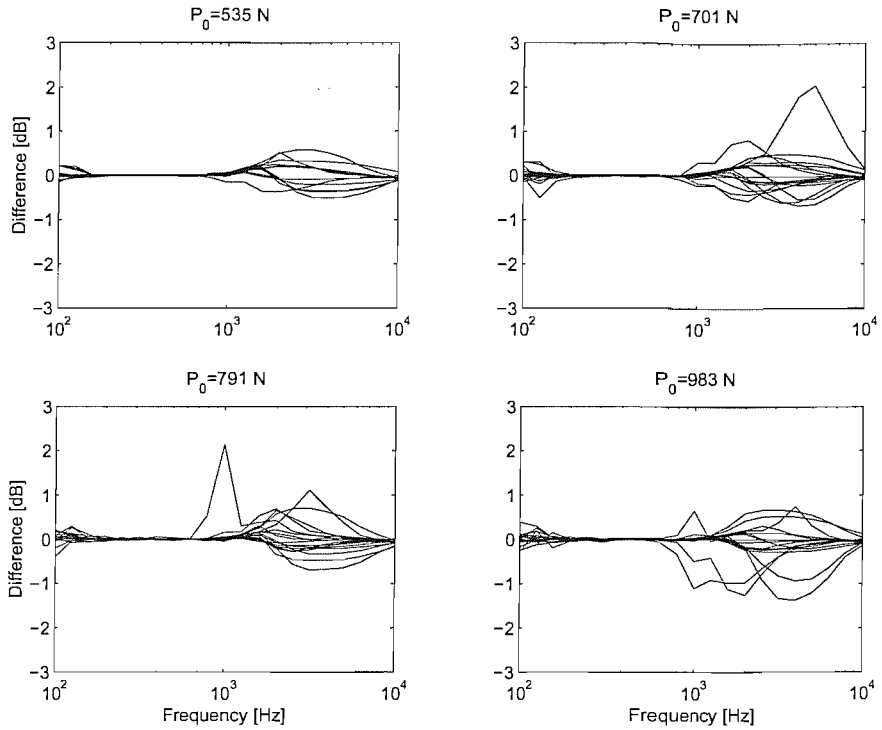

Figure 9–29 Comparisons of the modal wheel variant predicted contact force due to a 1mm dipped rail using non-linear and linear time stepping models.

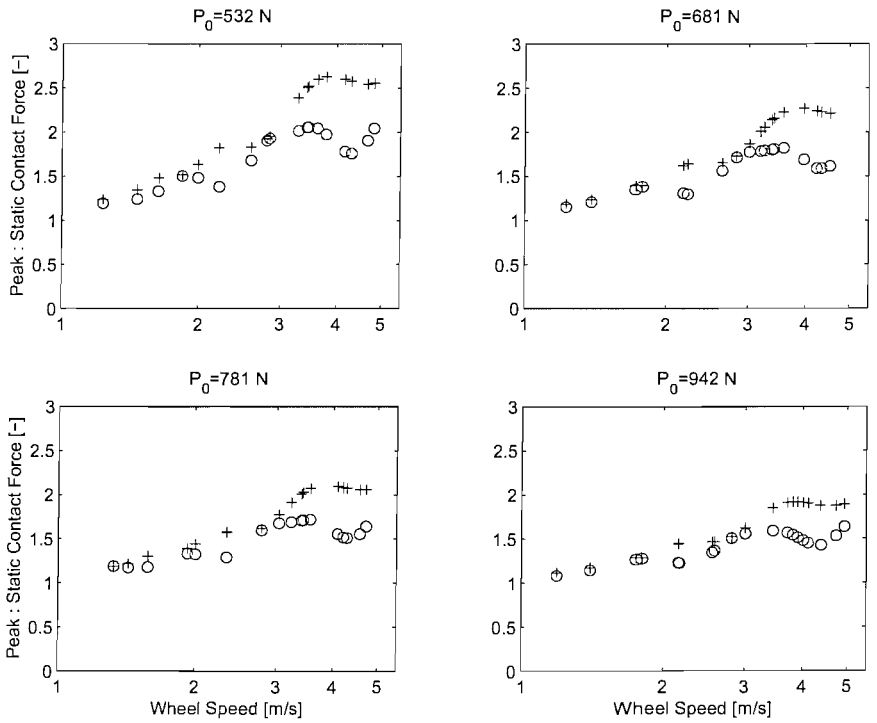

Figure 9–30 Simple variant and modal wheel variant predicted maximum contact force, due to a 2mm dipped rail, as a function of wheel speed for the four wheel pre-loads considered.

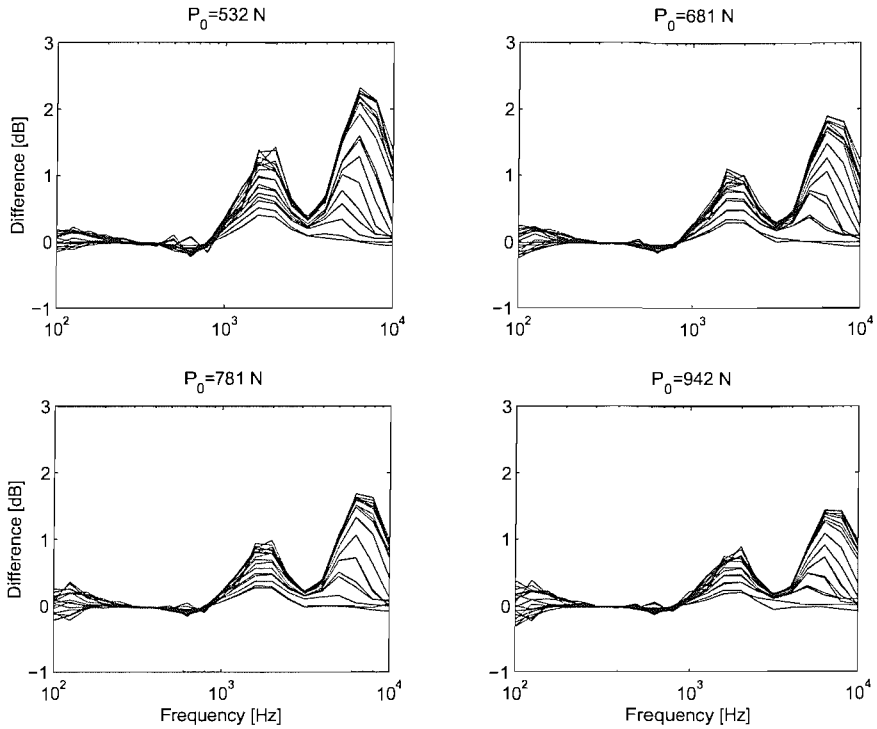

Figure 9–31 Simple variant predicted non-linear contact force level minus the linear contact force level due to a 2mm dipped rail.

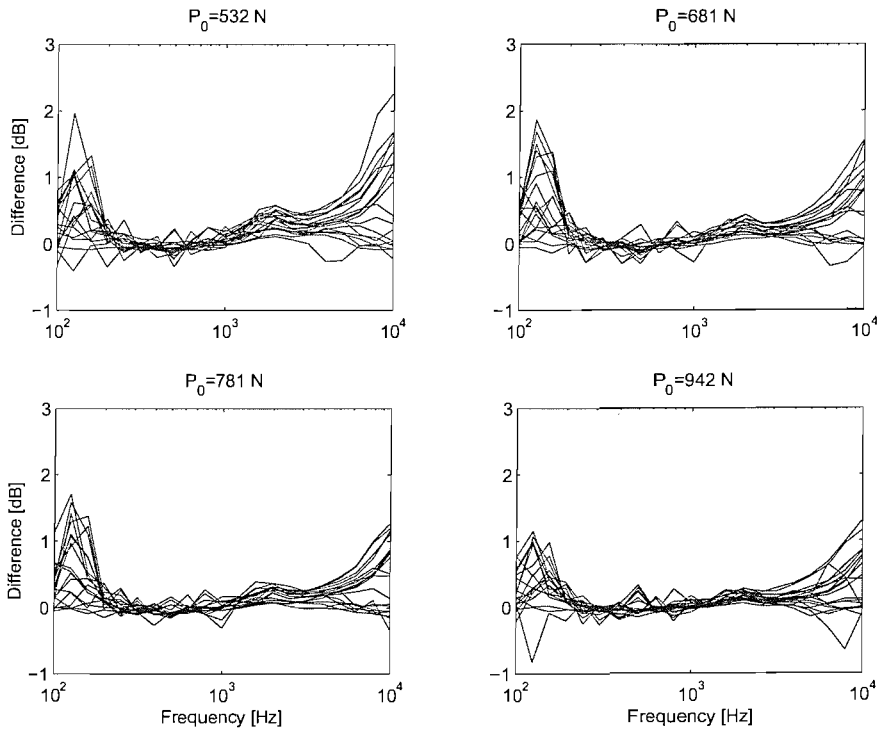

Figure 9–32 Modal wheel variant predicted non-linear contact force level minus the linear contact force level due to a 2mm dipped rail

are typically larger than the linear predictions, particularly in the high frequencies bands (above 1kHz). The largest differences are seen in the 10kHz one-third octave band. As for the simple variant results (see Figure 9–31), the differences are the largest for the lowest wheel pre-load, where a difference of 2.2dB is evident, and lowest (1.2dB) for the greatest wheel pre-load.

9.8 Conclusions

This chapter has presented measurements and predictions of wheel and rail vibration due to dip joint profiles. This was done by manufacturing a 1/5 scale representation similar to that used by [Wu and Thompson, 2001(b)] in their theoretical simulations. The basis for the geometry used in this chapter has therefore been based on a stylised representation of a dip joint rather than a full scale measurement.

Problems occurred with the reproduction of the required dipped joint geometry. It was found that the design requirement for each of the dipped joints could not be faithfully reproduced using the CNC machining technique. This not only resulted in a poor representation of the design requirement geometry but it also resulted in the CNC machined sections having larger surface roughness amplitudes than the rest of the dipped rail railhead. This is particularly noticeable for the 2mm dip joint, where the surface roughness contribution is shown in Figure 9–8.

In order to make predictions for this type of discontinuity, an alteration to the method of splitting the input into two parts (presented in Chapter 7) was required. This involved finding a cut-off point (as a function of wavelength) from which the two parts of the input were filtered by low pass and high pass filters in the time domain.

This method of forming the overall predicted vibration levels from predictions made with two inputs was beneficial in describing the effects of the discontinuity part of the input in conjunction with the surface roughness contribution of the dipped rail inputs. For example, for the studies of the 1mm dip, the discontinuity part of the input was found not to influence the overall predicted level until the higher wheel speeds were reached (greater than 2.5m/s). The geometry was found not to be sufficiently large to influence the prediction in the range 100Hz to 10kHz at wheel speeds below 3m/s. The 2mm dip was, however, found to influence the overall prediction at wheel speeds above 1.5m/s. This showed that the large wavelength (low frequency) effects of shallow dips at low wheel speeds can therefore effectively be ignored for predictions of rolling noise as the geometry excites frequencies that are not of interest. Larger changes (or increase

of amplitudes) in geometry have been seen to influence the predictions at lower wheel speeds.

Analysis of the 1mm dip predictions has shown that for the lowest wheel speeds the presence of the 1mm dip has almost no effect on the result. Therefore, the prediction generally consists of the vibration due to surface roughness. Results showing the differences in level between the 2mm dip joint predictions and measurements are impressive. They demonstrate that the predictions are almost as good as the predictions made due to a surface roughness input. Predictions formed from discontinuity inputs were not expected to improve upon the agreement of the predictions with the measurements presented in Chapter 6. Here they are just as good.

10 Wheel / rail vibration due to a simulated wheel flat

10.1 Introduction

Wheel flats are localised flat regions on the circular running surface of a railway wheel, caused by excessive braking. The work presented in this chapter uses a simulated wheel flat on the surface of a railhead in place of a flat on the surface of a wheel. This facilitates measurements of rail vibration as the location of the wheel flat on the rail is always known [Newton and Clark, 1979].

Predictions of wheel and rail vibration were made using the models presented in Chapter 2 together with a measurement of the surface profile. As in previous chapters the predictions were made for many wheel speeds at four wheel pre-loads and were compared with measurements of rig vibration.

10.2 Manufacture of a simulated wheel flat

A simulated wheel flat was machined on to the surface of a railhead that had previously been manufactured in the same manner to the railhead studied in Chapter 6. The shape of the simulated wheel flat was chosen to be an arc (the same radius as the rig wheel) with a depth of 0.5mm. This was cut into the surface of the railhead with a milling machine and an adjustable radius cutting tool. The resulting profile (that has been measured with an LVDT using the surface profile measurement method of Chapter 4) is shown in Figure 10–1. This also shows the design requirement of the wheel flat geometry, and a fitted arc of 0.1m radius but smaller depth that has been aligned to the measurement position.

As in the previous chapters, the surface profile of the discontinuity was not measured until many 'rolling wheel' measurements over the discontinuity had been made. This resulted in a line that was apparent on the surface of the rail showing a wheel / rail contact path distinguishable from the duller railhead surface, as shown in Figure 10–2. Measurements of the surface profile were made along the centre of this line, so that inputs to the prediction models were as representative as possible.

It can be seen from Figure 10–1 that the measured depth of the simulated wheel flat was only 0.35mm. This is smaller than the required depth of 0.5mm because the rig wheel did not run exactly in the centre of the railhead (see Figure 10–2). On average the wheel

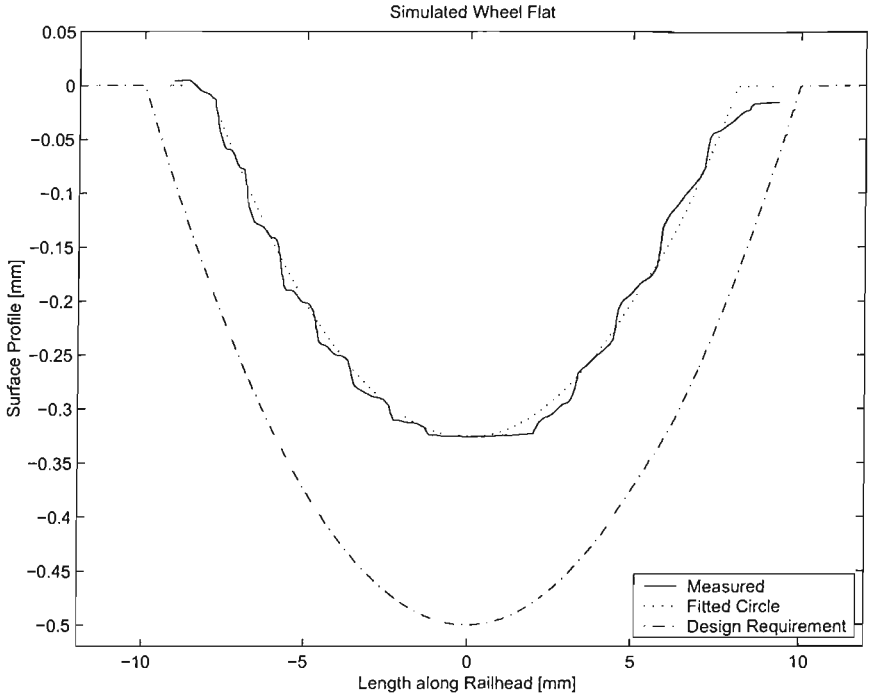

Figure 10–1 Measurement of simulated wheel flat compared with the design requirement and a curve that has been fitted to the measured profile.

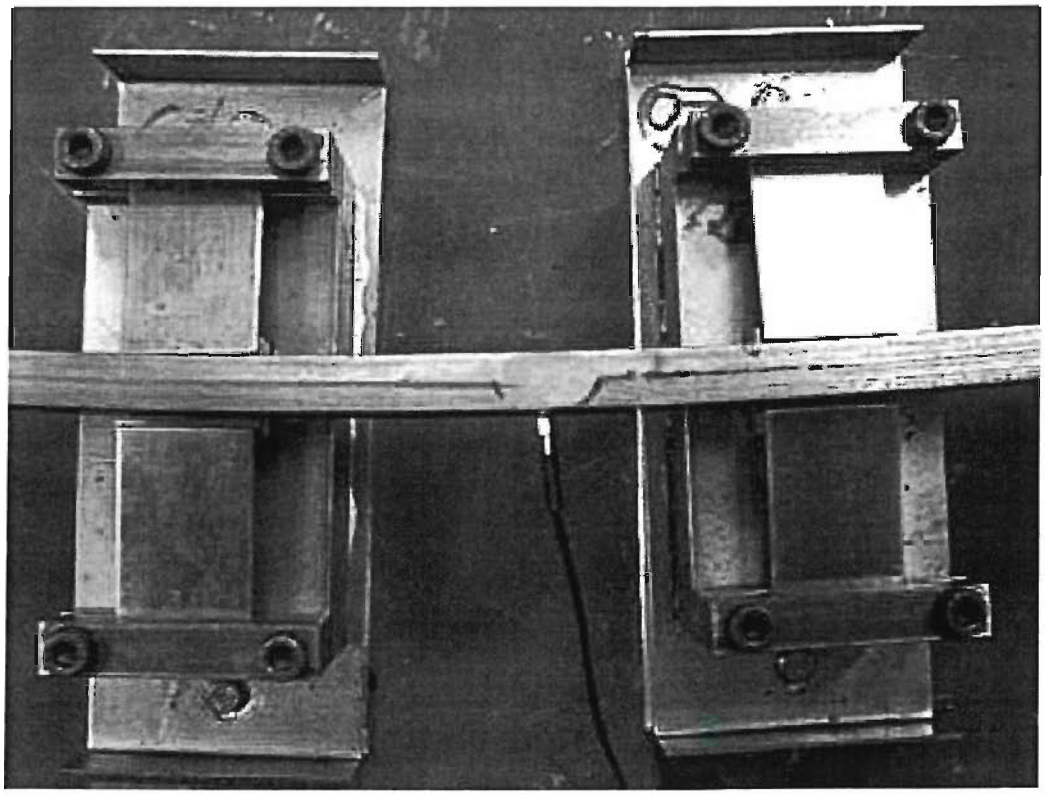

Figure 10–2 Photograph of the railhead containing the simulated wheel flat.

was found to run slightly to the outer side of the rail where the depth of the simulated wheel flat is only 0.35mm. Thus an impression of a shallower simulated wheel flat is seen rather than the one desired. This was unavoidable due to manufacturing restrictions of the rig rail and the way it was positioned on the track supports, and similar to the case for the dipped rail joints in the previous chapter.

The irregularities in the measurement seen in Figure 10–1 are thought to be due to the manufacturing process (only a single 'rough' cut was made) because several separate measurements of the simulated wheel flat resulted in similar profiles. The irregularities are highlighted in Figure 10–1 by comparing the measured surface profile with a fitted curve of 0.1m radius. To improve the surface finish of the cut, the geometry would ideally have to be a ground finish. This type of precision finish was not feasible due to the cost of grinding equipment for such a large diameter. The geometry of the simulated wheel flat was therefore made using an adjustable cutting tool that is not able to produce a surface finish much better than that shown.

10.3 Measurements of the surface profile

An enlarged view of the rail profile has already been presented in Figure 10–1. The simulated wheel flat, however, was not the only part of the railhead that had to be measured. The input used for the prediction models was a measurement of a long length of the railhead profile (along the path that the wheel takes on the railhead) that included the discontinuity. This measurement is shown in Figure 10–3 before trend removal.

The method of splitting a surface profile measurement into two parts, presented in Chapter 7, ensures that appropriate post-processing of the surface roughness contribution of the input is made. The separate inputs formed using this method are shown in Figure 10–4 and Figure 10–5.

Figure 10–4 shows the discontinuity part of the wheel flat input. This includes a section of the railhead measurement at the simulated wheel flat (shown in Figure 10–3), and two artificially smooth sections of rail. These artificially smooth extensions allow decay of any fluctuations due to the starting transients (of the numerical routine) or the simulated wheel flat discontinuity.

Figure 10–5 shows the remaining surface roughness contribution of the surface profile measurement. This input simply contains the remaining part of the surface profile measurement after the wheel flat discontinuity has been removed. The section where the discontinuity was removed is replaced by a smooth curve that joins the two lengths of

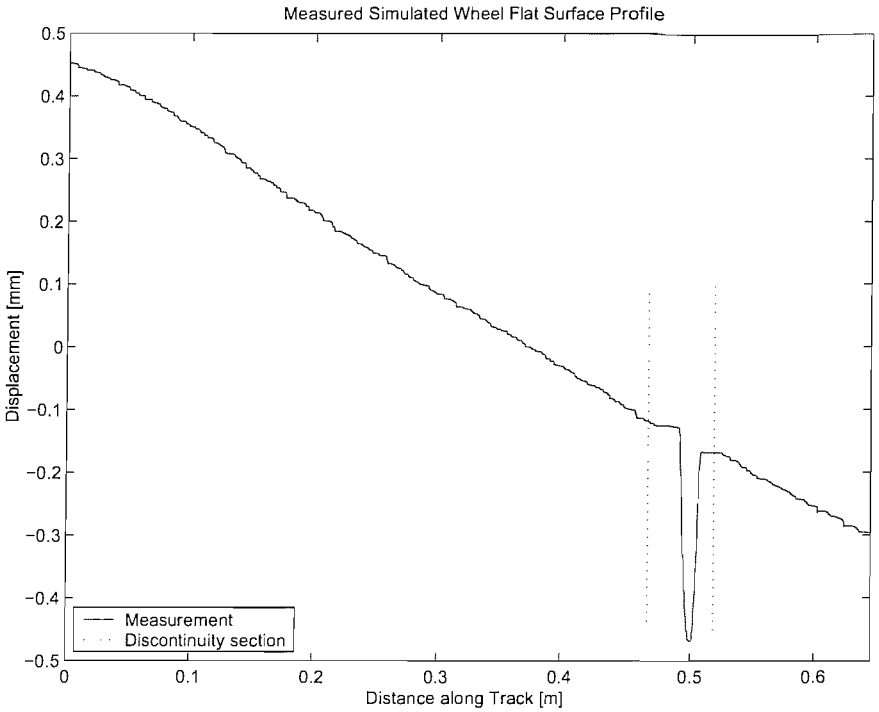

Figure 10–3 Measurement of simulated wheel flat (without any trend removal), and the position of the section removed for the discontinuity part of the input.

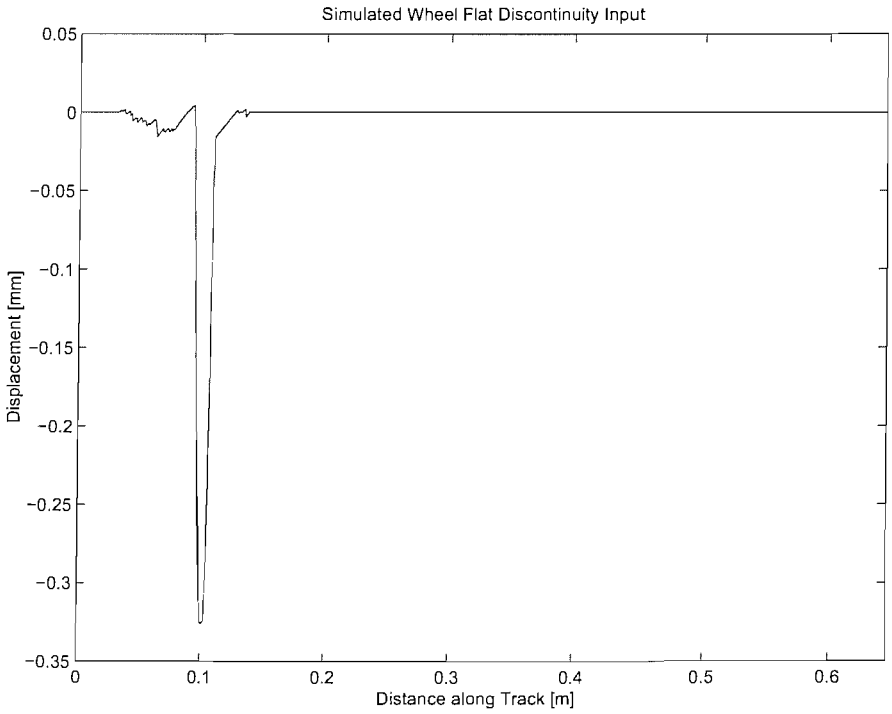

Figure 10–4 Discontinuity part of the simulated wheel flat input.

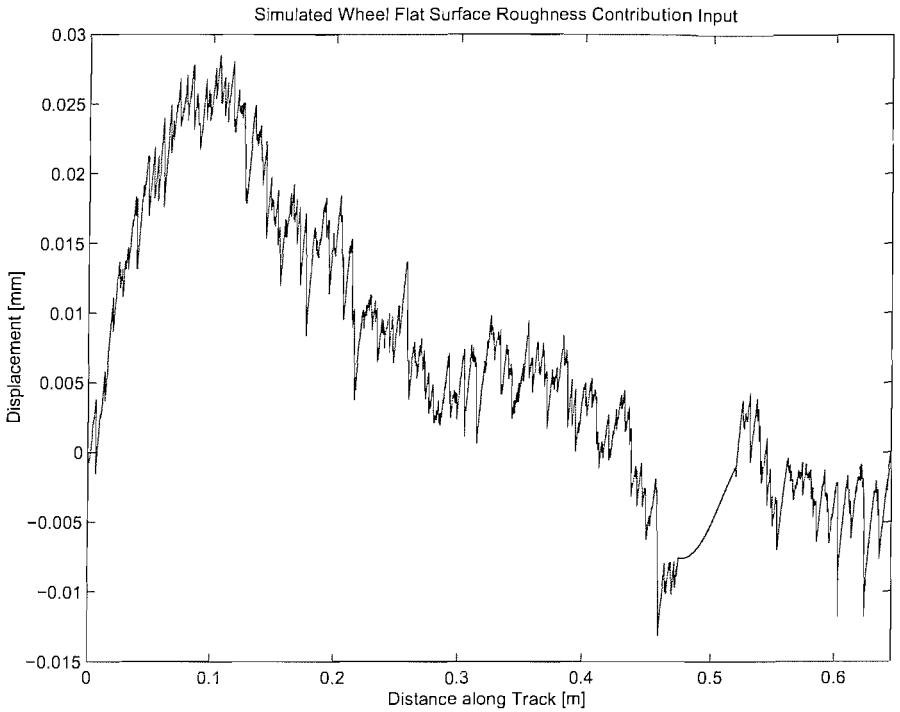

Figure 10–5 The remaining surface roughness part of the simulated wheel flat input.

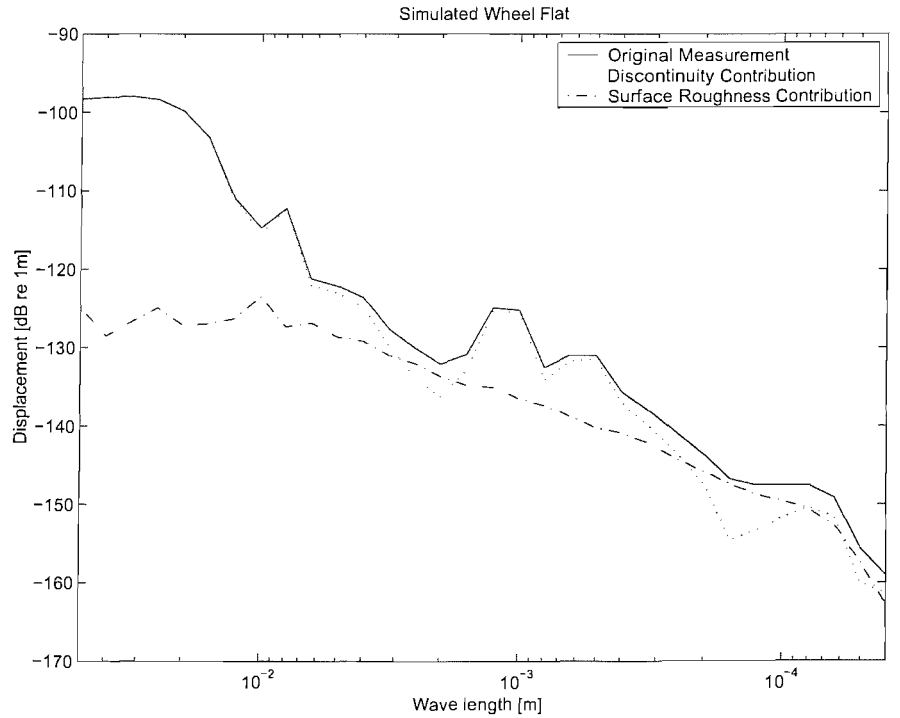

Figure 10–6 Spectra of the simulated wheel flat inputs.

surface roughness together. Both of the inputs in Figure 10–4 and Figure 10–5 were made to be of the same length so that comparisons could be easily made between the predictions using each of these inputs.

Spectra of these various parts of the surface profile are presented in Figure 10–6. This shows the spectra of the whole input (from the measurement shown in Figure 10–3), the discontinuity contribution (Figure 10–4), the surface roughness contribution (Figure 10–5), and the combined levels of the two part input. In Figure 10–6 the spectra from the whole input and the combined two part input are virtually indistinguishable, confirming the validity of the process of splitting the surface profile measurement into two parts.

Figure 10–6 shows that the surface roughness contribution is much lower than the level of the discontinuity contribution for wavelengths larger than 4mm. Similar levels are seen for both parts of the input at wavelengths smaller than 0.3mm. Unlike the step rail joints presented in Chapter 7, the wheel flat input in Figure 10–6 appears to have an effect at both long and short wavelengths. This, however, was not the case. Comparisons were made between the measured wheel flat surface profile and the fitted simulated wheel flat shape in Figure 10–1. The results are shown in Figure 10–7 where considerable differences for wavelengths less than 2mm are apparent. The spectrum of the ideal shape is more similar to the previous discontinuities as it appears to be dominated by large wavelengths. It can therefore be concluded that the short wavelength effects seen in the measured spectra of the simulated wheel flat are due to the ripples in the surface of the simulated wheel flat left by the manufacturing process (see Figure 10–1).

The effect of geometrical filtering is shown in Figure 10–8. Here it is apparent that the shorter wavelength effects due to the fluctuations on the surface of the simulated wheel flat are effectively not seen by the geometry of the wheel. At high frequencies the filtered discontinuity measurement has a similar amplitude to that of the surface roughness component. This suggests that the unwanted fluctuations within the simulated wheel flat geometry will not affect the rig vibration.

10.4 Measurements of vibration

Measurements of wheel and rail acceleration were made at several points on the 1/5 scale wheel / rail rig. The wheel and axle accelerometers were in the same positions as described in Chapter 5. Three accelerometers were again located on the rail at positions MRS6, MRS8 (the position of the simulated wheel flat), and MRS10 as in Chapter 6.

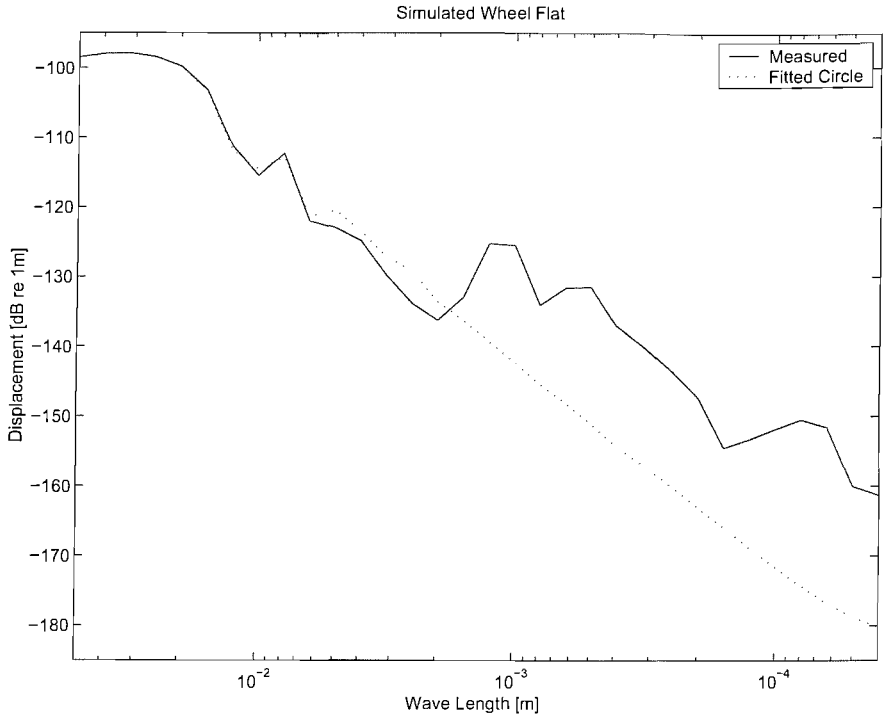

Figure 10–7 Comparisons between the measured input spectra and the spectra of the curve that was fitted to the measured profile.

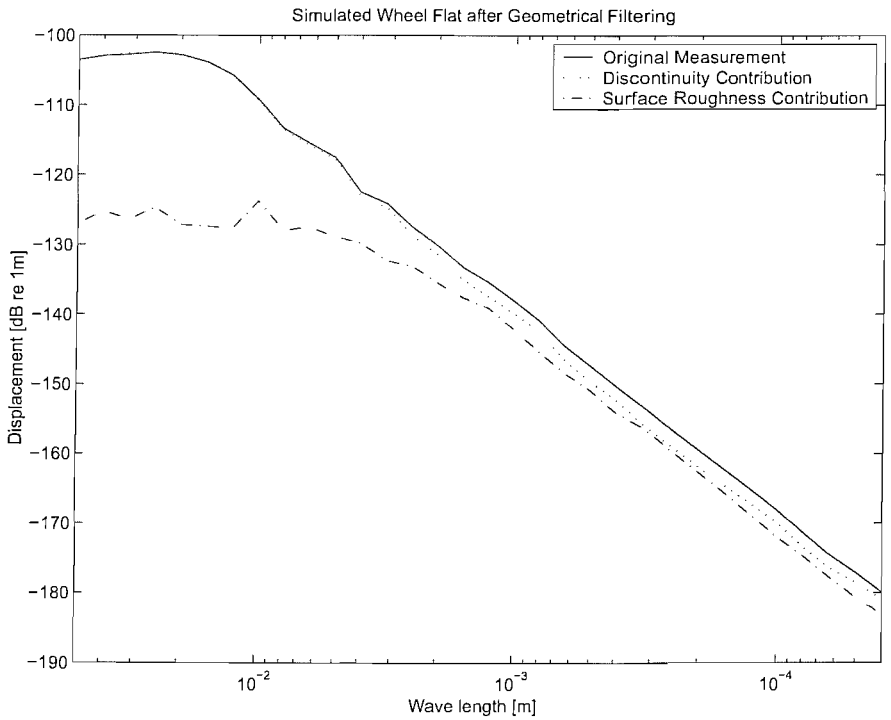

Figure 10–8 Spectra of the simulated wheel flat inputs after geometrical filtering.

As before, the wheel pre-load and wheel speed were recorded. Measurements were carried out for four wheel pre-loads and wheel speeds ranging from 1m/s to 5m/s.

An example of the measured rail acceleration is presented in Figure 10–9 for a wheel speed of 4.7m/s at a 925N wheel pre-load. Here time series from the three rail accelerometers are compared. This shows that (as for the step joints) the rail vibration is dominated by the presence of the discontinuity. The peak accelerations at MRS6 and MRS10 are seen to occur at a time where the wheel is at the point of the discontinuity rather than at the position of the accelerometer. This indicates that the inclusion of the effects of track decay may not be required to adjust the prediction formed from the discontinuity part of the input, providing the predictions are compared with a measurement made close to the discontinuity. It is also interesting to note that the vibration due to the surface roughness on the wheel and railhead is shown by an increase in acceleration close to each of the accelerometer positions at MRS6 and MRS10.

Figure 10–10 presents the corresponding outputs from the wheel and axle accelerometers. Again the peak accelerations occur at the same time (0.154s) as for the rail. Unfortunately, it is clear that the peak output from the wheel accelerometer is clipped. It is assumed that the wheel falling into the simulated wheel flat discontinuity on the railhead made such a large impact that the wheel accelerometer was not able to measure the peak acceleration. The axle accelerometer is seen to be within range but, for this wheel speed, it shows evidence of some cross talk (interference between channels) due to the overloading of the wheel accelerometer, as an additional spike is seen after the impact of the discontinuity. The wheel accelerometer measurements are therefore of no use and are not discussed further in this chapter.

Other measurements that were made through the slip rings were the wheel pre-load (which is a constant static value) and wheel velocity, which was calculated from a pulse from the tachometer that varied by large voltages (+/- 2V). Cross contamination of these channels was therefore of little importance, as any spikes were easily disregarded from the data that was required from these recordings. As measurements of the rail acceleration did not rely on the slip rings for their instrumentation, these measurements were unaffected by the problems described here. The measurements of rail acceleration used throughout the rest of this chapter are those made at MRS8, as this gives the result most representative of the wheel flat.

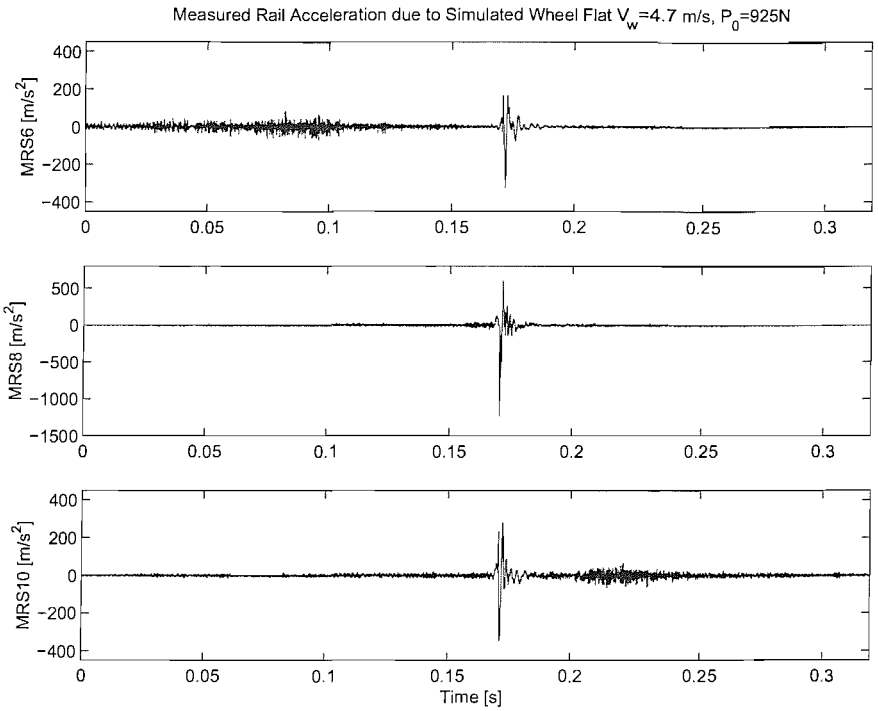

Figure 10–9 Time domain outputs from the three rail accelerometers for a wheel speed of 4.7m/s at a wheel pre-load of 925N.

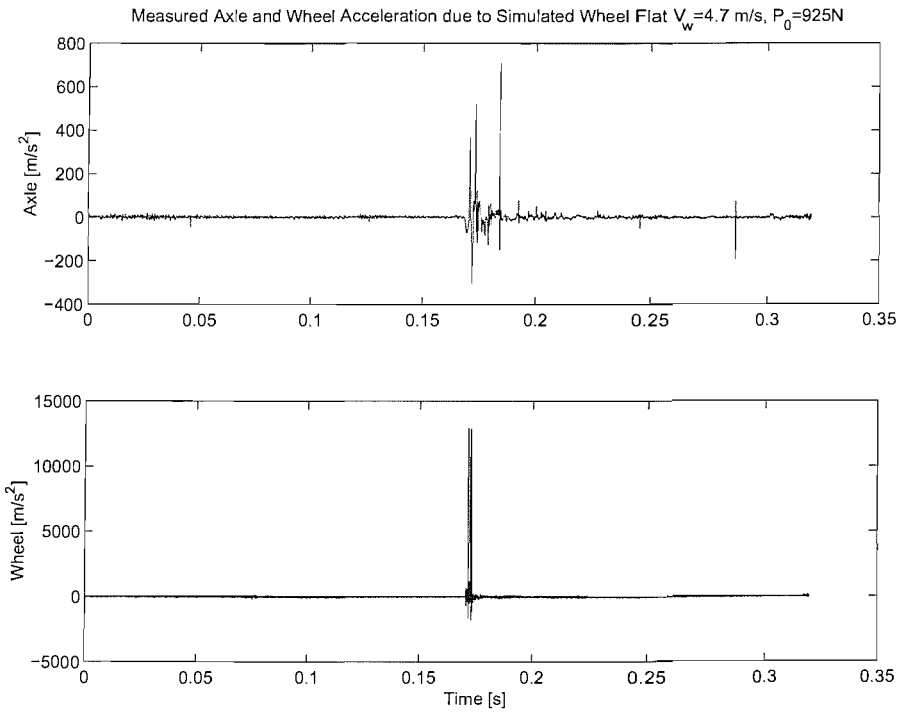

Figure 10–10 Time domain outputs from the wheel accelerometer and the axle accelerometer for a wheel speed of 4.7m/s at a wheel pre-load of 925N.

Measurements of the peak rail acceleration levels for each wheel pre-load are plotted as a function of wheel speed in Figure 10–11. These results show that the peak rail acceleration levels get larger with an increase of wheel speed. Variations in the results of the peak rail acceleration are seen with an increase in wheel pre-load. The highest wheel pre-load results are seen to follow a trend that rises at a rate of 10dB for a doubling of wheel speed. The results of the three lower wheel pre-loads appear to have two trends. A sudden increase in level is seen at about 2.3m/s for the 516N wheel pre-load, and at 3.2m/s and 3.9m/s for the 663N and 809N wheel pre-loads. These changes in level were thought to be related to the wheel losing contact with the rail. This observation is discussed when comparisons with the predictions are presented in the next section.

10.5 Comparisons of measured and predicted vibration

This section is concerned with comparisons of the measured and predicted vibration due to a simulated wheel flat on the 1/5 scale wheel / rail rig railhead. The modal wheel variant of the model has been used. Measurements and predictions of vibration are made for four wheel pre-loads ranging from 516N to 925N, at wheel speeds ranging from 1m/s to 5m/s.

Predictions were made using the two part input method described in Chapter 7. This allows adjustments (in the form of a correction to find the average rail vibration and a correction for contact filter effects) to be safely applied to the surface roughness part of the input. Only the contact filter adjustments were applied to the non-linear time-stepping model prediction formed from the discontinuity part of the input.

An example of the time-domain output from the non-linear model is shown in Figure 10–12 for a wheel pre-load of 925N and a wheel speed of 1.4m/s. This shows the predicted wheel and rail displacements together with the discontinuity input and the predicted contact force, as a function of distance along the track. It can be seen that, at this wheel speed, the wheel follows the surface of the railhead (shown by the input). When the wheel falls into the simulated wheel flat, a large impact is predicted, shown by a spike in the contact force at a value of 1.6kN. This is a relatively large value of contact force that is comparable with the step-up and step-down joints at similar low wheel speeds (see Chapter 8). Despite the large spike in the contact force, the modal wheel variant of the model does not predict loss of contact between the wheel and the rail for this low wheel speed.

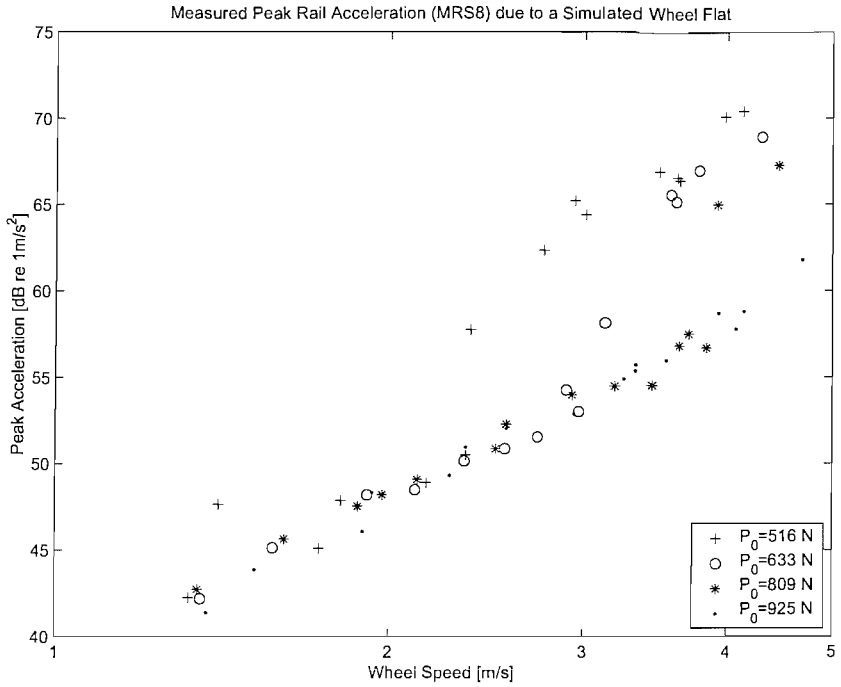

Figure 10–11 Peak rail acceleration levels as a function of measured wheel speed, for the lowest (516N) and highest (925N) wheel pre-loads considered.

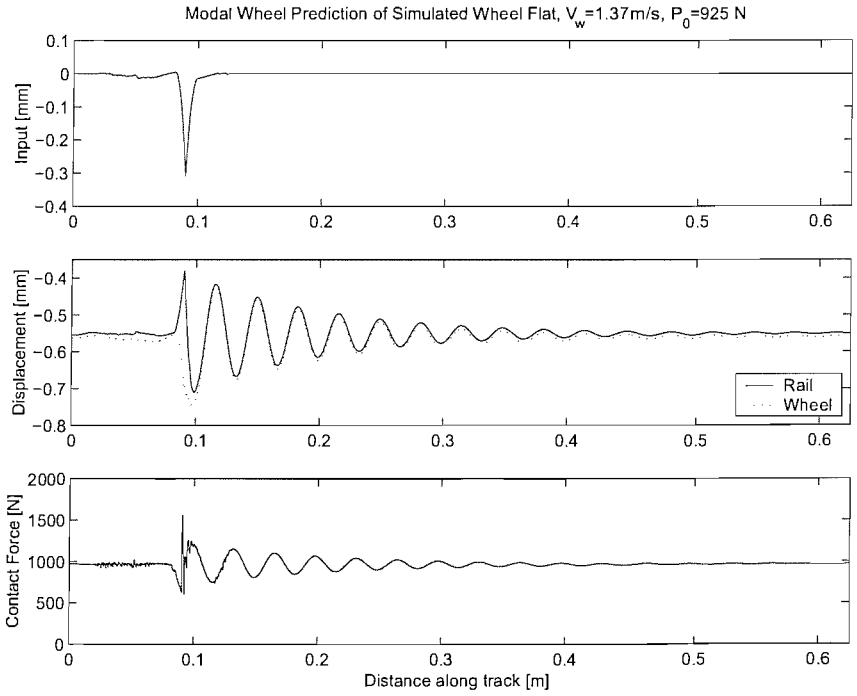

Figure 10–12 Wheel and rail displacements predicted using the modal wheel model compared with the input to the model, and the predicted contact force, for a wheel pre-load of 925N, at a wheel speed of 1.4m/s.

Further results are also shown in Figure 10–13 for the same wheel pre-load of 925N, but for a higher wheel speed of 4.7m/s. This shows that the wheel no longer follows the discontinuity on the surface of the railhead. The wheel is seen to fall slightly before it hits the far side of the simulated wheel flat. Loss of contact is predicted, as seen in the contact force both before and after the main impact. The maximum contact force is predicted to be 3.3kN, which is about two times the maximum value predicted for the lowest wheel speed and over three times the static pre-load.

Comparisons of the measured and predicted peak rail acceleration (made with the non-linear time-stepping model using the discontinuity part of the input) are presented in Figure 10–14 for the lowest wheel pre-load (516N) and the highest wheel pre-load (925N). The predicted values were found by differentiating the predicted displacements using a difference routine. As in previous chapters, the predictions were adjusted for contact filter effects by use of the FIR filter version of the approximate contact filter (see Chapter 5).

The predictions are seen to be much larger than the measurements by approximately 10dB at all the wheel speeds considered. The predictions, however, show a trend similar to that of the measurements where an increase of 10dB is seen for a doubling of wheel speed. The predictions do not however reproduce the behaviour seen in the measurements where the three lowest wheel pre-loads display sudden increases in the peak values at higher wheel speeds. It was thought that this might be due to the wheel unloading. A record of the wheel speed at which the predicted contact force (using both the simple variant and the modal wheel variant) became zero is presented in Table 10-1. This shows that the predictions made using the modal wheel variant are closest in agreement with the measured observations. These comparisons, however, do not demonstrate conclusively that the change in measured peak acceleration is in fact due to wheel unloading. Further investigations are required, where closer attention is paid to effects such as the wheel on track resonance.

An example of the predicted and measured rail acceleration spectra is presented in Figure 10–15 for a wheel pre-load of 925N and a wheel speed of 1.4m/s. It is clear that the prediction formed from the surface roughness part of the input has made no significant contribution to the overall predicted level. The predictions are greater than the measurements at all frequencies, with the largest differences (over 20dB) around 1-3kHz.

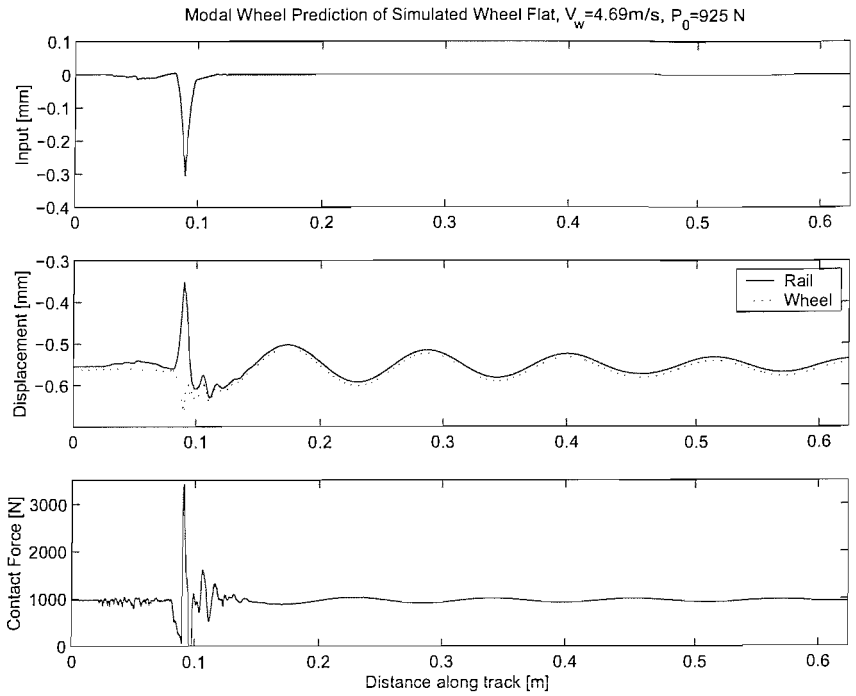

Figure 10–13 Wheel and rail displacements predicted using the modal wheel model compared with the input to the model, and the predicted contact force, for a wheel pre-load of 925N, at a wheel speed of 4.7m/s.

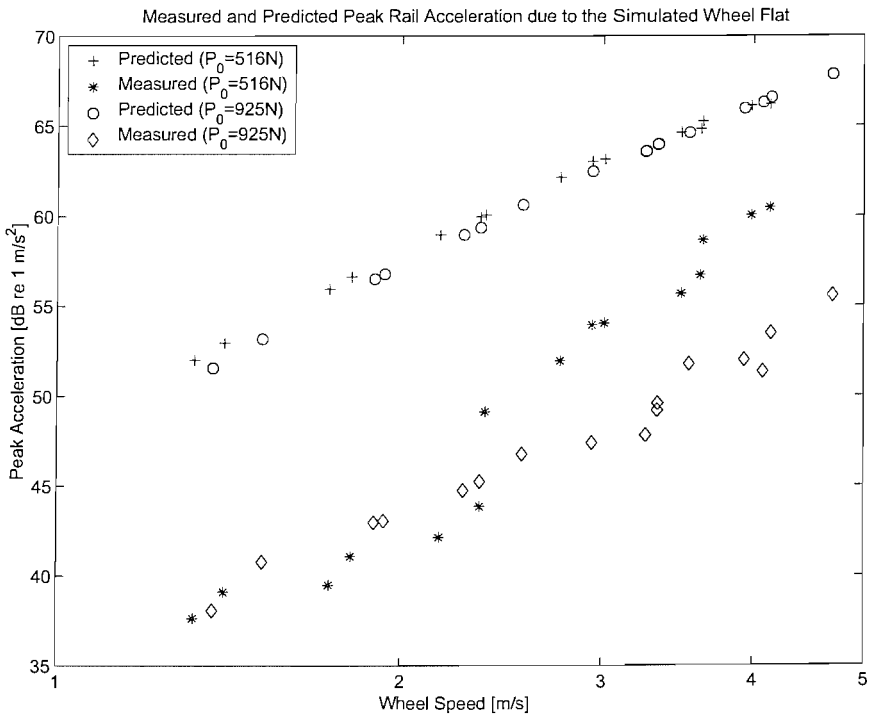

Figure 10–14 Measured and predicted (using the modal wheel model and the discontinuity part of the input) peak rail acceleration due to the simulated wheel flat as a function of wheel speed (1m/s to 5m/s).

Table 10-1 Measured and predicted wheel speeds at the point of wheel unloading

Wheel pre-load	Modal wheel variant	Simple variant	Measured observation
516N	2.2 m/s	1.8 m/s	2.3 m/s
663N	2.6 m/s	2.1 m/s	3.2 m/s
809N	3.2 m/s	2.5 m/s	3.9m/s
925N	3.3 m/s	2.9 m/s	-

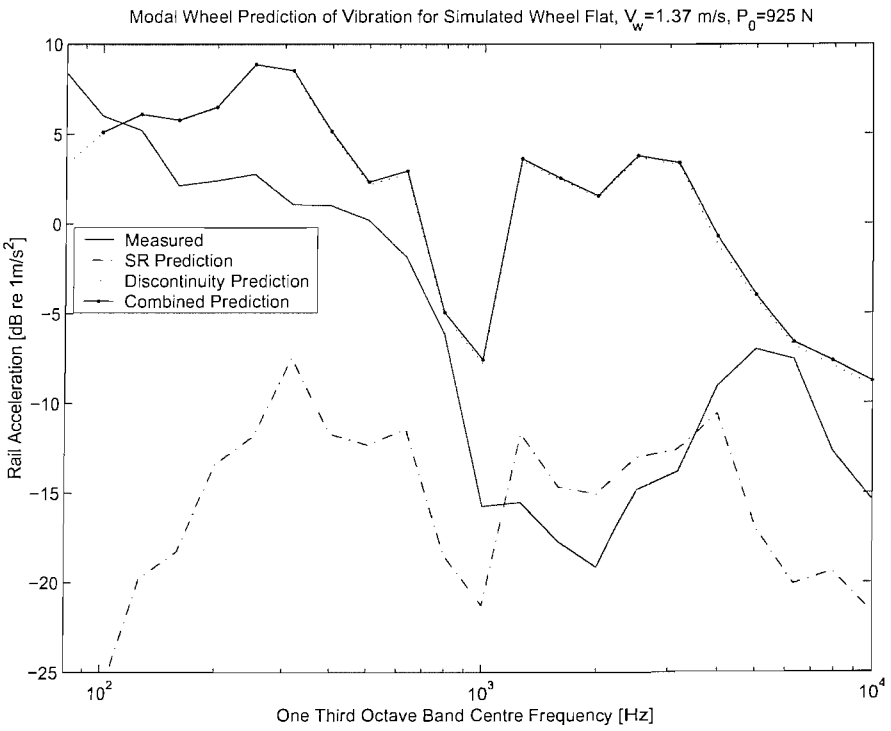

Figure 10–15 Modal wheel model predicted rail acceleration (using 2 inputs), including adjustments for contact filter effects, compared with the measured rail acceleration, for a wheel pre-load of 925N at a wheel speed of 1.4m/s

Figure 10–16 shows similar results as in Figure 10–15, but for a wheel speed of 4.7m/s. The same features are also evident here. Again, the predicted surface roughness contribution is much lower than the prediction formed from the discontinuity input. However the differences between the measurements and predictions are smaller in this case.

The difference between the overall predicted rail acceleration level (including the contact filter effects) and the measured rail acceleration level are presented for four wheel pre-loads and all the measured wheel speeds in Figure 10–17. This shows that the overall predicted level greatly exceeds the measured level at frequencies above 200Hz for the low wheel speeds. Better agreement is found for higher wheel speeds. Little variation is noticeable due to variations in wheel pre-load. Variations with wheel speed are seen at all frequencies above 1kHz. A possible reason why the predictions are in better agreement with the measurements at higher wheel speeds is discussed in section 10.7.

Results of the predicted wheel acceleration levels for the two parts of the input are presented in Figure 10–18 for a wheel speed of 1.4m/s and a wheel pre-load of 925N. These are compared with the measured axle acceleration levels, but as explained in section 10.4 the measurements were found not to be reliable. They are therefore only included as an approximate guide. Although the prediction due to the discontinuity part of the input is seen to dominate the overall prediction, as it does for the rail acceleration, the difference between the two components is smaller in the present case. The prediction due to the discontinuity input is only much larger than the prediction due to the surface roughness contribution below 400Hz. Similar results are shown in Figure 10–19 for a wheel speed of 4.7m/s and a wheel pre-load of 925N. Here the prediction formed from the discontinuity part of the input is seen to exceed that formed from the surface roughness contribution at frequencies up to 1.2kHz. Thus, as for other discontinuities the predictions formed from the discontinuity input are seen to make a greater impression on the overall predicted levels at higher wheel speeds.

10.6 Analysis of the predicted contact force

Predictions of the peak contact force formed from the simple variant and the modal wheel variant are presented in Figure 10–20. These results are presented as a ratio of peak predicted contact force to static wheel pre-load. The ratios formed from the simple variant are seen to be larger than the ratios formed from the modal wheel variant. In the

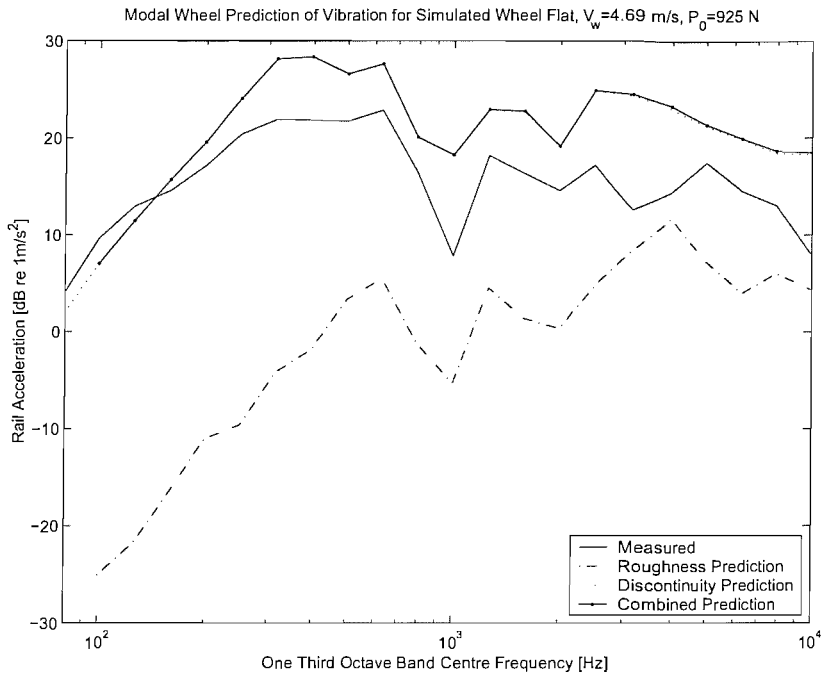

Figure 10–16 Modal wheel model predicted rail acceleration (using 2 inputs), including adjustments for contact filter effects, compared with the measured rail acceleration, for a wheel pre-load of 925N at a wheel speed of 4.7m/s

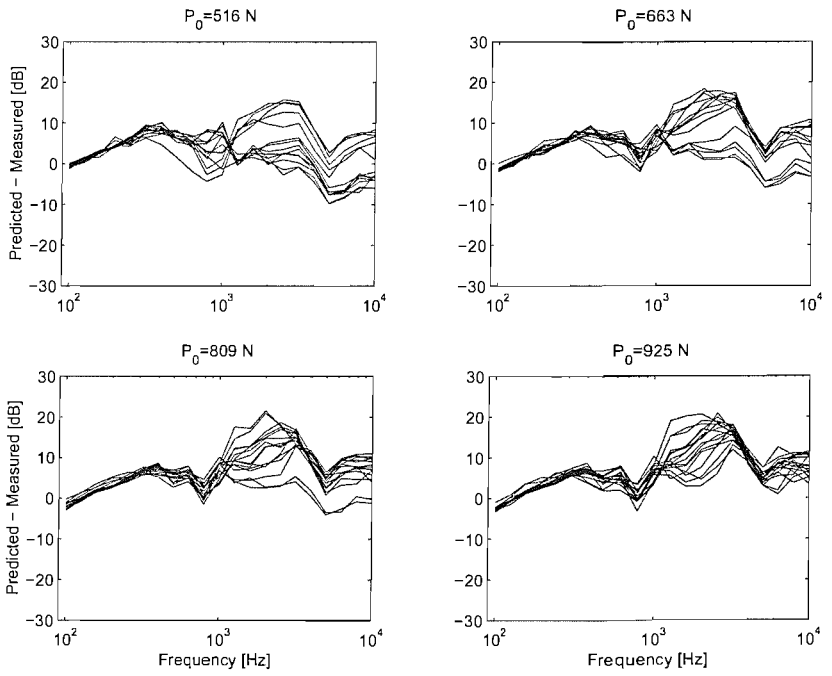

Figure 10–17 Modal wheel model predicted minus measured rail acceleration levels for four wheel pre-loads at speeds ranging from 1m/s to 5m/s. The overall prediction level used consists of a contribution due to the railhead surface roughness and the simulated wheel flat discontinuity. Predictions are adjusted for contact filter effects.

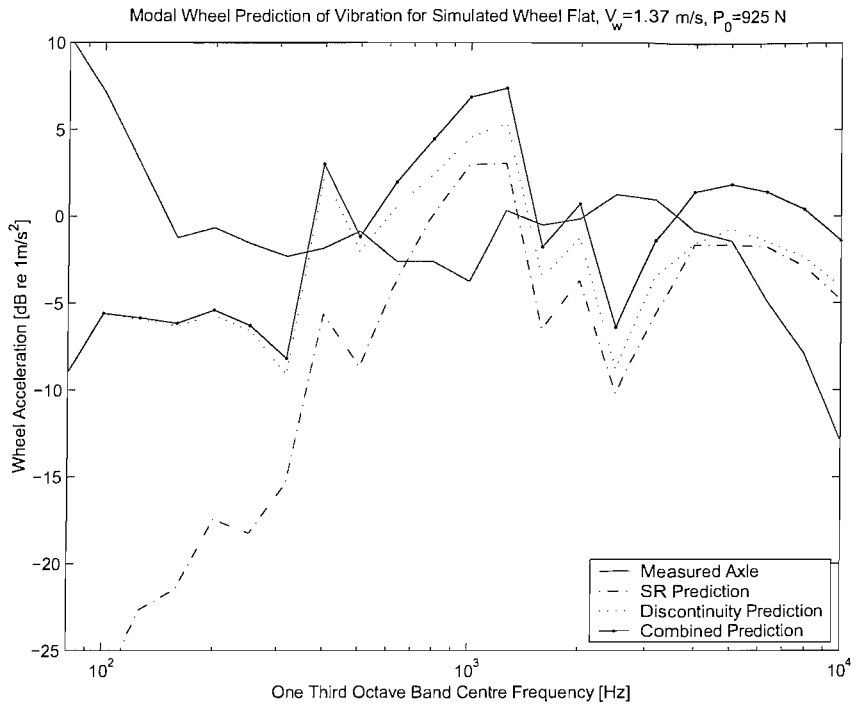

Figure 10–18 Modal wheel model predicted wheel acceleration (using 2 inputs), including adjustments for contact filter effects, compared with the measured wheel acceleration, for a wheel pre-load of 925N at a wheel speed of 1.4m/s

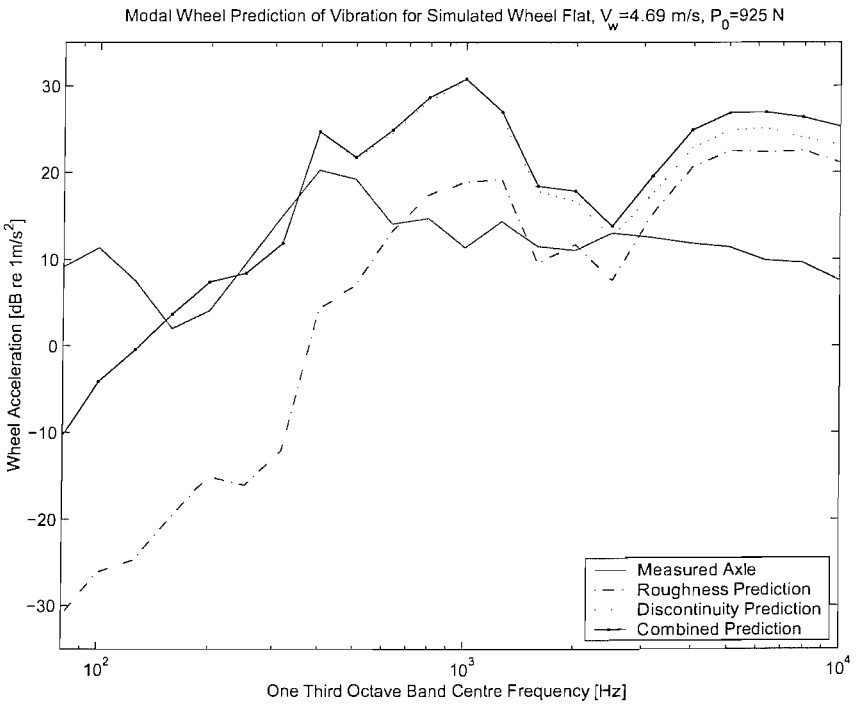

Figure 10–19 Modal wheel model predicted wheel acceleration (using 2 inputs), including adjustments for contact filter effects, compared with the measured wheel acceleration, for a wheel pre-load of 925N at a wheel speed of 4.7m/s

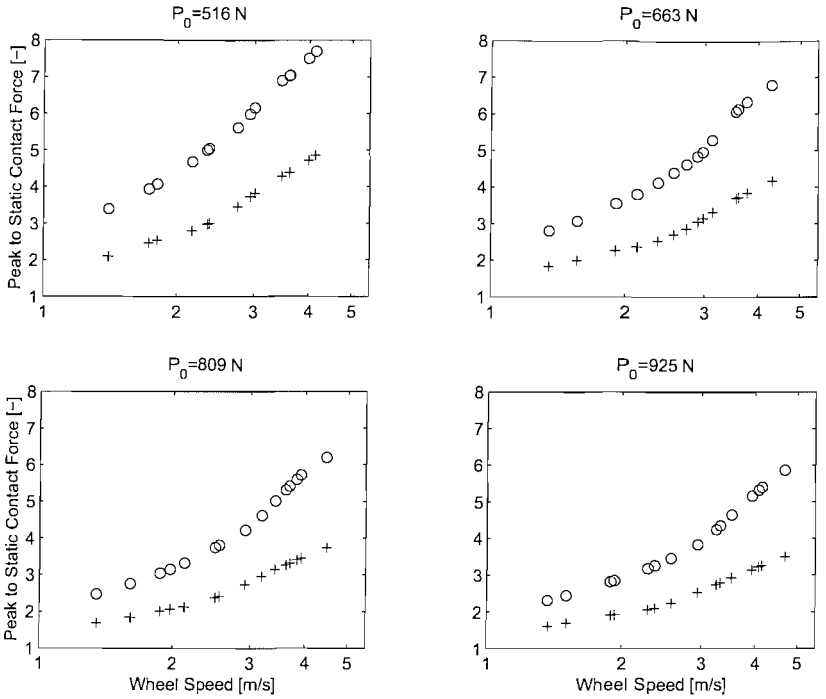

Figure 10–20 Ratio of predicted peak to static contact force due to a wheel rolling over a simulated wheel flat. Results are shown as a function of wheel speed for both the modal wheel variant (+) and the simple variant (o).

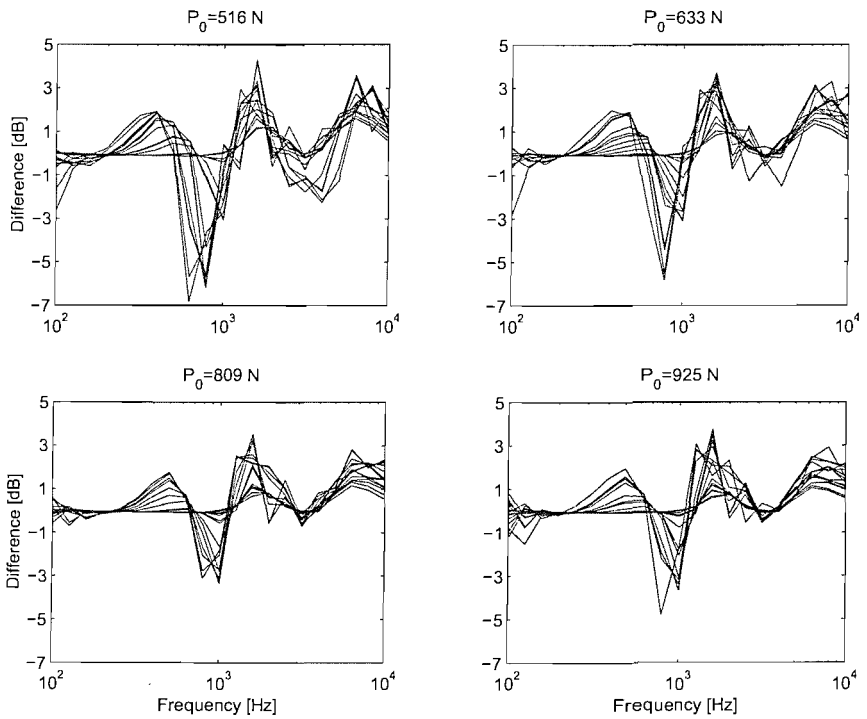

Figure 10–21 Difference in level between the non-linear predicted contact force due to the simulated wheel flat (using the simple model) and the linear predicted contact force due to the simulated wheel flat (using the simple model).

results from both of the variants the contact force changes slope at the speed at which the rig wheel is predicted to lose contact with the rail, as listed in Table 10-1. This result is discussed further in the conclusions.

Comparisons in the frequency domain between the time-stepping models using linear and non-linear contact spring relationships are considered next. These comparisons are made using the method introduced in Chapter 7. The difference in level for the simple variant non-linear and linear predicted contact force is shown in Figure 10–21. This shows that the maximum absolute difference between the two predictions is 7dB. This is found to occur for the lowest wheel pre-load (516N). Differences between the non-linear and linear predictions are seen to decrease as the wheel pre-load increases from 516N to 809N. This is to be expected as under lighter wheel pre-loads more non-linear behaviour is expected [Wu and Thompson 2000(a)]. Results of the highest wheel pre-load at 925N, however, are found to exhibit larger differences in the 800Hz to 1kHz frequency bands than for the 809N wheel pre-load. The differences in predicted contact force in Figure 10–21 are seen to be both positive and negative. Values of the linear and non-linear contact force are therefore seen to exceed each other in certain frequency bands. A similar trend was seen for the level joint (see Chapter 8), although the magnitudes of the differences are not similar.

Differences between the contact force from the non-linear and linear modal wheel variants of the time-stepping models are presented in Figure 10–22. These variations become smaller with an increase in wheel pre-load. The maximum absolute difference is seen to be smaller than for the simple variant. As for the simple variant results the differences in the predictions made using the modal wheel variant are seen to be both positive and negative in particular frequency bands.

10.7 Conclusions

Measurements and predictions of wheel and rail vibration have been made due to a simulated wheel flat for four wheel pre-loads and many wheel speeds ranging from 1m/s to 5m/s. The agreement between measurements and predictions has not been found to be as good as for the case of surface roughness. It is not clear whether this is due to deficiencies within the predictions or problems relating to the measurements. When the rig wheel rolled into the wheel flat discontinuity it was found to produce a large peak acceleration that exceeded the maximum limit of the transducer. This had not occurred for the other discontinuities. As such a large impact was produced, it is possible that this

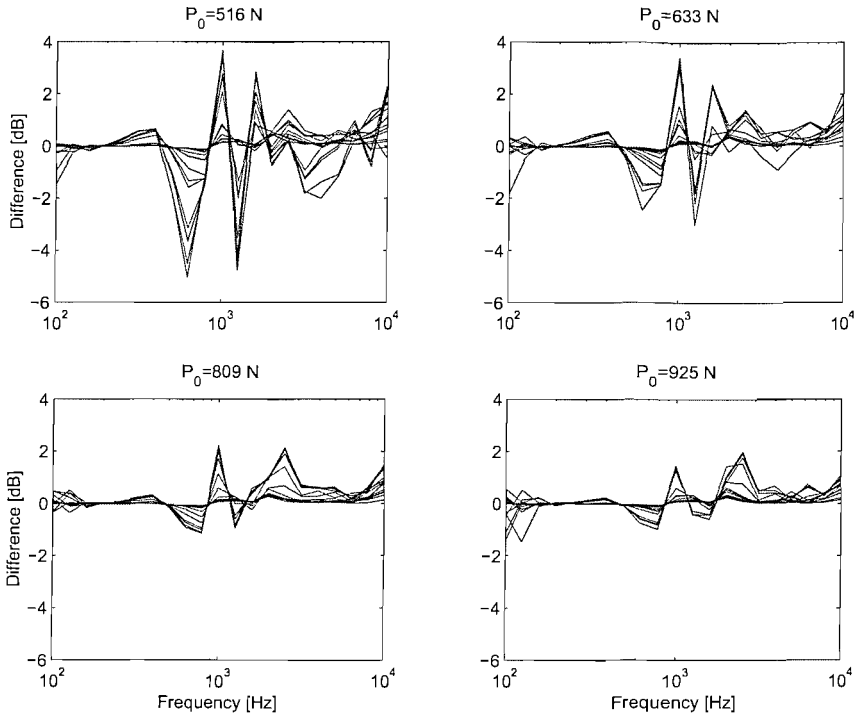

Figure 10–22 Difference in level between the non-linear predicted contact force due to the simulated wheel flat (using the modal wheel model) and the linear predicted contact force due to the simulated wheel flat (using the modal wheel model).

caused the track resilient elements to behave in a non-linear manner. This, however, would need to be verified. It is possible that a wheel flat with a smaller depth would have been more appropriate.

The results of the wheel flat investigations in Figure 10–17 show that the predicted rail acceleration levels are often greater than the measurements between 1kHz and 3kHz (depending on the wheel speed). This could indicate an under-attenuation of the contact filter adjustment (which strongly influences this frequency range), whereas over-attenuation has been indicated in similar frequency bands for the step-up joint (Figure 8-43). The comparisons between the overall predicted levels and the measured levels of rail acceleration have been encouraging. Perhaps the inclusion of a two dimensional elastic contact model would help to improve the predictions; reducing the variations with wheel speed above 1kHz shown in Figure 10–17.

The measured peak rail accelerations in Figure 10–11 demonstrated a trend that could be related to wheel unloading. However, the measured speeds at which this occurred did not correspond particularly well with predictions made with the modal wheel and simple variations of the non-linear time-stepping models (see Table 10-1). Whilst the predicted accelerations failed to show a trend similar to the measured rail acceleration, the predicted contact force (shown as a ratio of peak contact force to static wheel load) did demonstrate a change in slope at the speed at which the wheel unloaded. Further investigations should be made (perhaps with a smaller discontinuity depth). Future investigations should include a good representation of the wheel / rail contact dynamics, with an accurately modelled wheel-on-track resonance.

Comparisons between the predictions formed from the surface roughness part of the (simulated wheel flat) input and the predictions from the discontinuity part of the input have shown that the overall predicted level is dominated by the predictions formed from the discontinuity part of the input. This has been shown to be the case for both rail and wheel vibration. The surface roughness part of the input, however, has been seen to influence wheel vibration more than rail vibration. This has been found to occur for the other large sized discontinuities (for example the step-up and step-down joints) that have been investigated during this research.

11 Discussion and conclusions

This final chapter summarises the findings of the research presented in this thesis and presents recommendations for future work.

11.1 The 1/5 scale rig

The work contained within this thesis has been concerned with measurements and predictions of wheel / rail interaction on a 1/5 scale rig. Use of a scale model has been advantageous over measuring full scale situations because the measurements in the laboratory are controlled, and they are not hindered by the numerous operational requirements of a railway. The former is of particular interest as researchers have found that it is often difficult to obtain reliable data for comparisons with their predictions. The convenience of the scale rig, however, is not without problems. Broadly speaking these were related to measurement and manufacture of components at small scale.

Chapter 3 presented a set of scaling laws that were used to produce a track bed that was a 1/5 scale representation of a modern mainline concrete sleeper track. Whilst the track model was representative of the full size case, wheel loads applied to the track were not. This results in an incorrectly scaled contact patch dimension. Geometrical alterations were made to the railhead curvature to increase the contact patch length. Although this was a compromise as the lateral dimensions are incorrect, it was the only realistic method of adjustment available for the scale rig.

Accurate measurement of the surface profiles (introduced in Chapter 4) involved: careful examination of the requirements (or limits) of the predictions, measurement of the position along the surface being measured, and consideration of the properties of the measurement transducer. Despite the great care taken with the surface profile measurements, it was found that amplitudes of the shortest wavelengths (required for the predictions) were difficult to measure.

For practical measurements it is hard to find a transducer that can measure large bandwidths. This was demonstrated by the surface profile measurements made with the LVDT as well as the accelerometers that were used to measure wheel and rail vibration. For example, it was found that the measurement of properties such as the wheel-on-track resonance was not possible with the transducers used (although indications of the wheel-on-track resonance are shown in Figure 8-11 and Figure 8-12). This was unfortunate as it was discovered that the wheel-on-track resonance plays an important

role in the interaction of railway wheels and rails, particularly when predicting vibration due to a discontinuity on the railhead surface.

Other problems related to the use of small scale dimensions concerned the manufacture of the railhead profiles for the investigations. A good example of this is shown in Chapter 9, where a CNC milling process was unable to reproduce the subtle curves of the dipped rail profiles. Problems were also encountered with the simulated wheel flat where the manufacturing process resulted in a corrugated surface within the desired profile.

Nevertheless, despite these drawbacks of the 1/5 scale rig it has provided a controlled environment in which comparisons between measurements and predictions of vibration due to several different railhead profiles have been studied. Suggestions of improvements that could be made to the rig are listed later in section 11.5.1.

11.2 Comparisons of the measured and predicted vibration

Many comparisons of the measured and predicted vibration for different types of railhead surfaces have been presented in this thesis. The best agreement between the predictions and measurements was for rail vibration due to a surface roughness input, where the measured variant of the FRF model was used to form the predictions. Worst agreement was found for the comparisons of wheel and axle vibration, as the measurements were thought to have been strongly influenced by noise. These comparisons were therefore not pursued.

The performance of the measured variant of the FRF model was used as a benchmark. It was not expected that the predictions of vibration (due to other railhead profiles) would be in as good agreement as for the case of surface roughness. Some comparisons, however, were in almost as good agreement, for example for the 2mm dipped rail.

Unfortunately, the majority of the comparisons were not as good as the benchmark case. Reasons for poor agreement with the measurements have been attributed to:

- contact filter effects,
- the effect of track decay rates,
- and poor measurements.

The requirement for a reliable two-dimensional contact filter was realised at an early stage of the research. Published methods failed to yield predictions for the 1/5 scale rig that gave good agreement with the measurements. It is not known why these methods did not work on the 1/5 scale rig. It may be related to the small radius of curvature of the railhead, which was introduced to obtain a realistic contact patch length. Nevertheless as the existing methods were shown not to work, an approximate contact filter was derived using measured data. The performance of this approximate contact filter was verified at wheel pre-loads within the range 500N to 1kN for a surface roughness input. It is not known how the contact filter effects behave outside of this range of wheel pre-loads, or for surfaces other than low amplitude roughness. This might explain why the differences in level between the predictions and the measurements existed for some surface profiles at high frequencies (>1kHz).

A more accurate two-dimensional contact filter is currently being developed [Ford and Thompson, 2003] which combines both the contact filter effect and the geometrical filtering effects described in Chapter 4. It is hoped that this model will be able to help improve the performance of the wheel / rail interaction models described within this thesis.

Even for the best case of agreement between the predictions and measurements, (rail vibration due to a surface roughness input using the measured FRF variant) the resulting differences (between measured and predicted levels) ranged between –6dB and +6dB in each one-third octave band. These are large differences, but they are similar to the performance of other prediction models. Efforts have been made previously to try to improve the performance of prediction models which often involve complicated representations of the wheel and the track (for example [Grassie et al, 1982, Gavric 1995, Thompson 1993(c), and Knothe 1994]). There is little doubt that they enhance the representations of the separate parts of the wheel / rail interaction model, but these improvements have not dramatically reduced the differences between the measurements and predictions (such as those presented in Chapter 6). It can therefore be concluded that a better understanding of wheel / rail interaction is required.

A factor based on the track decay rates was used to determine the average rail vibration during the passage of a wheel from that at the wheel / rail contact point. This adjustment was applied to the predictions based on the surface roughness contributions for each input considered. For the component of vibration due to the discontinuity part of the

input, this adjustment was not included in the predictions of rail vibration. However, since the transient due to the discontinuity decays rapidly in time and the measurements were made at a position close to the discontinuity, the effect of track decay is not likely to influence these results strongly.

The non-linear prediction model could also be improved by inclusion of effects such as lateral vibration and wheel rotation. These effects might improve agreement between measurements and predictions, and could follow a process of gradual improvement and development much like the evolution of the TWINS package.

Chapter 5 described investigations into the performance of several variants of the prediction models. The linear models were expressed as transfer functions between roughness and vibration. These transfer functions have the form of an attenuation at high frequencies. As the wheel / rail contact stiffness reduces, the attenuation increases at high frequencies and shifts towards lower frequencies. Pole and zero plots of the simple variant and the modal wheel variant transfer functions showed that the prediction models remained stable as the contact stiffness between the wheel and the rail was varied. The method of evaluating the performance of the predictions model as a transfer function has been shown to be a useful way of studying the performance of the prediction model.

The surface profile measurement is a potential source of errors. Chapter 4 presents a method that attempts to improve the quality of measured profiles, but the LVDT that was used for the measurements was limited by a small frequency bandwidth necessitating very low measurement speeds. Further research is required in this area. The existing methods of post processing the roughness inputs also need development. The existing geometrical filter, for example, does not allow for localised deformation between the wheel and the rail. This would be included in a 2D contact model such as [Ford and Thompson, 2003].

It was noted during the investigations of the step-down joint and the simulated wheel flat that the differences between predictions and measurements of rail vibration for these large discontinuities were not in as good agreement as for situations with smaller discontinuities. This might be explained by the possibility that the resilient elements of the scale model track bed were compressed so much due to wheel / rail impacts that they behaved in a non-linear fashion. However, this needs to be verified.

The measurements of wheel and axle acceleration were found to be contaminated by noise. This was believed to be associated with the slip rings. Consequently the comparisons between measurements and predictions were not pursued for the axle and wheel comparisons. Other measurement noise problems occurred in the static measurements of the wheel and track accelerances where frequencies below 80Hz were poorly measured by the accelerometers. This prevented a reliable appraisal of the wheel-on-track resonance with both static and rolling wheel measurements.

Despite the various problems encountered throughout this research, the overall performance of the non-linear wheel / rail interaction models based on [Wu and Thompson, 2000(a)] was very good.

By way of summary, the next section gives a list of the contributions that have been made in this thesis.

11.3 Contributions of the research in this thesis

The following unique contributions have been made to the study of wheel and rail vibration:

1. A 1/5 scale railway track has been designed and manufactured that behaves dynamically (at 1/5 scale) much like that of a full scale mainline track (see Chapter 3).

2. A simple method has been devised that compares evidence of reflections in the manufactured 1/5 scale track with the behaviour of a clamped-clamped beam. This was done by comparing fluctuations in the modulus and phase of a point accelerance measurement of the track with the behaviour of a continuously supported (double elastic layer) rail model, and the behaviour of a clamped-clamped beam (see Chapter 3).

3. A new surface profile measurement method using an LVDT has been developed so that an adequate quality input is obtained for the prediction models (see Chapter 4). This has involved the development and manufacture of a wheel and tachometer assembly which is used to provide an accurate representation of the distance travelled along the length of a surface during a measurement. An anti-aliasing filter and data re-sampling technique have been used to ensure good quality data.

4. An alternative method of surface roughness measurement was formulated where the force gauge and the rig wheel pre-loading spring were used to measure the combined wheel and rail roughness (see Chapter 4). This method was only found to be suitable for the measurement of roughness wavelengths greater than about 1mm.

5. A method of estimating the acceleration at the point of wheel / rail contact from measured rail vibration data has been developed for the case of surface roughness on the wheel and railhead surfaces (see Chapter 5).

6. From the estimate of point acceleration (item 5 above), a method of estimating the track vibration decay rate has been made (see Chapter 5). This measurement of track decay was found to be different than the track decay calculated from static test measurements. This difference is attributed to a defect in the construction of the rig track bed. Resilient elements that were used to represent the ballast layer were found not to be securely adhered. This caused the vertical stiffness and damping of the rig track bed to be different when it was compressed under the weight of the rig wheel from when it was unloaded.

7. A method of approximating contact filter effects using a linear FRF prediction and the estimated point acceleration (item 5 above) was derived for the case of surface roughness of the wheel and railhead. From these results, an approximate contact filter was formed both as a frequency domain adjustment, and as a (FIR) filter (see Chapter 5). The behaviour of this approximation has been analysed both in the form of its FRF and in the position of its poles and zeros.

8. A method of modelling the frequency response of the rig wheel as though it was a set of mass-spring-dampers has been successfully implemented to form what has been called the modal wheel variant (see Chapter 5). This model has been successfully used in the time-domain simulations throughout.

9. Studies of the transfer functions between roughness and wheel, rail, and contact spring vibration have been made. Whilst these studies are only relevant when the wheel and the rail remain in contact, they demonstrate the (linearised) contact stiffness behaviour for different contact force values (see Chapter 5). These studies have been presented in the form of frequency response functions and pole and zero plots.

10. A method of splitting a surface profile measurement into two parts has been devised and used to allow corrections to be applied to the prediction formed from the surface roughness part of the input. This method allows the effect of any adjustments made to the predictions to be monitored.

11. An extensive set of measurements and predictions of railway vibration have been made and compared for different railhead profiles on the 1/5 scale wheel / rail rig (see Chapter 3 to 10). Predictions of rail vibration due to surface roughness have been shown to be in good agreement with the measurements.

12. For predictions of vibration due to a discontinuity on the railhead (using the method in item 10), it was found that rail vibration is mostly dominated by the effects of the discontinuity part of the input, whilst wheel vibration is more influenced by the surface roughness contribution.

13. The wheel-on-track resonance has been shown to be an important aspect of a prediction model, particularly for situations where large discontinuities are present on the railhead. The wheel-on-track resonance has been found to dominate the vibration of the predicted displacements, and for the case of a step joint, where loss of wheel / rail contact occurs, the measured rail acceleration.

14. An alternative method of predicting wheel and rail vibration has been developed from the form of the models developed by [Wu and Thompson, 2000(a)]. This is presented in Appendix B.

11.4 Comparisons of predicted contact force

The method of estimating the degree of non-linear behaviour experienced by the prediction models that was presented in Chapter 7 was used for each of the railhead profiles studied in this thesis. The results for the smooth railhead are presented in Figure 7-8 and Figure 7-9 for the simple model and the modal wheel model respectively. Here differences in the one-third octave band spectra were less than 0.5dB. This suggests that predictions of this surface geometry can be made with either a non-linear or linear contact spring relationship for the wheel pre-loads and wheel speeds considered.

Results for the railheads with intended discontinuities, however, were found to produce larger differences in the predicted one-third octave band spectra. The results for the dipped rail inputs in Figure 9-28 to Figure 9-32 show differences that can be as much as 6dB, but they are generally less than 2dB for the frequency range considered (100Hz to

10kHz). Comparing the results of the dipped rail with the smooth rail it is clear that the dipped rail differences are often greater in magnitude, but as these differences are often small (less than 2dB) they suggest that the linear model prediction provides an adequate approximation of the non-linear model prediction. Predictions of the dipped joints for the wheel pre-loads and wheel speeds considered can therefore be approximated with the linear model.

The differences in the predicted non-linear and linear contact force spectra for the simulated wheel flat and the step joints were found to be much larger than for the smooth rail. Use of the non-linear contact spring relationship is therefore advisable for these inputs. This is particularly the case for the step down joint (see Figure 8-50 and Figure 8-51) that was found to have the largest differences in predicted contact force spectra.

As well as estimating the degree of non-linear behaviour experienced by the prediction models this method (in Chapter 7) also demonstrated a difference between the two variants of the prediction models. Differences between the non-linear and linear predicted contact force spectra were found to be larger for the simple variant than for the modal wheel variant when the inputs contained discontinuities (dipped rails, simulated wheel flats, and step joints). This is an interesting result that deserves further investigation. The results of this method also demonstrated that an increase in wheel pre-load often resulted in smaller differences in predicted contact force spectra than for the lower wheel pre-loads.

11.5 Recommendations of future work

11.5.1 Improvements to the rig

The following parts of the rig should ideally be changed to improve its usefulness:

- The flat drive belt system was found to be particularly unreliable. Often it was hard to complete a full set of measurements without having to stop the measurements to clean and re-adjust the belt. A toothed belt drive might alleviate this problem, but a direct drive system would probably be better. For this, considerable redesigning of the rig would be necessary.
- The adhesive of the track bed supports should be replaced with better glue.

- The slip-ring assemblies should be removed from the instrumentation and replaced by a non-contact telemetry system so that reliable measurements of the wheel and the axle can be made.
- A wider frequency bandwidth of vibration should be measured in future experiments, ideally in the range 10Hz to 25kHz.

11.5.2 Suggested future experiments

It is expected that the outcome of the following experiments would be of particular interest:

- Investigate the behaviour of the model track bed, to ascertain whether large impacts of the wheel hitting the track cause the support structure to behave in a non-linear manner. This should help to clarify whether the discrepancies between the predicted and measured vibration due to the step-down joint and the simulated wheel flat were influenced in this way.
- Measure the low frequency response of the wheel and track to ascertain the frequency of the wheel-on-track resonance more reliably. Adjust the models accordingly and compare measurements with predictions (at low frequencies) to evaluate the damping of the wheel-on-track resonance.
- Repeat some of the experiments due to railhead discontinuities to check the agreement with the axle and wheel measurements.
- Investigate the alternative method of measuring the combined surface profile using the force gauge. Attempt to find out why noise contaminates the measurements at wavelengths shorter than 1mm.
- Attempt to find an alternative transducer with a larger bandwidth for the measurement of surface profiles. Compare its performance with the LVDT, and the force gauge method at large wavelengths.

11.5.3 Recommended improvements to the existing prediction models

The following improvements to the prediction models would be beneficial for both full scale and 1/5 scale predictions:

- Include a more realistic representation of the wheel-on-track resonance (see above).
- Include a two dimensional contact filter model within the prediction process. This should be possible using the work of [Ford and Thompson, 2003].
- Much like the way in which the TWINS package was developed, inclusion of effects such as lateral vibration and wheel rotation would ultimately be of benefit to the time domain models.

11.6 Concluding remarks

The work contained within this thesis has been of a particular nature that has necessitated direct comparisons with measured data. This has not been an easy process. For example, a large part of the thesis documents the alterations that had to be made to ensure a reasonable agreement between the outputs from existing prediction models and the measurements. Not only have the processes for each of these alterations been shown to be reasonable adjustments, they have greatly improved the understanding of the rig behaviour. A major achievement of this research is that the measurements made on the 1/5 scale rig have now been shown to be consistent with theoretical models, whereas previous research [ORE report C163/RP11, 1988, and ORE report C163/RP16, 1990] failed to find such consistency.

Comparisons of the non-linear time-stepping model [Wu and Thompson 2000(a)] with measurements of vibration due to discontinuities on the railhead surface were generally quite good. The requirement for a reliable two dimensional contact filter, however, was evident from an early stage of the research. Improvement in this area of the prediction process is badly needed.

References

JD Anderson, JR 1991 Fundamentals of aerodynamics (2nd edition) McGraw-Hill.

C Andersson, and T Dahlberg 1998 Wheel/rail impacts at a railway turnout crossing Proceedings of the Institution of Mechanical Engineers 212, part F, 123-134.

FG de Beer, M Janssens, PP Kooijman, and WJ van Vliet 2000 Curve squeal of railbound vehicles (Part 1): Frequency domain calculation model Internoise 2000, 1560-1563.

E Berghaus 1964 The history of railways Barrie and Rockliff, London.

BSI 1964 Specification for octave and one-third octave band-pass filters British Standards Institution BS2475: 1964.

RA Clark, PA Dean, JA Elkins, and SG Newton 1982 An investigation into dynamic effects of railway vehicles running on corrugated track Journal of Mechanical Engineering Science (24), 65-76.

RA Clark, GA Scott, and W Poole 1988 Short wave corrugations an explanation based on slip vibrations Applied Mechanics Rail Transportation Symposium, AMD vol.96, RTD vol. 2 ASME 1988.

AR Crockett, and JR Pyke 2000 Viaduct design for minimisation of direct and structure radiated train noise Journal of Sound and Vibration 231(3), 883-897.

PC Dings, and MG Dittrich 1996 Roughness on Dutch railway wheels and rails Journal of Sound and Vibration 193(1), 103-112.

RC Dorf, and RH Bishop 1995 Modern control systems (7th Edition) Addison Wesley Publishing Company.

S East 1998 The preparation and commissioning of a 1/5 scale test rig for investigation into wheel - rail rolling noise ISVR BEng Final Year Report, University of Southampton.

C Esveld 1989 Modern railway track MRT Productions, Germany.

NS Ferguson 1988 The vibration of rolling discs Ph.D. Thesis, University of Southampton.

R Ford and DJ Thompson 2003 Contact filters in wheel / rail noise prediction ISVR Technical Memorandum 907, University of Southampton.

G de France 1998 Railway track: Effect of rail support stiffness on vibration and noise ISVR MSc Dissertation, University of Southampton.

CO Frederick 1987 A rail corrugation theory Proceedings of the second international symposium on contact mechanics and wear of rail / wheel systems held at Kingston / RI July 1986; Waterloo Ontario: University of Waterloo Press, 181-211.

AG Galaitsis, and EK Bender 1976 Wheel / rail noise part V: Measurement of wheel and rail roughness Journal of Sound and Vibration 46(3), 437-451.

L Gavric 1995 Computation of propagative waves in free rail using a finite element technique Journal of Sound and Vibration 185(3), 531-543.

AC Geerlings, DJ Thompson, and JW Verheij 2001 Model-based acoustic substitution source methods for assessing shielding measures applied to trains Applied Acoustics 62, 878-1000.

J Golten, and A Verwer 1991 Control system design and simulation McGraw-Hill.

SL Grassie, RW Gregory, D Harrison, and KL Johnson 1982 The dynamic response of railway track to high frequency vertical vibration Journal of Mechanical Engineering Science 24(2) 77-90.

SL Grassie, and J Kalousek 1993 Rail corrugation: characteristics, causes and treatments Proceeding of the Institution of Mechanical Engineers 207F, 57-68.

SL Grassie, MJ Saxon, and JD Smith 1999 Measurement of longitudinal rail irregularities and criteria for acceptable grinding Journal of Sound and Vibration 227(5), 949-964.

MA Heckl 1995 Railway noise – can random sleeper spacings help? Acta Acustica 81, 559-564.

MA Heckl 1998 Curve squeal of trains – which wheel modes are prone to squeal? Euro-noise 1998, 85-90.

B Hemsworth 1979 Recent developments in wheel/rail noise research Journal of Sound and Vibration 66, 297-310.

P Holm 1999 Roughness measurement devices Proceedings of the Workshop Roughness Measurements 1999, 17-28.

A Igeland 1997 Dynamic train / track interaction: Simulation of railhead corrugation growth under a moving bogie using mathematical models combined with full-scale measurements Ph.D. Thesis, Chalmers University of Technology.

SD Iwnicki and AH Wickens 1998 Validation of a MATLAB railway vehicle simulation using a scale roller rig Vehicle System Dynamics 30, 257-270.

M Jaecker-Cueppers 2001 Railway noise abatement in the European Union – the working group railway noise of the European Commission Inter-noise 2001 (5), 2699-2704.

A Jaschinski, H Chollet, S Iwnicki, A Wickens, and J Von Wurzen 1999 The application of roller rigs to railway vehicle dynamics Vehicle System Dynamics, 31, (1999), 345-392.

MHA Janssens, and DJ Thompson 1996 A calculation model for the noise from steel railway bridges Journal of Sound and Vibration 193(1), 295-305.

HH Jenkins, JE Stephenson, GA Clayton, GW Morland, and D Lyon 1974 The effect of track vehicle parameters on wheel / rail vertical dynamic forces REJ January 1974, 2-16.

KL Johnson 1985 Contact mechanics Cambridge University Press, Cambridge.

CJC Jones, and DJ Thompson 2000 Rolling noise generated by railway wheels with visco-elastic layers Journal of Sound and Vibration 231(3), 779-790.

JJ Kalker 1979 Survey of wheel – rail rolling contact theory Vehicle System Dynamics 5, 317-358.

WF King 1990 The components of wayside noise generated by high-speed tracked vehicles Inter-noise 1990 (1), 375-378.

LE Kinsler, AR Frey, AB Coppens, and JV Sanders 1982 Fundamentals of acoustics (3rd Edition) John Wiley and Sons.

KL Knothe, Z Strzyzakowski, and K Willner 1994 Rail vibrations in the high frequency range Journal of Sound and Vibration 169(1), 111-123.

JT Nelson 1996 Recent developments in ground-borne noise and vibration control Journal of Sound and Vibration 193(1), 367-376.

JCO Nielsen 1993 Train / track interaction. Coupling of moving and stationary dynamic systems – theoretical and experimental analysis of railway structures

considering wheel and track imperfections Ph.D. Thesis, Chalmers University of Technology.

JCO Nielsen, and A Igeland 1995 Vertical dynamic interaction between train and track-influence of wheel and track imperfections Journal of Sound and Vibration 187(5), 825-839.

SG Newton, and RA Clark 1979 An investigation into dynamic effects on the track of wheel flats on railway vehicles Journal of Mechanical Engineering Science 21, 287-297.

AV Oppenheim and RW Schafer 1975 Digital signal processing Prentice Hall.

ORE Report 1985 Wheel / rail contact noise -
ORE, Question C163 Railway Noise, Report Number 9.

ORE Report 1988 Wheel / rail contact noise – Investigation into the application of a one-eighth scale wheel-rail roughness test rig ORE, Question C163 Railway Noise, Report Number 11.

ORE Report 1990 Wheel / rail contact noise – Further development of a $1/8^{th}$ scale wheel / rail roughness test rig ORE, Question C163 Railway Noise, Report Number 16.

O Palluat de Besset 1998 Study of novel railway wheel designs using a scale model rig ISVR MSc Dissertation, University of Southampton.

W Poole 1986 The measurement of the contact area between opaque objects under static and dynamic rolling conditions Contact mechanics and wear of rail / wheel systems II, Proceedings of the International Symposium, University of Rhode Island, Kingston, RI, 59-71.

Railway Gazette International 2001 White paper charts rail future Railway Gazette International 157(10), 651.

PJ Remington 1976 Wheel / rail noise-part IV: Rolling noise Journal of Sound and Vibration 46(3), 419-436.

PJ Remington 1987 Wheel/rail rolling noise I: theoretical analysis Journal of the Acoustical Society of America 81, 1805-1823.

PJ Remington 1988 Wheel / rail rolling noise: What do we know? What don't we know? Where do we go from here? Journal of Sound and Vibration 120(2), 203-226.

PJ Remington, and J Webb 1996 Wheel / rail noise reduction through profile modification Journal of Sound and Vibration 193(1), 335-348.

B Ripke, and K Hempelmann 1994 Model prediction of track loads and rail corrugation Railway Gazette International, July 1994, 447-450.

MJ Rudd 1976 Wheel / rail noise – Part II: Wheel squeal Journal of Sound and Vibration 46, 381-394.

DJ Thompson 1990 Wheel-rail noise: theoretical modelling of the generation of vibrations Ph.D. Thesis, University of Southampton.

DJ Thompson 1993(a) Wheel-rail noise generation, part I: introduction and interaction model Journal of Sound and Vibration 161, 387-400.

DJ Thompson 1993(b) Wheel-rail noise generation, Part II: Wheel vibration Journal of Sound and Vibration 161, 401-419.

DJ Thompson 1993(c) Wheel-Rail noise generation, part V: Inclusion of wheel rotation Journal of Sound and Vibration 161(3), 467-482.

DJ Thompson 1993(d) Wheel-rail noise generation, part III: Rail vibration Journal of Sound and Vibration 161(3), 421-446.

DJ Thompson 1993(e) Wheel-rail noise generation, part IV: Contact zone and results Journal of Sound and Vibration 161(3), 447-466.

DJ Thompson 1996 On the relationship between wheel and rail surface roughness and rolling noise Journal of Sound and Vibration 193(1), 149-160.

DJ Thompson 1997 Experimental analysis of wave propagation in railway tracks Journal of Sound and Vibration 203(5), 867-888.

DJ Thompson 1999 Non-linear effects at the wheel / rail interface and their influence on noise generation Grant application to Engineering and Physical Sciences Research Council, grant number GR/M82455.

DJ Thompson 2003 The influence of the contact zone on the excitation of wheel / rail noise Journal of Sound and Vibration 267, 523-535.

DJ Thompson, AR Briscoe, and CJC Jones 2000 Measurements of material properties of various visco-elastic materials, Part 2: Moduli for additional materials and temperature dependence ISVR Contract report No 00/06, University of Southampton.

DJ Thompson, B Hemsworth, and N Vincent 1996 Experimental validation of the TWINS prediction program for rolling noise, Part 1: Description of the model and method Journal of Sound and Vibration 193(1), 123-135.

DJ Thompson, and MHA Janssens 1997 Track-wheel interaction noise software theoretical manual (version 2.4) TNO-report, TPD-HAG-RPT-93-0214, revised.

DJ Thompson, and CJC Jones 2000 A review of the modelling of wheel/rail noise generation Journal of Sound and Vibration 231(3), 519-536.

DJ Thompson, and CJC Jones 2002 Sound radiation from a vibrating railway wheel Journal of Sound and Vibration 253(2), 401-419.

DJ Thompson, and N Vincent 1995 Track dynamic behaviour at high frequencies. Part 1: Theoretical models and laboratory measurements Vehicle System Dynamics Supplement 24, 86-99.

TX Wu, and DJ Thompson 1999(a) A double Timoshenko beam model for vertical vibration analysis of railway tracks at high frequencies Journal of Sound and Vibration 224, 329-348.

TX Wu, and DJ Thompson 1999(b) Analysis of lateral vibration behaviour of railway track at high frequencies using a continuously supported multiple beam model Journal of the Acoustical Society of America 106(3), 1369-1376.

TX Wu, and DJ Thompson 1999(c) The effects of local pre-load on the foundation stiffness and vertical vibration of railway track Journal of Sound and Vibration 219, 881-904.

TX Wu, and DJ Thompson 2000(a) Theoretical investigation of wheel/rail non-linear interaction due to roughness excitation Vehicle System Dynamics 34 (2000), 261-282.

TX Wu, and DJ Thompson 2000(b) The influence of random sleeper spacing and ballast stiffness on the vibration behaviour of railway track Acta Acustica 86 (2000), 313-321.

TX Wu, and DJ Thompson 2001(a) Vibration analysis of railway track with multiple wheels on the rail Journal of Sound and Vibration 239(1), 69-97.

TX Wu, and DJ Thompson 2001(b) On impact noise generation due to a wheel passing over rail joints ISVR Technical Memorandum number 863.

TX Wu, and DJ Thompson 2002 A hybrid model for noise generation due to railway wheel flats Journal of Sound and Vibration 251(1), 115-139.

IL Ver, CS Ventres, and MM Myles 1976 Wheel / rail noise-part III: Impact noise generation by wheel and rail discontinuities Journal of Sound and Vibration 46(3), 395-417.

JG Walker, NS Ferguson, and MG Smith 1996 An investigation of noise from trains on bridges Journal of Sound and Vibration 193(1), 307-314.

Appendix A

Derivation of the frequency domain model (equations (2-1) and (2-2)) is given in this appendix for vertical vibration based on a more general derivation of wheel / rail contact presented by [Thompson, 1993(a)].

Provided that the wheel and rail remain in contact the relative displacement of each part can be found by considering the free body diagram shown in Figure A1. Here a positive deflection is defined to be in a downwards direction. The contact between the wheel and the rail is modelled as a spring which is divided into two parts that describe the local deformations of the two bodies. A combined surface roughness (r) of the wheel and the rail is assumed to act between the wheel and the rail causing deflections in the contact springs (x_{cw} , x_{cr}) which result in deflections of the wheel (x_w) and the rail (x_r). The force (f) that is produced by the surface roughness input (r) acts upward on the wheel and downward on the rail.

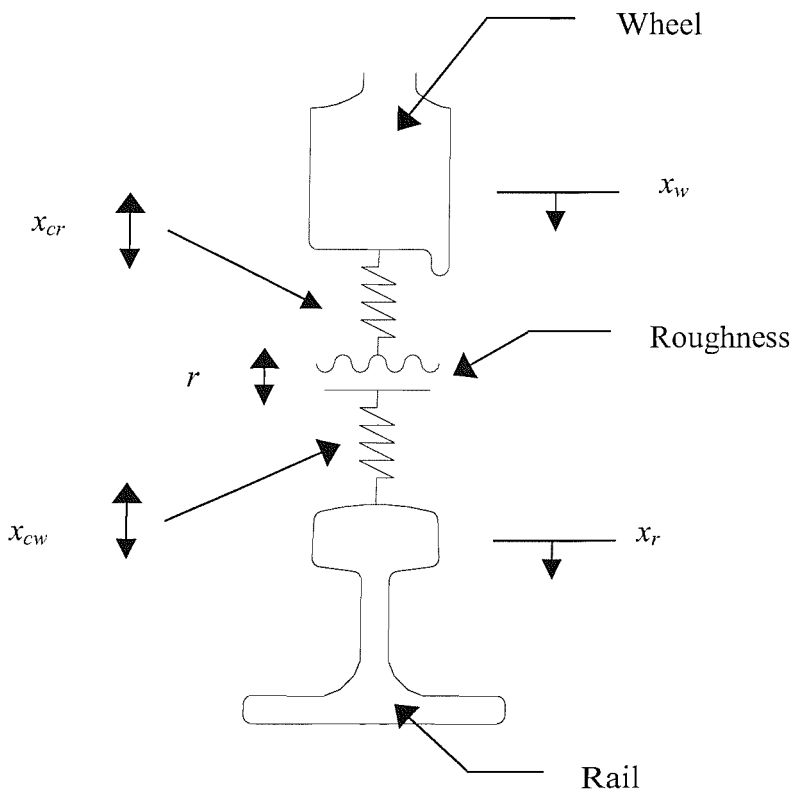

Figure A1 Relative displacements between wheel and rail

Thus by considering the relative displacements in Figure A1 the (vertical) deflection of the rail in the time domain is:

$$x_r = x_w - x_{cw} - x_{cr} + r \tag{A-1}$$

As it is assumed that the wheel and the rail remain in contact (i.e. a linear contact relationship is assumed), each part of the model in Figure A1 can also be expressed in the frequency domain. The frequency domain version of equation (A-1) is therefore:

$$X_r = X_w - X_{cw} - X_{cr} + R \tag{A-2}$$

Capital letters are used to denote the complex amplitudes of the corresponding quantities at frequency ω.

Provided that a linear contact relationship exists, each part of the model (the wheel, rail, and contact springs) can be expressed as receptances. This is shown in the following equations:

$$X_r = \alpha_r F \tag{A-3a}$$

$$X_w = -\alpha_w F \tag{A-3b}$$

$$X_{cw} = \alpha_{cw} F \tag{A-3c}$$

$$X_{cr} = \alpha_{cr} F \tag{A-3d}$$

Substitution of equations (A-3) into equation (A-2) produces:

$$R = (\alpha_r + \alpha_{cr} + \alpha_{cw} + \alpha_w) F \tag{A-4}$$

The receptances of the contact springs can be described by a single receptance (α_c) which is defined as:

$$\alpha_c = \alpha_{cr} + \alpha_{cw} \tag{A-5}$$

Equations (A-4) and (A-5) can be combined to provide a relationship for the contact force amplitude:

$$F = \frac{1}{\alpha_r + \alpha_c + \alpha_w} R \tag{A-6}$$

Substitution of equation (A-6) into (A-3a) produces the rail displacement amplitude (similar to equation (2-1)):

$$X_r = \frac{\alpha_r}{\alpha_r + \alpha_c + \alpha_w} R \tag{A-7}$$

Finally, substitution of equation (A-6) into (A-3b) produces the wheel displacement amplitude (similar to equation (2-2)):

$$X_w = \frac{-\alpha_w}{\alpha_r + \alpha_c + \alpha_w} R \tag{A-8}$$

Appendix B

Alternative method of predicting vibration based on FIR filters

An alternative method is introduced here for determining the rail or wheel vibration. This method was developed towards the end of the project and is not included within the previous chapters as it essentially reproduces the predictions of the linear time-stepping model. It is a result of the investigations of the behaviour of wheel / rail interaction as though it were a transfer function (see Chapter 5). Whilst, at present, this model is just an alternative way of reproducing the same results, the way in which the results are obtained could hopefully be adapted to allow for time varying quantities during the prediction. The greatest advantage of this method is that it is much quicker than the existing methods as the wheel / rail contact model is converted into a FIR filter.

As an example, the alternative method of predicting wheel / rail vibration is demonstrated for the prediction of rail vibration. Chapter 5 presents analysis of the transfer functions formed from the frequency response of both measurements and assumed parts of the wheel / rail contact model. This helped to show how the wheel, rail, and contact spring interact to form a transfer function between the roughness input and vibration output. For a linear contact spring relationship, the simple variant 'rail' transfer function (U_r / R) was found to be similar to both the modal wheel variant and the measured FRF variant. Further developments within Chapter 5 show the behaviour of the simple variant transfer function (U_r / R) in the form of its poles and zeros. This is described by equations (5-8). By converting the transfer function into its poles and zeros, it is possible (as for the approximate contact filter) to convert the wheel / rail interaction model for a fixed contact stiffness into a pole and zero representation in the z-plane (using equation (5-17)). This means that a time-domain surface roughness input can be filtered with both the modulus and phase of the simple variant thus forming a time-domain prediction of the displacement of the rail. An example of this is given below for the surface roughness input (results of which are presented in Chapter 6) for a wheel pre-load of 528N at a 1.3m/s wheel speed. But first, an example of the formation of the difference equations for the FIR filter at a specific wheel pre-load is presented. In order to do this, the following method is adopted:

1. Estimate the Hertzian contact stiffness that applies to the wheel pre-load (equation (2-10)).

2. Convert the Hertzian contact stiffness into an estimate of the contact spring receptance using equation (5-2a).
3. Use this constant value together with the values from the curve fitted track model, and the mass of the wheel, to form the s-plane version of transfer function U_r / R as shown in equation (5-8).
4. Map the s-plane representation of the transfer function U_r / R into the z-plane with the Bilinear transform (equation (5-17)).

Table B1 shows the variables used for the s-plane and z-plane representation of the simple model transfer function with a contact receptance associated with a 528N wheel pre-load. To demonstrate that the formation of the difference equation filter works as intended, a random (white noise) signal was constructed in MATLAB and then filtered using the MATLAB function FILTER with the (z-plane) coefficients presented in Table B1. If the PSD of the filtered output is divided by the PSD of the random input, the square of the frequency response of the filter transfer function is obtained. This is shown in Figure B1 where it is seen to be the same as the s-plane frequency response formed from receptances of each part of the interaction model.

The result in Figure B1 demonstrates that the difference equation filter is working correctly. The filter was then used to predict the rail displacement, previously predicted in Chapter 6 by the (simple variant) non-linear time-stepping model. As the contact receptance corresponds with the average value of the predicted contact force (or the wheel pre-load) this prediction replicates a linear time stepping result. The time domain outputs from both the linear time-stepping model and that from the filter are shown in Figure B2. An additional comparison of these results made in the frequency domain is shown in Figure B3. This demonstrates that the FIR filter representation for a fixed contact force replicates the previous rail vibration prediction in Chapter 6.

It is interesting to note, however, that if the FIR filter (version of equation (5-8)) were allowed to vary as a function of time according to a two dimensional contact prediction such as [Ford and Thompson, 2003] then a form of 'adaptive' filter could be produced. This could allow for non-linear contact and possibly provide a more efficient method of predicting the non-linear wheel / rail interaction than by using the existing time-stepping model.

Further possible advantages could be that other elements of the model such as the track transfer function could be permitted to vary with time. For example, the variations of frequency response along a track with a step joint could be incorporated.

Table B1 Filter coefficients for simple variant transfer function U_r/R with a 528N wheel pre-load.

s-plane Numerator		s-plane Denominator	
a_1	2.4×10^{5}	b_1	15
a_2	8.3×10^{9}	b_2	3.8×10^{5}
a_3	4.6×10^{13}	b_3	1.3×10^{10}
a_4	2.9×10^{17}	b_4	5×10^{13}
a_5	0	b_5	3.5×10^{17}
a_6	0	b_6	2.3×10^{19}
		b_7	3.4×10^{22}
z-plane Numerator		z-plane Denominator	
a_1	0.1343	b_1	1
a_2	-0.4707	b_2	-5.4649
a_3	0.4784	b_3	12.5362
a_4	0.1208	b_4	-15.4811
a_5	-0.5391	b_5	10.8763
a_6	0.3499	b_6	-4.1297
a_7	-0.0736	b_7	0.6632

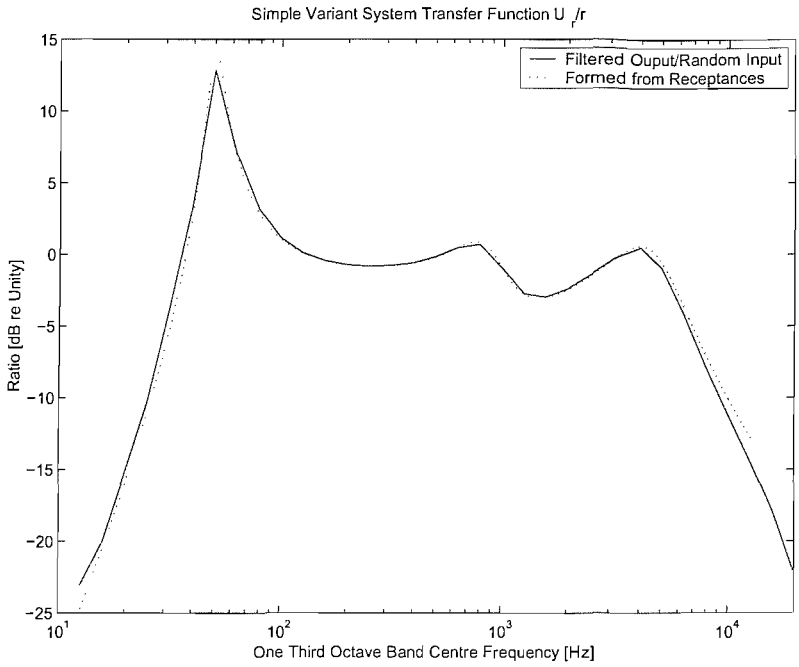

Figure B1 Transfer function U_r/r formed from a PSD of a filtered output divided by the PSD of a random signal input. This is compared with the transfer function U_r/r formed from receptances of the simple model.

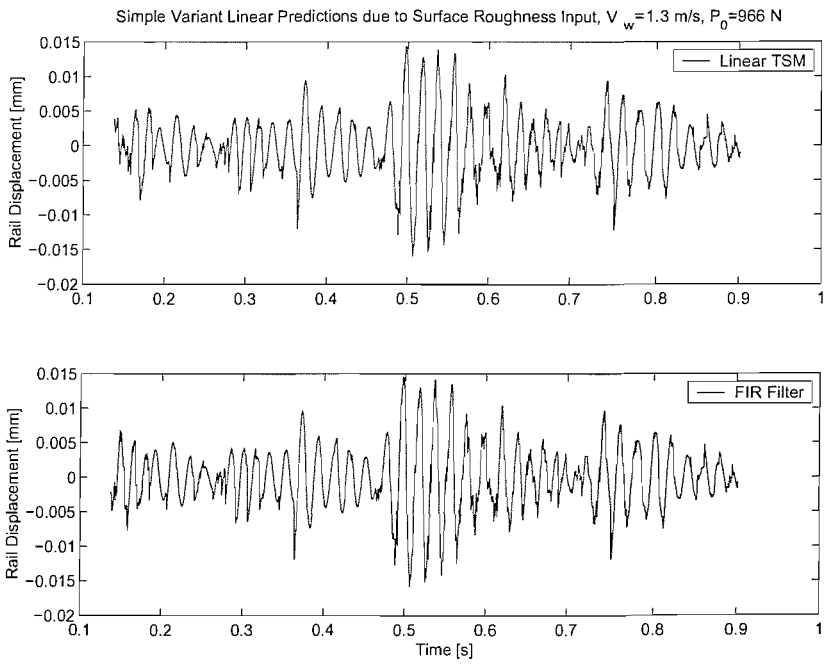

Figure B2 Example of the linear time-stepping model rail displacement (where starting transients have been omitted because of the linear time-stepping model) compared with the output of the simple model filter version for a wheel speed of 1.3m/s at a 966N wheel pre-load.

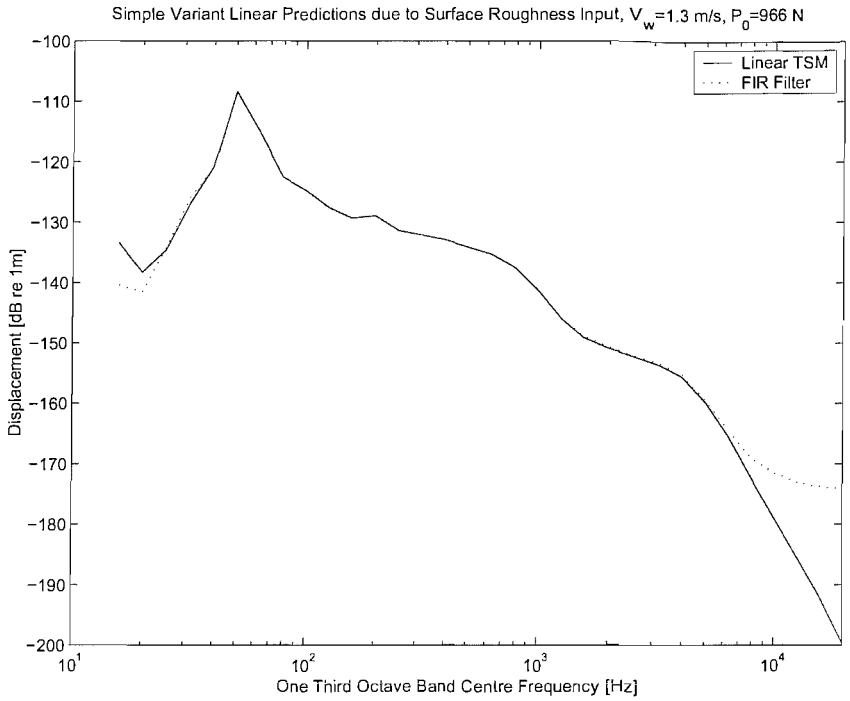

Figure B3 Spectra of the non-linear time-stepping model rail displacement and the output of the simple model FIR version results shown in Figure B2 above.